Mise en évidence du potentiel biomédical de nouveaux nanovecteurs

Morgane Daurat

THÈSE POUR OBTENIR LE GRADE DE DOCTEUR DE L'UNIVERSITÉ DE MONTPELLIER

En Biologie Santé

École doctorale
Sciences Chimiques et Biologiques pour la Santé

Unité de recherche
Institut des Biomolécules Max Mousseron UMR 5247

Mise en évidence du potentiel biomédical de nouveaux nanovecteurs

Présentée par Morgane DAURAT
Le 30 octobre 2019

Sous la direction de Magali GARY-BOBO

Devant le jury composé de

M. Jochen Rössler, Professeur en médecine, Centre médical universitaire (Berne, Suisse)	Président du jury
M. Vincent Sol, Professeur, LCSN (Limoges, France)	Rapporteur
M. Olivier Siri, Directeur de Recherche, UMR CNRS 6521 (Marseille, France)	Rapporteur
Mme. Virginie Lafont, Chargé de Recherche, IRCM (Montpellier, France)	Examinateur
M. Marcel Garcia, Directeur Général, NanoMedSyn (Montpellier, France)	Membre invité
Mme. Marie Maynadier, Chargé de Recherche, NanoMedSyn (Montpellier, France)	Co-encadrante
Mme. Magali Gary-Bobo, Chargé de Recherche, UMR CNRS 5247 IBMM (Montpellier, France)	Directrice de Thèse

UNIVERSITÉ DE MONTPELLIER

Remerciements

Je tiens tout d'abord à remercier le Professeur Vincent Sol et le Docteur Olivier Siri d'avoir accepté de juger ce travail en tant que rapporteur. Je tiens également à remercier le Professeur Jochen Rössler et le Docteur Virginie Lafont qui me font l'honneur d'être membres de mon jury.

Je remercie également les membres du jury du comité de thèse, le docteur Jean-Olivier Durand, le Docteur Frédérique Cunin, le Professeur Joël Chopineau et le Docteur Martine Cérutti. Merci pour vos conseils qui ont permis de faire avancer le projet.

Je tiens à remercier Monsieur Henry-Vincent Charbonné pour m'avoir permis de rejoindre NanoMedSyn et sa fabuleuse équipe.

Avant tout, je remercie tous les membres de l'équipe « Glyco et nanovecteurs pour le ciblage thérapeutique », de NanoMedSyn ainsi que les collaborateurs qui ont participés de près ou de loin à cette thèse.

J'attache une importance particulière à exprimer mes remerciements et ma profonde estime à ma directrice de thèse, Magali, qui a été la chef-chef idéale. Merci de m'avoir fait confiance et de m'avoir donné l'opportunité de faire cette thèse. C'était un réel plaisir de travailler avec toi : toujours de bonne humeur, à l'écoute et de très bons conseils. Cette thèse n'aurait pas pu aboutir sans toi, alors merci pour tout. Merci d'avoir toujours été de mon côté quand la pression montait. Je retiendrai beaucoup de choses de ces quatre années passées au laboratoire, que des bons moments mais ton imitation parfaite d'un animal si mignon me marquera à vie…

Je tiens également à remercier sincèrement ma co-encadrante de thèse, Marie, qui a été une co-chef-chef géniale. Toujours de bons conseils tant professionnels que personnels accompagnés de jeux de mots hilarants ! Merci pour ton soutien dans les moments de pression. Merci également pour toutes ces séances de sport…ta merveilleuse coordination m'aura permis quelques exercices d'abdos supplémentaires.

A présent, je souhaite vivement remercier Marcel, à vos côtés j'ai beaucoup appris, merci pour toutes ces conversations scientifiques qui ont permis de faire avancer le projet. Travailler avec vous a été une vraie chance. Je profite de ces remerciements pour me lancer et TE dire merci pour m'avoir donné l'opportunité de faire ma thèse dans cette superbe équipe. Je tenais également à vous remercier Marie et toi de me donner la chance de travailler à NanoMedSyn, je suis enchantée de continuer l'aventure avec vous.

A Laure, tu es pour moi bien plus qu'une collègue, tu as été présente dans tous les moments de la thèse, ça a été émotionnellement les montagnes russes mais tu as su me faire rester sur les rails. Tu m'as accompagnée et surtout supportée pour mon congrès à Londres, tu as su gérer mon stress à merveille et en plus tu as été une guide au top. Je ne pourrai jamais assez te remercier pour tout ce que tu as fait pour moi. Alors tout simplement merci et surtout n'oublies pas le plus important : Hakuna Matata !

A Ilaria, pour tes conseils, ta bienveillance et ta bonne humeur. Et ne t'en fais pas mes kilos en trop voudraient te dire qu'ils ne t'en veulent pas pour tous ces gâteaux délicieux !

A Christophe, le nouveau petit thésard, le petit nouveau en biologie…blague à part, ce fut un réel plaisir de travailler à tes côtés Mr Pointilleux, Grincheux, Gigi la grincheuse…merci pour ta bienveillance, ta bonne humeur et le travail que tu as réalisé avec Sofia. Grâce à vous j'ai pu faire la manip' du siècle. Malgré tout, l'enfer t'attend toujours ! En parlant de manip' du siècle, je souhaite également remercier ton chouchou préféré Denis, merci pour ta bonne humeur. Par contre on attend toujours ton Banofee…

A Lamiaa, travailler avec toi était un plaisir, nous avons passé des heures et des heures dans le froid de la salle de microscopie, mais grâce à ta gentillesse et ton humour, ces heures sont passées très vite ! Merci pour tous tes conseils, ton soutien et ta bonne humeur, tu es un vrai rayon de soleil ! A présent, je souhaite remercier Nabila et bien entendu ses nabilades. Tu m'auras bien fait rire, écrire mon manuscrit à tes côtés a été un vrai plaisir, toujours un petit mot pour détendre l'atmosphère. Je te souhaite bonne chance pour la fin de ta thèse, ne t'inquiètes pas tu vas assurer ! Je souhaite également remercier Nadir, merci pour tes conseils. Je remercie également Anastasia pour tout le travail que nous avons accomplis.

Je souhaite à présent remercier, Corentin, Marine et Marianne, vous avez été présents plus ou moins longtemps au laboratoire durant ma thèse, mais vous avez tous apporté quelque chose. Merci pour votre bonne humeur !

Aux chimistes de l'équipe, Khaled et Alain. Merci pour tous vos conseils, vous avez toujours pris le temps de répondre à mes questions de biologiste, j'ai presque compris la chimie grâce à vous. Je souhaite également bonne chance à Geoffrey pour la suite de sa thèse : force et honneur !

Un grand merci aux équipes de chimistes de Jean-Olivier Durand, Peter Hesemann, Yannick Guari et plus particulièrement à Sofia et Ekaterina. Merci d'avoir pris le temps de me montrer et m'expliquer la chimie.

Cette thèse n'aurait pas été la même sans le soutien infaillible de ma famille et mes amis. Tout d'abord, je n'en serai pas arrivée jusqu'ici sans le soutien de mes parents. Papa, maman, vous avez toujours cru en moi et vous m'avez toujours suivi dans mes choix. Vous avez été à l'écoute, de très bons conseils et toujours présents. Je suis fière d'être devenue la personne que je suis aujourd'hui, grâce à vous.

Mon petit frère, ta gentillesse et ta générosité font de toi un frère en or, merci pour tous tes bons petits plats, tu es un cuisiner hors pair, continues comme ça je suis fière de toi.

A mes grands-parents paternel et maternel. Vous avez été des papis et mamies en or. Je souhaite cependant remercier tout particulièrement mon Pépé. Merci de m'avoir donné le tuyau pour le stage de master 2 avec Magali car grâce à toi j'ai rencontré des gens formidables et un cadre de travail idéal.

A présent, je souhaite remercier ma Marraine, ma deuxième maman ainsi que mes cousins Floriane, Yoan et leurs pièces rapportées Mikael et Virginie. Merci pour tout ce que vous avez fait pour moi et d'être toujours présents. J'ai une pensée toute particulière pour ma cousine Manon, la vie nous demande tous les jours de nous battre, tu es pour moi un exemple de force et de courage. Malgré les coups durs, tu as été là, tu as cru en moi et n'a jamais douté que j'y arriverai. Je serai toujours là derrière toi pour te soutenir : « Toujours se relever, toujours recommencer, interdit d'abandonner ♪ ».

A mon parrain Gilles, ma tatie Maryline, mon tonton Philippe, ma tatie Evelyne et mes cousins Lily, Zoé, Kévin et Océane. Merci pour tout, merci d'être toujours présents. J'ai une attention particulière pour Zoé, je suis fière d'être la marraine d'une si belle et intelligente jeune fille.
A Virginie, ma tatie de cœur, depuis que je suis petite tu as toujours su que j'irai loin, merci d'avoir été présente dans les bons comme dans les mauvais moments. Je remercie également tous les amis de mes parents qui sont pour moi ma deuxième famille.

A ma belle-famille, merci pour tous ces moments partagés.

Enfin je remercie mes amis. Chacun à votre manière vous avez été présents pour moi. Cependant, je ne peux pas écrire ces remerciements sans citer mes meilleures amies, mes cramées Gréta et Cécile, votre soutien ne date pas d'hier, on se connait depuis tellement d'années, je ne dirai pas combien exactement, ça nous vieillirait trop. Merci pour tout, merci d'être vous, même si on est aujourd'hui à des kilomètres les unes des autres, vous êtes toujours présentes pour moi car la vraie amitié ce n'est pas d'être inséparable, c'est d'être séparé et que rien ne change. Vous avez toujours su que votre petit Newton y arriverait, alors merci d'avoir cru en moi.

Hélène, ma poulette, on se connait depuis moins longtemps mais ton amitié m'est précieuse. Tu vis à cent à l'heure mais je sais que tu n'es jamais loin. Merci pour tout !

Au noyau dur de la Fafa, Candice, Hélène et Manon. J'ai passé les meilleures années étudiantes à vos côtés. La coloc aura laissé des traces mais une belle amitié est née. Merci d'être vous, merci pour tous ces moments : les nombreux karaokés, les séances Harry Potter, les week-end aux quatre coins de la France.

A Sophie, nous nous sommes rencontrées sur les bancs de la fac de Médecine. Plus précisément dans la salle bleue où nous avons passé des heures et des heures à réviser. Tu as été et tu es toujours d'un soutien sans faille. Je n'oublierai jamais nos jeudis de folie, nos purée-jambon blanc en rentrant de soirée…et encore tant de choses que je ne peux pas citer ici. Merci d'avoir été là pendant toutes ces années.

A Dina, Jeff et Leïla nous nous sommes rencontrés au laboratoire mais vous êtes devenus rapidement des amis. Qu'on se le dise ces trois années de thèse n'ont pas été de tout repos mais vous avez toujours su trouver les mots pour me remotiver. Toujours présents pour me changer les idées. Dina et Jeff, vous m'abandonnez pour vivre de nouvelles aventures marseillaises mais attention vous n'allez pas vous débarrasser de moi comme ça, dommage, je suis sûre que vous espériez ça (surtout toi Jeff…). Je ne manquerai pas d'apporter mon sombrero pour une nouvelle tournée ! Je vous souhaite de vous épanouir dans votre vie professionnelle et personnelle car vous le méritez. Vous êtes de belles personnes ! Quant à toi Leïla, la force tranquille du groupe, merci d'être toi tout simplement. Tu es toujours de très bons conseils. Merci de m'avoir accompagnée en Thaïlande, ce voyage n'aurait pas été le même sans toi, j'attends le prochain avec impatience !

Aux animateurs, nous avons vécu de belles années au centre aéré Les Sablières. Vous apportez tous quelque chose de différent et c'est ça qui fait la force du groupe. Même si on ne se voit pas régulièrement, je tenais à vous dire merci pour toutes ces années de bonheur, en espérant qu'il y en ait encore beaucoup d'autres.

Aux garçons, Boubou, Franck, Arnaud, Mimi, Loïc, Erwan, Adrien, Sacha, Momo et toute la bande, vous m'avez petit à petit intégré dans votre groupe. Merci d'être vous, merci pour ces folles soirées qui m'ont permis de décompresser pendant ces trois années de thèse. En espérant qu'il y en ait encore, je compte bien fêter les 20, 30 … ans d'amitié avec vous !

Je finirai ces remerciements par toi, Victor, car tu es la personne la plus importante dans ma vie. Tu es près de moi depuis maintenant huit ans et tu as su me soutenir comme personne pendant ces trois années de thèse. Quand je te raconte mes soucis, tu me remontes le moral, quand je suis triste tu me réconfortes, quand je doute tu me pousses à aller de l'avant. Pour toutes ces choses je te remercie, merci d'être toi, merci pour ton soutien. Je t'aime.

Résumé

Le développement de thérapies ciblées est un enjeu majeur en santé et l'essor des nanovecteurs permet de répondre à ces besoins cliniques. Le premier axe de cette thèse est consacré à l'étude du potentiel thérapeutique de nanoparticules multifonctionnelles pour l'imagerie médicale, la thérapie photothermique et la délivrance de drogue pour le traitement du cancer. Le deuxième axe de recherche s'oriente vers le ciblage thérapeutique actif. L'entreprise NanoMedSyn a pour objectif de développer un ciblage actif du récepteur du mannose 6-phosphate, permettant un meilleur adressage des médicaments et des traitements plus efficaces. Ce type de ciblage peut avoir des retombées multiples pour la thérapie anticancéreuse mais également pour la thérapie des maladies lysosomales qui sont des maladies génétiques rares. NanoMedSyn développedes dérivés synthétiques de glycovecteurs innovants, appelés AMFA, qu'elle exploite en exclusivité. Les AMFA ont une bonne affinité pour le récepteur du mannose 6-phosphate et ont été greffés sur des nanoparticules multifonctionnelles dans le but d'améliorer l'adressage et la thérapie photodynamique biphotonique d'un cancer pédiatrique : le rhabdomyosarcome ; et sur des enzymes lysosomales pour le traitement de maladies lysosomales telle que la maladie de Pompe.

Mots-clés : Cancer, ciblage thérapeutique, nanomédecine, maladies lysosomales

Abstract

The development of targeted therapies is a major health issue and the rise of nanovectors makes it possible to meet these clinical needs. The first approach of this thesis is dedicated to the study of the therapeutic potential of multifunctional nanoparticles for medical imaging, photothermal therapy and drug delivery in cancer treatment. The second line of research focuses on active therapeutic targeting. The NanoMedSyn company aims to develop an active targeting of the mannose 6-phosphate receptor, allowing a better addressing of drugs and more effective treatments. This type of targeting may have multiple benefits for cancer therapy but also for the treatment of the lysosomal diseases which are rare genetic diseases. NanoMedSyn develops innovative synthetic derivatives of glycovectors, called AMFA, which it exploits exclusively. AMFA have a good affinity for the mannose 6-phosphate receptor and have been grafted on multifunctional nanoparticles in order to improve addressing and two-photon photodynamic therapy of a pediatric cancer: the rhabdomyosarcoma; and on lysosomal enzymes for the lysosomal diseases treatment such as for Pompe disease.

Keywords: Cancer, therapeutic targeting, nanomedicine, lysosomal diseases

Sommaire

Avant-propos

Avant de commencer cette thèse, j'ai effectué un Master Sciences du Médicament (option Aging et Stratégies Anti-Age) à la Faculté de Pharmacie de Montpellier. Ce master m'a permis de réaliser un stage dans l'équipe « Glyco et nanovecteurs pour le ciblage thérapeutique », sous la direction du Dr Magali Gary-Bobo. Au cours de ce stage, je me suis spécialisée dans le domaine de la recherche appliquée et plus particulièrement l'utilisation de nanoparticules pour des applications biomédicales comme l'imagerie, le ciblage de cellules ou tissus malades et la thérapie. Une collaboration avec l'équipe du Dr Peter Hesemann m'a permis de faire une étude pour décrire l'efficacité biologique de nanoparticules ioniques, synthétisées pour le traitement de maladies inflammatoires[1]. En effet, en tant que biologiste, j'ai travaillé plus particulièrement sur l'étude du potentiel thérapeutique de nanoparticules multifonctionnelles. Au cours de cette thèse, j'ai étudié l'efficacité de nanoparticules anti-cancéreuses. Aujourd'hui le ciblage thérapeutique constitue un challenge majeur pour améliorer l'efficacité des traitements de nombreuses pathologies. C'est dans cette optique que s'inscrit l'ensemble des activités de l'équipe « Glyco et nanovecteurs pour le ciblage thérapeutique » de l'Institut des Biomolécules Max Mousseron de Montpellier, qui est une équipe pluridisciplinaire intégrant des chimistes, des biologistes et des cliniciens. Le travail en collaboration avec les cliniciens est primordial pour axer les recherches vers les besoins cliniques les plus urgents. L'activité de l'équipe concerne le développement de glyconanovecteurs pour le ciblage thérapeutique des maladies lysosomales et de certains cancers. Les résultats issus de cette recherche académique ont fait l'objet d'un transfert de technologie vers le domaine industriel et l'entreprise NanoMedSyn a été créée en 2012. L'activité de l'entreprise est basée sur l'exploitation d'un brevet déposé par l'équipe sur des analogues du mannose 6-phosphate fonctionnalisés sur l'aglycone, appelés AMFA, qui ciblent efficacement le récepteur du mannose 6-phosphate dont la fonction principale est l'adressage des enzymes lysosomales aux lysosomes. L'objectif de NanoMedSyn est de valoriser la technologie AMFA pour le traitement des maladies lysosomales ainsi que pour le traitement de certains cancers.

C'est dans ce contexte que s'inscrit cette thèse qui s'effectue dans le cadre d'une bourse CIFRE mettant en jeu un contrat de collaboration entre l'équipe « Glyco et nanovecteurs pour le ciblage thérapeutique » et l'entreprise NanoMedSyn. Les travaux de thèse portent sur l'étude du

potentiel thérapeutique de nanoparticules multifonctionnelles synthétisées par des équipes de chimistes avec qui nous collaborons étroitement. De plus, j'ai étudié le ciblage thérapeutique par la technologie AMFA pour le traitement du rhabdomyosarcome qui est un cancer rare et la maladie de Pompe qui est une maladie lysosomale. Ces trois années m'ont permis d'être co-auteur de plusieurs articles scientifiques dont certains sont discutés au travers de ce manuscrit.

Chapitre 1 : Le cancer

1. Cancer : épidémiologie et définition

Selon l'Organisation Mondiale de la Santé (OMS), le cancer est un « terme général appliqué à un grand groupe de maladies qui peuvent toucher n'importe quelle partie de l'organisme. L'une de ses caractéristiques est la prolifération rapide de cellules anormales qui peuvent essaimer dans d'autres organes, formant ainsi les métastases »[2]. En 2018, le cancer touchait 18,1 millions de personnes dans le monde et était responsable de 9,6 millions de décès[3]. Les experts estiment que ces chiffres ne pourront qu'augmenter pour atteindre 26,4 millions de nouveaux cas et 17 millions de décès par an d'ici 2030[4]. Ceci est dû à trois facteurs principaux :

- l'augmentation de la population mondiale,
- le vieillissement de la population,
- la dégradation des modes de vies.

On estimait, en 2018 en France, 382 000 nouveaux cas et 157 400 décès. Les cancers les plus répandus chez les hommes sont les cancers de la prostate, des poumons et colorectaux tandis que chez les femmes ce sont les cancers du sein, colorectaux et des poumons[5]. Ces chiffres démontrent bien que la lutte contre le cancer représente un défi majeur de santé publique.

On compte actuellement plus de 200 types de cancers différents que l'on peut répartir en quatre grands types histologiques, en fonction de la nature du tissu dans lequel ils se développent. Ainsi on distingue :

- Les carcinomes qui apparaissent dans un épithélium (cancers du sein, des poumons, de la prostate, etc.).
- Les sarcomes qui sont issus des cellules des tissus conjonctifs comme les os, le tissu adipeux ou les muscles.
- Les cancers hématopoïétiques qui sont des cancers du sang (leucémie) ou des organes lymphoïdes (lymphome).
- Les cancers neuroectodermiques qui se développement à partir de cellules nerveuses.

Il existe une autre manière de répartir les cancers qui opposent les cancers solides (carcinomes et sarcomes) et les cancers « liquides » ou sanguins. Les cancers solides représentent 90 % des cancers humains.

Le développement du cancer se fait généralement en trois étapes[6] : l'initiation, la prolifération (ou promotion) et la progression. L'oncogenèse est initiée lorsqu'une cellule normale subit des mutations génétiques qui échappent aux mécanismes de contrôle de la cellule et qui au cours des divisions successives s'accumulent. Ces mutations peuvent être dues à un facteur génétique héréditaire ou à l'exposition à un facteur de risque (rayonnements ionisants, composés du tabac, alcool, facteurs environnementaux tels que la pollution, etc.) La transformation d'une cellule normale en cellule cancéreuse est un processus long qui apparaît après l'accumulation des mutations génétiques. Ces mutations génétiques peuvent entraîner une surexpression d'oncogènes ou la perte de gènes suppresseurs de tumeurs conduisant à une dérégulation des voies de signalisation intracellulaire. Par conséquent, la cellule ne répond plus à la régulation normale du cycle cellulaire et va alors proliférer très rapidement, de manière incontrôlée et autonome dans l'organisme. A ce stade, les cellules ont acquis les caractéristiques d'une cellule cancéreuse : leur croissance est augmentée et elles ont la capacité d'échapper au programme d'apoptose ; on parle alors de dysplasie puis de carcinome *in situ* lorsque les cellules ont un phénotype très anormal mais n'ont pas encore envahi les tissus voisins. Ces états sont considérés comme des tumeurs bénignes ou précancéreuses dans le cas du carcinome *in situ*. Lorsque la tumeur bénigne atteint une taille de 1 à 2 mm^3, les cellules cancéreuses sécrètent des facteurs angiogéniques tels que VEGF qui entraînent la prolifération des cellules endothéliales pour former de nouveaux vaisseaux sanguins[7]. Cette néoangiogenèse est indispensable à la progression de la tumeur car les vaisseaux sanguins vont apporter l'oxygène et les nutriments nécessaires à sa croissance. Ce phénomène est l'élément clé permettant aux cellules précancéreuses de développer un cancer invasif et de former des métastases (Figure 1). Cependant, ce développement des néo-vaisseaux sanguins est mal régulé et donne naissance à un réseau vasculaire tumoral désorganisé présentant une perméabilité plus grande que le réseau vasculaire normal.

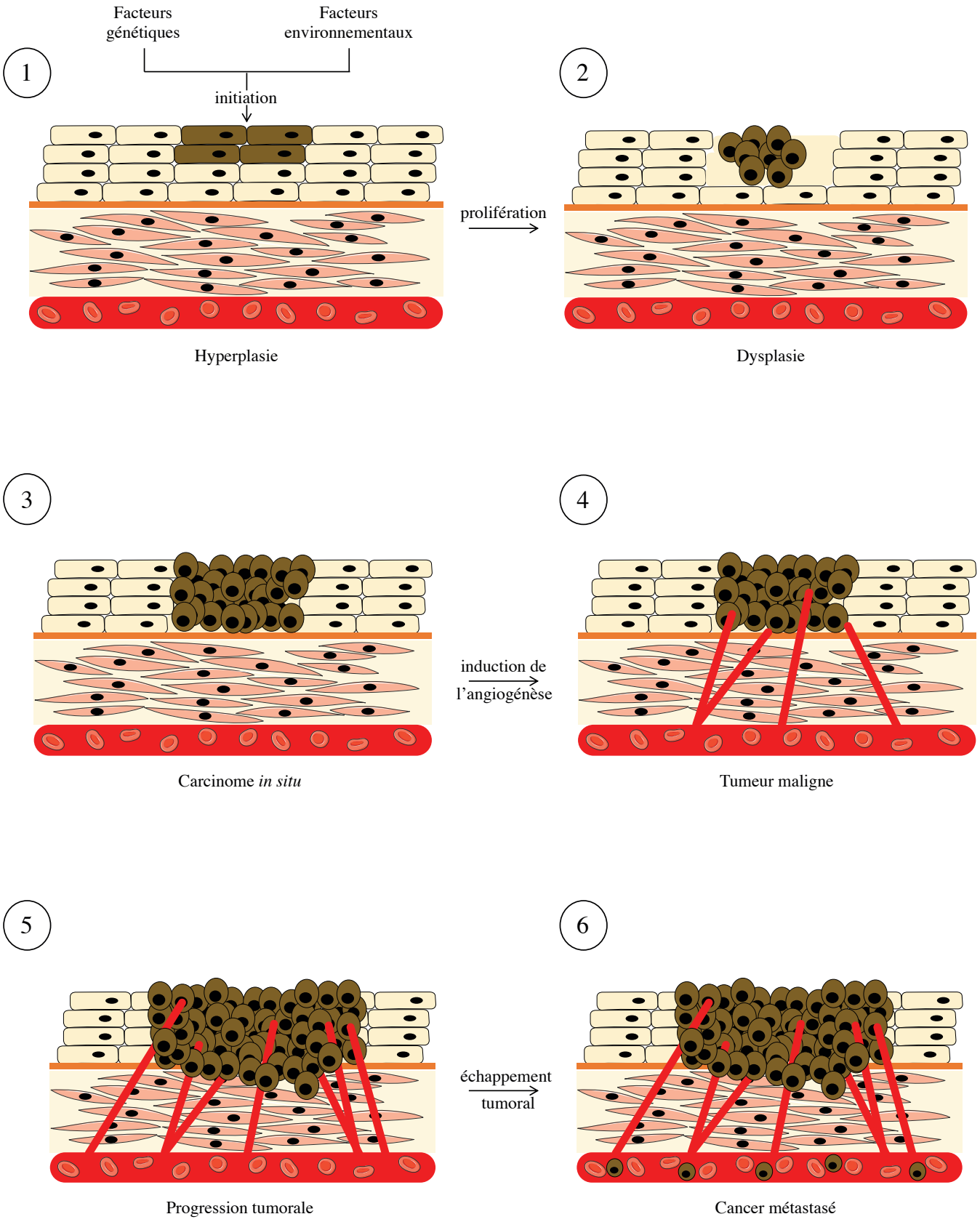

Figure 1 : Étapes de la cancérogenèse

(d'après https://www.cancer.ca)

2. Les traitements actuels

A l'heure actuelle, les équipes médicales disposent de plusieurs types de thérapies pour le traitement du cancer. Les plus courants sont la chirurgie, la radiothérapie et la chimiothérapie. Chaque patient a une prise en charge appropriée selon plusieurs critères : le type et le degré de progression du cancer, la présence d'autres maladies, l'âge du patient, etc. :

- La chirurgie a pour objectif l'ablation de la tumeur et des ganglions lymphatiques proches affectés. Le chirurgien enlève également du tissu sain environnant pour empêcher la réapparition de la tumeur.
- La radiothérapie utilise des radiations de haute énergie. Les radiations endommagent l'ADN des cellules cancéreuses entraînant l'arrêt de la division cellulaire et la mort de la cellule. Cependant, les tissus sains environnants sont également affectés par les radiations.
- La chimiothérapie consiste à administrer des drogues qui agissent et tuent les cellules à division rapide comme les cellules cancéreuses. Cependant, les drogues ne sont pas ciblées et peuvent aussi agir sur des cellules saines qui engendrent de nombreux effets secondaires sévères[8].

L'amélioration de ces thérapies est aujourd'hui un enjeu majeur et passe par le développement de nouvelles thérapies adaptées qui ciblent préférentiellement les cellules cancéreuses. Le ciblage actif des cellules cancéreuses permettrait d'augmenter l'efficacité thérapeutique du traitement et de diminuer considérablement les effets secondaires. De plus, les dernières décennies de recherche ont permis de démontrer des points communs entre les différents types de cancers : des mécanismes généraux ont été mis en évidence permettant de comprendre l'évolution du processus cancéreux. Bien que différents, les cancers ont des mécanismes d'apparition et d'évolution très similaires. La compréhension de ces différents mécanismes permettra de concevoir de nouvelles thérapies anticancéreuses plus ciblées et plus efficaces.

3. Les besoins cliniques : vers un traitement plus sélectif

Actuellement, les thérapies ciblées utilisées en clinique sont des médicaments qui bloquent la croissance et la propagation du cancer en interférant avec des molécules spécifiques considérées comme les cibles moléculaires. Ces molécules interviennent dans la croissance, la progression et la propagation de la tumeur. Les mécanismes d'action des thérapies ciblées

diffèrent des chimiothérapies standards, principalement parce que ces thérapies agissent sur une cible moléculaire associée à la cellule cancéreuse ou au microenvironnement tumoral alors que les chimiothérapies classiques agissent sur toutes les cellules à division rapide que la cellule soit cancéreuse ou normale.

Ces médicaments sont de deux types : les biomédicaments ou inhibiteurs extracellulaires qui sont généralement des anticorps monoclonaux (immunothérapie) et des petites molécules chimiques ou inhibiteurs intracellulaires qui sont des inhibiteurs de voies de signalisation ou des antagonistes de récepteurs (hormonothérapie). L'hormonothérapie et l'immunothérapie sont considérées comme des thérapies ciblées car elles agissent sur des mécanismes oncogéniques. Le premier médicament ciblé mis sur le marché a été le tamoxifène dans les années 70 pour le traitement des cancers du sein hormonodépendant[9]. L'hormonothérapie bloque l'action oncogénique des hormones qui permettent aux cellules cancéreuses hormonosensibles de proliférer rapidement. Dans ce type de cancer, les cellules cancéreuses ont dans leur noyau des récepteurs des œstrogènes. Le tamoxifène va se lier à ces récepteurs et bloquer ainsi l'action mitogène des œstrogènes. Le tamoxifène bloque les cellules en phase G1 du cycle cellulaire conduisant à une apoptose. En immunothérapie, il existe deux grands types de traitement : le ciblage du système immunitaire et le ciblage des cellules cancéreuses. Le système immunitaire est capable de détecter les cellules tumorales comme un danger pour l'organisme et les détruire mais les cellules cancéreuses sont capables de détourner les points de contrôle des cellules immunitaires en les inactivant afin d'éviter leur élimination. Pour cela, les cellules cancéreuses se lient aux cellules immunitaires *via* des récepteurs spécifiques entraînant l'inactivation de la cellule immunitaire. Pour empêcher cette liaison, les traitements les plus couramment utilisés sont des inhibiteurs de points de contrôle qui vont permettre l'activation de la cellule immunitaire et par conséquent l'élimination de la cellule cancéreuse. Le deuxième type de traitement en immunothérapie est le ciblage des cellules cancéreuses. Ce ciblage est basé sur l'utilisation d'anticorps monoclonaux qui ciblent directement les cellules tumorales afin de bloquer leur croissance et de les détruire.

En 2015, on dénombrait 43 thérapies ciblées autorisées par les agences de santé du médicament[10]. Cependant, ces thérapies ont des limites :

- Certains types de tumeurs n'ont pas encore de thérapie ciblée car les recherches n'ont pas permis de déterminer de cible moléculaire spécifique des cellules cancéreuses.
- Certaines cibles moléculaires ne sont exprimées que dans un faible pourcentage d'un type de cancer ainsi les thérapies ciblées ne s'adressent qu'à une minorité de patients.

- Les cellules cancéreuses peuvent devenir résistantes aux médicaments ciblés entraînant une perte totale d'efficacité du traitement.
- Les thérapies ciblées peuvent également entraîner des effets indésirables qui sont souvent moins sévères que les chimiothérapies classiques (problèmes de peau, de coagulation, de cicatrisation, d'hypertension).

Au vu de ces limites, il est nécessaire de continuer le développement de nouvelles thérapies dans le but d'améliorer le ciblage des cellules cancéreuses afin d'augmenter de manière significative l'efficacité thérapeutique, de réduire au maximum les effets indésirables, et de contourner la résistance des cellules cancéreuses. Les recherches se sont alors tournées vers les nanotechnologies et plus précisément vers le développement de nanoparticules pour le ciblage des cellules cancéreuses. Les nanoparticules sont le résultat du concept de vectorisation imaginé par l'immunologiste et médecin allemand Paul Ehrlich en 1906[11]. Il énonça la théorie du « Magic Bullet » : une « balle magique » capable de transporter des molécules à l'intérieur de l'organisme et possédant une excellente capacité et spécificité de ciblage.

Chapitre 2 : La nanomédecine pour le traitement des cancers

1. La nanomédecine

Les limites des traitements conventionnels ont entraîné le développement de nouvelles approches telle que la nanomédecine qui est l'application des nanotechnologies dans le domaine de la santé pour le diagnostic et la thérapie. Les nanotechnologies sont en constante évolution et naissent de la convergence de plusieurs domaines : la chimie, la biologie, la physique, les mathématiques et l'ingénierie, dans le but de développer et d'étudier des matériaux de l'ordre du nanomètre. A l'heure actuelle, les nanotechnologies sont déjà utilisées notamment pour traiter des cancers[12], des maladies cardio-vasculaires[13], des maladies neurodégénératives[14] et inflammatoires[15] mais également pour le diagnostic[16]. Le volet de la nanomédecine qui nous intéresse ici concerne le développement de nanovecteurs pour le traitement des cancers.

2. Les nanovecteurs

2.1 Généralités

De nombreuses molécules thérapeutiques classiques sont déjà utilisées en clinique mais connaissent de nombreuses contraintes biologiques : instabilité, toxicité, mauvaise solubilité, difficulté à franchir les barrières biologiques, etc. De plus, la quantité finale de médicaments atteignant la cible est faible car il va s'accumuler dans tout l'organisme sans discriminer les tissus malades des tissus sains entraînant des effets secondaires. La vectorisation de ces molécules thérapeutiques dans des nanovecteurs permet de pallier à certaines de ces contraintes[17]. Cette technique de vectorisation consiste à encapsuler des agents thérapeutiques à un système de transport, appelé nanoparticule, permettant de délivrer le médicament dans la zone cible. En effet, le nanovecteur permet de franchir certaines barrières biologiques tout en protégeant la molécule thérapeutique afin de la délivrer sous forme active et en grande quantité au niveau de la zone à traiter, conduisant ainsi à une meilleure efficacité thérapeutique. La première étude scientifique sur le sujet a été publiée en 1964 et décrivait la structure des liposomes[18]. Il faudra attendre 1995 pour qu'un premier nanovecteur reçoive une autorisation de mise sur le marché par la « Food and Drug Administration » (FDA). Ce nanovecteur, appelé Doxil, est composé de liposomes dans lequel de la doxorubicine a été encapsulée pour le

traitement du cancer de l'ovaire[19]. Aujourd'hui de nombreux nanovecteurs ont reçu une autorisation de mise sur le marché ou sont utilisés en phase clinique et de nombreuses études s'intéressent au développement de nouveaux nanovecteurs. Le tableau 1 décrit quelques exemples[20].

Thérapie	Nom du médicament	Type de nanovecteur	Agent thérapeutique	Type de cancer	Statut
Délivrance de drogues non ciblée	Doxil	Liposome pégylé	Doxorubicine	Cancer de l'ovaire, myélomes multiples, sarcome de Kaposi	Approuvé par la FDA
	Abraxane	Nanoparticule d'albumine	Paclitaxel	Cancers du sein, des poumons et du pancréas	Approuvé par la FDA
	Myocet	Liposome	Doxorubicine	Cancer du sein métastatique	Approuvé en Europe et au Canada
Délivrance de drogues ciblée	MM-302	Liposome avec greffage de HER2	Doxorubicine	Cancer du sein positif HER2	Phase II/III
	Immuno liposome	Liposome greffé avec EGFR	Doxorubicine	Tumeurs solides	Phase I
Délivrance de drogues par réponse aux stimuli	ThermoDox	Liposome	Doxorubicine	Carcinome hépatocellulaire	Phase III
Délivrance combinée de drogues	CPX-1	Liposome	Irinotecan et flocuridine	Cancer colorectal avancé	Phase II
Hyperthermie	NanoTherm	Nanoparticule d'oxyde de fer	/	Glioblastome	Approuvé en Europe
Radiothérapie	NBTXR3	Nanoparticule d'oxyde d'afnium	/	Sarcome des tissus mous (adulte)	Phase II/III
Thérapie génique ou ARN interférent	PNT2258	Liposome	Oligonucléotide d'ADN dirigé contre BCL-2	Lymphome cellules B large	Phase II
Immunothérapie	CYT6091	Nanoparticule d'or colloïdal	TNF	Tumeurs solides avancées	Phase 1

Tableau 1 : Exemples de thérapies à base de nanoparticules pour le traitement du cancer

2.2 Généralités sur les systèmes de vectorisation

Le développement des nanoparticules pour la délivrance de drogues anticancéreuses est une voie très étudiée. L'utilisation de nanoparticules doit permettre une délivrance contrôlée et locale au niveau de la tumeur. Pour répondre à ces critères, de nombreux types de nanovecteurs ont été développés mais ils doivent répondre à un cahier des charges très précis pour être efficaces et utilisables en clinique :

- ils doivent être stables,
- ils doivent être biocompatibles et biodégradables,
- ils doivent pouvoir transporter une quantité suffisante de médicament sans altérer sa stabilité et son activité,
- la libération de la drogue doit être contrôlée au niveau de la zone à traiter grâce aux caractéristiques intrinsèques du nanovecteur (sensibilité à une variation du milieu comme le pH, liaison réversible, photoinduite, etc.),
- leur surface doit être modifiable pour greffer des molécules de ciblage,
- leur taille doit être contrôlée pour permettre une circulation, une diffusion à travers les barrières physiologiques et une distribution dans les tissus.

Ce dernier point est important car les nanoparticules de taille inférieure à 5,5 nm sont filtrées par les reins ainsi elles quittent la circulation systémique très tôt sans pouvoir atteindre la zone tumorale[21,22]. De plus, les nanoparticules de plus de 100 nm sont généralement opsonisées avant d'atteindre la tumeur[23]. En 2011, la Commission Européenne a publié ses recommandations relatives à la définition des nanoparticules, dont leur taille qui doit être comprise entre 1 et 100 nm. Cependant, des experts ont montré que cette limitation de taille était une erreur car certains nanomatériaux peuvent avoir des propriétés uniques seulement si leur taille est supérieure à 100 nm (amélioration de la biodisponibilité, de la solubilité, réduction de la dose, etc.)[24].

La molécule encapsulée dans le vecteur est également un point important dans le domaine de la vectorisation car elle conditionne la méthode d'encapsulation. La molécule peut être de diverses natures selon le type de thérapie envisagée. Il peut s'agir de :

- matériel génétique (ADN[25], ARN[26], ARNi[27]) dans le cadre de la thérapie génique,
- d'agents anticancéreux pour la délivrance de drogues[28],
- de photosensibilisateurs pour la thérapie photodynamique[29],
- de marqueurs fluorescents dans le cadre du diagnostic[30].

Dans le cadre de cette thèse, nous avons étudié différents types de nanoparticules pour la thérapie du cancer avec des approches thérapeutiques différentes : des nanoparticules dans lesquelles un agent anticancéreux a été encapsulé pour de la délivrance de drogues, des nanoparticules d'analogue de bleu de prusse pour la thérapie photothermique et pour finir des nanoparticules dans lesquelles un photosensibilisateur a été encapsulé pour la thérapie photodynamique. Ces différentes approches seront détaillées dans la partie résultat (partie 1 : chapitres 1 et 2 ; partie 2 : chapitre 2) de ce manuscrit.

2.3 Caractéristiques des nanoparticules

Il existe plusieurs types de vecteurs, ils peuvent être d'origine biologique (lipoprotéines), naturelle (virus modifiés), ou synthétique (nanoparticules). Dans ce manuscrit, nous nous intéresserons uniquement aux nanoparticules. La recherche sur le développement des nanoparticules a permis de mettre au point trois générations (Figure 2) :

- Les nanoparticules de première génération sont des liposomes renfermant la molécule active. Cependant, ces liposomes vont être reconnus et marqués par des protéines plasmatiques appelées opsonines qui sont des protéines impliquées dans l'immunologie. Le complexe liposome-opsonine est alors reconnu comme du non-soi et va être capté par les macrophages dans le foie entraînant leur destruction et la libération de la molécule active[31]. Ces nanoparticules de première génération sont donc très utiles pour le traitement des cancers du foie mais sont inutilisables pour tout autre type de cancers.
- Afin d'éviter le phénomène d'opsonisation et d'augmenter le temps de demi-vie plasmatique, les nanoparticules de deuxième génération ont été développées. Ces nanoparticules sont recouvertes de polymères hydrophiles comme les polyéthylènes glycols (PEG) qui vont empêcher la fixation des opsonines. Ainsi, la nanoparticule devient « furtive » lui permettant d'éviter une internalisation totale par le foie et par conséquent d'augmenter le temps de circulation dans la circulation systémique afin d'atteindre d'autres organes[32].
- Ces nanoparticules de deuxième génération ont ensuite été améliorées par le greffage de molécules de ciblage à la surface de la nanoparticule qui sont capables de reconnaître des marqueurs spécifiques présents à la surface des cellules cancéreuses. Ces nanoparticules appelées nanoparticules de troisième génération sont très intéressantes pour obtenir une thérapie ciblée.

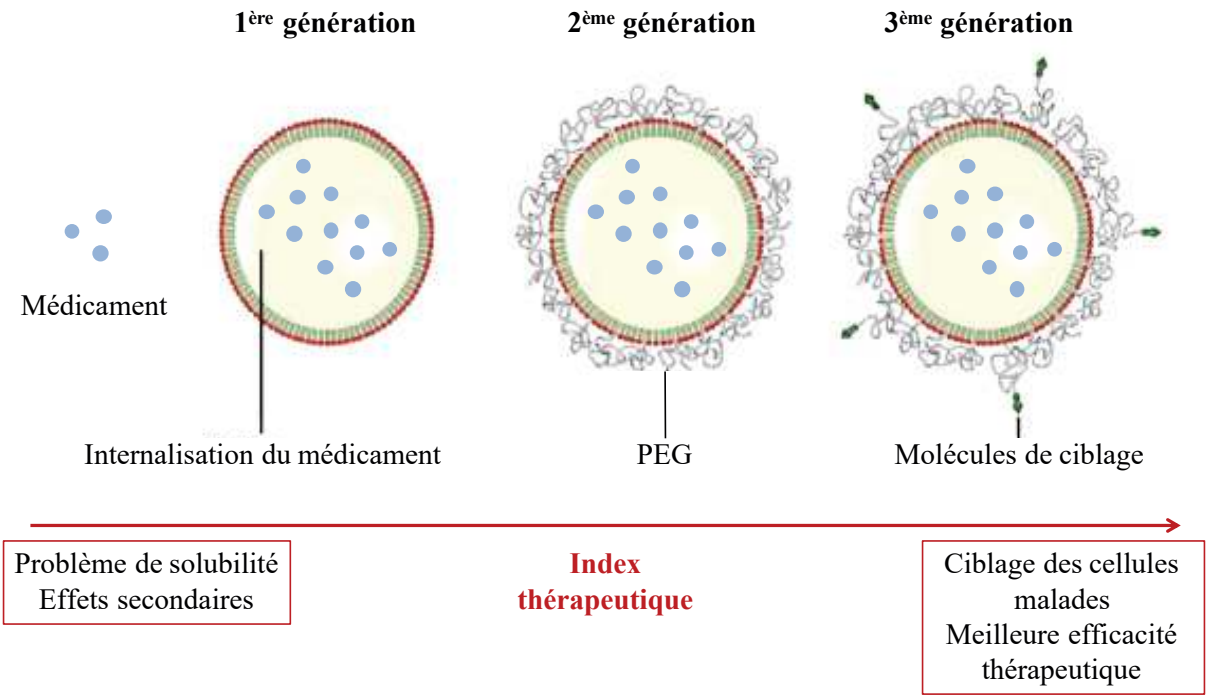

Figure 2 : Schéma des trois générations de nanoparticules

En fonction de la nature chimique de leur structure, plusieurs types de nanoparticules sont utilisés en vectorisation (Figure 3). Les nanoparticules peuvent être classées en deux grandes familles : les nanoparticules organiques et les nanoparticules inorganiques[33]. Une revue exhaustive des différents types de nanoparticules étant impossible, seules les principales nanoparticules utilisées à l'heure actuelle seront décrites ci-dessous.

2.3.1 Les nanoparticules organiques

- Les liposomes

Les liposomes ont été synthétisés pour la première fois en 1964 par l'équipe de Bangham[18]. Les liposomes sont des vésicules d'auto-assemblage dont la membrane est constituée d'une ou plusieurs bicouches lipidiques. Dans l'eau, une suspension de phospholipides forme spontanément des vésicules en raison de la structure amphiphile de ces molécules : les phospholipides possèdent une tête hydrophile et une queue hydrophobe entraînant l'organisation d'une bicouche avec les têtes polaires au contact de l'eau et les queues apolaires au centre de la bicouche. Les liposomes ont été les premières nanoparticules utilisées

pour l'adressage de médicament, ils sont aujourd'hui encore largement utilisés et continuent d'être étudiés.

- Les nanoparticules polymériques

Ces nanoparticules sont des polymères dans lesquelles les médicaments sont dissouts ou conjugués à leur surface. On distingue dans les nanoparticules polymériques :

- Les micelles qui sont composées de molécules amphiphiles. En milieu aqueux, les têtes hydrophiles sont dirigées vers l'eau et les queues hydrophobes sont dirigées vers l'intérieur tandis que dans un solvant organique ce sont les têtes hydrophiles qui sont orientées vers l'intérieur de la micelle. Ces propriétés particulières des micelles sont très intéressantes car elles permettent d'encapsuler des molécules hydrophiles et hydrophobes. Les micelles sont totalement biocompatibles et biodégradables[34,35].
- Les dendrimères qui sont des polymères homogènes hyper-ramifiés. Ils ont une vaste surface sur laquelle peuvent être liés des agents thérapeutiques ou des molécules biologiquement actives[36].
- Les nanoémulsions qui constituent une classe très particulière des émulsions, ont une taille de gouttes comprise entre 20 et 300 nm stabilisées par des surfactants. Les gouttelettes, composées généralement d'huile, permettent de solubiliser et d'encapsuler des médicaments, des agents de contraste, des sondes pour l'imagerie, etc., à de très grandes concentrations[37,38].

- Les nanotubes de carbone

Ils sont composés soit par une couche simple de paroi de graphène, soit par des couches multiples concentriques. Ils peuvent être utilisés par exemple pour encapsuler des drogues anticancéreuses ou des radionucléides[39].

2.3.2 Les nanoparticules inorganiques

- Les quantum-dots

Les quantum-dots sont des semi-conducteurs composés de minces cristaux fluorescents, qui en fonction de leur taille, peuvent émettre de la lumière dans le domaine du visible une fois stimulés par la lumière ultra-violette (UV). Ils peuvent être conjugués à un ligand par

l'intermédiaire d'une couche polymérique et ils sont utilisés pour le marquage cellulaire et l'imagerie des cancers[40].

- Les nanoparticules magnétiques

A l'heure actuelle, en clinique, les nanoparticules magnétiques sont principalement utilisées comme agent de contraste en Imagerie par Résonance Magnétique (IRM). Ces nanoparticules sont composées de cobalt, de nickel ou plus généralement d'oxyde de fer[41]. Un exemple de ce type de nanoparticules à base de bleu de Prusse sera développé dans la partie résultat (partie 1 : chapitre 2) de ce manuscrit.

- Les nanoparticules fonctionnalisées

Les nanoparticules fonctionnalisées sont des nanoparticules modifiées chimiquement à leur surface. Pour des applications biologiques, la surface des nanoparticules doit être polaire c'est-à-dire avoir une solubilité aqueuse élevée afin d'empêcher l'agrégation. Pour cela, des groupements hydrophiles tels que les PEG sont généralement utilisés pour diminuer le nombre d'interactions non spécifiques[42]. De plus, des molécules biologiques telles que les anticorps, les carbohydrates, les aptamères ou les peptides, sont utilisées pour diriger les nanoparticules vers des sites spécifiques dans l'organisme[43]. Ces agents de ciblage sont idéalement liés de façon covalente à la nanoparticule et présents en quantité contrôlée[44].

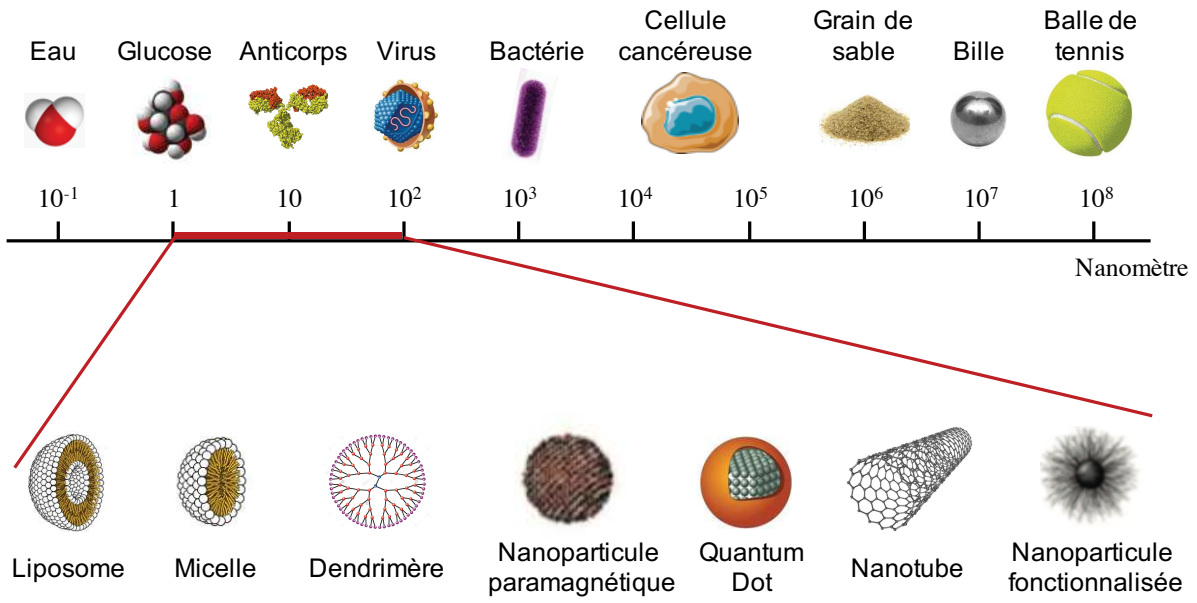

Figure 3 : Les principaux nanovecteurs utilisés en vectorisation

(d'après http://ocg.cancer.gov)

3. Les nanoparticules pour le traitement des cancers

Dans le cadre de la thérapie des cancers, les molécules utilisées en chimiothérapie ont plusieurs limites[45] :

- la faible solubilité de certains agents anticancéreux,
- leur faible sélectivité vis-à-vis des cellules cancéreuses entraînant une forte toxicité pour les tissus sains,
- leur faible perméabilité dans les tissus tumoraux,
- la résistance des cellules cancéreuses.

L'encapsulation de médicaments dans les nanoparticules permet de pallier à ces problèmes car la nanoparticule protège le médicament et le transporte jusqu'à la zone tumorale grâce à un ciblage passif appelé effet EPR pour « Enhanced Permeability and Retention effect »[46].

3.1 Le ciblage passif : l'effet EPR

Comme dit précédemment, les traitements classiques de chimiothérapie sont des molécules qui présentent une toxicité non négligeable car elles ne discriminent pas la tumeur des tissus normaux. Il est donc nécessaire de développer de nouveaux médicaments qui seront délivrés sélectivement à la tumeur afin d'éviter les effets indésirables. Une des possibilités est d'exploiter les anomalies anatomiques et physiopathologiques des tumeurs solides, en particulier leur réseau vasculaire. Nous savons que les cellules cancéreuses se multiplient beaucoup plus rapidement que les cellules saines environnantes. Elles monopolisent donc les nutriments, l'oxygène, le glucose, etc. et génèrent beaucoup de déchets toxiques pour les cellules saines. Lorsque la tumeur atteint une taille de 1 à 2 mm^3, ses besoins en oxygène et nutriments deviennent de plus en plus importants, les cellules saines ne peuvent plus rivaliser pour avoir un approvisionnement suffisant et elles ne peuvent plus gérer les grandes concentrations de déchets toxiques entraînant le remplacement des cellules saines par les cellules cancéreuses. Dans cet environnement devenu hostile pour les cellules saines, les cellules cancéreuses, à l'inverse, peuvent survivre en stimulant l'angiogenèse. En effet, sans circulation sanguine elles arrêtent leur croissance[47] et deviennent nécrotiques ou apoptotiques[48]. Par conséquent, l'angiogenèse est un facteur primordial pour la progression de la tumeur.

Dans des conditions physiologiques normales, le réseau vasculaire se développe selon deux mécanismes : la vasculogenèse et l'angiogenèse. La vasculogenèse est décrite par la différenciation des précurseurs des cellules endothéliales en un réseau vasculaire primitif. Ce phénomène est observé au cours des premières étapes du développement embryonnaire. L'étape suivante, appelée angiogenèse, est le développement du réseau vasculaire à partir de ce réseau primitif, par prolifération et bourgeonnement des cellules endothéliales. L'angiogenèse est contrôlée et joue un rôle dans le développement embryonnaire, les fonctions reproductrices (cycle menstruel, grossesse), et lors d'une réparation tissulaire (blessures musculaires, ischémies cardiaques)[49]. Le système vasculaire forme le réseau principal impliqué dans l'acheminement de l'oxygène et des nutriments aux organes. Cette fonction physiologique est détournée en conditions pathologiques, elle permet alors la progression de la maladie comme les rétinopathies, les hémangiomes infantiles, l'arthrite rhumatoïde, le psoriasis, les ulcères duodénaux et bien évidemment la progression tumorale[7].

Les cellules endothéliales sont des cellules qui se divisent très peu : leur taux de renouvellement est d'environ 1000 jours, et il est sous le contrôle d'un équilibre strict entre facteurs activateurs et inhibiteurs[50]. Cependant ces cellules sont réactives aux facteurs environnementaux et au cours de la croissance tumorale, un déséquilibre entre ces différents facteurs, appelé « switch angiogénique », est observé. Le processus d'angiogenèse est alors déclenché :

- Les cellules cancéreuses ainsi que les composants du microenvironnement tumoral (cellules inflammatoires, fibroblastes) vont sécréter des molécules angiogéniques telles que le VEGF. Ces molécules vont diffuser à travers le tissu tumoral pour atteindre les vaisseaux sanguins environnants entraînant l'activation des cellules endothéliales, ce qui permettra de guider la formation du néo-vaisseau.
- Dans un deuxième temps, les molécules angiogéniques vont stimuler la sécrétion de protéases par les cellules endothéliales permettant la dégradation de la membrane basale entourant le vaisseau.
- Cette dégradation va entraîner la migration des cellules endothéliales vers la source du stimulus angiogénique permettant le bourgeonnement d'un nouveau vaisseau.

Contrairement aux conditions physiologiques normales, les néo-vaisseaux qui irriguent la tumeur ont une forme irrégulière, ils sont dilatés et présentent des fenestrations dues à une désorganisation des cellules endothéliales[51]. Cette déficience anatomique entraîne une fuite

importante des composants du plasma sanguin par les fenestrations dont la taille a été estimée à 0,2 ± 0,5 μm[52,53]. De plus, le faible retour veineux dans le tissu tumoral[54] et la faible clairance lymphatique entraînent une rétention des macromolécules dans la tumeur[55]. Ce phénomène appelé effet EPR, a été décrit il y a 33 ans et constitue la base du ciblage passif des nanoparticules au niveau des tumeurs solides : les nanoparticules injectées par voie intraveineuse vont se déplacer dans la circulation sanguine jusqu'à la zone tumorale, les nanoparticules vont pouvoir traverser les fenestrations des néo-vaisseaux et être retenues dans la tumeur. La taille optimale des nanoparticules pour une pénétration par effet EPR n'est pas clairement définie et diffère selon le type de tumeur, mais il est généralement admis que les nanoparticules doivent mesurer entre 50 et 300 nm[56].

3.2 Le ciblage actif

Le ciblage passif de la tumeur par effet EPR est limité car il existe une hétérogénéité significative entre les tumeurs de même type ou de types différents[57]. De plus, une analyse de données précliniques sur l'administration de nanovecteurs publiées au cours des dix dernières années a montré qu'un faible pourcentage de la dose injectée atteignait les tumeurs[58]. Pour améliorer l'adressage et ainsi augmenter l'efficacité des nanoparticules, les recherches se sont tournées vers le ciblage actif des cellules cancéreuses. Ce ciblage est basé sur la conjugaison de biomolécules à la surface des nanoparticules. Les principaux objectifs du ciblage actif sont :

- la reconnaissance spécifique des cellules cancéreuses et l'absence d'interaction avec les cellules saines,
- l'augmentation de la concentration en nanoparticules au niveau des cellules cancéreuses.

Pour cela, le choix de la cible biologique est très important et doit répondre à différents critères :

- la cible doit être accessible pour la nanoparticule, c'est-à-dire que la cible doit être exprimée à la surface des cellules cancéreuses,
- la cible doit être spécifique des cellules cancéreuses, elle doit être exprimée plus fortement au sein de la tumeur que dans les tissus sains,
- le ligand doit avoir une grande sélectivité ainsi qu'une forte affinité pour la cible choisie pour éviter toute interaction non spécifique,
- le ligand peut être de différentes natures (anticorps, aptamères, glucides, etc.) suivant la cible choisie.

A l'heure actuelle, il existe quelques nanovecteurs pour le ciblage actif dont les plus courants sont les anticorps. On retrouve deux types d'anticorps : certains agissent sur la croissance des cellules en bloquant un récepteur d'un facteur de croissance comme le trastuzumab qui cible la surexpression du récepteur HER2 dans les cellules cancéreuses du sein. Tandis que d'autres peuvent être conjugués à des molécules thérapeutiques comme le Mylotarg® qui est un anticorps monoclonal dirigé contre le récepteur CD33 surexprimé quand le cadre des leucémies aiguës myéloïdes et qui est lié à un agent cytotoxique libéré dans la cellule pour induire des ruptures des doubles brins d'ADN induisant un arrêt du cycle cellulaire. Cependant, ces traitements sont généralement associés à d'autres traitements de chimiothérapie : on observe donc toujours des effets secondaires dus à la chimiothérapie[59,60].

En résumé, le ciblage passif des cellules cancéreuses guidé par l'effet EPR et l'activité métabolique importante des cellules cancéreuses conduisent à la rétention des nanoparticules dans la zone tumorale. Quant au ciblage actif, les nanoparticules fonctionnalisées avec des ligands spécifiques peuvent se lier préférentiellement aux récepteurs présents à la surface des cellules cancéreuses permettant une internalisation rapide et plus efficace, ce qui entraîne une plus grande quantité de nanoparticules à l'intérieur des cellules cancéreuses (Figure 4).

Nous décrirons dans ce manuscrit un exemple de nanoparticules fonctionnalisées par un carbohydrate pour le ciblage d'un cancer rare dans la partie résultat (partie 2 : chapitre 2) de ce manuscrit.

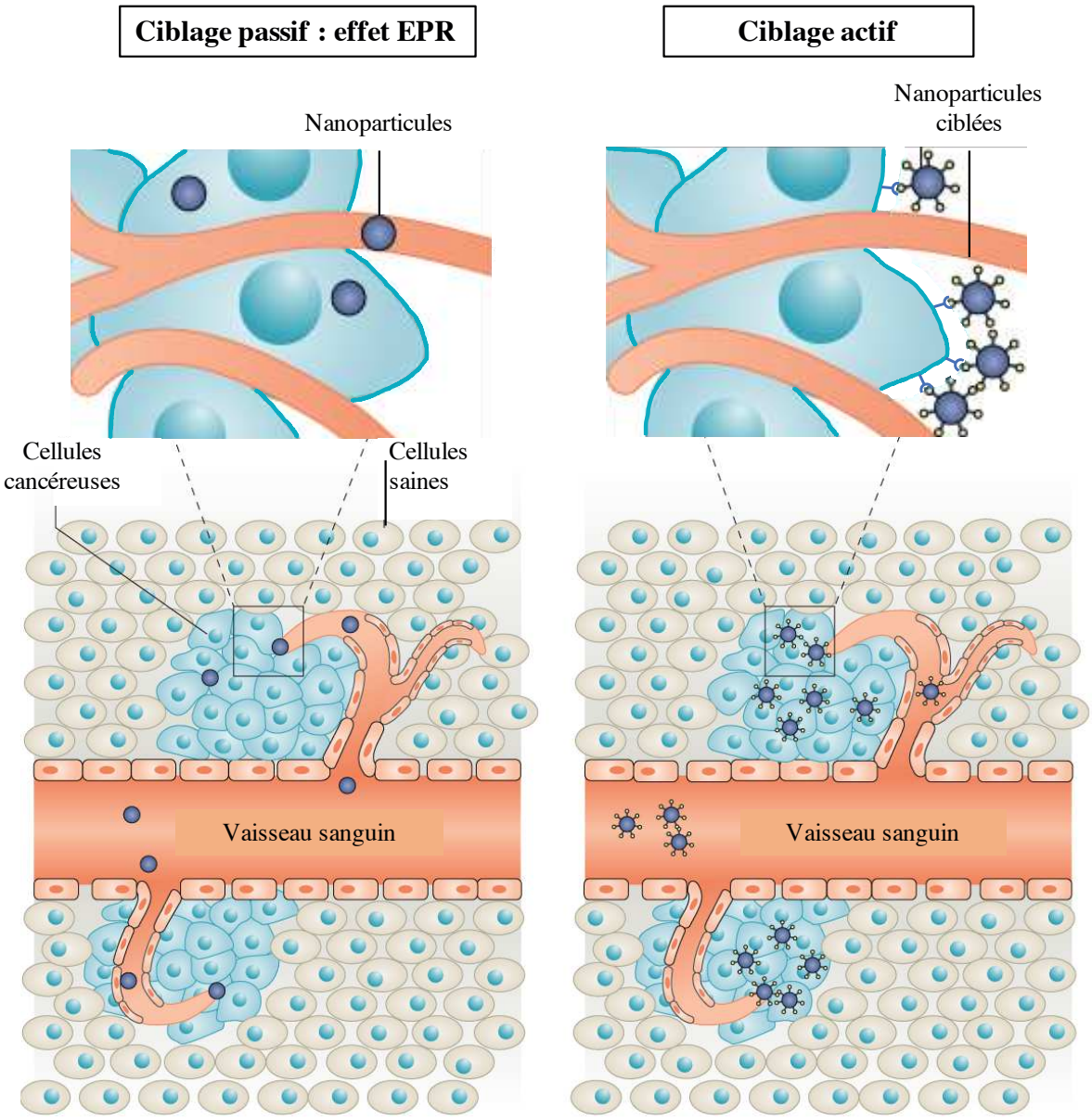

Figure 4 : Ciblages passif et actif par les nanoparticules[61]

Les effets à court et à long terme de ces nanomatériaux sont encore inconnus et des questions subsistent : serait-il possible de détecter et traiter un cancer avec la même nanoparticule ? Un nanovecteur pourrait-il détecter de manière spécifique une cellule cancéreuse pour savoir quand le médicament doit être libéré ? Est-il possible de synthétiser d'autres types de nanoparticules pour la thérapie, utilisable en clinique en première intention et sans association avec de la chimiothérapie ? Toutes ces questions rendent complexe la synthèse de nanovecteurs intelligents. Dans ce manuscrit, nous essayerons d'y répondre en partie par la synthèse de nanoparticules multifonctionnelles permettant de cibler, d'imager et de traiter la tumeur.

Chapitre 3 : Ciblage thérapeutique des lectines membranaires

Comme nous venons de l'aborder dans le chapitre précédent, un des moyens permettant le ciblage actif par les nanoparticules est d'utiliser les récepteurs membranaires exprimés à la surface des cellules cancéreuses. Pour cela, il faut connaître le niveau d'expression du récepteur membranaire ciblé. Dans ce chapitre, nous nous intéresserons plus particulièrement aux lectines. Quels rôles jouent-elles dans la cancérogenèse ? Est-ce qu'elles peuvent être une bonne cible thérapeutique pour le traitement des cancers ?

1. Les lectines

1.1 Définition

Les lectines sont des protéines ou glycoprotéines qui sont capables d'interagir de manière spécifique et réversible avec des carbohydrates (mono- ou oligosaccharides) sous forme de liaisons non covalentes (liaisons hydrogènes, hydrophobes, de coordination avec des ions métalliques)[62,63]. Les lectines sont souvent multivalentes car elles possèdent plusieurs sites de liaisons (lectines di- ou polyvalentes). Elles participent d'une manière générale aux processus de reconnaissances moléculaire et cellulaire pour tous les organismes vivants (virus, bactéries, plantes, animaux, humains)[64]. De plus, les lectines peuvent être circulantes, intracellulaires ou membranaires et ont par conséquence des rôles précis suivant leur localisation dans l'organisme :

- Les lectines circulantes jouent un rôle très important dans le système immunitaire[65].
- Les lectines membranaires reconnaissent des ligands extracellulaires et permettent leur endocytose. Elles possèdent également des propriétés de recyclage par la voie d'endocytose. Au pH lysosomal (pH acide), le complexe ligand-lectine se dissocie pour permettre à la lectine d'être recyclée à la membrane[66].
- Les lectines intracellulaires sont impliquées dans le trafic et le tri des glycoprotéines vers les endosomes ou vers d'autres voies de sécrétion[67].

Les lectines sont également impliquées dans plusieurs processus biologiques comme les mécanismes d'adhésion bactérienne, les interactions cellule-cellule et cellule-matrice extracellulaire, mais également les processus de phagocytose, de différenciation cellulaire et d'apoptose[68].

1.2 Les différentes catégories de lectines animales

La première classification des lectines a été réalisée à partir des lectines de plante et était basée selon leur spécificité pour leurs ligands saccharidiques[64]. Ce n'est qu'avec le développement du clonage moléculaire, qu'une classification plus rigoureuse a été mise en place, organisée sur la base de l'homologie des séquences d'acides aminés. La première classification de ce type a été proposée par Kurt Drickamer qui a identifié des séquences conservées dans les sites de reconnaissance appelés « carbohydrate recognition domain » (CRD). A partir de cette classification, huit familles ont pu être distinguées (Figure 5)[69] :

- Quatre familles pour les lectines extracellulaires : les lectines de type C, de type R, de type I et les Galectines.
- Quatre familles pour les lectines intracellulaires : les lectines de type P, de type M, de type L et les Calexines.

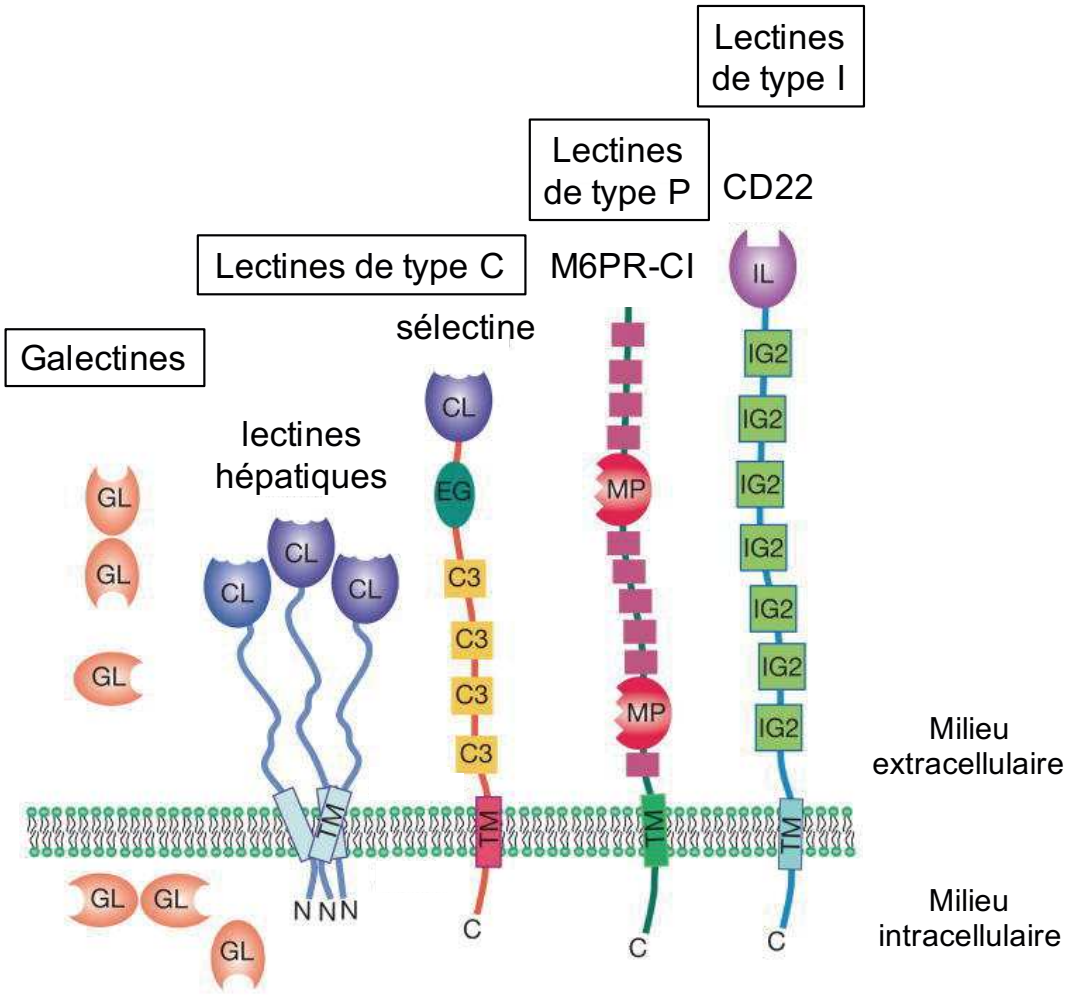

Figure 5 : Schéma des types majeurs des lectines animales[70]

Chaque famille de lectine est composée de groupes de lectines qui ont des ligands différents (Tableau 2).

Famille de lectine	Exemple de groupe	Exemple de ligands	Localisation cellulaire	Exemple de fonctions
Type C[71]	Récepteurs du mannose	Mannose, fucose, N-acétylglucosamine	Membranaire et extracellulaire	Rôle dans l'immunité innée Clairance des hormones glycosylées Reconnaissance de pathogène Rôle dans la migration cellulaire Rôle dans les interactions cellules dendritiques-cellules T
	Lectines hépatiques	Galactose, N-acétylgalactosamine		
	Sélectines	Résidus sialate-galatose-N-Acétylglucosamine-fucose		
Type R[72]	ß-trefoil	Galactose, N-acétylgalactosamine	Golgi et membranaire	Cible les enzymes Assure la production d'hormones glycosylées
Type I[73]	Sialoadhesin	Acide sialique N- et O-glycosylé	Membranaire	Rôle dans l'adhésion cellulaire Interactions cellule-cellule dans le système immun et le système nerveux
	CD22			
	CD33			
	MAG			
Galectines[74] (Type S)	Galectin-1	ß-galactose	Cytoplasme et extracellulaire	Régule la croissance cellulaire et l'apoptose Régule le cycle cellulaire Module les interactions cellule-cellule et cellule-substrat
	Galectin-2			
	Galectin-3			
Type P[75]	CD-M6PR	Mannose 6-phosphate	Membranaire, intracellulaire et extracellulaire	Cible les enzymes lysosomales et les glycoprotéines portant le mannose 6-phosphate Rôle dans le trafic et la dégradation de glycoprotéines
	CI-M6PR			
Type M[76]	EDEM1	Glycanes mannosylés	Réticulum endoplasmique	Rôle dans la dégradation des glycoprotéines
	EDEM2			
	EDEM3			
Type L[77]	ERGIC-53	Glycanes mannosylés	Réticulum endoplasmique et Golgi	Contrôle la sécrétion des glycoprotéines du réticulum endoplasmique
	VIP36			
Calnexines[78]	Calmegin	Glycoprotéines avec $Glc_1Man_9GlcNAc_2$	Réticulum endoplasmique	Contrôle la biosynthèse des glycoprotéines
	Calreticulin2			

Tableau 2 : Les différentes familles de lectines animales

1.3 Les carbohydrates

Les quatre principales classes de molécules organiques dans les systèmes vivants sont les protéines, les lipides, les acides nucléiques et les carbohydrates (ou glucides). Les carbohydrates sont les molécules organiques les plus importantes dans la nature et une majorité

des organismes vivants synthétisent et métabolisent ces glucides[79]. Les carbohydrates sont la principale source d'énergie ingérée par le corps humain. Ils sont transportés par les vaisseaux sanguins vers toutes les cellules de l'organisme pour participer au métabolisme énergétique[80]. Ils peuvent augmenter le temps de circulation sanguine de certaines protéines recombinantes en diminuant leur clairance par les reins[81] et permettre le passage de certaines barrières biologiques, comme la barrière hémato-encéphalique[82]. De plus, les carbohydrates peuvent être liés entre eux ou à d'autres molécules biologiques pour former des glycoconjugués : les glycoprotéines et les glycolipides qui sont les glycoconjugués les plus abondants dans les cellules animales et représentent les principaux ligands des lectines.

1.4 Les lectines comme cible thérapeutique

De plus en plus de stratégies thérapeutiques sont basées sur ce type d'interaction carbohydrates-lectines : ce concept a été établi pour la première fois en 1988 par Woodley et Naisbett qui ont proposé d'utiliser la lectine de tomate pour cibler la surface luminale de l'intestin grêle[83]. A partir de ces travaux, deux principaux types de ciblage ont été mis au point : le ciblage direct et le ciblage indirect. Le ciblage direct consiste à conjuguer le principe actif à un ou plusieurs carbohydrates qui seront reconnus par les lectines endogènes exprimées à la surface des cellules. Concernant le ciblage indirect, le principe actif est couplé à des lectines exogènes qui reconnaîtront, dans ce cas, les glycoconjugués présents à la surface des cellules (Figure 6).

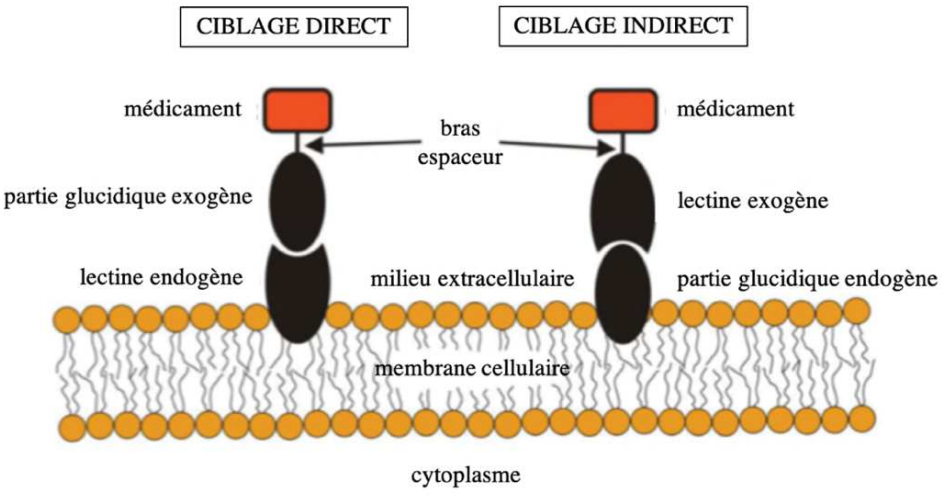

Figure 6 : Schéma illustrant les ciblages direct et indirect des lectines[81]

Dans ce manuscrit, nous allons nous intéresser plus particulièrement au ciblage direct des lectines. Ce ciblage est basé sur l'exploitation de l'expression des lectines à la surface des cellules malades dans le but d'adresser spécifiquement le médicament. Pour le traitement des cancers, il existe de nombreux exemples de ce type d'interaction comme le ciblage du récepteur CD44 qui peut lier l'acide hyaluronique et dont la surexpression a été démontrée dans différents types de cancers comme les mélanomes, les lymphomes, le cancer du sein, le cancer colorectal et le cancer des poumons[84–88]. Ce récepteur est connu pour jouer un rôle dans les processus d'invasion du cancer et les propriétés métastasiques. De nombreuses études ont montré que ce récepteur pouvait être ciblé, par exemple avec des liposomes fonctionnalisés par de l'acide hyaluronique dans lesquels a été encapsulé de la doxorubicine ou de la mitomycine C. L'efficacité thérapeutique du ciblage du récepteur a été démontré *in vitro* sur des lignées de cellules cancéreuses humaines[89] et *in vivo* chez des modèles de souris[90].

D'une manière générale, des études ont montré que les lectines étaient présentes à la surface des cellules cancéreuses et que leur profil d'expression était modulé[91]. De plus, certaines lectines jouent un rôle important dans le cancer car elles contribuent à l'angiogenèse et la perte de l'adhésion cellulaire permettant la formation de métastases[92,93]. Dans ce manuscrit, nous nous concentrerons sur le ciblage d'une lectine en particulier : le récepteur du mannose 6-phosphate cation indépendant.

2. Les récepteurs du mannose 6-phosphate (RM6P)

Deux RM6P ont été décrits : le récepteur du mannose 6-phosphate cation-dépendant (RM6P-CD) et le récepteur du mannose 6-phosphate cation-indépendant (RM6P-CI). Tous les deux composent les seuls récepteurs de la famille des lectines P et appartiennent à la famille des glycoprotéines transmembranaires de type I. Le clonage de leur ADN complémentaire a permis de définir leur structure, représentée schématiquement dans la figure 7 et qui est composée d'une séquence signal, d'un domaine extracellulaire (extrémité N-terminale), d'une région transmembranaire hydrophobe et d'un domaine cytoplasmique (extrémité C-terminale)[94].

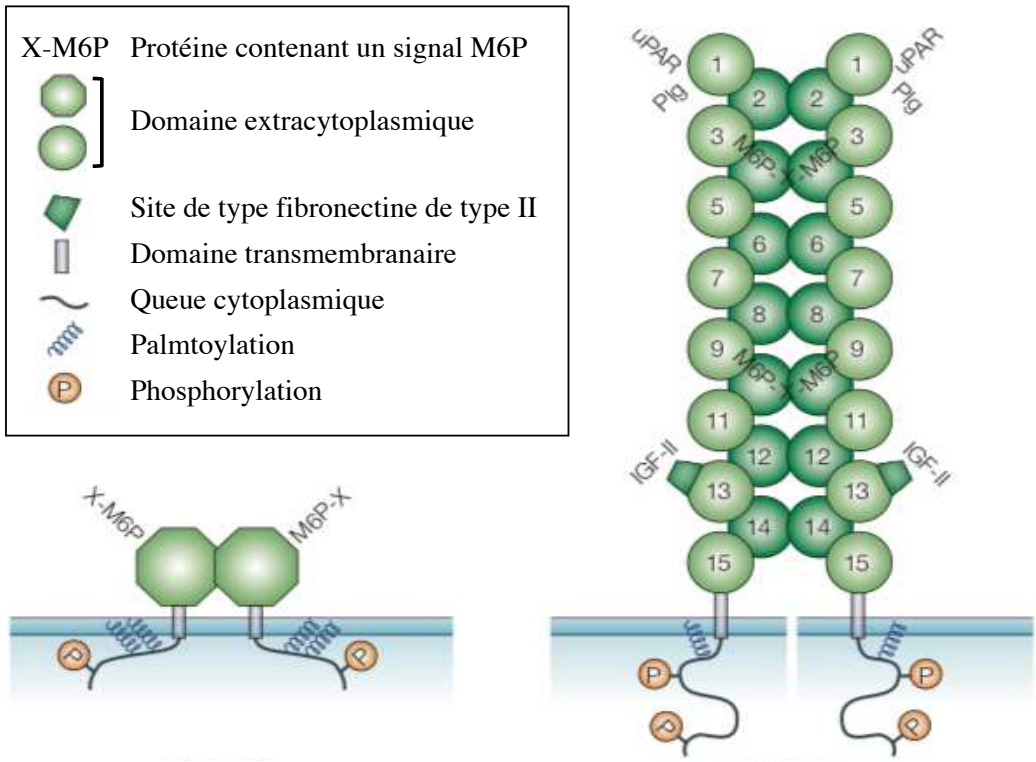

Figure 7 : Structure des récepteurs du mannose 6-phosphate[95]

2.1 Le RM6P-CD

2.1.1 Structure

Le RM6P-CD est de faible poids moléculaire (46 kDa) et il est caractérisé de cation-dépendant car il a besoin de cations divalents pour lier le ligand. L'analyse séquentielle du RM6P-CD humain a montré qu'il était composé d'une séquence signal en N-terminal de 20 résidus, un domaine transmembranaire de 19 résidus, un domaine extracellulaire de 164 résidus et d'une extrémité C-terminale de 68 résidus[96]. Ce récepteur possède cinq sites de glycosylation sur le domaine extracellulaire, dont au moins quatre sont utilisés, et aucun site de glycosylation sur le domaine intracellulaire. Son domaine extracellulaire est similaire aux quinze domaines répétés du RM6P-CI indiquant que ces deux récepteurs proviennent d'un gène ancestral commun[97]. Il est sous la forme d'un homodimère non covalent dans la membrane[75] et sous forme de dimère ou tétramère en solution[98]. Il peut être internalisé comme le RM6P-CI : les séquences d'internalisation sont situées dans l'extrémité C-terminale[99].

2.1.2 Fonctions

Le RM6P-CD reconnaît le mannose 6-phosphate (M6P) comme ligand et c'est le seul ligand connu à ce jour. Le RM6P-CD participe au transport des enzymes lysosomales synthétisées au niveau du réseau trans-golgien vers les endosomes qui les transfèrent jusqu'aux lysosomes. Ce récepteur n'a aucune fonction transmembranaire même s'il peut être présent à la membrane[100] car il ne possède pas la capacité de lier et d'internaliser les enzymes au pH extracellulaire qui est de 7,4[101].

2.2 Le RM6P-CI

2.2.1 Structure

Le RM6P-CI est de haut poids moléculaire (300 kDa). Il est composé d'une séquence signal en N-terminal de 40 résidus, un domaine transmembranaire de 23 résidus, un domaine extracellulaire de 2264 résidus composés de 15 domaines répétitifs contenant les sites de liaison des ligands, et d'une extrémité C-terminale de 164 résidus[102]. Le domaine extracellulaire a dix-neuf sites de glycosylation potentiels[103]. Le RM6P-CI est sous forme de dimère à la membrane et sous forme de monomère en solution[104].

2.2.2 Fonctions

Le RM6P-CI est principalement localisé dans les compartiments intracellulaires (90 à 95%), en particulier dans le réseau trans-golgien et les endosomes, 5 à 10% étant présent à la surface des cellules[97]. Ce récepteur participe donc, comme le RM6P-CD, au transport des enzymes lysosomales synthétisées vers le lysosome. De plus, le RM6P-CI participe à l'endocytose des molécules ayant un signal M6P, mais également d'autres ligands. En effet, la spécificité de ce récepteur est dans la nature des ligands qu'il est capable de lier : les ligands peuvent être de nature lipidique (acide rétinoïque), protéique (Insulin-like Growth Factor II ou IGF-II) et glucidique (M6P) sur des sites de liaison bien distincts.

- L'acide rétinoïque

L'acide rétinoïque est la forme active de la vitamine A. Il est impliqué dans de nombreux processus biologiques comme la croissance cellulaire, la différenciation et l'apoptose

cellulaire[105]. Ce ligand se fixe sur la partie C-terminale du récepteur[106] et permet de favoriser la liaison du M6P, ceci est également vrai dans le sens inverse[107].

- L'IGF-II

L'IGF-II est un facteur de croissance impliqué dans le contrôle de la croissance cellulaire. Le récepteur est capable de lier en même temps l'IGF-II et le M6P c'est pour cela que le RM6P-CI est également appelé : le « mannose 6-phosphate/insulin-like growth factor II receptor ». Le récepteur lie sur le domaine 11 l'IGF-II entraînant son internalisation afin qu'il soit dégradé dans les lysosomes[108]. Les sites de liaisons du M6P et de l'IGF-II sont distincts mais la liaison de chacun peut influencer la liaison de l'autre : c'est le cas des enzymes lysosomales qui portent le signal M6P et qui altèrent la liaison de l'IGF-II. Ceci a été démontré avec la cathepsine D : la liaison de la cathepsine D va interférer avec l'IGF-II qui se déplace alors vers le récepteur à l'IGF-I entraînant un effet mitogène[109]. Des études indiquent que le RM6P-CI joue un rôle primordial dans la croissance et la motilité des cellules. L'importance de la dégradation de l'IGF-II a été démontrée chez des souris knock-out pour le RM6P-CI qui présentaient des taux élevés d'IGF-II dans la circulation sanguine et une augmentation de la taille des organes. Ces souris mourraient alors à la naissance suite à une insuffisance cardiaque due à une cardiomégalie. Cependant si le gène du récepteur de l'IGF-II est également invalidé, les souris ne meurent plus à la naissance ce qui démontre que la dégradation de l'IGF-II est une fonction essentielle et vitale du récepteur[110–112].

- Le M6P

Le récepteur est capable de lier deux molécules de M6P ou une chaîne oligosaccharidique diphosphorylée par monomère. Sur les 15 unités répétitives qui composent la partie extracellulaire du récepteur, seulement les domaines 1-3 et 7-11 sont impliqués dans la liaison du M6P[113]. Plus précisément il a été démontré le rôle primordial des domaines 3 et 9 dans la liaison du M6P[114]. De plus le récepteur est capable de lier toutes autres molécules ayant un signal M6P répertoriés dans le tableau 3.

Ligands	Fonction du RM6P-CI	Maladies ou processus biologiques associés
Ligand avec un signal M6P		
Enzymes lysosomales	Biogenèse des lysosomes Dissémination tumorale	Maladies lysosomales Métastases
Complexe TGFß latent	Activation de TGFß	Cicatrisation
Granzyme B	Endocytose et apoptose	Réponse immunitaire
Facteur inhibiteur de leucémie et facteur de stimulation des colonies de macrophages	Endocytose et dégradation dans lysosome	Désordres hématopoïétiques, myélomes, maladie de Castelman, polycythémie
Prolifférine	Croissance cellulaire et angiogenèse	Fibrosarcomes
Glycoprotéine du virus de l'herpès (gD)	Endocytose des virus	Infection virale
Rénine	Internalisation de la (pro)rénine cardiaque	Désordres cardiovasculaires
Ligands sans signal M6P		
IGF-II	Endocytose et dégradation dans le lysosome	Croissance cellulaire dans l'embryogenèse et oncogenèse
Récepteur urokinase (uPAR) et plasminogène	Régulation de uPAR à la surface cellulaire, activation de l'urokinase (uPA)	Fibrinolyse, adhésion et migration cellulaire
Acide rétinoïque	Modulation de l'action de l'acide rétinoïque	Croissance cellulaire dans l'embryogenèse et oncogenèse

Tableau 3 : Récapitulatif des différents ligands et fonctions du RM6P-CI[115]

3. Ciblage du RM6P-CI pour le traitement des maladies lysosomales et des cancers

3.1 RM6P-CI et maladies lysosomales

Nous avons vu que les RM6P étaient des récepteurs indispensables permettant l'acheminement des enzymes lysosomales vers les lysosomes. Les lysosomes sont des organites intracytoplasmiques présents dans toutes les cellules nucléées. Ils constituent les compartiments acides de la cellule qui établissent la communication entre le milieu extracellulaire et intracellulaire par le biais de l'endocytose, la phagocytose et l'exocytose. La fonction principale des lysosomes est la dégradation et le recyclage de molécules intracellulaires par les enzymes lysosomales. Les enzymes ont une activité optimale à un pH acide (5,2 à 5,5) qui correspond au pH à l'intérieur des lysosomes : les enzymes sont donc aussi appelées hydrolases acides. On dénombre une cinquantaine d'enzymes lysosomales (phosphatases, glycosidases, lipases, nucléases, sulfatases et protéases) qui sont caractérisées par un ou plusieurs signaux M6P leur permettant d'être acheminées vers les lysosomes *via* les RM6P. Il existe deux voies de transport des enzymes lysosomales vers les lysosomes :

- le transport du réseau trans-golgien,
- l'endocytose des enzymes extracellulaires.

3.1.1 Le transport du réseau trans-golgien vers les lysosomes

Ce transport correspond à la voie de biosynthèse des enzymes lysosomales. Ces enzymes sont synthétisées par les polysomes liés à la membrane du réticulum endoplasmique rugueux (RER). Chacune de ces protéines contient un signal peptide hydrophobe en position N-terminale qui permet le transport de la protéine en cours de traduction vers la lumière du RER[116]. Une fois dans le RER, les enzymes vont perdre le peptide signal et subir des modifications post-traductionnelles, appelées glycosylation qui ont pour but d'additionner des oligosaccharides. Cette addition est appelée N-glycosylation car elle a lieu sur le groupement amine d'un résidu asparagine (Asn ou N). L'oligosaccharide est composé de trois glucoses, neuf mannoses et deux résidus N-acétyl-glucosamine ($Glc_3Man_9GlcNac_2$)[117]. Par des transports vésiculaires, les glycoprotéines se dirigent vers l'appareil de Golgi où l'oligosaccharide va être maturé par clivage et addition de sucres pour diversifier les oligosaccharides sur chaque type

de glycoprotéines[118]. Dans le cas des enzymes lysosomales, elles vont acquérir le signal M6P grâce à l'action de deux enzymes[119] (Figure 8):

- la N-acétylglucosamine-1-phosphotransférase (ou phosphotransférase) qui permet la liaison d'un résidu N-acétylglucosamine-1-phosphate en position 6 d'un mannose,
- la N-acétylglucosamine-1-phosphodiester α-N-acétylglucosaminidase (phosphoglycosidase) qui hydrolyse le résidu Glc-NAc pour laisser apparaître la fonction monoester M6P.

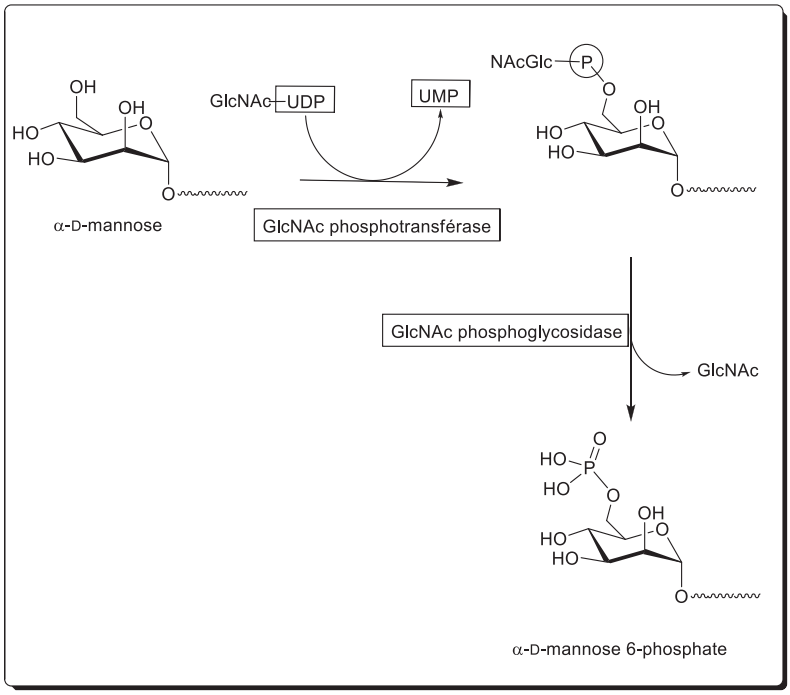

Figure 8 : Acquisition du signal mannose 6-phosphate par une enzyme lysosomale

Grâce au signal M6P, les enzymes lysosomales peuvent se lier au RM6P-CD mais vont majoritairement se lier au RM6P-CI au niveau du réseau trans-golgien à pH 7. Des clathrines, protéines structurelles constituant l'enveloppe des vésicules, se fixent au RM6P-CI et forment des vésicules qui vont transporter le complexe pro-enzyme/RM6P-CI vers les prolongations du Golgi puis les endosomes précoces pour finir dans les endosomes tardifs. Le pH acide des endosomes tardifs (pH entre 5 et 7) permet la dissociation du complexe pro-enzyme/RM6P-CI, les enzymes vont alors pouvoir se diriger vers les lysosomes où elles seront déphosphorylées[120]. Après avoir libéré les enzymes, les RM6P sont recyclés dans des vésicules de transport qui bourgeonnent des endosomes tardifs vers la membrane du réseau trans-golgien pour être réutilisés pour un nouveau cycle de transport. Le RM6P-CI est également envoyé vers la

membrane plasmique afin d'internaliser les enzymes extracellulaires ayant échappées au processus de transport du réseau trans-golgien vers les lysosomes[121].

3.1.2 L'endocytose des enzymes extracellulaires

Une partie des enzymes lysosomales échappe au processus décrit précédemment et sont par conséquent sécrétées à l'extérieur de la cellule. Le RM6P-CI à la membrane plasmique joue alors un rôle primordial dans l'endocytose de ces enzymes sécrétées. Le transport du complexe pro-enzyme/RM6P-CI depuis la membrane plasmique vers les lysosomes s'effectue globalement comme celui du réseau trans-golgien. Des protéines adaptatrices AP2 reconnaissent des signaux cytosoliques du récepteur et vont pouvoir se fixer sur le complexe pro-enzyme/RM6P-CI afin de recruter des clathrines qui vont recouvrir la membrane plasmique pour qu'elle puisse bourgeonner et former des vésicules qui contiennent le complexe[122]. Les vésicules sont alors dirigées vers les endosomes précoces puis tardifs où le complexe va se dissocier à pH acide. Les enzymes libérées sont ensuite acheminées vers les lysosomes et les récepteurs seront recyclés vers la membrane plasmique ou le réseau trans-golgien. La figure 9 représente schématiquement les deux voies de transport des enzymes lysosomales.

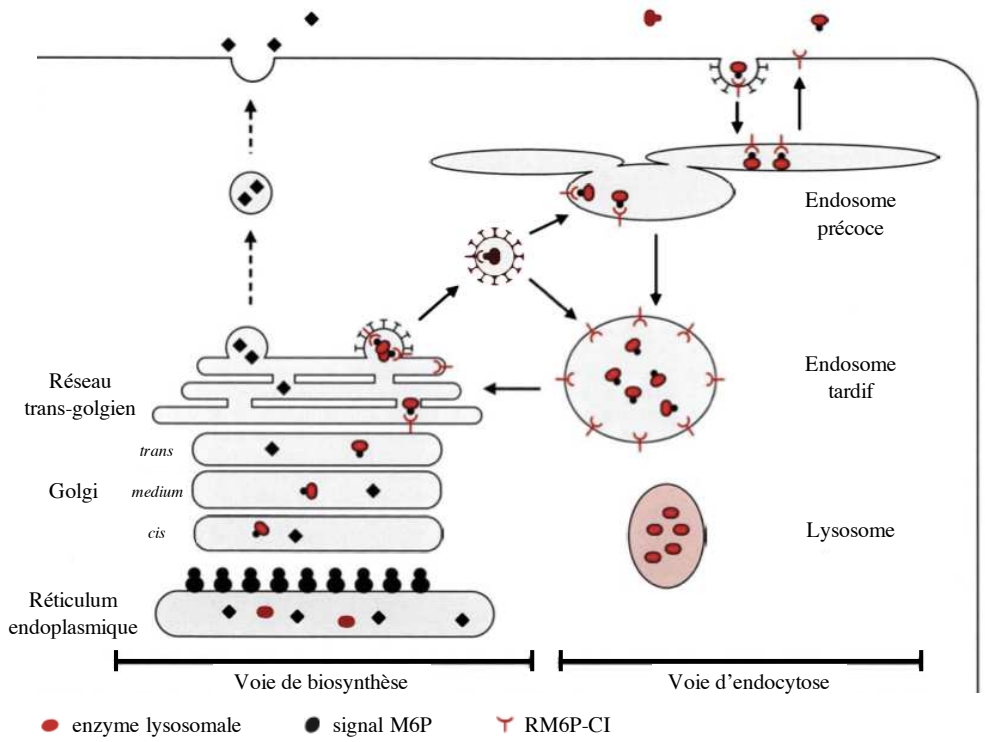

Figure 9 : Les deux voies de transport des enzymes lysosomales vers les lysosomes[123]

3.1.3 *Cible thérapeutique pour les maladies lysosomales*

Une des applications majeures du ciblage du RM6P-CI est le traitement des maladies lysosomales. On dénombre aujourd'hui une cinquantaine de maladies lysosomales qui sont des maladies génétiques. Chaque maladie lysosomale est liée à l'absence ou la déficience d'une enzyme lysosomale spécifique dont la conséquence est l'accumulation du substrat de cette enzyme dans le lysosome. Nous avons vu précédemment que le RM6P-CI est responsable de l'acheminement des enzymes lysosomales ainsi que des ligands ayant un signal M6P jusqu'aux lysosomes. De Duve a alors proposé en 1964 que les déficiences en enzymes lysosomales pourraient être rectifiées en administrant une enzyme exogène[124]. Aujourd'hui, neuf maladies lysosomales sont traitées par enzymothérapie substitutive[125]. Cependant, le ciblage par le M6P présente quelques limites dont :

- l'instabilité du signal M6P dans le sang car il est sensible aux phosphatases sériques empêchant un adressage efficace aux organes[126],
- l'incapacité à apporter les enzymes administrées à certains tissus spécifiques de la maladie comme le système nerveux central *via* la barrière hémato-encéphalique[127],
- le coût annuel du traitement estimé entre 87000 et 600000 euros par patient selon la maladie[128].

L'inconvénient majeur du M6P est la sensibilité aux phosphatases présentes dans le sérum mais également dans tous les organes entraînant une déphosphorylation : le M6P ne peut plus être reconnu par le RM6P-CI. Il s'en suit une diminution de l'adressage de l'enzyme aux organes ainsi qu'une augmentation des doses administrées au patient (et donc du coût du traitement). La stabilité de ce signal est donc un élément indispensable pour son utilisation dans le transport de molécules bioactives. Afin d'éviter cette déphosphorylation, les équipes du Professeur Alain Morère et du Docteur Marcel Garcia ont développé des analogues du M6P où le phosphate est remplacé par un phosphonate, un carboxylate, un malonate ou un sulfate. Ces analogues, appelés AMFA (Analogue du Mannose 6-phosphate Fonctionnalisé sur l'Aglycone), ont été brevetés puis l'entreprise NanoMedSyn a acquis une licence exclusive d'exploitation. Dans le cadre de cette thèse, nous avons étudié ces analogues pour le ciblage du RM6P-CI pour le traitement d'une maladie lysosomale : la maladie de Pompe.

3.2 Cible thérapeutique pour le traitement des cancers

La capacité du RM6P-CI à interagir avec plusieurs facteurs de croissance impliqués dans la cancérogenèse tels que l'IGF-II et le TGFß1 indique qu'il pourrait être un gène suppresseur de tumeur car il aurait un pouvoir régulateur négatif sur la prolifération cellulaire. En effet, l'IGF-II est capable de se lier au RM6P-CI mais également au récepteur de l'IGF-I. Le RM6P-CI permet la dégradation de l'IGF-II et joue ainsi un rôle d'inhibiteur et de modulateur de la croissance cellulaire car l'IGF-II ne peut plus se fixer sur le récepteur de l'IGF-I qui est le seul à pouvoir envoyer un signal de prolifération à la cellule. Plusieurs études ont démontré que le RM6P-CI pourrait être potentiellement un gène suppresseur de tumeur car il a été observé dans différents types de cancers (hépatocarcinomes[129], seins[130], poumon[131], ovaire[132], tumeurs adéno-corticales[133], carcinomes épidermoïques[134]) et il présentait une altération de fonction suite à une perte d'hétérozygotie du gène et de mutations sur l'allèle restant participant à la progression tumorale. Cette perte d'hétérozygotie entraîne une diminution de l'expression du récepteur par rapport aux tissus sains. Cependant, pour que le RM6P-CI soit une bonne cible thérapeutique, il faut que le récepteur soit surexprimé à la membrane lorsque la cellule devient cancéreuse, ainsi nous pourrions discriminer les cellules cancéreuses des cellules saines. La surexpression du RM6P-CI a été démontrée dans plusieurs lignées cellulaires cancéreuses humaines ainsi que dans des tissus humains tels que le cancer du sein[135], du pancréas[136], gastrique[137], le mélanome[138] et le cancer de la prostate[139]. La première étude concernant la délivrance de drogues aux cellules cancéreuses *via* le RM6P-CI a été publiée par l'équipe de Jai Prakash en 2009[140] : l'albumine de sérum humain a été fonctionnalisée avec du M6P puis conjuguée avec de la doxorubicine (M6P-HSA-DOX). Cette étude a été menée sur des lignées cellulaires cancéreuses humaines de mélanome et de colon et a démontré que M6P-HSA-DOX était internalisée plus efficacement que la HSA non fonctionnalisée par le M6P et *via* une endocytose active par le RM6P-CI. L'efficacité du système ciblé a été évaluée *in vivo*, chez le modèle animal de la souris dans lequel des xénogreffes de tumeurs sous-cutanées ont été réalisées. Les résultats démontrent que le M6P-HSA-DOX s'accumule dans les tumeurs et permet la diminution significative de la tumeur par rapport à la doxorubicine libre qui est distribuée dans tous les organes sains. Cependant, cette étude ne montre pas de résultats sur HSA-DOX comme contrôle, alors qu'il aurait été indispensable de confirmer que l'efficacité thérapeutique du système ciblé est due à la fonctionnalisation du M6P et non pas seulement à l'encapsulation de la doxorubicine dans la HSA. Une autre étude menée au sein du laboratoire a permis de démontrer l'efficacité

thérapeutique de nanoparticules ciblées pour le ciblage du RM6P-CI dans le cas du traitement de la prostate[139]. La surexpression du RM6P-CI a été démontrée sur 84 % des tissus humains prostatiques (126 cas) tandis que dans les tissus humains normaux aucune surexpression n'a été observée (39 cas). Dans cette étude, l'équipe a fonctionnalisé un analogue du M6P sur des nanoparticules dans lesquelles a été encapsulé un photosensibilisateur pour permettre une thérapie photodynamique. Les résultats ont démontré une meilleure efficacité thérapeutique des nanoparticules ciblées comparées aux nanoparticules non fonctionnalisées avec l'analogue du M6P. Donc contrairement aux études réalisées sur différents types de cancers dans lesquelles le RM6P-CI était décrit comme étant un gène suppresseur de tumeur, ces deux dernières études ont montré que dans certains cas précis de cancers solides, la surexpression du RM6P-CI permettait de considérer ce récepteur comme une bonne cible thérapeutique. Dans ce manuscrit, nous étudierons le ciblage du RM6P-CI par des nanoparticules fonctionnalisées avec un analogue du M6P dans le cadre d'un cancer rare : le rhabdomyosarcome.

Chapitre 4 : Le rhabdomyosarcome

1. Les cancers pédiatriques

Les cancers pédiatriques sont des tumeurs malignes survenant chez l'enfant avant l'âge de 18 ans. Dans le monde, on dénombre entre 50 et 200 millions d'enfants qui sont atteints d'un cancer[141]. En France, 1700 nouveaux cas de cancers ont été diagnostiqués chez les enfants et les adolescents, et un enfant sur 440 sera atteint d'un cancer avant l'âge de 15 ans[142]. Le taux de guérison chez les enfants a considérablement augmenté et dépasse aujourd'hui 80% tous cancers confondus. Cependant, cette maladie reste la deuxième cause de mortalité des enfants de plus d'un an, après les accidents[143]. Les cancers pédiatriques sont complètement différents de ceux diagnostiqués chez les adultes : il s'agit de maladies rares (1 à 2% des cancers) et les principales localisations chez l'adulte (poumons, seins, prostate…) ne sont pas retrouvées chez les enfants. A l'heure actuelle, de nombreuses études ont cherché à comprendre les causes de l'apparition d'un cancer pédiatrique mais il est très rare que les facteurs environnementaux soient à l'origine d'un cancer et on estime qu'environ 10% des enfants ont une prédisposition génétique à développer un cancer : les recherches doivent donc se poursuivre pour déterminer exactement les facteurs impliqués. Les cancers pédiatriques les plus fréquents sont les leucémies (29%), les tumeurs cérébrales (25%) et les lymphomes (10%)[144,145]. Les cancers de l'enfant ont été répertoriés en différents groupes selon « l'International Classification of Childhood Cancer » (ICCC) et deux registres pédiatriques français enregistrent en continu des informations sur les cancers pédiatriques : le Registre National des Hémopathies malignes de l'Enfant (RNHE) dont l'enregistrement a commencé en 1990 et le Registre National de Tumeurs Solides de l'Enfant (RNTSE) qui a débuté en 2000 (Tableau 4). Dans ce manuscrit, nous nous concentrerons uniquement sur un cancer pédiatrique : le rhabdomyosarcome (RMS).

Groupes diagnostiques selon l'ICC	Effectif moyen annuel	En %	Incidence (par million)			
			< 1 an	1-4 ans	5-9 ans	10-14 ans
I. Leucémies	524	28,9%	35,7	71,5	38,3	29,4
II. Lymphomes	184	10,3%	1,1	7,5	13,8	27,1
III. Tumeurs du système nerveux central	442	24,9%	38,9	46	37,2	31,8
IV. Tumeurs du système nerveux sympathique	142	8%	72,8	21,7	3,4	1,5
V. Rétinoblastomes	48	2,7%	25,8	8,2	0,5	0
VI. Tumeurs rénales	98	5,5%	18,1	18	5,7	1,3
VII. Tumeurs hépatiques	20	1,1%	6,8	3	0,5	0,7
VIII. Tumeurs malignes osseuses	82	4,6%	0,5	1,5	5,5	14,4
IX. Sarcomes des tissus mous et extraosseux (dont RMS)	112	6,3%	16,6	12	8	7,8
X. Tumeurs germinales, trophoblastiques et gonadiques	60	3,4%	15,8	3,7	2,4	7,0
XI. Mélanomes malins et autres tumeurs malignes épithéliales	64	3,6%	2,1	2,1	3,0	11,4
XII. Autres tumeurs malignes	4	0,2%	2,1	0,6	0,2	0,1
Total	1770		236,3	195,8	118,3	132,5

Tableau 4 : Les différents types de cancer chez l'enfant et leur incidence sur la période 2010-2014[146,147]

2. Le rhabdomyosarcome

2.1 Généralités et épidémiologie

Le RMS est un sarcome des tissus mous. Les sarcomes sont des tumeurs malignes rares, appelées également tumeurs mésenchymateuses, qui apparaissent à partir des tissus mous situés dans n'importe quelle partie du corps. Les tissus mous relient, soutiennent et entourent les organes du corps humain. Ces tumeurs sont très hétérogènes car elles peuvent se développer à partir des tissus de soutien qu'ils soient conjonctifs, vasculaires, musculaires, nerveux ou adipeux. Le RMS a été décrit pour la première fois en 1854 par Weber : à l'heure actuelle c'est

le sarcome des tissus mous le plus courant chez les enfants (6% de l'ensemble des cancers pédiatriques) avec une incidence d'une centaine de cas par an en France. Néanmoins, comme tous les cancers de l'enfant, c'est une maladie rare. Il y a deux pics d'incidence : entre 2 et 5 ans et entre 15 et 19 ans avec une prédominance chez les garçons[148]. Le RMS se développe à partir du tissu musculaire squelettique normal : il peut donc se développer dans n'importe quelle partie du corps humain. Cependant, il y a des localisations plus fréquentes au niveau de la tête et du cou (40%), de l'appareil génito-urinaire (25%) et des membres (20%). La plupart des enfants atteints de RMS n'ont pas de facteur de risque connu pour développer un cancer. Cependant, un faible pourcentage de cas a été associé à des troubles génétiques connus tels que :

- le syndrome de Li-Fraumeni qui est associé à une mutation du gène p53 entraînant un risque accru de développer simultanément plusieurs cancers (tissus mous, seins, os, peau, cerveau, sang…)[149,150].
- La neurofibromatose de type 1 qui affecte le développement et la croissance des cellules nerveuses[151].
- Le syndrome de Beckwith-Widemann qui a un effet dès la deuxième moitié de grossesse : la croissance du fœtus est excessive avec une hypertrophie des organes[152].
- Le syndrome de Costello qui est dû à une mutation du proto-oncogène HAS qui est impliqué dans le contrôle de la croissance et de la division cellulaire entraînant un risque accru de développer un cancer. Ce syndrome entraîne un retard de croissance (petite taille, déficit intellectuel), une flexibilité des articulations, une dysmorphie faciale et une atteinte cardiaque et neurologique[153].

2.2 Les origines de la tumeur

2.2.1 Caractéristiques histologiques

Histologiquement, les RMS ont été classés en deux sous-types histologiques majeurs[154,155] :

- le RMS embryonnaire (60 à 70% des cas) qui touche généralement les enfants avant l'âge de 5 ans et qui apparaît préférentiellement au niveau de la région de la tête et du cou et de l'appareil génito-urinaire,

- le RMS alvéolaire (20 à 30% des cas) qui touche les enfants plus âgés et qui apparaît dans la région des membres et la région du périnée.

Il existe d'autres variantes, toutes considérées comme des sous-groupes du RMS embryonnaire, comprenant le sous-type botryoïde, le sous-type à cellules fusiformes et le sous-type pléomorphe, que l'on trouve principalement chez les adultes. Les RMS botryoïdes apparaissent sous la muqueuse des orifices corporels tandis que les RMS à cellules fusiformes sont le plus souvent observés dans la région para-testiculaire. Les patients atteints d'un RMS embryonnaire ont généralement un pronostic favorable alors que les patients atteints d'un RMS alvéolaire ont un pronostic défavorable avec un taux de survie à 5 ans inférieur à 50%[156].

2.2.2 Caractéristiques moléculaires

- Les RMS alvéolaires

Près de 80% des RMS alvéolaires sont associés à une translocation chromosomique entraînant un gène de fusion entre PAX3 (chromosome 1) ou PAX7 (chromosome 2) et FOXO1a (chromosome 13) provenant respectivement de la translocation chromosomique suivante : t(1;13)(q35;q14) et t(2;13)(p36;q14). La fusion des gènes schématisée dans la figure 10 montre que la région du point de rupture est la même pour PAX3 et PAX7. Pour FOXO1a, le point de rupture a lieu au niveau du domaine de liaison à l'ADN. La protéine de fusion est composée en N-terminal des deux domaines de liaison à l'ADN de PAX3 ou PAX7 (PB et HB) et en C-terminal du domaine de transactivation de FOXO1a. Par l'intermédiaire des domaines de PAX3, la protéine de fusion peut se lier à plus d'un millier de sites du génome, principalement des régions promotrices entraînant l'activation de plusieurs centaines de gènes. Il semblerait que ces gènes contribuent au développement tumoral en influant sur le contrôle de la croissance, de l'apoptose, de la différenciation et de la motilité des cellules cancéreuses[157]. En effet, PAX3 et PAX7 sont des facteurs de transcription qui ont un rôle dans la différenciation des cellules satellites musculaires en myoblastes[158,159]. Le rôle physiologique de FOXO1a est l'induction d'une réponse adéquate aux changements environnementaux pour maintenir l'homéostasie : pour cela FOXO1a induit la transcription de gènes qui affectent différents processus cellulaires comme le cycle cellulaire, la survie cellulaire et le métabolisme[160]. Environ 60 à 70% des RMS alvéolaires présentent le gène de fusion PAX3-FOXO1a alors que seulement 20% ont le gène de fusion PAX7-FOXO1a. La recherche de ce gène de fusion est

très importante pour le pronostic, en effet les RMS alvéolaires avec PAX3-FOXO1a sont nettement plus agressifs qu'avec PAX7-FOXO1a.

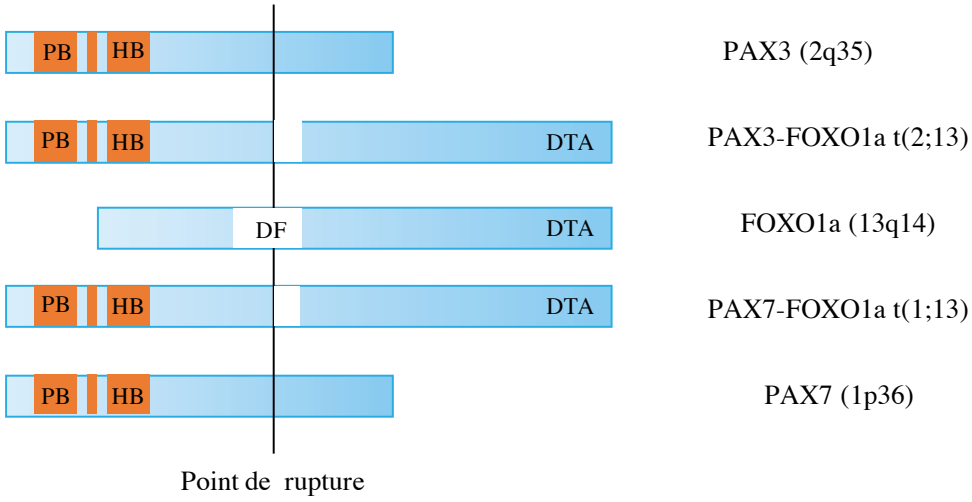

PB : domaine "paired-box" de liaison à l'ADN
HB : domaine homeobox de liaison à l'ADN
DF : domaine "Forkhead" de liaison à l'ADN
DTA: domaine de transactivation

Figure 10 : Schéma de la translocation chromosomique dans les RMS alvéolaires[155]

- Les RMS embryonnaires

Aucune translocation chromosomique n'est détectée dans les RMS embryonnaires. Cependant, une perte d'hétérozygotie est typiquement observée sur le chromosome 11 au niveau du locus 15 correspondant au gène codant pour l'IGF-II. Dans des conditions normales, une seule copie du gène est active tandis que l'autre est dite silencieuse. Dans le cas d'un RMS embryonnaire, une modification chimique de la structure de l'ADN, dans ce cas précis une méthylation va avoir lieu, entraînant l'activation de la copie du gène de l'IGF-II qui est normalement silencieuse. De plus, cette méthylation va permettre l'inactivation du gène voisin appelé H19 : ce gène est dans des conditions normales un suppresseur de croissance. La méthylation va donc entraîner l'activation de la copie silencieuse du gène IGF-II et l'inactivation du gène H19. Par conséquent, les deux copies de l'IGF-II sont actives entraînant une surexpression du facteur de croissance IGF-II et par conséquent un signal constant de prolifération qui ne sera plus régulé par H19 ce qui permettra le développement tumoral (Figure 11)[161,162].

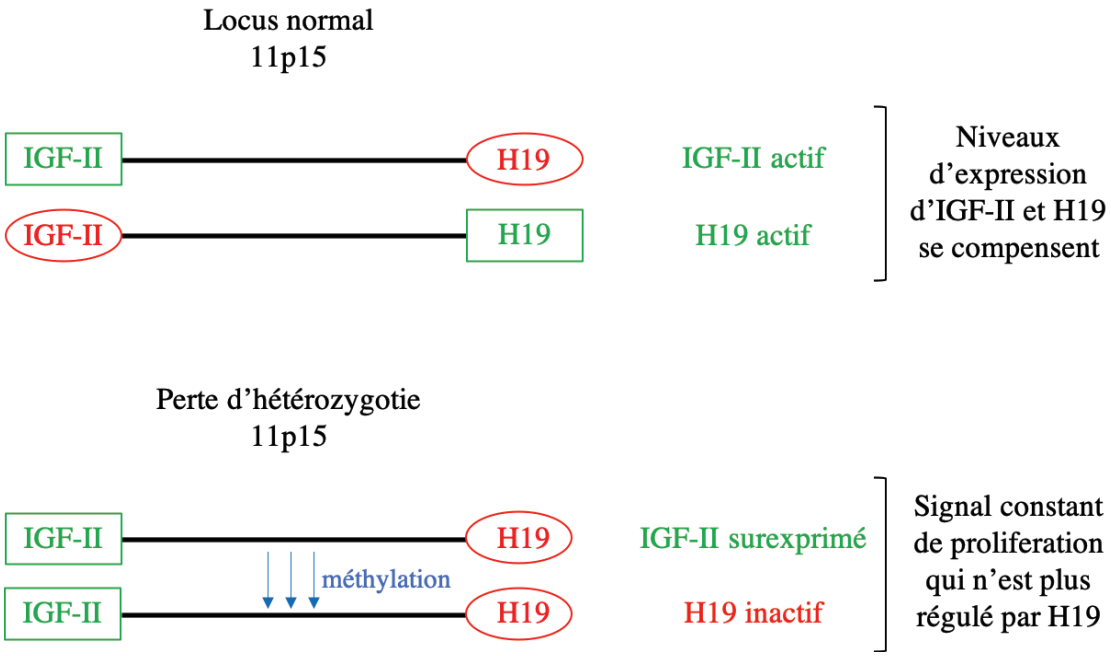

Figure 11 : Schéma de la perte d'hétérozygotie dans les RMS embryonnaires

2.2.3 Origine cellulaire

Comme nous l'avons décrit précédemment, les RMS sont des tumeurs du muscle strié squelettique. Ce muscle est constitué de fibres musculaires qui sont des cellules plurinucléées de forme polygonale dont les noyaux se situent en périphérie de la cellule. Chaque fibre est délimitée par une membrane (sarcolemme) et contient dans son cytoplasme (sarcoplasme) des myofibrilles qui permettent la contraction musculaire. Les myofibrilles ont une structure filamentaire régulière (myofilaments) qui donne l'aspect strié en microscopie. Lors de l'embryogenèse, des cellules non différenciées mononucléées appelées myoblastes vont fusionner pour former une fibre musculaire. Les myoblastes vont tout d'abord fusionner pour former un myotube où les noyaux seront en position centrale. Lorsque le myotube se différencie en fibre musculaire, les noyaux se déplacent vers la périphérie de la fibre appelée cellule musculaire (Figure 12).

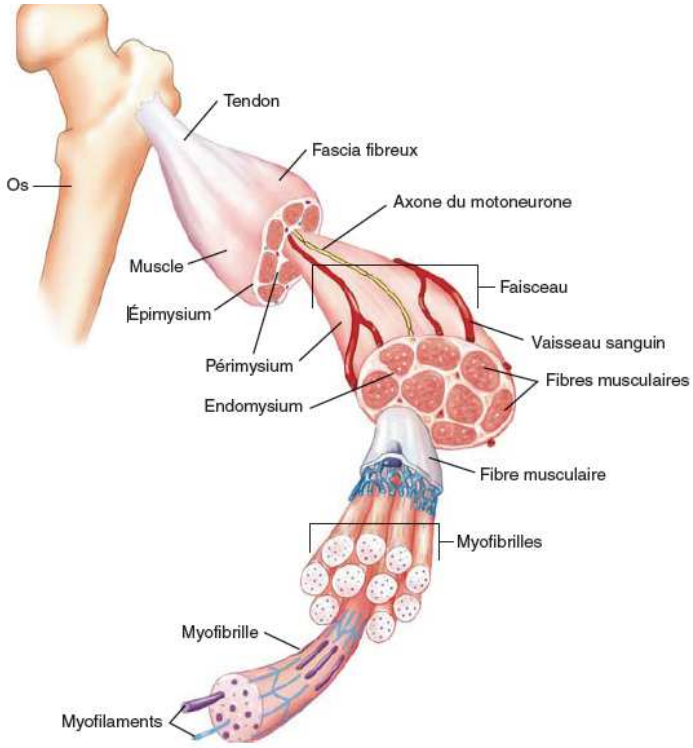

Figure 12 : Schéma d'un muscle strié squelettique

(http://www.toutsurlasarcopenie.fr/muscle/)

Bien que l'origine exacte du RMS ne soit encore pas totalement connue, il est suggéré que les cellules cancéreuses dérivent de cellules souches mésenchymateuses ou de cellules satellites musculaires[163]. En effet, de récentes études ont mis en évidence l'hétérogénéité des RMS suggérant qu'ils pourraient provenir d'origines diverses autres que musculaire comme les cellules souches mésenchymateuses. Ces cellules souches sont retrouvées dans de nombreux tissus et ont la capacité de circuler entre les organes offrant ainsi une possibilité d'apparition de RMS dans les tissus non musculaires ce qui pourrait expliquer l'hétérogénéité des RMS[164].

Dans l'embryon, les cellules mésodermiques génèrent des cellules myogéniques capables de se différencier pour produire les fibres musculaires squelettiques par l'action de facteurs de transcription myogéniques tels que PAX3 et PAX7. Cependant, une partie de ces cellules échappe à la différenciation musculaire et forme une population unique de cellules satellites qui agissent dans l'organisme comme des précurseurs myogéniques afin de maintenir la croissance musculaire si nécessaire. Par exemple, au cours d'une lésion musculaire, les cellules satellites, qui normalement sont quiescentes, vont s'activer pour se différencier et fusionner avec les myofibrilles déjà existantes *via* un processus hautement régulé impliquant

des facteurs myogéniques exprimés de manière séquentielle[165]. Selon différentes études, l'apparition d'un RMS est due à une perturbation de la croissance et de la différenciation des précurseurs myogéniques[166,167] (Figure 13).

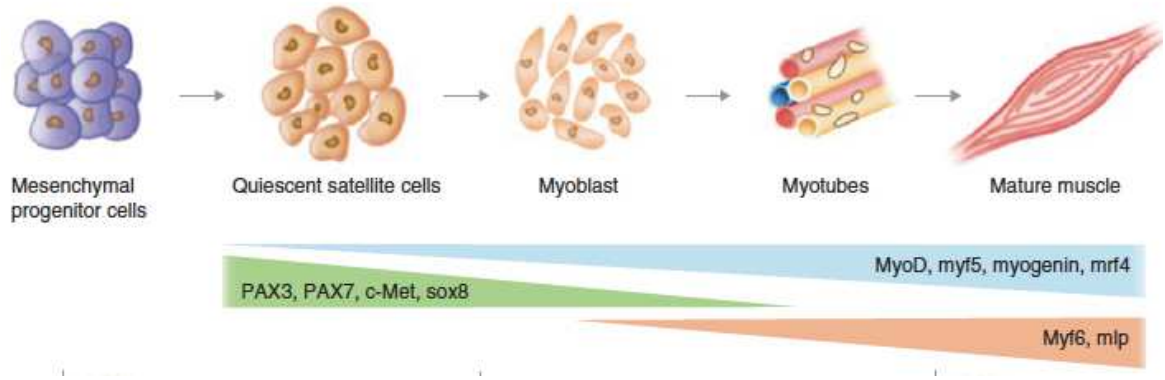

Figure 13 : Voies des facteurs myogéniques dans la tumorogenèse du RMS[168,169]

De plus, une analyse du transcriptome des cellules cancéreuses de RMS comparée à celui des cellules saines musculaires adultes et fœtales a été réalisée. Cette analyse a permis de démontrer un haut degré de similarité des profils d'expression entre les cellules de RMS et les cellules fœtales prouvant la nature myogénique indifférenciée des cellules cancéreuses. Plus précisément, les gènes exclusivement surexprimés dans le RMS (comme FGR4, NOTCH2, UBEC2, UHFR1 et YWHAB) contribuent à l'incapacité des cellules de mener à bien un développement normal du muscle et donc de progresser vers la tumorogenèse[170]. Le schéma d'expression des facteurs myogéniques régulant la différenciation myogénique a été étudié de manière approfondie dans les RMS. Tous ces facteurs sont activés au début ou pendant le processus de différenciation et sont ensuite inactivés pour achever la différenciation musculaire. Cependant, ces facteurs sont dérégulés dans le cas de RMS et restent activés en continu[171,172].

2.3 Symptômes et diagnostic

Un RMS est souvent indolore sauf en cas de métastases osseuses ou si la tumeur comprime la vessie. Les signes cliniques vont dépendre de la localisation de la tumeur[173] :

- les tumeurs touchant l'orbite vont entraîner une déviation de l'œil,
- les tumeurs qui touchent les sinus vont entraîner une sinusite chronique,
- les tumeurs de la vessie se manifestent par une rétention urinaire,

- pour les autres localisations, la tumeur est visible car elle forme une masse isolée.

Cependant si le RMS est d'emblée diffus, l'état général de l'enfant s'aggrave très rapidement (fièvre, anémie, problème de coagulation, douleurs osseuses).

Le diagnostic d'un RMS se fait après un examen clinique du médecin et des examens d'imagerie. Les examens d'imagerie (échographie, scanner, IRM, scintigraphie osseuse) sont indispensables car ils permettent de préciser la localisation de la tumeur et ses rapports anatomiques avec les organes environnants, ainsi que de rechercher une atteinte ganglionnaire et des métastases. De manière systématique, une biopsie est réalisée pour permettre un examen histologique afin de confirmer la malignité de la tumeur ainsi que le type de RMS (embryonnaire ou alvéolaire)[174] :

- les cellules cancéreuses d'un RMS seront positives au marquage de la myogénine[175],
- un RMS embryonnaire présente des cellules fusiformes en faible densité,
- un RMS alvéolaire présente des cellules plus petites, rondes et regroupées en amas séparées par des septa fibreux. Ces cellules ont l'aspect des cellules alvéolaires des poumons d'où le nom de RMS alvéolaire (Figure 14).

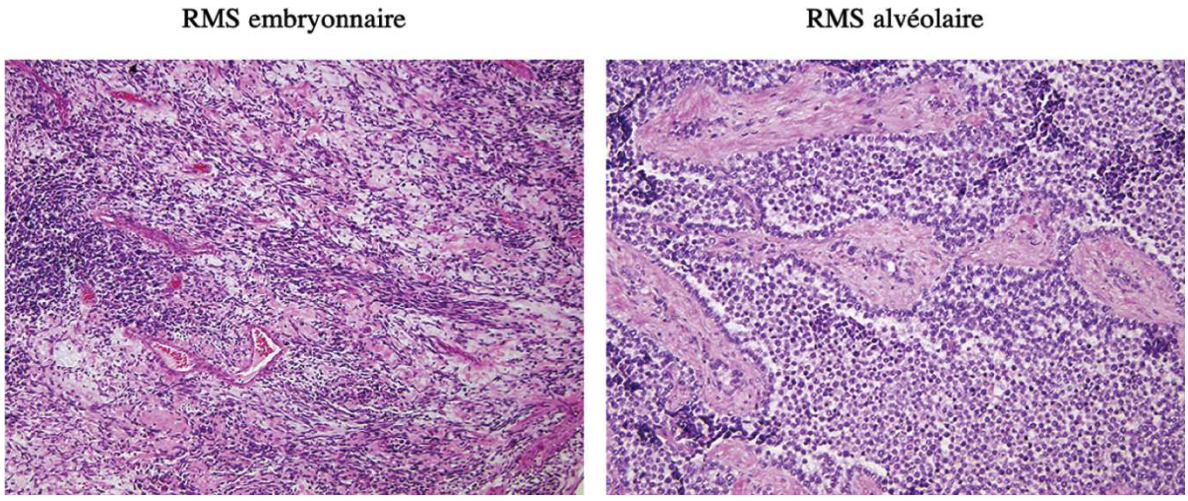

Figure 14 : Coupes histologiques des RMS principaux[176]

La mise en évidence de la translocation chromosomique t(2,13) est également recherchée pour confirmer un RMS alvéolaire[177]. De plus, les antécédents familiaux de l'enfant sont analysés afin de rechercher certains troubles génétiques décrits précédemment (syndrome

de Li-Fraumeni, de Beckwith-Wiedemann, de Costello, de Noonan, neurofibromatose de type 1).

2.4 Classification des rhabdomyosarcomes

Les RMS n'évolueront pas de la même manière suivant leur localisation, leurs caractéristiques histologiques, leur taille, l'absence ou la présence de métastases et l'âge du patient au moment du diagnostic. Ces facteurs sont appelés pronostiques car ils permettent d'évaluer les probabilités de guérison. Les médecins utilisent deux types de terminologie pour décrire ces facteurs : le stade et le groupe clinique.

2.4.1 Les stades

Les stades dépendent de trois facteurs[178] :

- la partie du corps dans laquelle la tumeur initiale s'est formée. La localisation est classée comme étant favorable (orbite, paupière, région tête et cou sauf région proches des méninges, appareil génito-urinaire sauf la vessie et la prostate) ou défavorable (vessie, prostate, zone paraméningée, membres, tronc, partie arrière de l'abdomen),
- la taille de la tumeur initiale symbolisée par les lettres a (< 5 cm) ou b (> 5 cm),
- l'atteinte ganglionnaire,
- la présence ou absence de métastases.

Les stades sont répertoriés selon la classification TNM qui est un système international proposé par le chirurgien français Pierre Denoix en 1940[179]. Les trois lettres font référence à la propagation de la tumeur sur le site initial (T), dans les ganglions lymphatiques (N) et à distance pour la formation de métastases (M). Chaque lettre est associée à un coefficient :

- T0 (tumeur initiale localisée) à T4 (tumeur étendue aux tissus environnants). Ces coefficients dépendent du volume de la tumeur calculé selon le diamètre de la tumeur et la fixation aux organes voisins,
- N0 (les ganglions ne sont pas atteints), N1 (les ganglions sont atteints) ou NX (pas de données sur les ganglions),
- M0 (absence de métastases) ou M1 (présence de métastases),

Le tableau 5 répertorie le système de classification pour les RMS.

Stade	Localisation	Statut T	Taille	Etat des ganglions	Métastases
1	Favorable	T1 ou T2	a et b	N0, N1 ou NX	M0
2	Défavorable	T1 ou T2	a	N0 ou N1	M0
3	Défavorable	T1 ou T2	a	N1	M0
			b	N0, N1 ou NX	
4	Tous les sites	T1 ou T2	a et b	N0 ou N1	M1

Tableau 5 : Système de classification du stade pour les patients atteints de RMS[180]

2.4.2 Les groupes

Quatre études cliniques, appelées « Intergroup Rhabdomyosarcoma Study » (IRS), sur des patients atteints de RMS réalisées entre 1972 et 1997 ont permis de catégoriser les RMS en groupes cliniques basés sur la qualité de la résection chirurgicale initiale[181,182,183]. En effet, après les examens d'imagerie lors du diagnostic, le chirurgien peut décider de réséquer totalement la tumeur. Après cette chirurgie initiale, les patients sont classés selon les groupes cliniques présentés dans le tableau 6.

Groupe	Incidence	Définition
I	13%	Tumeur localisée avec résection complète et pas d'atteinte ganglionnaire
II	20%	Tumeur localisée, cellules tumorales résiduelles après résection : (a) pas d'atteinte ganglionnaire locale (b) ganglions positifs réséqués localement (c) ganglions positifs réséqués localement mais atteinte d'un ganglion éloigné de la tumeur
III	49%	Tumeur localisée, tumeur résiduelle après résection, ganglions atteints localement
IV	18%	Pas de résection et présence de métastases

Tableau 6 : Système de classification des groupes cliniques de patients atteints de RMS

2.4.3 Modes de propagation

Les RMS peuvent se propager localement, de manière régionale ou à distance :

- localement, la tumeur va infiltrer les tissus environnants,
- de manière régionale, la tumeur va atteindre les ganglions qui drainent la zone de la tumeur initiale, ceci est observé pour des RMS qui se sont développés au niveau des membres et de la zone para-testiculaire,
- à distance, les cellules cancéreuses vont pouvoir se détacher de la tumeur initiale, et être disséminées par les vaisseaux sanguins pour atteindre une autre partie du corps et former des métastases. Les organes les plus courants sont les poumons, les os et la moelle osseuse[184].

2.4.4 Groupes de risque

Quand le diagnostic est posé (imagerie, biopsie, histologie, classe et groupe connus), il est possible de déterminer un pronostic et de classer les patients dans quatre groupes à risque. Ce classement est réalisé en fonction du stade, du groupe, du type histologique (embryonnaire ou alvéolaire), de la présence ou de non de métastases et de l'âge du patient. Ces informations sont très importantes pour déterminer la curabilité du RMS et adapter au mieux le traitement. Les groupes ont été organisés suivant les études cliniques IRS[185–189] :

- Risque standard, sous-groupe A : ces patients ont un taux de survie de 85% après un traitement de chimiothérapie peu intensif.
- Risque standard, sous-groupe B : ces patients ont un taux de survie de 80% après un traitement de chimiothérapie combinant trois médicaments et généralement de la radiothérapie.
- Risque intermédiaire : ce groupe représente la majorité des patients qui ont un taux de survie de seulement 50% après une chimiothérapie combinant trois médicaments et de la radiothérapie.
- Risque élevé : ce groupe représente les patients atteints de RMS alvéolaire et embryonnaire métastatiques. Ces patients reçoivent une chimiothérapie très agressive, de la radiothérapie et de la chirurgie mais le taux de guérison est de seulement 20%. Les enfants de moins d'un an atteint d'un RMS embryonnaire métastatique ont un taux de survie inférieur à 20%.

Le tableau 7 résume la classification des RMS.

Risque	Stade	Groupe	Localisation	Taille	Histologie	Métastases	Ganglions
Standard Sous-groupe A	1	I	Favorable	a ou b	Embryonnaire	M0	N0, N1 ou NX
	1	II	Favorable	a ou b	Embryonnaire	M0	N0 ou NX
	1	III	Seulement l'orbite	a ou b	Embryonnaire	M0	N0 ou NX
	2	I	Défavorable	a	Embryonnaire	M0	N0 ou NX
Standard Sous-groupe B	1	II	Favorable	a ou b	Embryonnaire	M0	N1
	1	III	Seulement l'orbite	a ou b	Embryonnaire	M0	N1
	1	III	Favorable (sauf orbite)	a ou b	Embryonnaire	M0	N0, N1 ou NX
	2	II	Défavorable	a	Embryonnaire	M0	N0 ou NX
	3	I ou II	Défavorable	a	Embryonnaire	M0	N1
	3	I ou II	Défavorable	a	Embryonnaire	M0	N0, N1 ou NX
Intermédiaire	2	III	Défavorable	a	Embryonnaire	M0	N0 ou NX
	3	III	Défavorable	a	Embryonnaire	M0	N1
	3	III	Défavorable	a ou b	Embryonnaire	M0	N0, N1 ou NX
	1, 2 ou 3	I, II ou III	Favorable ou défavorable	a ou b	Alvéolaire	M0	N0, N1 ou NX
	4	IV	Favorable ou défavorable	b	Embryonnaire	M1	N0, N1 ou NX
Elevé	4	IV	Favorable ou défavorable	a ou b	Embryonnaire	M1	N0, N1 ou NX
	4	IV	Favorable ou défavorable	a ou b	Alvéolaire	M1	N0, N1 ou NX

Tableau 7 : Résumé de la classification des RMS[178]

2.5 Les traitements actuels

La planification du traitement des patients atteints de RMS est une démarche pluridisciplinaire décidée en Réunion de Concertation Pluridisplicinaire (RCP). Les professionnels de santé vont se baser sur les examens radiologiques et histologiques pour adapter au mieux le traitement à administrer. Ils prennent en considération : la localisation, le type, le stade, et le groupe de risque. Les traitements actuels sont la chimiothérapie, la radiothérapie et la chirurgie.

2.5.1 La chirurgie initiale

Le protocole de traitement commence toujours par une chirurgie initiale :

- si la tumeur est petite, bien localisée, accessible et sans conséquence pour les organes environnants, le chirurgien peut procéder à une résection complète. Ce cas est toutefois très rare.
- dans les autres cas, la chirurgie initiale est réalisée pour faire une biopsie et réséquer au maximum la tumeur.

A partir de cette biopsie et des analyses histologiques et génétiques, les médecins peuvent adapter le protocole de traitement.

2.5.2 La chimiothérapie

La chimiothérapie peut être administrée pour[190] :

- détruire les cellules cancéreuses résiduelles après la chirurgie initiale afin de réduire le risque de réapparition du cancer (chimiothérapie adjuvante),
- réduire la taille de la tumeur pour faciliter une chirurgie ou une radiothérapie (chimiothérapie néoadjuvante),
- soulager la douleur et contrôler les symptômes d'un RMS de stade avancé (chimiothérapie palliative).

La chimiothérapie consiste en l'administration de médicaments en intraveineux. Selon le stade et le groupe de risque, les agents anticancéreux peuvent être administrés en combinaison. La plupart des patients reçoivent la chimiothérapie pour une durée de six à douze mois. Les

médicaments les plus courants sont : vincristine, ifosfamide, actinomycine D et doxorubicine. L'association ifosfamide, vincristine et actinomycine (IVA) est la plus souvent utilisée[178,184,190].

2.5.3 La radiothérapie

Tous les patients atteints de RMS alvéolaire, et une partie des patients classés dans les groupes II et III sont traités par radiothérapie après avoir reçu une chimiothérapie[174]. La radiothérapie est généralement mise en place après quatre à cinq cycles de chimiothérapie (environ douze semaines)[191]. Ce traitement est risqué car les tissus en développement chez l'enfant vont être également irradiés causant des effets secondaires irréversibles.

2.5.4 La chirurgie retardée

Après les cycles de chimiothérapie, certains patients peuvent subir une chirurgie retardée si la tumeur est réduite de manière significative. Ce traitement peut permettre d'éviter ou de réduire les doses de radiothérapie. La chirurgie retardée, tout comme une résection complète pendant une chirurgie initiale, dépend de la localisation de la tumeur[192].

2.5.5 Les effets des traitements

Les différentes études cliniques IRS ont permis d'évaluer sur plus de trois mille patients les effets des traitements administrés. Ces études ont permis une augmentation de la survie à cinq ans de 25% à 40%. Cependant, il reste des disparités entre les patients selon le stade clinique et le type histologique de RMS[189,193] :

- Selon le stade clinique : au stade 1 les patients ont un taux de survie de 80%, alors qu'il est de 66% et 60% respectivement pour les stades 2 et 3. Les patients à un stade 4 n'ont que 20% de taux de survie à 5 ans.
- Selon le type histologique : le taux de survie pour les patients atteints d'un RMS embryonnaire est de 78% alors qu'il n'est que de 38% pour les patients atteints de RMS alvéolaire.

De plus, le traitement d'un RMS est particulier car il touche des enfants en plein développement. La thérapie doit être adaptée afin de minimiser le développement de

complications à court et long terme. Cependant, les traitements actuels entraînent de nombreux effets secondaires pendant la thérapie (perte de cheveux, vomissements, inflammation de la bouche et des intestins, aplasie…)[8] mais aussi sur du long terme. En effet, il est possible qu'une tumeur maligne secondaire se développe suite aux traitements : des cas de leucémies et d'ostéosarcomes ont été décrits dans la littérature[194]. De plus, les patients atteints de RMS au niveau de la vessie ou de la prostate peuvent avoir des complications suite à la chirurgie ou à la radiothérapie, cinq à quinze ans après le diagnostic (perte de fonction, cystite hémorragique, déficience hormonale)[195]. La chimiothérapie peut également causer des effets secondaires sur le long terme, par exemple l'ifosfamide qui fait partie de la combinaison d'agents anti-cancéreux utilisés habituellement cause très souvent des dommages rénaux, plus particulièrement chez les jeunes enfants de moins de trois ans[196]. Les traitements actuels doivent donc être améliorés pour permettre un meilleur taux de survie pour les cancers les plus agressifs et diminuer les effets secondaires graves engendrés pendant et après le traitement.

2.6 A la recherche de nouveaux traitements

Sans thérapie ciblée, le taux de survie des patients ne s'améliore pas, en particulier pour les patients à haut risque avec un mauvais pronostic[197]. De plus, les options de traitement sont limitées pour les stades avancés de RMS dues à la résistance des cellules cancéreuses aux chimiothérapies entraînant une réduction de l'efficacité thérapeutique[198]. Certaines études ont identifié des cibles thérapeutiques potentielles associées aux deux types de RMS qui sont des voies moléculaires spécifiques et plus particulièrement des kinases qui sont impliquées dans la croissance et la progression du cancer[199]. En effet, il a été démontré que certains récepteurs tyrosine kinase (RTK) sont surexprimés dans les RMS tels que les récepteurs de l'IGF-I, MET, EGFR, HER2, FGFR qui sont des récepteurs dont les voies de signalisation sont impliquées dans la prolifération, la différenciation et la migration cellulaire[200–203]. De plus, FGFR4 et le récepteur de l'IGF-I sont des cibles directes du gène de fusion PAX3-FOXO1a impliqué dans la tumorogenèse des RMS alvéolaires[204]. Cependant, cibler un seul de ces récepteurs ne semble pas être une stratégie optimale parce que les voies de signalisation sont beaucoup trop complexes : bloquer une seule voie ne suffit pas à tuer les cellules cancéreuses[202]. Il a alors été proposé de combiner plusieurs thérapies ciblées :

- L'association d'un inhibiteur du récepteur de l'IGF-I et du HER2 est significativement plus efficace comparée aux drogues seules *in vitro* et *in vivo*[202].

- L'association d'un anticorps monoclonal contre le récepteur de l'IGF-I et de la rapamycine induit une diminution significative de la progression de la tumeur *in vivo*[202].

Ces résultats sont prometteurs mais des études supplémentaires sont nécessaires pour approfondir la compréhension de ces cibles potentielles.

Dans ce manuscrit, nous proposons une autre cible thérapeutique pour le traitement des RMS dont nous étudierons le potentiel thérapeutique.

Chapitre 5 : La maladie de Pompe

1. Généralités

La maladie de Pompe également connue sous le nom de glycogénose de type 2 ou déficit en maltase acide est causée par un défaut de l'enzyme alpha-glucosidase acide (GAA). Cette enzyme permet de dégrader le glycogène en glucose dans les lysosomes. Une déficience de l'enzyme entraîne une accumulation du glycogène dans les lysosomes au sein de différents tissus et plus particulièrement dans les muscles cardiaque, respiratoires et squelettiques responsable d'une myopathie progressive et mortelle[205]. La maladie de Pompe a été découverte en 1932 par le pathologiste néerlandais Johannes Cassianus Pompe qui a décrit la maladie pour la première fois chez un nourrisson de sept mois qui souffrait de faiblesse musculaire et qui décéda d'une cardiomyopathie sévère. De plus, les tissus examinés ont montré une accumulation massive de glycogène[206]. Mais ce n'est qu'en 1963 que le biochimiste belge Henri-Gery Hers démontra que la GAA était localisée dans le lysosome et que c'était la seule enzyme responsable de la dégradation du glycogène en glucose, c'est pourquoi la maladie a été caractérisée de maladie de surcharge lysosomale. De plus, il observa que l'enzyme était absente des lysosomes chez les patients atteints de la maladie de Pompe. Il a également fait l'hypothèse que certaines maladies encore inconnues pouvaient être expliquées par l'absence d'autres enzymes lysosomales[207]. Grâce à ses découvertes, le concept de maladie lysosomale a été établi et depuis une cinquantaine de maladies ont été répertoriées.

2. Étiologie et épidémiologie

La maladie de Pompe est une maladie génétique causée par une mutation du gène codant pour la GAA localisé sur le chromosome 17q25. Les deux copies du gène doivent contenir une mutation pour que la maladie se manifeste : c'est donc une maladie à transmission autosomique récessive[208]. A l'heure actuelle, plusieurs centaines de mutations ont été dénombrées à partir du clonage du gène[209,210] et approximativement 400 mutations ont été répertoriées comme étant pathogéniques[211]. Plusieurs mutations sont couramment retrouvées chez certaines origines ethniques : c.32-13T>G est la mutation la plus connue chez les caucasiens, c.1935C>A est fréquente dans la population taïwanaise, c.del525, del exon18 et Arg309 sont communes aux Pays-Bas, c.2650C>T est la mutation la plus fréquente chez les afro-américains et enfin

c.2238G>C est retrouvée plus particulièrement chez les chinois. Ces mutations entraînent une perte totale de l'activité de la GAA[205]. D'un point de vue épidémiologique, la maladie de Pompe, comme toutes les maladies lysosomales, est une maladie rare. La prévalence est estimée entre 1/140000 et 1/250000. En février 2019, le registre français de la maladie de Pompe recensait 212 patients[212].

3. Caractéristiques physiopathologiques

La maladie de Pompe peut se déclarer à tout âge et les signes cliniques sont hétérogènes et plus ou moins sévères. Cependant, la communauté scientifique a récemment adopté une nomenclature internationale pour décrire trois formes caractéristiques de la maladie[213] : la forme infantile classique, la forme juvénile et la forme adulte. Les formes juvénile et adulte peuvent être associées et sont nommées formes tardives.

Les variations pathologiques des fibres musculaires squelettiques sont identiques dans les différentes formes cliniques de la maladie. En effet, l'analyse en microscopie électronique de myocytes a montré une évolution hiérarchisée de la structure des fibres musculaires (Figure 15)[214] :

- Stade 1 : Les cellules au stade précoce de la maladie contiennent des lysosomes remplis de glycogène dans des myofibrilles intactes. Les cellules ont un aspect vacuolaire.
- Stade 2 : Le glycogène continue de s'accumuler entraînant une augmentation de la taille des lysosomes. Il a été observé que le glycogène pouvait s'échapper des lysosomes et ainsi se répandre dans le cytoplasme. Les myofibrilles commencent à être atteintes et à se fragmenter.
- Stade 3 : Les cellules contiennent de nombreux lysosomes saturés en glycogène. Les membranes lysosomales se rompent et le glycogène s'accumule dans le cytoplasme causant des dommages irréversibles aux éléments contractiles de la cellule. La structure des mitochondries est anormale et les myofibrilles se fragmentent totalement.
- Stade 4 : La majorité du glycogène est dans le cytoplasme entraînant une perturbation des éléments contractiles dans la cellule. Il n'y a plus de structure myofibrillaire.
- Stade 5 : La taille des cellules augmente fortement due à l'afflux d'eau qui entraîne une dissolution ou une dilution du glycogène.

De plus, une étude a montré que le glycogène s'accumule dans les muscles striés mais il peut également s'accumuler dans les muscles lisses, les nerfs et le système nerveux central[215].

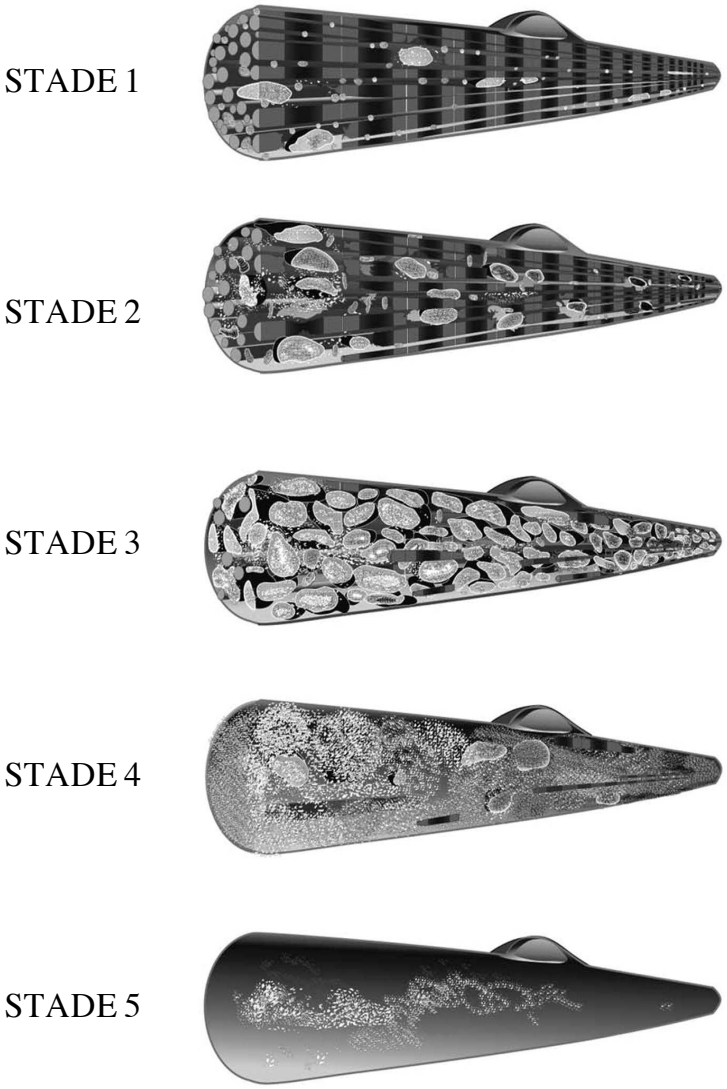

Figure 15 : Evolution de la maladie de Pompe, du stade 1 à 5 observée par TEM dans une fibre musculaire[214]

Une autre caractéristique de la maladie de Pompe est l'autophagie. C'est un processus qui permet la dégradation d'une partie des composants cytoplasmiques (protéines, organites cellulaires…) par les lysosomes[216]. Des études ont démontré que les patients avaient d'une part une augmentation du nombre de lysosomes et d'autre part une accumulation de vacuoles autophagiques, appelées autophagosomes, ce qui confirme une défaillance autophagique chez les patients atteints de la maladie de Pompe. La défaillance autophagique participe à l'atrophie musculaire tout comme l'accumulation de glycogène[217,218]. Dans les biopsies musculaires, il a

été également observé une surexpression des phosphatases acides présentes dans les lysosomes. Ce niveaux élevé d'expression est une caractéristique de la maladie de Pompe qui peut être utilisée comme alternative pour le diagnostic lorsque les biopsies musculaires ne présentent pas de signes spécifiques de la maladie[219].

4. Symptômes et diagnostic

4.1 Les symptômes

La maladie de Pompe peut toucher aussi bien les enfants que les adultes. Cependant, la progression de la maladie dépend principalement de la nature de la mutation qui déterminera le niveau d'activité résiduelle de la GAA et par conséquent les manifestations cliniques[220]. La maladie de Pompe est classée en différentes formes cliniques selon l'âge des patients (Tableau 8)[221–224].

- La forme infantile

C'est la forme la plus sévère car l'activité résiduelle de la GAA est inférieure à 1%. Elle apparaît chez le nourrisson avant l'âge de six mois et les premiers symptômes apparaissent généralement vers 1 ou 2 mois. Cette forme est caractérisée par :

- Des troubles moteurs qui se manifestent par une diminution du tonus musculaire (hypotonie).
- Une atteinte respiratoire caractérisée par une faiblesse des muscles respiratoires (diaphragme) entraînant une toux et une insuffisance respiratoire.
- Une atteinte cardiaque causée par un dysfonctionnement du muscle du cœur. La sévérité de la forme infantile est due à cette cardiomyopathie : ce dysfonctionnement progresse rapidement entraînant une insuffisance cardiaque ainsi que d'autres anomalies comme des arythmies avec un risque de mort subite. Dans les premiers stades de la maladie, les nourrissons ont une cardiomyopathie hypertrophique avec ou sans obstruction de l'orifice de sortie du ventricule gauche et dans les derniers stades de la maladie, les nourrissons ont une cardiomyopathie dilatée caractérisée par la dilation des ventricules et une faiblesse de contraction musculaire.
- D'autres manifestations cliniques ont été répertoriées comme l'atteinte des muscles de la bouche et de la gorge qui empêchent le nourrisson de se nourrir correctement et la

macroglossie (augmentation du volume de la langue). Une hépatomégalie légère (hypertrophie du foie) est souvent observée.

Une autre variante de la forme infantile peut être diagnostiquée. Il s'agit de la forme infantile non classique qui peut apparaître dans la première année du nourrisson. Les symptômes sont les mêmes que pour la forme infantile mais le cœur est moins touché : l'hypertrophie du coeur est moins importante et l'obstruction ventriculaire n'est pas observée ce qui permet de conserver une fonction cardiaque normale.

Les patients vont être mis sous assistance respiratoire très rapidement car ils souffriront d'une faiblesse musculaire sévère causée par les insuffisances cardiaque et respiratoire. Cependant, les patients atteints de la forme infantile non classique vont survivre au-delà de la première année contrairement aux patients atteints de la forme infantile classique.

- La forme tardive juvénile

La forme tardive juvénile se déclare avant l'âge de vingt ans. Cette forme se caractérise par une faiblesse musculaire, des troubles de la marche et une atteinte respiratoire. Le cœur n'est généralement pas touché. Plus précisément, cette forme est caractérisée par :

- Des troubles moteurs des muscles qui relient les membres au tronc. La maladie va d'abord toucher les muscles des hanches et du bassin ce qui va entraîner des difficultés pour marcher. Les muscles qui maintiennent la colonne vertébrale sont également touchés. Il peut aussi y avoir une atteinte des muscles de la gorge et de la langue causant des problèmes pour s'alimenter et parler.
- Une atteinte respiratoire qui apparaît après les troubles moteurs.
- L'atteinte cardiaque est très faible et peut se traiter.
- D'autres manifestations cliniques comme l'hépatomégalie et la macroglossie peuvent être présentes.

- La forme tardive adulte

Elle se déclare généralement autour des trente-quarante ans. Elle est caractérisée par :

- Des troubles moteurs qui touchent les muscles des membres inférieurs entraînant des difficultés pour marcher.
- Une atteinte respiratoire qui cause une difficulté à respirer, des maux de têtes et des somnolences. Les patients ont une toux moins efficace, les sécrétions ne peuvent pas

être bien expulsées entraînant des infections respiratoires fréquentes. L'atteinte respiratoire conduit généralement à une insuffisance respiratoire grave qui est la première cause de décès.

	Forme infantile	Forme infantile non classique	Forme tardive
Activité GAA	< 1%	< 1%	Juvénile : 1 à 10% Adulte : 2 à 40%
Apparition des symptômes	1 à 2 mois	1 an	Enfance ou adolescence (forme juvénile), 30-40 ans (forme adulte)
Progression	Rapide	Modérée	Lente
Cardiomyopathie	Sévère	Modérée	Rare
Myopathie squelettique	Sévère	Modérée	Progressif
Décès	Avant l'âge d'un an dû à une insuffisance cardio-respiratoire	Petite enfance dû à une insuffisance respiratoire	Décès dû à une insuffisance respiratoire

Tableau 8 : Les différentes formes de la maladie de Pompe

4.2 Diagnostic

Le diagnostic de la maladie de Pompe présente des difficultés en raison de la rareté et de la nature non spécifique des manifestations cliniques de la maladie[225]. Un algorithme de diagnostic a été mis en place et se base sur les principales manifestations cliniques de la maladie[226]. Les figures 16 et 17 présentent les algorithmes pour les formes infantile et tardives.

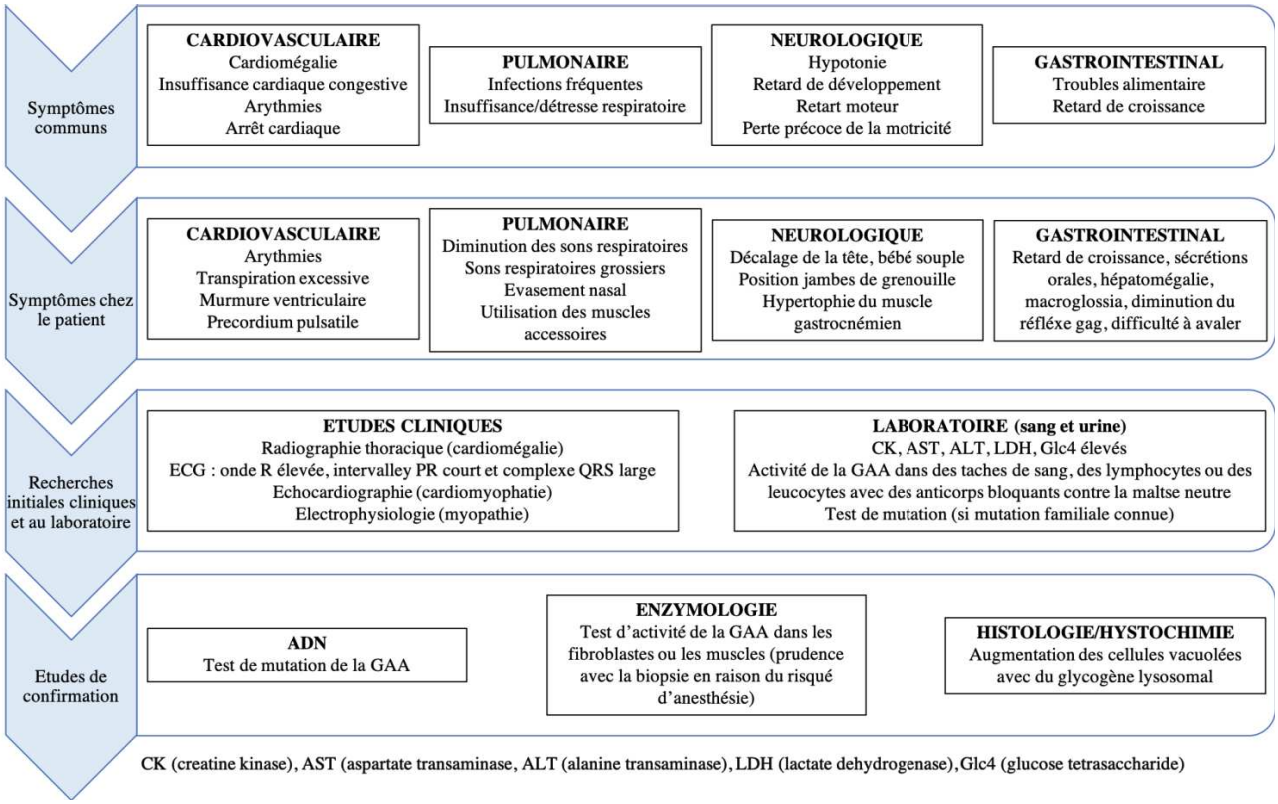

Figure 16 : Algorithme de diagnostic chez les patients atteints de la forme infantile[226]

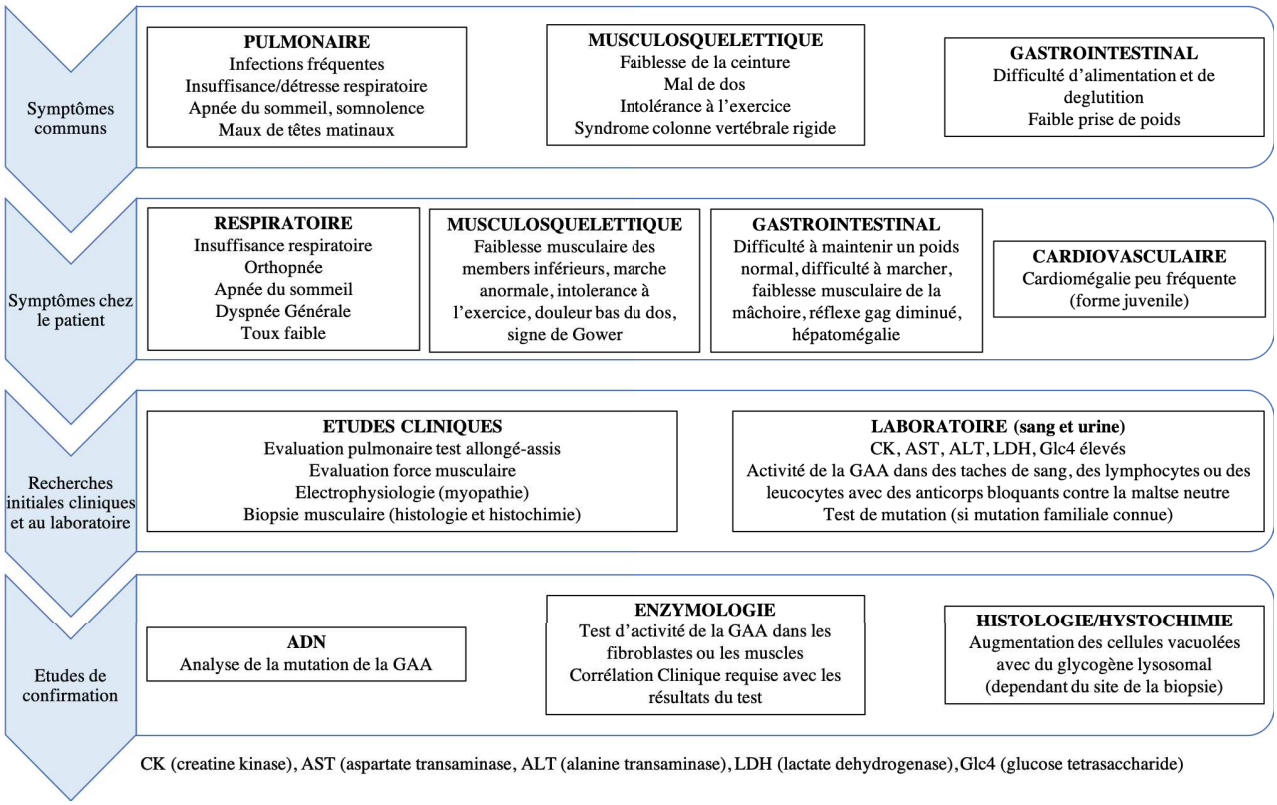

Figure 17 : Algorithme de diagnostic pour les patients atteints des formes tardives[226]

D'après les algorithmes cités précédemment, le diagnostic est basé sur des tests biologiques et histologiques pour la maladie de Pompe.

- L'activité de la GAA

Le diagnostic est confirmé par l'absence quasi-totale (forme infantile) ou nettement réduite (formes tardives) de l'activité de la GAA. La mesure de l'activité de la GAA est réalisée par dosage de l'activité enzymatique sur substrat synthétique (4-méthylumbelliféryl-α-D-glucopyranoside) ou naturel (glycogène) sur des échantillons de patients. Les premiers tests étaient effectués sur des fibroblastes cutanés prélevés par biopsie. Les fibroblastes étaient ensuite mis en culture jusqu'à confluence pour faire le dosage enzymatique. Cependant, il faut attendre un délai de six semaines pour avoir les résultats ce qui peut constituer de graves risques pour les patients atteints de la forme infantile dont la progression de la maladie est très rapide. Les tests pouvaient également être réalisés à partir de biopsies musculaires permettant d'obtenir des résultats de dosage immédiat ; cependant ce type de biopsie est très invasif pour les patients notamment pour les nourrissons et les jeunes enfants[227,228]. Ces tests ont donc été remplacés par des tests sanguins pour un diagnostic plus rapide, moins coûteux et surtout moins invasif[229].

- Les biopsies musculaires

Les biopsies sont réalisées sur les patients atteints des formes tardives afin d'évaluer la santé du muscle. Les biopsies permettent d'évaluer l'histologie de la maladie : l'emplacement et la quantité de glycogène (présence de vacuoles), la présence d'autophagosomes et la surexpression de phosphatases acides. Les vacuoles sont observables par immunohistochimie (Figure 18E, I et M) et en microscopie électronique (Figure18G, K et Q). L'accumulation de glycogène est observable par la coloration à l'acide périodique de Schiff : on observe des vacuoles positives à la coloration démontrant la présence de glycogène (Figure 18F, J et N) ainsi qu'une coloration positive des phosphatases acides (Figure 18H, L et P). Les résultats obtenus sur les biopsies musculaires sont différents selon la forme clinique de la maladie. La fréquence de vacuolisation des cellules résultant de l'accumulation de glycogène varie en fonction de la forme clinique : de 75% à 100% dans la forme infantile, supérieur à 50% dans la forme juvénile et de 10% à 50% dans la forme tardive adulte[230,231]. Cependant, cette technique est risquée pour les nourrissons et les jeunes enfants et l'accumulation de glycogène varie en fonction du site de la biopsie ce qui peut engendrer des faux négatifs[225].

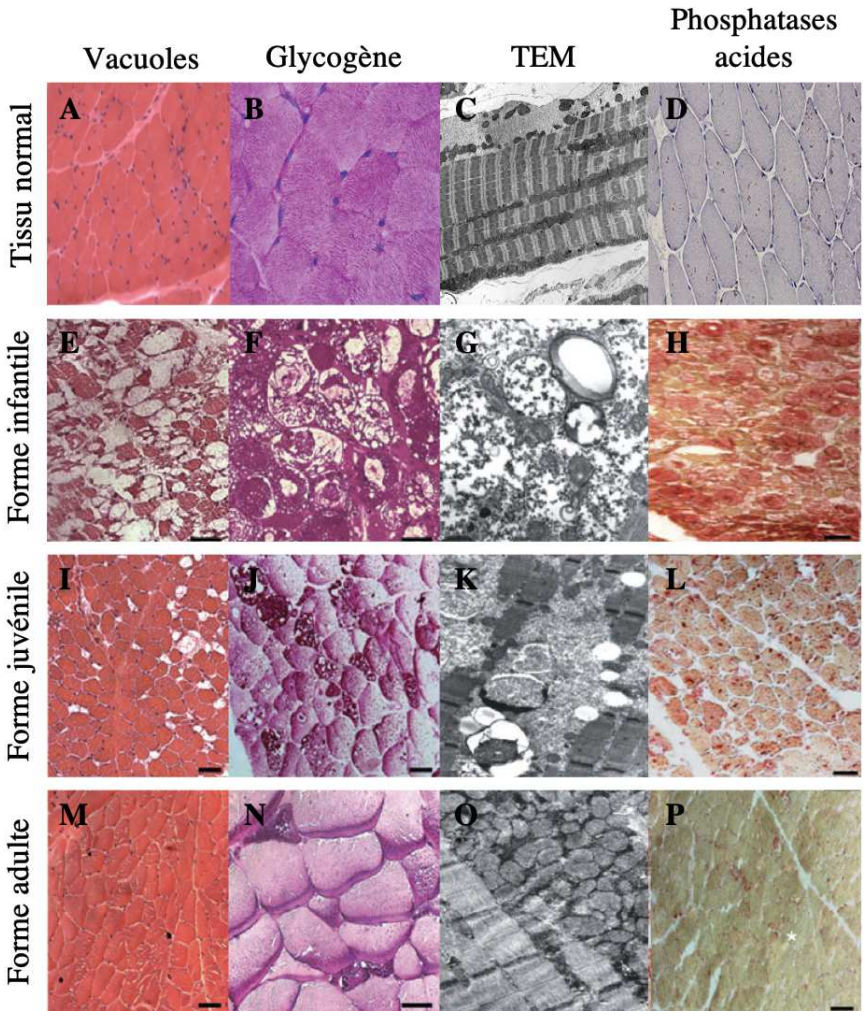

Figure 18 : Biopsies musculaires de patients atteints de la maladie de Pompe[231–233]

- Les tests génétiques

Bien que le dosage enzymatique soit le test de choix pour les patients atteints de la maladie de Pompe, l'analyse des mutations est un outil fiable pour la confirmation du diagnostic. Il est particulièrement utile dans l'identification des porteurs lorsqu'une mutation familiale est connue : ceci est très important pour un diagnostic prénatal. Ce test est effectué à partir d'ADN génomique isolé du sang ou des fibroblastes cutanés[234,235].

- Quantification de l'expression de la GAA

La quantification de l'expression de la GAA permet de déterminer le statut « CrossReactive Immunological Material » (CRIM). Ce statut est un important prédicteur de la réponse clinique[234,235]. Les patients CRIM-négatifs sont incapables de synthétiser une GAA native en raison de la présence de mutations délétères sur le gène GAA. Environ 20% des

patients atteints de la forme infantile sont CRIM-négatifs. Le système immunitaire de ces patients reconnaît la GAA comme étant du non-soi ce qui engendre une réaction immunitaire croisée. Au contraire, les patients CRIM-positifs peuvent produire une quantité résiduelle de GAA native qu'elle soit fonctionnelle ou non, ce qui prévient la réaction immunitaire. Les patients CRIM-négatifs vont donc déclencher une forte réponse immunitaire contre l'enzyme recombinante administrée pour l'enzymothérapie substitutive réduisant ainsi l'efficacité thérapeutique. De même, certains patients CRIM-positifs développent une forte réaction immunitaire après le traitement : ces patients sont appelés CRIM-positifs à haut titrage (HTCP). Les patients CRIM-négatifs et HTCP ont un pronostic négatif et ont aucune chance de guérison. La détermination du statut CRIM est donc très importante pour la mise en place des traitements : les patients CRIM-négatifs et HTCP devront subir une thérapie immunomodulatrice dans le but de répondre à l'enzymothérapie[236,237].

Pour compléter le diagnostic, il est possible d'effectuer d'autres tests, cependant ils sont non spécifiques de la maladie de Pompe :

- La concentration sérique en créatine kinase (CK) :

Les patients atteints des formes infantile et juvénile ont une concentration sérique en CK très élevée : 2000 $UI.L^{-1}$ (concentration normale en CK entre 60 et 305 $UI.L^{-1}$) alors que chez les patients atteints de la forme adulte le taux peut être normal[238]. Ce test est très sensible mais il est non spécifique de la maladie de Pompe. En effet, un taux anormalement élevé de CK peut être trouvé dans d'autres pathologies telles que la sclérose latérale amyotrophique[238], des tumeurs musculaires[239], etc.

- La concentration urinaire en glucose tétrasaccharide (Glc4)

Les patients atteints de la maladie de Pompe ont une concentration élevée de Glc4 dans les urines. Ce test est très sensible mais cette augmentation est également observée dans d'autres maladie de stockage du glycogène[239].

5. Les traitements actuels

A l'heure actuelle, un seul traitement est approuvé par les autorités de santé pour le traitement de la maladie de Pompe. C'est un traitement de remplacement de l'enzyme ou

enzymothérapie substitutive. Pour compléter ce traitement, les médecins ont recours à des traitements symptomatiques qui consistent à soulager au mieux les manifestations de la maladie.

5.1 Les traitements symptomatiques[192,240]

Ces traitements sont administrés pour toutes les formes de la maladie. Cependant, la sévérité étant liée à l'âge d'apparition, les conditions de prise en charge sont adaptées à l'âge du patient.

- L'atteinte cardiaque :

La base du traitement est le suivi constant du cœur avec plusieurs examens (radiographie du thorax, électrocardiogramme, échocardiographie) qui permettent d'adapter régulièrement le traitement symptomatique par rapport à l'évolution du volume du cœur et des anomalies rythmiques. Le traitement administré est propre à chaque patient car l'utilisation de médicaments standards peut être contre-indiquée suivant l'âge du patient et le stade de la maladie.

- L'atteinte respiratoire :

Dans un premier temps, des séances de kinésithérapie sont mises en place pour éliminer les sécrétions bronchiques qui aggravent l'insuffisance respiratoire. Selon l'évolution de la maladie, les patients peuvent être mis sous assistance respiratoire non invasive qui consiste à insuffler mécaniquement de l'air dans les poumons à l'aide d'un masque. Lorsque l'insuffisance respiratoire devient sévère, le patient doit être placé sous assistance respiratoire continue et lorsque l'assistance n'est plus suffisante, une trachéotomie peut être effectuée.

- La gestion des troubles musculo-squelettiques :

Les patients suivent des séances de kinésithérapie et de physiothérapie. Ces séances permettent aux nourrissons d'atteindre des étapes de développement normal telles que la capacité à s'asseoir, les passages entre différentes positions, le contrôle du port de tête, etc. Pour les patients plus âgés, le but est de garder une bonne amplitude des mouvements et d'éviter le blocage des articulations. Des appareils peuvent être mis en place comme des coques moulées en plastique pour les nourrissons qui ne tiennent pas assis ou le port d'un corset pour maintenir

le tronc. Chez les enfants, la kinésithérapie est très importante pour éviter toute déformation du squelette (scoliose). A terme, si la maladie s'aggrave, les patients auront besoin d'un fauteuil roulant pour se déplacer.

- Prise en charge de la nutrition :

Les nourrissons sont les plus touchés par ces problèmes de nutrition, ils ont besoin d'une assistance (sonde nasogastrique ou gastrostomie) dès les premiers mois de leur vie. Il est également important de dégager le pharynx des sécrétions nasales et buccales par des séances de kinésithérapie pour permettre aux patients de se nourrir normalement.

- Prévention des infections :

Une majorité des patients auront au cours de leur maladie une insuffisance respiratoire et seront par conséquent sensibles aux infections pulmonaires. Ces infections peuvent être traitées par des antibiotiques.

- Prévention de l'ostéoporose :

Les patients ont un suivi régulier pour leur équilibre, leur capacité de marche et la minéralisation de leurs os. Si une déminéralisation est observée, le patient doit prendre des compléments de calcium et de la vitamine D.

5.2 Traitement médicamenteux : l'enzymothérapie substitutive

L'enzymothérapie substitutive consiste à administrer une enzyme recombinante aux patients pour pallier au défaut d'une enzyme endogène causée par une maladie lysosomale[124]. A ce jour, le seul traitement spécifique pour la maladie de Pompe approuvé par les autorités compétentes européennes et américaines depuis mars 2006 est un traitement d'enzymothérapie substitutive commercialisé par Sanofi-Genzyme sous le nom de Myozyme® en Europe et Lumizyme® aux Etats-Unis. La Myozyme® est une Alpha Glucosidase Acide recombinante humaine (rhGAA) produite chez une lignée cellulaire d'ovaires de cochon d'Inde (CHO). La composition de Myozyme® est répertoriée dans le tableau 9. La posologie recommandée est de 20 mg/kg, administrée une fois toutes les deux semaines en perfusion intraveineuse, elle doit être réalisée dans un hôpital.

Composés	Quantité
rhGAA	52,5 mg
Mannitol	210 mg
Polysorbate 80	0,5 mg
Phosphate de sodium dibasique heptahydraté	9,9 mg
Phosphate de sodium monobasique monohydraté	31,5 mg

Tableau 9 : Composition de Myozyme®[241]

L'évaluation de l'efficacité thérapeutique de Myozyme® a été montrée à partir de trois essais cliniques qui ont été comparés à une étude épidémiologique basée sur les dossiers médicaux des patients qui n'avaient reçu aucun traitement. L'efficacité thérapeutique a d'abord été étudiée sur des patients atteints de la forme infantile : deux essais cliniques AGLU01602 et AGLU01702 ont été réalisés respectivement sur 18 patients âgés de 6 mois et 21 patients âgés de 6 mois à 3,5 ans. Les patients ont reçu 20 ou 40 mg/kg toutes les deux semaines pendant 52 semaines en perfusion intraveineuse. Les résultats n'étaient pas différents entre les deux posologies, seule la dose de 20 mg/kg a été retenue pour l'autorisation de mise sur le marché (AMM). Ces études ont montré l'efficacité thérapeutique de Myozyme®[242,243] :

- le taux de survie était significativement augmenté, les patients ont survécu au-delà de 18 mois,
- la cardiomyopathie a régressé avec une diminution de 58% de la masse ventriculaire gauche,
- la fonction motrice a été améliorée avec une acquisition de la marche à un âge normal pour certains patients,
- les fonctions respiratoires ont été significativement améliorées chez certains patients qui n'ont plus eu besoin d'assistance respiratoire,
- pour les patients plus âgés l'effet thérapeutique est conservé.

Pour les patients CRIM-négatifs, différents protocoles ont été étudiés pour éviter une réponse immunitaire élevée suite à l'administration de Myozyme®. Le plus courant est l'association de rituximab et méthotrexate avec ou sans gamma globulines. De plus, l'addition de bortezomib aux précédents immunomodulateurs s'est montrée efficace pour moduler la forte réponse immunitaire[244].

Un essai clinique sur les formes tardives a également été réalisé (AGLU02804). Les patients étaient âgés de plus de 8 ans et ont reçu 20 mg/kg toutes les deux semaines pendant 78 semaines. Soixante patients ont reçu le traitement alors que 30 patients ont reçu un placebo. Sur ces formes cliniques de la maladie, Myozyme® permet une amélioration modeste de la marche et de la fonction respiratoire. De plus, une grande variabilité dans la réponse au traitement a été observée et l'état de santé de certains patients a continué à s'aggraver[245]. D'autres études ont complété cet essai clinique. Elles ont permis le suivi de 438 patients pendant 3 à 48 mois. Les principales conclusions de cette étude sont les suivantes[246,247] :

- le taux de mortalité est cinq fois plus faible chez les patients traités que chez les patients qui ont reçu le placebo,
- la fonction respiratoire s'est améliorée au cours des premiers mois de traitement mais est revenue progressivement au niveau de base pour diminuer légèrement après 2 à 3 ans de traitement,
- la fonction motrice a été améliorée au cours des 20 premiers mois de traitement puis a stagné.

6. A la recherche d'un nouveau traitement

La Haute Autorité de Santé (HAS) a reconnu que Myozyme® apportait une amélioration « importante » du service médical rendu dans la forme infantile car le traitement est très efficace sur la cardiomyopathie qui est le symptôme le plus sévère. Suite aux essais cliniques sur les formes tardives, la HAS a considéré une amélioration « modérée » du service médical rendu. De plus, au vu des résultats chez la forme adulte, la HAS confirme le progrès thérapeutique mineur du fait de son efficacité limitée. En effet, la réponse des muscles squelettiques chez les adultes est variable et moins importante comparée à d'autres maladies lysosomales traitées par enzymothérapie substitutive[245]. L'efficacité de l'enzymothérapie substitutive dépend du nombre de M6P que contient l'enzyme recombinante ainsi que du niveau d'expression du RM6P-CI dans les tissus cibles. La limite d'efficacité de l'enzymothérapie substitutive au niveau des muscles squelettiques a été attribuée au faible nombre de M6P sur Myozyme® ainsi qu'à la faible expression de RM6P-CI à la surface des cellules musculaires squelettiques[248]. Il est donc indispensable de développer un traitement plus efficace sur les formes tardives. Pour cela, plusieurs industries pharmaceutiques ont essayé de développer une nouvelle enzymothérapie substitutive.

- Sanofi-Genzyme :

Genzyme a mis au point une rhGAA de nouvelle génération, appelée néo-GAA, sur laquelle des ligands oligosaccharidiques synthétiques portant des résidus M6P mono- et biphosphorylés ont été greffés dans le but de mieux cibler les muscles. Les résultats précliniques montrent une meilleure efficacité (2,5 à 5 fois plus élevée) chez les souris jeunes mais presque aucune amélioration sur les souris âgées de plus de 10 mois[248]. La phase clinique 1/2 réalisée sur des patients préalablement traités avec Myozyme® ne présente pas d'augmentation de la mobilité, seule une légère amélioration de la fonction respiratoire a été observée. Cependant, une phase 3 qui durera trois ans a été initiée en 2017 sur 86 patients âgés de plus de trois ans[248].

- Biomarin :

Biomarin a développé une enzyme recombinante fusionnée à l'IGF-II (BMN-701) qui est un des ligands naturels du RM6P-CI ce qui permettrait d'améliorer le ciblage du récepteur. Les études précliniques sur des souris modèle de la maladie de Pompe ont montré que BMN-701 était significativement plus efficace que rhGAA pour éliminer le glycogène dans de nombreux tissus musculaires squelettiques. De plus, après douze semaines de traitement à 20 mg/kg, BMN-701 améliore la fonction respiratoire[249]. La société Biomarin a annoncé en 2016 les résultats préliminaires de l'essai clinique de phase II : sur 24 participants, 6 patients ont interrompu le traitement avant la fin de l'essai dont 2 pour des effets indésirables graves. Chez les 18 participants restants, les critères d'évaluation étaient légèrement améliorés mais sans être significatifs après 6 mois de traitement[250]. Au vu de ces résultats décevants, Biomarin a annoncé l'interruption de l'essai clinique.

- Amicus

Amicus a développé une protéine chaperonne (AT2200) dans le but de stabiliser Myozyme®. L'essai clinique de phase II a été réalisé sur 25 patients âgés de 18 à 25 ans. AT2200 a permis d'augmenter l'activité de Myozyme® dans le sang ainsi que dans les tissus musculaires. En parallèle, Amicus développe également une nouvelle enzyme recombinante qui comporte plus de M6P à sa surface afin de mieux cibler le RM6P-CI dans le but d'être mieux adressée aux lysosomes. Des études précliniques sur des souris modèles de la maladie de Pompe ont montré que l'association de cette nouvelle enzyme recombinante avec AT2200 était plus efficace que Myozyme® pour diminuer le glycogène dans les muscles[251]. Un essai clinique de phase I/II est en cours sur des patients âgés de 18 à 65 ans. Les résultats

intermédiaires après 9 mois de suivi ont montré une diminution du glycogène dans les muscles. De plus, une tendance à l'amélioration de la marche et de la fonction respiratoire semble ressortir. Cependant, il faut confirmer cette tendance sur une période plus longue[252].

Le ciblage du RM6P-CI est donc un point crucial pour augmenter l'efficacité thérapeutique de l'enzymothérapie substitutive. Dans ce manuscrit, nous étudierons le potentiel des AMFA greffés sur Myozyme® dans le but d'améliorer le ciblage lysosomal *via* le RM6P-CI et ainsi améliorer l'efficacité thérapeutique de l'enzyme recombinante.

Partie 1 : Nanoparticules multifonctionnelles pour le traitement des cancers

Dans cette première partie consacrée à un des axes de ma thèse, l'étude de nanoparticules multifonctionnelles pour la thérapie photothermique et la délivrance de drogue est décrite et illustrée par trois articles scientifiques dont je suis co-auteur. Ces travaux ont été menés en collaboration avec les équipes du Dr Yannick Guari, du Dr Jean-Olivier Durand et du Dr Peter Hesemann de l'Institut Charles Gerhardt de Montpellier.

Chapitre 1 : Nanoparticules de bleu de Prusse pour le traitement par hyperthermie et l'imagerie médicale des cancers

1. Les nanoparticules de bleu de Prusse (PB)

Le bleu de Prusse est un pigment bleu foncé découvert en 1706 utilisé pour deux applications principales : la peinture et la médecine. En médecine, il a été approuvé par les autorités de santé en 2016 et est connu sous le nom de Radiogardase®. Il est utilisé pour prévenir ou traiter les contaminations radioactives au thallium et au césium radioactifs ou non. Il joue un rôle de chélateur pour empêcher le passage des radionucléides dans le sang et ainsi réduire leur temps de demi-vie[253]. Les PB sont des nanoobjets inorganiques composés d'ions de métal de transition ou de lanthanides assemblés par des ponts cyano (Figure 19)[254–256].

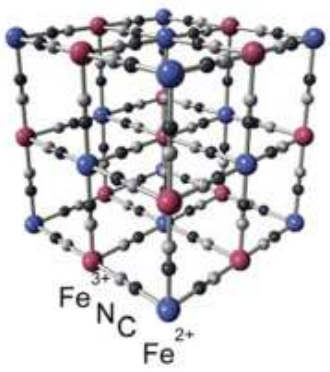

Figure 19 : Schéma d'une nanoparticule de bleu de Prusse[257]

Ces PB ont un potentiel pour les applications biomédicales dues à leurs caractéristiques intrinsèques comme la flexibilité de leur structure, la composition variable, les propriétés physico-chimiques, la porosité, la grande stabilité et la biocompatibilité[258]. Pour ces raisons, les PB sont utilisées couramment en biologie comme agent de contraste pour différents types d'imagerie (IRM[259,260], scintigraphie[261], imagerie photoacoustique[262]), comme nanovecteurs pour la délivrance de drogue[263,264] ou comme agent thérapeutique[265]. Le plus récent développement de PB à des fins thérapeutiques est lié à son remarquable potentiel pour la thérapie photothermique des cancers[266,267].

2. La thérapie photothermique (PTT)

Le principe de base de la PTT est l'augmentation localisée de la température des cellules cancéreuses afin de provoquer la mort cellulaire. Le concept d'utilisation de la chaleur pour traiter le cancer date de la fin du XIXème siècle : à cette époque il n'y avait pas d'essais cliniques encadrés comme aujourd'hui mais de nombreux rapports de médecins et scientifiques ont décrit la guérison de patients après un traitement d'hyperthermie sur des tumeurs superficielles[268]. L'hyperthermie peut également être utilisée pour administrer plus rapidement des agents anti-cancéreux en augmentant le débit sanguin ou en radiothérapie en sensibilisant les cellules cancéreuses au rayonnement car elles sont plus sensibles aux rayons que les cellules saines[269]. Des études ont démontré que des températures allant de 41 à 47°C peuvent rompre les membranaires cellulaires en dénaturant les protéines ce qui déclenche un mécanisme d'apoptose alors que des températures supérieures à 50°C engendrent un phénomène de nécrose[270,271]. Divers protocoles ont été mis en place mettant en jeu des lasers, des micro-ondes, des fréquences radio et des ultrasons mais ces techniques ne permettent pas d'obtenir une homogénéité de la température au sein de la tumeur et entraînent la destruction des tissus sains environnants[272]. Afin de mieux cibler les cellules cancéreuses, il a été proposé d'utiliser des agents photothermiques qui pourraient s'accumuler dans la tumeur et être irradiés par la suite avec un laser[257,273–275]. Cette technique a été nommée thérapie photothermique car les agents photothermiques convertissent la lumière en chaleur. La société MagForce basée en Allemagne, fut la première à développer en clinique des nanoparticules d'oxyde de fer (NanoTherm®) pour réaliser la PTT afin de traiter les tumeurs du cerveau. Ce traitement a obtenu le marquage CE en 2011 pour le traitement du glioblastome multiforme au stade avancé. Aux Etats-Unis, la FDA a accordé une IDE (Investigational Device Exemption) en février 2018, pour conduire un

essai clinique pour traiter des patients atteints d'un cancer de la prostate avec un risque intermédiaire[276]. Ce traitement est cependant invasif car les nanoparticules doivent être injectées directement dans la tumeur[276].

3. Description des travaux

3.1 Publication n°1 : Multifunctional manganese-doped Prussian blue nanoparticles for two-photon Photothermal Therapy and Magnetic Resonance Imaging.

- Introduction :

Dans le cadre de cette thèse, nous avons travaillé sur des PB synthétisées par l'équipe de Yannick Guari afin d'être étudiées comme agent thérapeutique pour la PTT. En effet, les PB présentent une forte absorption dans le proche infrarouge due à la présence d'une bande de transfert de charge, comprise entre 650 et 900 nm, entre les métaux Fe^{2+} et Fe^{3+} qui composent la nanoparticule. Les PB ont donc un rendement photothermique élevé et sont stables même sous irradiation[277,278]. Récemment, des études *in vitro* et *in vivo* ont démontré que des PB dopées au manganèse ou au gadolinium étaient capables de convertir l'irradiation laser monophotonique en énergie thermique provoquant une élévation de la température et par conséquent la mort des cellules cancéreuses[279–282]. Les résultats de ces différentes études sont difficilement comparables car l'efficacité dépend de la concentration en nanoparticules, de leur densité optique et du temps d'irradiation. Il a également été démontré que les PB présentaient une efficacité supérieure aux molécules organiques utilisées conventionnellement en tant qu'agent photothermique[283]. Cependant, l'éradication des cellules tumorales sous excitation monophotonique est incomplète en raison de la répartition hétérogène de la chaleur dans les cellules cancéreuses et de la faible pénétration du laser dans les tissus. De plus, une concentration relativement élevée d'agents photothermiques est nécessaire pour ce type de traitement[277,280,284]. Pour pallier à ces problèmes, nous avons démontré pour la première fois que les PB pouvaient être des agents photothermiques efficaces sous irradiation biphotonique. La PTT biphotonique présente des avantages par rapport à une excitation monophotonique, car elle a une meilleure pénétration tissulaire, une meilleure résolution 3D ce qui permet une destruction ciblée, efficace et rapide des cellules cancéreuses en évitant les tissus sains environnants[285].
Ce travail est issu d'une collaboration étroite avec l'équipe du Dr Yannick Guari de l'Institut Charles Gerhardt de Montpellier, et le Dr Lamiaa Ali, post-doctorante dans notre équipe

« Glyco et nanovecteurs pour le ciblage thérapeutique » de l'Institut de Biomolécules Max Mousseron. Nous avons démontré sur des lignées cellulaires du cancer du sein que des PB dopées ou non avec des pourcentages différents de manganèse entraînaient une mort cellulaire drastique 24 h après une irradiation biphotonique à 808 nm (5% de puissance) pendant 10 mn. En effet, après internalisation des PB, l'irradiation entraîne l'oscillation des électrons des atomes qui composent la nanoparticule et lors du retour à l'état stable, il y a une production de chaleur causant la mort cellulaire (Figure 20)[286].

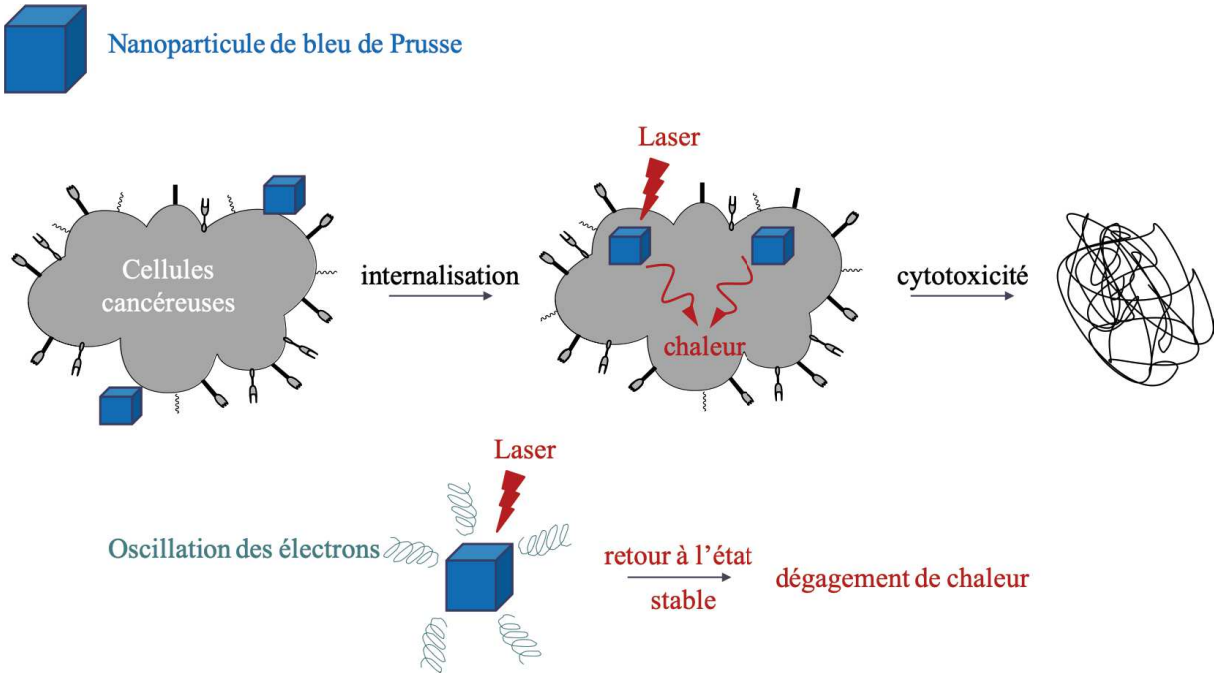

Figure 20 : Schéma du mécanisme de la thérapie photothermique *in vitro*

Photodiagnosis and Photodynamic Therapy 22 (2018) 65–69

Contents lists available at ScienceDirect

Photodiagnosis and Photodynamic Therapy

journal homepage: www.elsevier.com/locate/pdpdt

Multifunctional manganese-doped Prussian blue nanoparticles for two-photon photothermal therapy and magnetic resonance imaging

Lamiaa M.A. Ali[a,1], Emna Mathlouthi[b,c], Marilyn Kajdan[b], Morgane Daurat[a,d], Jérôme Long[b], Rahima Sidi-Boulenouar[e], Maïda Cardoso[e], Christophe Goze-Bac[e], Nourredine Amdouni[c], Yannick Guari[b], Joulia Larionova[b,*], Magali Gary-Bobo[a,*]

[a] Institut des Biomolécules Max Mousseron, UMR5247, Université de Montpellier, CNRS, ENSCM, Faculté de Pharmacie, 15 Avenue Charles Flahault, 34093, Montpellier, Cedex 05, France
[b] Institut Charles Gerhardt, Equipe Ingénierie Moléculaire et Nano-Objets, Université de Montpellier, CNRS, ENSCM, Place Eugène Bataillon, 34095, Montpellier, Cedex 5, France
[c] Université de Tunis el Manar, Faculté des Sciences, UR/11/ES/19, Physico-Chimie Des Matériaux à l'état Condensé, 2092, Tunis, Tunisie
[d] NanoMedSyn, 15 Avenue Charles Flahault, 34093, Montpellier, France
[e] L2C, UMR 5221 CNRS-UM2, Equipe BioNanoNMRI, Université de Montpellier, Place Eugène Bataillon, 34095, Montpellier, Cedex 5, France

ARTICLE INFO

Keywords:
Prussian blue
Nanoparticles
Photo-thermal therapy
Two-photon irradiation
Photo-thermal agent
MRI
Multifunctional
Cancer cells' eradication

ABSTRACT

Here we demonstrate for the first time that Mn^{2+}-doped Prussian blue nanoparticles of *c.a.* 70 nm act as effective agents for photothermal therapy under two-photon excitation with an almost total eradication of malignant cells (97 and 98%) at a concentration of 100 μg mL^{-1} 24 h after NIR excitation. This effect combined with interesting longitudinal NMR relaxivity values offer new perspectives for effective imaging and cancer treatment.

Prussian Blue (PB) type nanoparticles are a new family of inorganic nano-objects made of transition metal ions or lanthanides assembled through cyano-bridging ligands in nano-sized architectures. They have attracted a great deal of interest during the past ten years due to their specific molecule-based nature that is different compared to conventional inorganic nanoparticles [1–4]. They present a remarkable potential for biomedical applications due to many advantages from their flexible molecule-based structure, adjustable composition, tunable physical and chemical properties, porosity, high stability in aqueous media even at low pH, and biocompatibility [5]. Moreover, in its so-called "soluble" form, PB has been approved by the Food and Drug Administration (FDA) for human use as a radioactive Cs^+ antidote or Tl^+ poisoning [6–10]. For these reasons, PB type nano-objects have been proposed as contrast agents for several types of imaging including Magnetic Resonance Imaging (MRI) [11–21], scintigraphy [22], photoacoustic imaging [23,24], as nano-carriers for drug delivery [25–28], or as therapeutic agents for different kinds of therapy and treatment [26,29].

The most extensive recent development of PB type nanoparticles for therapeutic purposes is linked with their exceptional potential as Photothermal Therapy (PTT) agent for cancer treatment. The principle of this newly developed hyperthermia strategy for the therapeutic treatment of tumour cells consists in the ablation of the malignant cells by laser irradiation at energetically low wavelengths in the presence of a Near Infrared Region (NIR) photo-absorbing agent [30–32]. PB nanoparticles exhibit a strong absorption in the NIR arising from a metal-to-metal charge transfer band (from Fe^{2+} to Fe^{3+}) situated between 650 and 900 nm, a high photothermal conversion efficiency and an outstanding stability over irradiation. Recently, it has been demonstrated *in vitro* and *in vivo* that PB and Mn^{2+}- or Gd^{3+}-doped PB nanoparticles are able to convert the laser irradiation into thermal energy under single-photon irradiation, which provides an important temperature elevation and a tumour necrosis [11,12,20,33–43]. The efficiency depends on the nanoparticles' concentration, their chemical composition, the optical density and the irradiation time which makes it difficult to compare different PB-based systems. It has been shown

* Corresponding authors.
E-mail addresses: joulia.larionova@umontpellier.fr (J. Larionova), magali.gary-bobo@inserm.fr (M. Gary-Bobo).
[1] On sabbatical leave from Medical Research Institute, Alexandria University, Egypt.

https://doi.org/10.1016/j.pdpdt.2018.02.015
Received 24 November 2017; Received in revised form 15 January 2018; Accepted 20 February 2018
Available online 22 February 2018

Table 1
Some characteristics for nanoparticles **1–3**.

Label	Formula	d[a](nm)	Zeta potential (mV)
1	$Na_{0.41}Fe[Fe(CN)_6]_{0.85}$	67 ± 6	−31.3
2	$Na_{0.27}Mn_{0.14}Fe[Fe(CN)_6]_{0.89}$	73 ± 9	−36.1
3	$Na_{0.19}Mn_{0.44}Fe[Fe(CN)_6]$	61 ± 6	−40.5

[a] Core diameter determined from TEM analysis.

that they present higher efficiency in comparison with Au nano-objects and better photothermal stability than organic dyes used as conventional PTT agents [12,42]. However, complete eradication of tumour cells with single-photon excitation PTT treatments is rather difficult due to the heterogeneous laser heat distribution and a limited light penetration. Moreover relatively high concentrations of PTT agents are needed for this treatment [12,37,42,43]. In this line of thought, PTT under two-photon excitation provides well-known advantages over single-photon irradiation due to its increased penetration depth and focalization allowing selective, efficient, and rapid destruction of the targeted tumour cells with less damages of healthy tissues [44,45,46].

Yet, to the best of our knowledge, such treatment has never been applied using PB type nanoparticles.

In this communication, we demonstrate for the first time that PB and Mn^{2+}-doped PB nanoparticles of *c.a.* 70 nm act as efficient PTT agents under two-photon excitation inducing an almost total eradication of malignant cells (97 and 98%) at a concentration of 100 μg mL^{-1} 24 h after NIR excitation. These results highlight a significant improvement related to the use of a lower concentration of PTT agent and superior efficacy compared to previously published one-photon PTT treatment. Moreover, due to their interesting r_1 longitudinal relaxivity values, they may be considered as promising theranostic agents.

PB and Mn^{2+}-doped PB nanoparticles were synthesized using the controlled self-assembly reaction between molecular precursors, $Na_4[Fe(CN)_6]\cdot 10H_2O$ and $FeCl_3\cdot 6H_2O$ with various amounts of $MnCl_2\cdot 6H_2O$ to give $Na_{0.41}Fe[Fe(CN)_6]_{0.85}$ (**1**), $Na_{0.27}Mn_{0.14}Fe[Fe(CN)_6]_{0.89}$ (**2**) and $Na_{0.19}Mn_{0.44}Fe[Fe(CN)_6]$ (**3**) nanoparticles. All samples exhibit the bulk PB structural features as confirmed by their stretching vibration around 2080 cm^{-1} (Fig. S1, SI). Obtained Zeta potential values of −31.3, −36.1 and −40.5 mV for **1**, **2** and **3**, respectively (Table 1), confirm their negative surface charge arising from the presence of the cyanometallate groups localized on the nanoparticles' surface. Transmission Electronic Microscopy (TEM) images show the typical cubic shape of PB nanoparticles with a mean diameter ranging from 61 to 73 nm (Fig. 1, Fig. S2, Table 1). Note that in the previously published work, a significant size change (from 60 to 160 nm) occurred with the modification of the Mn^{2+} amount, which makes difficult to compare the nanoparticles' properties [12]. The absorption spectra of samples **1–3** show a broad band in the range 600–900 nm with a maximum at 735 nm for PB nanoparticles **1**, which is red-shifted to 777 and 783 nm for **2** and **3**, respectively. Such bathochromic shift has previously been observed for manganese-doped PB hollow cubes [12]. Concomitantly, a decrease in absorbance is also observed with increased manganese amounts.

In order to study the therapeutic efficiency of these nanoparticles as PTT agents, we used a human breast adenocarcinoma MDA-MB-231 cell line expressing green fluorescent protein (GFP) which provides the visualization of nuclei in green. After 24 h of cell growth, the cells were incubated with nanoparticles **1**, **2** and **3** at a concentration of 100 μg mL^{-1}. 24 h after treatment, the cells were visualized with LSM-confocal microscope by using the excitation at 488 nm (green fluorescence) (Fig. 2, images before irradiation). Then, irradiation with a pulsed laser for two-photon excitation at 808 nm (3.7 W, 5% of total laser power) for 10 min was performed. The cells were visualized immediately and 24 h after irradiation (Fig. 2).

The safety of the two-photon irradiation on control cells (*i.e.* without nanoparticles) is clearly observable immediately after irradiation. In addition, 24 h after irradiation, an increase in the green fluorescence was observed for control cells, indicating a cell proliferation, which confirms the laser safety and the availability of normal conditions for the cell growth. On the contrary, a visible reduction of the cell number was observed for cells treated with sample **2** immediately after irradiation, while, no changes were observed in cells containing samples **1** and **3**. However, 24 h after irradiation, all samples **1–3** induce a dramatic decrease of cell numbers (Fig. 2).

These results were confirmed by a quantitative cell counting using ImageJ program, as shown in Fig. 3a. Indeed, sample **2** is the only one that induces a pronounced effect immediately after irradiation by

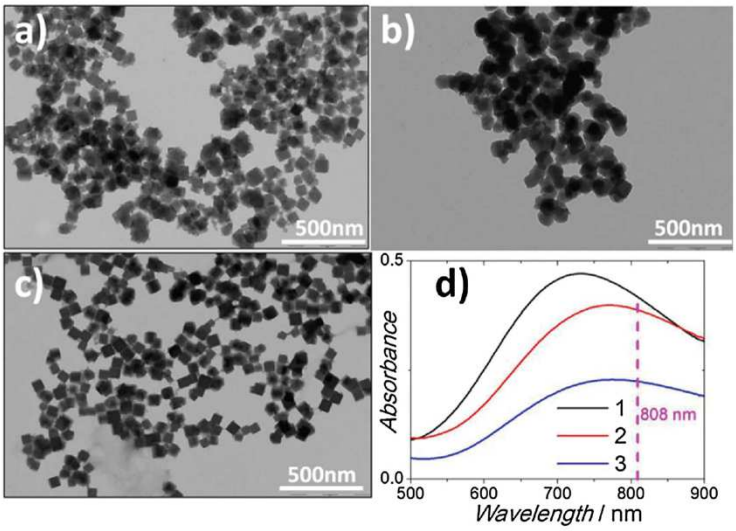

Fig. 1. TEM images of the **1** (a), **2** (b) and **3** (c); d) UV–vis spectra of the aqueous suspensions of **1**, **2** and **3** (0.033 mg mL^{-1}).

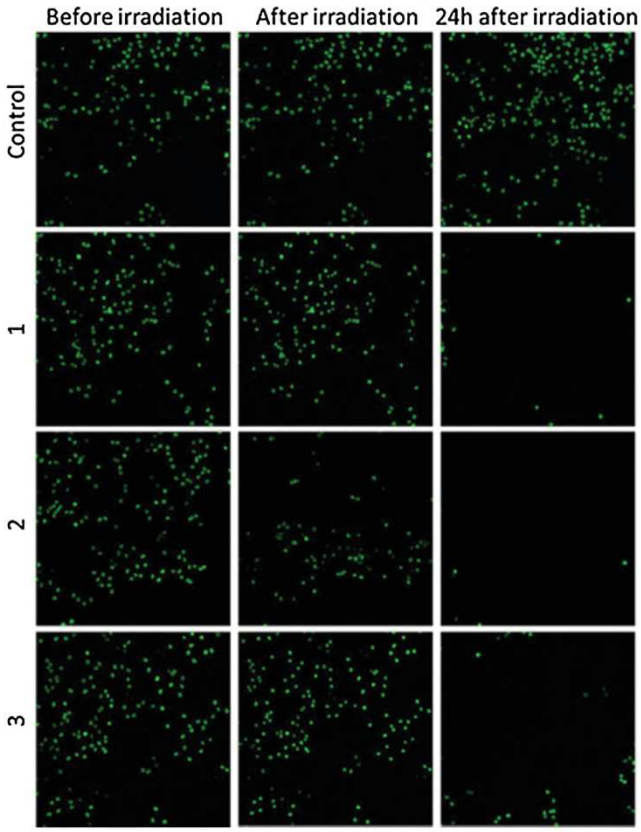

Fig. 2. Fluorescence imaging of living MDA-MB-231 cells treated for 24 h with nanoparticles **1**, **2** and **3** at a concentration of 100 μg mL^{-1}, before irradiation, immediately after irradiation and 24 h after irradiation with a two-photon excitation laser at 808 nm (3.7 W, 5% power) for 10 min.

causing 33% of cell death. One day after irradiation, **1**, **2** and **3** induce 96, 97 and 85% of cell death, respectively. The observed effect is much better in terms of cell death in comparison to that is observed for a single photon irradiation (0.8 W/cm^2, 5 min) for incubated PB nanoparticles of 65 nm or 15% manganese-doped PB hollow cubes of 60–160 nm with a similar concentration where only *ca.* 65–67% of cell death was found [12,40], for Gadolinium doped PB nanoparticles [43] (less than 20% of cell death with a similar concentration) or for 500 nm hollow nanoparticles presenting little PTT effect [37]. The difference in behavior observed between samples **2** and **3** may be explained by the lower absorbance value of the latter.

In order to investigate the influence of the nanoparticles' concentration on the PTT, lower concentrations (50, 10 or 1 μg mL^{-1}) of **2** were used in the same experimental conditions. Fig. 3b shows that the presence of the nanoparticles has no effect immediately after irradiation at these concentrations. A significant cell death (88%) was observed 24 h after irradiation at the concentration of 50 μg mL^{-1}, while below 10 μg mL^{-1} the loss of the photothermal properties is indicated by steady/increase in cell number.

NMR relaxivity measurements were performed for Mn^{2+}-doped PB nanoparticles **2** and **3** to confirm their potential as contrast agents for MRI. The room temperature proton relaxation time T_1 measurements were done for aqueous solutions of **2** and **3** with different concentrations at an applied magnetic field of 4.7 T by using a spectrometer Tecmag Apollo operating at 200 MHz. The longitudinal, r_1, relaxivity was determined from the slopes of the plot of $1/T_1$ *vs* nanoparticles' concentration and is equal to 2.58 and 5.30 $mM^{-1}s^{-1}$ for **2** and **3**, respectively (Fig. S3, SI). These values are higher or comparable with the ones obtained for the commercial contrast agent known as the trademark Prohance® (3.00 $mM^{-1}s^{-1}$) and comparable with r_1 values found for other Mn^{2+}-doped PB nanoparticles [12,37]. This result indicates that these nanoparticles may be used as T_1 MRI contrast agents.

Nanoparticles' safety was evaluated by investigating the cytotoxicity in MDA-MB-231 cells treated with different concentrations (50, 100 and 150 μg mL^{-1}) of nanoparticles **1**–**3**, 3 days after nanoparticles' incubation. The results indicate over 90% cell viability, allowing to consider that these nanoparticles do not exhibit toxicity at these concentrations (Fig. S4, SI). This is in agreement with other studies, which however were carried out for a shorter period of time [37]. Moreover, the kinetic of the cells' division was not altered by the presence of the nanoparticles. In order to prove this, an assay of the cell cycle phases in MDA-MB-231 cells treated with different concentrations (0, 50, 100 and 150 μg mL^{-1}) of sample **2** for 3 days, was carried out. Results presented in Fig. S5, SI show that the increase in the nanoparticles concentrations is associated with a slight increase in the G1 phase, suggesting the initiation of cell arrest mechanism at the highest concentrations

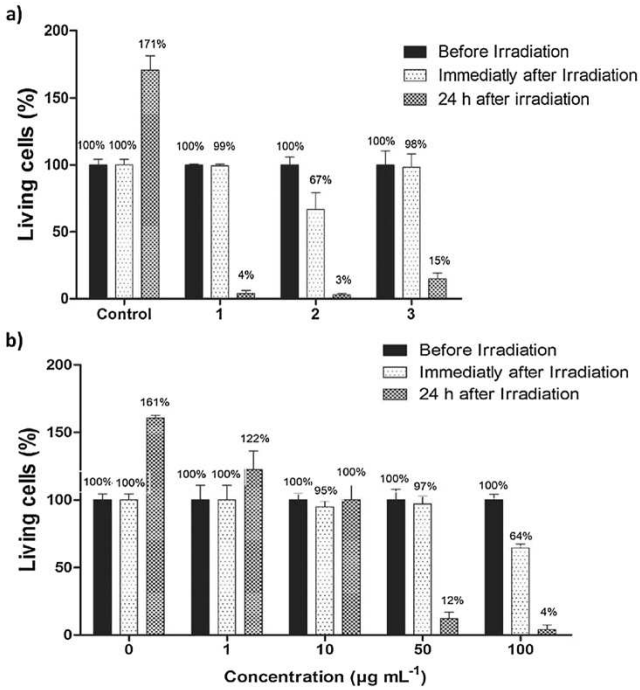

Fig. 3. a) Cell counting% of living MDA-MB-231 cells treated with nanoparticles **1–3** at a concentration of 100 µg mL^{-1} before irradiation, immediately after irradiation and 24 h after irradiation with a two-photon excitation laser at 808 nm (3.7 W, 5% power) for 10 min. Data are presented as (mean ± SEM), n = 3; b) Cell counting% of living cells MDA-MB-231 treated with different concentrations of Mn-doped PB nanoparticles **2** before irradiation, immediately after irradiation and 24 h after irradiation with a two-photon excitation laser at 808 nm (3.7 W, 5% power) for 10 min using different concentrations of nanoparticles (1, 10, 50 and 100 µg mL^{-1}). Data are presented as (mean ± SEM), n = 3.

(150 µg mL^{-1}). Consequently we can observe a small decrease in the G2 phase. No apoptosis was been observed here (no detectable Sub-G1 peak). This result obtained with flow cytometer is in agreement with the data of cytotoxicity study.

In summary, we report here the synthesis of cubic PB nanoparticles of *c.a.* 70 nm doped with different amounts of Mn^{2+} and their investigations as efficient agents for two-photon excited photothermal therapy. All nanoparticles have similar diameter and possess different amount of Mn^{2+} allowing to compare the efficiency of these systems for PTT. They show a great photothermal potential under two-photon excitation, as indicated by an almost total eradication of malignant cells (97 and 98%) in the case of Mn^{2+} doped nanoparticles 24 h after NIR excitation at a concentration of 100 µg mL^{-1}. Such result is much better than previously reported ones concerning single-photon PTT for other PB nano-objects. Even if the investigated nanoparticles do not present the same size, shape and composition, we can reasonably suppose that this difference mainly comes from two-photon irradiation conditions. Further, these results in terms of efficiency as well as the advantages of two-photon irradiation (high penetration depth and light focalization) constitute favorable elements for the use of this type of nanoparticles for PTT under bi-photonic irradiation rather than under one-photonic one. In addition, Mn^{2+}-doped nanoparticles exhibit longitudinal relaxivity values higher or comparable to the commercial contrast agent Prohance®. Finally a cytotoxicity study showed that these nanoparticles had no cytotoxic effect up to a concentration of 150 µg mL^{-1} after 3 days of incubation. This study demonstrates that PB and Mn^{2+}-doped PB nanoparticles exhibit remarkable efficacy for PTT under two-photon excitation and longitudinal relaxivity providing an additional lane to the reflections conducted for the development of novel theranostic agents.

The authors thank the University of Montpellier, CNRS, for financial support, PAC ICGM and BionanoMRI platforms for measurements. Lamiaa M. A. Ali acknowledges the support from the French and the Egyptian Governments through a cofinanced fellowship granted by the French Embassy in Egypt (Institut Français d'Egypte) and the Science and Technology Development Fund (STDF). Magali Gary-Bobo is grateful to the Région Languedoc-Roussillon for Research Grant "Chercheur(se)s d'Avenir".

Appendix A. Supplementary data

Supplementary data associated with this article can be found, in the online version, at https://doi.org/10.1016/j.pdpdt.2018.02.015.

References

[1] E. Dujardin, S. Mann, Adv. Mater. 16 (2004) 1125–1129.
[2] L. Catala, F. Volatron, D. Brinzei, T. Mallah, Inorg. Chem. 48 (2009) 3360–3370.
[3] J. Larionova, Y. Guari, C. Sangregorio, C. Guerin, New J. Chem. 33 (2009) 1177–1190.
[4] L. Catala, T. Mallah, Coord. Chem. Rev. 346 (2017) 32–61.
[5] J. Long, Y. Guari, C. Guerin, J. Larionova, Dalton Trans. 45 (2016) 17581–17587.
[6] V. Nigrovic, Phys. Med. Biol. 10 (1965) 81–92.
[7] D.R. Melo, J.L. Lipsztein, C.A.N. Oliveira, L. Bertelli, Health Phys. 66 (1994) 245–252.
[8] J. Pearce, Food Chem. Toxicol. 32 (1994) 577–582.
[9] D.F. Thompson, C.O. Church, Pharmacotherapy, J. Hum. Pharmacol. Drug Ther. 21 (2001) 1364–1367.
[10] J. Ruprecht, Toxicology 233 (2007) 20–22.
[11] X. Cai, W. Gao, L. Zhang, M. Ma, T. Liu, W. Du, Y. Zheng, H. Chen, J. Shi, ACS Nano 10 (2016) 11115–11126.
[12] W. Zhu, K. Liu, X. Sun, X. Wang, Y. Li, L. Cheng, Z. Liu, ACS Appl. Mater. Interfaces 7 (2015) 11575–11582.
[13] M. Perrier, A. Gallud, A. Ayadi, S. Kennouche, C. Porredon, M. Gary-Bobo, J. Larionova, C. Goze-Bac, M. Zanca, M. Garcia, I. Basile, J. Long, J. de Lapuente, M. Borras, Y. Guari, Nanoscale 7 (2015) 11899–11903.
[14] G. Paul, Y. Prado, N. Dia, E. Riviere, S. Laurent, M. Roch, L.V. Elst, R.N. Muller, L. Sancey, P. Perriat, O. Tillement, T. Mallah, L. Catala, Chem. Commun. 50 (2014) 6740–6743.

[15] M.F. Dumont, S. Yadavilli, R.W. Sze, J. Nazarian, R. Fernandes, Int. J. Nanomed. 9 (2014) 2581–2595.
[16] M.F. Dumont, H.A. Hoffman, P.R.S. Yoon, L.S. Conklin, S.R. Saha, J. Paglione, R.W. Sze, R. Fernandes, Bioconjugate Chem. 25 (2014) 129–137.
[17] M. Perrier, S. Kenouche, J. Long, K. Thangavel, J. Larionova, C. Goze-Bac, A. Lascialfari, M. Mariani, N. Baril, C. Guérin, B. Donnadieu, A. Trifonov, Y. Guari, Inorg. Chem. 52 (2013) 13402–13414.
[18] E. Chelebaeva, J. Larionova, Y. Guari, R.A.S. Ferreira, L.D. Carlos, A.A. Trifonov, T. Kalaivani, A. Lascialfari, C. Guerin, K. Molvinger, L. Datas, M. Maynadier, M. Gary-Bobo, M. Garcia, Nanoscale 3 (2011) 1200–1210.
[19] M. Shokouhimehr, E.S. Soehnlen, A. Khitrin, S. Basu, S.D. Huang, Inorg. Chem. Commun. 13 (2010) 58–61.
[20] M. Shokouhimehr, E.S. Soehnlen, J. Hao, M. Griswold, C. Flask, X. Fan, J.P. Basilion, S. Basu, S.D. Huang, J. Mater. Chem. 20 (2010) 5251–5259.
[21] Y. Guari, J. Larionova, M. Corti, A. Lascialfari, M. Marinone, G. Poletti, K. Molvinger, C. Guerin, Dalton Trans. (2008) 3658–3660.
[22] M. Perrier, M. Busson, G. Massasso, J. Long, V. Boudousq, J.P. Pouget, S. Peyrottes, C. Perigaud, C. Porredon-Guarch, J. de Lapuente, M. Borras, J. Larionova, Y. Guari, Nanoscale 6 (2014) 13425–13429.
[23] L. Jing, X. Liang, Z. Deng, S. Feng, X. Li, M. Huang, C. Li, Z. Dai, Biomaterials 35 (2014) 5814–5821.
[24] X. Liang, Z. Deng, L. Jing, X. Li, Z. Dai, C. Li, M. Huang, Chem. Commun. 49 (2013) 11029–11031.
[25] S. Mukherjee, B.R. Rao, B. Sreedhar, P. Paik, C.R. Patra, Chem. Commun. 51 (2015) 7325–7328.
[26] M.S. Kandanapitiye, F.J. Wang, B. Valley, C. Gunathilake, M. Jaroniec, S.D. Huang, Inorg. Chem. 54 (2015) 1212–1214.
[27] W. Shao-Jen, C. Chun-Sheng, C. Lin-Chi, Sci. Technol. Adv. Mater. 14 (2013) 044405.
[28] H.-Y. Lian, M. Hu, C.-H. Liu, Y. Yamauchi, K.C.W. Wu, Chem. Commun. 48 (2012) 5151–5153.
[29] C. Lavaud, M. Kajdan, E. Compte, J.-C. Maurel, J. Lai, Kee Him, P. Bron, E. Oliviero, J. Long, J. Larionova, Y. Guari, New J. Chem. 41 (2017) 2887–2890.
[30] L.W. Zou, H. He, L. Zeng, T. Tan, H. Cao, X. He, Z. Zhang, S. Guo, Y. Li, Theranostics 6 (2016) 762–772.
[31] V. Shanmugam, S. Selvakumar, C.-S. Yeh, Chem. Soc. Rev. 43 (2014) 6254–6287.
[32] A.M. Alkilany, L.B. Thompson, S.P. Boulos, P.N. Sisco, C.J. Murphy, Adv. Drug Del. Rev. 64 (2012) 190–199.
[33] E.E. Sweeney, R.A. Burga, C. Li, Y. Zhu, R. Fernandes, Sci. Rep. 6 (2016) 37035.
[34] L. Jing, S. Shao, Y. Wang, Y. Yang, X. Yue, Z. Dai, Theranostics 6 (2016) 40–53.
[35] W.-P. Li, C.-H. Su, L.-C. Tsao, C.-T. Chang, Y.-P. Hsu, C.-S. Yeh, ACS Nano (2016), http://dx.doi.org/10.1021/acsnano.6b05858.
[36] R.A. Burga, S. Patel, C.M. Bollard, C.R.Y. Cruz, R. Fernandes, Nanomedicine 11 (2016) 1759–1767.
[37] X. Jia, X. Cai, Y. Chen, S. Wang, H. Xu, K. Zhang, M. Ma, H. Wu, J. Shi, H. Chen, ACS Appl. Mater. Interfaces 7 (2015) 4579–4588.
[38] X. Cai, X. Jia, W. Gao, K. Zhang, M. Ma, S. Wang, Y. Zheng, J. Shi, H. Chen, Adv. Funct. Mater. 25 (2015) 2520–2529.
[39] X. Cai, W. Gao, M. Ma, M. Wu, L. Zhang, Y. Zheng, H. Chen, J. Shi, Adv. Mater. 27 (2015) 6382–6389.
[40] H.A. Hoffman, L. Chakrabarti, M.F. Dumont, A.D. Sandler, R. Fernandes, RSC Adv. 4 (2014) 29729–29734.
[41] L. Cheng, H. Gong, W. Zhu, J. Liu, X. Wang, G. Liu, Z. Liu, Biomaterials 35 (2014) 9844–9852.
[42] G. Fu, W. Liu, S. Feng, X. Yue, Chem. Commun. 48 (2012) 11567–11569.
[43] Y. Li, C.H. Li, D.R. Talham, Nanoscale 7 (2015) 5209–5216.
[44] J.L. Li, D. Day, M. Gu, Adv. Mater. 20 (2008) 3866–3871.
[45] J. Kim, S. Park, J.E. Lee, S.M. Jin, J.H. Lee, I.S. Lee, I. Yang, J.-S. Kim, S.K. Kim, M.-H. Cho, T. Hyeon, Angew. Chem. Int. Ed. 45 (2006) 7754–7758.
[46] S. Madadi Ardekani, A. Dehghani, M. Hassas, M. Kianinia, I. Aharonovich, V.G. Gomes, Chem. Eng. J. 330 (2017) 651–662.

SUPPORTING INFORMATION

Multifunctional manganese-doped Prussian blue nanoparticles for two-photon Photothermal Therapy and Magnetic Resonance Imaging

Lamiaa M.A. Ali,[a1] Emna Mathlouthi,[b,c] Marilyn Kajdan,[b] Morgane Daurat,[a,d] Jérôme Long,[b] Rahima Sidi-Boulenouar,[e] Maida Cardoso,[e] Christophe Goze-Bac,[e] Nourredine Amdouni,[c] Yannick Guari,[b] Joulia Larionova,[b*] Magali Gary-Bobo[a*]

[a] *Institut des Biomolécules Max Mousseron, UMR5247, Université de Montpellier, CNRS, ENSCM, Faculté de Pharmacie, 15 Avenue Charles Flahault, 34093 Montpellier Cedex 05, France*

[b] *Institut Charles Gerhardt Montpellier, UMR 5253, Ingénierie Moléculaire et Nano-Objets, Université de Montpellier , CNRS, ENSCM, place E. Bataillon, 34095 Montpellier Cedex 5, France.*

[c] *Université de Tunis el Manar, Faculté des Sciences, UR/11/ES/19, Physico-chimie des matériaux à l'état condensé, 2092, Tunis, Tunisie*

[d] *NanoMedSyn, 15 avenue Charles Flahault, 34093 Montpellier, France.*

[e] *L2C, UMR 5221 CNRS-UM2, Equipe BioNanoNMRI, Université de Montpellier, Place Eugène Bataillon, 34095 Montpellier Cedex 5, France.*

[1] On sabbatical leave from Medical Research Institute, Alexandria University, Egypt

Experimental

Synthetic procedures

Materials. All chemical reagents were purchased and used without further purification: potassium ferricyanide (Acros Organics, 99%), Iron(III) chloride hexahydrate ($FeCl_3 \cdot 6H_2O$, 97% Chimica), ultra-pure water. The $Na_3[Fe(CN)_6]$ complex was obtained by passing the $K_3[Fe(CN)_6]$ through an ion-exchange resin (acidic form) followed by neutralisation with NaOH.

Synthesis of Prussian Blue nanoparticles (1). At 25°C, aqueous solutions of $FeCl_3 \cdot 6H_2O$ (10 mM, 10 mL) and $Na_4[Fe(CN)_6] \cdot 10H_2O$ (11.25 mM, 10 mL) were added simultaneously to 100 mL of pure water at 2 mL/h rate, using a syringe pump. After completion of the addition, the mixture was stirred one hour before being centrifuged at 35,700 x g (20,000 rpm) during 10 min. The supernatant was removed and the NPs were washed successively with water and ethanol and dried under vacuum.

IR (KBr): $\nu(C\equiv N) = 2085\ cm^{-1}$. EDS: 18.07/81.93 (Na/Fe). Formula found: $Na_{0.41}Fe[Fe(CN)_6]_{0.85}$.

Synthesis of Mn^{2+}-doped Prussian Blue nanoparticles (2). The protocol is identical than for **1** except that a mixture of $FeCl_3 \cdot 6H_2O$ (7.6 mM) and $MnCl_2 \cdot 4H_2O$ (0.4 mM) in 10 mL was used. IR (KBr): $\nu(C\equiv N) = 2085\ cm^{-1}$. EDS: 11.90/6.06/82.05 (Na/Mn/Fe). Formula found: $Na_{0.27}Mn_{0.14}Fe[Fe(CN)_6]_{0.89}$.

Synthesis of Mn^{2+}-doped Prussian Blue nanoparticles (3). The protocol is identical than for **1** except that a mixture of $FeCl_3 \cdot 6H_2O$ (5.6 mM in 10mL) and $MnCl_2 \cdot 4H_2O$ (2.4 mM in10mL) was used. IR (KBr): $\nu(C\equiv N) = 2081\ cm^{-1}$. EDS: 7.04/16.62/76.34 (Na/Mn/Fe). Formula found: $Na_{0.19}Mn_{0.44}Fe[Fe(CN)_6]$.

Characterisation methods

Infrared spectra were recorded as KBr disks on a Nicolet Model 510P spectrophotometer. UV-Vis spectra were collected on a SPECOORD 210 UV-VIS spectrometer in water. Transmission Electron Microscopy (TEM) observations were carried out at 100 kV (JEOL 1200 EXII). Samples for TEM measurements were deposited from solutions on copper grids. Nanoparticles' size distribution histograms were determined using enlarged TEM micrographs taken at magnification of 100 K on a statistical sample of ca. 300 nanoparticles. HRTEM measurements were performed on a JEOL 2200FS. Scanning Electronic Microscopy (EDS) analyses were performed on a FEI Quanta FEG 200 instrument. The powders were deposited on an adhesive carbon film and analysed under vacuum. The quantification of the heavy elements was carried out with the INCA software, with a dwell time of 3 µs. Hydrodynamic diameter and zeta potential were determined using a Nano ZS apparatus (Malvern). Data were collected from the He-Ne laser light source (633 nm) at 173° from the transmitted beam. Results were presented as Z-average obtained in intensity mode, associated to the polydispersity index (PDI).

The ^{1}H NMR relaxometry characterizations have been performed by using aqueous solutions of the nanoparticles prepared from powder samples by their redispersion in water. The longitudinal (T_1) relaxation times measurements for different concentrations of nanoparticles were performed on a Tecmag Apollo spectrometer operating at 10 *MHz*. An saturation-recovery followed by Hahn echo detection sequence (SAT – τ – Hahn) was used to measure the longitudinal relaxation time T_1. τ was varied from 100 ms to 3 s. For each concentration of the nanoparticles, the table of delay (τ) was chosen such that the instantaneous magnetization $M_z(t)$ recovers its equilibrium value M_0. Thereby each T_1 value was obtained by curve fitting using the relation: $M_z(t) = M_0 \times [1 - exp(-t/T_1)]$, where $M_z(t)$ represents the longitudinal magnetization at time τ following the saturation pulse train. The r_1 relaxivity was then calculated from the slope of a linear regression of $R_{1,2} = T^{-1}_1$ against the concentration of the nanoparticles (C), following : $R_1 = R^0_1 + r_1 \times C$, where R^0_1 is the relaxation rate without nanoparticles.

Cell culture

Human breast adenocarcinoma MDA-MB-231 cell line was used. Here this cell line stably expresses GFP inducing the visualization of green nuclei. Cells were cultured in Dulbecco's Modified Eagle's Medium (DMEM) supplemented with 10% fetal bovine serum and antibiotic (0.05 mg mL^{-1} gentamicin). These cells grown in humidified atmosphere at 37°C and under 5% CO_2.

Cytotoxicity experiments

MDA-MB-231 cells were seeded in 384-well plates. After 24 hours of cell growth, cells were treated with increasing concentrations (0, 50, 100 and 150 µg mL^{-1}) of Prussian blue nanoparticles (**1-3**). 3 days after treatment, cells were visualized with LSM-confocal microscope; green fluorescence was excited at 488 nm, cells were counted using ImageJ program.

Cell-cycle analysis

MDA-MB-231 cells were seeded in 12-well plate and let to grow for 24 h. After 24 h of cell growth, cells were treated with different concentrations (0, 50, 100 and 150 µg mL^{-1}) of sample **2**. After 3 days of treatment, cells were harvested and fixed with ethanol overnight at 4°C. After fixation, the cells were incubated with RNase A and Propidium iodide (PI) at concentrations 1 mg mL^{-1} and 40 µg mL^{-1}, respectively, for 2 h at room temperature in dark followed by 24 h at 4°C in dark. Flow cytometric analysis was performed using NovoCyte flow cytometer and the data were analyzed by NovoExpress software (ACEA Biosciences, Inc.). The evaluation of the intracellular DNA content was carried out in 10,000 events.

Hyperthermia experiments

MDA-MB-231 cells were seeded in 384-well plates. After 24 hours of cell growth, cells were treated with Prussian blue nanoparticles (**1-3**) at concentration 100 µg mL^{-1} and with different concentrations (0, 1, 10, 50 and 100 µg mL^{-1}) of PB nanoparticles **2**. 24 hours after treatment, cells were visualized

with LSM-confocal microscope; green fluorescence was excited at 488 nm. Then cells were irradiated with pulsed laser at 808 nm (3,7 W, 5% of total laser power) for 10 min. Cells were observed and exposed to imaging immediately after irradiation and 24 h after irradiation. For quantification, cells were counted using ImageJ program.

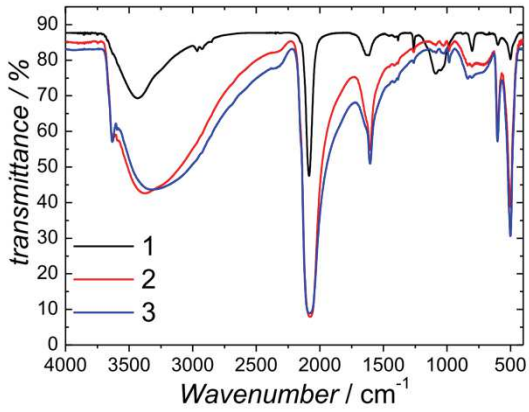

Fig. S1. IR spectra of samples **1**, **2** and **3**.

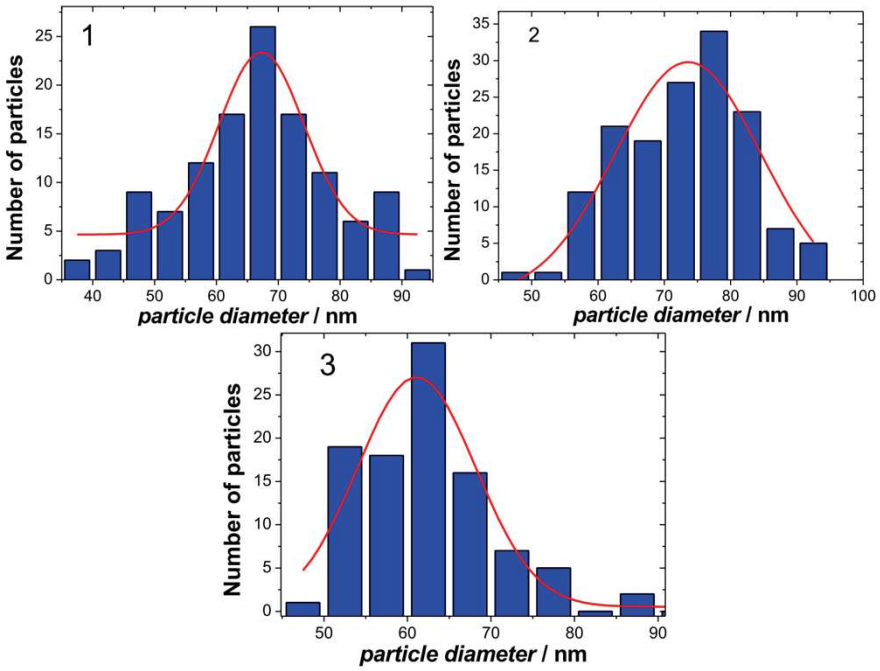

Fig. S2. Size distribution for samples **1-3**. The red solid line corresponds to the fit with a Gaussian function.

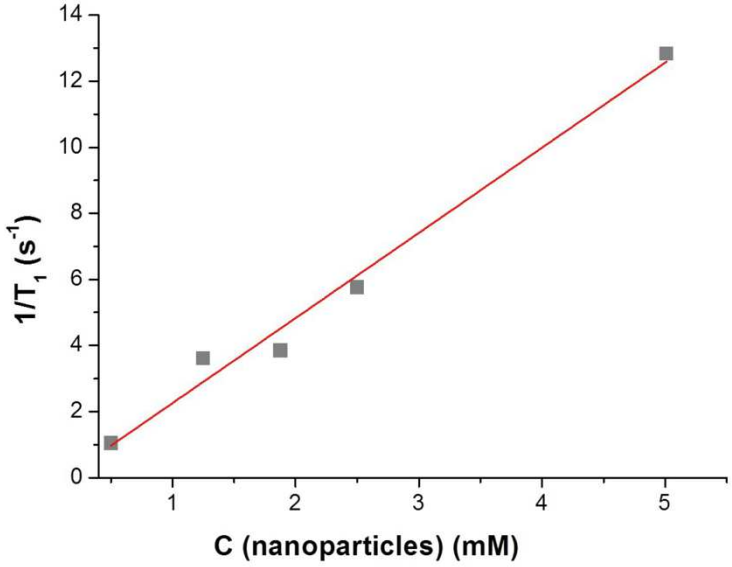
14
12
10
8
6
4
2
0
1
2
3
4
5
1/T1 (s-1)
C (nanoparticles) (mM)

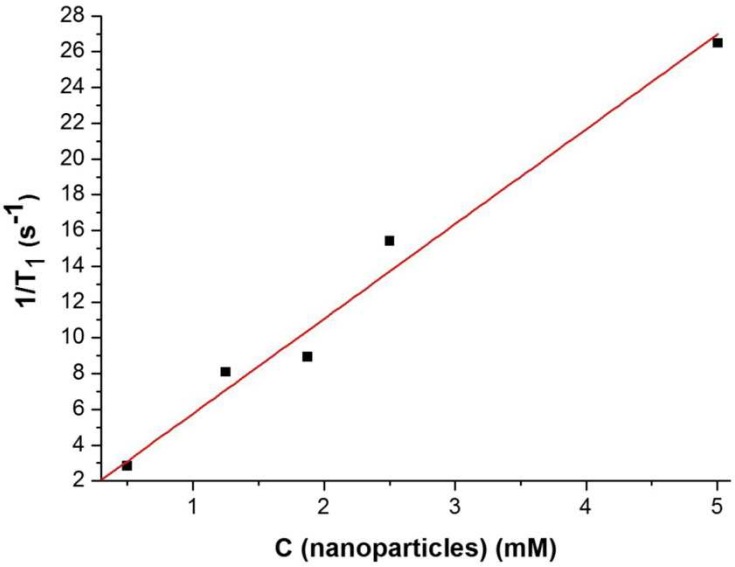
28
26
24
22
20
18
16
14
12
10
8
6
4
2
1
2
3
4
5
1/T1 (s-1)
C (nanoparticles) (mM)

Fig. S3. T_1 relaxation rate measurements *vs* concentration of aqueous solutions of the nanoparticles **2** (top) and **3** (down) performed at an applied magnetic field of 4.7 T.

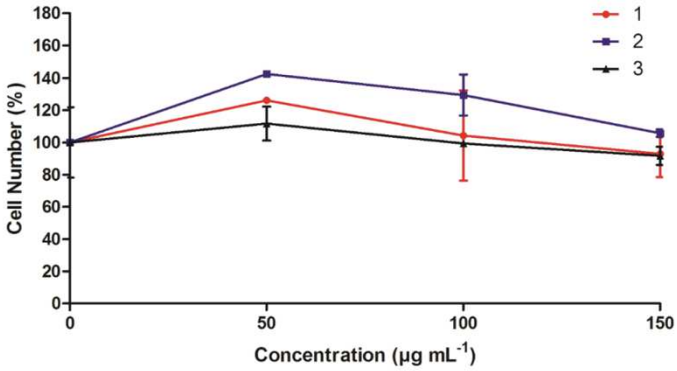

Fig. S4. Cell viability (%) of MDA-MB-231 cells treated with increasing concentrations of nanoparticles **1** – **3** after 3 days of incubation. Data are presented as (mean ± SEM), n=2. No significant differences where observed with the 3 batches of nanoparticles at the studied doses.

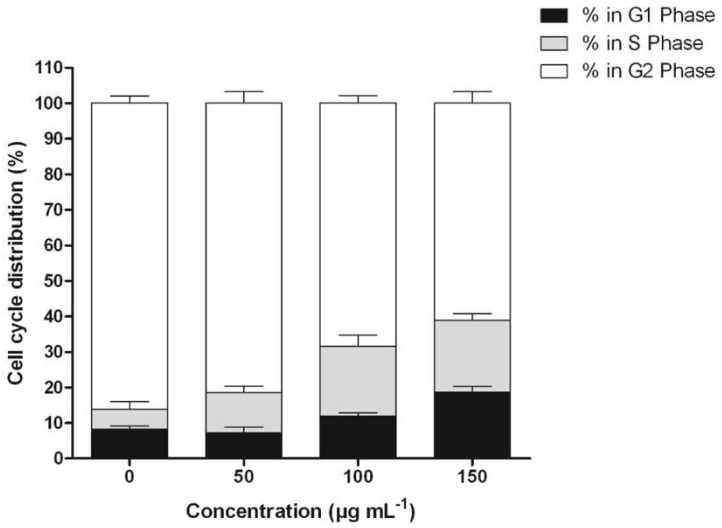

Fig. S5. Cell cycle analysis of MDA-MB-231 breast cancer cells treated with different concentrations of sample **2** for 3 days and then stained with PI. Data are presented as (mean ± SEM), n=2.

- Conclusion :

Dans ce travail, nous avons décrit la synthèse de PB cubiques dopées ou non avec différentes quantités de manganèse et étudié ces PB comme agent photothermique efficace sous irradiation biphotonique. Les PB entraînent quasiment 100% de mort cellulaire 24 h après l'irradiation à des concentrations inférieures à celles rapportées dans la littérature pour une irradiation monophotonique. De plus, nous avons démontré la biocompatibilité des PB même à des concentrations élevées. L'efficacité thérapeutique de ces PB ainsi que les avantages d'une irradiation biphotonique constituent des éléments favorables pour l'utilisation de ce type de nanoparticules en PTT. De plus, du fait de leur intéressant temps de relaxation longitudinale grâce au manganèse, ces PB pourraient être utilisées en tant qu'agent de contraste. En effet, leur temps de relaxation est supérieur ou comparable à ceux de l'agent de contraste commercial Prohance®. Les PB dopées en manganèse présentent donc une remarquable efficacité thérapeutique et un potentiel en tant qu'agent de contraste offrant une voie de développement de ces PB comme nouveaux agents théranostiques.

- Perspective :

Ce travail devra être complété par la mesure de l'élévation de la température dans les cellules cancéreuses après une irradiation biphotonique. Pour cela, nous avons obtenu un contrat de l'Agence Nationale de la Recherche qui permettra entre autres de nous procurer une caméra thermique nécessaire à la mesure de la température. Certaines études ont déjà démontré l'efficacité thérapeutique par PTT avec une irradiation biphotonique de nanoparticules d'or qui sont connues pour avoir un excellent potentiel photothermique[287–290].

3.2 Publication n°2 : Implementing luminescence in Prussian blue nanoparticles : synthesis, properties and *in vitro* imaging.

- Introduction :

Dans la continuité du travail décrit précédemment, nous avons étudié le potentiel des PB en imagerie par fluorescence. Cette technique plus simple et moins coûteuse que celles citées précédemment (IRM, scintigraphie, imagerie photo-acoustique) bénéficie d'une sensibilité élevée[285] et est indispensable pour exploiter pleinement les propriétés des PB afin de les visualiser pour étudier leur biodistribution et comprendre leur efficacité. Cependant, les études sur l'implémentation de la luminescence dans les PB sont peu nombreuses : nous pouvons citer les exemples de PB dopées au manganèse et fonctionnalisées à la surface avec de l'avidine[285] ou un cœur de polypyrrole[291] qui ont permis *in vitro* d'observer l'internalisation des PB dans les cellules. Par conséquent, de nouveaux exemples de PB luminescentes avec différentes gammes d'émissions sont nécessaires. Pour ce travail, l'équipe du Dr Yannick Guari et plus particulièrement, Mme Ekaterina Mamontova, doctorante, ont mis en évidence une stratégie originale visant à rendre luminescente des PB par une fonctionnalisation après la synthèse des nanoparticules par deux fluorophores différents, le 2-aminoanthracène (AA) et la Rhodamine B (RhB), afin de produire un système magnéto-luminescent permettant de suivre le devenir des nanoparticules dans les cellules cancéreuses. Cet article où je suis co-premier auteur fera l'objet d'une future soumission.

Journal Name

COMMUNICATION

Implementing luminescence in Prussian blue nanoparticles: synthesis, properties and *in vitro* imaging

Received 00th January 20xx,
Accepted 00th January 20xx

DOI: 10.1039/x0xx00000x

www.rsc.org/

Ekaterina Mamontova,[a,§] Morgane Daurat,[b,c,§] Jérôme Long*, Anastasia Godefroy,[b,c] Fabrice Salles,[d] Yannick Guari,[a] Magali Gary-Bobo*[b] and Joulia Larionova[a]

We report in this communication the post-synthetic functionalization of Prussian Blue (PB) nanoparticles by two different luminiphores (2-aminoanthracene and rhodamine B). The photoluminescence properties of the fluorophores are found modified by confinement effet upon adsorption. We demonstrate that such multifunctional nanosized systems could be used for *in vitro* imaging.

Prussian Blue (PB) and their analogues are widely recognized as the first coordination network materials in which transition metal ions are assembled through cyano-bridges that generate a 3D cubic structure. PB is a valence mixed system exhibiting the general formula $A_{1-x}Fe^{III}[Fe^{II}(CN)_6]_{1-x/4}\square_{x/4}$ in which A is an alkaline ion and $\square$ denotes the hexacyanoferrate vacancies. The synthesis of PB at the nanoscale has recently attracted a great interest due to their specific molecule-based character that differs with respect to classical inorganic nanoparticles.[1-3] More specifically a recent upturn has recently been taken to utilize PB nanoparticles for biomedical applications thanks to their adjustable physical and chemical properties, their porosity and their chemical robustness in water over a large pH range[4] while benefiting from an excellent biocompatibility since the soluble form of PB has been approved by the Food and Drug Administration (FDA) as an antidote for radioactive Cs^+ and Tl^+ poisoning.[5-9] Consequently, the efficiency of nanosized PB has been demonstrated for a myriad of biomedical applications including contrast agents for Magnetic Resonance Imaging (MRI),[10-20] scintigraphy,[21] photo-acoustic imaging,[22-23] nano-carriers for drug delivery[24-27] or as therapeutic agents for different kinds of therapy and treatment[25, 28] including photothermal therapy.[29-32]

On the other hand, others simple and affordable techniques such as fluorescence imaging benefiting from a high temporal resolution and high sensitivity[33] is therefore highly needed to fully exploit the potentialities of nanosized PB with the aim to locate the nanoparticles, understand their biodistribution and monitor the efficiency of the targeted treatment. However, efforts to implement luminescence in these intrinsically multifunctional PB nanosystems remain almost unexplored. One can cite the examples of Mn-doped PB nanoparticles with an avidin functionalized surface or core@shell made of polypyrrole@PB nanoparticles.[14, 34] Although *in vitro* fluorescence imaging was performed, the internalization of the nanoparticles into the cells needs to be clearly confirmed. Hence, new examples of luminescent PB nanoparticles with different emission ranges are therefore required. Besides, from a fundamental point of view, elucidation of the adsorption mechanism and studies of their photophysical properties are also of critical importance to ultimately optimize the systems.

In this sense, we have recently reported an original strategy to render magnetic nickel hexacyanochromate nanoparticles luminescent by a post-synthetic functionalization by the 2-aminoanthracene (**AA**) fluorophore to yield a bifunctional magneto-luminescent system.[35] Taking advantage of this simple methodology, we propose here to extend this strategy to PB nanosystems by functionalization with two different fluorophores, **AA** and Rhodamine B (**RhB**). We demonstrate that differences in the luminophore adsorption mechanism are readily observed while *in vitro* fluorescence imaging unambiguously confirms the potential of such functional PB nanosystems.

Implementing luminescence properties in our PB nanosized systems was therefore performed by a two-steps procedure

[a] *Institut Charles Gerhardt, UMR 5253, Equipe Ingénierie Moléculaire et Nano-Objets, Université de Montpellier, ENSCM, CNRS. Place Eugène Bataillon, 34095 Montpellier Cedex 5, France, E-mail : jerome.long@umontpellier.fr*
[b] *Institut des Biomolécules Max Mousseron, UMR5247, Université de Montpellier, CNRS, ENSCM, Faculté de Pharmacie, 15 Avenue Charles Flahault, 34093 Montpellier Cedex 05, France.*
[c] *NanoMedSyn, 15 Avenue Charles Flahault, 34093 Montpellier Cedex 5, France*
[d] *Institut Charles Gerhardt Montpellier, UMR 5253, Equipe Agrégats, Interfaces et Matériaux pour l'Energie ENSCM/CNRS/UM, Place Eugène Bataillon, 34095 Montpellier Cedex 5, France.*

§. Both authors contributed equally to this work.

Electronic Supplementary Information (ESI) available: [details of any supplementary information available should be included here]. See DOI: 10.1039/x0xx00000x

luminophores. In this study, two fluorophores that differs from their size and emission features were selected (Scheme S1). Firstly, the **AA** luminophore was selected since: *i*) the amine function allows its anchorage *via* the formation of hydrogen or coordination bonds to the Fe^{3+} metal ions of PB located close to the cyanometallate vacancies; *ii*) its small molecular size that can fit into the pores generated by the hexacyanoferrate vacancies; *iii*) its green color emission upon various excitation wavelengths ranging from 300 to 450 nm,[36] which makes it widely used in applications, such as reagents and assay kits. The second luminophore is the well-known **RhB**, extensively used in different applications including nanoparticles functionalization.[37] In contrast to **AA**, the large size of **RhB** most likely prevents its adsorption within the PB porosity but surface functionalization may be achieved either by electrostatic (ammonium interacting with negatively charged PB nanoparticles) or coordination (carboxylic moieties) interactions. Additionally, the excitation wavelength in the visible (500-600 nm) may be taken as an advantage for bioimaging and induces a red emission.[37]

Surfactant free PB nanoparticles $Na_{0.30}Fe^{III}[Fe^{II}(CN)_6]_{0.82}\cdot 3.7H_2O$ (**1**) of 72 ± 6 nm (Fig. S1) were obtained using our previously reported method in aqueous solution by the controlled addition of the molecular precursors $Na_4[Fe(CN)_6]\cdot 10H_2O$ and $FeCl_3\cdot 6H_2O$.[32, 38] **1** was subsequently redispersed in either ethanol or water with **AA** or **RhB** respectively, and the mixture was reacted for 24H before being thoroughly washed and next dialyzed to fully remove any residual luminophores. Elemental and Thermogravimetric (TGA) analyses (Fig. S2-S3) on the obtained solids allows estimating the water and luminophores content to give $Na_{0.30}Fe^{III}[Fe^{II}(CN)_6]_{0.83}@(AA)_{0.08}\cdot 3.6H_2O$ (**1@AA**) and $Na_{0.23}Fe^{III}[Fe^{II}(CN)_6]_{0.81}@(RhB)_{0.02}\cdot 3.7H_2O$ (**1@RhB**). This corresponds to a loading capacity, defined as the luminiphore's weight divided by the total weight of the nanoparticles, of 4.8 and 2.9 % for **1@AA** and **1@RhB** respectively. Besides, TGA analyses indicate that in both cases the luminophore's decomposition occurs at higher (**1@AA**) or similar temperatures (**1@RhB**) compared to the individual entities and concomitantly with that of PB suggesting a strong interaction between the luminophores and the nanoparticles. In comparison with the pristine nanoparticles, **1@AA** and **1@RhB** exhibit similar structural features such as a stretching cyanide $\nu(Fe^{II}\text{-}CN\text{-}Fe^{III})$ band located around 2080 cm^{-1} in the FT-IR spectra (Fig. S4-S5), and a Powder X-Ray Diffraction Patterns showing the typical *fcc* structure with a lattice parameter a = 10.0 Å (Fig. S6, Table S1). The post-functionalization with the luminophores is confirmed by the typical vibrations of either **AA** and **RhB** in the 600-1700 cm^{-1} region (Fig. S5). Scherrer analysis does not reveal a modification in the crystallite sizes with respect to the pristine nanoparticles (*i.e.* 55 nm, Table S1) which is in good accordance with the Transmission Electronic Microscopy (TEM) analyses showing cubic nanoparticles with a mean diameter of 72 ± 5 nm and 73 ± 5 nm for **1@AA** and **1@RhB** respectively (Fig. 1, Fig. S7-S8). The negative values of the zeta potentials for **1** and **1@AA** are rather similar indicating a similar surface state (Table S2). In contrast, a significant increase of the zeta potential is observed for **1@RhB** while no chloride ion (that may originate from **RhB**) could be detected by EDS analysis. All these results indicate that **AA** may be adsorbed within the porosity of the PB whereas **RhB** interacts electrostatically with the negatively charged surface of PB nanoparticles.

To validate such assumptions, molecular simulations (Monte Carlo and classical force field-based calculations) were performed (ESI). The pores size distribution of **1** (Fig. S9) highlights two distinct porosity in the coordination network, namely the tetrahedral sites of the *fcc* structure and the distorted larger pores of 8 Å × 8 Å × 11 Å generated by cyanometallate vacancies and suitable to accommodate only **AA** (10 Å × 5 Å × 1 Å). In contrast, the size of **RhB** (16 Å × 12 Å × 7 Å) is clearly too large to enter into these cavities, suggesting rather an interaction at the nanoparticles surface.

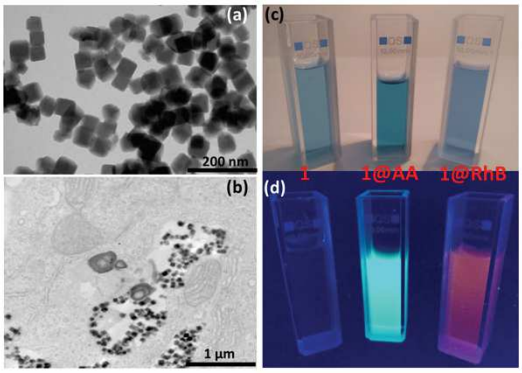

Figure 1. TEM images of **1@AA** (a) and MDA-MB-231 cancer cells exposed with **1@AA** (b); Photographs of **1**, **1@AA** and **1@RhB** (c) and under excitation with an UV lamp at 365 nm (d).

Additionally, the **AA** amount adsorbed at saturation can be obtained by Monte Carlo simulations by taking the hypothesis of the **AA** loading in an empty structure is estimated at 0.13 **AA** molecules per unit cell (as defined below), which is slightly higher than the experimental value of 0.08. This corresponds to a loading capacity of 7.6 wt% to compare with the experimental one of 4.8 wt%. This discrepancy could be rationalized by the presence of solvent molecules which are able to chemically interact with unsaturated metal centers (CUS) and enters in competition with **AA**. To go further, the distribution of the **AA** molecules in the pores reveals that this latter is adsorbed within the largest pores generated by cyanometallate vacancies (Fig. S10). Complementary calculations have also been performed to calculate the interaction energy when the **AA** adsorption is mainly governed by physisorption (since Universal Force Field is unable to predict the formation of a covalent interaction). Firstly, the enthalpy corresponding to a physisorption at low coverage (1 molecule per cell) is estimated at −30 $kcal.mol^{-1}$, while the chemisorption involving a coordination bond between **AA** and Fe^{3+} gives a larger value of 120 $kcal.mol^{-1}$. Such difference suggests a favorable interaction by coordinative bonds. Fig.

S10 illustrates this interaction between NH_2 from **AA** and Fe^{3+} of 2.7-2.9 Å described by Monte-Carlo simulations (physisorption), but it should be mentioned that interaction between NH_2 and cyano-groups can be observed. In contrast, by considering chemisorption, a shorter distance of 1.96 Å between **AA** and Fe^{3+} is found.

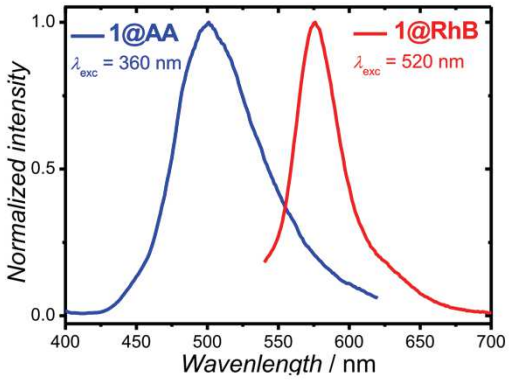

Figure 2. Room temperature normalized emission spectra for **1@AA** (excited at 360 nm) and **1@RhB** (excited at 520 nm) re-dispersed in ethanol (1 mg.mL^{-1}).

The optical properties of the resulting functionalized PB nanoparticles were investigated in both suspension and solid-state. Firstly, the electronic absorption spectra of **1@AA** and **1@RhB** show the typical broad band in the NIR associated with the intervalence Fe^{2+}/Fe^{3+} charge transfer of PB (Fig. S11). Moreover, the typical absorption bands related to the fluorophores could also discerned around 400 nm and 550 nm for **AA** and **RhB** respectively. As regards the photoluminescence features, Fig. 1 shows that while a suspension of **1** is optically inactive, both **1@AA** and **1@RhB** exhibit a blue-green and orange emission respectively when excited by a UV-lamp. For both functionalized systems, the photoluminescence spectra acquired in suspension exhibit a blue-shift (*e.g.* 10 nm) with respect to the isolated luminophores (Fig. 2, Fig. S12). Such phenomenon was previously observed in related functionalized PBA nanoparticles and could be ascribed to a modification of the environment of the luminophores upon adsorption.[35] Thus, when excited in the UV to blue spectral region, suspension of **1@AA** exhibits a broad emission band located at 500 nm while excitation of **1@RhB** at 520 nm shows an asymmetric emission band centered at 575 nm (Fig.1, Fig. S13-S14). In solid-state, **1@AA** displays a comparable green emission feature at the exception of a weak emission component located in the 400-430 nm region (Fig. S15) and previously identified as being dependent on the chromophore's concentration upon adsorption in PBA.[35] In contrast, the solid-state emission spectrum for **1@RhB** (Fig. S16) is comparable to that obtained in aqueous suspension while only a red-shifted emission band is observed for the **RhB** due to the well-known concentration effect.[39]

Release experiments were carried out to confirm the strong interaction of the fluorophores with the PB nanoparticles. For both **1@AA** and **1@RhB**, no release of the luminophores could be detected after dialysis in water during 24H (Fig. S17). These results suggest that the luminescence properties of PB nanoparticles could be used to follow their cells internalization. Hence, *in vitro* experiments on human breast adenocarcinoma cells (MDA-MB-231) were performed. Fluorescent imaging of the MDA-MB-231-GFP living cells showed that the nanoparticles were efficiently internalized by cancerous cells. After 20 h incubation, **1@AA** and **1@RhB** are localized in cell cytoplasm.

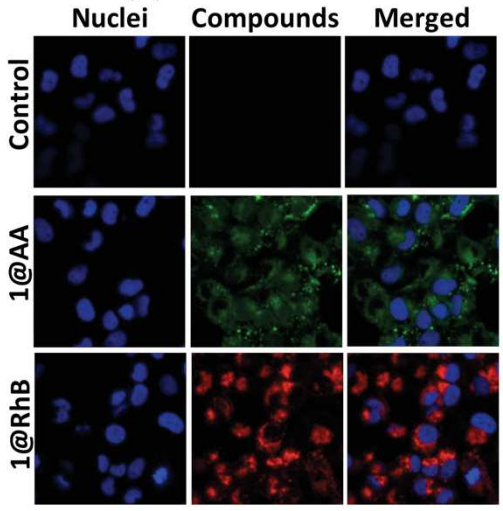

Figure 3. Human breast adenocarcinoma MDA-MB-231-GFP cells uptake of nanoparticles. Cancerous cells were incubated or not for 20 h with **1@AA** or **1@RhB** at a concentration of 100 µg.mL^{-1}.

Moreover, comparison between **1@AA** and **1@RhB** internalization with the independent luminophores indicates that **AA** was not internalized by the cells in contrast to **RhB** (Fig. 3, S18). This later is indeed known to cross the membranes of cells[40]. Moreover, control experiments were performed with **1** using similar conditions (Fig. S19). No fluorescence could be detected demonstrating the efficiency of the post-functionalization. To ultimately confirm the cancer cell internalization of the functionalized **1@AA** and **1@RhB**, TEM imaging was performed after 20 h of incubation. The results point out a clear localization of the functionalized PB into the MDA-MB-231 cells (Fig. 1, Fig. S20), in accordance with the results from fluorescence imaging.

Finally, quantification of the **1@RhB** internalization by cancerous cells by flow cytometry experiments was performed (Fig. S21). **1@RhB** was incubated in the culture cells at a concentration of 100 µg.mL^{-1} during different times (1 h, 3 h, 6 h and 24 h). After 3 h of incubation, a high internalization level (55% stained cells) was reached and after 24 h, 79% of cells were stained. All together, these biological experiments

demonstrate the potential of such PB nanoparticles to highly penetrate the cancer cells.

In conclusion, we have demonstrated that PB nanoparticles could be easily post-functionalized by various luminophores to render them luminescent. Depending on the luminophore's nature, different adsorption mechanisms could be observed as confirmed by molecular modeling. Additionally, we unambiguously show that these simple functionalized nanosized probes could be efficiently used to monitor the cell internalization of the nanoparticles by fluorescence imaging. This opens exciting perspectives for using these PB functionalized nanoparticles for multimodal imaging.

Conflicts of interest

There are no conflicts to declare.

Acknowledgements

The authors thank the University of Montpellier, CNRS and PAC of ICGM. The Portugal–France bilateral action, PESSOA Program (Hubert Curien) "Magneto-optical Multifunctional Nanoparticles" (40773PE) is also acknowledged.

Notes and references

1 J. Larionova, Y. Guari, C. Sangregorio and C. Guerin, *New Journal of Chemistry*, 2009, **33**, 1177-1190.
2 L. Catala, F. Volatron, D. Brinzei and T. Mallah, *Inorg. Chem.*, 2009, **48**, 3360-3370.
3 E. Dujardin and S. Mann, *Adv. Mater.*, 2004, **16**, 1125-1129.
4 J. Long, Y. Guari, C. Guerin and J. Larionova, *Dalton Trans.*, 2016, **45**, 17581-17587.
5 V. Nigrovic, *Phys. Med. Biol.*, 1965, **10**, 81-92.
6 D. R. Melo, J. L. Lipsztein, C. A. N. Oliveira and L. Bertelli, *Health Physics*, 1994, **66**, 245-252.
7 J. Pearce, *Food Chem. Toxicol.*, 1994, **32**, 577-582.
8 D. F. Thompson and C. O. Church, *Pharmacotherapy: The Journal of Human Pharmacology and Drug Therapy*, 2001, **21**, 1364-1367.
9 J. Ruprecht, *Toxicology*, 2007, **233**, 20-22.
10 X. Cai, W. Gao, L. Zhang, M. Ma, T. Liu, W. Du, Y. Zheng, H. Chen and J. Shi, *ACS Nano*, 2016, **10**, 11115-11126.
11 W. Zhu, K. Liu, X. Sun, X. Wang, Y. Li, L. Cheng and Z. Liu, *ACS Appl. Mater. Interfaces*, 2015, **7**, 11575-11582.
12 M. Perrier, A. Gallud, A. Ayadi, S. Kennouche, C. Porredon, M. Gary-Bobo, J. Larionova, C. Goze-Bac, M. Zanca, M. Garcia, I. Basile, J. Long, J. de Lapuente, M. Borras and Y. Guari, *Nanoscale*, 2015, **7**, 11899-11903.
13 G. Paul, Y. Prado, N. Dia, E. Riviere, S. Laurent, M. Roch, L. V. Elst, R. N. Muller, L. Sancey, P. Perriat, O. Tillement, T. Mallah and L. Catala, *Chem. Commun.*, 2014, **50**, 6740-6743.
14 M. F. Dumont, S. Yadavilli, R. W. Sze, J. Nazarian and R. Fernandes, *Int. J. Nanomed.*, 2014, **9**, 2581-2595.
15 M. F. Dumont, H. A. Hoffman, P. R. S. Yoon, L. S. Conklin, S. R. Saha, J. Paglione, R. W. Sze and R. Fernandes, *Bioconjugate Chem.*, 2014, **25**, 129-137.
16 M. Perrier, S. Kenouche, J. Long, K. Thangavel, J. Larionova, C. Goze-Bac, A. Lascialfari, M. Mariani, N. Baril, C. Guérin, B. Donnadieu, A. Trifonov and Y. Guari, *Inorg. Chem.*, 2013, **52**, 13402-13414.
17 E. Chelebaeva, J. Larionova, Y. Guari, R. A. S. Ferreira, L. D. Carlos, A. A. Trifonov, T. Kalaivani, A. Lascialfari, C. Guerin, K. Molvinger, L. Datas, M. Maynadier, M. Gary-Bobo and M. Garcia, *Nanoscale*, 2011, **3**, 1200-1210.
18 M. Shokouhimehr, E. S. Soehnlen, A. Khitrin, S. Basu and S. D. Huang, *Inorg. Chem. Commun.*, 2010, **13**, 58-61.
19 M. Shokouhimehr, E. S. Soehnlen, J. Hao, M. Griswold, C. Flask, X. Fan, J. P. Basilion, S. Basu and S. D. Huang, *J. Mater. Chem.*, 2010, **20**, 5251-5259.
20 Y. Guari, J. Larionova, M. Corti, A. Lascialfari, M. Marinone, G. Poletti, K. Molvinger and C. Guerin, *Dalton Trans.*, 2008, 3658-3660.
21 M. Perrier, M. Busson, G. Massasso, J. Long, V. Boudousq, J. P. Pouget, S. Peyrottes, C. Perigaud, C. Porredon-Guarch, J. de Lapuente, M. Borras, J. Larionova and Y. Guari, *Nanoscale*, 2014, **6**, 13425-13429.
22 L. Jing, X. Liang, Z. Deng, S. Feng, X. Li, M. Huang, C. Li and Z. Dai, *Biomaterials*, 2014, **35**, 5814-5821.
23 X. Liang, Z. Deng, L. Jing, X. Li, Z. Dai, C. Li and M. Huang, *Chem. Commun.*, 2013, **49**, 11029-11031.
24 S. Mukherjee, B. R. Rao, B. Sreedhar, P. Paik and C. R. Patra, *Chem. Commun.*, 2015, **51**, 7325-7328.
25 M. S. Kandanapitiye, F. J. Wang, B. Valley, C. Gunathilake, M. Jaroniec and S. D. Huang, *Inorg. Chem.*, 2015, **54**, 1212-1214.
26 W. Shao-Jen, C. Chun-Sheng and C. Lin-Chi, *Sci. Techno. Adv. Mater.*, 2013, **14**, 044405.
27 H.-Y. Lian, M. Hu, C.-H. Liu, Y. Yamauchi and K. C. W. Wu, *Chem. Commun.*, 2012, **48**, 5151-5153.
28 C. Lavaud, M. Kajdan, E. Compte, J.-C. Maurel, J. Lai Kee Him, P. Bron, E. Oliviero, J. Long, J. Larionova and Y. Guari, *New J. Chem.*, 2017, **41**, 2887-2890.
29 L. W. Zou, H.; He, B.;, Zeng, L.; Tan, T.; Cao, H.; He, X.; Zhang, Z.; Guo, S.; Li, Y. , *Theranostics*, 2016, **6**, 762-772.
30 V. Shanmugam, S. Selvakumar and C.-S. Yeh, *Chem. Soc. Rev.*, 2014, **43**, 6254-6287.
31 A. M. Alkilany, L. B. Thompson, S. P. Boulos, P. N. Sisco and C. J. Murphy, *Adv. Drug Del. Rev.*, 2012, **64**, 190-199.
32 L. M. A. Ali, E. Mathlouthi, M. Kajdan, M. Daurat, J. Long, R. Sidi-Boulenouar, M. Cardoso, C. Goze-Bac, N. Amdouni, Y. Guari, J. Larionova and M. Gary-Bobo, *Photodiagnosis Photodyn. Ther.*, 2018, **22**, 65-69.
33 F. Leblond, S. C. Davis, P. A. Valdés and B. W. Pogue, *Journal of Photochemistry and Photobiology B: Biology*, 2010, **98**, 77-94.
34 S. Ye, Y. Liu, S. Chen, S. Liang, R. McHale, N. Ghasdian, Y. Lu and X. Wang, *Chem. Commun.*, 2011, **47**, 6831-6833.
35 E. Mamontova, J. Long, R. Ferreira, A. M. P. Botas, F. Salles, Y. Guari, L. A. D. Carlos and J. Larionova, *Nanoscale*, 2019, **11**, 7097-7101.
36 Q. Yao, A. Bermejo Gómez, J. Su, V. Pascanu, Y. Yun, H. Zheng, H. Chen, L. Liu, H. N. Abdelhamid, B. Martín-Matute and X. Zou, *Chem. Mater.*, 2015, **27**, 5332-5339.
37 M. J. Snare, F. E. Treloar, K. P. Ghiggino and P. J. Thistlethwaite, *J. Photochem.*, 1982, **18**, 335-346.
38 G. Maurin-Pasturel, E. Rascol, M. Busson, S. Sevestre, J. Lai-Kee-Him, P. Bron, J. Long, J. Chopineau, J.-M. Devoisselle, Y. Guari and J. Larionova, *Inorg. Chem. Front.*, 2017, **4**, 1737-1741.
39 K. Itoh, Y. Chiyokawa, M. Nakao and K. Honda, *J. Am. Chem. Soc.*, 1984, **106**, 1620-1627.

Please do not adjust margins

Electronic Supporting Information

Implementing luminescence in Prussian blue nanoparticles: synthesis, properties and *in vitro* imaging

Ekaterina Mamontova,[a,§] Morgane Daurat,[b,c,§] Jérôme Long*,[a] Anastasia Godefroy,[b,c] Fabrice Salles,[d] Yannick Guari,[a] Magali Gary-Bobo*[b] and Joulia Larionova[a]

a. Institut Charles Gerhardt, Equipe Ingénierie Moléculaire et Nano-Objets, Université de Montpellier, ENSCM, CNRS. Place Eugène Bataillon, 34095 Montpellier Cedex 5, France, E-mail : jerome.long@umontpellier.fr

b. Institut des Biomolécules Max Mousseron, UMR5247, Université de Montpellier, ENSCM, CNRS, Faculté de Pharmacie, 15 Avenue Charles Flahault, 34093 Montpellier Cedex 5, France

c. NanoMedSyn, 15 Avenue Charles Flahault, 34093 Montpellier Cedex 5, France

d. Institut Charles Gerhardt, Equipe Agrégats, Interfaces et Matériaux pour l'Energie, ENSCM, CNRS, Université de Montpellier. Place Eugène Bataillon, 34095 Montpellier Cedex 5, France.

§. Both authors contributed equally to this work.

Table of Contents

Table of Contents

Fig. S14. Left: Room temperature normalized excitation spectra for RhB and 1@RhB re-dispersed in water (500 µg.mL-1) monitored at 500 nm. Right: Room temperature emission spectra for 1@RhB re-dispersed in water excited at different wavelengths. 14

Fig. S15. Room temperature emission (left) and excitation (right) spectra excited at 360 and monitored around 500 nm, respectively, for powdered AA and 1@AA. 17

Fig. S16. Left: Room temperature emission spectra for powdered RhB and 1@RhB excited at 467 nm and 520 nm, respectively; Right: Room temperature excitation spectra for powdered RhB and 1@RhB monitored around 690 nm and 580 nm, respectively. 17

Fig. S17. Electronic spectra of dialysis medium (water) after release's experiments for 1@AA (left) and 1@RhB (right). 18

Fig. S18. MDA-MB-231 were incubated for 20 h with AA and RhB at a concentration of 100 $\mu g.mL^{-1}$. One photon fluorescence imaging was performed on living cells with similar parameters that 1@AA and 1@RhB imaging, respectively. 18

Fig. S19. MDA-MB-231 were incubated for 20 h with 1 at a concentration of 100 $\mu g.mL^{-1}$. One photon fluorescence imaging was performed on living cells with similar parameters that 1@AA (a) and 1@RhB (b) imaging, respectively. 19

Experimental section

Synthetic procedures

Materials. All chemical reagents were purchased and used without further purification: Iron (III) chloride hexahydrate (Sigma Aldrich, 97%), Sodium hexacyanoferrate (II) decahydrate (Alfa Aesar, 99%), 2-aminoanthracene (Alfa Aesar, 94%), Rhodamine B (Acros Organics, 98+%), ultra-pure water, ethanol 96% vol (TechniSolv), SnakeSkin Dialysis Tubing (3,5000 MWCO, 22 mm × 35 feet dry diameter, 34 mm dry flat width, ThermoScientific).

Synthesis of $Na^+/Fe^{3+}/[Fe^{II}(CN)_6]^{4-}$ PB nanoparticles (1). The PB nanoparticles were obtained following the general procedures.[1-2] At 25°C, aqueous solutions of $FeCl_3{\cdot}6H_2O$ (10.00 mM, 10 mL) and $Na_4[Fe(CN)_6]{\cdot}10H_2O$ (11.25 mM, 10 mL) were added simultaneously to 100 mL of pure water at 2 $mL.h^{-1}$ rate, using a syringe pump. After addition, the mixture was stirred one hour before being centrifuged at 37,500 × *g* (20,000 rpm) during 15 min. The supernatant was removed and the NPs were washed successively with water and ethanol and dried under vacuum. Dark blue powder.
IR (KBr): ν(O-H) = 3630 cm^{-1} (coordinated water), ν(O-H) = 3400 cm^{-1} (crystallized water), ν(C≡N) = 2082 cm^{-1} (Fe^{III}–C≡N–Fe^{II}), δ(O–H) = 1606 cm^{-1} (crystallized water), ν(Fe^{II}-CN) = 602 cm^{-1}, δ(Fe^{II}-CN) = 501 cm^{-1}.
EDS: 14.04/85.96 (Na/Fe). Formula found: $Na_{0.30}Fe^{III}[Fe^{II}(CN)_6]_{0.82}{\cdot}3.7H_2O$.
Elemental analysis calcd (%): C, 19.49; H, 2.44; N, 22.72; found (%): C, 19.22; H, 3.36; N, 22.15.

Post-synthetic functionalization of $Na^+/Fe^{3+}/[Fe^{II}(CN)_6]^{4-}$ PBA nanoparticles with 2-aminoanthracene (1@AA). The post-functionalization was performed by mixing the pristine $Na^+/Fe^{3+}/[Fe^{II}(CN)_6]^{4-}$ NPs (30 mg, 0.10 mmol) with the 2-aminoanthracene (96 mg, 0.50 mmol) in ethanol for 24 h under stirring. Then, the solution was centrifuged at 37,500 × *g* (20,000 rpm) during 15 min. The supernatant was removed and the NPs were washed with ethanol several times. The NPs were dispersed in the minimum of ethanol to perform a 2-days dialysis using SnakeSkin Dialysis Tubing. Finally, the solid was recovered by centrifugation at 37,500 × *g* (20,000 rpm) during 15 min and dried under vacuum. Blue solid.
IR (KBr): ν(O-H) = 3630 cm^{-1} (coordinated water), ν(O-H) = 3390 cm^{-1} (crystallized water/primary alcohol groups), ν(C≡N) = 2078 cm^{-1} (Fe^{III}–C≡N–Fe^{II}), ν(N-H) = 1635 cm^{-1} (N-H amine), δ(O–H) = 1609 cm^{-1} (crystallized water), ν(C-C) = 1485-1410 cm^{-1} (aromatic), ν(C-H) = 1346-600 cm^{-1} (aromatic), ν(Fe^{II}-CN) = 600 cm^{-1}, δ(Fe^{II}-CN) = 501 cm^{-1}.
EDS: 15.12/84.88 (Na/Fe).
Elemental analysis calcd (%): C, 21.60; H, 2.49; N, 21.05. Found (%): C, 21.33; H, 2.56; N, 20.78.
Estimated formula for **1@AA**: $Na_{0.30}Fe^{III}[Fe^{II}(CN)_6]_{0.83}@(AA)_{0.08}{\cdot}3.6H_2O$.

Post-synthetic functionalization of $Na^+/Fe^{3+}/[Fe^{II}(CN)_6]^{4-}$ PBA nanoparticles with Rhodamine B (1@RhB). The post-functionalization was performed by mixing the pristine $Na^+/Fe^{3+}/[Fe^{II}(CN)_6]^{4-}$ NPs (30 mg, 0.1 mmol) with the rhodamine B (240 mg, 0.50 mmol) in ultrapure water for 24 h under stirring. Then, the solution was centrifuged at 37,500 × *g* (20,000 rpm) during 15 min. The supernatant was removed and the NPs were washed with water several times. The NPs were dispersed in minimum of water to perform a 2-days dialysis using SnakeSkin Dialysis Tubing. Finally, the solid was recovered by centrifugation at 37,500 × g (20,000 rpm) during 15 min, washed with water and ethanol and dried under vacuum. Blue solid.

IR (KBr): ν(O-H) = 3630 cm^{-1} (coordinated water), ν(O-H) = 3400 cm^{-1} (crystallized water/primary alcohol groups), ν(C≡N) = 2082 cm^{-1} (Fe^{III}–C≡N–Fe^{II}), ν(C=O) = 1691 cm^{-1} (COOH acide), ν(C=N) = 1635 cm^{-1}, ν(C-C) = 1485-1410 cm^{-1} (aromatic), ν(C-H) = 1346-600 cm^{-1} (aromatic), ν(Fe^{II}-CN) = 603 cm^{-1}, δ(Fe^{II}-CN) = 501 cm^{-1}.
EDS: 11.59/88.06 (Na/Fe).
Elemental analysis calcd (%): C, 18.29; H, 2.53; N, 20.45. Found (%): C, C, 18.57; H, 2.62; N, 20.95
Estimated formula for **1@RhB**: $Na_{0.23}Fe^{III}[Fe^{II}(CN)_6]_{0.81}@(RhB)_{0.02}\cdot 3.7H_2O$.

Luminophore's release
In order to estimate the release kinetics, the NPs **1@AA** or **1@RhB** (10 mg) were dispersed in 3 mL of ultrapure water to perform 24-hours dialysis using SnakeSkin Dialysis tubing in 10 mL of water. The receiving medium was studied by UV-Vis spectroscopy.

Cell culture
Human breast adenocarcinoma MDA-MB-231-GFP and MDA-MB-231 cell lines were used. MDA-MB-231 cell line stably expresses GFP inducing the visualization of green nuclei in contrast to MDA-MB-231. Cells were cultured in Dulbecco's Modified Eagle's Medium (DMEM) supplemented with 10% fetal bovine serum and antibiotic (0.05 $mg.mL^{-1}$ gentamicin). These cells grown in humidified atmosphere at 37°C and under 5% CO_2.

Characterization methods

Infrared spectroscopy
Infrared spectra were recorded as KBr disks on a PerkinElmer Spectrum two spectrophotometer.

Ultraviolet-visible spectroscopy
UV-Vis spectra were collected on a JASCO V-650 spectrometer in water or ethanol (C = 500 $\mu g.mL^{-1}$).

X-ray powder diffraction
X-ray powder diffraction patterns were recorded in the 2θ interval 5-60° at room temperature with the PANalytical X'Pert Powder diffractometer analytical diffractometer mounted in a Debye−Scherrer configuration and equipped with Cu radiation (λ = 1.5418 Å).

TGA analysis
Thermogravimetric analyses were obtained with a thermal analyzer STA 409 Luxx® (Netzsch) in the range 25 – 650 °C at heating speed of 5 $°C.min^{-1}$.

Electron microscopy
Transmission Electron Microscopy (TEM) observations were carried out at 100 kV (JEOL 1200 EXII). Samples for TEM measurements were deposited from solutions on copper grids. Nanoparticles' size distribution histograms were determined using enlarged TEM micrographs taken at magnification of 100 K on a statistical sample of ca. 300 nanoparticles.

TEM imaging
MDA-MB-231 cells were seeded on glass coverslips for 24 h. After controlling their adherence and growing, cells were exposed or not to 100 $\mu g\ mL^{-1}$ of **1@AA** and **1@RhB** for 20 h The medium was removed and cells were washed twice with DPBS. Cells were fixed by incubation with 2.5% (v/v) glutaraldehyde in DPBS buffer and stored at 4°C. Then, cells were extensively washed with DPBS. The staining of samples was obtained upon incubation with 1% osmium tetroxide. Samples were dehydrated

by ascending grades of EtOH; for impregnation, the samples were firstly treated with a mix EtOH/EPON resin (1:1, v/v) for 1 h, and twice in EPON for 2 h. The polymerization was performed by embedding cells in EPON resin for 12 h at 60°C, plunged in liquid nitrogen at -195°C to detach the coverslip, and placed for two days at 60°C for completing polymerization. The ultrathin sections (70 nm) were obtained using an ultramicrotome (Leica Ultracut) and disposed on the copper grids. The grids were incubated in uranyl acetate for 2 min, rinsed in water, and then incubated in lead citrate for 2 min, and finally rinsed with water.

Scanning Electronic Microscopy

Scanning Electronic Microscopy (EDS) analyses were performed on a FEI Quanta FEG 200 instrument. The powders were deposited on an adhesive carbon film and analysed under vacuum. The quantification of the heavy elements was carried out with the INCA software, with a dwell time of 3 µs.

Photoluminescence measurements

The emission and excitation spectra were recorded at 295 K using an Edinburgh FLS-920 spectrofluorimeter in water or ethanol suspension (C = 500 $\mu g.mL^{-1}$) or for powdered samples. The excitation source was a 450 W Xe arc lamp. The emission spectra were corrected for detection and optical spectral response of the spectrofluorometer.

Cellular uptake

The cellular uptake experiment was performed using confocal fluorescence microscopy on living cells. MDA-MB-231-GFP cells were plated onto bottom glass dishes (World Precision Instrument, Stevenage, UK) in 1 mL culture medium for 24 h. Cancerous cells were treated or not for 20 h with **1@AA** or **1@RhB** at a concentration of 100 $\mu g.mL^{-1}$, and **AA** or **RhB** at the same grafted concentration on **1**. Before the visualization, cells were washed two times with culture medium. Confocal fluorescence microscopy observations were carried out at Carl Zeiss Microscope. The measurements were performed on living cells under a 488 nm wavelength excitation for nucleus, 458 nm for **AA** and 561 nm for **RhB** using. All images were performed with a high magnification (63x/1.4 OIL DIC Plan-Apo).
Conventionally, GFP signal was represented in green, here GFP is in blue in order to show the **AA** fluorescence in green. In addition, MDA-MB-32-GFP cells were used for confocal imaging to have nuclei labeling other than DAPI, in order to avoid excitation spectrum overlap between DAPI and 2-AA.

Internalization quantification by FACS

MDA-MB-231 cells were treated or not with 100 µg.mL-1 of **1@RhB** for 1, 3, 6 and 24 h. After treatment, control and treated cells were washed once in cold Phosphate Buffer Saline (PBS), harvested and centrifuged (1300 rpm, 5 min). Cell pellet were resuspended in PBS enriched with $CaCl_2$, $MgCl_2$ and stained by propidium iodide (1 µg.mL-1) (Sigma-Aldrich Chimie, Lyon, France), a cell death indicator. Flow cytometric determination of living cells and micelles with FITC positive cells was done by FACS CytoFlex Flow Cytometer (Beckman Coulter, France) with a minimum of 10.000 living cells collected.

Computational section

To complete the study, Monte Carlo simulations were performed at 300 K to determine the amount adsorbed at saturation for both **RhB** and **AA** in the PB structure **1** as well as the adsorption energy between the first molecule and the framework. For that purpose, 5×10^6 steps for equilibration and 5×10^6 steps of production were considered for calculations using Universal Force Field (UFF) combined with

partial charges for both the molecules and the framework. The force fields were implemented in the home-made Monte Carlo code. Following the strategy proposed in Rojas et al.,[3] ESP charges were extracted from DMol[3] calculations for **RhB** and **AA** molecules while qEq partial charges (corresponding to the partial charges obtained from the electronegativity equalization method) were considered for the solid framework and formal charges for the compensating cations. Concerning the Lennard Jones interactions, the Lorentz-Berthelot rules were applied with a cut-off radius fixed at 12.5 Å. Ewald summation for the electrostatic part was handled to increase the convergence for the energy calculations. The structures considered for the solid have already been presented in the literature.
In addition, classical calculations performed with GULP have been used to optimize the geometry of the solid considering a chemical interaction with the **AA** in order to compare the physical interaction (similar to adsorption of the molecule) and the chemical interaction (similar to chemisorption of the molecule on the unsaturated metal center). For these calculations, the same parameters used before have been considered.
Keep in mind that the molecular simulations have focused on the microscopic pores and not on the mesopores which were present in the structure. From Monte Carlo simulations, the adsorption enthalpy at low coverage (1 molecule per cell) is estimated at –30 kcal.mol^{-1}, which is weaker than the chemical interaction between **AA** and **1** (evaluated at –120 kcal.mol^{-1}) calculated using similar force fields. This value is obtained from the difference between the energy of the {PB + AA} structure (where the **AA** is interacting with the Fe^{3+} cation by NH_2 group) and the sum of the energy of the empty PB structure and the energy of the **AA** molecule. These results point out that **AA** should interact with **1** by strong chemical coordination interactions.

In complement, the pore size distribution has been calculated using the same parametrization for the framework (UFF) and the methodology developed by Gelb and Gubbins.[4]. The pores size distribution shows two different types: the tetrahedral sites of the fcc structure (with pore diameter close to 4 Å) and larger pores (with pore radius estimated at 7.5 Å from Figure S9 if we consider a spherical ball to probe the porosity, but the pores are elongated and dimensions are close to 7.5 Å x 7.5 Å x 20 Å)) formed by cyanometallates vacancies which are suitable to accommodate **AA** of 10 Å x 5 Å x 1 Å but are unable to accommodate **RhB** of 16 x 12 x 7 Å.

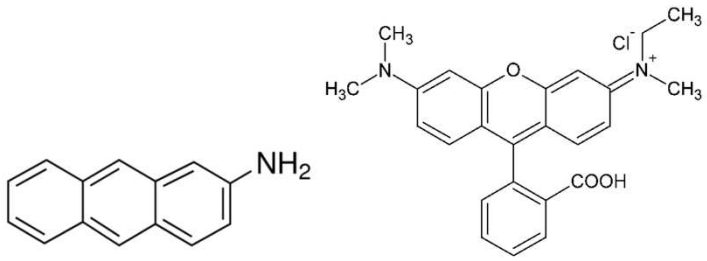

Scheme S1. Chemical structures of **AA** (left) and **RhB** (right).

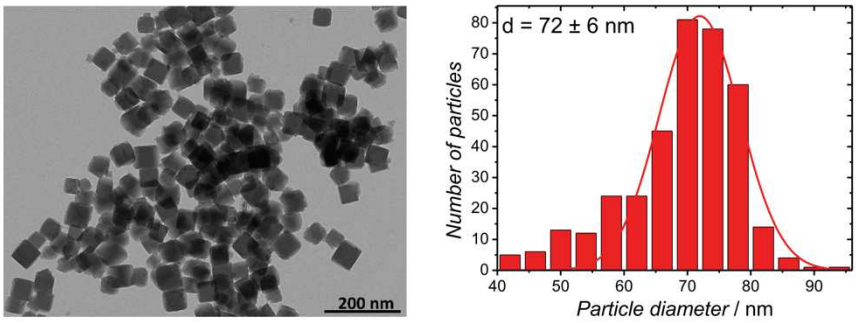

Fig. S1. TEM image (left) and size distribution (right) for **1**.

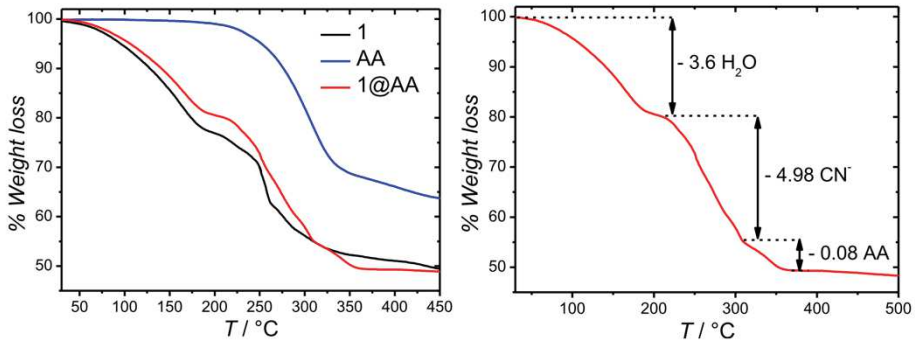

Fig. S2. Left: TGA analysis obtained with a 5°C.min^{-1} heating rate for **1**, **AA** and **1@AA**; Right: TGA curve obtained with a 5°C.min^{-1} heating rate demonstrating the decomposition of **1@AA**.

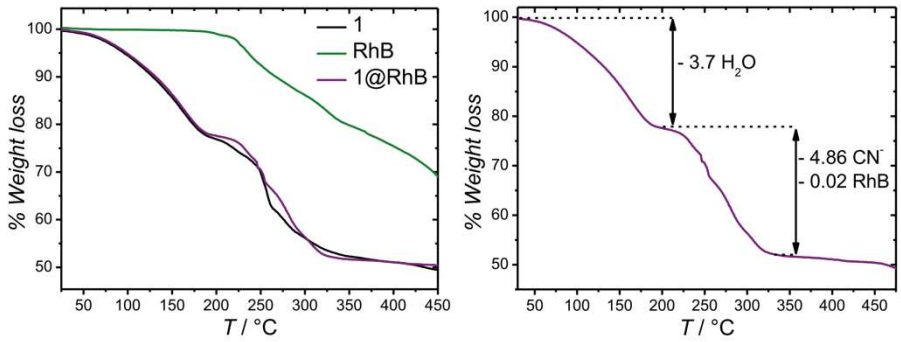

Fig. S3. Left: TGA analysis obtained with a 5°C.min^{-1} heating rate for **1**, **RhB** and **1@RhB**; Right: TGA curve obtained with a 5°C.min^{-1} heating rate demonstrating the decomposition of **1@RhB**.

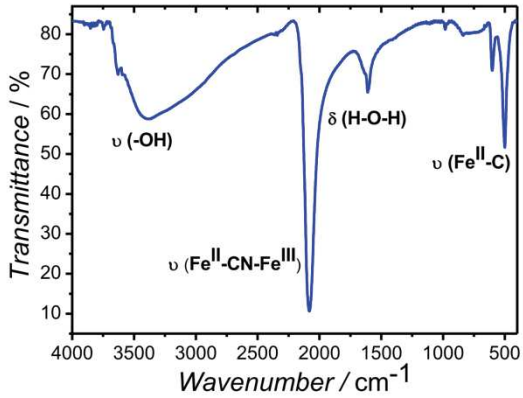

Fig. S4. IR spectra of **1**.

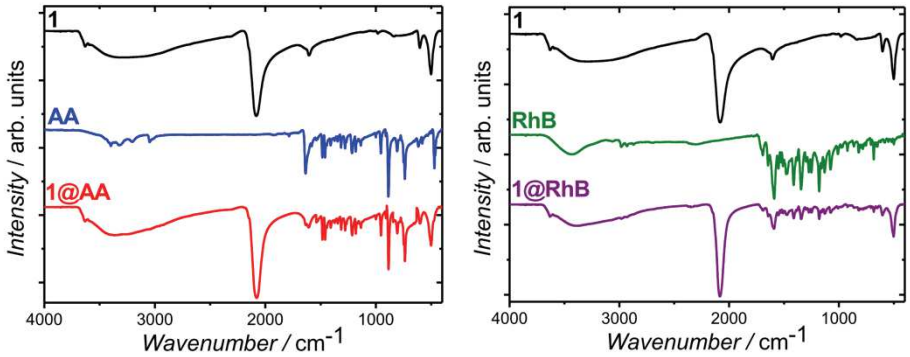

Fig. S5. Comparison between IR spectra of **AA**, **1** and **1@AA** (left) and between **RhB**, **1** and **1@RhB** (right).

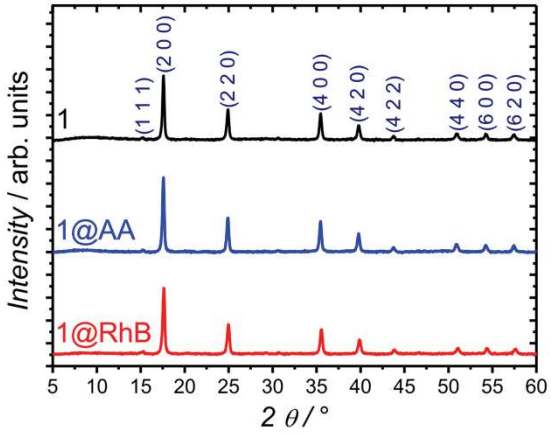

Fig. S6. PXRD patterns of **1** (black), **1@AA** (blue), **1@RhB** (red).

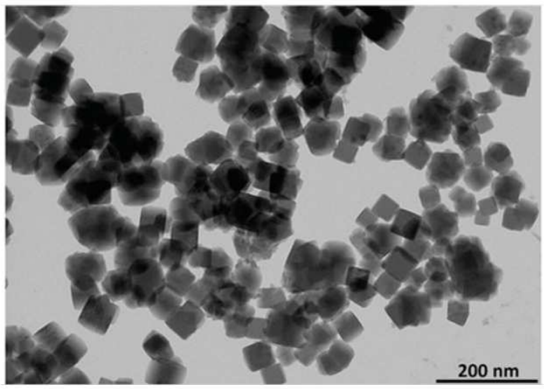

Fig. S7. TEM image of **1@RhB**.

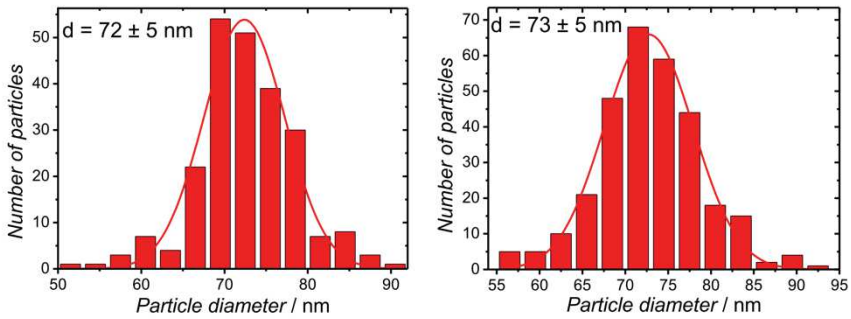

Fig. S8. Size distribution for **1@AA** (left) and for **1@RhB** (right).

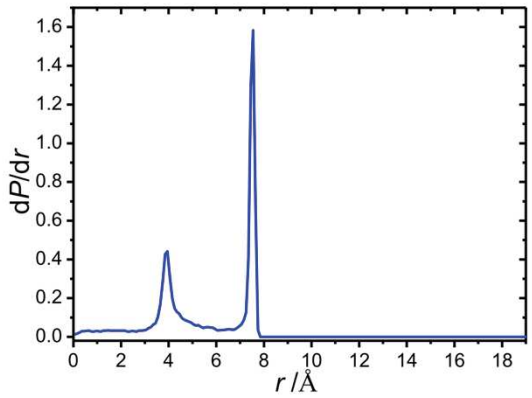

Fig. S9. Pore size distribution of **1** obtained from Monte Carlo simulations illustrating the presence of two types of pores corresponding to the channels and the larger pores formed by the vacancies.

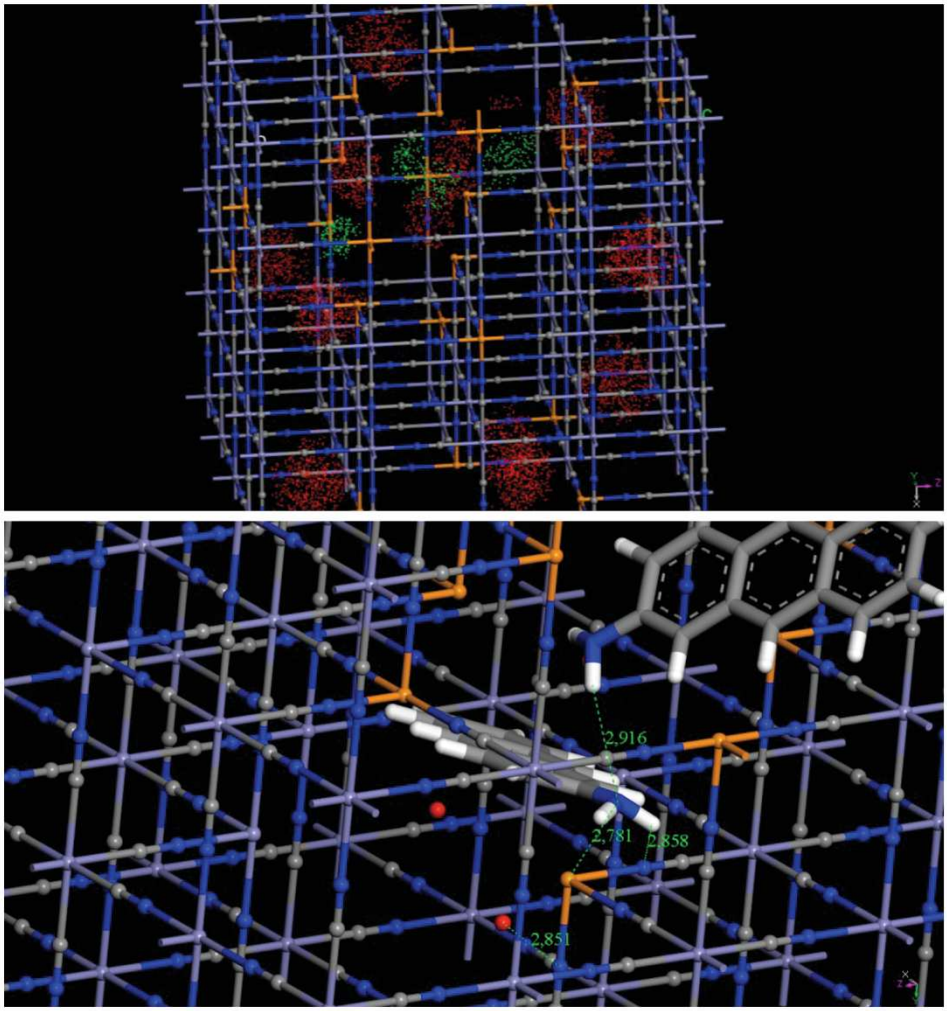

Fig. S10. Top: Snapshot illustrating the density of presence of the **AA** molecules (green) and of the alkaline ions (red) in the empty PB structure **1** from Monte Carlo simulations. Color code for **1**: orange Fe^{3+}, light violet Fe^{2+}, blue N, grey C. Bottom: Plausible configuration of the **AA** molecule in PB structure **1** from Monte Carlo simulations at saturation.

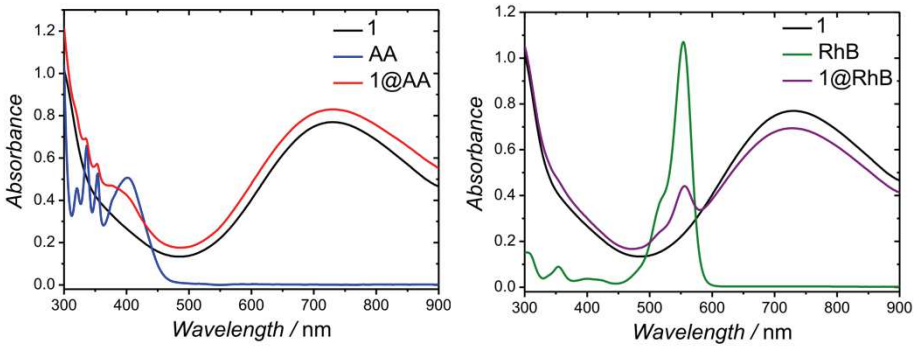

Fig. S11. Left: Room temperature absorption spectra for **1, AA** and **1@AA** in ethanol (500 μg.mL^{-1}). Right: Room temperature absorption spectra for **1, RhB** and **1@RhB** in water (500 μg.mL^{-1}).

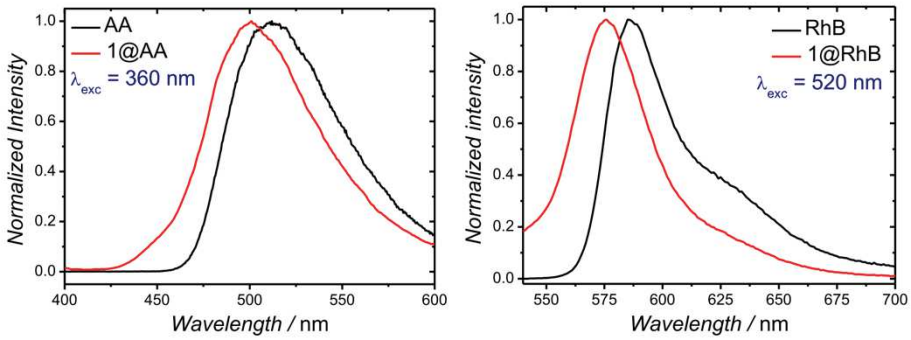

Fig. S12. Left: Room temperature normalized emission spectra for **AA** and **1@AA** re-dispersed in ethanol (1 mg.mL^{-1}) and excited at 360 nm. Right: Room temperature normalized emission spectra for **RhB** and **1@RhB** re-dispersed in water (1 mg.mL^{-1}) and excited at 520 nm.

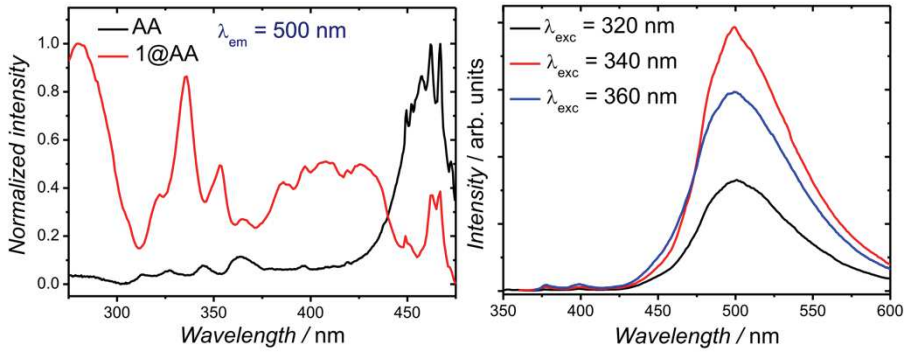

Fig. S13. Left: Room temperature normalized excitation spectra for **AA** and **1@AA** re-dispersed in ethanol (500 μg.mL^{-1}) monitored at 500 nm. Right: Room temperature emission spectra for **1@AA** re-dispersed in ethanol excited at different wavelengths.

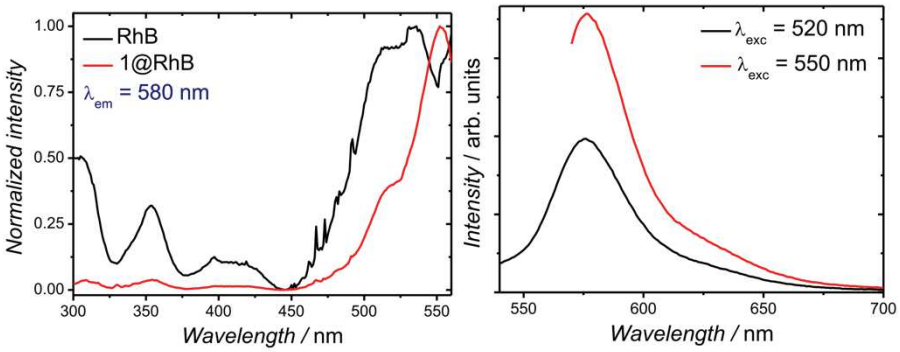

Fig. S14. Left: Room temperature normalized excitation spectra for **RhB** and **1@RhB** re-dispersed in water (500 µg.mL^{-1}) monitored at 500 nm. Right: Room temperature emission spectra for **1@RhB** re-dispersed in water excited at different wavelengths.

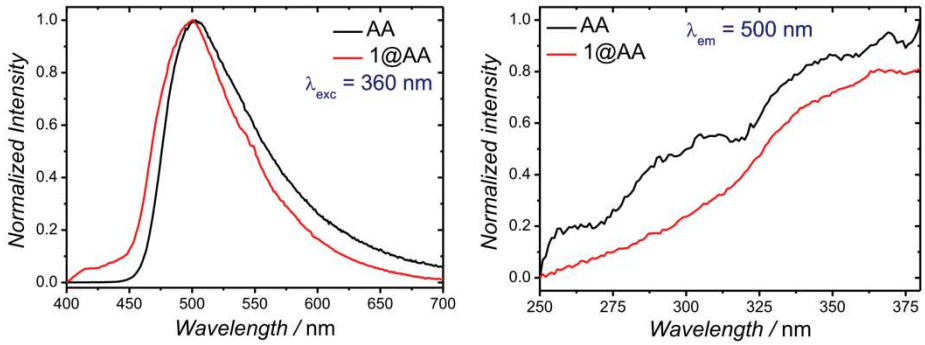

Fig. S15. Room temperature emission (left) and excitation (right) spectra excited at 360 and monitored around 500 nm, respectively, for powdered **AA** and **1@AA**.

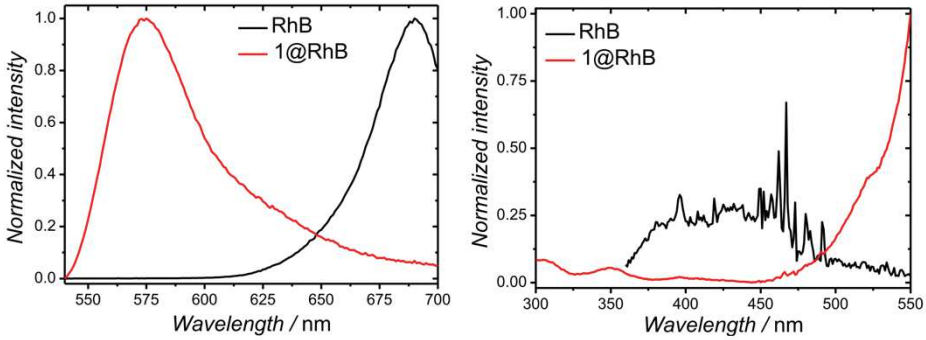

Fig. S16. Left: Room temperature emission spectra for powdered **RhB** and **1@RhB** excited at 467 nm and 520 nm, respectively; Right: Room temperature excitation spectra for powdered **RhB** and **1@RhB** monitored around 690 nm and 580 nm, respectively.

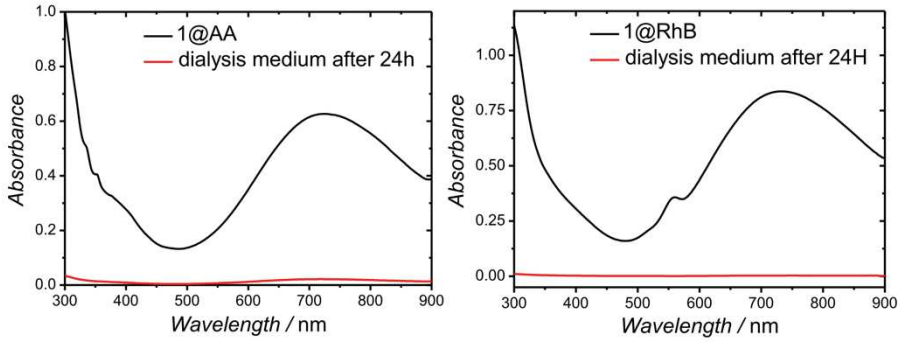

Fig. S17. Electronic spectra of dialysis medium (water) after release's experiments for **1@AA** (left) and **1@RhB** (right).

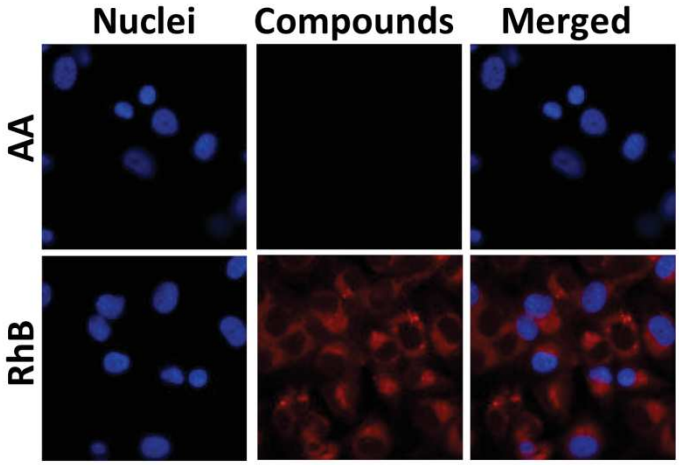

Fig. S18. MDA-MB-231 were incubated for 20 h with **AA** and **RhB** at a concentration of 100 $\mu g.mL^{-1}$. One photon fluorescence imaging was performed on living cells with similar parameters that **1@AA** and **1@RhB** imaging, respectively.

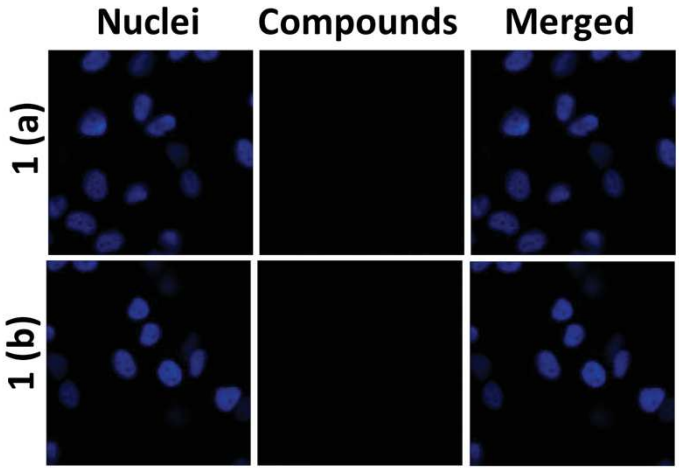

Fig. S19. MDA-MB-231 were incubated for 20 h with **1** at a concentration of 100 µg.mL^{-1}. One photon fluorescence imaging was performed on living cells with similar parameters that **1@AA (a)** and **1@RhB (b)** imaging, respectively.

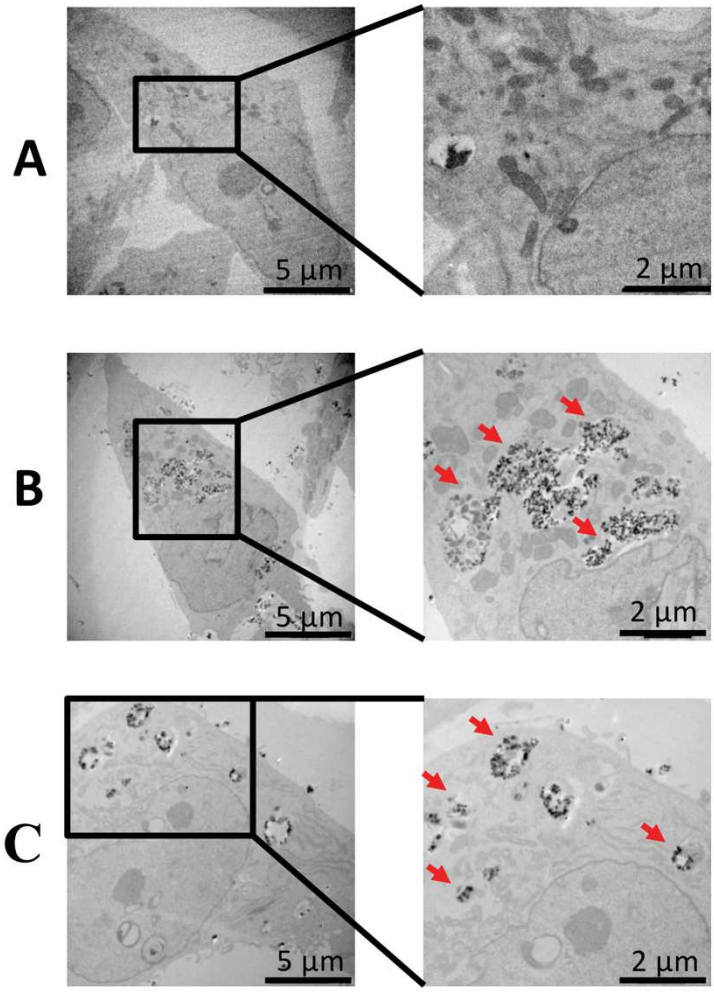

Fig. S20. TEM imaging of MDA-MB-231 cancer cells (A, control) and exposed with **1@AA** (B), **1@RhB** (C) for 20 h at a concentration of 100 µg.mL^{-1}. The nanoparticles are localized by arrows in the cells.

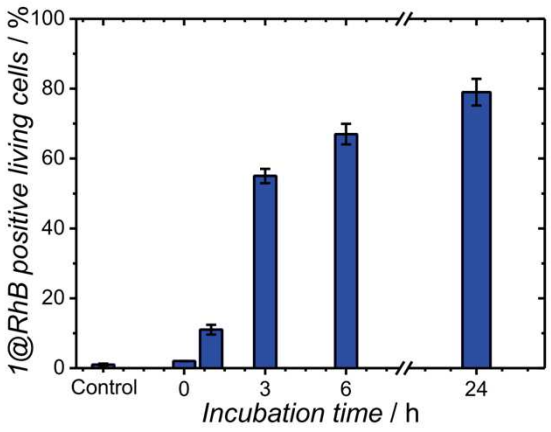

Fig. S21. Internalization of **1@RhB** by living MDA-MB-231 cells by flow. Cells were treated or not with 100 µg.mL^{-1} of **1@RhB** for 1, 3, 6 and 24 h. Non-fixed cells were incubated with propidium iodide (1 µg.mL^{-1}) to remove dead cells and **1@RhB** fluorescence was analyzed. Data represent means ± SEM of two experiments.

Table S1. Crystallographic parameters for **1**, **1@AA** and **1@RhB**

Sample	*Lattice parameter (Å)*	*Crystallite size (nm)*
1	10.07	55
1@AA	10.08	55
1@RhB	10.06	54

Table S2. Values of the zeta potential for **1** and **1@AA**

Sample	*Zeta potential (mV)*
1	−27 ± 5
1@AA	−25 ± 5
1@RhB	−15 ± 5

References

1 G. Maurin-Pasturel, E. Rascol, M. Busson, S. Sevestre, J. Lai-Kee-Him, P. Bron, J. Long, J. Chopineau, J.-M. Devoisselle, Y. Guari and J. Larionova, *Inorg. Chem. Front.*, 2017, **4**, 1737-1741.

2 L. M. A. Ali, E. Mathlouthi, M. Kajdan, M. Daurat, J. Long, R. Sidi-Boulenouar, M. Cardoso, C. Goze-Bac, N. Amdouni, Y. Guari, J. Larionova and M. Gary-Bobo, *Photodiagnosis Photodyn. Ther.*, 2018, **22**, 65-69.

3 S. Rojas, I. Colinet, D. Cunha, T. Hidalgo, F. Salles, C. Serre, N. Guillou and P. Horcajada, *ACS Omega*, 2018, **3**, 2994-3003.

4 L. D. Gelb and K. E. Gubbins, *Langmuir*, 1999, **15**, 305-308.

- Conclusion :

Dans cette étude, nous avons démontré que les PB pouvaient être fonctionnalisées après leur synthèse par divers luminophores afin de suivre leur devenir dans les cellules cancéreuses. Dans un premier temps, les chimistes ont confirmé la forte interaction des luminophores avec les PB. En effet, après dialyse dans de l'eau pendant 24 h, aucune libération du 2-AA ou de la RhB n'a été détectée. Par conséquent, ces PB fonctionnalisées avec les luminophores peuvent être utilisées pour suivre le devenir des nanoparticules dans les cellules. J'ai donc par la suite réalisé des expériences *in vitro* sur des lignées cellulaires du cancer du sein. L'imagerie confocale sur cellules vivantes a montré que les nanoparticules étaient internalisées efficacement et s'accumulaient dans le cytoplasme après 20 h d'incubation. De plus, j'ai confirmé l'internalisation des PB fonctionnalisées par les cellules cancéreuses par microscopie électronique en transmission (TEM). Pour finir, j'ai quantifié par cytométrie en flux l'internalisation des PB fonctionnalisées avec la RhB à différents temps ce qui nous a permis de conclure que les cellules cancéreuses les internalisaient rapidement : dès 3 h d'incubation. Tous ces résultats permettent d'ouvrir des perspectives intéressantes pour l'utilisation de ces nanoparticules en imagerie.

Chapitre 2 : Les nanoparticules pour la délivrance de drogue

Pour cette partie de travail de ma thèse, nous avons travaillé en étroite collaboration avec les équipes du Dr Jean-Oliver Durand et du Dr Peter Hesemann de l'Institut Charles Gerhardt de Montpellier.

1. Les nanoparticules organosiliciées

Ces nanoparticules sont synthétisées à partir de précurseurs organiques, d'agents directeurs de structure et en absence de silice. Des études récentes ont montré leur excellente biocompatibilité[292]. Les analogues poreux (PMO) de ce type de nanoparticules sont très couramment utilisés pour différentes applications telles que l'adsorption[293], la catalyse[294], la délivrance de drogue[295] et la théranostique[296]. Le travail de Inagaki, Ozin et Stein en 1999, a décrit pour la première fois la synthèse des nanoparticules organosiliciées : ces matériaux sont obtenus grâce à des réactions d'hydrolyse et de polycondensation (réaction sol-gel)[297–299]. Une grande variété de matériaux a déjà été synthétisée à partir de différents précurseurs organosiliciés[300]. Contrairement aux nanoparticules de silice mésoporeuse (MSN), qui sont aussi couramment utilisées, les PMO sont des solides poreux c'est-à-dire qu'ils présentent des arrangements en trois dimensions d'atomes laissant apparaître dans leurs structures des pores répartis de manière périodique. Ces pores sont basés sur des groupes fonctionnels organiques liant de manière covalente les domaines siloxanes de formule chimique R_2SiO où R est un groupe radical organique (Figure 21).

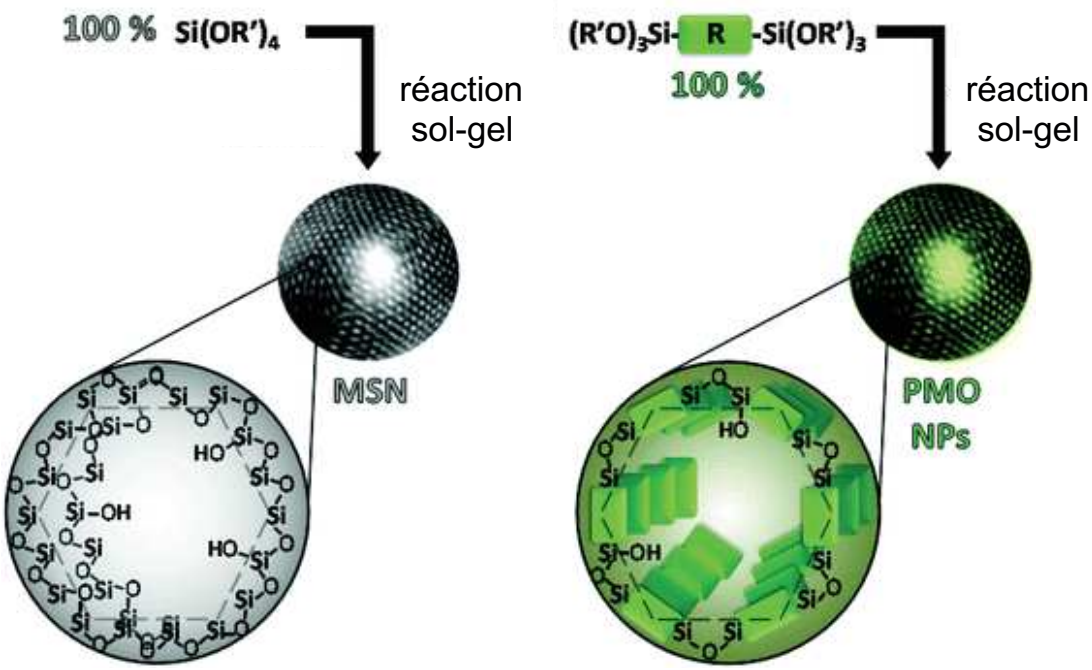

Figure 21 : Représentation schématique des MSN et PMO[296]

2. Description des travaux

Publication n°3 : « Organosilica nanoparticles for gemcitabine monophosphate delivery in cancer cells »

- Introduction :

Pour cette étude, deux types de nanoparticules ont été synthétisés par l'équipe du Dr Jean-Olivier Durand et du Dr Peter Hesemann, et plus particulièrement par le Dr Saher Rahamni et le Dr Roza Bouchal. Ces nanoparticules ont été développées pour la délivrance de drogue anti-cancéreuse, dans notre cas la gemcitabine monophosphate qui est utilisée notamment dans le traitement du cancer du sein. Les drogues hydrophiles ne peuvent pas être encapsulées dans des MSN sans la présence de bouchons qui bloquent les pores[301,302]. Par conséquent, nous avons décidé d'étudier l'encapsulation de la gemcitabine dans des nanoparticules organosiliciées. L'encapsulation de la gemcitabine monophosphate est difficile et peu de systèmes covalents comme la squalénisation (vésicules formées de gemcitabine monophosphate greffée sur des molécules de squalène), des formulations basées sur des liaisons de coordination avec des ions métalliques et des nanoparticules où la gemcitabine se lient à du calcium phosphate ont été décrits[303–305].

Dans cette étude, nous proposons deux stratégies innovantes pour l'encapsulation et la libération de la gemcitabine monophosphate :

- l'utilisation de nanoparticules organosiliciées à base d'amine obtenues à partir du bis(3-trimethoxysilylpropyl)-N-methylamine qui est composée de porphyrines (POR-NP) afin de pouvoir imager et localiser les nanoparticules dans les cellules,
- l'utilisation de nanoparticules organosiliciées à base d'ammonium, qui sont appelées nanoparticules ionosiliciées (INP) et qui sont obtenues à partir d'un précurseur d'ammonium trimethoxysilane.

J'ai étudié l'efficacité biologique de ces nanoparticules sur des lignées cellulaires du cancer du sein afin de démontrer leur potentiel thérapeutique en tant que véhicule de drogue anti-cancéreuse et leur potentiel d'imagerie. Les résultats ont été publiés dans un article dont je suis premier auteur dans le journal ChemNanoMat. Nous avons également été sélectionnés pour faire la couverture du journal.

CHEMNANOMAT

CHEMISTRY OF NANOMATERIALS FOR ENERGY, BIOLOGY AND MORE

www.chemnanomat.org

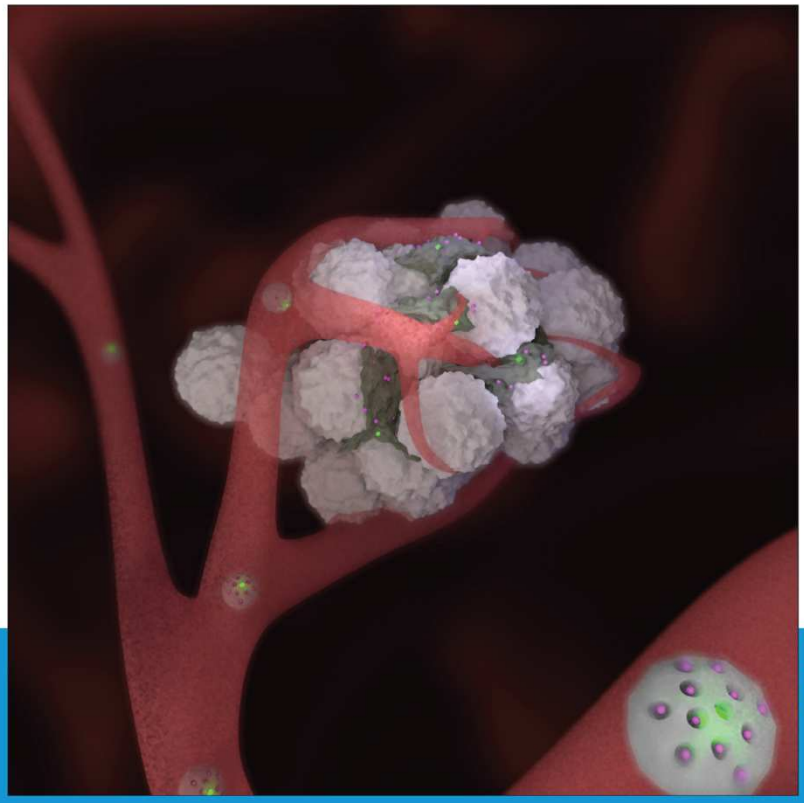

7/05
2019

A Journal of

ACES
Asian Chemical Editorial Society

A sister journal of **Chemistry – An Asian Journal** and the **Asian Journal of Organic Chemistry**

Front Cover:
Magali Gary-Bobo, Jean-Olivier Durand, Peter Hesemann et al.
Organosilica Nanoparticles for Gemcitabine Monophosphate Delivery in Cancer Cells

WILEY-VCH

ACES Asian Chemical Editorial Society
DOI: 10.1002/cnma.201900202
CHEMNANOMAT
Full Paper

Organosilica Nanoparticles for Gemcitabine Monophosphate Delivery in Cancer Cells

Morgane Daurat,[b, c] Saher Rahmani,[a] Roza Bouchal,[a] Alia Akrout,[a] Jelena Budimir,[a] Christophe Nguyen,[b] Clarence Charnay,[a] Yannick Guari,[a] Sébastien Richeter,[a] Laurence Raehm,[a] Nadir Bettache,[b] Magali Gary-Bobo,*[b] Jean-Olivier Durand,*[a] and Peter Hesemann*[a]

Abstract: Organosilica nanoparticles hold great promise for nanomedicine applications. These nanoparticles are synthesized from polytrialkoxysilylated precursors without any silica source. In this work we present two kinds of organosilica nanoparticles with either amine or ammonium walls constituting their structure. Both types of nanoparticles are very efficient for gemcitabine monophosphate delivery, a small hydrophilic anticancer drug whose encapsulation is still a challenge. The nanoparticles are endocytosed by MCF-7 breast cancer cells as monitored by confocal microscopy. They are efficient and lead to 60% cancer cell death.

1. Introduction

The use of organosilica nanoparticles for biological applications has attracted much attention during the last decade and the field has been recently reviewed.[1,2] These nanoparticles are prepared from polytrialkoxysilylated organic precursors, which are condensed in mild conditions using the sol-gel procedure, without the presence of any silica source. Recent studies have shown the excellent biocompatibility of these nanoparticles.[3] Of interest are their porous analogues, which have also been reviewed and are particularly suitable for theranostic applications and drug delivery.[4–6] Indeed, their properties are very different from that of well-known mesoporous silica nanoparticles (MSN).[7] Hydrophilic drugs such as anti-cancer drug gemcitabine cannot be encapsulated in MSN without the elaboration of stimuli-responsive stoppers to block the pores.[8–12] We recently demonstrated that gemcitabine and gemcitabine monophosphate (GMP) could be loaded in 1,2-bis (triethoxysilyl)ethane-based periodic mesoporous organosilica nanoparticles (PMO NPs) with high capacity. In order to extend the scope of stimuli-triggered GMP delivery, we decided to study methyl amine and methylammonium-based organosilica nanoparticles as gemcitabine monophosphate carriers. Indeed the encapsulation of GMP is still very challenging and covalent systems such as squalenization,[13,14] formulations with metal ions (MOF,[15,16] Zn^{2+}[17–19]or Gd^{3+}[20]-based coordination systems), calcium phosphate-based nanoparticles[21–25] have been reported. Here, we describe two innovative strategies for GMP transport and release, based on different types of organosilica materials: *i)* the use of new amine-based organosilica nanoparticles (POR-organosilica) obtained from *bis*(3-trimethoxysilylpropyl)-*N*-methylamine, incorporating a porphyrin derivative in the structure for near-infrared (NIR) imaging, and *ii)* the use of ammonium based mesoporous ionosilica nanoparticles, which we already described for dichlofenac delivery,[26] obtained from a *tris*-trialkoxysilylated ammonium precursor. In the first case, GMP release was controlled through pH change; in the second case, the release was triggered through anion exchange. Both GMP-loaded systems were incubated with MCF-7 cancer cells and were very efficient in inducing cancer cell death.

[a] Dr. S. Rahmani, Dr. R. Bouchal, A. Akrout, J. Budimir, Dr. C. Charnay, Dr. Y. Guari, Dr. S. Richeter, Dr. L. Raehm, Dr. J.-O. Durand, Dr. P. Hesemann
Institut Charles Gerhardt Montpellier,
UMR-5253 CNRS-UM-ENSCM cc 1701
Place Eugène Bataillon, 34095, Montpellier cedex 05 France
E-mail: jean-olivier.durand@umontpellier.fr
peter.hesemann@umontpellier.fr
[b] M. Daurat, C. Nguyen, Dr. N. Bettache, Dr. M. Gary-Bobo
Institut des Biomolécules Max Mousseron,
UMR 5247 CNRS, UM-Faculté de Pharmacie,
Avenue Charles Flahault, 34093, Montpellier cedex 05 France
E-mail: magali.gary-bobo@inserm.fr
[c] M. Daurat
NanoMedSyn
Institut des Biomolécules Max Mousseron
UMR 5247 CNRS, UM-Faculté de Pharmacie
Avenue Charles Flahault, 34093, Montpellier cedex 05 France

2. Results and Discussion

2.1. Studies of POR-Organosilica Nanoparticles

POR-Organosilica nanoparticles were elaborated by co-condensation of bis (3-methoxysilyl propyl)-N-methylamine (95% mol) with tetraethoxysilylated 5,10,15,20-*(tetra-4-aminophenyl)porphyrin* (5% mol) under basic conditions with the use of CTAB as the surfactant. The sol-gel reaction was carried out for 2 h at 75 °C, then the nanoparticles were centrifuged and the surfactant was extracted by exchange with NH_4NO_3. The POR-Organosilica carriers were first characterized with transmission electron microscopy (TEM) which showed the presence of nanoparticles with a mean diameter centered at 80 nm ± 30 nm (Figure 1A,D). UV – visible spectra showed the presence of adsorption bands (Soret-band: 424, Q-bands 522, 562, 580 and 652 nm) which confirmed the successful incorporation of the

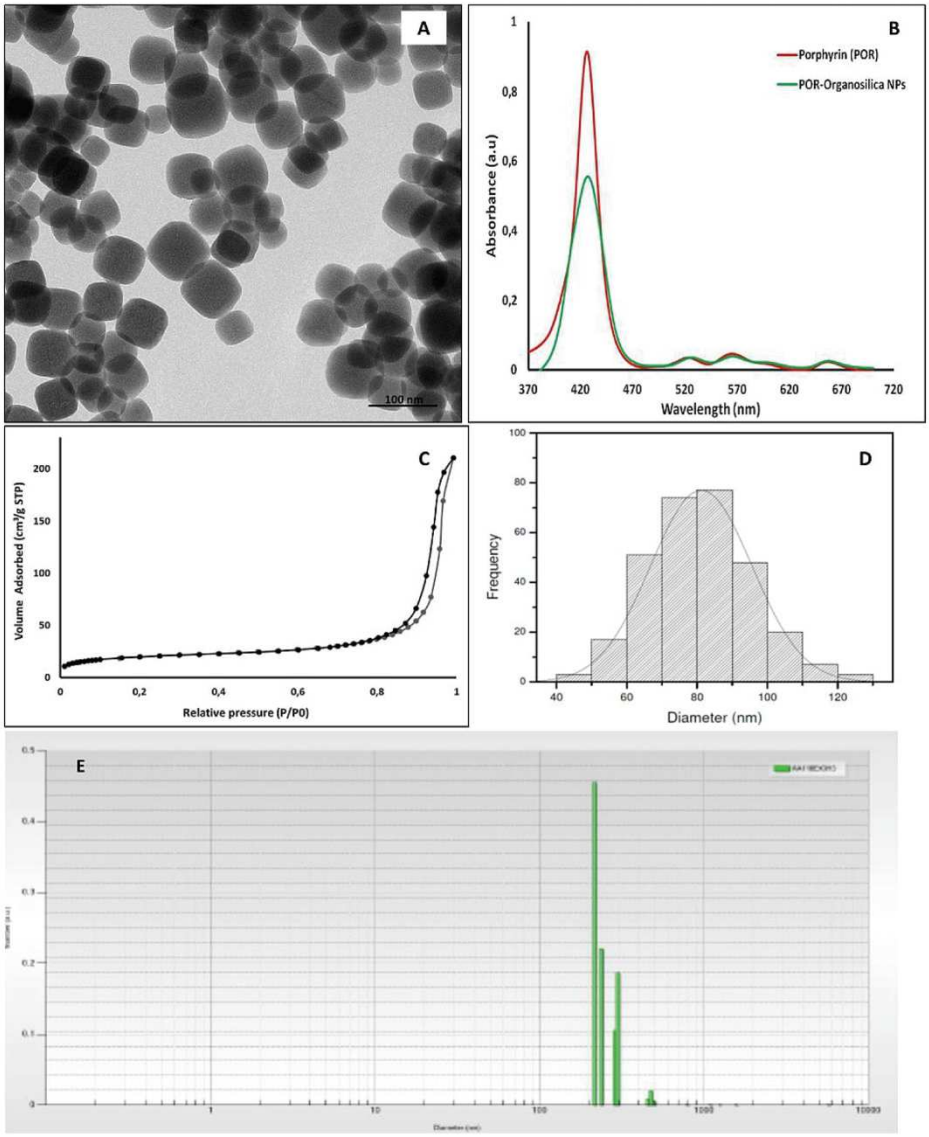

Figure 1. A) TEM micrographs, scale Bar 100 nm. B) UV-vis absorbance spectra of the porphyrin derivative and of the nanoparticles in EtOH, C) N_2 adsorption-desorption isotherms, D) Particle size distribution from TEM analysis. E) Dynamic Light scattering of POR-organosilica nanoparticles in absolute EtOH.

porphyrin derivative in the organosilica matrix (Figure 1B). No red shift of the UV-Vis spectrum was noticed after incorporation of the porphyrin, suggesting that no aggregation of the photosensitizer occurred in the matrix. Quantification allowed determining 0.0057 mmol of porphyrin/g of nanoparticles. The nitrogen adsorption-desorption experiments (BET) were carried out. A low specific surface area of 68 m^2/g (Figure 1C) was measured in agreement with a restricted accessibility of nitrogen molecules to the internal volume and surface of POR-Organosilica nanoparticles at cryogenic temperature (77 K).

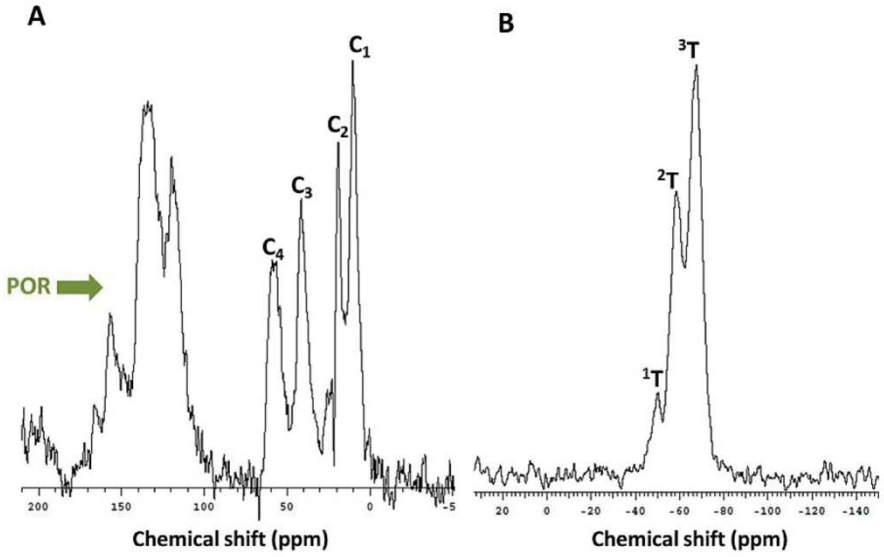

Figure 2. A) ^{13}C CP MAS solid-state NMR of PORorganosilica nanoparticles B) ^{29}Si CP MAS solid state NMR of PORorganosilica nanoparticles.

Dynamic Light Scattering (DLS) was measured in water at pH 5. The dispersibility of the nanoparticles was very good after sonication, with a hydrodynamic diameter of 311 nm (Dn 50%) with a PDI of 0.28. The size distribution in absolute EtOH is displayed in Figure 1E and shows nanoparticles with a narrow statistical distribution centered at 215 nm. The zeta potential was measured at 33 mV at pH 7 in agreement with the protonation of amine groups constituting the organosilica matrix.

The structure of POR-organosilica nanoparticles was studied by ^{13}C and ^{29}Si CP-MAS, solid-state NMR spectroscopy (figure 2). The ^{13}C spectrum displayed the characteristic signals of the phenylporphyrin derivative between 100 and 150 ppm, and the signals of the aliphatic chain at 60 ppm (CH_3N), 43 ppm (CH_2N), 17 ppm (–CH_2–), 7 ppm (CH_2Si). The ^{29}Si CP-MAS spectrum displayed the signals of well condensed triethoxysilyl groups at 50, 60 and 70 ppm.

We then studied the adsorption of GMP by the POR-Organosilica nanoparticles at neutral pH for 48 hours, at room temperature. The loading capacity was very good (42%). Interestingly the zeta potential was still measured at 33 mV showing that GMP was adsorbed inside the POR-Organosilica structure.

The release of GMP was monitored in water following standard published protocols,[27,28] in order to show that the release was pH sensitive (Figure 3).

The absence of release at pH 7.4 indicated that the negatively charged drug was strongly interacting through electrostatic interactions with the ammoniums constituting the structure of POR-organosilica nanoparticles. The addition of HCl to adjust the pH at 5.5 led to the protonation of GMP (second pKa of phosphate is 6) and this induced the drug release. 30% of the drug was released after 4 hours.

In vitro cytotoxicity study was then performed on MCF-7 breast cancer cell line incubated with GMP anticancer drug loaded- POR-Organosilica nanoparticles (Figure 4). MCF-7 cells were incubated with empty or loaded nanoparticles in biological conditions for 72 h. The colorimetric assay used to determine cell death level (MTT) showed that unloaded nanoparticles presented a low toxicity in the tested conditions. In contrast, nanoparticles loaded with GMP induced 50% cell death at low concentrations such as 1 $\mu g\,mL^{-1}$ and reached the maximal effect at 10 $\mu g\,mL^{-1}$ with 60% cancer cell death. This demonstrated the efficiency of POR-Organosilica nanoparticles to deliver GMP in cancer cells.

Secondly, near-infrared (NIR) confocal imaging was realized on MCF-7 breast cancer cells incubated for 24 h with 50 $\mu g\,mL^{-1}$ of POR-Organosilica nanoparticles. The excitation was performed at 750 nm with a femtosecond pulsed laser allowing detection of intense luminescence of porphyrins which demonstrated the efficient endocytosis and the imaging potential of the POR-Organosilica nanoparticles.

2.2. Studies of Ionosilica Nanoparticles

As a second way to transport GMP, we studied ionosilica nanoparticles as drug carrier vehicles. Ionosilicas, defined as silica-based materials containing covalently anchored ionic groups, recently emerged as a new family of functional organo-

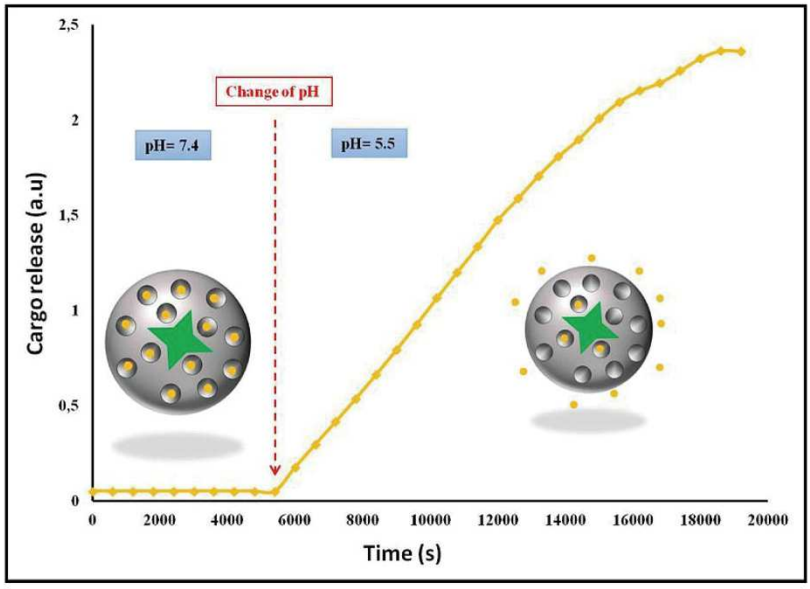

Figure 3. Release experiment of GMP loaded in POR-Organosilica nanoparticles. The experiment was performed in water upon addition of hydrochloric acid (0.2 M). The release profile was plotted from the UV-visible spectra over time.

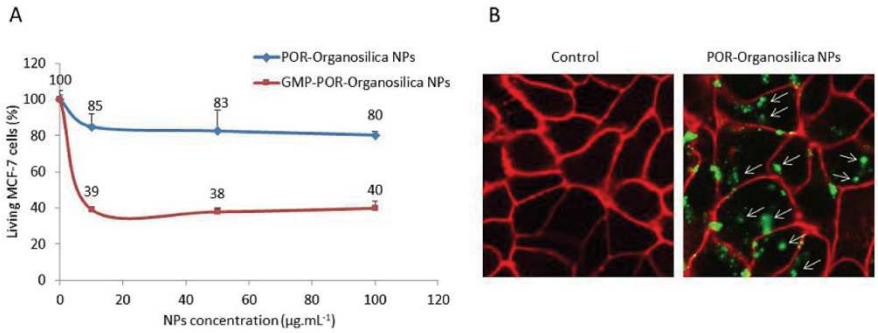

Figure 4. (A) GMP delivery in human breast cancer cells (MCF-7) *via* POR-Organosilica nanoparticles. Cytotoxic study of a range (from 0.1 to 100 µg mL^{-1}) of nanoparticles loaded or not with GMP, incubated for 72 h with MCF-7. (B) NIR fluorescence imaging of POR-Organosilica nanoparticles, demonstrating the cellular uptake of 50 µg mL^{-1} nanocarrier (green) by MCF-7 cells whose membranes are stained in red.

silicas. These materials are synthesized *via* hydrolysis-polycondensation reactions starting from ionic precursors.[29,30] Ionosilicas combine high porosity, regular architecture on the mesoscopic scale with an unmatched chemical versatility, induced by the high number of incorporated ionic sites and the high variability of possible anion-cation combinations. In analogy to ionic liquids, which are considered as *'designer solvents'*, ionosilicas can be regarded as *'designer materials'*.[31] Ionosilicas are particularly efficient anion exchange materials. In relationship to biomedical applications, we already reported that ionosilicas could efficiently trap a large variety of anionic species among them oxo-anions, halides or anionic drugs and dyes.[32–35]

Ionosilica nanoparticles (INPs) display several interesting features that makes them systems of choice for a use as drug nanocarriers and make them particularly interesting for applications in the biomedical field. First, INPs display low cytotoxicity and therefore high biocompatibility. Second, the synthesis

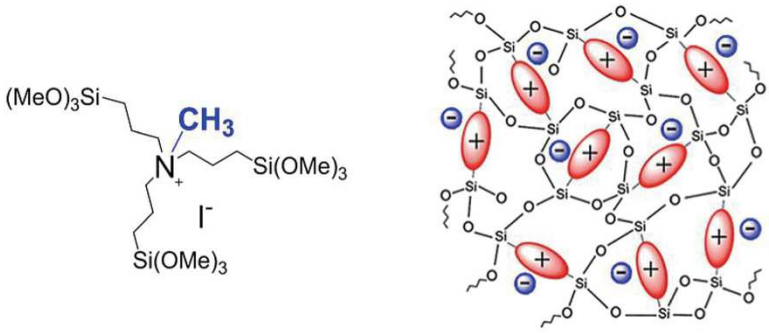

Figure 5. A. trisalkopxysliylated precursor used for the synthesis of ionosilica material. **B**. Schematic constitution of an ionosilica material.

process of INPs does not use highly cytotoxic compounds, in particular cationic porogens such as CTAB. This synthesis approach further enhances the biocompatibility and makes complex purification steps of the nanoparticles needless. Due to the high number of immobilized ionic sites, INPs are highly hydrophilic and therefore easily dispersible in aqueous and physiological media. INPs display high adsorption capacity towards anionic drugs, as a high number of anion exchange sites is present within the particles. Finally, loaded INPs display slow and progressive release kinetics that is controlled by anion exchange.[26]

We recently reported the first example of INPs for the vectorization of a model drug, *i.e.* diclofenac.[32] The very promising results obtained in this study prompted us to extend our studies to another field, in particular anticancer therapy. Here, we used INPs as nanocarriers to vehicle GMP.

INPs were obtained with a modified Stöber method in aqueous ammoniac solution. We used a *tris*-trialkoxysilylated ammonium precursor for the synthesis of these nano-objects. Hydrolysis-polycondensation reaction of this compound afforded INPs exclusively constituted of ionic ammonium building blocks. The synthesis involved a combination of an anionic surfactant, which generates mesoporosity within the particles through a templating approach, and a neutral PEO-PPO-PEO triblock copolymer as surfactant (F127). This latter compound limits the particle growth, being adsorbed on the surface of the formed primary particles.

In this work, we synthesized INPs with a slight modification of the previously published procedure.[26] In particular, we used a procedure that gets on without the silylated PEG precursor, allowing accessing INPs using only the neutral and physisorbed F127 surfactant. Similarly to the previously reported procedure, the INPs were synthesized from a *tris*-trimethoxysilylated ammonium precursor (Figure 5A). The constitution of ionosilica material from this compound is schematized in Figure 5B.

The INPs were characterized with several characterization techniques to elucidate in particular their morphological and surface properties.

DLS with the INPs indicated the formation of objects with a particle size of 158 nm (±29 nm, PDI 0.17) (Figure 6A). DLS often overestimates the particle size as it determines the hydrodynamic diameter of the particles. DLS therefore takes into account the hydration sphere of the particles, including the surface located F127 surfactant. The particle size analysis from electron microscopy results in a considerably lower diameter of INPs of 87±22 nm (Figure 6B).

TEM and SEM images are given in Figure 6C/D. An average particle size of about 50–100 nm can be estimated from these images. Particle size analysis of the TEM indicates an average diameter of 87±22 nm. These results are in line with our former works, where INPs with a diameter of 104 nm have been reported. The slightly lower diameter can be explained with the absence of surface located PEG-groups. The particle size strongly depends on several reaction parameters such as concentration, temperature, and pH of the hydrolysis-polycondensation mixture. The fact that the formed nanoparticles show a very similar size compared to the previously reported ones shows the good reproducibility of the ionosilica nanoparticle synthesis.

For efficient anion exchange processes, porosity and well-defined textures are essential characteristics. We therefore focused on the determination of the surface properties of the INPs. First, we performed nitrogen sorption experiments with the INPs. The nitrogen sorption isotherm is given in Figure 7A. The INPs are highly porous and show a specific surface area S_{BET} of 826 m^2/g. The nitrogen sorption isotherm also gives information regarding the pore size and pore volume. The isotherm indicates two regions of nitrogen adsorption, namely at $P/P_0 < 0.3$ and $P/P_0 > 0.8$. The first region corresponds to the filling of small mesopores. From the shape of the adsorption isotherm, we can deduce a pore size of 2 nm, in line with our former results. The strong nitrogen adsorption at higher relative pressures indicates much larger pores and can be attributed to intergrain porosity. Secondly, we characterized the nanoparticles with X-ray diffraction. The diffractogram (Figure 7B) only displays a shoulder at $2\theta = 2.3°$, thus indicating the presence of

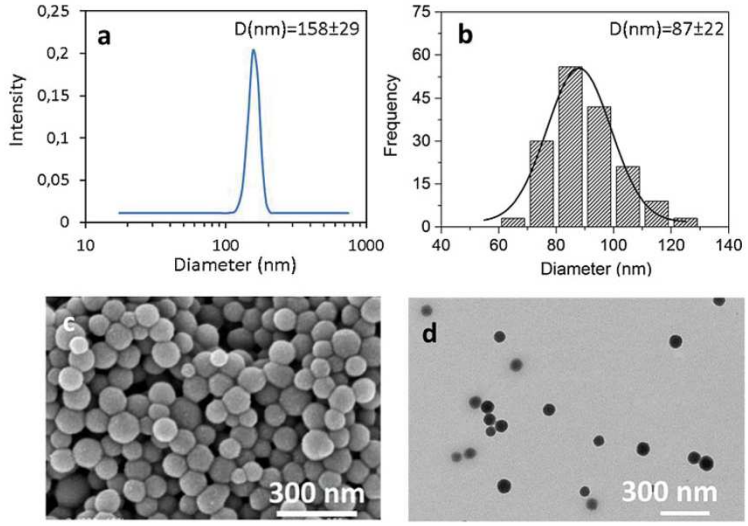

Figure 6. A. and B. Particle size distribution of the ionosilica nanoparticles, obtained by DLS and TEM-analysis. **C**. SEM image **D**. TEM image of the ionosilica nanoparticles.

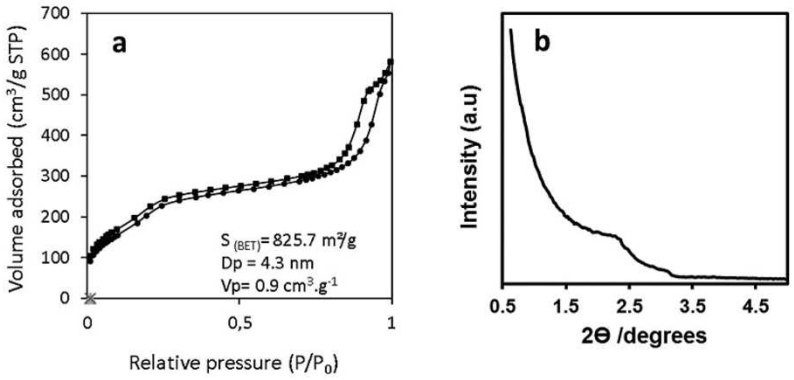

Figure 7. A. Nitrogen sorption isotherms of ionosilica nanoparticles **B**. Small-angle X-ray diffractogram of ionosilica nanoparticles.

nanoparticles with low long-range order. This result is not surprising, as the nanoparticles are too small to exhibit regular long-range architectures.

The characterization of INPs therefore confirms that highly porous ionosilica nanoparticles can be exclusively obtained from a silylated ammonium precursor. These nano-objects contain a very high number of immobilized ionic groups, and show high porosity and therefore display some interesting features for applications for drug-delivery.

In a second time, we used these nanoparticles for anion exchange with GMP. For this purpose, an aqueous dispersion of INPs was dispersed with a solution of GMP. The anion exchange was monitored with UV-Vis spectroscopy. This technique allowed for a precise determination of the quantity of exchanged GMP. The anion exchange occurred very smoothly and UV/Vis analysis of the supernatant indicated that the GMP was efficiently adsorbed by the INPs. With this anion exchange technique, we obtained ionosilica nanoparticles INP/GMP with a loading of 1.76 mmol of GMP/g of nanoparticles. This value is in line with formerly observed loadings of ionosilica materials.

To investigate the drug delivery potential of the INP/GMP system, a cytotoxicity study on MCF-7 cells was performed with

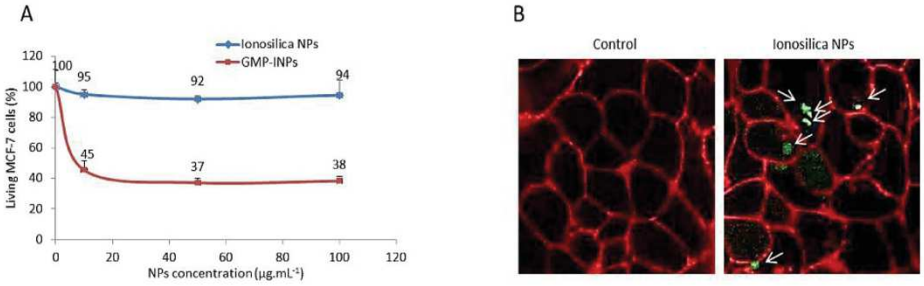

Figure 8. A. Cytotoxic effect of INPs on human breast cancer MCF-7 cells. Cells were incubated with INPs (from 5 to 100 $\mu g\,mL^{-1}$) loaded or not with gemcitabine for 72 h and submitted to a MTT assay. The level of living cells was measured and expressed as the percent of control cells. Values are means ± standard deviations of 3 experiments. **B.** Confocal microscopy of MCF-7 cells incubated with INPs (50 $\mu g\,mL^{-1}$) conjugated with FITC for 24 h. Imaging was performed on living cells at a wavelength of 485 nm.

INPs loaded or not with GMP. For this purpose, cancer cells were incubated with increasing concentrations of INPs. As depicted on Figure 8A, INP + GMP induced 63% of cell death after 72 h incubation at concentration of 50 $\mu g\,mL^{-1}$ whereas bare INPs were not toxic. This effect could be attributed to the efficient drug release after endocytosis of these nanoparticles by MCF-7 cells as demonstrated in Figure 8B. In fact, INPs conjugated with FITC were incubated in culture cells at concentration of 50 $\mu g\,mL^{-1}$ for 24 h. Confocal microscopy imaging of living cells showed that nanoparticles are efficiently internalized by MCF-7 cells after this period.

All together, these data demonstrated the efficacy of INPs. Importantly, unloaded INPs showed no cytotoxicity at the studied concentrations, thus demonstrating good biocompatibility.

3. Conclusion

In this paper, we performed the synthesis of two different kinds of organosilica nanoparticles for GMP delivery. The first system obtained by the condensation of bis(triethoxysilylpropyl)methylamine led to amine-based organosilica nanoparticles of 80 nm average diameter incorporating a porphyrin in the structure. These nanoparticles allowed a significant loading capacity of GMP of 42% and the release of GMP was pH-triggered. These nanoparticles were very efficient for NIR imaging of cancer cells, and led to 60% of cancer cell death at low concentration. Alternatively mesoporous ionosilica nanoparticles loaded with FITC were endocytosed by MCF-7 cancer cells. When loaded with GMP, these nanoparticles were very efficient in inducing cancer cell death with 60% of mortality. Therefore, organosilica nanoparticles are promising candidates for nanomedicine applications.

Experimental Section

Chemicals and Materials

The following chemicals, cetyltrimethylammonium bromide (CTAB, 95%), THF, DIPEA, DIC, ammonium hydroxide, ammonium nitrate (NH_4NO_3), were purchased from Sigma-Aldrich. Bis (3-methoxysilyl propyl)-N-methylamine was purchased from Abcr GmbH&Co, hydrochloric acid from VWR PROLABO and 5,10,15,20-*meso*-tetra(4-aminophenyl)porphyrin from porphyChem.

TEM analysis was performed on a JEOL 1200 EXII instrument. Statistical distribution diameters of the nanoparticles was determined by measuring the diameters of 300 nanoparticles. Dynamic light scattering analyses were performed using a Cordouan Technologies DL 135 Particle size analyzer instrument. BET analyses were determined using a TRISTAR 3000 gas adsorption analyzer instrument. ^{1}H NMR spectra were recorded on a Bruker AC 400 spectrometer and were calibrated to TMS on the basis of the relative chemical shift (δ in ppm) of the residual non-deuterated solvent as an internal standard.

Synthesis of Nanoparticles

The synthesis of POR-Organosilica nanoparticles was obtained in two steps which are detailed in the following paragraphs:

Silylated Porphyrin

Firstly, a mixture of 5,10,15,20-*meso*-tetra(4-aminophenyl)porphyrin (200 mg, $1.4*10^{-2}$ mmol), DIPEA (11.2 mg), isocyanatopropyltriethoxysilane (362.8 mg) was stirred in anhydrous THF (7 mL) under argon at 80 °C overnight (scheme 1). After evaporation of the solvent, the POR precursor was washed with AcOEt and recrystallized in hexane. This process was repeated 4 times. Finally, the precursor was dried under vacuum. ^{1}H NMR (300 MHz, DMSO-d6) was done to prove the silylation of the porphyrin (Figure). (δ (ppm) 8.88 (s, 8H, $H\beta_{pyrrole}$), 8.86 (s, 4H,CO–N**H**–CH_2), 8.06 (d, ^3J = 9.0 Hz, 8H, $H_{3,5\ aryl}$), 7.84 (d, ^3J = 9.0 Hz, 8H, $H_{2,6\ aryl}$), 6.40 (t, 4H, ^3J = 4.5 Hz, CO–N**H**–Ph), 3.81 (q, ^3J = 7.5 Hz, 24H, O–C**H**$_2$–CH_3), 1.20 (t, ^3J = 7.5 Hz, 36H, O–CH_2–C**H**$_3$), 0.66 (t, ^3J = 9.0 Hz, 8H, C**H**$_2$–Si).

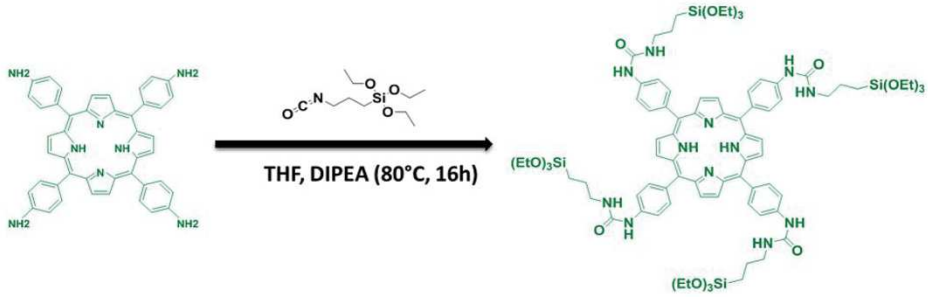

Scheme 1. Design of silylated porphyrin.

Synthesis of POR-Organosilica Nanoparticles

In a 250 mL three necks round bottom flask, 19.2 mg of CTAB, sodium hydroxide (39 µl, 1 M), 300 µL of absolute ethanol and 60 mL of ultrapure water was stirred at 75 °C for 50 minutes at 1000 rpm. In the mean time, bis (3-trimethoxysilyl propyl) -N-methylamine (21.33×10^{-3} mmol) and silylated porphyrin 5% (1.07×10^{-5} mol) were sonicated in 9 mL of ethanol. Then, the alcoholic solution was added to the template, the stirring speed was changed to 1400 rpm and the condensation process was performed for 2 hours at 80 °C. Afterwards, the solution was cooled at room temperature while stirring. POR-Organosilica nanoparticles were collected by centrifugation for 20 minutes at 20000 rpm. The sample was then extracted three times with an alcoholic solution of ammonium nitrate (6 $g\,L^{-1}$) in order to remove the CTAB surfactant, and washed several times with ethanol. Finally, the sample was dried under air flow for few hours.

Gemcitabine Monophosphate Loading in Nanoparticles

A mixture of POR-organosilica nanoparticles based porphyrin (7.3 mg), deionized water (5 ml) and GMP (2 mg) was sonicated for 10 minutes and stirred for 48 hours at room temperature at 320 rmp. Then, the sample was centrifuged at 10000 rpm for 20 min and was washed 4 times with water and dried for few hours under vacuum.

The loading capacities were calculated from the UV-Vis analysis of the supernatant of the GMP in solution.

$$\text{Loading Capacity (wt\%)} = [\text{mass of loaded drug}/(\text{mass of loaded drug} + \text{mass of NPs})]^{*}100$$

$$\text{GMP (wt\%)} = 42\%$$

Ionosilica Nanoparticles

Precursor's Synthesis

The synthesis of methyl-(tris(3-trimethoxysilyl)propyl) ammonium iodide was carried out according to the literature.[29,30]

Ionosilica Nanoparticles Synthesis

In a typical synthesis procedure, a solution of sodium hexadecyl sulfate SHS (100 mg, 0.3 mmol) and deionized water (30 ml) was stirred for 1 hour to form a clear solution at 70 °C. The hybrid precursor (methyl-(tris(3-trimethoxysilyl)propyl) ammonium iodide) (200 mg, 0.31 mmol) dissolved in 2 ml of 1-propanol was added drop by drop under vigorous stirring to promote the precursor hydrolysis during 20 min. Then a mixture of nonionic surfactant triblock copolymer F127 (20 mg) in 1 ml of water was added to the solution, followed after 5 min by 1 ml of ammonia (0.1 M). The condensation process was conducted for 24 h at 1250 rpm at 70 °C. The as-synthesized NPs were collected by centrifugation and washed twice with water and ethanol before template extraction with an ethanolic ammonium chloride solution. Finally, the nanoparticles were washed three times with water.

GMP Loading

Gemcitabine monophosphate (GMP) loaded nanoparticles were synthesized by dissolving 2.9 mg GMP with 75 mg of ionosilica nanoparticles already dispersed in 500 µl of deionized water under stirring for 24 hours at room temperature. The resulting nanoparticles (INP- GMP) were then washed with water to remove all physisorbed GMP. The loading of GMP on ionosilica nanoparticles was quantitatively determined by UV-visible spectroscopy. We obtained a loading of C = 1.7636 mmol/g (mol GMP/1 g of nanoparticles) corresponding to the concentration of 38%.

In Vitro Studies

Cell Culture

Human breast cancer cells (MCF-7) were purchased from ATCC (American Type Culture Collection, Manassas, VA). Cells were cultured in Dulbecco's Modified Eagle's Medium (DMEM-F12) supplemented with 10% foetal bovine serum and 50 $\mu g\,mL^{-1}$ gentamycin. These cells were allowed to grow in humidified atmosphere at 37 °C under 5% CO2.

Cytotoxic Study

MCF-7 cells were seeded into 96-well plates at 5000 cells per well in 200 µL culture medium and allowed to grow for 24 h. Increasing concentrations of POR-organosilica NPs with or without Gemcitabine were added in culture medium of MCF-7 cells. Three days after

treatment, a MTT assay was performed to determine the drug delivery potential of the nanoparticles. Briefly, cells were incubated for 4 h with 0.5 mg mL^{-1} of MTT (3-(4,5-dimethylthiazol-2-yl)-2,5-diphenyltetrazolium bromide; Promega) in media. The MTT/media solution was then removed and the precipitated crystals were dissolved in EtOH/DMSO (v/v). The solution absorbance was read at 540 nm in a microplate reader.

NIR-Imaging

MCF-7 cells were plated onto bottom glass dishes (World Precision Instrument, Stevenage, UK) at a density of 10^6 cells cm^{-2}. Twenty four hours after seeding, cells were then washed once and incubated in 1 mL culture medium containing POR-organosilica nanoparticles at a concentration of 80 µg mL^{-1} for 24 h. Fifteen min before the end of incubation, cells were loaded with CellMask™ plasma membrane stain (Invitrogen, Cergy Pontoise, France) at a final concentration of 5 µg mL^{-1}. Prior the observation, cells were washed gently with phenol red-free DMEM. Cells were then visualized with a LSM 780 LIVE confocal microscope (Carl Zeiss, Le Pecq, France), at 750 nm using a high magnification (63x/1.4 OIL DIC Plan-Apo).

Acknowledgements

The grant "Chercheur d'Avenir Languedoc-Roussillon" attributed to MGB and the Erasmus Mundus program for SR are gratefully acknowledged. We thank L. Lichon for technical assistance. We thank MRI (Montpellier RIO Imaging platform) for confocal imaging facilities. M Daurat, S. Rahmani and R. Bouchal contributed equally to this work.

Conflict of Interest

The authors declare no conflict of interest.

Keywords: gemcitabine monophosphate · organosilica nanoparticles · drug delivery · cancer · ionosilica

[1] J. G. Croissant, X. Cattoen, J.-O. Durand, M. Wong Chi Man, N. M. Khashab, *Nanoscale* **2016**, *8*, 19945–19972.
[2] M. Nakamura, *Nanotechnol. Rev.* **2012**, *1*, 469–491.
[3] J. G. Croissant, Y. Fatieiev, N. M. Khashab, *Adv. Mater.* **2017**, *29*, 1604634.
[4] X. Du, X. Li, L. Xiong, X. Zhang, F. Kleitz, S. Z. Qiao, *Biomaterials* **2016**, *91*, 90–127.
[5] Y. Chen, J. Shi, *Adv. Mater.* **2016**, *28*, 3235–3272.
[6] J. G. Croissant, X. Cattoen, M. W. C. Man, J.-O. Durand, N. M. Khashab, *Nanoscale* **2015**, *7*, 20318–20334.
[7] J. G. Croissant, Y. Fatieiev, A. Almalik, N. M. Khashab, *Adv. Healthc. Mater.* **2018**, *7*, 1700831.
[8] M. R. Zeiderman, D. E. Morgan, J. D. Christein, W. E. Grizzle, K. M. McMasters, L. R. McNally, *ACS Biomater. Sci. Eng.* **2016**, *2*, 1108–1120.
[9] A. Pourjavadi, Z. M. Tehrani, *Mater. Sci. Eng. C* **2016**, *61*, 782–790.
[10] H. Meng, M. Wang, H. Liu, X. Liu, A. Situ, B. Wu, Z. Ji, C. H. Chang, A. E. Nel, *Acs Nano* **2015**, *9*, 3540–3557.
[11] J. G. Croissant, D. Zhang, S. Alsaiari, J. Lu, L. Deng, F. Tamanoi, A. M. Al Malik, J. I. Zink, N. M. Khashab, *J. Control. Release* **2016**, *229*, 183–191.
[12] Z. Bahrami, A. Badiei, G. M. Ziarani, *J. Nanopart. Res.* **2015**, *17*, 1–12.
[13] A. Maksimenko, J. Caron, J. Mougin, D. Desmaele, P. Couvreur, *Int. J. Pharm.* **2015**, *482*, 38–46.
[14] J. Caron, E. Lepeltier, L. H. Reddy, S. Lepetre-Mouelhi, S. Wack, C. Bourgaux, P. Couvreur, D. Desmaele, *Eur. J. Org. Chem.* **2011**, 2615–2628, S2615/2611-S2615/2627.
[15] V. Rodriguez-Ruiz, A. Maksimenko, V. Agostoni, P. Couvreur, R. Gref, R. Anand, M. Lampropoulou, K. Yannakopoulou, S. Monti, *J Drug Target* **2015**, *23*, 759–767.
[16] T. Simon-Yarza, M. Gimenez-Marques, R. Mrimi, A. Mielcarek, R. Gref, P. Horcajada, C. Serre, P. Couvreur, *Angew. Chem., Int. Ed.* **2017**, *56*, 15565–15569.
[17] C. Poon, C. He, D. Liu, K. Lu, W. Lin, *J. Control. Release* **2015**, *201*, 90–99.
[18] C. Poon, X. Duan, C. Chan, W. Han, W. Lin, *Mol. Pharmaceutics* **2016**, *13*, 3665–3675.
[19] C. He, C. Poon, C. Chan, S. D. Yamada, W. Lin, *J. Am. Chem. Soc.* **2016**, *138*, 6010–6019.
[20] L. Li, R. Tong, M. Li, D. S. Kohane, *Acta Biomater.* **2016**, *33*, 34–39.
[21] Y. Zhang, N. M. J. Schwerbrock, A. B. Rogers, W. Y. Kim, L. Huang, *Mol. Ther.* **2013**, *21*, 1559–1569.
[22] Y. Zhang, L. Peng, R. J. Mumper, L. Huang, *Biomaterials* **2013**, *34*, 8459–8468.
[23] Y. Zhang, W. Y. Kim, L. Huang, *Biomaterials* **2013**, *34*, 3447–3458.
[24] L. Miao, S. Guo, J. Zhang, W. Y. Kimb, L. Huang, *Adv. Funct. Mater.* **2014**, *24*, 6601–6611.
[25] J. Zhang, L. Miao, S. Guo, Y. Zhang, L. Zhang, A. Satterlee, W. Y. Kim, L. Huang, *J. Control. Release* **2014**, *182*, 90–96.
[26] R. Bouchal, M. Daurat, M. Gary-Bobo, A. Da Silva, L. Lesaffre, D. Aggad, A. Godefroy, P. Dieudonne, C. Charnay, J.-O. Durand, P. Hesemann, *ACS Appl. Mater. Interfaces* **2017**, *9*, 32018–32025.
[27] Z. Li, D. L. Clemens, B.-Y. Lee, B. J. Dillon, M. A. Horwitz, J. I. Zink, *ACS Nano* **2015**, *9*, 10778–10789.
[28] J. Croissant, X. Cattoen, M. W. C. Man, A. Gallud, L. Raehm, P. Trens, M. Maynadier, J.-O. Durand, *Adv. Mater.* **2014**, *26*, 6174–6178.
[29] T. P. Nguyen, P. Hesemann, M. L. T. Thi, J. J. E. Moreau, *Journal of Materials Chemistry* **2010**, *20*, 3910–3917.
[30] S. El Hankari, B. Motos-Perez, P. Hesemann, A. Bouhaouss, J. J. E. Moreau, *Journal of Materials Chemistry* **2011**, *21*, 6948–6955.
[31] U. D. Thach, P. Trens, B. Prelot, J. Zajac, P. Hesemann, *Journal of Physical Chemistry C* **2016**, *120*, 27412–27421.
[32] R. Bouchal, I. Miletto, U. D. Thach, B. Prelot, G. Berlier, P. Hesemann, *New Journal of Chemistry* **2016**, *40*, 7620–7626.
[33] U. D. Thach, P. Hesemann, G. Yang, A. Geneste, S. Le Caer, B. Prelot, *Journal of Colloid and Interface Science* **2016**, *482*, 233–239.
[34] U. D. Thach, B. Prelot, P. Hesemann, *Separation and Purification Technology* **2018**, *196*, 217–223.
[35] U. D. Thach, B. Prelot, S. Pellet-Rostaing, J. Zajac, P. Hesemann, *ACS Applied Nano Materials* **2018**, *1*, 2076–2087.

Manuscript received: April 5, 2019
Accepted manuscript online: April 5, 2019
Version of record online: April 30, 2019

- Conclusion :

Dans cet article, nous avons réalisé la synthèse de deux types de nanoparticules organosiliciées pour la délivrance de gemcitabine monophosphate. Les POR-NP à base d'amine ont permis d'encapsuler une quantité significative de gemcitabine monophosphate et la libération a été déclenchée à pH acide dans la cellule cancéreuse. A pH neutre aucune libération n'a été détectée. En effet, à pH 7,4 la drogue chargée négativement interagit fortement par le biais d'interactions électrostatiques avec les ammoniums constituant la structure de la nanoparticule, alors qu'un pH acide de 5,5 entraîne la protonation de la gemcitabine monophosphate induisant sa libération. De plus, ces nanoparticules dans lesquelles ont été incorporées des porphyrines sont très efficaces et ont permis de visualiser les nanoparticules dans le cytoplasme des cellules cancéreuses. Parallèlement, les INP chargées en FITC ont été internalisées efficacement par les cellules cancéreuses permettant la libération de la gemcitabine monophosphate par échange d'ions présents dans la cellule cancéreuse. L'efficacité d'internalisation des deux types de nanoparticules a conduit à environ 60% de mort cellulaire même à faible concentration (dès 10 μg.mL^{-1}). Ces nanoparticules organosiliciées ont donc un potentiel pour des applications d'imagerie médicale et thérapeutique : ce sont donc de bons candidats pour des applications théranostiques.

Partie 2 : Le ciblage thérapeutique du récepteur du mannose 6-phosphate

Chapitre 1 : Les analogues du mannose 6-phosphate pour le ciblage du RM6P-CI membranaire

1. Les travaux antérieurs entrepris au sein du laboratoire

La finalité de ma thèse est de développer un ciblage thérapeutique innovant basé sur le ciblage du RM6P-CI pour deux applications thérapeutiques : le traitement du cancer et plus particulièrement le RMS et le traitement de la maladie de Pompe. Nous avons vu précédemment que le signal M6P (ligand naturel du RM6P-CI) est un élément clé dans de nombreux processus biologiques ainsi que dans le ciblage de molécules bioactives vers les lysosomes. Cependant, la stabilité du M6P est un facteur limitant car il est sensible aux phosphatases présentes dans le sérum mais également celles présentes dans tous les organes entraînant une déphosphorylation : le M6P ne peut plus être reconnu par le RM6P-CI. Afin d'éviter cette déphosphorylation, les équipes du Professeur Alain Morère et du Docteur Marcel Garcia ont développé des analogues du M6P où le phosphate est remplacé par un phosphonate, un carboxylate ou un malonate. Ces analogues, appelés AMFA (Analogue du Mannose 6-phosphate Fonctionnalisé sur l'Aglycone), ont été brevetés puis l'entreprise NanoMedSyn a acquis une licence exclusive d'exploitation. Dans un premier temps, l'équipe a dû prendre en compte les différents éléments structuraux du M6P qui sont indispensables ou qui peuvent être modifiés pour ne pas altérer le phénomène de reconnaissance par le récepteur (Figure 22)[306] :

- L'hydroxyle en position 2 du saccharide doit être obligatoirement en position axiale. En effet le glucose 6-phosphate dont l'hydroxyle est en position équatoriale ou le 2-desoxy-glucose 6-phosphate ne présentent qu'une très faible affinité pour le RM6P-CI.
- L'hydroxyle en position anomère peut être modifié. Le fructose-1-phosphate qui ne présente pas l'hydroxyle en position anomère a une affinité comparable pour le RM6P-CI démontrant que le groupement substituant la position anomère du M6P n'a pas d'influence sur la reconnaissance du récepteur.

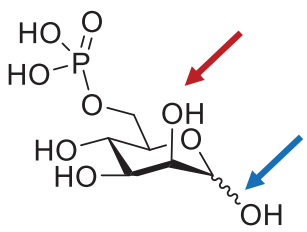

Mannose 6-phosphate
$K_i = 10^{-6}$ M

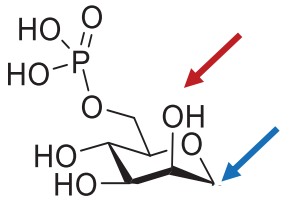

Fructose 1-phosphate
$K_i = 7.10^{-6}$ M

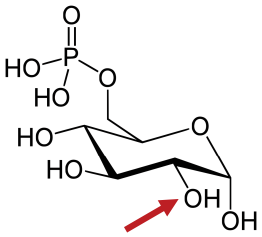

Glucose 6-phosphate
$K_i = 8.10^{-2}$ M

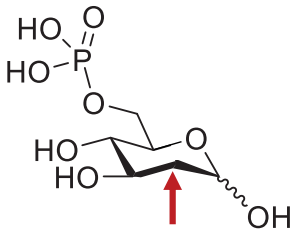

2-Desoxy glucose 6-phosphate
$K_i = 8.10^{-2}$ M

→ Hydroxyle en position axiale

→ Position anomère

Figure 22 : Elements structuraux importants du M6P pour la reconnaissance du RM6P-CI[306]

Dans un deuxième temps, le groupement phosphate a été remplacé par un phosphonate, carboxylate ou malonate ce qui a permis d'augmenter significativement la stabilité dans le sérum puisque ces groupements de remplacement sont insensibles aux phosphatases sériques. De plus les AMFA ont une affinité pour le RM6P-CI plus élevée ou comparable à celle du M6P[307]. Les AMFA sont aussi modifiés sur la position aglycone (fonction hydroxyle anomérique) où un bras est ajouté afin de limiter les encombrements stériques du vecteur sur lequel il est fonctionnalisé dans le site de liaison du RM6P-CI permettant une meilleure interaction entre l'AMFA et le récepteur.

Chapitre 2 : Ciblage thérapeutique du rhabdomyosarcome

Dans cette étude, des PMO ciblées pour la thérapie photodynamique et l'imagerie du rhabdomyosarcome ont été développées. Ce travail a été effectué en collaboration avec l'équipe du Dr Jean-Olivier Durand et plus particulièrement avec Mme Sofia Dominguez-Gil, doctorante à l'Institut Charles Gerhardt de Montpellier et Mr Christophe Nguyen, doctorant en cotutelle dans notre équipe « Glyco et nanovecteurs pour le ciblage thérapeutique » à l'Institut des Biomolécules Max Mousseron et celle du Dr Jean-Olivier Durand.

1. La thérapie photodynamique (PDT)

1.1 Principe et mécanisme

La concept de la PDT est né au début du XXème siècle avec les travaux de Niels Finsen qui lui ont permis d'obtenir un prix Nobel de médecine en 1903[308]. Cependant, l'application clinique de la PDT pour le traitement des cancers est récente. La PDT a émergé comme une nouvelle alternative à la chimiothérapie et à la radiothérapie pour le traitement des cancers. Cette technique est basée sur l'association d'un photosensibilisateur (PS), de lumière et d'oxygène. Après avoir été administré, le PS s'accumule dans les cellules cancéreuses, puis la zone tumorale est irradiée avec une lumière à la longueur d'onde d'excitation spécifique du PS. Cette irradiation permet l'activation du PS et entraîne une cascade de réactions :

(1) le PS absorbe un photon qui le fait passer d'un état fondamental (S_0) à un état excité (S_n),

(2) le PS va ensuite se retrouver dans un état singulet excité (S_1) de plus basse énergie que S_n. Cet état est très court de l'ordre de 10^{-10} à 10^{-7} seconde,

(3) L'excès d'énergie S_1 est restitué selon deux mécanismes : en émettant un photon par fluorescence ou en passant par un état intermédiaire appelé « état triplet » qui possède une durée de vie plus longue de l'ordre de 10^{-6} à 1 seconde. Le PS va alors revenir vers l'état fondamental S_0 soit par phosphorescence soit en transférant l'excès d'énergie aux molécules du milieu.

Il existe deux types de réactions conduisant à l'effet phototoxique du PS : les réactions d'oxydo-réduction de type I qui permettent la production de radicaux libres toxiques ou les réactions de

type II qui impliquent un transfert d'énergie du PS vers l'oxygène du milieu produisant de l'oxygène singulet (Figure 23).

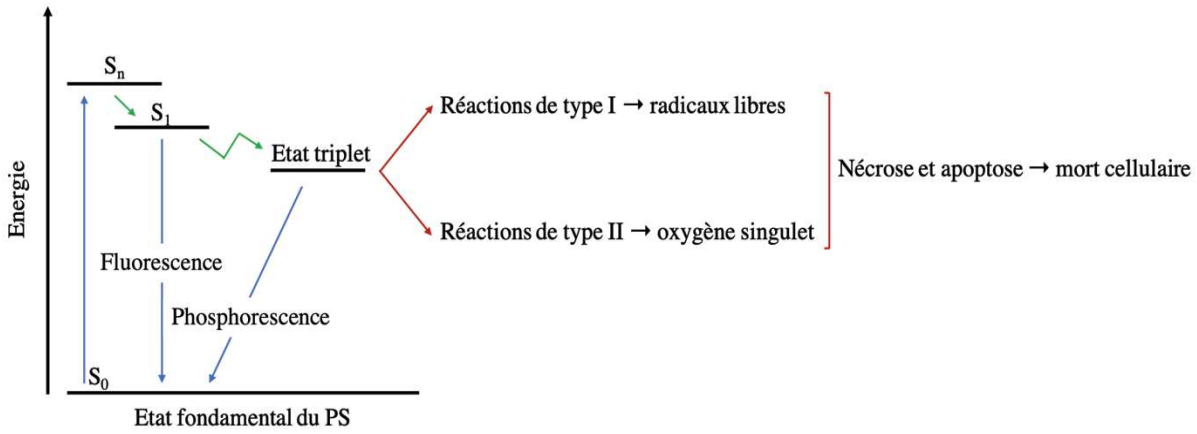

Figure 23 : Diagramme de niveau d'énergie de Jablonski pour la thérapie photodynamique[309]

Généralement, les réactions de type II sont prépondérantes et concernent la plupart des PS utilisés en PDT[309,310]. L'oxygène singulet réagit avec de nombreuses molécules de la cellule, il est donc très toxique car il entraîne la production d'espèces réactives oxygénées, l'oxydation d'acides aminés, de bases nucléiques, des lipides membranaires insaturés ce qui engendre la destruction des organites et des membranes plasmiques induisant une mort cellulaire par nécrose seulement deux heures après le traitement[311]. De plus, l'oxygène singulet peut entraîner dans la mitochondrie le relargage du cytochrome C responsable de l'activation de l'apoptose : ce mécanisme de mort cellulaire est plus lent que la nécrose[312]. La PDT va également affecter la vascularisation tumorale par thrombose privant la tumeur d'oxygène (hypoxie) et de nutriments nécessaires à sa survie. Ces phénomènes vont enclencher une réponse inflammatoire et immunitaire contre les cellules cancéreuses et les métastases éventuelles[313–316].

1.2 Utilisation clinique

La PDT est une thérapie ciblée qui se limite aux tumeurs solides, de petite taille et accessibles à l'irradiation lumineuse (tumeurs cutanées ou accessibles par voie endoscopique). Le PS est un élément clé de la PDT. Il est préférable qu'il absorbe la lumière dans le rouge ou le proche infrarouge avec un fort coefficient d'absorption molaire afin de pouvoir traiter les

tissus en profondeur et générer assez d'oxygène singulet et d'espèces réactives oxygénées pour être toxiques à la cellule cancéreuse[316]. Les lumières bleues sont à éviter car elles causent des dommages à l'ADN et elles sont moins pénétrantes dans les tissus[317]. Cependant, d'une manière générale, les PS sont des molécules très intéressantes car elles ne sont actives qu'après excitation lumineuse à une puissance et une longueur d'onde déterminées. Elles sont donc utilisées en tant qu'agents thérapeutiques dans le cadre de la PDT mais elles peuvent également servir à la détection et donc au diagnostic d'un cancer grâce à leur propriété de fluorescence précédemment décrite dans le diagramme de Jablonski. Ces molécules ont donc des propriétés théranostiques[318]. Malgré leur fort potentiel biomédical, seulement quelques PS sont approuvés par les autorités de santé ou sont en cours d'essais cliniques car ils doivent pouvoir dans l'idéal s'accumuler dans les tumeurs, ne pas engendrer de toxicité sans excitation lumineuse et être rapidement éliminés par les cellules saines[319] (Tableau 10).

Photosensibilisateur	Famille chimique	Longueur d'onde de traitement (nm)	Cancer
Photofrin®	Porphyrine	630	Poumon, œsophage, vessie, cerveau, ovaire, canal biliaire
Levelun®	Précurseur de porphyrine	635	Peau, vessie, cerveau, œsophage
Metvix®	Précurseur de porphyrine	630	Peau
Hexvix®	Précurseur de porphyrine	Lumière blanche	Cellules basales
Visudyne®	Benzoporphyrine	690	Pancréas, sein
Tookad®	Porphyrine	762	Œsophage, prostate
Foscan®	Chlorine	652	Tête et cou, poumon, cerveau, canal biliaire, pancréas, peau, sein
Laserphyrin®	Chlorine	660	Foie, colon, cerveau, poumon, sein, peau
Photochlor®	Chlorine	665	Tête et cou, œsophage, poumon
Purlytin®	Chlorine	660	Peau, sein
Amphinex®	Chlorine	633	Cancers superficiels, colon
Lutex®	Texaphyrine	732	Sein

Tableau 10 : Photosensibilisateurs utilisés en clinique dans le traitement du cancer[320]

1.3 Excitation biphotonique

Les PS cités précédemment ont comme inconvénient majeur d'être excités uniquement avec une irradiation monophotonique. Le challenge est de synthétiser des PS capables d'absorber deux photons. Ces PS sont photo-activables par de très brèves impulsions laser (de l'ordre de la femtoseconde) à moins haute puissance et dans le proche infra-rouge. La PDT biphotonique permet une pénétration plus profonde dans les tissus (jusqu'à 2 cm), une meilleure résolution 3D et une réduction des photo-dommages sur les tissus environnants de la tumeur car l'irradiation a lieu uniquement au point focal contrairement à l'irradiation monophotonique où l'irradiation se fait tout au long de la trajectoire du laser[321,322].

2. Description des travaux

- Introduction :

L'objectif de cette étude était d'étudier le potentiel thérapeutique de PMO en PDT biphotonique pour le traitement ciblé du cancer. Le ciblage actif des cellules cancéreuses permet de cibler préférentiellement les cellules cancéreuses dans le but de réduire significativement les effets indésirables et d'augmenter l'efficacité thérapeutique. Le but étant de cibler un récepteur qui est surexprimé lorsque la cellule devient cancéreuse ce qui permet de discriminer les cellules cancéreuses des cellules saines. Cette étude s'est basée sur les travaux antérieurs de l'équipe qui ont permis de démontrer que le RM6P-CI était une bonne cible thérapeutique pour le cancer de la prostate. En effet, la surexpression du récepteur a été observée dans les tissus de patients atteints du cancer de la prostate alors qu'aucun tissu sain ne surexprimait le récepteur. Dans cette étude, le potentiel thérapeutique de MSN-AMFA a été démontré en PDT monophotonique et biphotonique[139].

Dans le cadre de ma thèse, j'ai étudié le profil d'expression du RM6P-CI dans différents cancers. Pour ce faire, j'ai étudié le niveau d'expression du récepteur dans différentes lignées cellulaires cancéreuses par western blot et j'ai montré que les trois lignées cellulaires de RMS disponibles pour cette étude exprimaient un niveau très élevé de RM6P-CI. Cette expression a été comparée à des lignées cellulaires saines pour confirmer que la surexpression était observée uniquement dans les cellules cancéreuses. La preuve de concept de la PDT utilisant des PMO a été déjà réalisée auparavant sur d'autres types de cancers[323–325] permettant d'envisager

l'utilisation de ces outils pour le traitement du RMS. Des PMO ont donc été synthétisées et fonctionnalisées par les AMFA par l'équipe du Dr Jean-Olivier Durand et plus particulièrement par Mme Sofia Dominguez-Gil et Mr Christophe Nguyen. Pour cette étude, nous avons décidé de fonctionnaliser un mannose 6-carboxylate avec un bras phényl squarate (M6C-PhSq) dont la synthèse a été décrite précédemment[139]. La première étape de fonctionnalisation est le greffage à la surface des PMO de PEG triethoxysilane permettant la furtivité de la nanoparticule et de l'aminoundecyltriethoxysilane pour avoir une fonction amine libre à la surface de la nanoparticule. Cette amine libre sert alors de base pour le greffage du M6C-PhSq (Figure 24). J'ai pu ensuite étudier le potentiel thérapeutique de ces PMO en PDT biphotonique sur les lignées cellulaires de RMS ainsi que sur des lignées de myoblastes sains correspondantes. Cette étude fait l'objet de la rédaction d'un article pour lequel je suis co-premier auteur.

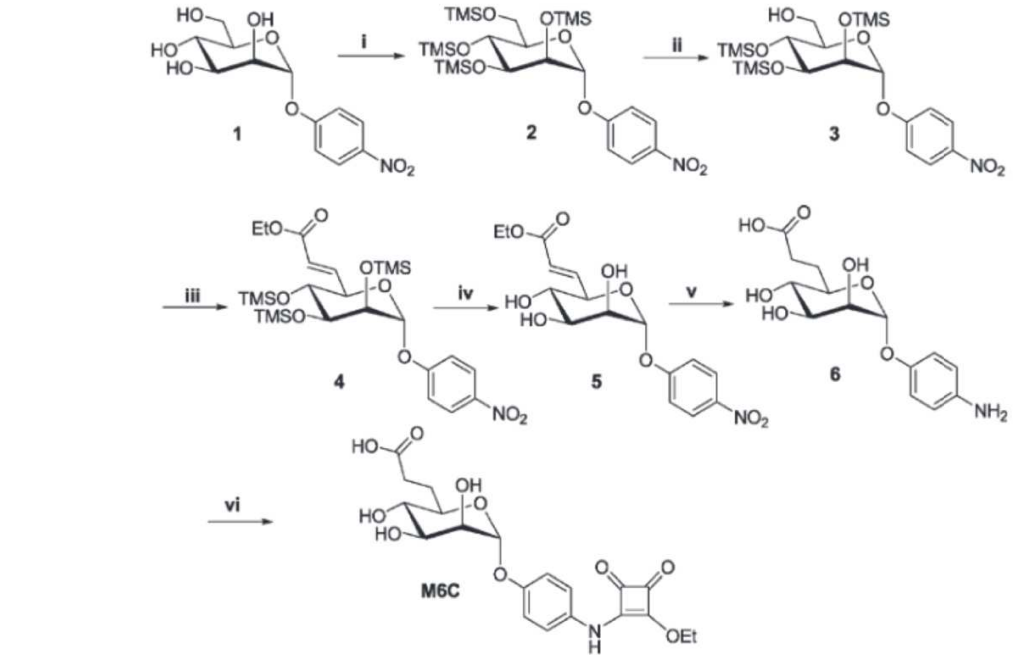

i) TMSCl, CH2Cl2, Et3N, RT, 21 h, 95%; ii) K2CO3, MeOH, 0°C, 15 min, 50%; iii) 1. DMSO, (COCl)2, Et3N, THF, -78°C, 2. triethyl phosphonoacetate, NaH, THF, RT, 90 min, 73%; iv) HCl 0,5N, THF, RT, 10 min, 91%; v) 1.H2, Pd/C, ethanol/H2O (4:1) RT, overnight, 98% 2. NaOH 0,1N, THF, RT, 6 h, 91%; vi) diethyl squarate, EtOH/H2O (2:5:1), RT, 4 h, 56%. DMSO : dimethylsulfoxide, THF : tetrahydrofuran, TMS : trimethylsilyl

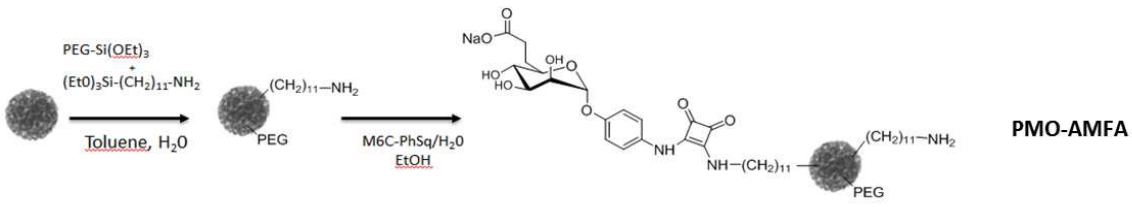

Figure 24 : Schéma de la fonctionnalisation de l'AMFA sur les PMO

Mannose 6-phosphate receptor targeted with porphyrin-based periodic mesoporous organosilica nanoparticles for Rhabdomyosarcoma therapy

Morgane Daurat,†[a] Christophe Nguyen,†[b] Sofia Dominguez Gil,†[c] Clarence Charnay,[c] Laurence Raehm,[c] Khaled El Cheikh,[a] Alain Morère,[b] Marcel Garcia,[a] Frédérique Cunin,[c] Jochen Roessler,[e] Jean-Olivier Durand,[c] Magali Gary-Bobo[b]

a NanoMedSyn Avenue Charles Flahault, 34093, Montpellier cedex 05 France

b Institut des Biomolécules Max Mousseron, UMR 5247 CNRS, UM-Faculté de Pharmacie, Avenue Charles Flahault, 34093, Montpellier cedex 05 France. e-mail: magali.gary-bobo@inserm.fr

c Institut Charles Gerhardt Montpellier, UMR-5253 CNRS-UM-ENSCM cc 1701 Place Eugène Bataillon, 34095, Montpellier cedex 05 France. e-mail: durand@univ-montp2.fr

d Laboratoire PEIRENE, EA 7500, Université de Limoges, Faculté des Sciences et Techniques, 123 avenue Albert Thomas, 87060 Limoges France

e INSELSPITAL, Universitätsspital Bern, Universitätsklinik für Kinderheilkunde, Abteilung für Pädiatrische Hämatologie/Onkologie, 3010 Bern

† these authors contribute equally to this work

Abstract

Recently, we described porphyrin-based periodic mesoporous organosilica (PMO) nanoparticles synthesized from a large functional octatriethoxysilylated porphyrin precursor. The framework of the nanoparticles was formed by J-aggregates of porphyrins allowing two-photon excitation (TPE) and biomedical potential for photodynamic therapy (PDT) and imaging. In this study, we functionalized these PMOPOR with polyethylene glycol (PEG) moieties and analogues of mannose 6-phosphate functionalized at the anomeric position (AMFA). These AMFA are known to target efficiently the mannose 6-phosphate receptor (M6PR) that is overexpressed in various cancer cell lines (breast, prostate). Here we show that M6PR could be an efficient target to address a therapy and discriminate Rhabdomyosarcoma (RMS) cells from healthy myoblasts.

1. Introduction

Rhabdomyosarcomas (RMS) are the most common soft tissue sarcomas of childhood. There are two major subtypes, the embryonal and the alveolar (most aggressive) RMS. Despite intensified multimodality treatments, the overall survival of high-risk population has remained at 5% to 20% over the last decades. This rate stays insufficient and new innovative selective treatments based on nanomedicine are urgently needed. Very few examples of nanoparticles for treatment of RMS have

been described in the literature. Abraxane has been investigated in RMS-xenografted mice,[1] magnetic drug targeting was reported in rat models of RMS,[2] chitosan nanoparticles have been used to silence TGFβ1 (transforming growth factor) in cells with small hairpin RNA[3] or mesoporous silica nanoparticles functionalized with polyethyleneimine have been used in cells to silence ELMO1, a protein involved in cell migration.[4] None of these nanoparticles were functionalized with a biomolecule to target RMS. Targeting an overexpressed receptor in cancer research is very important to differentiate between malignant and normal tissues. Gold nanoparticles have been functionalized with TAT peptide to target RMS cells, and induced cell death[5] but TAT peptide is not specific of RMS. Liposomes loaded with tubulin binding agent epothilone B in order to target RMS were developed. These liposomes have been shown to inhibit endothelial and tumor cell viability to the same extends as the free drug. Furthermore, potent antitumor growth activity could be demonstrated *in vivo* by using vascular endothelial cell targeting. Indeed, the RGD peptide was attached on the surface of the liposomes. These liposomes interact with the integrin receptor and show a beneficial effect in comparison to the untargeted formulation, by increasing cumulative survival of mice bearing RMS. [6] However the RGD peptide is not sufficiently specific for RMS as integrins are also overexpressed in all the vascular endothelial cells of children.

Identification of cation-independent mannose 6-phosphate receptor (M6PR) overexpression on prostate cancer cells [7] led us to study the expression level of M6PR on other types of cancer such as RMS. In the present paper, overexpression of M6PR on RMS cells versus healthy myoblasts was studied and confirmed. We therefore decided to target RMS cells using M6PR pathway and more particularly using analogues of mannose 6-phosphate functionalized at the anomeric moiety (AMFA) grafted on nanoparticles.

We recently synthesized very efficient porphyrin-based periodic mesoporous organosilica nanoparticles (PMOsPOR NPs, 250 nm diameter) showing interconnected cavities (from 10 to 80 nm) for breast cancer treatment using two-photon excited photodynamic therapy (TPE-PDT). [8] For this, a large functional octatriethoxysilylated porphyrin precursor was condensed without any silica source. The framework of the nanoparticles was formed with J-aggregates of porphyrins inside the pore of the walls allowing two-photon excitation (TPE).[9] TPE is of particular interest for biological applications because it allows a deep penetration of the near-infrared beam down to 2 cm in soft tissues and a high spatiotemporal resolution for imaging and cancer detection. Importantly, TPE-PDT has demonstrated a high potential for cancer therapy, in particular, for the treatment of small-sized tumor.[10]

Therefore, we present here the combination of PMO with AMFA to target M6PR overexpressed in rhabdomyosarcoma cells for TPE-PDT of RMS. The strong therapeutic potential and selectivity of PMO grafted with PEG and AMFA are demonstrated.

2. Material and Methods

2.1. Material

Cetyltrimethylammonium bromide (CTAB, 99%), sodium hydroxide (NaOH, 97%), toluene, and ammonium nitrate (NH_4NO_3) were purchased from Sigma-Aldrich. Ethanol (EtOH) was purchased from Carlo Erba. Aminoundecyltriethoxysilane and PEG-triethoxysilane were purchased from SIKEMIA. *p*-[*N*-

(2-Ethoxy-3,4-dioxocyclobut-1-enyl)amino]phenyl 6-deoxy-7-hydroxycarbonyl-α-D-manno-heptopyranoside [M6C-PhSq] was synthesized as described by E. Bouffard *et al*. [11] PMO were synthetized following the protocol previously describe by C. Mauriello Jimenez *et al*.[8]

2.2. Analytical techniques

UV-vis absorption spectra were recorded on a Hewlett-Packard 8453 spectrophotometer using correction factors supplied by the manufacturer. TEM analysis was performed on a JEOL 1200 EXII instrument. Dynamic light scattering analyses were performed using a Cordouan Technologies DL 135 Particle Size Analyzer instrument and analyzed with NanoQ software. IR spectra were recorded on a Perkin-Elmer 100 FT spectrophotometer. Zeta potential measures were performed with a Malvern Zetasizer NanoSeries Instrument.

2.3. Silylation of POR Precursor

A mixture of the octapropargyl porphyrin derivative (100 mg, 9.0×10^{-2} mmol), bromotris(triphenylphosphine)-copper(I) ([CuBr(PPh3)3], 13 mg, 1.5×10^{-2} mmol), and anhydrous THF (3 mL) was placed in a 10 mL sealable microwave reactor, and 3-azidopropyltriethoxysilane (178 mg, 7.1×10^{-1} mmol) was added. Then, the tube was flushed with argon and the microwave irradiation was conducted for 30 min at 100 °C (maximum power 200 W). After evaporation of the solvent, the POR precursor was quantitatively obtained as a purple solid (225 mg, 7.25×10^{-2} mmol).

2.4. Synthesis of Porous Porphyrin-Based Organosilica Nanoparticles (PMO)

A mixture of CTAB (120 mg, 0.39 mmol), distilled water (60 mL), and NaOH (0.2 M aqueous solution, 437 µL) was stirred at 80°C for 2 hours at 750 rpm in a 250 mL three-neck round bottom flask. Then, the octasilylated porphyrin (55 mg, 0.018 mmol, in 1 mL of absolute ethanol) was added, and the mixture was stirred for 30 hours at 80°C. Afterwards, the solution was cooled to room temperature while stirring. The crude mixture was centrifuged (20 000 rpm, 20 min). The supernatant was removed, and the PMO were washed with ethanol and were stored at 4°C.

2.5. Synthesis of PMO-PEG/NH_2 nanoparticles

After centrifugation, PMO (48.8 mg) were resuspended in 6 ml of toluene at 100 °C. Then a mix of 11-aminoundecyltriethoxysilane (29.3 mg - 87.8 µmoles) and PEG-triethoxysilane (36 mg - 87.8 µmoles) was dissolved in 1 mL of toluene and added to the NPs. 20 µL of water were added to the reaction. The reaction was kept under stirring overnight at 100 °C. Then, it was cooled down to room temperature and centrifuged for 30 minutes at 20 000 rpm. The supernatant was removed and the solid was washed with EtOH leading to 40 mg of grafted PMO-PEG/NH_2 in EtOH. DLS measurement in water showed a hydrodynamic diameter of 443 nm. *Zeta* potential in water gave a value of + 36.5 mV.

2.6. Synthesis of PMO-AMFA nanoparticles

10 mg of PMO-PEG/NH_2 were resuspended in ethanol at 50°C. A water solution (2 mL) of 3.6 mg of AMFA, more precisely in this study, it is a mannose 6-carboxylate with a phenyl squarate arm (M6C-PhSq), was added dropwise to the PMO. The reaction was kept under stirring at 50 °C overnight. Then, the resulting mixture was cooled down to room temperature and centrifuged. The supernatant was then removed and the solid washed with a solution of Ammonium Nitrate in ethanol (6 g/L), water,

and ethanol leading to 9.3 mg of grafted PMO-AMFA in EtOH. DLS measurement in water showed a hydrodynamic diameter of 399 nm. *Zeta* potential in water gave a value of -22.9 mV.

2.7. Cell Culture

For cell culture, RMS-YM, RD and RMS human rhabdomyosarcoma cancer cells from INSELSPITAL, University hospital (Bern), SK-1111 normal myoblasts from CookMyoSite, and MH38 normal myoblasts provided by G. Carnac (Inserm U1046-UMR CNRS 9214, Montpellier, France) were used. RMS-YM, RD and RMS were cultured in RPMI-1640 medium supplemented with 10 % FBS and 1% penicillin/streptomycin. SK-1111 and MH38 were cultured in Ham F10 medium plus 20% fetal bovine serum, 1% insulin, 25 $ng.mL^{-1}$ FGF, 10 $ng.mL^{-1}$ EGF and 1% penicillin/streptomycin. All cell types were allowed to grow in humidified atmosphere at 37 °C under 5% CO_2.

2.8. Western Blotting

To study the expression level of M6PR, RMS-YM, RD, RMS, SK-1111 and MH38 were subjected to Western blot analysis. The cells were harvested, washed three times in PBS and lysed by three freeze-thaw cycles in buffer containing 50 mM HEPES, 150 mM NaCl, 1 mM EDTA, 2.5 mM EGTA, 0,1% Tween 20, 10% glycerol, 1 mM NaF, 1 mM $NaNO_3$, 10 mM glycerophosphate and protease inhibitors (dilution 1:25 Complete, Roche Diagnostics). The lysates were precleared by centrifugation at 10,000 × g for 15 min at 4°C. Samples were tested for protein concentration by the Bradford method and equal amounts (25 µg) of cell extract and 1 µg bovine purified M6PR were resolved by 12% SDS-PAGE electrophoresis. After blotting, the gel was transferred onto PVDF membrane and M6PR protein was detected by probing with anti-human M6PR (cation independent) antibody (dilution 1:50000, Abcam). β-actin detected by a monoclonal mouse antibody was used as the loading control. Immunoblotting was performed using secondary antibody coupled with horseradish peroxidase and revealed by ECL detection system (Amersham).

2.9. Cytotoxicity Measurement

For cytotoxicity analysis, RMS-YM and SK-1111 cells were seeded into a 96 well plate, 2000 cells per well in 200 µL of culture medium and allowed to grow for 24 h. Then cells were treated with increasing concentrations of nanoparticles (from 1 to 100 $µg.mL^{-1}$). Three days after treatment, a MTT assay was performed to determine the cell viability. Briefly, cells were incubated for 4 h with 0.5 $mg.mL^{-1}$ of MTT (3-(4,5-dimethylthiazol-2-yl)-2,5-diphenyltetrazolium bromide; Promega) in media. The MTT/media solution was then removed and the precipitated crystals were dissolved in EtOH/DMSO (v/v). The solution absorbance was read at 540 nm in a microplate reader.

2.10. Two-Photon Excitation Photodynamic Therapy

RMS-YM and SK-1111 cells were seeded into a 384 multi-well glass-bottomed plate (thickness 0.17 mm) with a black polystyrene frame at a concentration of 1000 cells per well in 50 µL of culture medium, and allowed to grow for 24 h. Then, cells were treated with nanoparticles (40 $µg.mL^{-1}$) for 16 h. For mannose 6-phosphate (M6P) reversion assay, the cells were incubated or not with 10 mM of M6P for 10 min prior to the incubation with PMO-AMFA (40 $µg.mL^{-1}$) and again 10 mM of M6P, for 4 h. The cells were submitted or not to laser irradiation with the LSM 780 live confocal microscope (Carl Zeiss Microscope) at 800 nm by three scans of 1.57 s duration in 4 different areas of the well with a focused laser at a maximum laser power (lase power input 3W). The laser beam was focused by a

microscope objective lens (Carl Zeiss 10×/0.3 EC Plan-Neofluar). After 2 days, the MTT assay was performed as previously described and was corrected according to the following formula: Abs control – 2 × (Abs control – Abs nanoparticles).

2.11. Two-photon fluorescence imaging

RMS-YM cells were grown on tissue culture dish with cover glass bottom (FluoroDish from WPI) in complete culture medium. The next day, the cells were treated or not with 10 mM of M6P for 10 min, then the cells were incubated with PMO-AMFA (40 $\mu g.mL^{-1}$) and again 10 mM of M6P, for 4 h. Fifteen minutes before the end of incubation, cells were loaded with Hoechst 33342 (5 $\mu g.mL^{-1}$, Invitrogen) for nuclear staining. Before visualization, cells were washed three times with cell media. Cells were examined under LSM 780 live confocal microscope (Carl Zeiss Microscope) and scanned at 760 nm for nuclei and 800 nm for PMO-AMFA. All images were performed with a high magnification (63×/1.4 OIL DIC Plan-Apo).

2.12. Statistical analysis

Statistical analysis was performed using the Student's t test to compare paired groups of data. A p-value of <0.05 was considered to be statistically significant.

3. Results and Discussion

3.1. Overexpression of M6PR on RMS

The first step of this work was the study of M6PR expression on RMS cells and healthy myoblasts. For this, we have analysed the protein expression level of M6PR in 3 different RMS cells lines and healthy myoblasts by Western blot (Figure 1).

As showed in Figure 1A, the protein expression level of M6PR is clearly higher in the 3 cell lines of RMS than in the 3 cell lines of healthy myoblasts. The quantification of M6PR level by Image J software corrected by the expression level of an invariant (β-actin) indicated that in mean, there was a 7 fold-increase in M6PR expression in RMS cells than in healthy cells. This suggested that the increase in M6PR expression could be considered as a biomarker of RMS development.

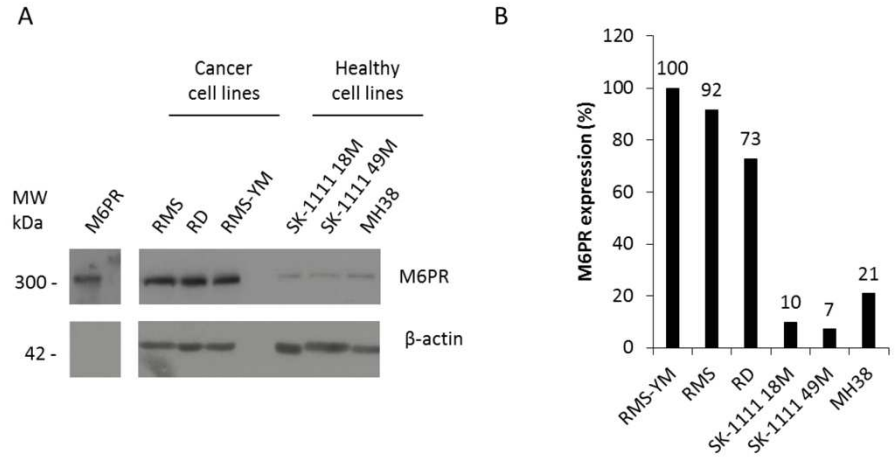

Figure 1. M6PR expression in different cell lines. (A) The cell extracts (25 µg) were analyzed by Western blots using human M6PR or β-actin antibodies. β-actin is a control for total protein loading. **(B)** Quantification with Image J software of 300 kDa M6PR protein corrected by β-actin expression. RMS-YM cells are considered as 100%.

3.2. Synthesis of PMO grafted with PEG ad AMFA

We then investigated the functionalization of PMO with AMFA (Figure 2). To do this, aminoundecyltriethoxysilane and PEG triethoxysilane were first grafted[12] on the surface of PMO. Then AMFA was grafted on the surface of functionalized PMO to target RMS cells. Here, the AMFA used was the M6C-PhSq, and the reaction of its squarate moeity with the amino groups led to a covalent attachment of AMFA on the surface of PMO.

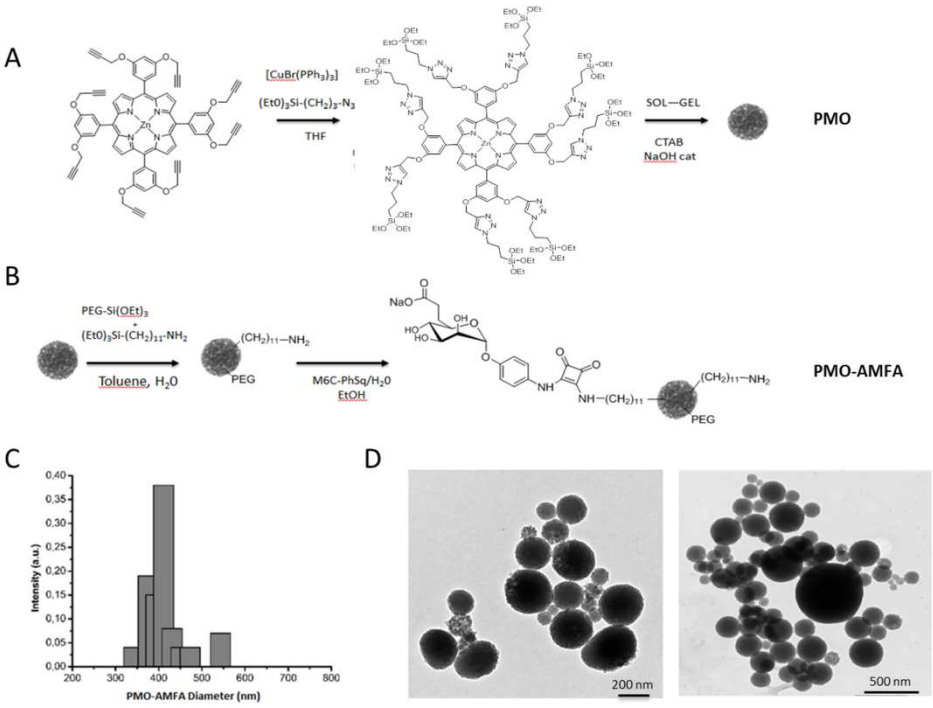

Figure 2. Synthesis and characterization of PMO-AMFA. (**A**) Synthesis of PMO. (**B**) Schematic representation of coupling of the mannose 6-carboxylate with a phenyl squarate arm (M6C-PhSq) also called AMFA in order to obtained PMO-AMFA. (**C**) DLS in intensity of PMO-AMFA. (**D**) Microscopy images of PMO-AMFA by TEM at different magnifications.

3.3 Biocompatibility of PMO on different cell lines

Then, a cytotoxic study was realized by a 3 days incubation time with increasing concentrations of PMO grafted with PEG and AMFA. This study was performed on one RMS and one healthy cell lines: RMS-YM and SK-1111, respectively. These data demonstrated that for both cell lines, the batch of PMO, which are grafted with PEG and AMFA, did not show any cytotoxicity (Figure 3). In contrast, pristine PMO (here called PMO) and PMO-PEG/NH_2 generated slight cell death. In fact, in RMS-YM cells, the incubation with PMO at 100 µg.mL^{-1} induced 30% cell death (Figure 3A). In SK-1111, PMO and PMO-PEG/NH_2 at 100 µg.mL^{-1} induced approximately the same percentage of cell death (Figure 3B).

However, until 40 µg.mL^{-1} no significant cell death was observed in any cell lines. So for further biological experiments we decided to work at this concentration.

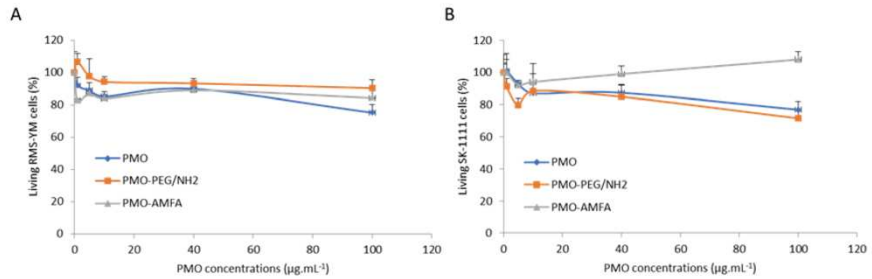

Figure 3. Cytotoxicity of PMO on cancer and healthy cells. (**A**) RMS-YM cancer cells and (**B**) SK-1111 healthy cells were treated with increasing concentrations of nanoparticles. After three days of incubation, a MTT assay was performed. Data are presented as (mean ± SEM), n=2.

3.4. Study of TPE-PDT and fluorescence imaging potential

Then the biological activity and more particularly the ability of PMO-AMFA to target and treat RMS cells under near infrared two-photon excitation was studied (Figure 4). For this, we incubated RMS-YM cancer cells and SK-1111 healthy cells with 40 µg.mL^{-1} of PMO, PMO-PEG/NH_2 or PMO-AMFA for 16 h. Then, the cells were irradiated or not at 800 nm for a short time (3 x 1.57 s) at maximal laser power (Figure 4A, 4B and 4D). First, after TPE, PMO and PMO-PEG/NH_2 induced 62% and 57% cell death respectively on RMS-YM cancer cells and 50% and 51% on SK-1111 healthy cells. Interestingly, PMO-AMFA was efficient on cancer cells by inducing after TPE 94% cell death, but not on healthy cells (no significant cell death). This result demonstrated the importance of the targeting to be specific for rhabdomyosarcoma cancer cells.

The involvement of M6PR in the active endocytosis of PMO-AMFA was shown by the competitive inhibition of PMO-AMFA endocytosis using an excess of M6P, which is the natural ligand of M6PR. RMS-YM cancer cells were incubated for 4 h with PMO-AMFA in the presence or absence of an excess of M6P. First, after 4 h of incubation, TPE-PDT with PMO-AMFA induced 58% cancer cell death. Importantly, the addition of M6P inhibited totally cancer cell death suggesting that M6P prevented the internalization of PMO-AMFA *via* the M6PR pathway (Figure 4C). This result was confirmed by two-photon fluorescence imaging (Figure 4D).

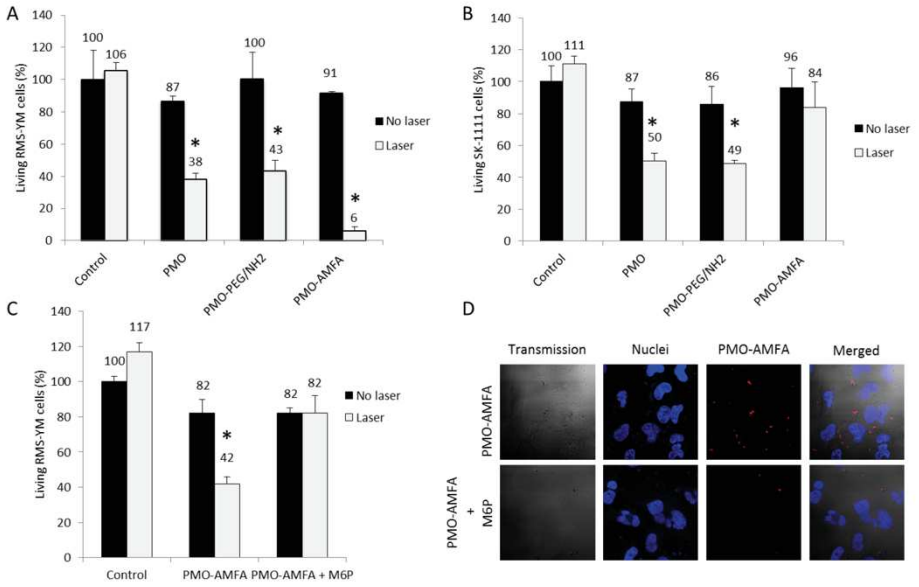

Figure 4. TPE-PDT and fluorescence imaging *in vitro* with PMO. Cancer cells (RMS-YM) (**A**) and normal cells (SK-1111) (**B**) were irradiated at 800 nm (3 x 1.57s) after 16 h of treatment with nanoparticles (40 µg.mL^{-1}). (**C**) and (**D**) Cancer cells (RMS-YN) were treated during 4 h with PMO-AMFA (40 µg.mL^{-1}) with an excess or not of M6P. Data are mean values ± standard deviations from three independent experiments. *Statistically significant versus non irradiated nanoparticles ($p < 0.05$ from Student's t test).

Conclusion

In this study, we have demonstrated that M6PR could be considered as a new target for rhabdomyosarcoma therapy. In fact, we have observed an overexpression of this receptor in different RMS cancer cells allowing the discrimination between cancer cells and healthy cells which present a normal expression level of M6PR. The targeting of M6PR was performed using AMFA and more precisely by the grafting of mannose 6-carboxylate bearing a phenyl squarate arm on the PEG/NH_2 moities of PMO.

Altogether, the results presented here showed that PMO-AMFA were highly efficient for targeting and therapy of RMS-YM cells by a mechanism involving M6PR dependent endocytosis. Moreover, PMO-AMFA did not show any effect on healthy cells demonstrating the specificity of the targeting toward cancer cells. Targeted TPE-PDT could be considered as a new therapeutic strategy for rhabdomyosarcoma.

References

1. L. Zhang, P. Marrano, S. Kumar, M. Leadley, E. Elias, P. Thorner and S. Baruchel, *Clin. Cancer Res.*, 2013, **19**, 5972-5983.
2. M. G. Krukemeyer, V. Krenn, M. Jakobs and W. Wagner, *J. Drug Target.*, 2012, **20**, 185-193.
3. S.-L. Wang, H.-H. Yao, L.-L. Guo, L. Dong, S.-G. Li, Y.-P. Gu and Z.-H. Qin, *Cancer Genet. Cytogenet.*, 2009, **190**, 8-14.
4. X. Huang, H. Townley and H. Townley, *Nanobiomedicine (Rij)*, 2016, **3**, 4.
5. A. A. Taha, S. M. H. Al-Jawad and L. F. A. Al-Barram, *J. Cluster Sci.*, 2019, **30**, 403-414.
6. V. Rengaswamy, D. Zimmer, R. Suss and J. Rossler, *J. Control. Release*, 2016, **235**, 319-327.
7. O. Vaillant, K. El Cheikh, D. Warther, D. Brevet, M. Maynadier, E. Bouffard, F. Salgues, A. Jeanjean, P. Puche, C. Mazerolles, P. Maillard, O. Mongin, M. Blanchard-Desce, L. Raehm, X. Rebillard, J.-O. Durand, M. Gary-Bobo, A. Morere and M. Garcia, *Angew. Chem., Int. Ed.*, 2015, **54**, 5952-5956.
8. C. Mauriello Jimenez, D. Aggad, J. G. Croissant, K. Tresfield, D. Laurencin, D. Berthomieu, N. Cubedo, M. Rossel, S. Alsaiari, D. H. Anjum, R. Sougrat, M. A. Roldan-Gutierrez, S. Richeter, E. Oliviero, L. Raehm, C. Charnay, X. Cattoen, S. Clement, M. Wong Chi Man, M. Maynadier, V. Chaleix, V. Sol, M. Garcia, M. Gary-Bobo, N. M. Khashab, N. Bettache and J. O. Durand, *Adv. Funct. Mater.*, 2018, **28**, 1800235.
9. S. Biswas, H.-Y. Ahn, M. V. Bondar and K. D. Belfield, *Langmuir*, 2012, **28**, 1515-1522.
10. J. R. Starkey, A. K. Rebane, M. A. Drobizhev, F. Q. Meng, A. J. Gong, A. Elliott, K. McInnerney and C. W. Spangler, *Clin. Cancer Res.*, 2008, **14**, 6564-6573.
11. E. Bouffard, C. Mauriello Jimenez, K. El Cheikh, M. Maynadier, I. Basile, L. Raehm, C. Nguyen, M. Gary-Bobo, M. Garcia, J.-O. Durand and A. Morère, *Int. J. Mol. Sci.*, 2019, **20**, 2809.
12. D. Warther, C. M. Jimenez, L. Raehm, C. Gerardin, J.-O. Durand, A. Morere, K. El Cheikh, A. Gallud, M. Gary-Bobo, M. Maynadier and M. Garcia, *RSC Adv.*, 2014, **4**, 37171-37179.

- Conclusion :

Dans cette étude, le RM6P-CI a été identifié dans les lignées cellulaires en tant que cible potentielle pour le traitement du RMS. Mes travaux ont permis de mettre en évidence la surexpression du récepteur dans les cellules de RMS : en effet, la quantification du niveau du RM6P-CI par Western blot indique un niveau d'expression sept fois plus élevé que dans les cellules saines correspondantes. Ceci suggère donc que la surexpression du RM6P-CI pourrait être un biomarqueur du développement du RMS et également une cible thérapeutique permettant de démontrer le potentiel des PMO-AMFA pour le traitement de cette maladie par la PDT biphotonique. Dans un premier temps, j'ai montré la biocompatibilité des PMO fonctionnalisées ou non sur les cellules cancéreuses ainsi que sur les cellules saines. Dans un deuxième temps, j'ai étudié le potentiel des PMO-AMFA pour cibler et traiter les cellules cancéreuses sous irradiation biphotonique. Les PMO non fonctionnalisées entraînent environ 50% de mort cellulaire sur les cellules cancéreuses mais également sur les cellules saines. Cependant, les PMO-AMFA sont efficaces sur les cellules cancéreuses en induisant 94% de mort cellulaire mais n'ont pas d'effet significatif sur les cellules saines. Ce résultat démontre le ciblage spécifique des cellules cancéreuses de RMS par les PMO-AMFA. Pour aller plus loin, l'implication du RM6P-CI dans l'endocytose active des PMO-AMFA a été démontrée par inhibition compétitive de l'endocytose des nanoparticules en utilisant un excès de M6P. L'addition de M6P inhibe totalement la mort cellulaire suggérant que le M6P a bloqué l'endocytose active des PMO-AMFA *via* le RM6P-CI. Ce résultat a été confirmé par imagerie. Nous avons donc démontré que le RM6P-CI pouvait être considéré comme une nouvelle cible pour le traitement du RMS car nous avons observé une surexpression du récepteur dans différentes lignées cellulaires de RMS permettant de discriminer les cellules cancéreuses des cellules saines. De plus, le M6C-PhSq est un bon ligand pour le ciblage du RM6P-CI car les PMO-AMFA sont très efficaces sur les cellules cancéreuses et n'ont pas d'effet sur les cellules saines démontrant la spécificité du ciblage des cellules cancéreuses. La PDT biphotonique pourrait donc être considérée comme une nouvelle stratégie thérapeutique pour le RMS.

Chapitre 2 : Ciblage thérapeutique de la maladie de Pompe

1. Les travaux antérieurs de NanoMedSyn

Dans la maladie de Pompe, l'enzymothérapie substitutive actuelle (Myozyme®) basée sur l'utilisation d'une GAA humaine recombinante qui porte naturellement un signal M6P est efficace sur les cardiomyopathies dans la forme infantile mais elle a une efficacité limitée sur les muscles squelettiques dans les formes tardives[246,326–328]. Comme nous l'avons vu précédemment l'efficacité relative de Myozyme® est attribuée notamment à sa faible affinité pour le RM6P-CI. En effet, la GAA est naturellement délivrée aux lysosomes *via* le RM6P-CI après la liaison de deux M6P présents sur une même enzyme. Cependant, les lots de Myozyme® contiennent en moyenne un faible nombre de M6P (entre 0,9 et 1,2 moles de M6P par mole d'enzyme) et donc une faible quantité de chaînes glycosylées portant deux résidus M6P. Or, les oligosaccharides avec un seul résidu M6P ont une affinité pour le récepteur 1000 fois inférieure expliquant pourquoi Myozyme® ne cible pas efficacement le récepteur[327,329,330]. NanoMedSyn a donc proposé une alternative dont le but est de greffer des AMFA sur l'enzyme recombinante afin d'augmenter l'efficacité du ciblage et par conséquent augmenter l'efficacité thérapeutique de Myozyme®. Les étapes nécessaires de production de l'enzyme recombinante fonctionnalisée sont les suivantes :

(1) Synthèse des AMFA

Les AMFA ont été décrits précédemment. Dans le cas de l'enzymothérapie substitutive, NanoMedSyn a décidé d'utiliser un AMFA dont le phosphate a été remplacé par un phosphonate car c'est l'analogue qui a la meilleure affinité pour le RM6P-CI (Figure 25A).

(2) Production de l'enzyme humaine recombinante

La production de l'enzyme a été effectuée par l'équipe du Dr Martine Cérutti (UPS3044, Saint Christol lès Alès). L'enzyme a été produite en utilisant le système Baculovirus/cellules Sf9 d'insecte. Ce système est déjà utilisé couramment pour la production de protéines thérapeutiques utilisées en clinique telles que Cervarix® (vaccin contre le cancer du col de l'utérus) ou Provenge® (vaccin contre le cancer de la prostate)[331]. Ce système d'expression génère des enzymes avec les chaînes d'oligosaccharides localisées sur la même position que les enzymes produites en système CHO comme la Myozyme®. Par contre, on note l'absence de résidus M6P et de chaînes d'oligosaccharides complexes qui sont remplacées par des chaînes

de mannose dans les cellules d'insecte[332]. Lorsque la production est terminée, l'enzyme est purifiée sur colonnes chromatographiques, concentrée et filtrée. L'enzyme recombinante ainsi obtenue est pure à plus de 95% avec un rendement de production de 30%.

(3) Greffage de l'AMFA sur l'enzyme humaine recombinante (Figure 25B)

Tout d'abord, les chaînes d'oligomannoses de l'enzyme sont oxydées par une solution de méta-periodate de sodium ($NaIO_4$) afin d'obtenir des fonctions aldéhydes. Ces fonctions vont alors pouvoir réagir avec les résidus O-alkylamine de l'AMFA de manière covalente formant ainsi des fonctions oxymes qui sont très stables[333]. La concentration d'AMFA greffée est de 4 ± 1 mole par mole d'enzyme ce qui est donc plus élevée que celle de M6P détectée sur Myozyme®.

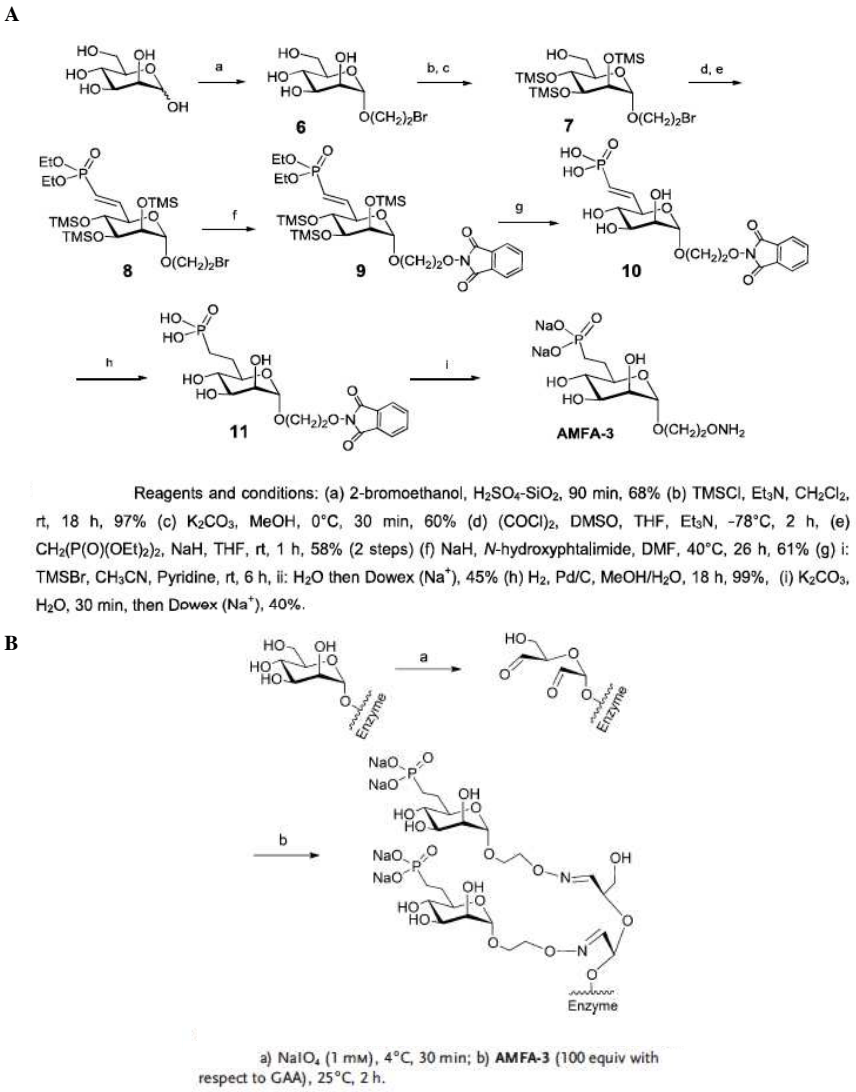

Figure 25 : Synthèse (A) et fonctionnalisation (B) de l'AMFA sur l'enzyme recombinante[334]

Le premier article publié par NanoMedSyn sur cette rhGAA-AMFA a permis de démontrer qu'elle était plus efficace que Myozyme® sur plusieurs critères : une meilleure internalisation dans les cultures primaires de fibroblastes de patients adultes de la maladie de Pompe, une meilleure réduction du taux de glycogène dans les quadriceps des souris modèles de la maladie de Pompe (âgées de 4,5 mois ou plus âgées (6,5 mois) qui sont mieux représentatives des formes tardives de la maladie) et une amélioration de la structure des fibres musculaires. Ces résultats se traduisent par une amélioration de la marche évaluée par le test du rotarod[334]. Suite à ces résultats très prometteurs, NanoMedSyn a décidé d'évaluer sa stratégie de ciblage sur Myozyme® et a publié un article sur cette étude qui a permis de démontrer pour la première fois l'efficacité thérapeutique de l'enzymothérapie substitutive chez des souris très âgées (10-12 mois) modèles de la forme adulte de la maladie de Pompe. Myozyme®-AMFA (aussi appelée rhGAA-AMFA) diminue le taux de glycogène et améliore la structure des fibres musculaires. En effet, comme il a été décrit précédemment, les noyaux des cellules musculaires sont en périphérie de la cellule alors que dans les muscles chez les patients atteints de la maladie de Pompe les noyaux migrent vers le centre des cellules. Les coupes histologiques de quadriceps des souris Pompe ont montré que rhGAA est inefficace alors que rhGAA-AMFA a diminué de 50% le nombre de noyaux centraux démontrant la régénération musculaire chez les souris âgées. De plus, aucun anticorps anti-AMFA n'a été détecté dans le sérum des souris[335]. Ces deux articles démontrent que les AMFA permettent d'améliorer significativement l'efficacité thérapeutique de l'enzyme chez les souris modèles de la maladie de Pompe.

Pourquoi l'AMFA permet-il cette amélioration ? Les premières réponses sont que le taux d'AMFA greffé sur l'enzyme est bien meilleur que le taux de résidus M6P sur rhGAA, par conséquent les AMFA ont une meilleure affinité pour le récepteur que rhGAA : ceci a été vérifié par des tests d'affinité qui ont démontré que l'affinité pour le récepteur était six fois plus élevée pour rhGAA-AMFA comparée à celle de rhGAA[335]. De plus, nous savons que le phosphonate est insensible aux phosphatases : est-ce que l'efficacité thérapeutique est améliorée grâce à cette insensibilité ? Est-ce que le fait que rhGAA-AMFA soit mieux internalisée explique à lui seul le gain d'efficacité thérapeutique ? Ces questions ont fait l'objet d'une étude que j'ai réalisée en collaboration avec Mme Anastasia Godefroy, doctorante, ainsi que toute l'équipe de NanoMedSyn.

2. Description des travaux

- Introduction :

L'augmentation de l'affinité de rhGAA-AMFA pour le RM6P-CI n'est probablement pas la seule raison de l'amélioration de l'efficacité thérapeutique car les études antérieures de Genzyme ou Biomarin, citées précédemment, dont le but était d'améliorer le ciblage de la GAA n'ont donné aucun résultat significatif pour l'amélioration de l'efficacité thérapeutique alors qu'un gain d'affinité pour le récepteur a été montré. Il semblerait donc que l'augmentation de l'effet thérapeutique de l'enzyme soit basée sur un mécanisme intracellulaire. Afin de mieux définir le mécanisme d'action de rhGAA-AMFA, nous avons étudié sa maturation endo-lysosomale. Le processus de maturation de rhGAA est complexe et nécessite plusieurs étapes : la maturation du précurseur (110 kDa) subit des protéolyses successives conduisant à une forme endosomale intermédiaire de 95 kDa, une forme active de 76 kDa et une forme lysosomale mature de 60-70 kDa (Figure 26) : les formes actives et matures montrent une activité 7 à 10 fois supérieure pour le glycogène par rapport au précurseur[220,336]. De plus, l'étude de Bali et al., a clairement établi que l'activité globale de l'enzyme dans les tissus des patients était corrélée à la présence de la forme mature à 60-70 kDa[220].

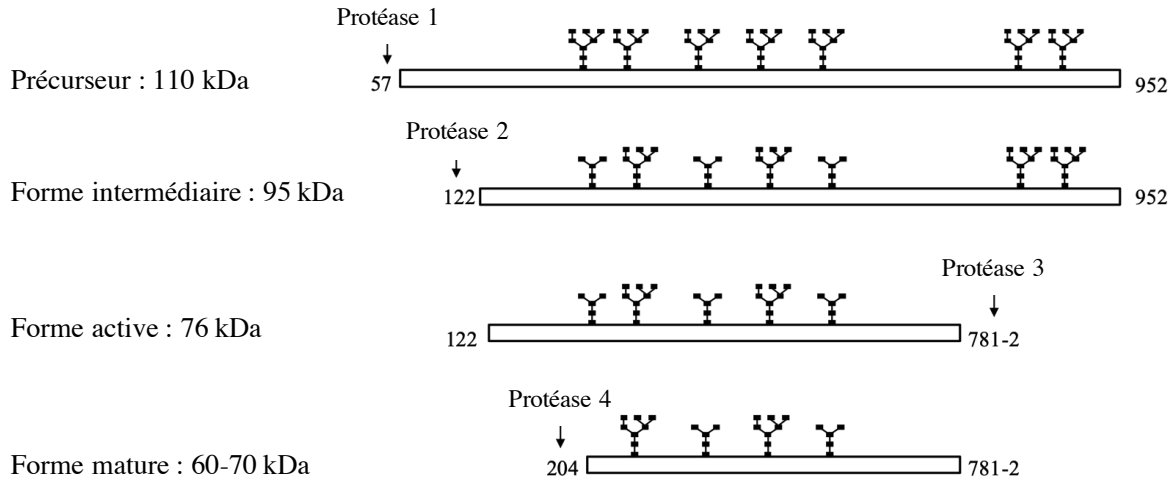

Figure 26 : Maturation intracellulaire de la GAA[336]

Nous avons donc étudié la maturation de rhGAA-AMFA en comparaison avec rhGAA. Pour cela j'ai réalisé, en collaboration avec Mme Anastasia Godefroy, le couplage de rhGAA-

AMFA et étudié la maturation des enzymes dans des cultures primaires de myoblastes de patients adultes atteints de la maladie de Pompe par Western blot. Les résultats obtenus ont fait l'objet d'une publication pour laquelle je suis co-premier auteur.

Received: 29 March 2019 | Revised: 5 June 2019 | Accepted: 11 June 2019

DOI: 10.1111/jcmm.14516

SHORT COMMUNICATION

WILEY

Mannose 6-phosphonate labelling: A key for processing the therapeutic enzyme in Pompe disease

Anastasia Godefroy[1,2] | Morgane Daurat[1,2] | Afitz Da Silva[1,2] | Ilaria Basile[2] | Khaled El Cheikh[2] | Catherine Caillaud[3] | Sabrina Sacconi[4] | Benedikt Schoser[5] | Henry-Vincent Charbonné[2] | Magali Gary-Bobo[1] | Alain Morère[1] | Marcel Garcia[1,2] | Marie Maynadier[2]

[1]IBMM, CNRS, ENSCM, University of Montpellier, Montpellier, France

[2]NanoMedSyn, Montpellier, France

[3]Biochimie Métabolique et Protéique, AH-HP, Hôpital Necker Enfants-Malades and Inserm U1151, Institut Necker Enfants Malades, Université Paris-Descartes, Paris, France

[4]Service Système Nerveux Périphérique, Muscle et SLA, Centre Hospitalier Universitaire de Nice, Centre National de la Recherche Scientifique, Institut National de la Santé et de la Recherche Médicale, Institute for Research on Cancer and Aging of Nice, Université Côte d'Azur, Nice, France

[5]Department of Neurology, Friedrich-Baur-Institute, Ludwig-Maximilians University Munich, Munich, Germany

Correspondence
Alain Morère, IBMM, CNRS, ENSCM, University of Montpellier, 15 avenue Charles Flahault, Montpellier 34093, France.
Email: alain.morere@umontpellier.fr

Marcel Garcia and Marie Maynadier, NanoMedSyn, 15 avenue Charles Flahault, Montpellier 34093, France.
Email: m.garcia@nanomedsyn.com (MG); m.maynadier@nanomedsyn.com (MM)

Funding information
APPI, Grant/Award Number: N°DOS0026362/00; French National Research Agency, Grant/Award Number: ANR-13-RPIB-0012; Association Nationale Recherche Technologie, Grant/Award Number: N°16/0628 and N°16/0629; NanoMedsyn; Vaincre les Maladies Lysosomales Suisse; Occitanie-Midi Pyrénées Region, Grant/Award Number: PILE 180060 and PILE 180064

Abstract

In the search of a better enzyme therapy in Pompe disease, the conjugation of mannose 6-phosphonates to the recombinant enzyme appeared as an enhancer of its efficacy. Here, we demonstrated that the increased efficacy of the conjugated enzyme is partly due to a higher intracellular maturation because of its insensitiveness to acid phosphatases during the routing to lysosomes.

KEYWORDS

acid phosphatases, acid α-glucosidase, enzyme replacement therapy, intracellular processing, lysosomal storage disease, mannose 6-phosphate receptor

Anastasia Godefroy, Morgane Daurat and Afitz Da Silva contributed equally to this work.

1 | INTRODUCTION

In Pompe disease, the current enzyme replacement therapy based on a human recombinant acid α-glucosidase (rhGAA) naturally bearing mannose 6-phosphate (M6P) has a limited efficacy.[1-4] We recently proposed a conjugation of rhGAA with a phosphonate analogue of mannose 6-phosphate (called AMFA) which enables never-before seen improvements on walking ability and on musculoskeletal health in the aged Pompe mouse model.[5,6] Here, we hypothesized that this new therapeutic efficacy is not solely due to a better internalization via M6P receptor pathway and we investigated the enzyme processing. The intracellular maturation of rhGAA (110 kD) is complex and consists in successive proteolyses up to an endosomal 95 kD intermediate form, a 76 kD active form and a 60-70 kD lysosomal mature form (Scheme S1).[7,8] The 76 and 60-70 kD GAA species show a 7-10-fold increased activity.[7] Bali et al[8] clearly established on patient biopsies that the overall activity was correlated with the presence of the 60-70 kD form.

Secondly, since an overexpression of acid phosphatases has been observed in several lysosomal storage disorders (LSD)[9,10] we also analysed the involvement of lysosomal acid phosphatases ACP2 and ACP5 in rhGAA maturation.

2 | MATERIALS AND METHODS

See Supporting Information for detailed description.

3 | RESULTS

3.1 | AMFA grafting on rhGAA enables in vitro and in vivo complete enzyme processing

A high uptake of 110 kD GAA precursor was observed in cultured myoblasts from adult Pompe patients for both rhGAA and rhGAA-AMFA treatments (Figure 1A); however, 76 kD form (Figure S1A) and 60-70 kD form (Figure S1B) are 3- and 5-fold more important for rhGAA-AMFA treated cells. As expected intracellular GAA activity was also significantly increased for rhGAA-AMFA as compared to rhGAA (Figure S1C). Similar results were found on different myoblasts (Figure S1D-G). GAA genetic mutations of the corresponding primary cultured cells are listed in Table S1.

We then differentiated myoblasts into myotubes according to the technique described by Nascimbeni et al 2012.[11] In myotubes, the 76 kD and 60-70 kD forms were significantly increased by rhGAA-AMFA treatment (4.1- and 2.2-fold) as compared to rhGAA (Figure 1B-C).

We also analysed the enzyme maturation in 10-month-old Pompe mice treated weekly with 5 mg/kg rhGAA, rhGAA-AMFA or vehicle during 3 months. While no specific band was detected in the control Pompe tissue, the 95 kD intermediary form was detected after rhGAA treatment (Figure 1D). In mice injected with rhGAA-AMFA, the 95 kD form, the 76 kD active form and/or the 60-70 kD mature form were observed. This higher maturation was also associated with a gain in GAA activity in muscle biopsies (data not shown). Together, these results indicate that AMFA conjugation increases rhGAA maturation both in patient cultured cells and in aged Pompe mice.

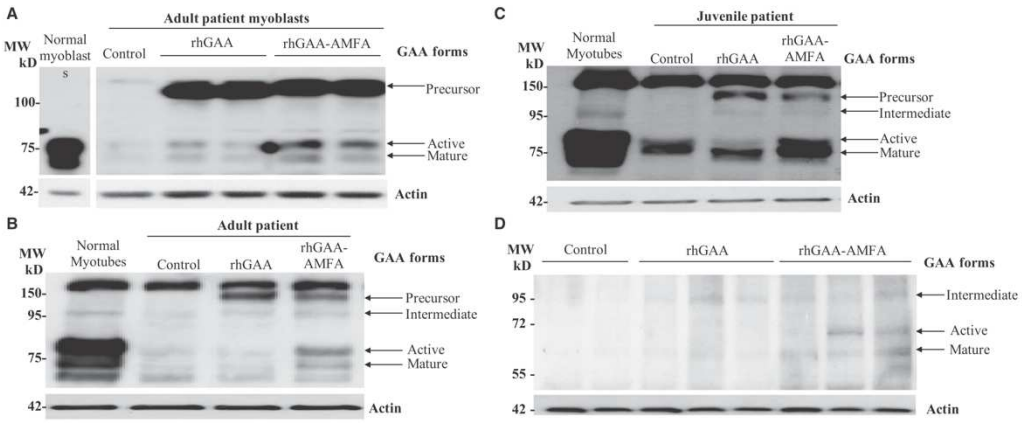

FIGURE 1 Uptake and maturation of rhGAA and rhGAA-AMFA in myoblasts and myotubes of Pompe patients (P12, P14) and in quadriceps of treated Pompe mice. A, P12 myoblasts. B, C, myotubes differentiated from myoblasts of adult (P12) and juvenile (P14) patients were incubated with 50 nmol/L rhGAA, rhGAA-AMFA or with vehicle (Control) for 8 h (myoblasts) or 48 h (myotubes) in culture medium. The cell extracts (5 µg) were analysed by Western blot using human GAA or actin antibodies. D, Maturation of rhGAA and rhGAA-AMFA in quadriceps of aged Pompe mice. The tests were performed on 10-month-old mice treated with 5 mg/kg/week of rhGAA or rhGAA-AMFA or by vehicle (Control), during 13 weeks. The maturation of the enzymes in quadriceps on aged Pompe mice is studied by Western blot on 20 µg tissue extract using human GAA or actin antibodies. Black arrows indicate respectively 110 kD (inactive precursor), 95 kD (inactive intermediary), 76 kD (active intermediary) and 60-70 kD GAA (mature active) forms and actin is a control for total protein loading

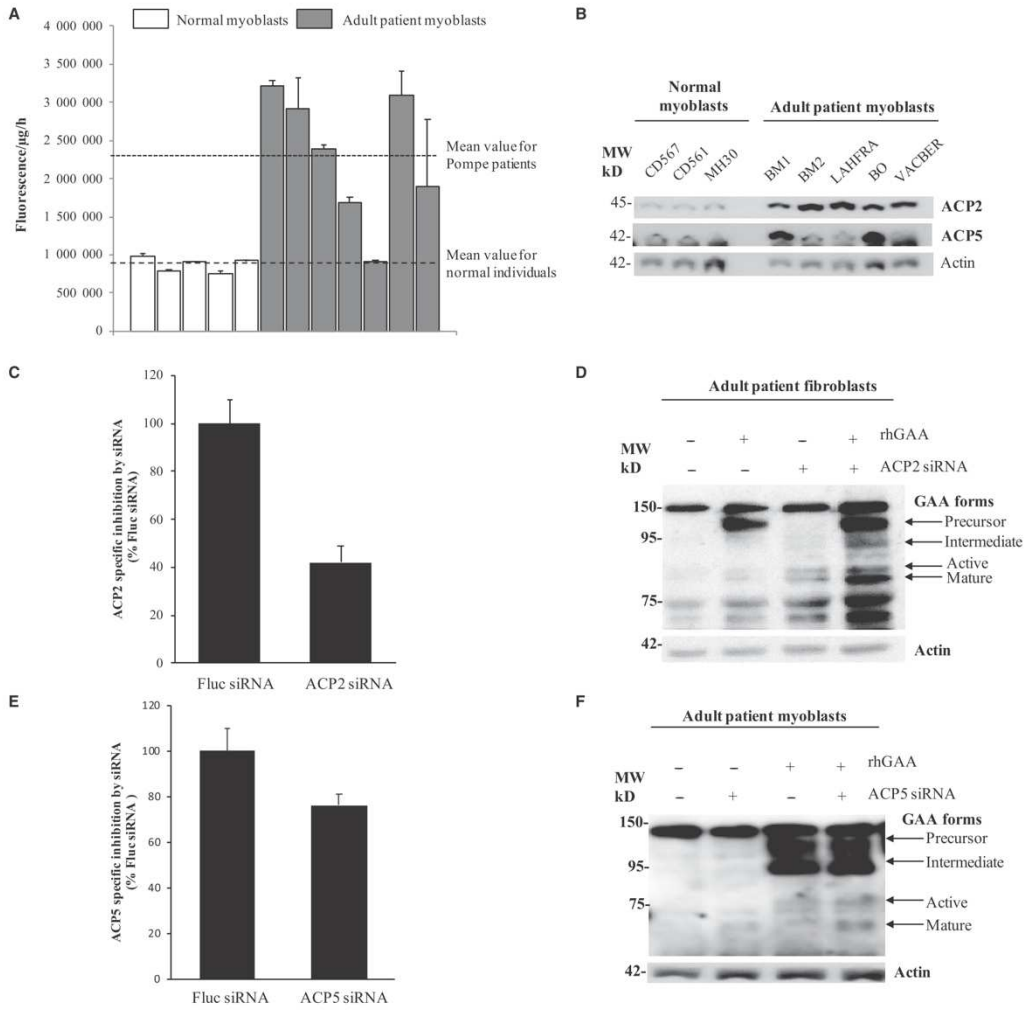

FIGURE 2 Overexpression of acid phosphatases and activation of rhGAA maturation by silencing phosphatases in cells from Pompe patients. A, The phosphatase activity was respectively measured in P1, P2, P4, P5, P6 myoblasts from healthy individuals and P7, P8, P9, P10, P11, P12, P13 myoblasts from adult Pompe patients. The quantification was assayed on cell extracts (10 µL) using a fluorescent substrate 6,8-difluoro-4-methylumbelliferyl phosphate (DiFMUP) (n = 2). B, Cell extracts (5 µg) of myoblasts from different origins were analysed by Western blots using anti-human ACP2, ACP5 or actin antibodies (used as loading control). C, D, With specific siRNA, ACP2 expression was inhibited in P15 fibroblasts. E, F, In P12 myoblasts, ACP5 expression was modulated through siRNA treatment . Western blot analysis of lysates from cells incubated with 50 nmol/L rhGAA for 8 h preceded or not by 48 h siRNA treatment. Lysates were immunoblotted with antibody against human GAA and actin as loading control (n = 2)

3.2 | Impact of acid phosphatases in GAA processing

The main difference between AMFA and Mannose 6-Phosphate is the replacement of the phosphate moiety by a phosphonate group insensitive to phosphatase in contrast to M6P. In agreement with a previous study,[9] we found that acid phosphatases activity is significantly increased in Pompe patient myoblasts (264 ± 96%) as compared to normal myoblasts (value set as 100 ± 11%, $P < 0.005$ Student's *t* test) (Figure 2A). As such phosphatases could be involved

in M6P signal deterioration on rhGAA, we demonstrated that the inhibition of overexpressed phosphatases with sodium fluoride or β−glycerophosphate allowed the processing of rhGAA into 76 kD and 60-70 kD active forms (Figure).

Expressions of ACP2 and ACP5, two major acid phosphatases involved in M6P dephosphorylation[9] were assessed (Figure 2B). ACP2 is overexpressed in almost all Pompe disease samples, whereas few ones overexpressed ACP5.

The inhibition with specific siRNAs of 58% ACP2 and 24% ACP5 expression (Figure 2C-E) was sufficient to enhance rhGAA maturation (Figure 2D-F) and partially that of the endogenous deficient enzyme.

4 | DISCUSSION

In this report, significant differences in the processing of rhGAA-AMFA and rhGAA are presented. Although both enzymes are well internalized, only rhGAA-AMFA undergoes cleavage to 76 kD active and 60-70 kD mature forms in primary cultures of fibroblasts, myoblasts and myotubes from Pompe patients and in aged Pompe mice after 3-month treatment. These data establish that the protease machinery necessary for enzymatic maturation is still functional in both adult patients and aged Pompe mice which were previously considered as ERT refractory.[4]

Then, we considered the role of phosphatases in GAA maturation. In LSD, several reports evidence an overexpression of lysosomal acid phosphatases. As already demonstrated for lysosomal enzymes in cancers,[12,13] we supposed that overexpressed phosphatases can overflow from lysosomes to nearby endo-lysosomal vesicles. Such abnormally localized phosphatases could prevent GAA-M6PR complexing before the enzyme reaches the lysosomes and thus impair enzyme endo-lysosomal maturation. Our present analysis indicates an increase of the acid phosphatases activity and more specifically, an elevation of ACP2 and ACP5. Using general inhibitors and specific siRNAs, we obtained a partial phosphatases inhibition sufficient to allow the formation of rhGAA active and mature forms. Although different cell types remain to be evaluated, these data already evidence that acid phosphatases overexpression prevents rhGAA processing.

The outcome of the unmatured rhGAA was not investigated here. However, aberrant localization of rhGAA into autophagosomes could be hypothesized.[14]

In conclusion, the higher therapeutic efficacy of rhGAA-AMFA observed in vitro and in vivo [5,6] is associated with an increase of enzyme maturation. Altogether, these data suggest that AMFA targeting may represent a potential therapeutic advantage for Pompe disease and also for other LSD which overexpress acid phosphatases.

ACKNOWLEDGEMENTS

We thank Dr Gilles CARNAC, from Inserm U1046-UMR CNRS 9214, and Pr François RIVIER, from the CHU Montpellier-Guy de Chauliac, for their scientific and medical advices. This work was supported by French National Research Agency ANR-13-RPIB-0012, by Association Nationale Recherche Technologie grant 2016/0628 and grant 2016/0629, by APPI grant N°DOS0026362/00 from BPI, by NanoMedSyn and by Occitanie-Midi Pyrénées Region grant PILE 180060 and PILE 180064, by Vaincre les Maladies Lysosomales Suisse. For sample providing, we thank Pr Schaeffer from CBC Biotec Biobank, the Reference Center for Neuromuscular Diseases and ALS of Nice University Hospital, and the Muscle Tissue Culture Collection MTCC. We thank the Biobank of Cells, Tissues and DNA from patients with neuromuscular diseases, member of the Telethon Network of Genetic Biobanks (project no. GTB12001), funded by Telethon Italy, and of the EuroBioBank network, for providing us specimens. The Muscle Tissue Culture Collection is part of the German network on muscular dystrophies (MD-NET, service structure S1, 01GM0601) and the German network for mitochondrial disorders (mito-NET, project D2, 01GM0862) funded by the German Ministry of Education and Research (BMBF, Bonn, Germany). The Muscle Tissue Culture Collection is a partner of EuroBioBank (www.eurobiobank.org) and TREAT-NMD (www.treat-nmd.eu). AG, MD, ADS are CIFRE PhD students from Association Nationale Recherche Technologie. IB, KEC, HVC, MG, MM are employees of NanoMedSyn. MG, MGB and AM are co-founders and have received consulting fees from NanoMedSyn.

CONFLICT OF INTEREST

The authors declare that they have no conflicts of interest with the contents of this article.

DATA AVAILABILITY

The data that support the findings of this study are available from the corresponding author upon reasonable request.

ORCID

Alain Morère https://orcid.org/0000-0002-3269-5172

REFERENCES

1. van der Ploeg AT, Clemens PR, Corzo D, et al. A Randomized study of alglucosidase alfa in late-onset Pompe's disease. *N Engl J Med*. 2010;362:1396-1406.
2. Schoser B, Stewart A, Kanters S, et al. Survival and long-term outcomes in late-onset Pompe disease following alglucosidase alfa treatment: a systematic review and meta-analysis. *J Neurol*. 2017;264:621-630.
3. Maga JA, Zhou J, Kambampati R, et al. Glycosylation-independent lysosomal targeting of acid α-glucosidase enhances muscle glycogen clearance in Pompe mice. *J Biol Chem*. 2013;288:1428-1438.
4. Zhu Y, Jiang J-L, Gumlaw NK, et al. Glycoengineered acid α-glucosidase with improved efficacy at correcting the metabolic aberrations and motor function deficits in a mouse model of Pompe disease. *Mol Ther*. 2009;17:954-963.

5. El Cheikh K, Basile I, Da Silva A, et al. Design of potent mannose 6-phosphate analogues for the functionalization of lysosomal enzymes to improve the treatment of pompe disease. *Angew Chem Int Ed Engl*. 2016;55:14774-14777.
6. Basile I, Da Silva A, El Cheikh K, et al. Efficient therapy for refractory Pompe disease by mannose 6-phosphate analogue grafting on acid α-glucosidase. *J Control Release*. 2018;269:15-23.
7. Moreland RJ, Jin X, Zhang XK, et al. Lysosomal acid α-glucosidase consists of four Different peptides processed from a single chain precursor. *J Biol Chem*. 2005;280:6780-6791.
8. Bali DS, Tolun AA, Goldstein JL, Dai J, Kishnani PS. Molecular analysis and protein processing in late-onset Pompe disease patients with low levels of acid α-glucosidase activity. *Muscle Nerve*. 2011;43:665-670.
9. Tsuburaya RS, Monma K, Oya Y, et al. Acid phosphatase-positive globular inclusions is a good diagnostic marker for two patients with adult-onset Pompe disease lacking disease specific pathology. *Neuromuscul Disord*. 2012;22:389-393.
10. Makrypidi G, Damme M, Muller-Loennies S, et al. Mannose 6 dephosphorylation of lysosomal proteins mediated by acid phosphatases Acp2 and Acp5. *Mol Cell Biol*. 2012;32:774-782.
11. Nascimbeni AC, Fanin M, Masiero E, Angelini C, Sandri M. The role of autophagy in the pathogenesis of glycogen storage disease type II (GSDII). *Cell Death Differ*. 2012;19:1698-1708.
12. Rochefort H, Liaudet E, Garcia M. Alterations and role of human cathepsin D in cancer metastasis. *Enzyme Protein*. 1996;49:106-116.
13. Aggarwal N, Sloane BF. Cathepsin B: multiple roles in cancer. *Proteom Clin Appl*. 2014;8:427-437.
14. Raben N, Ralston E, Chien Y-H, et al. Differences in the predominance of lysosomal and autophagic pathologies between infants and adults with Pompe disease: implications for therapy. *Mol Genet Metab*. 2010;101:324-331.

SUPPORTING INFORMATION

Additional supporting information may be found online in the Supporting Information section at the end of the article.

How to cite this article: Godefroy A, Daurat M, Da Silva A, et al. Mannose 6-phosphonate labelling: A key for processing the therapeutic enzyme in Pompe disease. *J Cell Mol Med*. 2019;00:1–5. https://doi.org/10.1111/jcmm.14516

SUPPORTING INFORMATIONS

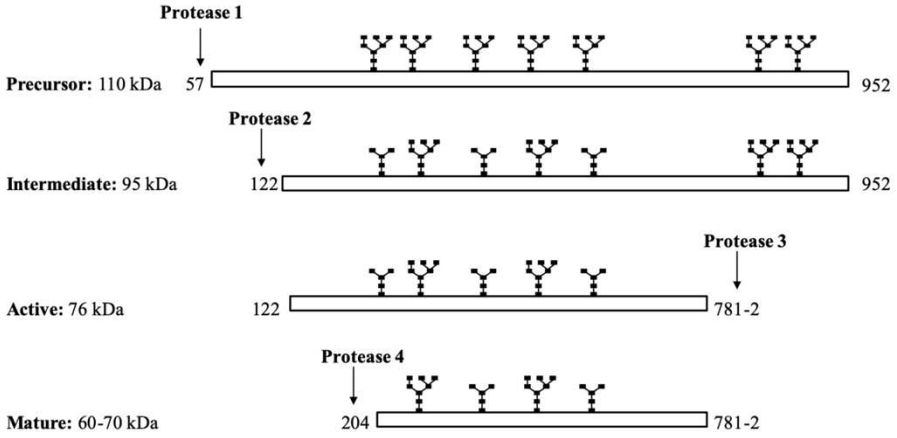

Scheme S1. Intracellular maturation of GAA under physiological conditions. Several successive cleavages of the inactive 110 kDa precursor GAA occur in the endolysosomal routing leading to the formation of an intermediate 95 kDa form, then an active 76 kDa form and finally the mature 60-70 kDa form in lysosomes (modified from [12]).

MATERIALS & METHODS

Materials

Primary cultures of myoblasts from 15 individuals (referred as P1 to 15) were provided by different biobanks. Normal myoblasts (referred as P1 to P6) were supplied by Dr. G. Carnac (Inserm U1046-UMR CNRS 9214, Montpellier, France) and the Reference Center for Neuromuscular Diseases and ALS of Nice University Hospital (Nice, France).

Pompe adult myoblasts (referred as P7 to P13) were provided by the Muscle Tissue Culture Collection (Munich, Germany), the Reference Center for Neuromuscular Diseases and ALS of Nice University Hospital (Nice, France) and the CBC Biotec Biobank BB-0033-00046 (Lyon, France). P14, a primary culture of myoblasts from a Pompe juvenile patient, was obtained from the Telethon Network of Genetic Biobanks [1] (Milan, Italy). P15 corresponds to fibroblasts from Pompe adult patient which were kindly provided by Dr. C. Caillaud (Necker Hospital Paris, France). The GAA gene alterations identified in Pompe patients from which the primary cultures were established are summarized in Table S1.

Table S1. *GAA* gene mutations in the Pompe patients used in this study

Patient	Allele 1	Allele 2
P7	c-32-13T>G	c.925G>A (p.Gly309Arg)
P8	c-32-13T>G	c.1075G>A (p.Gly359Arg)
P9	c-32-13T>G	c.1438-1G>C
P10	c.-32-13T>G	c.1396del (p.Val466Phefs*11)
P11	c.-32-13T>G	c.2738C>G (p.Pro913Arg)
P12	c-32-13T>G	c.1927G>A (p.Gly643Arg)
P13	c.119G>A (p.Arg40Gln)	c.1497G>A (p.Trp499*)
P14	c.-32-13T>G	c.2237G>A (p.Trp746*)
P15	c.-32-13T>G	c.2104C>T (p.Arg702Cys)

The rhGAA used was alglucosidase-alfa (Myozyme®) manufactured by Sanofi-Genzyme and recovered from excess material of the reconstituted commercial product used in patients. Pompe mice were a kind gift from Pr. Nina Raben [2] and were housed and cared according to protocols

approved by the Languedoc-Roussillon ethical committee CEEA-LR-36 with agreement N4987-2016101116132551.

Cell culture

Cells were cultured in a humidified atmosphere containing 5% CO_2 at 37°C. The myoblasts of Pompe disease patients and healthy persons were cultured in Ham F10 medium plus 20% fetal bovine serum (FBS), 1% insulin, 25 ng/mL FGF, 10 ng/mL EGF and 1% penicillin/streptomycin on collagen coated surface. In myotube experiments, successive steps of the differentiation of adult patient myoblasts are required. Myoblasts at confluence were induced to differentiate by lowering the FBS concentration to 2%. Cells were maintained in differentiation medium for 5 days. The myotubes obtained after 7 days of differentiation acquired contractile capacities (data not shown) and are therefore representative of the most abundant cells of skeletal muscles. For fibroblasts, they were cultured in DMEM supplemented with 10% FBS and 1% penicillin/streptomycin.

Chemical conjugation of AMFA onto rhGAA

The rhGAA was coupled with AMFA according to the method previously described [10] . Briefly, rhGAA was oxidized with 5 mM $NaIO_4$ for 30 min at 4°C in the dark. Oxidation reaction was stopped by addition of 2% glycerol. Oxidized enzyme was purified on a G-10 Sepharose column (GE Healthcare) according to manufacturer's instructions. AMFA was then grafted on rhGAA at a ratio of 300 equivalents per mole of enzyme during 2 h at 37°C in the dark under agitation. After conjugation reaction, rhGAA-AMFA was dialyzed against 25 mM sodium phosphate buffer (pH 6.2) containing 1% mannitol and 0.005% Tween 80 for 18 h at 4°C. The samples were aliquoted and stored at -20°C until used. The number of AMFA, determined using

MALDI-TOF mass spectrometry from 5 different coupling reactions, is approximately of 5.3 ± 1.8 mol AMFA per mol enzyme.

Western blot analysis

To study rhGAA-AMFA maturation, extracts from Pompe adult myoblasts were subjected to Western blot analysis. The cells were washed 3 times, harvested in PBS and lysed by 3 freeze-thaw cycles in buffer containing 50 mM HEPES, 150 mM NaCl, 1 mM EDTA, 2.5 mM EGTA, 0.1% Tween 20, 10% glycerol, 1 mM NaF, 1 mM $NaNO_3$, 10 mM glycerophosphate and protease inhibitors (dilution 1:25 Complete, Roche Diagnostics). The lysates were precleared by centrifugation at 10,000 g for 15 min at 4°C. Samples were tested for protein concentration by the Bradford method and equal amounts (5 or 20 µg) of cell extract were resolved by 12% SDS-PAGE. After blotting the gel into PVDF membrane, proteins were detected by probing with anti-human GAA (GeneTex), ACP2 (Santa Cruz Biotechnology) or ACP5 (Abcam) incubated with peroxidase-conjugated secondary antibodies (Amersham). Immunoreactive proteins were then analyzed by ECL detection system (Amersham). Actin detected by a monoclonal mouse antibody provided by Dr N. Bettache (CNRS UMR5247, Montpellier, France) was used as the loading control. Quantifications of the immunoreactive GAA forms were performed on unsaturated films with low exposures using Image J software.

Uptake assays

After enzyme treatment in triplicate for the indicated times at 37°C, cells were washed 3 times with PBS and lysed by sonication in GAA assay buffer (0.2 M $C_2H_3NaO_2$, 0.4 M KCl, pH 4.3) containing 0.1% Triton X-100. The lysates were centrifuged at 14,000 g for 10 min at 4°C. Samples were tested for protein concentration and enzymatic activity was measured by using the fluorescent substrate 4-methylumbelliferyl-α-D-glucopyranoside (4-MUG, Sigma Aldrich). Cell lysates were

incubated with 160 µM 4-MUG diluted in GAA assay buffer for 3 h at 37°C. The reaction was stopped by addition of 0.4 M glycine buffer pH 10.4 and the fluorescence was read with 355 nm excitation and 460 nm emission filters with a PerkinElmer 1420 VICTOR 2 microplate reader.

Total acid phosphatases activity quantification

Cells were cultured in 6-well plates and lysed in 0.2 M $C_2H_3NaO_2$, 0.4 M KCl, 0.1% Triton pH 4.3 and sonicated 3×6 s. The lysates were centrifuged at 14,000 g for 10 min at 4°C. Samples were assayed for protein concentration and the activity of phosphatases was determined using 6,8-difluoro-4-methylumbelliferyl phosphate (DiFMUP) (Molecular Probes) as a substrate. Extracts (5 µL) were incubated in 100 mM sodium acetate buffer pH 5.5 and 0.1 mM DiFMUP for 30 min at room temperature. Fluorescence intensity was monitored with a 355 nm excitation and a 460 nm emission filters with a PerkinElmer 1420 VICTOR 2 microplate reader.

Acid phosphatases inhibition

Cells were incubated with 50 nM enzymes and phosphatase inhibitors 2 mM NaF or 2.5 mM beta-glycerophosphate for 48 h at 37°C in RPMI medium enriched with 10% heat-inactivated calf serum. After incubation, cells were washed three times with PBS and stocked at -20°C until Western blot analysis.

siRNA silencing

Small interfering RNA (siRNA) duplex oligoribonucleotides for human acid phosphatases 2 (ACP2) and tartrate-resistant acid phosphatase (TRAP, ACP5) were synthesized by Santa Cruz Biotechnology, INC (accession number: sc-96327 and sc-44164). ACP2 siRNA and TRAP siRNA are a pool of 3 target-specific 19-25 nucleotides designed to knock down gene expression. Firefly luciferase-specific siRNA (siRNA Fluc) was used as controlled and purchase by Eurogentec. siRNA Fluc sequences were as followed: sense 5'-CUUACGCUGAGUACUUCGA55-3' and anti-sense 5'UCGAAGUACUCAGCGUAAG-3'. Cells were allowed to grow on 6-well plates

until reaching 50-70% confluency in appropriate culture medium. Cells were then transfected using, for one well, 50 pmol of siRNA and 8 µL of INTERFERin® (PolyplusTransfection) reagent in Opti-MEM™ medium and incubated 4 h. Following incubation, standard growth medium was added and FCS equilibrated at 10% in each well. Forty-eight h after transfection, wells were washed 2 times with PBS and treated with 50 nM enzymes or vehicle for 8 h in DMEM supplemented with 10% FCS. After incubation, cells were washed 3 times with PBS and plates were stored at -20°C until used.

Statistical analysis

The statistical analysis was performed using either the Student's test or the Newman-Keuls test for repeated measures. A probability value of $p < 0.05$ was considered statistically significant.

REFERENCES

[1] **Filocamo M, Mazzotti R, Corsolini F, et al.** Cell Line and DNA Biobank From Patients Affected by Genetic Diseases. *Open Journal of Bioresources* 2014; 1; e2. (methods)

[2] **Raben N, Nagaraju K, Lee E, et al.** Targeted disruption of the acid alpha-glucosidase gene in mice causes an illness with critical features of both infantile and adult human glycogen storage disease type II. *J. Biol. Chem.* 1998; 273; 19086–92(.Mettre in methods)

ADDITIONAL RESULTS

Maturation of rhGAA and rhGAA-AMFA in myoblasts of adult Pompe patient.

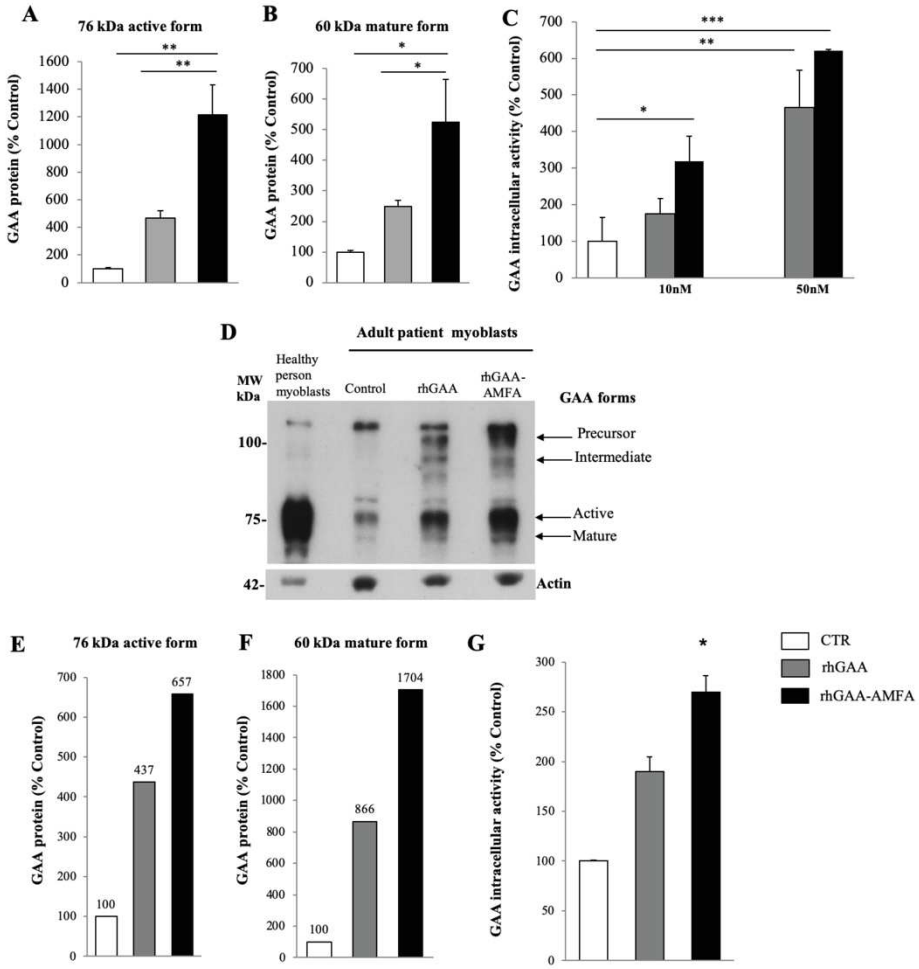

Figure S1: Maturation of rhGAA and rhGAA-AMFA in myoblasts of Pompe patient P12 (from A to C) and P7 (from D to G). Myoblasts were incubated with 50 nM rhGAA, rhGAA-AMFA or with vehicle (Control) for 8 h (P12) or 4 h (P7) in medium enriched with 10% human serum. (A, B) Quantification with Image J software of 76 kDa and 60-70 kDa GAA protein forms corrected by actin expression. Control cells are considered as 100%. (n=2) (C) GAA catalytic activities of myoblasts treated 3 h with vehicle or 10 nM or 50 nM rhGAA or rhGAA-AMFA. The tests were performed in cell lysates using synthetic substrate 4-MUG. Data are expressed as a percentage of vehicle treated cell activity (n=2), *p<0.05, **p<0.01 and ***p<0.001 (Newmann-Keuls multiple comparison test). **(**D) The cell extracts (5 µg) were analyzed by Western blots using human GAA or actin antibodies. Black arrows indicate respectively 110 kDa (inactive precursor), 95 kDa (inactive intermediate), 76 kDa (active intermediary) and 60-70 kDa GAA (mature active) forms. Actin is a control for total protein loading. (E, F) Quantification of GAA protein forms performed as in (A,B). (G) GAA activities in P7 myoblasts incubated for 3 h with 20 nM enzyme treatment (n=2), *p<0.05 vs control (Newmann-Keuls multiple comparison test).

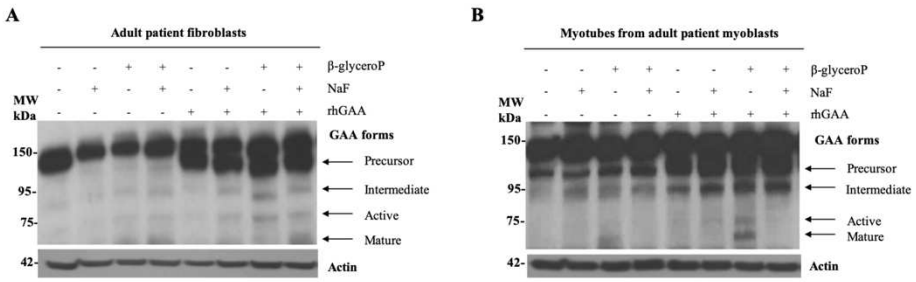

Figure S2: Activation of rhGAA maturation by phosphatase inhibitors in adult Pompe fibroblasts and myotubes. The internalization and processing of rhGAA in P15 adult fibroblasts (A), myotubes from P9 (B) was measured in the presence or absence of phosphatase inhibitors NaF

or beta-glycerophosphate. The enzymes (50 nM) were incubated for 48 h and the intracellular maturation was detected by Western blots using an anti-human GAA antibody. Actin was used as a control for total protein loading.

The combination of two inhibitors did not show additive effect on GAA maturation in fibroblasts and decreased the effect of beta-glycerophosphate in myotubes. These results indicate that the cellular acid phosphatases could play a repressive role in the maturation of rhGAA. In fibroblasts, the loss of the M6P signal on rhGAA would probably happen before the first proteolytic cleavage of the 110 kDa precursor since the 95 kDa is not detected. In myotubes and myoblasts the 95 kDa form is detected suggesting that phosphate group of M6P was removed later.

- Conclusion :

Dans cet article, nous avons étudié le mécanisme d'action de rhGAA-AMFA qui explique en partie l'amélioration de l'efficacité thérapeutique. Premièrement, nous avons démontré une différence significative dans le processus de maturation entre rhGAA-AMFA et rhGAA. En effet, nous avons observé une internalisation élevée du précurseur à 110 kDa pour rhGAA-AMFA et rhGAA dans des myoblastes provenant de différents patients adultes ; cependant la forme active à 76 kDa et la forme mature à 60-70 kDa sont respectivement 3 et 5 fois plus élevées pour rhGAA-AMFA. Des résultats similaires ont également été observés dans des myoblastes d'un patient adulte différenciés en myotubes. De plus, chez des souris modèles de la maladie de Pompe âgées de 10 mois et traitées avec 5 mg/kg par semaine pendant trois mois, nous observons 48 heures après le dernier traitement uniquement la forme intermédiaire à 95 kDa chez les souris traitées avec rhGAA alors que chez les souris traitées avec rhGAA-AMFA nous observons la forme active et chez certains individus les formes active et mature. Ces résultats montrent que les formes active et mature augmentent de manière significative avec rhGAA-AMFA ce qui signifie que le mécanisme impliquant les protéases nécessaires à la maturation enzymatique n'est pas altéré chez les patients adultes qui sont pourtant considérés habituellement comme non-répondeur à l'enzymothérapie de substitution[328]. Une différence majeure entre les AMFA et le M6P est l'insensibilité aux phosphatases. Nous avons donc émis l'hypothèse que les phosphatases acides intracellulaires seraient impliquées dans la détérioration du signal M6P empêchant le processus de maturation intracellulaire. Nos résultats démontrent, en accord avec des études précédentes, la surexpression des phosphatases acides intracellulaires totales et mettent en évidence la surexpression des phosphatases ACP2 et ACP5 dans les cultures de patients adultes. Des études antérieures avaient montré l'implication de ces deux phosphatases dans la déphosphorylation du M6P[219,337]. En utilisant des inhibiteurs de phosphatases et des siRNA spécifiques d'ACP2 et ACP5, nous avons obtenu une inhibition partielle des phosphatases, suffisante pour observer l'augmentation des formes active et mature de rhGAA. Bien que ces résultats doivent être approfondis, ils suggèrent tout de même que la surexpression des phosphatases acides empêche la maturation complète de rhGAA. D'une manière générale, ces résultats suggèrent que le ciblage du RM6P-CI par l'AMFA pourrait être un bon candidat thérapeutique pour la maladie de Pompe ainsi que pour d'autres maladies lysosomales dans lesquelles une surexpression des phosphatases acides est observé.

Conclusion générale et perspectives

Le développement de thérapies ciblées pour le traitement du cancer est un enjeu de santé publique. Il est nécessaire de développer des thérapies permettant de cibler préférentiellement les cellules cancéreuses afin d'augmenter l'efficacité thérapeutique dans la zone à traiter, d'éviter l'atteinte des tissus sains et ainsi diminuer considérablement les effets secondaires connus des thérapies classiques (chimiothérapie et radiothérapie). A l'heure actuelle, des thérapies ciblées ont déjà été autorisées par les autorités de santé mais ces thérapies ont des limites comme décrites précédemment. Ce projet de thèse s'inscrit dans ce contexte : l'objectif étant de développer des nanoparticules multifonctionnelles pour le traitement des cancers. Ce projet est donc à la frontière de plusieurs domaines scientifiques et la pluridisciplinarité de l'équipe « Glyco et nanovecteurs pour le ciblage thérapeutique » a permis de réaliser des études complètes me permettant d'être co-auteur d'articles scientifiques qui ont été soit décrits dans la partie résultat soit annexés dans ce manuscrit (Figure 27).

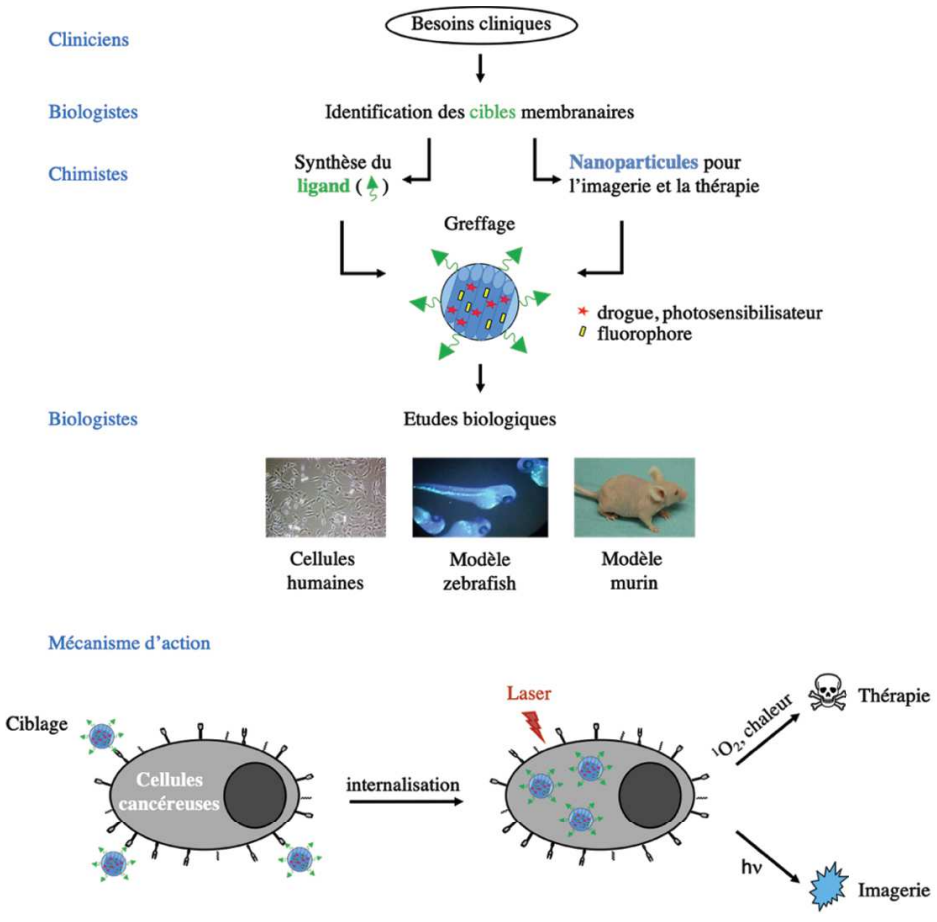

Figure 27 : Activités pluridisciplinaires du laboratoire

La première partie de la thèse concerne le développement de nanoparticules multifonctionnelles innovantes pour la thérapie et l'imagerie médicale des cancers. Les nanoparticules permettent un ciblage passif des tumeurs solides *via* l'effet EPR : les nanoparticules injectées en intraveineux vont se déplacer dans la circulation sanguine jusqu'à la zone tumorale et vont pouvoir traverser les fenestrations des néo-vaisseaux et ainsi être retenues dans la tumeur.

Dans ce contexte nous avons, tout d'abord, démontré pour la première fois le potentiel thérapeutique de nanoparticules de bleu de Prusse pour la PTT biphotonique. Cette technique est basée sur l'utilisation d'agents photothermiques capables de convertir la lumière en chaleur qui entraîne la mort des cellules cancéreuses. Ces nanoparticules ont été étudiées sous irradiation monophotonique et même si les résultats sont encourageants, ce type d'irradiation a des limites car elle ne permet pas une éradication complète des cellules cancéreuses due à l'hétérogénéité de la production de chaleur au sein de la tumeur et la faible distance de pénétration dans les tissus[338]. Dans notre étude, nous avons démontré que sous irradiation biphotonique les nanoparticules de bleu de Prusse entraînait quasiment 100% de mort cellulaire. Ces nanoparticules ont donc un grand potentiel de PTT. De plus, nous avons montré la possibilité de fonctionnaliser après synthèse des luminophores permettant de visualiser facilement le devenir des nanoparticules dans l'organisme.

Dans un deuxième temps, nous avons développé des nanoparticules organosiliciées pour la délivrance de drogue, dans notre cas la gemcitabine monophosphate utilisée en chimiothérapie notamment pour le traitement du cancer du sein. Cette étude était basée sur deux types de nanoparticules organosiliciées : des nanoparticules mésoporeuses et des nanoparticules ioniques. Dans le premier cas, les pores de la nanoparticule ont permis d'encapsuler la gemcitabine monophosphate et des porphyrines ont été incorporées à la matrice organosiliciée de la nanoparticule. Ce sont des molécules fluorescentes permettant la visualisation des nanoparticules dans l'organisme. Pour les nanoparticules ioniques, du FITC a été greffé à leur surface pour l'imagerie. Les études biologiques sur des cellules cancéreuses humaines du cancer du sein ont permis de démontrer le fort potentiel de ces nanoparticules pour transporter et libérer la gemcitabine monophosphate, car nous avons observé un taux élevé de mort cellulaire démontrant que l'encapsulation de la drogue n'altérait pas son activité thérapeutique. De plus, nous avons pu visualiser les deux types de nanoparticules dans les cellules cancéreuses et conclure qu'elles s'accumulaient dans le cytoplasme.

Les nanoparticules utilisées dans cette partie ont un point commun : elles peuvent être utilisées pour la thérapie mais également pour l'imagerie médicale. Ces nanovecteurs innovants sont appelés nanovecteurs théranostiques : c'est-à-dire la combinaison entre la thérapie et le diagnostic. Ils sont donc très prometteurs pour une utilisation clinique.

Cependant, le ciblage passif de ces nanoparticules est limité, c'est pourquoi les recherches se sont tournées vers le ciblage actif des cellules cancéreuses afin d'augmenter l'efficacité thérapeutique. Ce ciblage est basé sur la conjugaison de biomolécules à la surface des nanoparticules. L'équipe s'est alors spécialisée dans le développement de glycovecteurs pour le ciblage thérapeutique. La création de NanoMedSyn est basée sur l'exploitation d'un brevet déposé par l'équipe sur la synthèse d'un glycovecteur innovant : l'AMFA qui cible efficacement le RM6P-CI impliqué dans l'adressage des enzymes lysosomales aux lysosomes. La deuxième partie de cette thèse consiste à valoriser la technologie AMFA pour le traitement des maladies lysosomales ainsi que pour le traitement de certains cancers qui surexpriment le RM6P-CI, tel que le cancer de la prostate. L'équipe a démontré que le RM6P-CI était surexprimé et qu'il permettait d'augmenter significativement l'adressage et donc l'efficacité thérapeutique de nanoparticules.

Tout d'abord, nous avons étudié l'intérêt potentiel des AMFA dans le traitement d'un autre type de cancer en mettant en évidence la surexpression du RM6P-CI dans trois lignées cellulaires cancéreuses de RMS. En effet, nous avons démontré qu'en moyenne l'expression du récepteur était sept fois supérieure dans les cellules de RMS que dans les myoblastes sains de trois patients différents. Ceci suggère que le RM6P-CI pourrait être considéré comme un biomarqueur du développement du RMS. La deuxième étape a été la synthèse et la fonctionnalisation des AMFA de nanoparticules, plus particulièrement des PMO, pour faire de la PDT biphotonique grâce aux porphyrines incorporées dans la matrice de la nanoparticule. Les études biologiques effectuées sur une lignée cellulaire de RMS et une lignée de myoblastes sains ont permis de démontrer la biocompatibilité et l'efficacité thérapeutique de la PDT des PMO-AMFA. En effet, les PMO non fonctionnalisées induisent 50% à 60% de mort cellulaire sur les deux lignées cellulaires alors que les PMO-AMFA induisent quasiment 100% de mort cellulaire sur les cellules cancéreuses et aucun effet PDT sur les cellules saines dans les conditions étudiées. De plus, l'implication du RM6P-CI dans l'endocytose active des PMO-AMFA a été démontrée. Ces résultats démontrent que le RM6P-CI peut être considéré comme une bonne cible thérapeutique et que les AMFA ciblent spécifiquement les cellules cancéreuses dans lesquelles le récepteur est surexprimé. La PDT offre de nouvelles opportunités de thérapies non-invasives.

Cependant, en clinique, la PDT pour le traitement du RMS présente des limites car ce sont généralement des tumeurs profondes et difficiles d'accès. Afin d'optimiser ces résultats, nous proposons de conserver la fonctionnalisation de l'AMFA sur des nanoparticules pour conserver un ciblage actif efficace mais d'utiliser d'autres types de nanoparticules qui seraient autonomes, et qui n'auraient donc pas besoin d'un stimuli externe comme c'est le cas avec la PDT. Nous pourrions par exemple utiliser des nanoparticules pour la délivrance de drogue, comme décrites dans ce manuscrit, où la drogue est libérée uniquement à pH acide, c'est-à-dire, dans les vésicules endo-lysosomales ou directement dans les lysososmes. D'autres études ont montré l'efficacité de ces nanoparticules autonomes et ont confirmé leur fort potentiel thérapeutique : la drogue peut être liée à la nanoparticule par des liaisons hydrazones qui se rompent à pH acide[339], la drogue peut également être confinée dans la nanoparticule par des bouchons moléculaires qui forment des liaisons hydrogènes avec la nanoparticule et qui s'ouvrent à pH acide[340]. Nous pourrions également utiliser les nanoparticules comme vecteur de siRNA : ce sont des petits ARN interférents qui peuvent se lier spécifiquement à une séquence d'ARN messager pour bloquer l'expression du gène cible. Comme il a été décrit précédemment, les RMS alvéolaires sont caractérisés par un gène de fusion PAX3-FOXO1a. Une étude a démontré que le blocage de ce gène de fusion permettait de réduire significativement les xénogreffes de tumeurs chez les souris, un siRNA anti PAX3-FOXO1a a été encapsulé dans des liposomes et injecté à des souris. Les résultats ont montré une inhibition significative de l'initiation de la tumeur chez les souris[341]. Ces résultats nous permettent d'envisager ce type de thérapies (délivrance de drogue, utilisation de siRNA, combinaison des deux) avec les nanoparticules décrites dans cette thèse greffées par des AMFA pour le ciblage actif du RMS.

Nous avons étudié, par la suite, la possibilité d'utiliser l'AMFA pour le ciblage de la maladie de Pompe. Le traitement actuel par enzymothérapie substitutive a une efficacité limitée. Cependant, les résultats antérieurs de NanoMedSyn ont permis de montrer que le greffage de l'AMFA sur rhGAA permettait d'augmenter significativement l'efficacité du traitement chez les souris modèles de la maladie de Pompe : diminution du glycogène, amélioration de la santé musculaire permettant une meilleure motricité. Dans ce manuscrit, nous avons démontré une partie du mécanisme d'action de rhGAA-AMFA qui permettrait d'expliquer cette augmentation significative d'efficacité thérapeutique. RhGAA a une maturation intracellulaire très limitée contrairement à rhGAA-AMFA pour laquelle nous avons observé une maturation supérieure dans les cultures primaires (fibroblastes, myoblastes et myotubes) de patients adultes atteints de la maladie de Pompe. Cependant, nos résultats

montrent que l'inhibition partielle des phosphatases acides, surexprimées dans la maladie de Pompe, permet une augmentation significative de la maturation de rhGAA. Ceci pourrait expliquer l'efficacité thérapeutique relative de rhGAA observée chez les souris Pompe et chez les patients adultes. Ces résultats suggèrent que l'insensibilité de l'AMFA aux phosphatases sériques ainsi qu'aux phosphatases acides joue un rôle primordial dans la maturation de l'enzyme : elle est mieux reconnue et internalisée par le RM6P-CI et également mieux maturée. De plus, nous supposons que la surexpression des phosphatases acides entraînerait leur échappement hors des lysosomes vers les vésicules endo-lysosomales voisines entraînant la dégradation précoce du signal M6P et l'arrêt de l'acheminement de l'enzyme vers les lysosomes ainsi sa maturation serait interrompue. Sans maturation complète, l'enzyme ne peux pas être active et le traitement est alors peu efficace. Ces résultats prometteurs ont permis à NanoMedSyn d'obtenir une désignation de médicament orphelin auprès de l'Agence Européenne du Médicament en juillet 2016 démontrant l'intérêt de notre technologie par rapport au traitement existant. De plus, NanoMedSyn a signé un contrat de collaboration avec l'entreprise Shire (Boston, Etats-Unis), leader mondial des biotechnologies pour le traitement des maladies rares, nous permettant d'envisager à terme un protocole clinique.

La technologie AMFA pourrait également être utilisée pour développer un traitement pour d'autres maladies lysosomales traitées par enzymothérapie substitutive et permettre le ciblage thérapeutique d'autres types de cancers qui surexpriment le RM6P-CI

BIBLIOGRAPHIE

1. Bouchal R, Daurat M, Gary-bobo M, et al. Biocompatible Periodic Mesoporous Ionosilica Nanoparticles with 2 Ammonium Walls : Application to Drug Delivery. 2017. doi:10.1021/acsami.7b07264
2. OMS | Cancer. *WHO*. 2017. https://www.who.int/topics/cancer/fr/. Accessed April 24, 2019.
3. Iarc. Dernières données mondiales sur le cancer : le fardeau du cancer atteint 18,1 millions de nouveaux cas et 9,6 millions de décès par cancer en 2018. 2018:8-10. http://gco.iarc.fr/,.
4. Bray F, Ferlay J, Soerjomataram I, Siegel RL, Torre LA, Jemal A. 394 CA: A Cancer Journal for Clinicians Global Cancer Statistics 2018: GLOBOCAN Estimates of Incidence and Mortality Worldwide for 36 Cancers in 185 Countries. *CA CANCER J CLIN*. 2018;68:394-424. doi:10.3322/caac.21492
5. Les Cancers En France L ' Essentiel. 2019.
6. Uma Devi P. Basics of carcinogenesis. *Heal Adm*. 2004;(1):16-24. doi:10.1186/1471-2407-10-175
7. Folkman J. Angiogenesis in cancer, vascular, rheumatoid and other disease. *Nat Med*. 1995;1(1):27-30. doi:10.1038/nm0195-27
8. Nurgali K, Jagoe RT, Abalo R. Editorial: Adverse Effects of Cancer Chemotherapy: Anything New to Improve Tolerance and Reduce Sequelae? *Front Pharmacol*. 2018;9:245. doi:10.3389/fphar.2018.00245
9. Yan L, Rosen N, Arteaga C. Editorial Challenges in Targeted Cancer Drug Development. :1-4.
10. Thérapies LES, Dans C. / État des lieux en 2015 et enjeux. 2015.
11. Strebhardt K, Ullrich A. Paul Ehrlich's magic bullet concept: 100 Years of progress. *Nat Rev Cancer*. 2008;8(6):473-480. doi:10.1038/nrc2394
12. Ho BN, Pfeffer CM, Singh ATK. Update on Nanotechnology-based Drug Delivery Systems in Cancer Treatment. 2017;5981:5975-5981. doi:10.21873/anticanres.12044
13. Oh B, Lee CH. Nanofiber for cardiovascular tissue engineering. *Expert Opin Drug Deliv*. 2013;10(11):1565-1582. doi:10.1517/17425247.2013.830608

14. Nikalje AP. Nanotechnology and its Applications in Medicine. 2015;5:81-89. doi:10.4172/2161-0444.1000247
15. Ivanov V, Atolia E, Farias E, Mcnicholas TP. HHS Public Access. 2014;8(11):873-880. doi:10.1038/nnano.2013.222.In
16. Patel S, Nanda R, Sahoo S. Medicinal chemistry Nanotechnology in Healthcare : Applications and Challenges. 2015;5(12):528-533. doi:10.4172/2161-0444.1000312
17. Couvreur P. *Drug Vectorization or How to Modulate Tissular and Cellular Distribution of Biologically Active Compounds*. Vol 59.; 2001.
18. Mol J, Babraham AP. Negative Staining of Phospholipids and their Structural Modification by Surface-active Agents as observed in the Electron Microscope. 1964:660-668.
19. Barenholz YC. Doxil ® — The fi rst FDA-approved nano-drug : Lessons learned. 2012;160:117-134. doi:10.1016/j.jconrel.2012.03.020
20. Shi J, Kantoff PW, Wooster R, Farokhzad OC. Cancer nanomedicine : progress , challenges and opportunities. 2017;17(1):20-37. doi:10.1038/nrc.2016.108
21. Park J-H, Gu L, von Maltzahn G, Ruoslahti E, Bhatia SN, Sailor MJ. Biodegradable luminescent porous silicon nanoparticles for in vivo applications. *Nat Mater*. 2009;8(4):331-336. doi:10.1038/nmat2398
22. Choi HS, Liu W, Misra P, et al. Renal clearance of quantum dots. *Nat Biotechnol*. 2007;25(10):1165-1170. doi:10.1038/nbt1340
23. Barreto JA, Malley WO, Kubeil M, Graham B, Stephan H, Spiccia L. Nanomaterials : Applications in Cancer Imaging and Therapy. 2011. doi:10.1002/adma.201100140
24. Bawa R. Regulating Nanomedicine – Can the FDA Handle It ? Regulating Nanomedicine – Can the FDA Handle It ? 2017;(March). doi:10.2174/156720111795256156
25. Dobson J. Gene therapy progress and prospects : magnetic nanoparticle-based gene delivery. 2006:283-287. doi:10.1038/sj.gt.3302720
26. Chen J, Guo Z, Tian H, Chen X. Production and clinical development of nanoparticles for gene delivery. *Mol Ther - Methods Clin Dev*. 2016;3(December 2015):16023. doi:10.1038/mtm.2016.23
27. Jimenez CM, Aggad D, Croissant JG, et al. Porous Porphyrin-Based Organosilica Nanoparticles for NIR Two-Photon Photodynamic Therapy and Gene Delivery in Zebrafish. 2018;1800235:1-12. doi:10.1002/adfm.201800235

28. Jong WH De. Drug delivery and nanoparticles : Applications and hazards. 2008;3(2):133-149.
29. Secret E, Maynadier M, Gallud A, et al. Two-photon excitation of porphyrin-functionalized porous silicon nanoparticles for photodynamic therapy. *Adv Mater*. 2014;26(45):7643-7648. doi:10.1002/adma.201403415
30. Agasti SS, Rana S, Park M, Kim CK, You C, Rotello VM. NIH Public Access. 2011;62(3):316-328. doi:10.1016/j.addr.2009.11.004.Nanoparticles
31. Moghimi SM, Hunter AC. Recognition by Macrophages and Liver Cells of Opsonized Phospholipid Recognition by Macrophages and Liver Cells of Opsonized Phospholipid Vesicles and Phospholipid Headgroups. 2001;(January). doi:10.1023/A
32. Wang J, Sui M, Fan W. Nanoparticles for Tumor Targeted Therapies and Their Pharmacokinetics Nanoparticles for Tumor Targeted Therapies and Their Pharmacokinetics. 2010;(May 2014). doi:10.2174/138920010791110827
33. Chuto G. Les nanoparticules. 2010;34:370-376. doi:10.1016/j.mednuc.2010.03.003
34. Zhang Z, Sun Q, Zhong J, Yang Q. Magnetic Resonance Imaging-Visible and pH-Sensitive Polymeric Micelles for Tumor Targeted Drug Delivery. 2014;(June). doi:10.1166/jbn.2014.1729
35. Tag Y, Kale A, Hartner WC, Papahadjopoulos-sternberg B, Torchilin VP. Self-assembling micelle-like nanoparticles based on phospholipid – polyethyleneimine conjugates for systemic gene delivery. *J Control Release*. 2009;133(2):132-138. doi:10.1016/j.jconrel.2008.09.079
36. Gajbhiye V, Palanirajan VK, Tekade RK, Jain NK. Dendrimers as therapeutic agents : a systematic review. 2009:989-1003. doi:10.1211/jpp/61.08.0002
37. Sigward E, Mignet N, Rat P, Guigner J, Scherman D, Brossard D. Formulation and cytotoxicity evaluation of new self-emulsifying multiple W / O / W nanoemulsions. 2013:611-625.
38. Koga K, Takarada N, Takada K. European Journal of Pharmaceutics and Biopharmaceutics Nano-sized water-in-oil-in-water emulsion enhances intestinal absorption of calcein , a high solubility and low permeability compound. *Eur J Pharm Biopharm*. 2010;74(2):223-232. doi:10.1016/j.ejpb.2009.09.004
39. Bianco A, Kostarelos K, Prato M. Opportunities and challenges of carbon-based nanomaterials for cancer therapy. *Expert Opin Drug Deliv*. 2008;5(3):331-342. doi:10.1517/17425247.5.3.331

40. Fang M, Peng C, Pang D, Li Y. Quantum Dots for Cancer Research : Current Status , Remaining Issues , and Future Perspectives Characteristics of QDs for Biomedical. 2012.
41. Seifalian A, Green M, Seifalian AM. Stem cell tracking using iron oxide nanoparticles. 2014:1641-1653.
42. Demir HV. Conjugated polymer nanoparticles. 2010. doi:10.1039/b9nr00374f
43. Yasun E, Kang H, Erdal H, et al. Cancer cell sensing and therapy using affinity tag-conjugated gold nanorods. 2013:1-9.
44. Montenegro J, Grazu V, Sukhanova A, et al. Controlled antibody /(bio-) conjugation of inorganic nanoparticles for targeted delivery ☆. *Adv Drug Deliv Rev*. 2013;65(5):677-688. doi:10.1016/j.addr.2012.12.003
45. Qi X, Tester RF. Bioadhesive Properties of β -Limit Dextrin. 2011;14(1):60-66.
46. Danhier F. To exploit the tumor microenvironment : Since the EPR effect fails in the clinic , what is the future of nanomedicine ? *J Control Release*. 2016;244:108-121. doi:10.1016/j.jconrel.2016.11.015
47. Nishida N. Angiogenesis in cancer. 2006;2(3):213-219.
48. Holmgren L, O'Reilly MS, Folkman J. Dormancy of micrometastases: Balanced proliferation and apoptosis in the presence of angiogenesis suppression. *Nat Med*. 1995;1(2):149-153. doi:10.1038/nm0295-149
49. Folkman J, Shing Y. contrast, the FGFs are pleiotropic. They stimulate the growth of endothelial cells, smooth muscle cells, fibroblasts, and certain. 1992;267(16):10931-10934.
50. Denekamp J. Angiogenesis, neovascular proliferation and vascular pathophysiology as targets for cancer therapy. *Br J Radiol*. 1993;66(783):181-196. doi:10.1259/0007-1285-66-783-181
51. Iyer AK, Khaled G, Fang J, Maeda H. Exploiting the enhanced permeability and retention effect for tumor targeting. *Drug Discov Today*. 2006;11(17-18):812-818. doi:10.1016/j.drudis.2006.07.005
52. Yuan F, Dellian M, Fukumura D, et al. Vascular Permeability in a Human Tumor Xenograft: Molecular Size Dependence and Cutoff Size1. 1995:3752-3757.
53. Davies CDL, Berk DA, Pluen A, Jain RK. Comparison of IgG diffusion and extracellular matrix composition in rhabdomyosarcomas grown in mice versus in vitro as spheroids reveals the role of host stromal cells. 2002:1639-1644. doi:10.1038/sj/bjc/6600270
54. Iyer A, Greish K, Fang J. Enhanced Permeability and Retention (EPR) Effect and

Tumor-Selective Delivery of Anticancer Drugs. 2006;(April). doi:10.1142/9781860948039

55. Maeda H. THE ENHANCED PERMEABILITY AND RETENTION (EPR) EFFECT IN TUMOR VASCULATURE : THE KEY ROLE OF TUMOR-SELECTIVE MACROMOLECULAR. 2001;41(00):189-207.
56. Matsumura Y, Maeda H. A New Concept for Macromolecular Therapeutics in Cancer Chemotherapy : Mechanism of Tumoritropic Accumulation of Proteins and the Antitumor Agent Smancs1. 1986;(December):6387-6392.
57. Moghimi SM. Nanoparticle transport pathways into tumors. 2018:18-21.
58. Wilhelm S, Tavares AJ, Dai Q, et al. Analysis of nanoparticle delivery to tumours. *Nat Rev Mater*. 2016;1:16014. https://doi.org/10.1038/natrevmats.2016.14.
59. Vu T, Claret FX. Trastuzumab: updated mechanisms of action and resistance in breast cancer. *Front Oncol*. 2012;2:62. doi:10.3389/fonc.2012.00062
60. Intravenous FOR, Only USE, Reactions H, Anaphylaxis I, Events P. https://www.accessdata.fda.gov. :1-21.
61. Riley RS, June CH, Langer R, Mitchell MJ. Delivery technologies for cancer immunotherapy. *Nat Rev Drug Discov*. 2019;18(3):175-196. doi:10.1038/s41573-018-0006-z
62. Leonidas DD, Vatzaki EH, Vorum H, Celis JE, Madsen P, Acharya KR. Structural Basis for the Recognition of Carbohydrates by Human Galectin-7 †,‡. 1998;2960(98):13930-13940. doi:10.1021/bi981056x
63. Duverger E, Frison N, Roche A, Monsigny M. Carbohydrate – Lectin Interactions Assayed by SPR Carbohydrate-lectin interactions assessed by surface plasmon resonance. 2016;(September). doi:10.1007/978-1-60761-670-2
64. Lam SK, Ng TB. Lectins : production and practical applications. 2011:45-55. doi:10.1007/s00253-010-2892-9
65. Takahashi K, Ezekowitz RAB. The Role of the Mannose-Binding Lectin in Innate Immunity. 2005;41(figure 1).
66. Monsigny M, Roche A, Kieda C, et al. Characterization and biological implications of membrane lectins in tumor , lymphoid and myeloid cells. 1988;70:1633-1649.
67. Ni X, Canuel M, Morales CR. The sorting and trafficking of lysosomal proteins Histology and. 2006:899-913. doi:10.14670/HH-21.899
68. Ambrosi M, Cameron R, Davis BG. Lectins : Tools for the Molecular Understanding of

the Glycocode Lectins : tools for the molecular understanding of the glycocode. 2005;(May 2014). doi:10.1039/b414350g

69. Gupta A, Gupta GS. and mannan binding lectins Targeting cells for drug and gene delivery : Emerging applications of mannans and mannan binding lectins. 2014;(May).
70. Lavín de Juan L, García Recio V, Jiménez López P, Girbés Juan T, Cordoba-Diaz M, Cordoba-Diaz D. Pharmaceutical applications of lectins. *J Drug Deliv Sci Technol*. 2017;42:126-133. doi:https://doi.org/10.1016/j.jddst.2017.05.018
71. Drickamer K, Taylor ME. Recent insights into structures and functions of C-type lectins in the immune system. *Curr Opin Struct Biol*. 2015;34:26-34. doi:10.1016/j.sbi.2015.06.003
72. Cummings RD, Etzler ME. R-type Lectins. In: Varki A, Cummings RD, Esko JD, et al., eds. Cold Spring Harbor (NY); 2009.
73. Crocker PR, Varki A. Siglecs in the immune system. *Immunology*. 2001;103(2):137-145. doi:10.1046/j.0019-2805.2001.01241.x
74. Cedeno-Laurent F, Dimitroff CJ. Galectins and their ligands: negative regulators of anti-tumor immunity. *Glycoconj J*. 2012;29(8-9):619-625. doi:10.1007/s10719-012-9379-0
75. Dahms NM, Hancock MK. P-type lectins. *Biochim Biophys Acta*. 2002;1572(2-3):317-340. doi:10.1016/s0304-4165(02)00317-3
76. Mast SW, Diekman K, Karaveg K, Davis A, Sifers RN, Moremen KW. Human EDEM2, a novel homolog of family 47 glycosidases, is involved in ER-associated degradation of glycoproteins. *Glycobiology*. 2005;15(4):421-436. doi:10.1093/glycob/cwi014
77. Fiedler K, Simons K. A putative novel class of animal lectins in the secretory pathway homologous to leguminous lectins. *Cell*. 1994;77(5):625-626. doi:https://doi.org/10.1016/0092-8674(94)90047-7
78. Ohsako S, Hayashi Y, Bunick D. Molecular cloning and sequencing of calnexin-t. An abundant male germ cell-specific calcium-binding protein of the endoplasmic reticulum. *J Biol Chem*. 1994;269(19):14140-14148.
79. Wade Jr LG. Organic Chemistry, Chapter 17. *React Aromat Compd*. 1987:762-763.
80. Asif HM, Akram M, Saeed T, Khan MI, Akhtar N. Review Paper Carbohydrates 1. 2011;(February 2014).
81. Ghazarian H, Idoni B, Oppenheimer SB. A glycobiology review: carbohydrates, lectins and implications in cancer therapeutics. *Acta Histochem*. 2011;113(3):236-247. doi:10.1016/j.acthis.2010.02.004

82. Shaltiel-Karyo R, Frenkel-Pinter M, Rockenstein E, et al. A blood-brain barrier (BBB) disrupter is also a potent α-synuclein (α-syn) aggregation inhibitor: a novel dual mechanism of mannitol for the treatment of Parkinson disease (PD). *J Biol Chem*. 2013;288(24):17579-17588. doi:10.1074/jbc.M112.434787

83. Woodley JF, Naisbett B. The potential of lectins for delaying the intestinal transit of drugs. In: *Proc. Int. Symp. Control Rel. Bioact. Mater.* Vol 15. ; 1988:125-126.

84. Smadja-Joffe F, Legras S, Girard N, et al. CD44 and Hyaluronan Binding by Human Myeloid Cells. *Leuk Lymphoma*. 1996;21(5-6):407-420. doi:10.3109/10428199609093438

85. Zöller M. CD44: physiological expression of distinct isoforms as evidence for organ-specific metastasis formation. *J Mol Med*. 1995;73(9):425-438. doi:10.1007/BF00202261

86. Rudzki Z, Jothy S. CD44 and the adhesion of neoplastic cells. *Mol Pathol*. 1997;50(2):57-71. doi:10.1136/mp.50.2.57

87. Herrera-Gayol A, Jothy S. Adhesion Proteins in the Biology of Breast Cancer: Contribution of CD44. *Exp Mol Pathol*. 1999;66(2):149-156. doi:https://doi.org/10.1006/exmp.1999.2251

88. Tran TA, Kallakury BVS, Sheehan CE, Ross JS. Expression of CD44 standard form and variant isoforms in non-small cell lung carcinomas. *Hum Pathol*. 1997;28(7):809-814. doi:https://doi.org/10.1016/S0046-8177(97)90154-4

89. Cells T, Eliaz RE, Szoka FC. Liposome-encapsulated Doxorubicin Targeted to CD44 : A Strategy to Kill CD44-. 2001:2592-2601.

90. George T, Life SW, Faculty S. LOADING MITOMYCIN C INSIDE LONG CIRCULATING HYALURONAN TARGETED NANO-LIPOSOMES INCREASES ITS ANTITUMOR ACTIVITY. 2004;789(August 2003):780-789. doi:10.1002/ijc.11615

91. An RLOT, Avraham RAZ. Lectins in Cancer Cells. (Box 108).

92. Liu F-T, Rabinovich GA. Galectins as modulators of tumour progression. *Nat Rev Cancer*. 2005;5(1):29-41. doi:10.1038/nrc1527

93. Mannori G, Santoro D, Carter L, Corless C, Nelson RM, Bevilacqua MP. Inhibition of colon carcinoma cell lung colony formation by a soluble form of E-selectin. *Am J Pathol*. 1997;151(1):233-243. https://www.ncbi.nlm.nih.gov/pubmed/9212748.

94. Lobel P, Dahmss NM, Kornfeld S, Louis S. Cloning and Sequence Analysis of the Cation-independent Mannose 6-Phosphate Receptor*. 1988;263(5):2563-2570.

95. Ghosh P, Dahms NM, Kornfeld S. MANNOSE 6-PHOSPHATE RECEPTORS : NEW TWISTS IN THE TALE. 2003;4(MARCH):6-9. doi:10.1038/nrm1050
96. Pohlmann R, Nagel G, Schmidt B, et al. Cloning of a cDNA encoding the human cation-dependent mannose 6-phosphate-specific receptor X-. 1987;84(August):5575-5579.
97. Kornfeld S. STRUCTURE AND FUNCTION OF THE MANNOSE 6-PHOSPHATE/INSULINLIKE GROWTH FACTOR II RECEPTORS. *Annu Rev Biochem*. 1992;61(1):307-330. doi:10.1146/annurev.bi.61.070192.001515
98. Dahms NM, Lobel P, Breitmeyer J, Chirgwin JM, Kornfeld S. 46 kd mannose 6-phosphate receptor: cloning, expression, and homology to the 215 kd mannose 6-phosphate receptor. *Cell*. 1987;50(2):181-192. doi:10.1016/0092-8674(87)90214-5
99. Collawn JF, Kuhn LA, Liu LF, Tainer JA, Trowbridge IS. Transplanted LDL and mannose-6-phosphate receptor internalization signals promote high-efficiency endocytosis of the transferrin receptor. *EMBO J*. 1991;10(11):3247-3253.
100. Stein M, Zijderhand-Bleekemolen JE, Geuze H, Hasilik A, von Figura K. Mr 46,000 mannose 6-phosphate specific receptor: its role in targeting of lysosomal enzymes. *EMBO J*. 1987;6(9):2677-2681. https://www.ncbi.nlm.nih.gov/pubmed/2960521.
101. Ghosh P, Dahms NM, Kornfeld S. Mannose 6-phosphate receptors: new twists in the tale. *Nat Rev Mol Cell Biol*. 2003;4(3):202-212. doi:10.1038/nrm1050
102. Oshima A, Nolan CM, Kyle JW, Grubb JH, Sly WS. The human cation-independent mannose 6-phosphate receptor. Cloning and sequence of the full-length cDNA and expression of functional receptor in COS cells. *J Biol Chem*. 1988;263(5):2553-2562.
103. Sahagiansq GG, Steer CJ. Transmembrane Orientation of the Mannose 6-Phosphate Receptor in Isolated Clathrin-coated Vesicles *. 1985;260(17):9838-9842.
104. Byrd JC, Macdonald RG, Macdonald RG. *JBC Papers in Press. Published on April 11, 2000 as Manuscript M000010200*.; 2000.
105. Berbis P. [Retinoids: mechanisms of action]. *Ann Dermatol Venereol*. 2010;137 Suppl 3:S97-103. doi:10.1016/S0151-9638(10)70036-3
106. Dahms NM, Olson LJ, Kim J-JP. Strategies for carbohydrate recognition by the mannose 6-phosphate receptors. *Glycobiology*. 2008;18(9):664-678. doi:10.1093/glycob/cwn061
107. Kang JX, Bell J, Leaf A, Beard RL, Chandraratna RA. Retinoic acid alters the intracellular trafficking of the mannose-6-phosphate/insulin-like growth factor II receptor and lysosomal enzymes. *Proc Natl Acad Sci U S A*. 1998;95(23):13687-13691. doi:10.1073/pnas.95.23.13687
108. Nolan CM, Kyle JW, Watanabe H, Sly WS. Binding of insulin-like growth factor II

(IGF-II) by human cation-independent mannose 6-phosphate receptor/IGF-II receptor expressed in receptor-deficient mouse L cells. *Cell Regul*. 1990;1(2):197-213. doi:10.1091/mbc.1.2.197

109. Mathieu M, Rochefort H, Barenton B, Prebois C, Vignon F. Interactions of Cathepsin-D and Insulin-Like Growth Factor-II (IGF-II) on the IGF-II/Mannose-6-Phosphate Receptor in Human Breast CancerCells and Possible Consequences on Mitogenic Activity of IGF-II. *Mol Endocrinol*. 1990;4(9):1327-1335. doi:10.1210/mend-4-9-1327
110. Ludwig T, Eggenschwiler J, Fisher P, D'Ercole AJ, Davenport ML, Efstratiadis A. Mouse mutants lacking the type 2 IGF receptor (IGF2R) are rescued from perinatal lethality in Igf2 and Igf1r null backgrounds. *Dev Biol*. 1996;177(2):517-535. doi:10.1006/dbio.1996.0182
111. Wang ZQ, Fung MR, Barlow DP, Wagner EF. Regulation of embryonic growth and lysosomal targeting by the imprinted Igf2/Mpr gene. *Nature*. 1994;372(6505):464-467. doi:10.1038/372464a0
112. Lau MM, Stewart CE, Liu Z, Bhatt H, Rotwein P, Stewart CL. Loss of the imprinted IGF2/cation-independent mannose 6-phosphate receptor results in fetal overgrowth and perinatal lethality. *Genes Dev*. 1994;8(24):2953-2963. doi:10.1101/gad.8.24.2953
113. Westlund B, Dahms NM, Kornfeld S. The bovine mannose 6-phosphate/insulin-like growth factor II receptor. Localization of mannose 6-phosphate binding sites to domains 1-3 and 7-11 of the extracytoplasmic region. *J Biol Chem*. 1991;266(34):23233-23239.
114. Olson LJ, Castonguay AC, Lasanajak Y, et al. Identification of a fourth mannose 6-phosphate binding site in the cation-independent mannose 6-phosphate receptor. *Glycobiology*. 2015;25(6):591-606. doi:10.1093/glycob/cwv001
115. Gary-bobo M, Nirdé P, Jeanjean A, et al. Mannose 6-phosphate receptor targeting and its applications in human diseases . To cite this version : HAL Id : inserm-00230130. 2009.
116. Zimmermann R, Eyrisch S, Ahmad M, Helms V. Protein translocation across the ER membrane. *Biochim Biophys Acta - Biomembr*. 2011;1808(3):912-924. doi:https://doi.org/10.1016/j.bbamem.2010.06.015
117. Kornfeld S. Trafficking of lysosomal enzymes in normal and disease states. *J Clin Invest*. 1986;77(1):1-6. doi:10.1172/JCI112262
118. Schwarz F, Aebi M. Mechanisms and principles of N-linked protein glycosylation. *Curr Opin Struct Biol*. 2011;21(5):576-582. doi:https://doi.org/10.1016/j.sbi.2011.08.005
119. Sahagian GG. The mannose 6-phosphate receptor: function, biosynthesis and

translocation. *Biol cell*. 1984;51(2):207-214.

120. Gonzalez-Noriega A, Grubb JH, Talkad V, Sly WS. Chloroquine inhibits lysosomal enzyme pinocytosis and enhances lysosomal enzyme secretion by impairing receptor recycling. *J Cell Biol*. 1980;85(3):839-852. doi:10.1083/jcb.85.3.839
121. Dahms NM, Lobel P, Kornfeld S. Mannose 6-phosphate receptors and lysosomal enzyme targeting. *J Biol Chem*. 1989;264(21):12115-12118.
122. Jadot M, Canfield WM, Gregory W, Kornfeld S. Characterization of the signal for rapid internalization of the bovine mannose 6-phosphate/insulin-like growth factor-II receptor. *J Biol Chem*. 1992;267(16):11069-11077.
123. Meresse, S.; Bauer, U.; Ludwig, T.; Mauxion, F.; Schmidt, A.; Hoflack, B. Bases moléculaires du transport vers les lysosomes. *Med Sci*. 1993;Vol. 9(N° 2):p.148-156.
124. DEDUVE C. FROM CYTASES TO LYSOSOMES. *Fed Proc*. 1964;23:1045-1049.
125. Beck M. Treatment strategies for lysosomal storage disorders. 2017:13-18. doi:10.1111/dmcn.13600
126. Jeanjean A, Garcia M, Leydet A, Montero J-L, Morère A. Synthesis and receptor binding affinity of carboxylate analogues of the mannose 6-phosphate recognition marker. *Bioorg Med Chem*. 2006;14(10):3575-3582. doi:https://doi.org/10.1016/j.bmc.2006.01.024
127. Desnick RJ. Enzyme replacement and enhancement therapies for lysosomal diseases. *J Inherit Metab Dis*. 2004;27(3):385-410. doi:10.1023/B:BOLI.0000031101.12838.c6
128. Wyatt K, Henley W, Anderson L, et al. The effectiveness and cost of enzyme replacement and substrate reduction therapies : a longitudinal cohort study of people with lysosomal storage disorders. 2012;16(39).
129. De Souza AT, Hankins GR, Washington MK, Fine RL, Orton TC, Jirtle RL. Frequent loss of heterozygosity on 6q at the mannose 6-phosphate/insulin-like growth factor II receptor locus in human hepatocellular tumors. *Oncogene*. 1995;10(9):1725-1729.
130. Hankins GR, De Souza AT, Bentley RC, et al. M6P/IGF2 receptor: a candidate breast tumor suppressor gene. *Oncogene*. 1996;12(9):2003-2009.
131. Kong FM, Anscher MS, Washington MK, Killian JK, Jirtle RL. M6P/IGF2R is mutated in squamous cell carcinoma of the lung. *Oncogene*. 2000;19(12):1572-1578. doi:10.1038/sj.onc.1203437
132. Rey JM, Theillet C, Brouillet JP, Rochefort H. Stable amino-acid sequence of the mannose-6-phosphate/insulin-like growth-factor-II receptor in ovarian carcinomas with

loss of heterozygosity and in breast-cancer cell lines. *Int J cancer*. 2000;85(4):466-473. doi:10.1002/(sici)1097-0215(20000215)85:4<466::aid-ijc4>3.0.co;2-2

133. Leboulleux S, Gaston V, Boulle N, Le Bouc Y, Gicquel C. Loss of heterozygosity at the mannose 6-phosphate/insulin-like growth factor 2 receptor locus: a frequent but late event in adrenocortical tumorigenesis. *Eur J Endocrinol*. 2001;144(2):163-168.
134. Probst OC, Puxbaum V, Svoboda B, et al. The mannose 6-phosphate/insulin-like growth factor II receptor restricts the tumourigenicity and invasiveness of squamous cell carcinoma cells. *Int J cancer*. 2009;124(11):2559-2567. doi:10.1002/ijc.24236
135. Hebert E, Herbelin C, Bougnoux P. Analysis of the IGF-II receptor gene copy number in breast carcinoma. *Br J Cancer*. 1994;69(1):120-124. doi:10.1038/bjc.1994.19
136. Ishiwata T, Bergmann U, Kornmann M, Lopez M, Beger HG, Korc M. Altered expression of insulin-like growth factor II receptor in human pancreatic cancer. *Pancreas*. 1997;15(4):367-373.
137. Paper O. Gastric cancer : the role of insulin-like growth factor 2 (IGF 2) and its receptors (IGF 1R and M6-P / IGF 2R). 2003;2(September):430-438. doi:10.1002/path.1465
138. Laube F. Mannose-6-phosphate/insulin-like growth factor-II receptor in human melanoma cells: effect of ligands and antibodies on the receptor expression. *Anticancer Res*. 2009;29(4):1383-1388.
139. Vaillant O, Cheikh K El, Warther D, et al. Mannose-6-phosphate receptor: A target for theranostics of prostate cancer. *Angew Chemie - Int Ed*. 2015;54(20):5952-5956. doi:10.1002/anie.201500286
140. Prakash J, Beljaars L, Harapanahalli AK, Zeinstra-smith M, Jager-krikken A De. Tumor-targeted intracellular delivery of anticancer drugs through the mannose-6-phosphate/insulin-like growth factor II receptor. 2010;1981:1966-1981. doi:10.1002/ijc.24914
141. https://www.who.int/cancer/children/faq/fr/.
142. De RN des C. http://rnce.vjf.inserm.fr/index.php/fr/statistiques.
143. http://sfce.sfpediatrie.com/page/les-cancers-de-lenfant.
144. Priorities DC, Edition T. Cancer.
145. Steliarova-Foucher E, Colombet M, Ries LAG, et al. International incidence of childhood cancer, 2001-10: a population-based registry study. *Lancet Oncol*. 2017;18(6):719-731. doi:10.1016/S1470-2045(17)30186-9
146. Cancer IN du. *Soins En Cancérologie > 141*.
147. Steliarova-foucher E, Stiller C, Sc M, Lacour B, Kaatsch P, Ph D. International

Classification of Childhood Cancer , Third Edition. 2005;(February). doi:10.1002/cncr.20910

148. http://www.infosarcomes.org.

149. Li FP, Fraumeni JFJ. Soft-tissue sarcomas, breast cancer, and other neoplasms. A familial syndrome? *Ann Intern Med*. 1969;71(4):747-752. doi:10.7326/0003-4819-71-4-747

150. Diller L, Sexsmith E, Gottlieb A, Li FP, Malkin D. Germline p53 mutations are frequently detected in young children with rhabdomyosarcoma. *J Clin Invest*. 1995;95(4):1606-1611. doi:10.1172/JCI117834

151. Sung L, Anderson JR, Arndt C, Raney RB, Meyer WH, Pappo AS. Neurofibromatosis in children with Rhabdomyosarcoma: a report from the Intergroup Rhabdomyosarcoma study IV. *J Pediatr*. 2004;144(5):666-668. doi:10.1016/j.jpeds.2004.02.026

152. Steenman M, Westerveld A, Mannens M. Genetics of Beckwith-Wiedemann syndrome-associated tumors: common genetic pathways. *Genes Chromosomes Cancer*. 2000;28(1):1-13.

153. Hennekam RCM. Costello syndrome: an overview. *Am J Med Genet C Semin Med Genet*. 2003;117C(1):42-48. doi:10.1002/ajmg.c.10019

154. Dasgupta R, Fuchs J, Rodeberg D. Seminars in Pediatric Surgery Rhabdomyosarcoma. 2016;25:276-283. doi:10.1053/j.sempedsurg.2016.09.011

155. Rengaswamy V, Kontny U, Rössler J. New approaches for pediatric rhabdomyosarcoma drug discovery: targeting combinatorial signaling. *Expert Opin Drug Discov*. 2011;6(10):1103-1125. doi:10.1517/17460441.2011.611498

156. Ognjanovic S, Linabery AM, Charbonneau B, Ross JA. Trends in childhood rhabdomyosarcoma incidence and survival in the United States, 1975-2005. *Cancer*. 2009;115(18):4218-4226. doi:10.1002/cncr.24465

157. Barr FG. Gene fusions involving PAX and FOX family members in alveolar rhabdomyosarcoma. *Oncogene*. 2001;20(40):5736-5746. doi:10.1038/sj.onc.1204599

158. Kuang S, Chargé SB, Seale P, Huh M, Rudnicki MA. Distinct roles for Pax7 and Pax3 in adult regenerative myogenesis. *J Cell Biol*. 2006;172(1):103 LP - 113. doi:10.1083/jcb.200508001

159. Brzoska E, Przewozniak M, Grabowska I, Janczyk-Ilach K, Moraczewski J. Pax3 and Pax7 expression during myoblast differentiation in vitro and fast and slow muscle regeneration in vivo. *Cell Biol Int*. 2009;33(4):483-492. doi:10.1016/j.cellbi.2008.11.015

160. Eijkelenboom A, Burgering BMT. FOXOs: signalling integrators for homeostasis maintenance. *Nat Rev Mol Cell Biol*. 2013;14:83. https://doi.org/10.1038/nrm3507.

161. Zhan S, Shapiro DN, Helman LJ. Activation of an imprinted allele of the insulin-like growth factor II gene implicated in rhabdomyosarcoma. *J Clin Invest*. 1994;94(1):445-448. doi:10.1172/JCI117344

162. Visser M, Sijmons C, Bras J, et al. Allelotype of pediatric rhabdomyosarcoma. *Oncogene*. 1997;15(11):1309-1314. doi:10.1038/sj.onc.1201302

163. Charytonowicz E, Cordon-Cardo C, Matushansky I, Ziman M. Alveolar rhabdomyosarcoma: is the cell of origin a mesenchymal stem cell? *Cancer Lett*. 2009;279(2):126-136. doi:10.1016/j.canlet.2008.09.039

164. Lisboa S, Cerveira N, Vieira J, et al. Genetic diagnosis of alveolar rhabdomyosarcoma in the bone marrow of a patient without evidence of primary tumor. *Pediatr Blood Cancer*. 2008;51(4):554-557. doi:10.1002/pbc.21646

165. Bober E, Lyons GE, Braun T, Cossu G, Buckingham M, Arnold HH. The muscle regulatory gene, Myf-6, has a biphasic pattern of expression during early mouse development. *J Cell Biol*. 1991;113(6):1255-1265. doi:10.1083/jcb.113.6.1255

166. Walters ZS, Villarejo-Balcells B, Olmos D, et al. JARID2 is a direct target of the PAX3-FOXO1 fusion protein and inhibits myogenic differentiation of rhabdomyosarcoma cells. *Oncogene*. 2014;33(9):1148-1157. doi:10.1038/onc.2013.46

167. Rossi S, Stoppani E, Puri PL, Fanzani A. Differentiation of human rhabdomyosarcoma RD cells is regulated by reciprocal, functional interactions between myostatin, p38 and extracellular regulated kinase signalling pathways. *Eur J Cancer*. 2011;47(7):1095-1105. doi:10.1016/j.ejca.2010.12.010

168. Sun X, Guo W, Shen JK, Mankin HJ, Hornicek FJ, Duan Z. Rhabdomyosarcoma: Advances in Molecular and Cellular Biology. *Sarcoma*. 2015;2015:232010. doi:10.1155/2015/232010

169. Rengaswamy V, Kontny U, Jochen R. combinatorial signaling New approaches for pediatric rhabdomyosarcoma drug discovery : targeting combinatorial signaling. 2016;(October 2011). doi:10.1517/17460441.2011.611498

170. Schaaf GJ, Ruijter JM, Ruissen F Van, et al. Full transcriptome analysis of rhabdomyosarcoma, normal and fetal skeletal muscle: statistical comparison of multiple SAGE libraries. 2005;26:1-26.

171. Ciesla M, Dulak J, Jozkowicz A. MicroRNAs and epigenetic mechanisms of rhabdomyosarcoma development. *Int J Biochem Cell Biol*. 2014;53:482-492.

doi:10.1016/j.biocel.2014.05.003

172. Zhang M, Truscott J, Davie J. Loss of MEF2D expression inhibits differentiation and contributes to oncogenesis in rhabdomyosarcoma cells. *Mol Cancer*. 2013;12(1):150. doi:10.1186/1476-4598-12-150
173. https://www.mayoclinic.org/diseases-conditions/rhabdomyosarcoma/symptoms-causes/syc-20390962.
174. Dagher R, Helman L. Rhabdomyosarcoma: an overview. *Oncologist*. 1999;4(1):34-44.
175. Sebire NJ, Malone M. Myogenin and MyoD1 expression in paediatric rhabdomyosarcomas. *J Clin Pathol*. 2003;56(6):412-416. doi:10.1136/jcp.56.6.412
176. Parham DM, Barr FG. Classification of rhabdomyosarcoma and its molecular basis. *Adv Anat Pathol*. 2013;20(6):387-397. doi:10.1097/PAP.0b013e3182a92d0d
177. Barr FG, Qualman SJ, Macris MH, et al. Genetic heterogeneity in the alveolar rhabdomyosarcoma subset without typical gene fusions. *Cancer Res*. 2002;62(16):4704-4710.
178. http://sarcomahelp.org.
179. Brierley J, Staging NCI of CC on C. The evolving TNM cancer staging system: an essential component of cancer care. *CMAJ*. 2006;174(2):155-156. doi:10.1503/cmaj.045113
180. Lawrence WJ, Anderson JR, Gehan EA, Maurer H. Pretreatment TNM staging of childhood rhabdomyosarcoma: a report of the Intergroup Rhabdomyosarcoma Study Group. Children's Cancer Study Group. Pediatric Oncology Group. *Cancer*. 1997;80(6):1165-1170.
181. Crist WM, Garnsey L, Beltangady MS, et al. Prognosis in children with rhabdomyosarcoma: a report of the intergroup rhabdomyosarcoma studies I and II. Intergroup Rhabdomyosarcoma Committee. *J Clin Oncol*. 1990;8(3):443-452. doi:10.1200/JCO.1990.8.3.443
182. Crist W, Gehan EA, Ragab AH, et al. The Third Intergroup Rhabdomyosarcoma Study. *J Clin Oncol*. 1995;13(3):610-630. doi:10.1200/JCO.1995.13.3.610
183. Crist WM, Anderson JR, Meza JL, et al. Intergroup rhabdomyosarcoma study-IV: results for patients with nonmetastatic disease. *J Clin Oncol*. 2001;19(12):3091-3102. doi:10.1200/JCO.2001.19.12.3091
184. https://www.gustaveroussy.fr/fr/rhabdomyosarcome.
185. Meza JL, Anderson J, Pappo AS, Meyer WH. Analysis of Prognostic Factors in Patients With Nonmetastatic Rhabdomyosarcoma Treated on Intergroup Rhabdomyosarcoma

Studies III and IV: The Children's Oncology Group. *J Clin Oncol*. 2006;24(24):3844-3851. doi:10.1200/JCO.2005.05.3801

186. Raney RB, Walterhouse DO, Meza JL, et al. Results of the Intergroup Rhabdomyosarcoma Study Group D9602 protocol, using vincristine and dactinomycin with or without cyclophosphamide and radiation therapy, for newly diagnosed patients with low-risk embryonal rhabdomyosarcoma: a report from the Soft Tissue Sarcoma Committee of the Children's Oncology Group. *J Clin Oncol*. 2011;29(10):1312-1318. doi:10.1200/JCO.2010.30.4469
187. Arndt CAS, Stoner JA, Hawkins DS, et al. Vincristine, actinomycin, and cyclophosphamide compared with vincristine, actinomycin, and cyclophosphamide alternating with vincristine, topotecan, and cyclophosphamide for intermediate-risk rhabdomyosarcoma: children's oncology group study D9803. *J Clin Oncol*. 2009;27(31):5182-5188. doi:10.1200/JCO.2009.22.3768
188. Malempati S, Hawkins DS. Rhabdomyosarcoma: review of the Children's Oncology Group (COG) Soft-Tissue Sarcoma Committee experience and rationale for current COG studies. *Pediatr Blood Cancer*. 2012;59(1):5-10. doi:10.1002/pbc.24118
189. Breneman JC, Lyden E, Pappo AS, et al. Prognostic factors and clinical outcomes in children and adolescents with metastatic rhabdomyosarcoma--a report from the Intergroup Rhabdomyosarcoma Study IV. *J Clin Oncol*. 2003;21(1):78-84. doi:10.1200/JCO.2003.06.129
190. https://www.cancer.ca.
191. http://www.ihope.fr.
192. https://www.orpha.net.
193. Stevens MCG, Rey A, Bouvet N, et al. Treatment of nonmetastatic rhabdomyosarcoma in childhood and adolescence: third study of the International Society of Paediatric Oncology--SIOP Malignant Mesenchymal Tumor 89. *J Clin Oncol*. 2005;23(12):2618-2628. doi:10.1200/JCO.2005.08.130
194. Rich DC, Corpron CA, Smith MB, Black CT, Lally KP, Andrassy RJ. Second malignant neoplasms in children after treatment of soft tissue sarcoma. *J Pediatr Surg*. 1997;32(2):369-372. doi:10.1016/s0022-3468(97)90213-x
195. Xaney B, Heyn R, Hays DM, Rena I, Maurer HM, D M. Sequelae of Treatment in 109 Patients Followed for 5 to 15 Years after Diagnosis of Sarcoma of the Bladder and Prostate A Report from the Intergroup Rhabdomyosarcoma Study Committee. 1993:2387-2394.

196. Raney B, Ensign LG, Foreman J, et al. Renal toxicity of ifosfamide in pilot regimens of the intergroup rhabdomyosarcoma study for patients with gross residual tumor. *Am J Pediatr Hematol Oncol*. 1994;16(4):286-295.
197. Crose LES, Linardic CM. Receptor tyrosine kinases as therapeutic targets in rhabdomyosarcoma. *Sarcoma*. 2011;2011:756982. doi:10.1155/2011/756982
198. Melguizo C, Prados J, Rama ANAR, et al. Multidrug resistance and rhabdomyosarcoma (Review). 2011:755-761. doi:10.3892/or.2011.1347
199. Erp AEM Van, Versleijen-jonkers YMH, Graaf WTA Van Der, Fleuren EDG. Targeted Therapy – based Combination Treatment in Rhabdomyosarcoma. 2018. doi:10.1158/1535-7163.MCT-17-1131
200. Maulik G, Shrikhande A, Kijima T, Ma PC, Morrison PT, Salgia R. Role of the hepatocyte growth factor receptor, c-Met, in oncogenesis and potential for therapeutic inhibition. *Cytokine Growth Factor Rev*. 2002;13(1):41-59.
201. Wieduwilt MJ, Moasser MM. Review The epidermal growth factor receptor family : Biology driving targeted therapeutics. 2008;65:1566-1584. doi:10.1007/s00018-008-7440-8
202. Martins AS, Olmos D, Missiaglia E, Shipley J. Targeting the insulin-like growth factor pathway in rhabdomyosarcomas: rationale and future perspectives. *Sarcoma*. 2011;2011:209736. doi:10.1155/2011/209736
203. Tiong KH, Mah LY, Leong C-O. Functional roles of fibroblast growth factor receptors (FGFRs) signaling in human cancers. *Apoptosis*. 2013;18(12):1447-1468. doi:10.1007/s10495-013-0886-7
204. Cao L, Yu Y, Bilke S, et al. Genome-wide identification of PAX3-FKHR binding sites in rhabdomyosarcoma reveals candidate target genes important for development and cancer. *Cancer Res*. 2010;70(16):6497-6508. doi:10.1158/0008-5472.CAN-10-0582
205. van der Ploeg AT, Reuser AJJ. Pompe's disease. *Lancet (London, England)*. 2008;372(9646):1342-1353. doi:10.1016/S0140-6736(08)61555-X
206. Pompe JC. Over idiopathische hypertrophie van het hart. *Ned Tijdschr Geneeskd*. 1932;76:304-311.
207. HERS HG. alpha-Glucosidase deficiency in generalized glycogenstorage disease (Pompe's disease). *Biochem J*. 1963;86(1):11-16. doi:10.1042/bj0860011
208. Kroos M, Hoogeveen-westerveld M, Ploeg ANSVANDER, Reuser AJJ. The Genotype – Phenotype Correlation in Pompe Disease. 2012;68:59-68. doi:10.1002/ajmc.31318
209. De Filippi P, Saeidi K, Ravaglia S, et al. Genotype-phenotype correlation in Pompe

disease, a step forward. *Orphanet J Rare Dis*. 2014;9:102. doi:10.1186/s13023-014-0102-z

210. Hermans MMP, van Leenen D, Kroos MA, et al. Twenty-two novel mutations in the lysosomal alpha-glucosidase gene (GAA) underscore the genotype-phenotype correlation in glycogen storage disease type II. *Hum Mutat*. 2004;23(1):47-56. doi:10.1002/humu.10286
211. Stenson PD, Mort M, Ball E V, Shaw K, Phillips A, Cooper DN. The Human Gene Mutation Database: building a comprehensive mutation repository for clinical and molecular genetics, diagnostic testing and personalized genomic medicine. *Hum Genet*. 2014;133(1):1-9. doi:10.1007/s00439-013-1358-4
212. https://www.afm-telethon.fr.
213. Gungor D, Reuser AJJ. How to describe the clinical spectrum in Pompe disease? *Am J Med Genet A*. 2013;161A(2):399-400. doi:10.1002/ajmg.a.35662
214. Thurberg BL, Lynch Maloney C, Vaccaro C, et al. Characterization of pre- and post-treatment pathology after enzyme replacement therapy for Pompe disease. *Lab Invest*. 2006;86(12):1208-1220. doi:10.1038/labinvest.3700484
215. Halldorson J, Kazi Z, Mekeel K, et al. Successful combined liver / kidney transplantation from a donor with Pompe disease. *Mol Genet Metab*. 2015;115(4):141-144. doi:10.1016/j.ymgme.2015.05.007
216. Badadani M. Autophagy Mechanism , Regulation , Functions , and Disorders. 2012;2012(2). doi:10.5402/2012/927064
217. Nascimbeni AC, Fanin M, Masiero E, Angelini C, Sandri M. The role of autophagy in the pathogenesis of glycogen storage disease type II (GSDII). *Cell Death Differ*. 2012;19(10):1698-1708. doi:10.1038/cdd.2012.52
218. Raben N, Ralston E, Chien Y-H, et al. Differences in the predominance of lysosomal and autophagic pathologies between infants and adults with Pompe disease: implications for therapy. *Mol Genet Metab*. 2010;101(4):324-331. doi:10.1016/j.ymgme.2010.08.001
219. Tsuburaya RS, Monma K, Oya Y, et al. Acid phosphatase-positive globular inclusions is a good diagnostic marker for two patients with adult-onset Pompe disease lacking disease specific pathology. *Neuromuscul Disord*. 2012;22(5):389-393. doi:10.1016/j.nmd.2011.11.003
220. Bali DS, Tolun AA, Goldstein JL, Dai J, Kishnani PS. Molecular analysis and protein processing in late-onset Pompe disease patients with low levels of acid alpha-glucosidase activity. *Muscle Nerve*. 2011;43(5):665-670. doi:10.1002/mus.21933

221. Hirschhorn R, Reuser AJJ. Type II : Acid a -Glucosidase (Acid Maltase) Deficiency.
222. Chen YT, Amalfitano A. Towards a molecular therapy for glycogen storage disease type II (Pompe disease). *Mol Med Today*. 2000;6(6):245-251.
223. Limongelli G, Fratta F. S1.4 Cardiovascular involvement in Pompe disease. *Acta Myol*. 2011;30(3):202-203. https://www.ncbi.nlm.nih.gov/pmc/articles/PMC3298106/.
224. Slonim AE, Bulone L, Ritz S, Goldberg T, Chen A, Martiniuk F. Identification of two subtypes of infantile acid maltase deficiency. *J Pediatr*. 2000;137(2):283-285. doi:10.1067/mpd.2000.107112
225. Kishnani PS, Steiner RD, Bali D, et al. Pompe disease diagnosis and management guideline. *Genet Med*. 2006;8(5):267-288. doi:10.109701.gim.0000218152.87434.f3
226. Howell RR, Byrne B, Darras BT, Kishnani P, Nicolino M, van der Ploeg A. Diagnostic challenges for Pompe disease: An under-recognized cause of floppy baby syndrome. *Genet Med*. 2006;8(5):289-296. doi:10.1097/01.gim.0000204462.42910.b8
227. Katzin LW, Amato AA. Pompe disease: a review of the current diagnosis and treatment recommendations in the era of enzyme replacement therapy. *J Clin Neuromuscul Dis*. 2008;9(4):421-431. doi:10.1097/CND.0b013e318176dbe4
228. Diagnostic criteria for late-onset (childhood and adult) Pompe disease. *Muscle Nerve*. 2009;40(1):149-160. doi:10.1002/mus.21393
229. Goldstein JL, Young SP, Changela M, et al. Screening for Pompe disease using a rapid dried blood spot method: experience of a clinical diagnostic laboratory. *Muscle Nerve*. 2009;40(1):32-36. doi:10.1002/mus.21376
230. Schoser B. Muscle Biopsy as a Diagnostic Tool in Pompe Disease. *Clin Ther*. 2011;33(6):S6. doi:10.1016/j.clinthera.2011.05.084
231. Schoser B, Müller-Höcker J, Horvath R, et al. Adult-onset glycogen storage disease type 2: Clinico-pathological phenotype revisited. *Neuropathol Appl Neurobiol*. 2007;33:544-559. doi:10.1111/j.1365-2990.2007.00839.x
232. Golsari A, Nasimzadah A, Thomalla G, Keller S, Gerloff C. Prevalence of adult Pompe disease in patients with proximal myopathic syndrome and undiagnosed muscle biopsy. *Neuromuscul Disord*. 2018;28(3):257-261. doi:10.1016/j.nmd.2017.12.001
233. Escobar LF, Wagner S, Tucker M, Wareham J. Neonatal presentation of lethal neuromuscular glycogen storage disease type IV. *J Perinatol*. 2012;32:810-813. doi:10.1038/jp.2011.178
234. Martiniuk F, Chen A, Mack A, et al. Carrier frequency for glycogen storage disease type II in New York and estimates of affected individuals born with the disease. *Am J Med*

Genet. 1998;79(1):69-72.

235. Loonen MC, Schram AW, Koster JF, et al. Identification of heterozygotes for glycogenosis 2 (acid maltase deficiency). *Clin Genet*. 1981;19(1):55-63.
236. Banugaria SG, Prater SN, Ng Y-K, et al. The impact of antibodies on clinical outcomes in diseases treated with therapeutic protein: lessons learned from infantile Pompe disease. *Genet Med*. 2011;13(8):729-736. doi:10.1097/GIM.0b013e3182174703
237. Bali DS, Goldstein JL, Banugaria S, et al. Predicting cross-reactive immunological material (CRIM) status in Pompe disease using GAA mutations: lessons learned from 10 years of clinical laboratory testing experience. *Am J Med Genet C Semin Med Genet*. 2012;160C(1):40-49. doi:10.1002/ajmg.c.31319
238. Uni- D, Carolina N. Pompe disease in infants and children. 2004.
239. Sawabe S, Hara K, Maekawa M. [High creatine kinase MB concentration and activity in patients with rhabdomyosarcoma]. *Rinsho Byori*. 1999;47(11):1079-1082.
240. https://rarediseases.org/rare-diseases/pompe-disease/.
241. http://products.sanofi.ca/fr/myozyme-fr.pdf.
242. Kishnani PS, Hwu W-L, Mandel H, Nicolino M, Yong F, Corzo D. A retrospective, multinational, multicenter study on the natural history of infantile-onset Pompe disease. *J Pediatr*. 2006;148(5):671-676. doi:10.1016/j.jpeds.2005.11.033
243. Kishnani PS, Corzo D, Nicolino M, et al. Recombinant human acid [alpha]-glucosidase: major clinical benefits in infantile-onset Pompe disease. *Neurology*. 2007;68(2):99-109. doi:10.1212/01.wnl.0000251268.41188.04
244. Banugaria SG, Prater SN, McGann JK, et al. Bortezomib in the rapid reduction of high sustained antibody titers in disorders treated with therapeutic protein: lessons learned from Pompe disease. *Genet Med*. 2013;15(2):123-131. doi:10.1038/gim.2012.110
245. Kohler L, Puertollano R, Raben N. Pompe Disease : From Basic Science to Therapy Pompe Disease : From Basic Science to Therapy. 2018;(August). doi:10.1007/s13311-018-0655-y
246. Schoser B, Stewart A, Kanters S, et al. Survival and long-term outcomes in late-onset Pompe disease following alglucosidase alfa treatment: a systematic review and meta-analysis. *J Neurol*. 2017;264(4):621-630. doi:10.1007/s00415-016-8219-8
247. Anderson LJ, Henley W, Wyatt KM, et al. Effectiveness of enzyme replacement therapy in adults with late-onset Pompe disease: results from the NCS-LSD cohort study. *J Inherit Metab Dis*. 2014;37(6):945-952. doi:10.1007/s10545-014-9728-1

248. Wenk J, Hille A, von Figura K. Quantitation of Mr 46000 and Mr 300000 mannose 6-phosphate receptors in human cells and tissues. *Biochem Int*. 1991;23(4):723-731.
249. Peng J, Dalton J, Butt M, et al. Reveglucosidase alfa (BMN 701), an IGF2-Tagged rhAcid alpha-Glucosidase, Improves Respiratory Functional Parameters in a Murine Model of Pompe Disease. *J Pharmacol Exp Ther*. 2017;360(2):313-323. doi:10.1124/jpet.116.235952
250. http://investors.biomarin.com/2016-01-11-BioMarin-Announces-Interim-Analysis-of-INSPIRE-Clinical-Trial-in-Pompe- Disease-at-34th-Annual-J-P-Morgan-Annual-Healthcare-Conference.
251. Khanna R, Flanagan JJ, Feng J, et al. The pharmacological chaperone AT2220 increases recombinant human acid alpha-glucosidase uptake and glycogen reduction in a mouse model of Pompe disease. *PLoS One*. 2012;7(7):e40776. doi:10.1371/journal.pone.0040776
252. https://www.vml-asso.org/maladie-de-pompe-resultats-intermediaire-de-l-essai-clinique-atb200-at2221.
253. https://www.has-sante.fr/upload/docs/application/pdf/2018-04/radiogardase_synthese_ct15788.pdf.
254. Larionova J, Guari Y, Sangregorio C, Gue C. Cyano-bridged coordination polymer nanoparticles. 2009:1177-1190. doi:10.1039/b900918c
255. Catala L, Mallah T. Nanoparticles of Prussian blue analogs and related coordination polymers: From information storage to biomedical applications. *Coord Chem Rev*. 2017;346:32-61. doi:https://doi.org/10.1016/j.ccr.2017.04.005
256. Dujardin BE, Mann S. Morphosynthesis of Molecular Magnetic Materials. 2004;(13):1125-1129. doi:10.1002/adma.200400166
257. Hoffman HA, Chakrabarti L, Dumont MF, Sandler AD, Fernandes R. Prussian blue nanoparticles for laser-induced photothermal therapy of tumors. *RSC Adv*. 2014;4(56):29729-29734. doi:10.1039/C4RA05209A
258. Long J, Guari Y, Guérin C, Larionova J. Prussian blue type nanoparticles for biomedical applications. 2016;45(44). doi:10.1039/c6dt01299j
259. Perrier M, Gallud A, Ayadi A, et al. Investigation of cyano-bridged coordination nanoparticles Gd3+/[Fe(CN)6]3−/D-mannitol as T1-weighted MRI contrast agents. 2015;7(28). doi:10.1039/c5nr01557j
260. Shokouhimehr M, Soehnlen ES, Khitrin A, Basu S, Huang SD. Biocompatible Prussian blue nanoparticles: Preparation, stability, cytotoxicity, and potential use as an MRI

contrast agent. *Inorg Chem Commun*. 2010;13(1):58-61. doi:https://doi.org/10.1016/j.inoche.2009.10.015

261. Perrier M, Busson M, Massasso G, Long J, Boudousq V, Pouget J. 201Tl+-labelled Prussian blue nanoparticles as contrast agents for SPECT scintigraphy. 2014;(ii):13425-13429. doi:10.1039/c4nr03044c
262. Xiaolong Liang, za Zijian Deng, za Lijia Jing, zb Xiaoda Li, b Zhifei Dai a CL and MH. Prussian blue nanoparticles operate as a contrast agent for enhanced photoacoustic imaging. 2013;(207890):11029-11032. doi:10.1039/c3cc42510j
263. Wang S-J, Chen C-S, Chen L-C. Prussian blue nanoparticles as nanocargoes for delivering DNA drugs to cancer cells. *Sci Technol Adv Mater*. 2013;14:44405. doi:10.1088/1468-6996/14/4/044405
264. Lian H, Hu M, Liu C, Wu KC. ChemComm Highly biocompatible , hollow coordination polymer nanoparticles as cisplatin carriers for efficient intracellular drug delivery w. 2012:5151-5153. doi:10.1039/c2cc31708g
265. Him K, Bron P, Oliviero E. In situ synthesis of Prussian blue nanoparticles within a biocompatible reverse micellar system for in vivo Cs + uptake †. 2017:2887-2890. doi:10.1039/c6nj03770d
266. Ho HA, Chakrabarti L, Dumont MF, Sandler D. Prussian blue nanoparticles for laser-induced photothermal therapy of tumors. 2014:29729-29734. doi:10.1039/c4ra05209a
267. Dacarro G, Taglietti A, Pallavicini P. Prussian Blue Nanoparticles as a Versatile Photothermal Tool. *Molecules*. 2018;23(6):1414. doi:10.3390/molecules23061414
268. Bleehen NM. Hyperthermia in the treatment of cancer. *Br J Cancer Suppl*. 1982;5:96-100. https://www.ncbi.nlm.nih.gov/pubmed/6950783.
269. Hildebrandt B, Wust P, Ahlers O, et al. The cellular and molecular basis of hyperthermia. *Crit Rev Oncol Hematol*. 2002;43(1):33-56.
270. Wust P, Hildebrandt B, Sreenivasa G, et al. Hyperthermia in combined treatment of cancer. *Lancet Oncol*. 2002;3(8):487-497.
271. Milleron RS, Bratton SB. "Heated" debates in apoptosis. *Cell Mol Life Sci*. 2007;64(18):2329-2333. doi:10.1007/s00018-007-7135-6
272. Huang X, Jain PK, El-Sayed IH, El-Sayed MA. Plasmonic photothermal therapy (PPTT) using gold nanoparticles. *Lasers Med Sci*. 2007;23(3):217. doi:10.1007/s10103-007-0470-x
273. Feng Y, Fuentes D, Hawkins A, et al. Nanoshell-mediated laser surgery simulation for prostate cancer treatment. *Eng Comput*. 2009;25(1):3-13. doi:10.1007/s00366-008-

0109-y

274. Dickerson EB, Dreaden EC, Huang X, et al. Gold nanorod assisted near-infrared plasmonic photothermal therapy (PPTT) of squamous cell carcinoma in mice. *Cancer Lett*. 2008;269(1):57-66. doi:10.1016/j.canlet.2008.04.026
275. Fu G, Liu W, Feng S, Yue X. Prussian blue nanoparticles operate as a new generation of photothermal ablation agents for cancer therapy. *Chem Commun*. 2012;48(94):11567-11569. doi:10.1039/C2CC36456E
276. https://www.magforce.com.
277. Zou L, Wang H, He B, et al. Current Approaches of Photothermal Therapy in Treating Cancer Metastasis with Nanotherapeutics. *Theranostics*. 2016;6(6):762-772. doi:10.7150/thno.14988
278. Shanmugam V, Selvakumar S, Yeh C-S. Near-infrared light-responsive nanomaterials in cancer therapeutics. *Chem Soc Rev*. 2014;43(17):6254-6287. doi:10.1039/C4CS00011K
279. Sweeney EE, Burga RA, Li C, Zhu Y, Fernandes R. Photothermal therapy improves the efficacy of a MEK inhibitor in neurofibromatosis type 1-associated malignant peripheral nerve sheath tumors. *Nat Publ Gr*. 2016;(October):1-9. doi:10.1038/srep37035
280. Cai X, Jia X, Gao W, et al. A Versatile Nanotheranostic Agent for Efficient Dual-Mode Imaging Guided Synergistic Chemo-Thermal Tumor Therapy. *Adv Funct Mater*. 2015;25(17):2520-2529. doi:10.1002/adfm.201403991
281. Burga RA, Patel S, Bollard CM, Y Cruz CR, Fernandes R. Conjugating Prussian blue nanoparticles onto antigen-specific T cells as a combined nanoimmunotherapy. *Nanomedicine (Lond)*. 2016;11(14):1759-1767. doi:10.2217/nnm-2016-0160
282. Cheng L, Gong H, Zhu W, et al. PEGylated Prussian blue nanocubes as a theranostic agent for simultaneous cancer imaging and photothermal therapy. *Biomaterials*. 2014;35(37):9844-9852. doi:10.1016/j.biomaterials.2014.09.004
283. Zhu W, Liu K, Sun X, et al. Mn2+-Doped Prussian Blue Nanocubes for Bimodal Imaging and Photothermal Therapy with Enhanced Performance. *ACS Appl Mater Interfaces*. 2015;7(21):11575-11582. doi:10.1021/acsami.5b02510
284. Su S, Ding Y, Li Y, Wu Y, Nie G. Integration of photothermal therapy and synergistic chemotherapy by a porphyrin self-assembled micelle confers chemosensitivity in triple-negative breast cancer. *Biomaterials*. 2016;80:169-178. doi:10.1016/j.biomaterials.2015.11.058
285. Li JL, Day D, Gu M. Ultra-Low Energy Threshold for Cancer Photothermal Therapy

Using Transferrin-Conjugated Gold Nanorods. *Adv Mater*. 2008;20(20):3866-3871. doi:10.1002/adma.200800941

286. Melamed JR, Edelstein RS, Day ES. Elucidating the fundamental mechanisms of cell death triggered by photothermal therapy. *ACS Nano*. 2015;9(1):6-11. doi:10.1021/acsnano.5b00021
287. Du C, Wang A, Fei J, Zhao J, Li J. Polypyrrole-stabilized gold nanorods with enhanced photothermal effect towards two-photon photothermal therapy. *J Mater Chem B*. 2015;3(22):4539-4545. doi:10.1039/C5TB00560D
288. Minai L, Yeheskely-Hayon D, Yelin D. High levels of reactive oxygen species in gold nanoparticle-targeted cancer cells following femtosecond pulse irradiation. *Sci Rep*. 2013;3:2146. doi:10.1038/srep02146
289. Vickers ET, Garai M, Bonabi Naghadeh S, et al. Two-Photon Photoluminescence and Photothermal Properties of Hollow Gold Nanospheres for Efficient Theranostic Applications. *J Phys Chem C*. 2018;122(25):13304-13313. doi:10.1021/acs.jpcc.7b09055
290. Chen Z, Fan H, Li J, Tie S, Lan S. Photothermal therapy of single cancer cells mediated by naturally created gold nanorod clusters. *Opt Express*. 2017;25(13):15093-15107. doi:10.1364/OE.25.015093
291. Ye S, Liu Y, Chen S, et al. Photoluminescent properties of Prussian Blue (PB) nanoshells and polypyrrole (PPy)/PB core/shell nanoparticles prepared via miniemulsion (periphery) polymerization. *Chem Commun*. 2011;47(24):6831-6833. doi:10.1039/C1CC11424G
292. Croissant JG, Fatieiev Y, Khashab NM. Degradability and Clearance of Silicon , Organosilica , Silsesquioxane , Silica Mixed Oxide , and Mesoporous Silica Nanoparticles. 2017. doi:10.1002/adma.201604634
293. De Canck E, Ascoop I, Sayari A, Van Der Voort P. Periodic mesoporous organosilicas functionalized with a wide variety of amines for CO2 adsorption. *Phys Chem Chem Phys*. 2013;15(24):9792-9799. doi:10.1039/c3cp50393c
294. Melero JA, Iglesias J, Arsuaga JM, Sainz-Pardo J, de Frutos P, Blazquez S. Synthesis and catalytic activity of organic–inorganic hybrid Ti-SBA-15 materials. *J Mater Chem*. 2007;17(4):377-385. doi:10.1039/B610868G
295. Wu H, Shieh F, Kao H, Chen Y. Benzene-Bridged Periodic Mesoporous Organosilicas Functionalized with. 2013:6358-6367. doi:10.1002/chem.201204400
296. Croissant JG, Cattoën X, Wong Chi Man M, Durand J-O, Khashab NM. Syntheses and

applications of periodic mesoporous organosilica nanoparticles. *Nanoscale*. 2015;7(48):20318-20334. doi:10.1039/C5NR05649G

297. Melde BJ, Holland BT, Blanford CF, Stein A. Mesoporous Sieves with Unified Hybrid Inorganic/Organic Frameworks. *Chem Mater*. 1999;11(11):3302-3308. doi:10.1021/cm9903935
298. Inagaki S, Guan S, Fukushima Y, Ohsuna T, Terasaki O. Novel Mesoporous Materials with a Uniform Distribution of Organic Groups and Inorganic Oxide in Their Frameworks. *J Am Chem Soc*. 1999;121(41):9611-9614. doi:10.1021/ja9916658
299. Asefa T, MacLachlan MJ, Coombs N, Ozin GA. Periodic mesoporous organosilicas with organic groups inside the channel walls. *Nature*. 1999;402(6764):867-871. doi:10.1038/47229
300. Hoffmann F, Cornelius M, Morell J, Fröba M. Silica-Based Mesoporous Organic – Inorganic Hybrid Materials Angewandte. 2006:3216-3251. doi:10.1002/anie.200503075
301. Croissant JG, Zhang D, Alsaiari S, et al. Protein-gold clusters-capped mesoporous silica nanoparticles for high drug loading, autonomous gemcitabine/doxorubicin co-delivery, and in-vivo tumor imaging. *J Control Release*. 2016;229:183-191. doi:10.1016/j.jconrel.2016.03.030
302. Zeiderman MR, Morgan DE, Christein JD, Grizzle WE, McMasters KM, McNally LR. Acidic pH-targeted chitosan capped mesoporous silica coated gold nanorods facilitate detection of pancreatic tumors via multispectral optoacoustic tomography. *ACS Biomater Sci Eng*. 2016;2(7):1108-1120. doi:10.1021/acsbiomaterials.6b00111
303. Zhang Y, Schwerbrock NM, Rogers AB, Kim WY, Huang L. Codelivery of VEGF siRNA and gemcitabine monophosphate in a single nanoparticle formulation for effective treatment of NSCLC. *Mol Ther*. 2013;21(8):1559-1569. doi:10.1038/mt.2013.120
304. Li L, Tong R, Li M, Kohane DS. Self-assembled gemcitabine-gadolinium nanoparticles for magnetic resonance imaging and cancer therapy. *Acta Biomater*. 2016;33:34-39. doi:10.1016/j.actbio.2016.01.039
305. Maksimenko A, Caron J, Mougin J, Desmaële D, Couvreur P. Gemcitabine-based therapy for pancreatic cancer using the squalenoyl nucleoside monophosphate nanoassemblies. *Int J Pharm*. 2015;482(1):38-46. doi:https://doi.org/10.1016/j.ijpharm.2014.11.009
306. Tong PY, Kornfeld S. Ligand interactions of the cation-dependent mannose 6-phosphate receptor. Comparison with the cation-independent mannose 6-phosphate receptor. *J Biol*

Chem. 1989;264(14):7970-7975.

307. Garcia M, Morère A, Gary-Bobo M, et al. COMPOUNDS TARGETING THE CATION-INDEPENDENT MANNOSE 6-PHOSPHATE RECEPTOR. 2011.
308. FITZPATRICK TB, PATHAK MA. Historical aspects of methoxsalen and other furocoumarins. *J Invest Dermatol*. 1959;32(2, Part 2):229-231.
309. Sibata CH, Colussi VC, Oleinick NL, Kinsella TJ. Photodynamic therapy in oncology. *Expert Opin Pharmacother*. 2001;2(6):917-927. doi:10.1517/14656566.2.6.917
310. Luksiene Z. Photodynamic therapy: mechanism of action and ways to improve the efficiency of treatment. *Medicina (Kaunas)*. 2003;39(12):1137-1150.
311. Vrouenraets MB, Visser GWM, Snow GB, van Dongen GAMS. Basic principles, applications in oncology and improved selectivity of photodynamic therapy. *Anticancer Res*. 2003;23(1B):505-522.
312. Oleinick NL, Evans HH. The photobiology of photodynamic therapy: cellular targets and mechanisms. *Radiat Res*. 1998;150(5 Suppl):S146-56.
313. Henderson BW, Dougherty TJ. How does photodynamic therapy work? *Photochem Photobiol*. 1992;55(1):145-157.
314. Sterenborg H, de Wolf J, Koning M, Kruijt B, van den Heuvel A, Robinson D. Phosphorescence-Fluorescence ratio imaging for monitoring the oxygen status during photodynamic therapy. *Opt Express*. 2004;12(9):1873-1878. doi:10.1364/opex.12.001873
315. Ochsner M. Photophysical and photobiological processes in the photodynamic therapy of tumours. *J Photochem Photobiol B*. 1997;39(1):1-18.
316. Castano AP, Demidova TN, Hamblin MR. Mechanisms in photodynamic therapy: part one-photosensitizers, photochemistry and cellular localization. *Photodiagnosis Photodyn Ther*. 2004;1(4):279-293. doi:10.1016/S1572-1000(05)00007-4
317. Matsumura Y, Ananthaswamy HN. Toxic effects of ultraviolet radiation on the skin. *Toxicol Appl Pharmacol*. 2004;195(3):298-308. doi:10.1016/j.taap.2003.08.019
318. Kelkar SS, Reineke TM. Theranostics: Combining Imaging and Therapy. *Bioconjug Chem*. 2011;22(10):1879-1903. doi:10.1021/bc200151q
319. Nyman ES, Hynninen PH. Research advances in the use of tetrapyrrolic photosensitizers for photodynamic therapy. *J Photochem Photobiol B*. 2004;73(1-2):1-28.
320. Raquel D, Almeida Q De, Terra LF, Mauri S. Photodynamic therapy in cancer treatment - an update review. 2019. doi:10.20517/2394-4722.2018.83
321. Cheng S-H, Hsieh C-C, Chen N-T, et al. Well-defined mesoporous nanostructure

modulates three-dimensional interface energy transfer for two-photon activated photodynamic therapy. *Nano Today*. 2011;6(6):552-563. doi:https://doi.org/10.1016/j.nantod.2011.10.003

322. Starkey JR, Rebane AK, Drobizhev MA, et al. New two-photon activated photodynamic therapy sensitizers induce xenograft tumor regressions after near-IR laser treatment through the body of the host mouse. *Clin Cancer Res*. 2008;14(20):6564-6573. doi:10.1158/1078-0432.CCR-07-4162
323. Aggad D, Jimenez M, Dib S, et al. Gemcitabine Delivery and Photodynamic Therapy in Cancer Cells via Porphyrin-Ethylene-Based Periodic Mesoporous Organosilica Nanoparticles. 2018:46-51. doi:10.1002/cnma.201700264
324. Croissant J, Salles D, Maynadier M, et al. Mixed Periodic Mesoporous Organosilica Nanoparticles and Core–Shell Systems, Application to in Vitro Two-Photon Imaging, Therapy, and Drug Delivery. *Chem Mater*. 2014;26(24):7214-7220. doi:10.1021/cm5040276
325. Croissant JG, Picard S, Aggad D, et al. Fluorescent periodic mesoporous organosilica nanoparticles dual-functionalized via click chemistry for two-photon photodynamic therapy in cells. *J Mater Chem B*. 2016;4(33):5567-5574. doi:10.1039/C6TB00638H
326. Groeneveld GJ, Ph D, Herson S, et al. A Randomized Study of Alglucosidase Alfa in Late-Onset Pompe's Disease. 2010.
327. Maga JA, Zhou J, Kambampati R, et al. Glycosylation-independent lysosomal targeting of acid alpha-glucosidase enhances muscle glycogen clearance in pompe mice. *J Biol Chem*. 2013;288(3):1428-1438. doi:10.1074/jbc.M112.438663
328. Zhu Y, Jiang J-L, Gumlaw NK, et al. Glycoengineered acid alpha-glucosidase with improved efficacy at correcting the metabolic aberrations and motor function deficits in a mouse model of Pompe disease. *Mol Ther*. 2009;17(6):954-963. doi:10.1038/mt.2009.37
329. McVie-Wylie AJ, Lee KL, Qiu H, et al. Biochemical and pharmacological characterization of different recombinant acid alpha-glucosidase preparations evaluated for the treatment of Pompe disease. *Mol Genet Metab*. 2008;94(4):448-455. doi:10.1016/j.ymgme.2008.04.009
330. Zhu Y, Li X, McVie-Wylie A, et al. Carbohydrate-remodelled acid alpha-glucosidase with higher affinity for the cation-independent mannose 6-phosphate receptor demonstrates improved delivery to muscles of Pompe mice. *Biochem J*. 2005;389(Pt 3):619-628. doi:10.1042/BJ20050364

331. Cérutti M, Golay J. Lepidopteran cells, an alternative for the production of recombinant antibodies? *MAbs*. 2012;4(3):294-309. doi:10.4161/mabs.19942
332. Aeed PA, Elhammer AP. Glycosylation of Recombinant Prorenin in Insect Cells: The Insect Cell Line Sf9 Does Not Express the Mannose 6-Phosphate Recognition Signal. *Biochemistry*. 1994;33(29):8793-8797. doi:10.1021/bi00195a022
333. Kalia J, Raines RT. Hydrolytic Stability of Hydrazones and Oximes **. 2008:7523-7526. doi:10.1002/anie.200802651
334. El Cheikh K, Basile I, Da Silva A, et al. Design of Potent Mannose 6-Phosphate Analogues for the Functionalization of Lysosomal Enzymes To Improve the Treatment of Pompe Disease. *Angew Chem Int Ed Engl*. 2016;55(47):14774-14777. doi:10.1002/anie.201607824
335. Basile I, Da Silva A, El Cheikh K, et al. Efficient therapy for refractory Pompe disease by mannose 6-phosphate analogue grafting on acid alpha-glucosidase. *J Control Release*. 2018;269:15-23. doi:10.1016/j.jconrel.2017.10.043
336. Moreland RJ, Jin X, Zhang XK, et al. Lysosomal acid alpha-glucosidase consists of four different peptides processed from a single chain precursor. *J Biol Chem*. 2005;280(8):6780-6791. doi:10.1074/jbc.M404008200
337. Makrypidi G, Damme M, Müller-Loennies S, et al. Mannose 6 dephosphorylation of lysosomal proteins mediated by acid phosphatases Acp2 and Acp5. *Mol Cell Biol*. 2012;32(4):774-782. doi:10.1128/MCB.06195-11
338. Zhou M, Zhao J, Tian M, et al. Radio-photothermal therapy mediated by a single compartment nanoplatform depletes tumor initiating cells and reduces lung metastasis in the orthotopic 4T1 breast tumor model. *Nanoscale*. 2015;7(46):19438-19447. doi:10.1039/c5nr04587h
339. Ma X, Zhao Y, Ng KW, Zhao Y. Integrated hollow mesoporous silica nanoparticles for target drug/siRNA co-delivery. *Chemistry*. 2013;19(46):15593-15603. doi:10.1002/chem.201302736
340. Yang K-N, Zhang C-Q, Wang W, Wang PC, Zhou J-P, Liang X-J. pH-responsive mesoporous silica nanoparticles employed in controlled drug delivery systems for cancer treatment. *Cancer Biol Med*. 2014;11(1):34-43. doi:10.7497/j.issn.2095-3941.2014.01.003
341. Rengaswamy V, Zimmer D, Süss R, Rössler J. RGD liposome-protamine-siRNA (LPR) nanoparticles targeting PAX3-FOXO1 for alveolar rhabdomyosarcoma therapy. *J Control Release*. 2016;235:319-327. doi:10.1016/j.jconrel.2016.05.063

ANNEXES

Annexe 1

"Biocompatible Periodic Mesoporous Ionosilica Nanoparticles with Ammonium Walls: Application to Drug Delivery"

Roza Bouchal, Morgane Daurat, Magali Gary-Bobo, Afitz Da Silva, Leïla Lesaffre, Dina Aggad, Anastasia Godefroy, Philippe Dieudonné , Clarence Charnay, Jean-Oliver Durand and Peter Hesemann*

ACS Appl. Mater. Interfaces, **2017**, 9 (37), pp 32018–32025, DOI: 10.1021/acsami.7b07264

Annexe 2

"Biological Fate of Fe_3O_4 Core-Shell Mesoporous Silica Nanoparticles Depending on Particle Surface Chemistry"

Estelle Rascol, Morgane Daurat, Afitz Da Silva, Marie Maynadier, Christophe Dorandeu, Clarence Charnay, Marcel Garcia, Joséphine Lai-Kee-Him, Patrick Bron, Mélanie Auffan, Wei Liu, Bernard Angeletti, Jean-Marie Devoisselle, Yannick Guari, Magali Gary-Bobo* and Joël Chopineau*

Nanomaterials (Basel). **2017**, (7), 162, DOI: 10.3390/nano7070162

Annexe 3

"Stealth Biocompatible Si-Based Nanoparticles for Biomedical Applications."

Wei Liu, Arnaud Chaix, Magali Gary-Bobo, Bernard Angeletti, Armand Masion, Afitz Da Silva, Morgane Daurat, Laure Lichon, Marcel Garcia, Alain Morère, Khaled El Cheikh, Jean-Olivier Durand, Frédérique Cunin and Mélanie Auffan*

*Nanomaterials **2017***, 7(10), 288, DOI: 10.3390/nano7100288

Annexe 4

"Efficient therapy for refractory Pompe disease by mannose 6-phosphate analogue grafting on acid α-glucosidase"

Ilaria Basile[1], Afitz Da Silva[1], Khaled El Cheikh, Anastasia Godefroy, Morgane Daurat, Alice Harmois, Marce Perez, Catherine Caillaud, Henry-Vincent Charbonné, Bernard Pau, Magali Gary-Bobo, Alain Morère, Marcel Garcia and Marie Maynadier*

Journal of Controlled Relase. **2018**, (20) pp15-23, DOI: 10.1016/j.jconrel.2017.10.043

Annexe 5

"Biosafety of Mesoporous Silica Nanoparticles"

Estelle Rascol*, Cédric Pisani, Christophe Dorandeu, Jeff L. Nyalosaso, Clarence Charnay, Morgane Daurat, Afitz Da Silva, Jean-Marie Devoisselle, Jean-Charles Gaillard, Jean Armengaud, Odette Prat, Marie Maynadier, Magali Gary-Bobo, Marcel Garcia, Joël Chopineau and Yannick Guari

Biomimetics **2018**, 3(3), 22, DOI:10.3390/biomimetics3030022

Annexe 6

"Diazachlorin and diazabacteriochlorin for one- and two-photon photodynamic therapy"

Jean-François Longevial,[1] Ayaka Yamaji,[1] Dina Aggad,[1] Gakhyun Kim, Wen Xi Chia, Tsubasa Nishimura, Yoshihiro Miyake, Sébastien Clément, Juwon Oh, Morgane Daurat, Christophe Nguyen, Dongho Kim,* Magali Gary-Bobo,* Sébastien Richeter* and Hiroshi Shibokubo*

Chem Comm. **2018**, **54**, 13829-13832 DOI: 10.1039/c8cc07489e

Annexe 7

"Hollow Organosilica Nanoparticles for Drug Delivery"

Saher Rahmani, Alia Akrout, Jelena Budimir, Dina Aggad, Morgane Daurat, Anastasia Godefroy, Christophe Nguyen, Hanene Largot, Magali Gary-Bobo*, Laurence Raehm, Jean-Olivier Durand and Clarence Charnay*

*ChemistrySelec*t, **2018**, (3), 10439-42. DOI: 10.1002/slct.201802107

Annexe 8

"Large Pore Mesoporous Silica and Organosilica Nanoparticles for Pepstatin A Delivery in Breast Cancer Cells"

Saher Rahmani, Jelena Budimir, Mylene Sejalon, Morgane Daurat, Dina Aggad, Eric Vives, Laurence Raehm, Marcel Garica, Laure Lichon, Magali Gary-Bobo*, Jean-Olivier Durand and Clarence Charnay*

Molecules, **2019**, 24, 332, DOI:10.3390/molecules24020332

ANNEXE 1

* Unknown * | ACSJCA | JCA10.0.1465/W Unicode | research.3f (R3.6.i12 HF02:4458 | 2.0 alpha 39) 2016/10/28 09:46:00 | PROD-JCAVA | rq_10701667 | 9/04/2017 04:12:40 | 8 | JCA-DEFAULT

ACS APPLIED MATERIALS & INTERFACES

Research Article

www.acsami.org

Biocompatible Periodic Mesoporous Ionosilica Nanoparticles with Ammonium Walls: Application to Drug Delivery

Roza Bouchal,[†] Morgane Daurat,[‡,§] Magali Gary-Bobo,[‡] Afitz Da Silva,[‡,§] Leïla Lesaffre,[‡] Dina Aggad,[‡] Anastasia Godefroy,[‡,§] Philippe Dieudonné,[∥] Clarence Charnay,[†] Jean-Olivier Durand,[†] and Peter Hesemann*[,†]

[†]Institut Charles Gerhardt de Montpellier, UMR 5253 CNRS-UM-ENSCM, Université de Montpellier, Place Eugène Bataillon, 34095 Montpellier Cedex 05, France

[‡]Faculté de Pharmacie, Institut de Biomolécules Max Mousseron, UMR 5247 CNRS-UM, 15 Avenue Charles Flahault, 34093 Montpellier Cedex 05, France

[§]NanoMedSyn, 15 Avenue Charles Flahault, 34093 Montpellier Cedex 05, France

[∥]Laboratoire Charles Coulomb, UMR CNRS 5521, Université de Montpellier, Place Eugène Bataillon, F-34095 Montpellier Cedex, France

Supporting Information

ABSTRACT: Periodic mesoporous ionosilica nanoparticles with ammonium walls were synthesized exclusively from a trisilylated ammonium precursor. The nanoparticles display a uniform particle size, together with a high specific surface area and an ordered hexagonal pore architecture. Completely biocompatible in vitro and in vivo, the nanoparticles are efficiently endocytosed by RAW 264.7 macrophages and used as carrier vehicles for anionic drugs. Diclofenac-loaded ionosilica nanoparticles are very efficient in inhibiting lipopolysaccharides-induced inflammation.

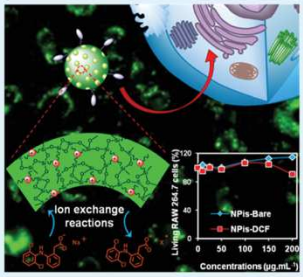

KEYWORDS: *ionosilica, periodic mesoporous organosilica, nanoparticles, anion exchange, drug delivery*

1. INTRODUCTION

Ionosilicas, defined as periodic mesoporous organosilicas (PMOs) constituting of ionic building blocks, recently emerged as a new family of functional materials. Due to their mixed ionic−mineral nature, ionosilicas are situated at the interface of functional silica mesophases and ionic liquids.[1−3] In the absence of silica sources such as tetraethyl-*ortho*-silicate, ionosilicas are obtained from oligosilylated ionic precursors via the hydrolysis−polycondensation procedures exclusively.[4,5] This synthetic strategy therefore affords materials that are entirely constituted of ionic building blocks. We recently showed that ionosilicas displaying a regular architecture on the mesoscopic level can be obtained from oligosilylated ionic precursors by the template-directed hydrolysis−polycondensation reactions in the presence of anionic surfactant.[6,7] This approach is particularly attractive because the organoionic group of the silylated precursor promotes the structuration process during the template-directed hydrolysis−polycondensation procedure.[8] Ionosilicas combine high porosity and regular architecture on the mesoscopic level with an unmatched chemical versatility, induced by the high variability and the high number of homogeneously distributed ionic species. They have a large potential for applications in catalysis[5] and separation.[3,9−11] Ionosilicas exhibit particularly hydrophilic properties, resulting in a particularly high affinity toward water.[12] This feature leads to an enhanced mass transfer and, in fine, to a high accessibility of ionic sites, in particular, in aqueous media. Finally, ionosilicas appear as efficient adsorbing materials for a large variety of anionic species such as iodide, chromate, perrhenate, and pertechnetate.[3,10,11,13] Recently, we demonstrated that ionosilicas also efficiently adsorb anionic drugs such as diclofenac (DCF) and sulindac, the two anionic nonsteroidal anti-inflammatory drugs (NSAID).[14]

Applications of ionosilicas necessarily require an efficient shaping of these materials, as powder-like morphologies are not always compatible with advanced applications. Here, we investigated the formation of ionosilica nanoparticles. The availability of ionosilica nanoparticles enables us to address new fields of applications of these nanomaterials, for example, as drug carrier vehicles in the biomedical area. Ionosilica

Received: May 23, 2017
Accepted: August 28, 2017
Published: August 28, 2017

DOI: 10.1021/acsami.7b07264
ACS Appl. Mater. Interfaces XXXX, XXX, XXX−XXX

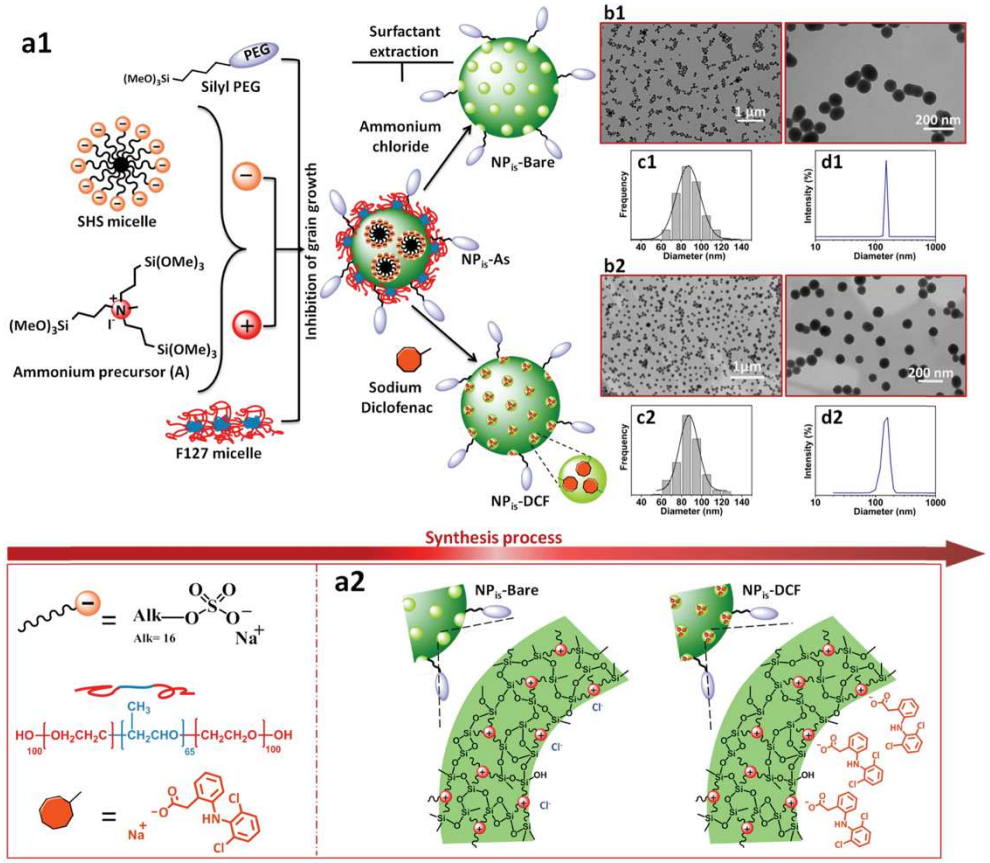

Figure 1. (a1) Illustration of the preparation of ionosilica nanoparticles and the template extraction; (a2) schematic illustration of ionosilica framework with ammonium group and the composition of internal pore of **NP$_{is}$-bare** and **NP$_{is}$-DCF**. (b1, b2) Transmission electron microscopy (TEM) images of **NP$_{is}$-bare** and **NP$_{is}$-DCF**. (c1, c2) Particle size distribution of **NP$_{is}$-bare** and **NP$_{is}$-DCF** obtained by TEM. (d1, d2) Dynamic light scattering (DLS) measurement of **NP$_{is}$-bare** and **NP$_{is}$-DCF**.

nanoparticles would be systems of choice for this field due to their high hydrophilicity, tunability, and high adsorption capacity for anionic drugs. However, reaching the nanoscale with conventional PMO materials is still a major challenge,[15−22] as examples of PMO-type nanoparticles are scarce. More specifically, ionosilicas are only available in bulk at the macroscopic scale so far.

Herein, we report for the first time ionosilica nanoparticles. These objects, obtained exclusively from a trisilylated ammonium precursor, constitute of ionic substructures. The nanoparticles display a narrow size distribution and a regular pore arrangement. Their ionic−mineral hybrid nature may confer particular surface properties to these nano-objects. These may further be adjusted when using appropriate ionic precursors, as the large variety of possible anion−cation combinations in ionosilicas provides a simple way to fine-tune the physicochemical properties of these functional materials.[12,23] Our recent results concerning the adsorption of anionic drugs by bulk ionosilica suggest potential applications of ionosilica nanoparticles in the area of drug delivery. We, therefore, performed in vitro, in vivo, and biodistribution investigations to address the cytotoxicity and biocompatibility of ionosilica nanoparticles. Finally, vectorization of drugs by the aid of ionosilica nanoparticles was investigated. We chose diclofenac (DCF) as the model drug to monitor the potential of the ionosilica nanoparticles to be used as drug carrier vehicles, as we previously studied adsorption of this non-steroidal anti-inflammatory drug (NSAID) from an aqueous solution. We observed that DCF is efficiently adsorbed by ionosilicas in bulk.[24]

2. RESULTS AND DISCUSSION

2.1. Synthesis and Characterization of Ionosilica Nanoparticles. The procedure for the preparation of the ionosilica nanoparticles containing ammonium substructures is schematized in Figure 1. The synthesis of the nanoparticles was

DOI: 10.1021/acsami.7b07264
ACS Appl. Mater. Interfaces XXXX, XXX, XXX−XXX

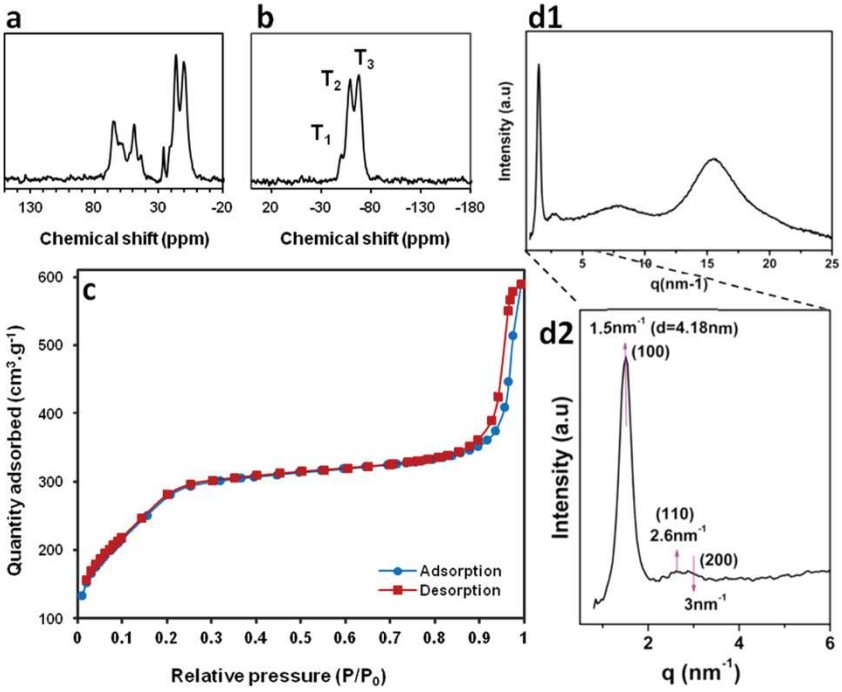

Figure 2. a) ^{13}C cross-polarization magic-angle spinning (CP-MAS) spectra of **NP$_{is}$-bare** nanoparticles. (b) ^{29}Si CP-MAS solid-state NMR spectra of **NP$_{is}$-bare** nanoparticles. (c) Nitrogen adsorption−desorption isotherm of **NP$_{is}$-bare** nanoparticles. (d1, d2) X-ray diffractogram of **NP$_{is}$-bare**.

carried out following a modified Stöber method using a binary surfactant system. The synthesis was based on the balance between the ordered assembly of cationic organic ammonium precursor (precursor A) and an anionic surfactant (SHS) to create mesoporosity within the nanoparticles via the formation of precursor−surfactant ion pairs. Simultaneously, the inhibition of grain agglomeration was achieved (i) by the addition of a nonionic surfactant (F127), which was efficiently adsorbed on the surface of the primary nanoparticles via hydrogen bonding and (ii) the addition of a silylated poly(ethylene glycol) precursor "silyl PEG." As PEG is a biocompatible group,[25−27] the surface functionalization of the ionosilica nanoparticles should further enhance their biocompatibility. Detailed information about the synthesis of the ionosilica nanoparticles can be found in the Supporting Information (page S2).

The successful formation of the as-synthesized ionosilica nanoparticles with surfactant-filled pores **NP$_{is}$-as** was indicated by transmission electron microscopy (TEM) and dynamic light scattering (DLS). The TEM images of these particles (SI, Figures S1 and S2) show spherical objects with a diameter of approximately 80−100 nm. The particle size determined by DLS is higher (148 nm), as DLS takes into account the surface-located PEG groups and the adsorbed F127 polymers, which increase the hydrodynamic diameter of the particles (SI, Figure S2).

The obtained **NP$_{is}$-as** ionosilica nanoparticles were then used to access bare particles with empty pores (**NP$_{is}$-bare**) via the washing procedures. For this purpose, the **NP$_{is}$-as** nanoparticles were treated with an ethanolic ammonium chloride solution. The obtained nanoparticles **NP$_{is}$-bare** were very similar to the **NP$_{is}$-as** particles in their size and shape. The TEM and scanning electron microscopy (SEM) images (Figures 1b1 and S3a,b, SI) indicate an average diameter of approximately 90 nm and a hydrodynamic diameter of 148 nm (Figure 1c1,d1), in nice agreement with the results obtained for **NP$_{is}$-as**.

We characterized the **NP$_{is}$-bare** nanoparticles more in detail to confirm the chemical integrity of the ionic building block and to determine their surface properties. For this purpose, we performed ^{13}C cross-polarization magic-angle spinning (^{13}C CP-MAS) and ^{29}Si CP-MAS solid-state NMR and infrared spectroscopy, nitrogen sorption, X-ray diffraction (XRD), and zeta-potential measurements.

First, the ^{13}C CP-MAS spectrum of **NP$_{is}$-bare** (Figure 2a) displays three signals related to *n*-propyl chains of the precursor at 10.7, 16.8, and 49.7 ppm, respectively. Additionally, the two signals around 60−70 ppm can be assigned to the methyl group directly attached to the nitrogen atom and to the PEG groups located on the surface of nanoparticles. The ^{29}Si CP-MAS NMR spectra of the material (Figure 2b) show three signals, which are characteristic of the T units, confirming the formation of a siloxane framework. The highest intensity was found for the T^2 and T^3 signals, which are assigned to $R\underline{Si}(OSi)_2OH$ and $R\underline{Si}(OSi)_3$ silicon centers, respectively. These results are in nice agreement with those obtained for the bulk ionosilica materials[4,5] and prove the presence of ammonium groups within the material. They confirm that no

DOI: 10.1021/acsami.7b07264
ACS Appl. Mater. Interfaces XXXX, XXX, XXX−XXX

degradation of the ionic precursor occurred during the hydrolysis−polycondensation procedure.

These results were confirmed by the Fourier transform infrared (FT-IR) spectroscopy. The FT-IR spectrum of **NP_{is}-bare** (SI, Figure S4) (green curve) shows (C−H) stretching vibrations of methylene groups at 3000−2840 cm^{-1}. Moreover, the spectrum is dominated by strong absorption bands between 1150 and 1000 cm^{-1}, which can be assigned to the siloxane network.[28] The FT-IR spectrum of the nanoparticles is in nice agreement with that of the previously reported bulk ionosilica.[4,5]

The textural properties of the **NP_{is}-bare** nanoparticles were determined via nitrogen sorption. The nitrogen sorption isotherm is given in Figure 2c. The Brunauer−Emmett−Teller surface area of the materials was 1034 $m^2 \cdot g^{-1}$. This result indicated that the anionic surfactant was eliminated in large extent from the pores. The nitrogen-adsorption isotherm of the **NP_{is}-bare** nanoparticles shows two separated adsorption steps. The first step occurred at a low partial pressure ($P/P_0 < 0.2$) and indicates mesoporosity with a pore size of ∼2.0 nm. This mesoporosity is due to the template effect of the anionic surfactant during the template-directed hydrolysis−polycondensation process.[7,8,29] Second, a strong nitrogen uptake at a high relative pressure ($P/P_0 > 0.8$) can be observed. This phenomenon can be related to the nitrogen adsorption by the void spaces between the nanoparticles and therefore indicates an intergranular porosity.

Finally, the XRD and small-angle X-ray scattering (SAXS) measurements were performed to get more information about the architecture of the material on the mesoscopic length scale and the crystallite size. Figure 2d1,d2 displays the XRD patterns of **NP_{is}-bare** nanoparticles. The diffractogram displays an intense reflection at $q = 1.5$ nm^{-1} and a low intense and larger contribution, which could fit with two contributions at $q = 2.6$ and 3 nm^{-1} (Figure 2d2). These three reflections with index (100), (110), and (200), respectively, indicate a regular repetition of the cylindrical pore arrangement, separated by hybrid silica walls, in accordance with a hexagonal two-dimensional (2D) structure. The low intensity of the (110) and (200) reflections can be explained by the size of the nanoparticles, limiting the long-range order within the particles to the maximum 20 unit cells. Considering the existence of walls between the cylinders, the distance D between the center of the cylinders should be $D = 2d_{100}/\sqrt{3}$ for a hexagonal 2D structure, with $d_{100} = 2\pi/q_{100} = 4.2$ nm. We found then $D = 4.8$ nm corresponding to the wall thickness plus the cylinders diameter. The broad peak centered at $q = 15$ nm^{-1} confirmed the amorphous nature of the silica hybrid walls,[30] as demonstrated in Figure 2d1. Small-angle X-ray scattering (SAXS) was performed to measure the average diameter size and the size polydispersity of the nanoparticles. The SAXS profile (the position of intensity oscillations of the form factor as shown in SI, Figure S5a) is directly related to the particle size and the size polydispersity. A fit profile was performed using the Sasfit software (SI, Figure S5a), giving a radius of 52 nm for **NP_{is}-bare** with a polydispersity of 0.18. The decrease in the intensity of the SAXS profile should follow a power law in q^{-4} for dense particles (as indicated in Figure S5a for a fitted curve). For the experimental data, the SAXS profile shows that the exponent of the power law is less than 4, indicating that the particle density is not homogeneous at the nm scale. This result is because of the presence of walls and pores, which have two different densities inside the nanoparticles.

The surface charge of **NP_{is}-bare** was checked using zeta-potential measurements at different pHs. We observed that the isoelectric point (IEP) of **NP_{is}-bare** was found in a slightly basic medium (pH ∼ 10.5; SI, Figure S6). This value, which is much higher compared with that for silica (IEP_{SiO_2}: pH ∼ 2), can be explained by the presence of cationic ammonium groups within the ionosilica framework, thus compensating the negative charge of silanolates (Si−O^-) located at the surface of the nanoparticles in an alkaline solution.

All of these results clearly indicate that highly porous ionosilica nanoparticles displaying ordered pore arrangements were obtained, starting from the tris-silylated ammonium precursor A. TEM, SEM, DLS, and SAXS gave concordant results regarding the particle size. Solid-state NMR and FT-IR spectroscopy confirmed the chemical constitution and the integrity of the ionic building blocks.

2.2. Vectorization of Diclofenac with Ionosilica Nanoparticles. In the following, we investigated the use of these functional ionosilica nano-objects in the area of drug delivery. For this purpose, we prepared diclofenac (**DCF**)-loaded nanoparticles directly via anion exchange on the as-synthesized **NP_{is}-as** nanoparticles, that is, loading and template elimination were carried out simultaneously to preserve the porosity of the material. For this purpose, the ionosilica nanoparticles **NP_{is}-as** were contacted with an ethanolic sodium diclofenac solution ($C = 0.51$ mM) under sonication for 25 min at room temperature. This procedure was repeated three times. The resulting nanoparticles (**NP_{is}-DCF**) were then washed three times with ethanol to remove all of the physisorbed surfactant and DCF. The loading of diclofenac on the ionosilica nanoparticles was monitored by UV−vis, FT-IR, and energy-dispersive X-ray (EDX) spectroscopies.

TEM, SEM, and SAXS measurements indicated that **NP_{is}-DCF** shows shape and size that are very similar to those of **NP_{is}-as** and **NP_{is}-bare** nanoparticles (TEM: 90 nm, SAXS: 94 nm) (Figures 1b2−d2, S3c,d and S5b, SI). Once again, the particle size determined by DLS is significantly higher (150 nm) due to the surface-located PEG groups. The fact that we measured very similar particle size for all of the three materials **NP_{is}-as**, **NP_{is}-bare**, and **NP_{is}-DCF** indicates that neither surfactant elimination nor anion exchange with **DCF-Na** into the ionosilica nanoparticles affects the particle geometry in terms of particle size, architecture, or particle size distribution. The pore arrangement of **NP_{is}-DCF** was verified using X-ray diffraction. The diffractogram (SI, Figure S5c) shows an intense (100) reflection at 1.5 nm^{-1}, as observed with **NP_{is}-bare**, but the (110) and (200) reflections are hardly identified. Finally, the surface charge of **NP_{is}-DCF** was checked by the zeta-potential measurements, which indicated that the positive charge is contributed by the presence of ammonium substructures (see Table S1).

The DCF loading onto the ionosilica nanoparticles was determined by UV−vis spectroscopy using eq 1

$$n_{DCF} = (n_{initial} - n_{final})/\text{nanoparticle mass} \quad (1)$$

where n_{DCF} is the number of moles of diclofenac in the nanoparticles and $n_{initial}$ and n_{final} are the number of moles of diclofenac in the supernatant before and after loading, respectively.

Using UV−vis spectroscopy, we observed that the ionosilica nanoparticles adsorbed 1.54 $mmol \cdot g^{-1}$ of **DCF-Na** (mol DCF/1 g of nanoparticles), corresponding to 49% w/w. This rather

DOI: 10.1021/acsami.7b07264
ACS Appl. Mater. Interfaces XXXX, XXX, XXX−XXX

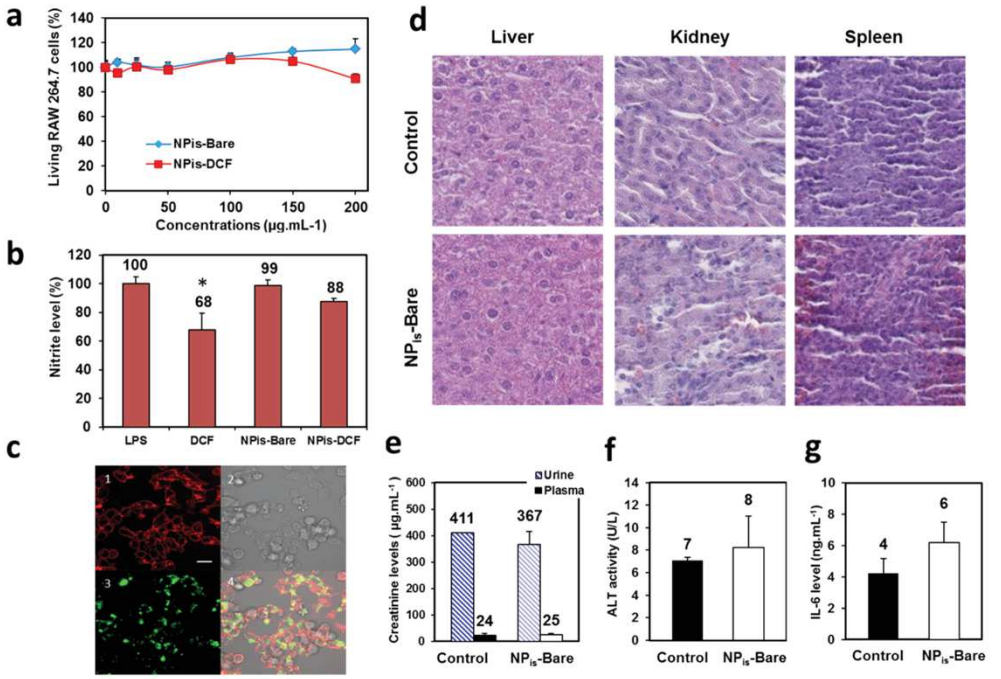

Figure 3. (a) Effect of NP_{is}-**bare** and NP_{is}-**DCF** nanoparticles on RAW 264.7 cells viability. RAW 264.7 cells incubated with increasing concentrations of NP_{is}-**DCF** and NP_{is}-**bare** nanoparticles during 24 h and submitted to a MTT assay. Results are percentage of living cells compared with untreated cells. Values are means ± standard deviations of three experiments. *$p < 0.05$ statistically different from control. (b) Effect of nanoparticles on lipopolysaccharides (LPS)-induced nitrite production in RAW 264.7 cells. Nitrite level assayed in the culture medium of RAW 264.7 cells stimulated with LPS (25 ng·mL^{-1}) for 2 h, followed by a 24 h treatment with 100 μg·mL^{-1} of NP_{is}-**bare**, NP_{is}-**DCF**, and **DCF-Na** in a concentration corresponding to the one contained in NP_{is}-**DCF**. Values are mean percentages ± standard deviations of two experiments. (c) Confocal fluorescent imaging of cell uptake of NP_{is}-fluorescein isothiocyanate (NP_{is}-**FITC**), membrane staining in red (1), transmission microscopy, (2) NP fluorescent imaging in green, and (3) merger of the three pictures demonstrates the internalization of NP in RAW 264.7 cells incubated during 24 h with NP_{is}-**FITC** (100 μg·mL^{-1}). Scale bar 10 μm. (d) Hematoxylin−eosin stained sections from paraffin-embedded tissues of control and treated mice observed at the magnification 100×. (e) Plasma and urine levels of renal biomarker (creatinine). (f) Plasma levels of biomarkers of the liver (alanine aminotransferase, ALT). (j) Plasma levels of systemic inflammation (IL-6).

high quantity of immobilized DCF is explained by the high affinity of the anionic drug toward the immobilized cationic ammonium groups.[14] We also analyzed an ethanolic suspension of the NP_{is}-**DCF** nanoparticles via UV−vis spectroscopy. The absorbance spectrum of the nanoparticles shows a strong absorption band characteristic of diclofenac, thus indicating the adsorption of diclofenac into the ionosilica nanoparticles (SI, Figure S7). Finally, the presence of DCF within the nanoparticles was also monitored via the FT-IR spectroscopy. The FT-IR spectrum of NP_{is}-**DCF** clearly shows the antisymmetric and symmetric stretching of the carboxylate group of DCF at 1576 and 1380 cm^{-1} (Figure S4), in addition to the characteristic absorption bands of the ionosilica nanoparticle NP_{is}-**as**. The slight shift in the lower-frequency absorption compared to the spectrum of **DCF-Na** indicates the interaction between the carboxylate ion and the cationic moiety of the ionosilica nanoparticle.[14]

To get information on the amount of anionic surfactant traces remaining in the loaded nanoparticles, the energy-dispersive X-ray spectroscopy (EDX) was performed on NP_{is}-**DCF**. In fact, the EDX analysis of NP_{is}-**DCF** indicates that approximately 70% of the anionic surfactant was replaced by DCF (SI, Figures S8 and S9), implying that a non-negligible amount of surfactant is still present in the nanoparticles after loading with DCF. However, the presence of a residual SHS in the sample does not raise toxicological problems due to the lower toxicity of sulfate/sulfonate surfactants,[31,32] especially compared with cationic surfactants such as cetyl trimethylammonium bromide, which are usually used in the syntheses of silica-based nanoparticles. These surfactants display considerable toxicity and often lead to cellular death even at low concentrations.[33] Our synthetic strategy based on the use of less-toxic anionic surfactants is therefore particularly adapted for the preparation of nano-objects for the biomedical use.

The cytotoxicity effect of NP_{is}-**bare** and NP_{is}-**DCF** nanoparticles was evaluated using the 3-(4,5-dimethylthiazol-2-yl)-2,5-diphenyltetrazolium bromide (MTT) assay on RAW 264.7 cells. As depicted in Figure 3a, a 24 h treatment with increasing concentrations of nanoparticles (NP_{is}-**bare** and NP_{is}-**DCF**) had no effect on RAW 264.7 cell growth. Even after 72 h, NP_{is}-**bare**

DOI: 10.1021/acsami.7b07264
ACS Appl. Mater. Interfaces XXXX, XXX, XXX−XXX

and **NP_{is}-DCF** displayed only a very slight effect on the RAW 264.7 cell growth (SI, Figure S10). In addition, a 72 h incubation time of **NP_{is}-DCF** was realized on human healthy fibroblasts (SI, Figure S11) to demonstrate the biocompatibility of a nonspecialized cell line and the results show the absence of toxicity at the concentrations tested (from 0 to 200 $\mu g \cdot mL^{-1}$). These results clearly demonstrate the in vitro biocompatibility of the ionosilica nanoparticles and their potential for further biomedical use.

Before focusing on the anti-inflammatory effect of the diclofenac-loaded ionosilica nanoparticles **NP_{is}-DCF**, we studied their drug release capacity. For this purpose, we performed the diclofenac release using deionized water at pH 5.5 and monopotassium phosphate (KH_2PO_4) aqueous solution at pH 5.6 as the release medium. We chose this composition as monopotassium phosphate is usually present in the culture medium. We observed that only 5% DCF was released in deionized water and 25% in KH_2PO_4 aqueous solution (SI, Figure S12). This result is due to the fact that the release of diclofenac proceeded via anion exchange in the presence of competing anionic phosphate species.

To estimate the biomedical potential of such nanoparticles loaded with **DCF**, their anti-inflammatory effect was studied. **NP_{is}-DCF** and **NP_{is}-bare** were incubated with RAW 264.7 cells in which the inflammation was induced by LPS. More precisely, RAW 264.7 cells were treated for 2 h with LPS (25 $ng \cdot mL^{-1}$), followed by the treatment with 100 $\mu g \cdot mL^{-1}$ of **NP_{is}-bare**, **NP_{is}-DCF** nanoparticles, and **DCF-Na** in a concentration equivalent to the one contained in **NP_{is}-DCF**. Figure 3b shows that **NP_{is}-DCF** could decrease the nitrite production of 12%, which is lower than the value observed for **DCF-Na** alone (32%), induced by LPS on RAW 264.7 cells. This lower anti-inflammatory effect is explained by slow **DCF** release from the nanoparticles, as indicated above. However, this result suggests that ionosilica nanoparticles can be of particular interest for long-term treatments, as the drug is progressively released over a rather long period. As expected, **NP_{is}-bare** have no effect on LPS-induced nitrite production. All of these results demonstrate the capacity of ionosilica nanoparticles to be used as efficient drug carrier system.

To confirm the drug delivery efficiency of **NP_{is}-DCF**, their capacity to reverse oxidative LPS-induced stress was analyzed by dichlorofluorescin diacetate assay on RAW 264.7 cells. These macrophages were treated for 2 h at a concentration of 25 $ng \cdot mL^{-1}$ with LPS to induce the reactive oxygen species (ROS) production. Then, the pretreatment was followed by an incubation of 100 $\mu g \cdot mL^{-1}$ of **NP_{is}-DCF** and **NP_{is}-bare** for 24 h. We observed that the cells incubated with LPS and **NP_{is}-DCF** exhibit a lower green fluorescence than the cells treated with LPS and **NP_{is}-bare** (SI, Figure S13). This confirmed that **NP_{is}-DCF** released **DCF** in the culture cells and decreased the inflammatory reactions induced by LPS treatment, such as ROS production.

This effect could be attributed to the efficient endocytosis of ionosilica nanoparticles by macrophages, as demonstrated in Figure 3c. We prepared the fluorescent ionosilica nanoparticles **NP_{is}-FITC** by contacting **NP_{is}-bare** with an ethanol solution of fluorescein isothiocyanate (FITC) at 0.1:1 (FITC/**NP_{is}-bare**) molar ratio. The adsorption of **FITC** on the ionosilica nanoparticles was performed via sonication (30 min at 30°C), followed by several washing steps with ethanol. Under the given conditions, the labeling with FITC involves an anion-exchange step, as FITC is present in the medium in its anionic carboxylate form.

The resulting fluorescent **NP_{is}-FITC** nanoparticles were then incubated in the culture cells at a concentration of 100 $\mu g \cdot mL^{-1}$. Fluorescent imaging of the living cells showed that the nanoparticles were progressively internalized by RAW 264.7 cells. After a 3 h incubation, **NP_{is}-FITC** are localized at the plasma membrane and after 6 h, **NP_{is}-FITC** are efficiently internalized to reach a maximal intracellular localization after 24 h (SI, Figure S14). This strong internalization of **NP_{is}-FITC** by macrophages after 24 h incubation time is represented in Figure 3c. In addition, an experiment of colocalization with endolysosomal compartments was realized and demonstrated that these **NP_{is}-FITC** are highly colocalized with lysosomes after 24 h (SI, Figure S15). Finally, to quantify the internalization kinetics of **NP_{is}-FITC**, fluorescence-activated cell sorting (FACS) experiments were performed, demonstrating the linear progression of **NP_{is}-FITC** endocytosis by macrophages to reach 93% of the cells containing **NP_{is}-FITC** after 24 h of incubation (SI, Figure S16). All together, these results demonstrate the highly efficient uptake of ionosilica nanoparticles by macrophages and their efficiency in drug delivery.

Finally, to estimate the in vivo biocompatibility of ionosilica nanoparticles, two groups of mice were constituted ($n = 4$) and injected intravenously with physiological serum supplemented or not (control) with **NP_{is}-bare** nanoparticles to reach a final concentration of 40 $mg \cdot kg^{-1}$ in the animals (Figure 3). This concentration is relatively high and corresponds to the already used doses for acute toxicity studies in mice.[34] However, the dispersibility of the solution of physiological serum added with nanoparticles was remarkably good, and we observed no difficulties related to the particles' agglomeration or precipitation over the whole time of the experiment. One week after the injection, the mice were sacrificed. The histological analysis did not show any structural modifications on the liver, kidney, and spleen (Figure 3d). Moreover, no significant differences between control and treated mice were observed for the biomarkers such as ALT (liver), IL-6 (systemic inflammation), and creatinine (kidney) (Figure 3e–g), confirming the functional integrity of the organs involved in the metabolism. These results obtained in mice demonstrated the good biocompatibility of the ionosilica nanoparticles and their potential for biomedical use.

3. CONCLUSIONS

We report novel ionosilica nanoparticles exclusively constituted of ammonium building blocks the silica network. These original nano-objects were synthesized solely from a silylated ammonium precursor and display a highly uniform particle size centered at 90 nm, together with a high specific surface area of up to 1000 $m^2 \cdot g^{-1}$ and a regular pore arrangement. The average pore size is centered at approximately 1.9 nm. Both in vitro and in vivo cytotoxicity investigations of the ionosilica nanoparticles displayed excellent biocompatibility. This feature is in part due to the original nanoparticles synthesis strategy involving anionic surfactants instead of more toxic cationic surfactants. The ionosilica nanoparticles can be used as drug carrier vehicles. We show that the nanoparticles can be loaded with anionic drugs via anion exchange. Here, we used a nonsteroidal anti-inflammatory drug, that is, diclofenac, as the model compound and to achieve a proof of concept. We observed that the drug release depends on the composition of

DOI: 10.1021/acsami.7b07264
ACS Appl. Mater. Interfaces XXXX, XXX, XXX−XXX

the release medium. Our results indicate a high potential for these functional and hydrophilic ionosilica nanoparticles in drug delivery and for opening new perspectives for the formation of tailor-made silica hybrid nanocarriers. Future studies will address the vectorization of other types of more challenging drugs, for example, for cancer therapy.

■ ASSOCIATED CONTENT

Supporting Information

The Supporting Information is available free of charge on the ACS Publications website at DOI: 10.1021/acsami.7b07264.

Brief description of experimental details of the precursor and nanoparticles synthesis, drug release, cell culture, cell death quantification, anti-inflammatory properties of nanoparticles, reactive oxygen species (ROS) measurements, cellular uptake and colocalization with lysosomes, internalization quantification by FACS, animals, and preliminary toxicological assessment and statistical analyses (PDF)

■ AUTHOR INFORMATION

Corresponding Author

*E-mail: peter.hesemann@umontpellier.fr. Tel: +33 (0) 467144528. Fax: +33 (0)467143852.

ORCID

Jean-Olivier Durand: 0000-0003-4606-2576

Author Contributions

The manuscript was written through contributions of all of the authors. All of the authors have given approval to the final version of the manuscript.

Notes

The authors declare no competing financial interest.

■ ACKNOWLEDGMENTS

R.B. acknowledges a doctoral fellowship from the Algerian government. The authors acknowledge financial support from the LabEx Chemistry of Molecular and Interfacial Systems (LabExCheMISyst) (ANR-10-LABX-05-01). M.G.-B. thanks the Région Languedoc-Roussillon for the grant "Chercheur d'Avenir." The authors thank Laure Lichon for technical assistance.

■ REFERENCES

(1) Gadenne, B.; Hesemann, P.; Moreau, J. J. E. Supported Ionic Liquids: Ordered Mesoporous Silicas containing Covalently Linked Ionic Species. *Chem. Commun.* **2004**, *40*, 1768−1769.

(2) Nguyen, T. P.; Hesemann, P.; Moreau, J. J. E. i-Silica: Nanostructured Silica Hybrid Materials containing Imidazolium Groups by Hydrolysis-Polycondensation of Disilylated bis-N,N′-Alkyl-Imidazolium Halides. *Microporous Mesoporous Mater.* **2011**, *142*, 292−300.

(3) Lee, B.; Im, H. J.; Luo, H. M.; Hagaman, E. W.; Dai, S. Synthesis and Characterization of Periodic Mesoporous Organosilicas as Anion Exchange Resins for Perrhenate Adsorption. *Langmuir* **2005**, *21*, 5372−5376.

(4) Nguyen, T. P.; Hesemann, P.; Tran, T. M. L.; Moreau, J. J. E. Nanostructured Polysilsesquioxanes bearing Amine and Ammonium Groups by Micelle Templating using Anionic Surfactants. *J. Mater. Chem.* **2010**, *20*, 3910−3917.

(5) El Hankari, S.; Motos-Perez, B.; Hesemann, P.; Bouhaouss, A.; Moreau, J. J. E. Pore Size Control and Organocatalytic Properties of Nanostructured Silica Hybrid Materials containing Amino and Ammonium groups. *J. Mater. Chem.* **2011**, *21*, 6948−6955.

(6) Hesemann, P.; Nguyen, T. P.; El Hankari, S. Precursor Mediated Synthesis of Nanostructured Silicas: From Precursor-Surfactant Ion Pairs to Structured Materials. *Materials* **2014**, *7*, 2978−3001.

(7) El Hankari, S.; Bouhaouss, A.; Hesemann, P. Anionic Surfactants as Versatile Soft-Templates to access Nanostructured Ionosilicas from Functional Amine and Ammonium Precursors. *Microporous Mesoporous Mater.* **2013**, *180*, 196−208.

(8) Che, S.; Garcia-Bennett, A. E.; Yokoi, T.; Sakamoto, K.; Kunieda, H.; Terasaki, O.; Tatsumi, T. A Novel Anionic Surfactant Templating Route for synthesizing Mesoporous Silica with Unique Structure. *Nat. Mater.* **2003**, *2*, 801−805.

(9) Ju, Y. H.; Webb, O. F.; Dai, S.; Lin, J. S.; Barnes, C. E. Synthesis and Characterization of Ordered Mesoporous Anion-Exchange Inorganic/Organic Hybrid Resins for Radionuclide Separation. *Ind. Eng. Chem. Res.* **2000**, *39*, 550−553.

(10) Zhu, L.; Zhang, C.; Liu, Y.; Wang, D.; Chen, J. Direct Synthesis of Ordered N-Methylimidazolium functionalized Mesoporous Silica as Highly Efficient Anion Exchanger of Cr(VI). *J. Mater. Chem.* **2010**, *20*, 1553−1559.

(11) Petrova, M.; Guigue, M.; Venault, L.; Moisy, P.; Hesemann, P. Anion Selectivity in Ion Exchange Reactions with Surface Functionalized Ionosilicas. *Phys. Chem. Chem. Phys.* **2015**, *17*, 10182−10188.

(12) Thach, U. D.; Trens, P.; Prelot, B.; Zajac, J.; Hesemann, P. Tuning the Interfacial Properties of Mesoporous Ionosilicas: Effect of Cationic Precursor and Counter Anion. *J. Phys. Chem. C* **2016**, *120*, 27412−27421.

(13) Thach, U. D.; Hesemann, P.; Yang, G.; Geneste, A.; Le Caer, S.; Prelot, B. Ionosilicas as Efficient Sorbents for Anionic Contaminants: Radiolytic Stability and Ion Capacity. *J. Colloid Interface Sci.* **2016**, *482*, 233−239.

(14) Bouchal, R.; Miletto, I.; Thach, U. D.; Prelot, B.; Berlier, G.; Hesemann, P. Ionosilicas as Efficient Adsorbents for the Separation of Diclofenac and Sulindac from Aqueous Media. *New J. Chem.* **2016**, *40*, 7620−7626.

(15) Hu, L.-C.; Shea, K. J. Organo-Silica Hybrid Functional Nanomaterials: how do Organic Bridging Groups and Silsesquioxane Moieties work Hand-in-Hand? *Chem. Soc. Rev.* **2011**, *40*, 688−695.

(16) Guan, B.; Cui, Y.; Ren, Z. Y.; Qiao, Z. A.; Wang, L.; Liu, Y. L.; Huo, Q. S. Highly Ordered Periodic Mesoporous Organosilica Nanoparticles with Controllable Pore Structures. *Nanoscale* **2012**, *4*, 6588−6596.

(17) Lu, N.; Tian, Y.; Tian, W.; Huang, P.; Liu, Y.; Tang, Y. X.; Wang, C. Y.; Wang, S. J.; Su, Y. Y.; Zhang, Y. L.; Pan, J.; Teng, Z. G.; Lu, G. M. Smart Cancer Cell Targeting Imaging and Drug Delivery System by Systematically Engineering Periodic Mesoporous Organosilica Nanoparticles. *ACS Appl. Mater. Interfaces* **2016**, *8*, 2985−2993.

(18) Wei, Y.; Li, X. M.; Zhang, R. Y.; Liu, Y.; Wang, W. X.; Ling, Y.; El-Toni, A. M.; Zhao, D. Y. Periodic Mesoporous Organosilica Nanocubes with Ultrahigh Surface Areas for Efficient CO_2 Adsorption. *Sci. Rep.* **2016**, *6*, No. 20769.

(19) Croissant, J. G.; Cattoen, X.; Man, M. W. C.; Durand, J. O.; Khashab, N. M. Syntheses and Applications of Periodic Mesoporous Organosilica Nanoparticles. *Nanoscale* **2015**, *7*, 20318−20334.

(20) Djojoputro, H.; Zhou, X. F.; Qiao, S. Z.; Wang, L. Z.; Yu, C. Z.; Lu, G. Q. Periodic Mesoporous Organosilica Hollow Spheres with Tunable Wall Thickness. *J. Am. Chem. Soc.* **2006**, *128*, 6320−6321.

(21) Urata, C.; Yamada, H.; Wakabayashi, R.; Aoyama, Y.; Hirosawa, S.; Arai, S.; Takeoka, S.; Yamauchi, Y.; Kuroda, K. Aqueous Colloidal Mesoporous Nanoparticles with Ethenylene-Bridged Silsesquioxane Frameworks. *J. Am. Chem. Soc.* **2011**, *133*, 8102−8105.

(22) Liu, J.; Yang, H. Q.; Kleitz, F.; Chen, Z. G.; Yang, T.; Strounina, E.; Lu, G. Q.; Qiao, S. Z. Yolk−Shell Hybrid Materials with a Periodic Mesoporous Organosilica Shell: Ideal Nanoreactors for Selective Alcohol Oxidation. *Adv. Funct. Mater.* **2012**, *22*, 591−599.

(23) Thach, U. D.; Hesemann, P.; Prelot, B. Design of Ionosilicas: Tailoring Ionosilicas for the Efficient Adsorption of p-Aminosalicylate *Sep. Purif. Technol.*, in press, 2017. 10.1016/j.seppur.2017.07.067.

DOI: 10.1021/acsami.7b07264
ACS Appl. Mater. Interfaces XXXX, XXX, XXX−XXX

564 (24) Agotegaray, M.; Palma, S.; Lassalle, V. Novel Chitosan Coated
565 Magnetic Nanocarriers for the Targeted Diclofenac Delivery. *J.*
566 *Nanosci. Nanotechnol.* **2014**, *14*, 3343−3347.
567 (25) Suzuki, K.; Ikari, K.; Imai, H. Synthesis of Silica Nanoparticles
568 having a Well-Ordered Mesostructure using a Double Surfactant
569 System. *J. Am. Chem. Soc.* **2004**, *126*, 462−463.
570 (26) Ikari, K.; Suzuki, K.; Imai, H. Structural Control of Mesoporous
571 Silica Nanoparticles in a Binary Surfactant System. *Langmuir* **2006**, *22*,
572 802−806.
573 (27) Chen, Z.; Li, X.; He, H. Y.; Ren, Z. H.; Liu, Y.; Wang, J.; Li, Z.;
574 Shen, G.; Han, G. R. Mesoporous Silica Nanoparticles with
575 Manipulated Microstructures for Drug Delivery. *Colloids Surf., B*
576 **2012**, *95*, 274−278.
577 (28) Chukin, G. D.; Malevich, V. I. Infrared Spectra of Silica. *J. Appl.*
578 *Spectrosc.* **1977**, *26*, 223−229.
579 (29) Yokoi, T.; Yoshitake, H.; Tatsumi, T. Synthesis of Anionic-
580 Surfactant-Templated Mesoporous Silica using Organoalkoxysilane-
581 containing Amino Groups. *Chem. Mater.* **2003**, *15*, 4536−4538.
582 (30) Kalapathy, U.; Proctor, A.; Shultz, J. A Simple Method for
583 Production of Pure Silica from Rice Hull Ash. *Bioresour. Technol.* **2000**,
584 *73*, 257−262.
585 (31) Krebs, F. C.; Miller, S. R.; Malamud, D.; Howett, M. K.;
586 Wigdahl, B. Inactivation of Human Immunodeficiency Virus Type 1 by
587 Nonoxynol-9, C31G, or an Alkyl Sulfate, Sodium Dodecyl Sulfate.
588 *Antiviral Res.* **1999**, *43*, 157−173.
589 (32) Young, F. M.; Phungtamdet, W.; Sanderson, B. J. S.
590 Modification of MTT Assay Conditions to examine the Cytotoxic
591 Effects of Amitraz on the Human Lymphoblastoid Cell Line, WIL2NS.
592 *Toxicol. In Vitro* **2005**, *19*, 1051−1059.
593 (33) Whitehead, K.; Karr, N.; Mitragotri, S. Safe and Effective
594 Permeation Enhancers for Oral Drug Delivery. *Pharm. Res.* **2008**, *25*,
595 1782−1788.
596 (34) Yu, Y.; Li, Y.; Wang, W.; Jin, M.; Du, Z.; Li, Y.; Duan, J.; Yu, Y.;
597 Sun, Z. Acute Toxicity of Amorphous Silica Nanoparticles in
598 Intravenously Exposed ICR Mice. *PLoS One* **2013**, *8*, No. e61346.

DOI: 10.1021/acsami.7b07264
ACS Appl. Mater. Interfaces XXXX, XXX, XXX−XXX

ANNEXE 2

nanomaterials

MDPI

Article

Biological Fate of Fe_3O_4 Core-Shell Mesoporous Silica Nanoparticles Depending on Particle Surface Chemistry

Estelle Rascol [1], Morgane Daurat [2,3], Afitz Da Silva [2,3], Marie Maynadier [2], Christophe Dorandeu [1], Clarence Charnay [1], Marcel Garcia [3], Joséphine Lai-Kee-Him [4], Patrick Bron [4], Mélanie Auffan [5], Wei Liu [5], Bernard Angeletti [5], Jean-Marie Devoisselle [1], Yannick Guari [1], Magali Gary-Bobo [3,*] and Joël Chopineau [1,6,*]

1 Institut Charles Gerhardt de Montpellier (ICGM), Montpellier University-Campus Triolet (CNRS UMR 5253/UM/ENSCM), Place Eugène Bataillon, CEDEX 5, 34095 Montpellier, France; estelle.rascol.c2i12@gmail.com (E.R.); christophe.dorandeu@umontpellier.fr (C.D.); clarence.charnay@umontpellier.fr (C.C.); jm.devoisselle@univ-montp1.fr (J.-M.D.); yannick.guari@umontpellier.fr (Y.G.)

2 NanoMedSyn, 15 Avenue Charles Flahault, 34093 Montpellier, France; morgane.daurat2@gmail.com (M.D.); afitz@hotmail.fr (A.D.S.); m.maynadier@nanomedsyn.com (M.M.)

3 IBMM, CNRS UMR 5247/UM/ENSCM Faculty of de Pharmaceutical Sciences of Montpellier 15, Avenue Charles Flahault, CEDEX 05, 34093 Montpellier, France; magali.gary-bobo@inserm.fr

4 Center of Structural Biochemistry (CNRS UMR 5048/INSERM U 1054/UM), 29 rue de Navacelles, 34090 Montpellier, France; josephine.laikeehim@cbs.cnrs.fr (J.L.-K.-H.); patrick.bron@cbs.cnrs.fr (P.B.)

5 Aix-Marseille Université, CNRS, IRD, Coll de France, CEREGE, 13001 Aix en Provence, France; auffan@cerege.fr (M.A.); wei.yanzi.liu@gmail.com (W.L.); angeletti@cerege.fr (B.A.)

6 Université de Nîmes, Rue Georges Salan, Nîmes 30000, France

* Correspondence: magali.gary-bobo@inserm.fr (M.G.-B.); joel.chopineau@enscm.fr (J.C.); Tel.: +33-4-11-75-96-17 (M.G.-B.); +33-4-11-75-94-49 (J.C.)

Received: 4 June 2017; Accepted: 23 June 2017; Published: 30 June 2017

Abstract: The biological fate of nanoparticles (NPs) for biomedical applications is highly dependent of their size and charge, their aggregation state and their surface chemistry. The chemical composition of the NPs surface influences their stability in biological fluids, their interaction with proteins, and their attraction to the cell membranes. In this work, core-shell magnetic mesoporous silica nanoparticles (Fe_3O_4@MSN), that are considered as potential theranostic candidates, are coated with polyethylene glycol (PEG) or 1,2-dimyristoyl-sn-glycero-3-phosphocholine (DMPC) lipid bilayer. Their biological fate is studied in comparison to the native NPs. The physicochemical properties of these three types of NPs and their suspension behavior in different media are investigated. The attraction to a membrane model is also evaluated using a supported lipid bilayer. The surface composition of NPs strongly influences their dispersion in biological fluids mimics, protein binding and their interaction with cell membrane. While none of these types of NPs is found to be toxic on mice four days after intravenous injection of a dose of 40 mg kg^{-1} of NPs, their surface coating nature influences the in vivo biodistribution. Importantly, NP coated with DMPC exhibit a strong accumulation in liver and a very low accumulation in lung in comparison with nude or PEG ones.

Keywords: nanoparticles; surface coating; cell-membrane interactions; biodistribution; safety

1. Introduction

In the past two decades, nanoparticles (NPs) for medical applications have been investigated by numerous researchers. The NPs based theranostic agents combine, in a unique formulation, tracking,

imaging, diagnosis, cell-targeting and drug delivery properties. In this emerging field of nanomedicine, Mesoporous Silica Nanoparticles (MSN) are considered as a promising platform for drug-delivery and cell targeting [1]. However, the major obstacle for NPs' accumulation at the site of interest is the rapid opsonization of the NPs by the liver and spleen macrophages. This opsonization is due to the formation of a protein corona at the surface of the NPs when they enter in contact with biological media [2]. The composition of the corona is particularly dependent on the NPs composition, surface charge and hydrophobicity [3]. Moreover, the protein corona influences the toxicity of the NPs [4]. Different proteins adsorb on native MSN [5], on liposomes prepared with various lipid compositions [6] and in the presence of polymeric groups [7–11]. Grafting of polyethylene glycol (PEG) groups on the NPs is well-known to induce a stealth effect of the NPs [12]. The NPs coated with PEG groups present a longer circulation time, and escape the reticuloendothelial system (RES) capture [13]. The PEG coating brings hydrophilicity at the surface of NPs. Water molecules interact via hydrogen bonds with the PEG moieties, enhancing the hydrodynamic diameter of the NPs [12]. However, this type of grafting induces aggregation in high saline concentration solution [14]. In fact, we previously demonstrated that MSN needed a precise amount of PEG in surface in order to avoid aggregation of particles. If the quantity was not optimized, PEG grafting did not improve colloidal stability [15]. Another strategy to produce a stealth effect, less investigated than the PEG coating, is to coat the surface of NPs with a lipid bilayer. The lipid bilayer, with an average thickness of 5 nm, does not change drastically the hydrodynamic diameter of the NPs [16]. Moreover, the lipid bilayer coating brings new functionalities to the NPs. Indeed, thermally controlled release can be performed by alternating magnetic field or phototherapy [17]. The biocompatibility of lipid coated NPs was generally tested using pegylated lipids [18]. The presence of a magnetic core add interesting functionalities to MSN [19]. The magnetic properties of Fe_3O_4 nanocrystals are useful to follow NPs using magnetic resonance imaging (MRI) [20] and produce thermally-controlled drug delivery or hyperthermia treatment [21]. In our previous study, the synthesis and functionalization of magnetic core shell MSN (Fe_3O_4@MSN) had been optimized [22]. The results, obtained using the classical MTT assay, showed that 1,2-dimyristoyl-sn-glycero-3-phosphocholine (DMPC) and PEG coated Fe_3O_4@MSN were less cytotoxic than the native NPs [22]. Moreover, an early effect of DMPC Fe_3O_4@MSN on cells has been observed using real-time dependent impedance measurements translating the difference in cell morphologies after NPs treatments.

These results supposed that the different physicochemical properties of PEG and lipid coated MSN influence the kinetics of their interaction with cells. Indeed, it was reported that the stability of NPs in biological media has a direct impact on interactions of NPs with cells [23]. To date, the relationships between physicochemical properties and biological effects of NPs are not well understood [24,25]. It has been shown that membrane models can be useful to understand the role of the physicochemical properties of NPs with their toxic effects [26]. Moreover, the behavior and effects of NPs on cell-membrane can be studied using membrane models [27] in well-defined conditions, as previously done for lipid coated silica NPs [5]. The quartz crystal microbalance with dissipation monitoring (QCM-D) is a well suited technique to follow the formation of membrane models, such as supported lipid bilayers (SLB) [28]. This technique provides estimation, in real-time, of a mass or a thickness adsorbed to the surface associated with the viscoelastic properties [29]. The deposition of the NPs, and the kinetics, on different surfaces have been studied using QCM-D as the analytical technique [10,30,31]. The characterization of the interactions between NPs and a supported lipid bilayer (SLB) has been performed to investigate the interaction of various types of NPs in different conditions [32–35]. However, to the best of our knowledge, the comparison of native, PEG and lipid coated MSN on a membrane model has not yet been studied. Plus, the relationship of physicochemical properties of these three different NPs surfaces in regard to cell internalization and in vivo biodistribution has not been compared before. The goal of this study was to understand the relation between surface chemistry, physicochemical properties, cell membrane interactions, in vivo biodistribution and toxic effects of NPs.

2. Results

2.1. Synthesis and Characterization of Fe_3O_4@MSN

Fe_3O_4@MSN core shell NPs were prepared by sol-gel reaction, following the optimized protocol previously described [22]. Fe_3O_4@MSN NPs present a magnetic core of 18 nm and a mesoporous silica shell of ca. 40 nm radius (Figure 1). Particles with an average primary diameter of ca. 100 nm were grafted in-situ by the addition of PEG_{2000} groups. The primary diameter of PEG Fe_3O_4@MSN NPs observed on TEM images was the same than for the native ones. The coating with DMPC lipid bilayers was performed after the synthesis, washing and drying of the native NPs. TEM images allow for the measurement of the primary diameter and the observation of the shape of the NPs (Figure 1a,b), while cryoTEM images revealed also the presence of DMPC lipid coating on Fe_3O_4@MSN (Figure 1c).

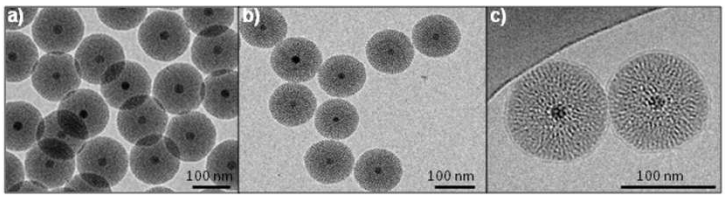

Figure 1. TEM and cryoTEM images of the nanoparticles (NPs); (**a**) Native magnetic mesoporous silica core-shell nanoparticles (Fe_3O_4@MSN); (**b**) polyethylene glycol (PEG) Fe_3O_4@MSN; (**c**) 1,2-dimyristoyl-sn-glycero-3phosphocholine (DMPC) Fe_3O_4@MSN observed by cryoTEM.

CryoTEM images revealed that the lipid bilayers measured 5 nm in thickness, so the primary diameter of DMPC Fe_3O_4@MSN is 10 nm higher than the native and PEG Fe_3O_4@MSN. The dispersion and stability of the NPs in suspension in different media were investigated by the measurement of the hydrodynamic diameter using Nano ZS apparatus (Figure 2). The NPs' surface chemistry influences their dispersion and stability when they were suspended in ethanol, HBS 5 (Hepes buffer 20 mM pH = 7.4 containing 5 mM NaCl), HBS 150 (Hepes buffer 20 mM pH = 7.4 containing 150 mM NaCl), complete cell culture medium Roswell Park Memorial Institute RPMI, and HBS 150 containing fetal calf serum (FCS) 10% (Figure 2). In ethanol, native and PEG Fe_3O_4@MSN present a hydrodynamic diameter (HD) of 144.5 $\pm$ 2.7 nm and 169.5 $\pm$ 0.9 nm, respectively (Figure 2a). These diameters are higher than the primary diameters observed by TEM, and the NPs stayed none aggregated in suspension after 2 and 15 h. Differently, DMPC Fe_3O_4@MSN suspended in ethanol presented a HD of 269.9 $\pm$ 15.9 nm, which increased to 643.5 $\pm$ 19.9 nm after 2 h and 1246 $\pm$ 48.2 nm after 15 h. The increase of HD of lipid coated Fe_3O_4@MSN in ethanol may be explained by a partial solubilization of the lipids in this solvent. In HBS 5, native Fe_3O_4@MSN presents a HD of 125.5 $\pm$ 1.2 nm at 0 h, 159.9 $\pm$ 1.9 nm after 2 h and 187.5 $\pm$ 3.3 nm after 15 h. PEG Fe_3O_4@MSN presents a HD of 141.8 $\pm$ 3.9 nm after 0 h, 202.1 $\pm$ 2.8 nm after 2 h and 232.5 $\pm$ 3.1 nm after 15 h. DMPC Fe_3O_4@MSN presents a HD of 167.1 $\pm$ 3.2 nm after 0 h, 171.6 $\pm$ 2.0 nm after 2 h and 177.1 $\pm$ 2.3 nm after 15 h. Thus, in HBS 5, native, PEG-grafted and lipid-coated NPs remained individually dispersed during 15 h after initial dispersion (Figure 2b). In HBS 150 buffer, native and PEG Fe_3O_4@MSN formed aggregates larger than 1 µm 2 h after initial dispersion (Figure 2c). However, coating with DMPC lipid bilayers was found to stabilize NPs suspension in buffer with high ionic strength (HBS 150). In this buffer, DMPC Fe_3O_4@MSN presented a HD of 171.6 $\pm$ 0.1 nm after 0 h, 198.0 $\pm$ 0.2 nm after 2 h, and 270.9 $\pm$ 0.2 nm after 12 h. In cell culture medium (RPMI containing 10% FCS) and HBS 150 containing 10% FCS, lipid coated DMPC Fe_3O_4@MSN were found always stable 15 h after dispersion (Figure 2d,e). The good dispersion of lipid coated DMPC Fe_3O_4@MSN in HBS 150 buffer and HBS 150 containing 10% FCS was also observed on cryoTEM images (data not shown). In RPMI and HBS 150 containing 10% FCS, native

NPs rapidly stabilized, presenting a HD of 128.2 ± 3.0 nm and 110.8 ± 2.0 nm at 0 h, in RPMI and HBS 150 10% FCS, respectively. However, the stabilization of PEG Fe_3O_4@MSN in protein-containing media took more time, presenting a HD close to the primary diameter only after 15 h. The zeta potentials (ZP) were measured in all media, except in ethanol (Figure 2f). Native Fe_3O_4@MSN presented a ZP of −18.9 ± 1.4 mV and −31.6 ± 0.8 mV, in HBS 150 and HBS 5, respectively. A decrease (in absolute value) of zeta potential to −16.1 ± 3.0 mV in HBS 150 and −28.4 ± 2.6 mV in HBS 5 by grafting by PEG groups was observed, and to −4.51 ± 1.1 mV in HBS 150 and −13.4 ± 0.3 mV in HBS 5, by coating by DMPC lipid bilayers. However, in protein-containing media, the zeta potential remained the same for native and lipid coated Fe_3O_4@MSN. The stabilization of native Fe_3O_4@MSN in RPMI and HBS 150 10% FCS is potentially due to the formation of a protein corona [23]. The stabilization of PEG Fe_3O_4@MSN in protein-containing media was longer due to the stealth effect of the PEG groups at the NPs surface impairing protein adsorption to the NPs surface.

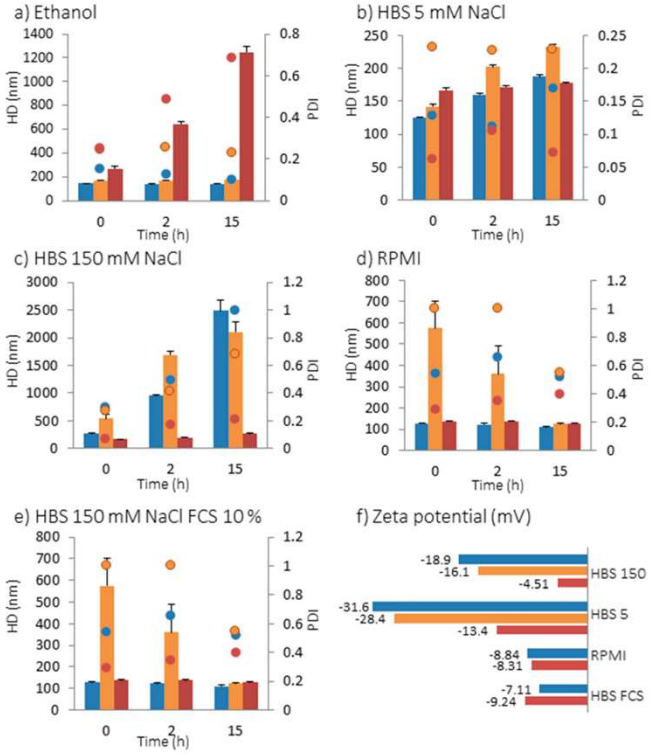

Figure 2. Hydrodynamic diameter (HD) represented by bars and polydispersity index (PDI) represented as dots of native (blue), PEG (orange) and DMPC (red) Fe_3O_4@MSN in different media: (**a**) in ethanol; (**b**) in HBS 5 mM NaCl, pH 7.4; (**c**) in HBS 150 mM NaCl, pH 7.4; (**d**) in RPMI cell culture medium (10% fetal calf serum (FCS), pH 7.4) and (**e**) in HBS 150 mM NaCl (pH 7.4) containing 10% FCS; (**f**) Zeta potential in HBS 150, HBS 5, RPMI and HBS 150 mM NaCl containing 10% FCS.

To conclude, the presence of a strong ionic strength or proteins did not modify the physicochemical behavior of DMPC Fe_3O_4@MSN, which are therefore the only ones to remain dispersed and stable in biological media.

2.2. Interaction of NPs with Model Membranes Depending of the Surface Coating

2.2.1. Changes at the Interface between NPs and a Supported Lipid Bilayer

The measurement of the interactions between NPs and a supported membrane model has been performed using a quartz crystal microbalance with dissipation monitoring (QCM-D). A SiO_2 coated 5 MHz quartz crystal was used. After injection of EPC (egg phosphatidyl choline) SUV (small unilamellar vesicles) suspension, a SLB (supported lipid bilayer) was formed, presenting a frequency shift of −26 Hz and a dissipation shift less than 0.5×10^{-6}; typically recorded for a supported bilayer [28]. The surface coated with the SLB was considered as the reference surface, and frequency and dissipation shifts induced by NPs deposition were measured from this surface. NPs were put in contact by flowing a NPs suspension on the top of the SLB in HBS 150 10% FCS medium (Figure 3). In this protein-containing medium, only very little NPs deposition on the lipid bilayer surface for PEG-Fe_3O_4@MSN and nativeFe_3O_4@MSN was observed. DMPC-Fe_3O_4@MSN interaction with the SLB surface resulted in more important frequency and dissipation shifts than those obtained for PEG-Fe_3O_4@MSN and native-Fe_3O_4@MSN. The kinetics of deposition were very different depending of the surface coating. The deposition of DMPC-Fe_3O_4@MSN occurred rapidly during the NPs flowing, inducing a frequency shift of -7.55 ± 1.49 Hz and a dissipation shift of $3.37 \pm 0.71 \times 10^{-6}$ after 1 h deposition. The maximum frequency shift observed was -9.81 ± 3.11 Hz and the maximum dissipation shift was $4.46 \pm 0.43 \times 10^{-6}$ after 10 h deposition. PEG-Fe_3O_4@MSN began to deposit at 4 h 07 ± 27 min, with a maximum frequency shift of -6.88 ± 0.75 Hz and a maximum dissipation shift of $1.49 \pm 0.30 \times 10^{-6}$ was obtained after 10 h deposition. NativeFe_3O_4@MSN began to deposit at 6 h 16 ± 33 min, with a maximum frequency shift of -3.69 ± 3.03 Hz and a maximum dissipation shift of $0.84 \pm 0.30 \times 10^{-6}$ was obtained after 10 h deposition. The deposition rates of the NPs were dependent of the aggregation state and the presence of a protein corona. DMPC-Fe_3O_4@MSN, which were well-dispersed and not influenced by the presence of proteins (Figure 2), were found to faster deposit on the SLB (Figure 3). PEG-Fe_3O_4@MSN were first aggregated and slowly dispersed due to the presence of proteins (Figure 2), allowing the deposition 4 h 07 ± 27 min after injection in the QCM-D cell (Figure 3). Native-Fe_3O_4@MSN stabilized by the presence of the protein corona at their surface (Figure 2), were very well dispersed, so these NPs began to deposit 6 h 16 ± 33 min (Figure 3).

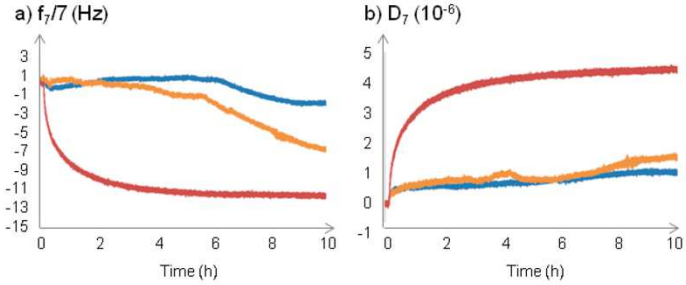

Figure 3. Quartz crystal microbalance with dissipation (QCM-D) sensorgrams following the interaction between NPs and egg phosphatidyl choline (EPC) supported lipid bilayer (SLB). Native (blue), PEG (orange) and DMPC (red) Fe_3O_4@MSN were flowed into HBS 150 mM NaCl 10% SCF medium on the top of EPC SLB, at a concentration of 0.25 mg mL^{-1} of NPs. After Fe_3O_4@MSN addition in the medium on the top of the EPC SLB during 15 min, the flow was stopped for 10 h. The results on the variations of frequency (**a**) and of the dissipation (**b**) are presented after offset of the lipid bilayer formation.

2.2.2. Time-Dependent Internalization of NPs in Hep-G2 cells

The uptake of native, PEG and DMPC Fe_3O_4@MSN by Hep-G2 cells (human hepatocyte carcinoma) after different incubation times were followed by TEM from ultrathin sections (Figure 4). After 3 h incubation period, native Fe_3O_4@MSN were observed aggregated near the cell membrane (Figure 4a). PEG Fe_3O_4@MSN were less aggregated than the native Fe_3O_4@MSN but were not observed in the cells (Figure 4d).

Conversely, DMPC Fe_3O_4@MSN were observed inside Hep-G2 cells after 3 h of exposure (Figure 4g). After 6 h incubation period, native Fe_3O_4@MSN were observed individually in vesicular structures in the cytoplasm (Figure 4b) and some PEG Fe_3O_4@MSN were internalized also (Figure 4e). DMPC Fe_3O_4@MSN were observed as small groups of NPs in vesicular structures (Figure 4h). These small groups were then observed for natives, PEG and DMPC Fe_3O_4@MSN after 24 h of NPs exposure with Hep-G2 cells (Figure 4c,f,i, respectively). This suggests a faster internalization of DMPC Fe_3O_4@MSN in human hepatic cells.

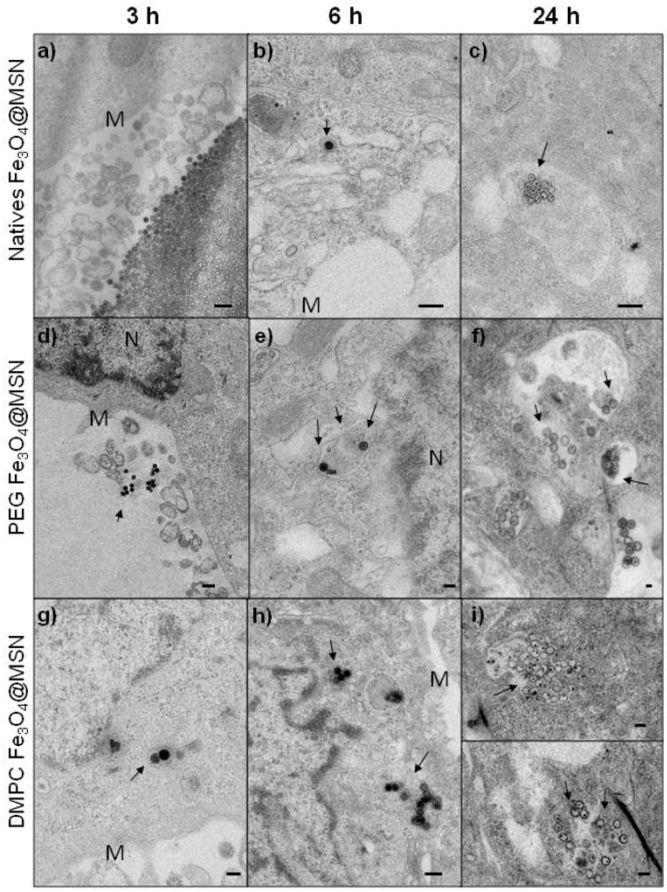

Figure 4. TEM imaging of Hep-G2 cells exposed for 3, 6, and 24 h at 50 μg mL^{-1} for native (**a**–**c**), PEG (**d**–**f**) or DMPC Fe_3O_4@MSN (**g**–**i**). The NPs are localized by arrows, near the cell membrane (M) or the nucleus (N).

2.3. In Vivo Experiments

2.3.1. In Vivo Biocompatibility

To estimate the biocompatibility of MSN, mice were injected intravenously with nanoparticles at a concentration of 40 mg kg^{-1}. This concentration is high and corresponds to concentration already used to evaluate the acute toxicity of NPs in mice [36]. Four days after the injection of NPs, mice were sacrificed and organs, urines and blood were collected. Histological analyses were performed. No noticeable structural modifications on liver, kidney and spleen were observed (Figure 5a). Moreover, as shown in Figure 5b–e, no significant differences between control and treated mice for the biomarkers such as creatinine (kidney), interleukine-6 (IL-6) and tumor necrosis factor alpha (TNF-α) (systemic inflammation), and alanine aminotransferase (ALT) (liver) were observed, confirming the functional integrity of organs. These results demonstrated the biocompatibility of the nanoparticles under consideration in this work.

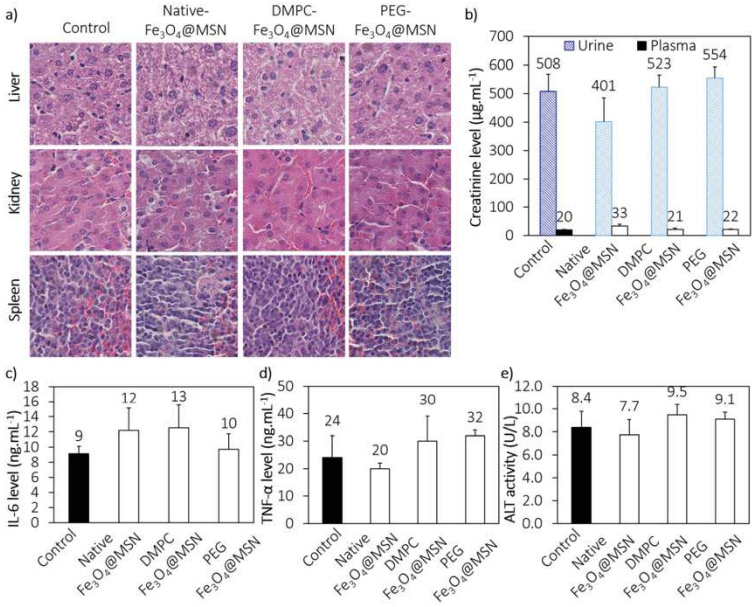

Figure 5. Preliminary toxicological assessment. (**a**) Hematoxylin-eosin sections from paraffin-embedded tissues (kidney, liver and spleen) of control and treated mice; (**b**) Plasma and urine levels of renal biomarker (creatinine); (**c**,**d**) Plasma levels of systemic inflammation biomarkers (IL-6 and TNF-α); (**e**) Plasma level of liver biomarker (ALT).

2.3.2. In Vivo Biodistribution

The amount of silicium has been quantified using inductively coupled plasma-mass spectrometry (ICP-MS) analysis. No significant elevation of silicium amount was detected in the kidneys and urines 4 days after injection. The quantities of silicium in the blood, the liver, the spleen, and the lungs were different depending of the NPs coating. These differences suggested changes in biodistribution and in pharmacokinetics of the NPs, due to the presence of the coating. Silicium amount in the liver 4 days after injection of DMPC Fe_3O_4@MSN is elevated compared to the level in liver of mice treated by native and PEG Fe_3O_4@MSN (Figure 6a). This shows a strong capture of DMPC Fe_3O_4@MSN by the liver.

However the accumulation in the spleen is almost similar between the 3 batches of MSN. Importantly, the lung is a biological barrier that is crucial to avoid and we can see that the amount of silicium in the lung is as low as the background level when mice were treated with DMPC Fe_3O_4@MSN. In contrast, this level is higher after injection of native and PEG Fe_3O_4@MSN.

In the blood, 2 h after injection, the levels of silicium are equally elevated between the different batches (Figure 6b). In contrast, 6 h after injection, we can see that the amount of circulating nanoparticles for natives and PEG Fe_3O_4@MSN decrease slowly, while DMPC Fe_3O_4@MSN do not circulate anymore (Figure 6b). This could be correlated to a rapid and strong uptake by the liver. We note that 24 h after the injection, PEG Fe_3O_4@MSN are still well present in blood, suggesting a better circulation time due to the coating.

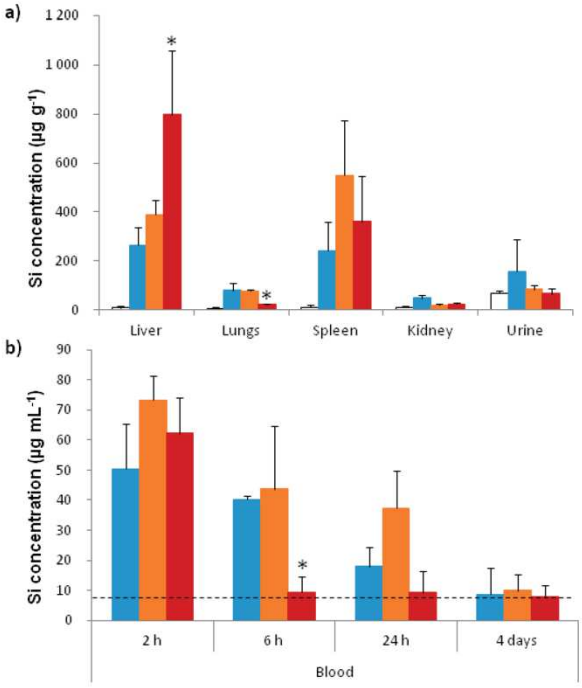

Figure 6. Biodistribution of Fe_3O_4@MSN in mice. (**a**) Quantification of silicium in different organs 4 days after injection. Inductively coupled plasma-mass spectrometry (ICPMS) was used after acid digestion to quantify the silicium in the liver, the lungs, the spleen, the kidneys, and urine 4 days after intravenous injection of native (blue), PEG (orange) and DMPC (red) Fe_3O_4@MSN at a concentration of 40 mg kg^{-1} in comparison to control mice (white); (**b**) NPs level in blood. The silicium was quantified in the blood 2 h, 6 h, 24 h, and 4 days after intravenous injection of native (blue), PEG (orange) and DMPC (red) Fe_3O_4@MSN at a concentration of 40 mg kg^{-1}. The dashed line indicates the silicium level found in the blood of control mice. For this experiment 20 mice were divided in 4 groups of 5 animals. Values of histograms represent mean ± SD of values of each animal of a group. * $p < 0.05$ statistically different from all other groups treated with NPs.

3. Discussion

The presented data demonstrate that native, DMPC and PEG Fe_3O_4@MSN stay dispersed and stable during 15 h when diluted in a medium having a low ionic strength (HBS 5 mM NaCl, pH 7.4).

When the ionic strength was increased to a more physiological amount of NaCl (HBS 150 mM NaCl, pH 7.4), native and PEG Fe_3O_4@MSN rapidly aggregated. The aggregation may be explained by a compression of the electrical double layer [23]. The coating with PEG is supposed to reduce the aggregation of NPs in suspension, by adding a steric repulsion between the NPs surfaces [37]. If the polymer grafting is heterogeneous, there is low electrostatic repulsion between the NPs, and the proteins are adsorbed on the non-coated surfaces leading to a progressive dispersion of the NPs. So the stabilizing effect of polymer grafting is not always obtained, depending of the polymer chain length, of the grafting density and the conformation of the chains at the NPs surface [6]. These different parameters influence the formation of a water shell [38] and the adhesion of some proteins at the surface [39]. Native Fe_3O_4@MSN rapidly dispersed in the presence of proteins (SVF 10%, in HBS 150 mM NaCl, pH 7.4 or RPMI). The electrostatic repulsion between negatively charged NPs surface and the proteins is reduced by the high ionic strength [40]. The protein corona forms a stabilizing shell around native Fe_3O_4@MSN. On the contrary, PEG Fe_3O_4@MSN are aggregated when diluted in HBS 150 mM NaCl, pH 7.4, in the presence or in the absence of proteins, or in RPMI containing SVF 10% and then slowly dispersed in the presence of proteins. The stealth effect expected by NPs coating with PEG is due to a significant reduction of the protein corona [41]. Yet, some proteins are still adsorbed because, as it has been previously described, the adsorption of proteins is a prerequisite to induce a stealth effect [8]. In our study, the adsorption of proteins onto the PEG Fe_3O_4@MSN surface was progressive, inducing a reduction of the aggregation state in suspension. DMPC Fe_3O_4@MSN stay stable in suspension during 15 h in HBS 150 mM NaCl, pH 7.4 or in cell culture medium (RPMI), containing or not SVF 10% proteins. The reduction of aggregation state of NPs by coating with a lipid bilayer was previously described [42]. The influence of proteins on the aggregation state of NPs has consequences on their interaction with the cell membrane, and potentially on their toxicity [4]. From QCM-D experiments performed in HBS 150 mM NaCl, pH 7.4, containing FCS 10%, DMPC-Fe_3O_4@MSN were found to rapidly deposit during the NPs flowing. Conversely, native and PEG Fe_3O_4@MSN were found to deposit more slowly. The stabilization of native Fe_3O_4@MSN and less importantly PEG Fe_3O_4@MSN by the presence of proteins in the medium seemed to reduce the deposition of the NPs on the membrane surface. On the contrary, the DMPC Fe_3O_4@MSN stability in suspension was not influenced by the presence of the proteins, and they were rapidly deposited on the membrane model.

The internalization of DMPC Fe_3O_4@MSN by Hep-G2 cells was also faster than the internalization observed for native and PEG Fe_3O_4@MSN. DMPC Fe_3O_4@MSN were observed inside intracellular vesicles after 3 h while native and PEG Fe_3O_4@MSN were observed inside cells after 6 h of incubation. These results suggest an early interaction between DMPC Fe_3O_4@MSN and Hep-G2 cell membrane than for the two other types of NPs. This is in accordance with the results obtained by real-time cell impedance measurements reported previously [22]. Using this indirect technique, an early variation of the cell index was observed when the Hep-G2 cell line was exposed to DMPC Fe_3O_4@MSN in comparison to native and PEG Fe_3O_4@MSN. To conclude on the impact of proteins on NPs cell membrane interactions, the more protein corona is important, the less NPs interact with the cellular membrane. Moreover, native Fe_3O_4@MSN, rapidly coated with serum proteins were slowly internalized by Hep-G2 cells, but remained the more cytotoxic according to the MTT assay and real-time cell impedance measurements. In this previous work, native Fe_3O_4@MSN induced 40% of cell death at a concentration of 100 $\mu g\ mL^{-1}$, when in the same conditions NPs recovered by PEG or DMPC induced 5% or 30% of cell death, respectively.

From in vivo experiments using mice, no toxic effect was observed four days after intravenous injection of native, PEG, or DMPC Fe_3O_4@MSN for a particle concentration of 40 $mg\ kg^{-1}$ on the renal or hepatic function, neither on inflammation factors. The histological observations show no difference between the liver, the spleen or kidneys of treated and non-treated mice. These results are in accordance with other published works on native MSN [19,36].

However, different biodistribution profiles were observed depending of the particle coating. Firstly, the DMPC Fe_3O_4@MSN were quickly cleared from the blood circulation, because no more

silicium was detected in comparison to control mice 6 h after injection of the NPs. This could be due, at least in part, to an efficient targeting of the liver. In addition, a large amount of in vivo data indicates that nanoparticles have the capacity to exert adverse pulmonary effects after different ways of exposure and systemic also, and it is a real challenge to avoid lung penetration [43]. Here, the very low level of silicium in the lungs of mice treated with DMPC Fe_3O_4@MSN translates the poor accumulation of these NPs in lungs, which is of major interest for a medical application.

Conversely, the amount of silicium 24 h after injection is not significantly different to 6 h for PEG Fe_3O_4@MSN, suggesting that the PEG coated NPs are slowly distributed in the organs. The presence of native and PEG Fe_3O_4@MSN in the lung may be due to the easier formation of aggregates than with DMPC Fe_3O_4@MSN. The prolonged circulation time observed for PEG Fe_3O_4@MSN is associated to a poor and slow cell internalization of the NPs. On the contrary, DMPC Fe_3O_4@MSN are rapidly internalized by cells; plus the absence of aggregation of DMPC Fe_3O_4@MSN at high ionic strength or in the presence of proteins, is a considerable advantage in the challenge of a translational objective. This is the first study on well-characterized monodisperse core-shell MSN comparing native or coated with PEG polymer or DMPC lipid bilayer by in vitro, in vivo experiments, and using cell membrane models.

4. Materials and Methods

4.1. Materials

All reagents were commercially available and used without any further purification. Hydrated iron oxide [FeO(OH), catalyst grade 30–50 mesh], oleic acid (90%), oleylamine (99%), diethylether (≥99.9%), anhydrous ethanol (≥99.8%), anhydrous pentane (99+%), anhydrous chloroform (99+%), tetraethoxysilane (TEOS, ≥99.9%), cetyltrimethylammonium bromide (CTAB), ammonium nitrate (NH_4NO_3), dimethyl sulfoxide (DMSO) and *N*-(2-hydroxyethyl)piperazine-*N*′-[2-ethanesulfonic acid] (Hepes), sodium dodecyl sulfate (SDS) were purchased from Sigma-Aldrich (Saint-Louis, MO, USA). Ultrapure Normatom® acids for trace metal analysis HNO_3 67–69% and HCl 34% were obtained from VWR (Atlanta, GA, USA). PlasmaPure H_2O_2 30% was obtained from SCP Science (Québec, QC, Canada). Sodium hydroxide (NaOH) and *n*-docosane (99%) were purchased from Acros (ThermoFisher Scientific, Waltham, MA, USA). Potassium chloride (KCl) was purchased from Prolabo (VWR, Atlanta, GA, USA). Hellmanex was purchased from Hellma (Müllheim, Germany). 1,2-dimyristoyl-sn-glycero-3-phosphocholine (DMPC) and L-α-phosphatidylcholine (EggPC) were purchased from Avanti polar lipids (Alabaster, AL, USA). DPBS buffer (KCl 2.66 mM, KH_2PO_4 1.47 mM, NaCl 137.93 mM, Na_2HPO_4-$7H_2O$ 8.05 mM, pH = 7.4) was provided by Gibco (ThermoFisher scientific, Waltham, MA, USA). Silanized PEG (CH_3O-PEG_{2000}-$Si(OCH_3)_3$) was purchased from Rapp polymer (Tuebingen, Germany).

Concerning cryo-electron microscopy, three microliters of suspension were applied to glow discharged Quantifoil R 2/2 grids (Quantifoil Micro Tools GmbH, Jena, Germany) or Lacey grid (Ted Pella Inc., Redding, CA, USA), blotted for 1s and then flash frozen in liquid ethane using a CP3 cryo-plunge (Gatan Inc., Pleasanton, CA, USA). Before freezing, the humidity rate was stabilized at about 95%. Cryo-EM was carried out on a JEOL 2200FS FEG operating at 200 kV under low-dose conditions (total dose of 20 electrons/$Å^2$) in the zero-energy-loss mode with a slit width of 20 eV. Images were taken at a nominal magnification of 50,000× corresponding to a calibrated magnification of 45,591× with defocus ranging from 1.4 to 2.5 µm.

4.2. Synthesis and Characterization of NPs

The native, PEG-grafted and lipid-coated Fe_3O_4@MSN were synthesized following the procedure recently described [22]. The same characterization methods were used. Hydrodynamic diameters and zeta potentials were determined using a Nano ZS apparatus (Malvern Instruments, Malvern, UK). Data were collected from the He-Ne laser light source (λ = 633 nm) at 173° from the transmitted light beam. Stock suspensions of the Fe_3O_4@MSN were prepared in stable conditions at a concentration

of 10 mg mL^{-1}. Pristines Fe_3O_4@MSN were dispersed in ethanol 95%, DMPC Fe_3O_4@MSN in HBS 150 mM NaCl and PEG Fe_3O_4@MSN in HBS 5 mM NaCl. The different suspensions were then diluted in different media at a concentration of 50 µg mL^{-1}. The dispersion behavior of the different Fe_3O_4@MSN was compared in 5 different media: ethanol, HBS 5 mM NaCl, HBS 150 mM NaCl, HBS 150 mM NaCl containing 10% FCS and complete RPMI (FCS 10%). The same suspensions were analyzed directly after dispersion, 2 h and 15 h later. Results are presented as Z-average obtained in intensity mode, associated to the polydispersity index (PDI).

4.3. Interaction of NPs with Membrane Models

The interactions of Fe_3O_4@MSN with model membranes were investigated using a QCM-D E1 setup (Biolin Scientific, Västra Frölunda, Sweden). The system is composed of a measurement chamber containing a 5 MHz quartz crystal sensor with a silica-coated surface. After each measurement, the chamber, the flow module, and the quartz were rinsed with 2 mL 2% Hellmanex and with 5 mL MilliQ water at a flow of 0.5 mL min^{-1}. The silica-coated quartz sensor was stored in a SDS 2% solution between two analyses. All measurements were performed at 25 °C. Firstly, the silica-coated surface was rinsed with MilliQ water, dried and placed during 15 min in UV-ozone chamber. Then, HBS 150 mM NaCl was flushed at 100 µL min^{-1}, and the quartz sensor was equilibrated for each overtone (1st to 13th). The baseline was obtained using HBS 150 mM NaCl both for the frequency and dissipation recordings. A supported lipid bilayer (SLB) is formed on a silica-coated surface of the QCM-D sensor after fusion of EPC small vesicles SUVs). For SUVs formation, a EPC lipid film was resuspended in Hepes 150 mM NaCl, ultrasonicated using a microtip (Digital Sonifier 250®, Branson Ultrasonics Corporation, Danbury, CT, USA), and then centrifuged at 20,000× *g* for 15 min (to remove titanium particles). The supernatant containing SUVs was collected and filtrated through 50 nm porous polycarbonate membrane before coating the SiO_2 QCM-D sensor. The SLB was formed by adding Egg PC SUVs (50 nm) in HBS 150 mM NaCl buffer at a lipid concentration of 0.1 mg mL^{-1} using a flow of 100 µL min^{-1} for 10 min. The formation of a continuous lipid bilayer is characterized by a frequency shift Δf of −26 Hz and a dissipation shift $\Delta D < 0.5 \times 10^{-6}$ followed on the 7th overtone. The membrane was washed during 1 h with HBS 150 mM NaCl under a flow of 100 µL min^{-1} for stabilization. Before adding NPs on top of the SLB, the NPs dispersant media was injected to recording Δf and ΔD changes due to the solvent composition. The NPs were dispersed at 0.25 mg mL^{-1} in HBS 150 mM NaCl containing 10% FCS, and then added on the membrane for 15 min (100 µL min^{-1}, 1.5 mL), and the flow was stopped for 10 h. Results were presented after offset of the SLB frequency and dissipation recordings, in order to analyze only the NPs effect.

4.4. Cellular Assays

4.4.1. Cell Culture

The Human hepatocyte carcinoma (Hep-G2) cell line was obtained from Sigma-Aldrich. Cells were cultured in RPMI 1640 (Invitrogen, Carlsbad, CA, USA) supplemented with 10% fetal calf serum (FCS) and 1% penicillin/streptomycin (100 U mL^{-1}, 100 µg mL^{-1}) and incubated in a cell incubator at 37 °C and 5% CO_2. Cells were used between passages 20 to 40. Cells were passed once a week and the medium was changed twice a week, keeping cells confluence below 80%.

4.4.2. Internalization Assay

Hep-G2 cells were seeded on glass coverslips for 24 h. After controlling their adherence and growing, cells were exposed to 50 µg mL^{-1} of NPs in RPMI for 3, 6 or 24 h at 37 °C and 5% CO_2. The medium was removed and cells were rinsed twice with DPBS. Cells were fixed by incubation with 2.5% (*v*/*v*) glutaraldehyde in DPBS buffer, for 1 h at room temperature (RT). Then, cells were extensively washed with DPBS. The staining of samples was obtained upon incubation with 1% osmium tetroxide. Samples were dehydrated by ascending grades of EtOH; for impregnation,

the samples were firstly treated with a mix EtOH/EPON^{TM} resin (1:1, v/v) for 1 h, and twice in EPON for 2 h. The polymerization was performed by embedding cells in EPON resin for 12 h at 60 °C, plunged in liquid nitrogen at −195 °C to detach the coverslip, and placed for two days at 60 °C for completing polymerization. The ultrathin sections (70 nm) were obtained using an ultramicrotome (Leica Ultracut, Wetzlar, Germany) and disposed on the copper grids. The grids were incubated in uranyl acetate for 2 min, rinsed in water, and then incubated in lead citrate for 2 min, and finally rinsed with water. For each condition (native, PEG and DMPC Fe_3O_4@MSN at 3, 6 or 24 h exposure time of Hep-G2 cells), almost 20 cells were observed, and then the observations were focused on the areas were NPs were observed.

4.5. Biodistribution in Mice

4.5.1. Animals

Female C57BL/6 mice (25 g) used for this study were procured from Charles River (Wilmington, MA, USA) and housed in the Institutional animal house under standard environmental conditions (23 ± 1 °C, 55 ± 5% humidity and 12/12 h, light/dark cycles) and maintained with free access to standard diet and water. To establish the preliminary toxicological analyses, 4 groups of 5 mice were injected intravenously with 200 µL of saline solution with or without MSN at a concentration of 40 mg kg^{-1}. (1) Control group (saline solution injection) (2) Native-Fe_3O_4@MSN (3) DMPC-Fe_3O_4@MSN (4) PEG-Fe_3O_4@MSN.

4.5.2. Preliminary Toxicological Assessment

Four days after treatment, mice were sacrificed and organs, blood and urine were collected for histological analysis and biochemical assays. The blood samples with heparin were centrifuged at 1300 rpm for 10 min. The plasma and urine were stored at −20 °C up to analysis. We measured plasma cytokines (TNF-α and IL-6) to assess the inflammatory reaction or systemic toxicity. Plasma TNF-α and IL-6 levels were quantified using commercial ELISA kits as described in the manufacturer's protocol (R&D systems, Minneapolis, MN, USA). The evaluation of renal function was determined by measuring creatinine levels in plasma and in urine using colorimetric assay at 495 nm with alkaline picrate. Liver function was determined from alanine aminotransferase (ALT) activity. Plasma ALT activity was measured according to standard protocol (Infinity, Thermo Scientific, Waltham, MA, USA). Moreover, liver, spleen and kidney were fixed in 10% paraformaldehyde, embedded in paraffin and cut 5 µm tick sections in a microtome. Sections were mounted on glass slides. After staining with hematoxylin-eosin, the sections were examined and imaged under a light microscope.

4.5.3. In Vivo Distribution and Degradation of MSN

Inductively coupled plasma-mass spectrometry (ICP-MS) was used to quantify silicium distribution in the digested tissue samples (liver, kidney and spleen). 2–100 mg of biological samples (urine, blood, or lyophilized and crushed kidney, spleen or liver) were digested in HNO_3 (1 mL, 67%) for 1 h, and then HCl (1 mL, 34%) and of H_2O_2 (0.5 mL, 30%) for 1 h. The digestion was completed by microwave in Teflon vials, by using UltraWAVE single reaction chamber (Milestone, Shelton, AL, USA). Silicium content was further analysed using a NexION™ 300 ICP-MS instrument (PerkinElmer, Waltham, MA, USA), from the analytical platform facilities of CEREGE (Aix en Provence, France).

4.6. Statistical Analysis

Statistical analysis was performed using the Student's *t*-test to compare paired groups of data. A p value < 0.05 was considered as statistically significant.

Acknowledgments: This work was supported by the French national research agency (ANR-13-NANO-0007, BioSiPharm project), and by "Chercheur d'Avenir Languedoc Roussillon". We thank the technological platform of microscopy of Montpellier University for the use of their electron microscope and their technical support,

in particular Franck Godiard and Véronique Richard. Patrick Bron et Joséphine Lai-Kee-Him would like to thank the French Infrastructure for Integrated Structural Biology (FRISBI) for its support, a national infrastructure supported by the French National Research Agency (ANR-10-INBS-05). We also thank Laure Lichon for technical assistance in the experiments.

Author Contributions: J.C., J.-M.D., Y.G. and C.C. conceived and designed the project of magnetic nanoparticles. M.G., M.M. and M.G.-B. devised the biological experiments to demonstrate the potential of magnetic nanoparticles. E.R. and C.D. synthetized the nanomaterials and performed the experiments with supported lipid bilayer models. M.D., A.D.S. and M.M., performed in vitro and in vivo experiments. M.A., W.L. and B.A. made the ICP-MS experiments. J.L.-K.-H. and P.B. made cryo-electron microscopy experiments.

Conflicts of Interest: The authors declare no conflict of interest.

References

1. Tarn, D.; Ashley, C.E.; Xue, M.; Carnes, E.C.; Zink, J.I.; Brinker, C.J. Mesoporous silica nanoparticle nanocarriers: Biofunctionality and biocompatibility. *Acc. Chem. Res.* **2012**, *46*, 792–801. [CrossRef] [PubMed]
2. Lazarovits, J.; Chen, Y.Y.; Sykes, E.A.; Chan, W.C. Nanoparticle-blood interactions: The implications on solid tumour targeting. *Chem. Commun.* **2015**, *51*, 2756–2767. [CrossRef] [PubMed]
3. Monopoli, M.P.; Walczyk, D.; Campbell, A.; Elia, G.; Lynch, I.; Bombelli, F.B.; Dawson, K.A. Physical-chemical aspects of protein corona: Relevance to in vitro and in vivo biological impacts of nanoparticles. *J. Am. Chem. Soc.* **2011**, *133*, 2525–2534. [CrossRef] [PubMed]
4. Westmeier, D.; Stauber, R.H.; Docter, D. The concept of bio-corona in modulating the toxicity of engineered nanomaterials (ENM). *Toxicol. Appl. Pharmacol.* **2015**, *299*, 53–57. [CrossRef] [PubMed]
5. Tada, D.B.; Suraniti, E.; Rossi, L.M.; Leite, C.A.; Oliveira, C.S.; Tumolo, T.C.; Calemczuk, R.; Livache, T.; Baptista, M.S. Effect of lipid coating on the interaction between silica nanoparticles and membranes. *J. Biomed. Nanotechnol.* **2014**, *10*, 519–528. [CrossRef] [PubMed]
6. Pozzi, D.; Caracciolo, G.; Capriotti, A.L.; Cavaliere, C.; La Barbera, G.; Anchordoquy, T.J.; Lagana, A. Surface chemistry and serum type both determine the nanoparticle-protein corona. *J. Proteom.* **2015**, *119*, 209–217. [CrossRef] [PubMed]
7. Hadjidemetriou, M.; Al-Ahmady, Z.; Mazza, M.; Collins, R.F.; Dawson, K.; Kostarelos, K. In vivo biomolecule corona around blood-circulating, clinically used and antibody-targeted lipid bilayer nanoscale vesicles. *ACS Nano* **2015**, *9*, 8142–8156. [CrossRef] [PubMed]
8. Schottler, S.; Becker, G.; Winzen, S.; Steinbach, T.; Mohr, K.; Landfester, K.; Mailander, V.; Wurm, F.R. Protein adsorption is required for stealth effect of poly(ethylene glycol)—And poly(phosphoester)—Coated nanocarriers. *Nat. Nanotechnol.* **2016**, *11*, 372–377. [CrossRef] [PubMed]
9. Dobrovolskaia, M.A.; Neun, B.W.; Man, S.; Ye, X.; Hansen, M.; Patri, A.K.; Crist, R.M.; McNeil, S.E. Protein corona composition does not accurately predict hematocompatibility of colloidal gold nanoparticles. *Nanomedicine* **2014**, *10*, 1453–1463. [CrossRef] [PubMed]
10. Xu, D.; Hodges, C.; Ding, Y.; Biggs, S.; Brooker, A.; York, D. Adsorption kinetics of laponite and ludox silica nanoparticles onto a deposited poly(diallyldimethylammonium chloride) layer measured by a quartz crystal microbalance and optical reflectometry. *Langmuir* **2010**, *26*, 18105–18112. [CrossRef] [PubMed]
11. Xu, F.; Reiser, M.; Yu, X.; Gummuluru, S.; Wetzler, L.; Reinhard, B.M. Lipid-mediated targeting with membrane-wrapped nanoparticles in the presence of corona formation. *ACS Nano* **2016**, *10*, 1189–1200. [CrossRef] [PubMed]
12. Pombo Garcia, K.; Zarschler, K.; Barbaro, L.; Barreto, J.A.; O'Malley, W.; Spiccia, L.; Stephan, H.; Graham, B. Zwitterionic-coated "stealth" nanoparticles for biomedical applications: Recent advances in countering biomolecular corona formation and uptake by the mononuclear phagocyte system. *Small* **2014**, *10*, 2516–2529. [CrossRef] [PubMed]
13. Choi, H.S.; Ipe, B.I.; Misra, P.; Lee, J.H.; Bawendi, M.G.; Frangioni, J.V. Tissue- and organ-selective biodistribution of nir fluorescent quantum dots. *Nano Lett.* **2009**, *9*, 2354–2359. [CrossRef] [PubMed]
14. Liu, X.; Situ, A.; Kang, Y.; Villabroza, K.R.; Liao, Y.; Chang, C.H.; Donahue, T.; Nel, A.E.; Meng, H. Irinotecan delivery by lipid-coated mesoporous silica nanoparticles shows improved efficacy and safety over liposomes for pancreatic cancer. *ACS Nano* **2016**, *10*, 2702–2715. [CrossRef] [PubMed]

15. Warther, D.; Jimenez, C.M.; Raehm, L.; Gerardin, C.; Durand, J.-O.; Morere, A.; El Cheikh, K.; Gallud, A.; Gary-Bobo, M.; Maynadier, M.; et al. Small sized mesoporous silica nanoparticles functionalized with mannose for retinoblastoma cell imaging. *RSC Adv.* **2014**, *4*, 37171–37179. [CrossRef]
16. Mashaghi, S.; Jadidi, T.; Koenderink, G.; Mashaghi, A. Lipid nanotechnology. *Int. J. Mol. Sci.* **2013**, *14*, 4242–4282. [CrossRef] [PubMed]
17. Bringas, E.; Koysuren, O.; Quach, D.V.; Mahmoudi, M.; Aznar, E.; Roehling, J.D.; Marcos, M.D.; Martinez-Manez, R.; Stroeve, P. Triggered release in lipid bilayer-capped mesoporous silica nanoparticles containing spion using an alternating magnetic field. *Chem. Commun.* **2012**, *48*, 5647–5649. [CrossRef] [PubMed]
18. Van Schooneveld, M.M.; Vucic, E.; Koole, R.; Zhou, Y.; Stocks, J.; Cormode, D.P.; Tang, C.Y.; Gordon, R.E.; Nicolay, K.; Meijerink, A.; et al. Improved biocompatibility and pharmacokinetics of silica nanoparticles by means of a lipid coating: A multimodality investigation. *Nano Lett.* **2008**, *8*, 2517–2525. [CrossRef] [PubMed]
19. Liu, J.; Qiao, S.Z.; Hu, Q.H.; Lu, G.Q. Magnetic nanocomposites with mesoporous structures: Synthesis and applications. *Small* **2011**, *7*, 425–443. [CrossRef] [PubMed]
20. Kang, H.; Mintri, S.; Menon, A.V.; Lee, H.Y.; Choi, H.S.; Kim, J. Pharmacokinetics, pharmacodynamics and toxicology of theranostic nanoparticles. *Nanoscale* **2015**, *7*, 18848–18862. [CrossRef] [PubMed]
21. Liu, J.; Detrembleur, C.; Pauw-Gillet, D.; Mornet, S.; Vander Elst, L.; Laurent, S.; Jérôme, C.; Duguet, E. Heat-triggered drug release systems based on mesoporous silica nanoparticles filled with a maghemite core and phase-change molecules as gatekeepers. *J. Mater. Chem. B* **2014**, *2*, 59–70. [CrossRef]
22. Nyalosaso, J.L.; Rascol, E.; Pisania, C.; Dorandeu, C.; Dumail, X.; Maynadier, M.; Gary-Bobo, M.; Lai Kee Him, J.; Bron, P.; Garcia, M.; et al. Synthesis, decoration, and cellular effects of magnetic mesoporous silica nanoparticles. *RSC Adv.* **2016**, *6*, 57275–57283. [CrossRef]
23. Moore, T.L.; Rodriguez-Lorenzo, L.; Hirsch, V.; Balog, S.; Urban, D.; Jud, C.; Rothen-Rutishauser, B.; Lattuada, M.; Petri-Fink, A. Nanoparticle colloidal stability in cell culture media and impact on cellular interactions. *Chem. Soc. Rev.* **2015**, *44*, 6287–6305. [CrossRef] [PubMed]
24. Nel, A.E.; Madler, L.; Velegol, D.; Xia, T.; Hoek, E.M.; Somasundaran, P.; Klaessig, F.; Castranova, V.; Thompson, M. Understanding biophysicochemical interactions at the nano-bio interface. *Nat. Mater.* **2009**, *8*, 543–557. [CrossRef] [PubMed]
25. Luyts, K.; Napierska, D.; Nemery, B.; Hoet, P.H. How physico-chemical characteristics of nanoparticles cause their toxicity: Complex and unresolved interrelations. *Environ. Sci. Process. Impacts* **2013**, *15*, 23–38. [CrossRef] [PubMed]
26. Chen, K.L.; Bothun, G.D. Nanoparticles meet cell membranes: Probing nonspecific interactions using model membranes. *Environ. Sci. Technol.* **2013**, *48*, 873–880. [CrossRef] [PubMed]
27. Rascol, E.; Devoisselle, J.M.; Chopineau, J. The relevance of membrane models to understand nanoparticles-cell membrane interactions. *Nanoscale* **2016**, *8*, 4780–4798. [CrossRef] [PubMed]
28. Keller, C.A.; Kasemo, B. Surface specific kinetics of lipid vesicle adsorption measured with a quartz crystal microbalance. *Biophys. J.* **1998**, *75*, 1397–1402. [CrossRef]
29. Richter, R.P.; Brisson, A.R. Following the formation of supported lipid bilayers on mica: A study combining AFM, QCM-D, and ellipsometry. *Biophys. J.* **2005**, *88*, 3422–3433. [CrossRef] [PubMed]
30. Li, W.; Liu, D.; Wu, J.; Kim, C.; Fortner, J.D. Aqueous aggregation and surface deposition processes of engineered superparamagnetic iron oxide nanoparticles for environmental applications. *Environ. Sci. Technol.* **2014**, *48*, 11892–11900. [CrossRef] [PubMed]
31. Quevedo, I.R.; Olsson, A.L.; Tufenkji, N. Deposition kinetics of quantum dots and polystyrene latex nanoparticles onto alumina: Role of water chemistry and particle coating. *Environ. Sci. Technol.* **2013**, *47*, 2212–2220. [CrossRef] [PubMed]
32. Bailey, C.M.; Kamaloo, E.; Waterman, K.L.; Wang, K.F.; Nagarajan, R.; Camesano, T.A. Size dependence of gold nanoparticle interactions with a supported lipid bilayer: A QCM-D study. *Biophys. Chem.* **2015**, *203*, 51–61. [CrossRef] [PubMed]
33. Liu, X.; Chen, K.L. Interactions of graphene oxide with model cell membranes: Probing nanoparticle attachment and lipid bilayer disruption. *Langmuir* **2015**, *31*, 12076–12086. [CrossRef] [PubMed]
34. Yi, P.; Chen, K.L. Interaction of multiwalled carbon nanotubes with supported lipid bilayers and vesicles as model biological membranes. *Environ. Sci. Technol.* **2013**, *47*, 5711–5719. [CrossRef] [PubMed]

35. Wang, Q.; Lim, M.; Liu, X.; Wang, Z.; Chen, K.L. Influence of solution chemistry and soft protein coronas on the interactions of silver nanoparticles with model biological membranes. *Environ. Sci. Technol.* **2016**, *50*, 2301–2309. [CrossRef] [PubMed]
36. Fu, C.; Liu, T.; Li, L.; Liu, H.; Chen, D.; Tang, F. The absorption, distribution, excretion and toxicity of mesoporous silica nanoparticles in mice following different exposure routes. *Biomaterials* **2013**, *34*, 2565–2575. [CrossRef] [PubMed]
37. Graf, C.; Gao, Q.; Schutz, I.; Noufele, C.N.; Ruan, W.; Posselt, U.; Korotianskiy, E.; Nordmeyer, D.; Rancan, F.; Hadam, S.; et al. Surface functionalization of silica nanoparticles supports colloidal stability in physiological media and facilitates internalization in cells. *Langmuir* **2012**, *28*, 7598–7613. [CrossRef] [PubMed]
38. Heuberger, M.; Drobek, T.; Voros, J. About the role of water in surface-grafted poly(ethylene glycol) layers. *Langmuir* **2004**, *20*, 9445–9448. [CrossRef] [PubMed]
39. Pasche, S.; Voros, J.; Griesser, H.J.; Spencer, N.D.; Textor, M. Effects of ionic strength and surface charge on protein adsorption at pegylated surfaces. *J. Phys. Chem. B* **2005**, *109*, 17545–17552. [CrossRef] [PubMed]
40. Fatisson, J.; Quevedo, I.R.; Wilkinson, K.J.; Tufenkji, N. Physicochemical characterization of engineered nanoparticles under physiological conditions: Effect of culture media components and particle surface coating. *Colloids Surf. B Biointerfaces* **2012**, *91*, 198–204. [CrossRef] [PubMed]
41. Pelaz, B.; del Pino, P.; Maffre, P.; Hartmann, R.; Gallego, M.; Rivera-Fernandez, S.; de la Fuente, J.M.; Nienhaus, G.U.; Parak, W.J. Surface functionalization of nanoparticles with polyethylene glycol: Effects on protein adsorption and cellular uptake. *ACS Nano* **2015**, *9*, 6996–7008. [CrossRef] [PubMed]
42. Bagwe, R.P.; Hilliard, L.R.; Tan, W. Surface modification of silica nanoparticles to reduce aggregation and nonspecific binding. *Langmuir* **2006**, *22*, 4357–4362. [CrossRef] [PubMed]
43. Card, J.W.; Zeldin, D.C.; Bonner, J.C.; Nestmann, E.R. Pulmonary applications and toxicity of engineered nanoparticles. *Am. J. Physiol. Lung Cell. Mol. Physiol.* **2008**, *295*, L400–L411. [CrossRef] [PubMed]

ANNEXE 3

nanomaterials

MDPI

Article

Stealth Biocompatible Si-Based Nanoparticles for Biomedical Applications

Wei Liu [1], Arnaud Chaix [2], Magali Gary-Bobo [3], Bernard Angeletti [1], Armand Masion [1], Afitz Da Silva [3,4], Morgane Daurat [3,4], Laure Lichon [3], Marcel Garcia [3], Alain Morère [3], Khaled El Cheikh [4], Jean-Olivier Durand [2], Frédérique Cunin [2] and Mélanie Auffan [1,*]

1 CNRS, IRD, Coll de France, CEREGE, Aix Marseille Université, 13545, Aix en Provence, France; wei.yanzi.liu@gmail.com (W.L.); angeletti@cerege.fr (B.A.); masion@cerege.fr (A.M.)
2 Institut Charles Gerhardt Montpellier, UMR 5253 CNRS-ENSCM-UM, Ecole Nationale Supérieure de Chimie Montpellier, 8 rue de l'Ecole Normale, 34296 Montpellier, France; arnaud.chaix@enscm.fr (A.C.); durand@univ-montp2.fr (J.-O.D.); frederique.cunin@enscm.fr (F.C.)
3 Institut des Biomolécules Max Mousseron, UMR 5247 CNRS-UM, 15 Avenue Charles Flahault, BP 14491, 34093 Montpellier CEDEX 05, France; magali.gary-bobo@inserm.fr (M.G.-B.); afitz@hotmail.fr (A.D.S.); morgane.daurat2@gmail.com (M.D.); laure.lichon@umontpellier.fr (L.L.); marcel.garcia@inserm.fr (M.G.); alain.morere@umontpellier.fr (A.M.)
4 NanoMedSyn, 15 Avenue Charles Flahault, BP 14491, 34093 Montpellier CEDEX 05, France; k.elcheikh@nanomedsyn.com
* Correspondence: auffan@cerege.fr; Tel.: +33-442-97-1543

Received: 31 August 2017; Accepted: 20 September 2017; Published: 23 September 2017

Abstract: A challenge regarding the design of nanocarriers for drug delivery is to prevent their recognition by the immune system. To improve the blood residence time and prevent their capture by organs, nanoparticles can be designed with stealth properties using polymeric coating. In this study, we focused on the influence of surface modification with polyethylene glycol and/or mannose on the stealth behavior of porous silicon nanoparticles (pSiNP, ~200 nm). In vivo biodistribution of pSiNPs formulations were evaluated in mice 5 h after intravenous injection. Results indicated that the distribution in the organs was surface functionalization-dependent. Pristine pSiNPs and PEGylated pSiNPs were distributed mainly in the liver and spleen, while mannose-functionalized pSiNPs escaped capture by the spleen, and had higher blood retention. The most efficient stealth behavior was observed with PEGylated pSiNPs anchored with mannose that were the most excreted in urine at 5 h. The biodegradation kinetics evaluated in vitro were in agreement with these in vivo observations. The biocompatibility of the pristine and functionalized pSiNPs was confirmed in vitro on human cell lines and in vivo by cytotoxic and systemic inflammation investigations, respectively. With their biocompatibility, biodegradability, and stealth properties, the pSiNPs functionalized with mannose and PEG show promising potential for biomedical applications.

Keywords: porous silicon nanoparticle; surface functionalization; PEG; mannose; stealth properties; biodegradation kinetic; biocompatibility

1. Introduction

The emergence of nanomedicine has opened up opportunities for the development of more efficient anti-cancer agents that induce fewer side effects. Among these, porous Si-based nanoparticles (NPs) were found to be promising nanocarriers due to their biodegradability and biocompatibility [1–6]. Si-based NPs display unique features such as high specific surface area and large porous volume [5,7] that are particularly interesting for: (i) the imaging of cancerous tissues [8–10]; (ii) selective binding to receptors overexpressed by target tissues or cells type in conjugation with specific ligands or

antibodies [11–19]; (iii) delivery of large concentrations of drugs and their controlled-release [1,20–22]; (iv) photosensitivity for photodynamic therapy (PDT) [23]; or (v) combination with two-photon excitation (TPE) in the near-infrared (IR) region that offers new perspectives for the treatment of solid tumors with an improved tissue penetration depth and spatial resolution [11,24].

One of the challenging issues concerning the development of such Si-based nanocarriers regards their recognition by the mononuclear phagocyte system (MPS) after their intravenous injection in the body. Such recognition will strongly decrease their performance and efficiency. With respect to NPs' clearance by the MPS, the liver and the spleen are the most active organs because of phagocytic cells as macrophages that act by surface opsonization [25] and generally express similar membrane receptors to those of tumors [26]. Given other constraints, such as the heterogeneities of tumors in terms of enhanced permeability and retention (EPR) and the multifactor impact such as electrolytes, proteins and lipids onto colloidal stability of nanocarriers, less than 10% of the total administered drug dose reaches the tumor [2]. Based on these considerations, there is a need to develop stealth nanocarriers with reduced uptake by the MPS and optimized for the EPR effect.

One way to design NPs with such stealth properties is surface functionalization by polyethylene glycol (PEG) to increase the surface hydrophilicity, improve the circulation time, and decrease the immune response by preventing interactions with blood proteins and MPS cells [27,28]. In this regard, PEG-functionalization efficiency has already been reported in vitro [29] and in vivo [10,30]. Another promising approach to increase the local concentration of Si-based NPs in tumor tissue is to conjugate these NPs with targeting molecules that have a high affinity for tumor cells. Sugars have been the focus of several studies since their receptors (lectins) are overexpressed in most of the cancer cells [31]. One possible targeting agent is low biomolecular weight mannose (Man), which was successfully used to target human cancer cells, including retina, breast and prostate, due to its high specificity to lectin receptors [11,15,32–34]. Previous studies by Gary-Bobo et al. have shown that the immobilization of Man derivatives at the surface of porous SiO_2 and Si NPs significantly increased the targeting of human breast (MCF-7, MDA-MB-231) and prostate (LNCaP) cancer cells by TPE–PDT therapy [11,15,32–34].

In this study, we designed porous silicon NPs (called pSiNPs) with PEG and/or Man functionalization in order to assess their stealth properties and biocompatibility in vivo after intravenous injection in mice. Biodistribution of pSiNP with PEG and mannose has not been studied yet to our knowledge. To quantify their avoidance by organs involved in the MPS and their clearance from the body, the Si content in target organs, blood and urine were measured using inductively coupled plasma mass spectrometry (ICP-MS). Complementary in vitro experiments were performed to assess the mechanisms of biodegradation and aggregation in standardized biological media. The chemical and colloidal stability of the formulations were compared by measuring the dissolution kinetics and aggregation states in the presence or not of fetal bovine serum (FBS). Finally, their biocompatibility was assessed in vivo by the plasma analysis of exposed mice and in vitro by measuring cell cytotoxicity.

2. Results and Discussion

2.1. Physico-Chemical Properties of Pristine and Formulated pSiNPs in Stock Suspensions

pSiNPs were synthesized by anodic etching of boron-doped crystalline silicon in a solution of aqueous hydrofluoric acid (HF) and ethanol, followed by electropolishing and fracturation of the porous layer. After centrifugation, NPs with a narrow-size distribution around 200 nm (using transmission electron microscopy (TEM)) were isolated. Oriented porosity with pore channels of 15–25 nm in diameter were observed, in agreement with average pore diameter calculated from the nitrogen adsorption/desorption analysis (19.4 nm). The pSiNPs also displayed a large surface area of 493 $m^2 \cdot g^{-1}$ (Figure S1).

The Bloch decay and cross-polarization magic angle spinning (CP-MAS) pulse sequences were used for the collection of ^{29}Si nuclear magnetic resonance (NMR) (Figure S2). While Bloch decay

collection gives information for all Si sites, CP-MAS is only sensitive to Si sites that are spatially close to protons i.e., the silanol groups at the surface of the NPs. In Bloch decay, only one peak was observed at approximately −110 ppm that was associated with siloxane and referred as Q4. In the ^{29}Si CP-MAS spectrum, two spectral features at −8 and −90 ppm were observed. With a NPs size of ~200 nm, the percentage of surface atoms described by these features was estimated to be less than 2%. The contribution with a chemical shift centered around −90 ppm (90% of total signal) is associated with surface silicon atoms that are predominantly in the Q2 configuration (i.e., with 2 hydroxyl groups). The peak with a chemical shift of approximately −8 ppm could be attributed to C–Si and represented <0.2% of Si. Based on these NMR observations we concluded that, once dispersed in absolute ethanol, the majority of the Si atoms of the pSiNPs were bound to oxygen.

Besides pristine pSiNPs, three formulations were prepared containing PEG and/or Man (Figure 1). The grafting of the PEG involved the functionalization of PEG diamine moiety with ICPES (isocyanopropyltriethoxysilane) prior to covalent attachment to the pSiNPs by silanization reaction, with the silanol present at the surface of the NPs (Figure S3). The mannose could then attach to the pendant PEG chain by reaction of the phenyl squarate with the amine function of the PEG (Figure S4). Finally, the grafting of mannose alone also involved chemical modification of a mannose phenyl squarate with APTES (aminopropyltriethoxysilane) for further grafting to the pSiNPs by silanization reaction (Figure S5). The covalent attachment of PEG and Man at the surface was confirmed by attenuated total reflectance Fourier transform infrared spectroscopy (ATR-FTIR) (Figure S6). Infrared spectroscopy confirmed the oxidation of the pSiNPs which is favorable for a successful surface chemical modification and functionalization by silanization chemistry. The amount of grafted Man was determined spectrophotometrically by reaction with resorcinol [24], at 36 μg and 28 μg of mannose phenyl squarate per mg of pSiNPs for pSiNPs–Man and pSiNPs–PEG–Man, respectively (Figure S7). These values are comparable for both grafting methods.

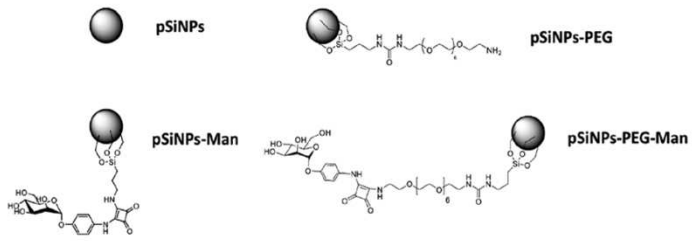

Figure 1. Schematic of the four pSiNPs formulations.

In ethanol, these oxidized pristine pSiNPs had average hydrodynamic diameters centered on 200 ± 20 nm (vol. %) and 185 ± 18 (num. %) with a moderate polydispersity index (PDI) around 0.16 ± 0.02 consistent with TEM images, and a negative zeta potential (−25 ± 1 mV). This negative zeta potential is due to the oxidation of the NPs and is attributed to the silanol groups present at the surface of the pSiNPs. After functionalization by PEG and/or Man, an increase of the average hydrodynamic diameters was observed for pSiNPs-PEG to 315 ± 26 nm (vol. %) and 185 ± 18 nm (num. %), for pSiNPs–Man to 488 ± 103 nm (vol. %) and 404 ± 33 nm (num. %), and for pSiNPs–PEG–Man to 530 ± 56 nm (vol. %) and 528 ± 77 nm (num. %). Moderate PDI values (0.35 ± 0.2 and 0.22 ± 0.1) were observed for pSiNPs–PEG and pSiNPs–Man, while for pSiNPs–PEG–Man the PDI values were higher (0.68 ± 0.3). The size distribution of hydrodynamic diameters is provided in supporting information (Figure S8). Zeta potential measurements also confirmed the successful chemical functionalization of the NPs observed by ATR-FTIR (Table 1). Indeed, the functionalization with PEG induced a charge inversion from negative (−25 ± 1 mV) to positive (28 ± 2 mV) in ethanol. This highlights that the surface of the pSiNPs was successfully functionalized by the cationic aminated PEG molecules (Table 1).

In comparison, modification of pSiNPs with Man slightly increased the zeta potential to -18 ± 1 mV in agreement with the successful functionalization of the surface by Man. Modifying the surface by both PEG and Man give a zeta potential value of 10 ± 0.2 mV showing the grafting of Man on PEG-functionalized pSiNPs.

Table 1. Zeta potential and hydrodynamic diameters (mean size value in vol. % and num. %) and PDI (polydispersity index) of pristine and functionalized pSiNPs in absolute ethanol. Data are the mean ± SD (n = 3).

Nanoparticles	pSiNPs	pSiNPs–PEG	pSiNPs–Man	pSiNPs–PEG–Man
Zeta potential (mV)	-25 ± 1	28 ± 2	-18 ± 1	10 ± 0.2
Hydrodynamic diameter (nm) vol. %	200 ± 20	315 ± 26	488 ± 103	530 ± 56
Hydrodynamic diameter (nm) num. %	185 ± 18	276 ± 35	404 ± 33	528 ± 77
PDI	0.16 ± 0.02	0.35 ± 0.2	0.22 ± 0.1	0.68 ± 0.3

2.2. In Vitro Biodegradability Kinetics

It is well known that the interactions between Si-based NPs and cancer cells depend not only on cell strains [5,35], but also on the size, surface properties, and solubility of the NPs in biological media [2,7,21,36,37]. Porous silicon has already been shown to be biodegradable in physiological environments, and to dissolve into orthosilicic acid, which is necessary for normal bone and connective tissue homeostasis [38]. Understanding the physical–chemical behavior of the pristine and formulated pSiNPs in standardized nutritive cellular media in vitro provided useful insights about their relative aggregation states and dissolution rates. The aggregation state (hydrodynamic diameter and zeta potential) and the dissolution rate were assessed in FBS-free and 10% FBS-supplemented Dulbecco's modified Eagle's medium DMEM/F12 (Figures 2 and 3).

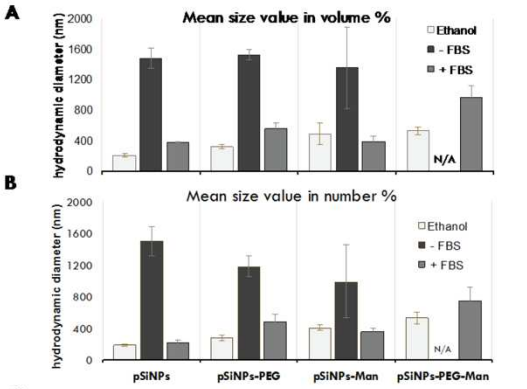

C

		pSiNPs	pSiNPs-PEG	pSiNPs-Man	pSiNPs-PEG-Man
ζ (mV)	- FBS	18.1±1.1	5.4±0.4	-7.8±0.4	N/A
	+ FBS	-9.3±1.4	-4.2±0.2	-8.1±0.6	-6.8±0.3
PDI	- FBS	0.45±0.1	0.21±0.1	0.34±0.1	N/A
	+ FBS	0.29±0.1	0.53±0.1	0.65±0.2	0.80±0.2

Figure 2. Average hydrodynamic diameters expressed as vol. % (**A**), num. % (**B**), and (**C**) ζ potential measurements and polydispersity index (PDI) for pristine or formulated pSiNPs after 10 min in DMEM/F12 ± 10% fetal bovine serum (FBS). The hydrodynamic diameters are mean size value (in vol. %). N/A denotes the absence of data due to strong aggregation. Data are the mean ± SD (n = 3).

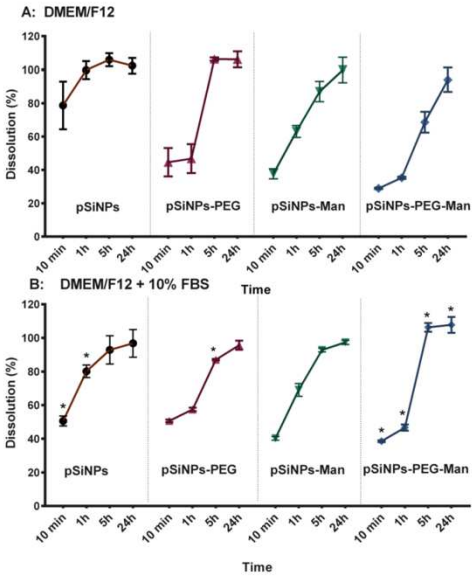

Figure 3. Dissolution kinetics of pSiNPs, pSiNPs–PEG, pSiNPs–Man, and pSiNPs–PEG–Man formulations after 10 min, 1, 5, and 24 h in DMEM/F12 ± 10% FBS. Results are expressed as a percentage of dissolved Si versus the total Si contents: (**A**) FBS-free DMEM/F12 medium; (**B**) 10% FBS-supplemented DMEM/F12 medium. Data are the mean ± SD (n = 3). Asterisk (*) denote statistical significant difference between dissolution rate in DMEM/F12 ± 10% FBS for pSiNPs formulations, * $p < 0.05$.

Aggregation state was first assessed 10 min after incubation in the FBS-free culture media. While well dispersed in their stock suspension, a strong aggregation occurred for all formulations. Aggregates with mean hydrodynamic diameters of around 1350–1520 nm (vol. %) and 1000–1500 nm (num. %) were quickly formed for pSiNPs, pSiNPs–PEG, and pSiNPs–Man. The pSiNPs–PEG–Man appeared to be the more destabilized (large and polydisperse aggregates), which makes them unmeasurable with dynamic light scattering (DLS). It is well established that in cell culture media, the neutral pH, the elevated ionic strength, and the presence of a divalent cation such as Ca^{2+} and Mg^{2+} can interact with the surface of the particles, decrease their surface charges, and cause their aggregation. This was also confirmed by zeta potential measurements in the FBS-free culture media (Figure 2B) that were closer to neutral in abiotic cell media at pH 7.4 (18.1 ± 1 mV for the pSiNPs, 5.4 ± 0.4 mV for pSiNPs–PEG, −7.8 ± 0.4 mV for pSiNPs–Man). This highlights the decrease of the electrostatic repulsion forces between NPs, which favored their colloidal destabilization [39,40] in standardized culture media.

As well as a colloidal instability, we also observed that formulated NPs were chemically unstable in the FBS-free DMEM/F12 medium. After 24 h, 100% of the Si from the four pSiNPs formulations were released as Si dissolved species. The dissolution kinetics were formulation-dependent. In FBS-free DMEM/F12 medium (Figure 3A), pristine pSiNPs shows the fastest degradation kinetic with 78 ± 14% of Si release in less than 10 min. Once functionalized with PEG and/or Man, Si mass loss from the NPs was reduced (~40% in 10 min). Indeed, after 1 h the percentages of dissolution were 99 ± 5% for pristine pSiNPs, 63 ± 4% for pSiNPs–Man, 46 ± 8% for pSiNPs–PEG, and 35 ± 1% for pSiNPs–PEG–Man. This highlights a chemical stabilization of the surface of the pSiNPs by the functionalization with organic molecules such as PEG and/or Man; the PEG–Man-functionalized NPs being the more stable in pure DMEM/F12 even after 5 h.

Alongside formulation-dependency, the dissolution kinetics of the pristine pSiNPs were also serum-dependent (Figures 2 and 3). Interaction with proteins is known to play a great role in the kinetics of biodegradation and cellular uptake [25,36,41]. Herein, in 10% FBS-supplemented media, the dissolution of pristine pSiNPs was significantly lower (50 ± 3%) than in FBS-free medium (78 ± 14%) after 10 min. This can likely be attributed to the adsorption of anionic proteins from the serum at the surface of pSiNPs [12,42–44]. These pSiNPs-protein interactions were confirmed by size and zeta-potential measurements. The addition of proteins in DMEM/F12-FBS media decreased the size of the pSiNPs aggregates and made their zeta potential negative (Figure 2).

Similar decreases in the hydrodynamic diameters were observed for the pSiNPs–Man, pSiNPs–PEG, and pSiNPs–PEG–Man between the FBS-free DMEM/F12 and the DMEM/F12 complemented with 10% FBS. These aggregates had PDI values that were not statistically different compared to those measured in ethanol (large standard deviation) except for the pSiNPs–Man in the FBS-complemented DMEM/F12. Moreover, the zeta potential of these three formulations were all ranged between −4 and −8 mV in the FBS-complemented DMEM/F12. The comparable negative charge of these formulations suggested that protein adsorption dominated the surface charge distribution. However, such a protein adsorption did not impact the dissolution kinetics of pSiNPs–Man and pSiNPs–PEG. A similar release of Si was observed for the FBS-free and FBS-supplemented DMEM/F12, excepting pSiNP–PEG at 5 h ($p < 0.05$) (Figure 3B). PEG is known to be an efficient way to prevent non-specific protein adsorption at the surface of materials [45–47]. We hypothesized that, once formulated by PEG and Man, the Si atoms localized at the surface of the pSiNPs were less available to directly interact with proteins limiting their complexation–dissolution. Regarding pSiNPs–PEG–Man formulation, a significant difference in the dissolution kinetics was observed between the FBS-free and FBS-supplemented DMEM/F12 at all time points. The combined PEG–Man formulation dissolved faster in the presence of FBS, which shows that the combination had an effect on the accessibility of the Si atoms at the surface and their dissolution kinetics.

2.3. Biocompatibility Studies In Vitro

In order to assess the biocompatibility of these 4 pSiNPs formulations, we studied their effects on the cell growth of human breast cancer cells (MCF-7). Cells were incubated for 72 h with increasing concentrations of each formulation (from 5 to 100 mg·L^{-1}). After three days, the number of living cells did not show any significant decrease compared to the control (Figure 4). Consequently, all the tested formulations did not induce any cell death or growth for the range of concentrations studied. This suggests an absence of cytotoxicity.

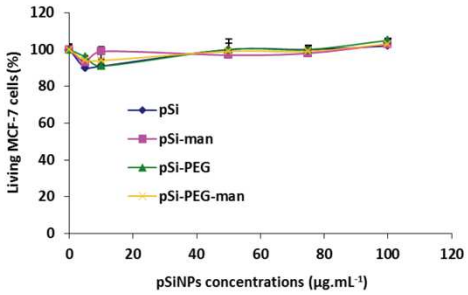

Figure 4. Cytotoxicity assessment of pSiNPs, pSiNPs–PEG, pSiNPs–Man, pSiNPs–PEG–Man. Human breast cancer cells (MCF-7) were incubated for 3 days with the 4 pSiNPs suspensions. Quantification of living cells was performed using (3-(4,5-dimethylthiazol-2-yl)-2,5-diphenyltetrazolium bromide (MTT) assay.

2.4. Biodistribution and Clearance of the pSiNps Formulation In Vivo

Based on the in vitro biodegradation result, the biodistribution of pristine and functionalized pSiNPs was assessed in vivo 5 h after intravenous injection into healthy mice. We observed that the Si biodistribution following injection of pSiNPs depended on the surface functionalization (Figure 5). As with other Si-based NPs [6,37,48], Si (dissolved or nanoparticulate forms) from pristine pSiNPs accumulated mainly in the MPS-related organs such as the liver and spleen (Figure 5B). This is likely due to pSiNPs being trapped by the Kupffer cells and splenic macrophages. Compared with pristine pSiNPs, pSiNPs functionalized with PEG induced less accumulation of Si in the liver. This suggests that the pSiNPs–PEG could partially escape from recognition and phagocytosis by liver phagocytes. Surprisingly, Si contents in the lung and spleen after pSiNPs–PEG treatment were higher than with pristine pSiNPs ($p < 0.05$) (Figure 5C), demonstrating that the PEGylated NPs could be captured by lung and splenic macrophages and hardly removed from the MPS organs. Faure et al. have shown the splenic capture of NH_2-ended PEG grafted on hybrid nanoparticles, in agreement with a positive zeta potential [49].

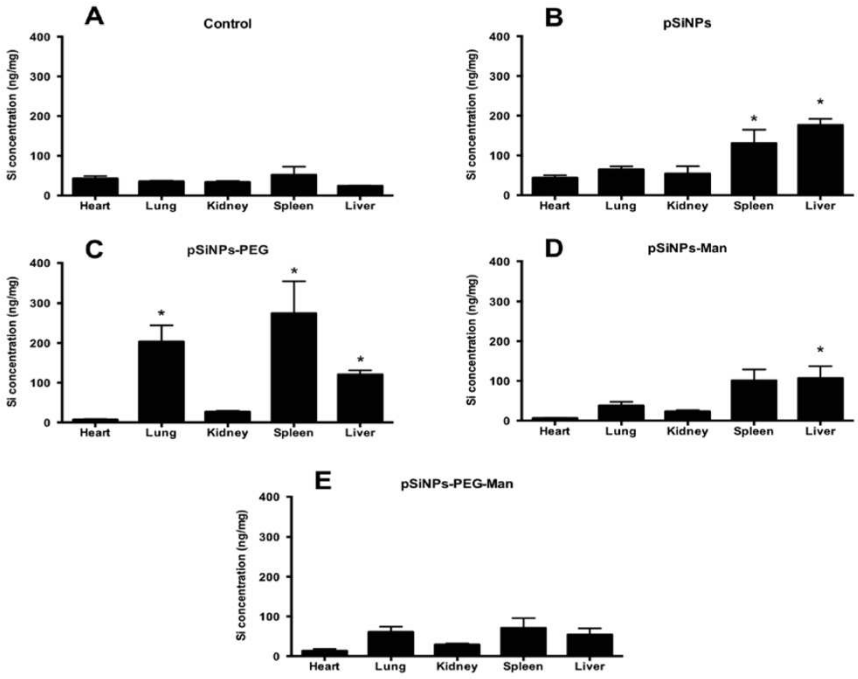

Figure 5. Si concentrations in organs of mice 5 h after intravenous injection. Control group (**A**), pSiNPs (**B**), pSiNPs–PEG (**C**), pSiNPs–Man (**D**) and pSiNPs–PEG–Man (**E**). Data are the mean ± SD ($n = 3$). Asterisk (*) denote statistical significant difference between pSiNPs-exposed mice and control group, * $p < 0.05$.

On the contrary, functionalization with mannose significantly decreased the accumulation of Si in the organs. As shown in Figure 5D, only liver accumulation was significantly higher than the control group for pSiNPs–Man formulation ($p < 0.05$), likely due to the presence of Kupffer cells in this organ which express mannose receptors [50]. The best stealth effect was obtained for the pSiNPs–PEG–Man formulation. No significant accumulation of Si in the studied organs was observed

for pSiNPs–PEG–Man (Figure 5E), indicating that PEGylation of pSiNPs and the post-functionalization with Man effectively reduced their uptake by the MPS.

The main objective of the surface modification of pSiNPs by PEG and Man was to escape from the MPS organs, increasing their blood-circulation lifetime and their excretion by urines. Figure 6 shows the Si concentration following injection of pristine pSiNPs, pSiNPs–PEG, pSiNPs–Man, and pSiNPs–PEG–Man in mice blood and urine 5 h after injection. For the pSiNPs, pSiNPs–PEG, and pSiNPs–Man, significant accumulation in the liver, spleen, and lung resulted in non-statistically different Si concentration in the blood and urine compared to the control group. However, for the pSiNPs–PEG–Man formulations, the absence of accumulation in the MPS organs is associated with a significant increase of Si concentration in the blood and urine compared to the control group ($p < 0.05$). In vivo, the mechanism of Si clearance is attributed to degradation of pSiNPs into soluble silicic acid followed by renal excretion. Such a biodegradation has been observed in vitro in the presence of FBS where a complete dissolution of the pSiNPs–PEG–Man was reached after 5 h. It is noteworthy that pSiNPs functionalized with PEG and Man was more destabilized in the FBS complementary DMEM/F12 medium. This indicates that differences in stealth behavior of the pSiNPs–PEG–Man formulation, compared to other three formulations in biological contexts, cannot be ascribed to a larger aggregate formation, but only to the differences in their surface functionalization.

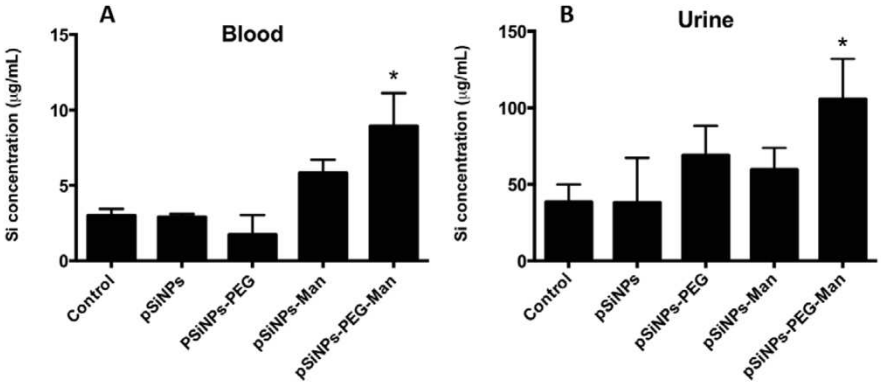

Figure 6. Si concentrations in blood (**A**) and urine (**B**) of mice after 5 h of intravenous injection. Mice were exposed to the four pSiNPs formulations. Data are the mean ± SD ($n = 3$). Asterisks (*) denote statistical significant difference between pSiNPs exposed mice and control group, $p < 0.05$.

Both in vitro and in vivo experiments agreed on the fact that the PEGylated Man-modified pSiNPs are quickly biodegraded in the bloodstream allowing for their excretion by renal filtration in less than 5 h. By contrast, other studies have shown clearance of Si from the mice bodies following pSiNPs intravenous injection (130–180 nm) after one week [6]. Our results clearly evidence that PEG and Man protected pSiNPs from MPS system and prolonged their lifetime in blood circulation, and hence could enhance the dissolved Si excretion in urine.

2.5. Biocompatibility Studies In Vivo

At the sacrifice, the blood of the mice was collected and plasma were prepared. In order to mesure the level of TNFα. Figure 7 shows that no significant increase in TNFα plasma level was observed in animals treated with each formulation. This suggests an absence of systemic inflammation at least within 5 h after injection.

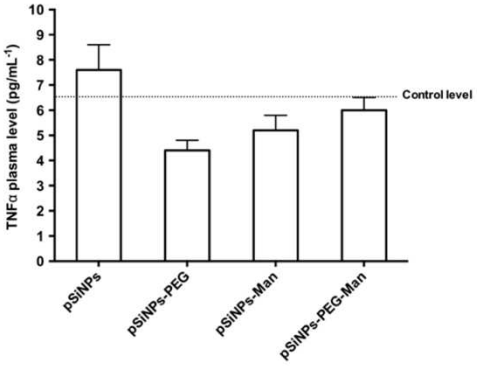

Figure 7. TNFα plasma level of mice treated intravenously by pSiNPs, pSiNPs–PEG, pSiNPs–Man, pSiNPs–PEG–Man at the final concentration of 40 mg·kg^{-1}. Plasma were collected during the sacrifice, 5 h after treatment. Values are means ± standard deviation.

3. Materials and Methods

3.1. pSiNPs Synthesis

Boron-doped p^{++}-type Si (0.8–1.2 mΩ.cm resistivity, <100> orientation) from Siltronix (France) was electrochemically etched in a 3:1 (*v*:*v*) solution of aqueous 48% hydrofluoric acid (HF): absolute ethanol (Sigma-Aldrich, Saint Quentin Fallavier, France). Etching was performed in a Teflon cell with a platinum ring counter electrode. A constant current of 167 mA·cm^{-2} was applied for 150 s, and then the sample was rinsed three times with ethanol. The porous layer was then removed from the substrate by application of a constant current of 4 mA·cm^{-2} for 250 s in an electrolyte solution containing 1:20 (*v*:*v*) aqueous 48% hydrofluoric acid: absolute ethanol. After rinsing three times with ethanol, the porous layer was put in ethanol in a glass vial. After 20 min of degassing under a nitrogen stream, the porous silicon film was fractured by ultrasonication for 16 h. The largest particles were then removed by spinning them down by centrifugation at 2700× *g* for 2 min (Minispin, Eppendorf, AG, Hamburg, Germany). In order to remove the smallest particles, the solution was finally centrifuged at 22,000× *g* for 30 min (centrifuge Eppendorf 5804, AG, Hamburg, Germany). The pellet was then dispersed in absolute ethanol.

3.2. pSiNPs Functionalization With PEG

0.5 mmol of polyethylglycoldiamine (368.5 g·mol^{-1}) and 0.25 mmol of isocyanopropyltriethoxysilane (ICPES) were added with 2 mL of dried tetrahydrofuran (THF) in a 25 mL round-bottomed flask. The mixture was stirred overnight at 50 °C and under nitrogen. Freshly prepared pSiNPs were centrifuged at 22,000× *g* for 30 min in ethanol, then centrifuged once with THF. 30 mg of pSiNPs were dispersed in 2 mL of THF with ICPES-PEG and reacted overnight at 50 °C under nitrogen. After the reactions, the pSiNPs–PEG were centrifuged at 22,000× *g* and washed 5 times with absolute ethanol to remove the PEGdiamine physisorbed onto their surface. 20 mg of pSiNPs–PEG were finally dispersed in 10 mL of absolute ethanol.

3.3. pSiNPs–PEG Functionalization With Man

0.03 mmol of mannose (*p*-[*N*-(2-Ethoxy-3,4-dioxocyclobut-1-enyl)amino]phenyl-α-D-mannopyranoside) (395.6 g·mol^{-1}), 0.07 mmol of trimethylamine, and 30 mg of pSiNPs–PEG were added with 2 mL of DMF in a 25 mL round-bottomed flask. The mixture was stirred overnight at 60 °C under nitrogen. After the reactions, the pSiNPs–PEG–Man were centrifuged at 22,000× *g* and

washed 5 times with absolute ethanol to remove the mannose physisorbed onto their surface. 20 mg of pSiNPs–PEG–Man were finally dispersed in 10 mL of absolute ethanol.

3.4. pSiNPs Functionalization With Man

0.03 mmol of mannose (*p*-[*N*-(2-Ethoxy-3,4-dioxocyclobut-1-enyl)amino]phenyl-α-D-mannopyranoside) (395.6 g·mol^{-1}), 0.04 mmol of aminopropyltriethoxysilane (APTES), and 11 µL (0.07 mmol) of triethylamine were added in 2 mL of dried THF in a 25 mL round-bottomed flask,. The mixture was stirred overnight at room temperature and under nitrogen. Freshly prepared pSiNPs were centrifuged at 22,000× *g* for 30 min in ethanol, then centrifuged once with DMF. 30 mg of pSiNPs were dispersed in 3 mL of DMF with APTES-Man and reacted overnight at 60 °C under nitrogen. After the reactions, the pSiNPs–Man were centrifuged at 22,000× *g* and washed 5 times with absolute ethanol to remove the mannose physisorbed onto their surface. 20 mg of pSiNPs–Man were finally dispersed in 10 mL of absolute ethanol.

3.5. Characterizations of pSiNPs Initial Suspensions in Ethanol

Solid-state ^{29}Si nuclear magnetic resonance (NMR) was used to assess the Si speciation of pSiNPs before functionalization by PEG and Man, or in vivo/in vitro studies. NMR spectra were obtained on a Bruker Advance 400 WB spectrometer (Bruker BioSpin Corporation, Billerica, ME, USA) at 79.5 MHz. Spectra were acquired in both single pulse and solid-state cross polarization magic angle spinning (CP-MAS) modes. In both cases the spin rate was 10 kHz and the number of scans was 4096. Recycle delays were 20 s and 5 s for the single pulse and the CP-MAS experiments respectively. Free induction decay (FID) was processed using the MestRecNova software (Mestrelab Research, Santiago de Compostela, Spain). A 50 Hz line broadening was applied prior to the Fourier transform, and phase and baseline correction were done manually. The relative proportion of the surface Si species was calculated from peak integration.

TEM images of the NPs were obtained on the JEOL 1200 EXII instrument (Jeol Ltd., Tokyo, Japan). The specific surface area and pore-size distribution of the samples were estimated using nitrogen adsorption–desorption isotherms with a Micrometrics ASAP 2020 instrument (ASAP 2020, Micromeritics Inc., Norcross, GA, USA). Before the sorption measurement, the samples were degassed at 80 °C for 6 h under reduced pressure. The specific surface area of the sample (S_{BET}) was calculated according to the Brunauer, Emmett, Teller (BET) method from the linear part of the nitrogen adsorption isotherm, and the pore-size distribution were analyzed according to the Barrett, Joyner and Halenda (BJH) method. Infrared spectra were recorded on a Nicolet IS5 spectrometer (Nicolet Instrument, Thermo Company, Waltham, MA, USA) with the attenuated total reflectance (ATR) ID5 module to study the covalent attachement of PEG and Man at the surface of the pSiNPs.

Hydrodynamic diameters and zeta potentials of the initial and functionalized NPs were measured in absolute ethanol by DLS using the NanoZS (Malvern Instruments Ltd., Worcestershire, UK) and the zeta potential measurements using the Zetasizer (Malvern Instruments Ltd., Worcestershire, UK). For data acquisition, a refractive index (RI) of 1.54 was used, and the reading was carried out at 173° with respect to the incident beam.

3.6. Dosing of the Phenyl Squarate Mannose Grafted on the pSiNPs–Man and pSiNPs–PEG–Man Formulations

The amounts of phenyl squarate-mannose grafted on the pSiNPs were determined by specific colorimetric reaction using a lambda 35 de Perkin Elmer UV–Vis spectrometer. The molar absorption coefficient of the mannose was determined using a solution of mannose in hydrated sulfuric acid and resorcinol (1,3-dihydroxybenzene) at different concentrations. The mannose amounts ranging from 1 to 4 mg were dissolved in 20 mL of acetic acid (0.01 mol·L^{-1}). Then, 200 µL of each solution was added to the solution containing 1 mL of 75% sulfuric acid and 200 µL of resorcinol. The samples were vortexed for 5 min and heated at 90 °C for 30 min. The samples were placed in the fridge and in

darkness for 30 min. The absorbance of the solution was recorded between 350 and 600 nm. Calibration curves were also recorded, in order to determine the molar absorption coefficient of the mannose under the same conditions (ε_{422} = 11651 L·mol^{-1}·cm^{-1}). The 75% sulfuric acid (1 mL), resorcinol (200 µL) and acetic acid (200 µL) solution was used as a reference solution. The dosing of the mannose grafted onto the pSiNPs followed the procedure described above. Here, the mannose solution was replaced using a known quantity of NPs functionalized with mannose phenyl squarate. A loading of 36 µg and 27.6 µg of mannose phenyl squarate per mg of pSiNPs was obtained for pSiNPs–Man and pSiNPs–PEG–Man respectively.

3.7. Physico-Chemical Stability In Vitro

The colloidal stability of the pSiNPs, pSiNPs–PEG, pSiNPs–Man, pSiNPs–PEG–Man was studied in vitro in abiotic cell culture media. Before use, each formulation was sonicated in a water bath for 5 min. The NPs were then diluted at 40 mg·L^{-1} in Dulbecco's modified Eagle's medium supplemented with Glutamax (DMEM/F-12) with and without 10% FBS and 1% penicillin-streptomycin (Gibco Laboratories, Grand Island, NY, USA). The samples were stirred (100 rpm) at a constant temperature of 37 °C for 10 min, 1 h, 5 h and 24 h. At each selected time, 2 mL of mixing solution was used for DLS and zeta potential measurements (using NanoZS and Zetasizer, Malvern Instruments Ltd., Worcestershire, UK).

The chemical stability (release of dissolved species) of the pSiNPs, pSiNPs–PEG, pSiNPs–Man, pSiNPs–PEG–Man was studied in vitro in abiotic DMEM/F-12 medium with and without 10% FBS. After 10 min, 1 h, 5 h and 24 h, aliquots (4 mL) of stirred (100 rpm) suspensions were ultrafiltrated using centrifugal filter units (Amicon ultra4, 3 kDa molar mass membrane cutoff, Beckman Coulter, Inc., Fullerton, CA, USA). The collected fractions were diluted 10-fold in ultrapure water with 2% nitric acid before ICP-MS analysis (Thermo X series II model equipped with a collision cell, Fisher Corp., MA, USA). To avoid the loss of Si on filter membranes, the recovery of soluble silicon was tested and found to be close to 100%. Concentrations of Si in stock suspensions were also measured by ICP-MS by transferring 2 mL of suspension into 1 mL of HCl (35%) and 1 mL of HNO_3 (67%) for NPs, followed by 45 min of microwave digestion. Samples were left in acid overnight for the digestion to complete. Appropriate dilutions were made for ICP-MS analysis. Results of the ICP-MS measurement are presented as means (n = 3) and standard deviations (SD).

3.8. In Vitro Cytotoxicity on Cell Line

Human breast cancer cells (MCF-7) were purchased from ATCC (American Type Culture Collection, Manassas, VA, USA). Cells were cultured in DMEM-F12 supplemented with 10% FBS and 50 µg·mL^{-1} gentamycin. These cells were allowed to grow in a humidified atmosphere at 37 °C under 5% CO_2. To study the effects of NPs on cell growth, MCF-7 cells were seeded into 96-well plates at 2000 cells per well in 200 µL culture medium and allowed to grow for 24 h. Increasing concentrations of pSiNPs, pSiNPs–PEG, pSiNPs–Man, pSiNPs–PEG–Man were incubated in a culture medium of MCF-7 cells during 72 h. Then, a MTT assay was performed to evaluate the toxicity. Briefly, cells were incubated for 4 h with 0.5 mg·mL^{-1} of MTT (3-(4,5-dimethylthiazol-2-yl)-2,5-diphenyltetrazolium bromide; Promega, Madison, WI, USA) in media. The MTT/media solution was then removed and the precipitated crystals were dissolved in EtOH/DMSO (1:1). The solution absorbance was read at 540 nm.

3.9. Biodistribution in Mice

Female C57/BL6 mice aged 8 weeks were provided by Charles River and, housed in the institutional animal house under standard environmental conditions (23 ± 1 °C, 55 ± 5% humidity and 12 h/12 h light/dark cycles) and maintained with free access to standard diet and water. All animals (3 mice per condition) were intravenously exposed to the four pSiNPs formulations (pSiNPs, pSiNPs–PEG, pSiNPs–Man, pSiNPs–PEG–Man) at the final concentration of 40 mg·kg^{-1}.

Control mice were injected with the vehicle alone (200 µL of physiological serum). The mice were sacrificed 5 h after intravenous injection. Their blood, urine and major organs (heart, lung, spleen, kidney and liver) were collected. Si concentration was then quantified by ICP-MS.

For quantification of the Si concentration in each organ (lung, kidney, spleen, heart and liver) of the exposed or control mice, the organs were freeze-dried, crushed and homogenized. Then, 1 mL of HNO_3 (67%) and 1 mL of H_2O_2 were added to approximately 30–50 mg of organ powder. For quantification of Si in bio fluids, 100 µL of blood and 5 to 100 µL of urine were separately mixed with 1 mL of HNO_3 (67%) and 1 mL of H_2O_2. The samples were left in acid overnight for digestion, and this was followed by 45 min of microwave digestion. Then, all the samples were diluted in HNO_3 (2%) to reach a final volume of 10 mL, and Si concentrations were measured by ICP-MS. The ICP-MS measurement data are presented as means (n= 3 mice per condition) and standard deviations (SD). The data were analyzed using a two-way analysis of variance (ANOVA) test followed by a Sidak's multiple comparisons test (Graphpad Prism 6, Graphpad Sofeware Inc., San Diego, CA, USA). A level of $p < 0.05$ was considered significant.

3.10. TNFα Plasma Levels Measurement

A blood sample for each mouse was collected to determine the level of inflammatory biomarkers such as TNFα. Plasma was separated from the blood by centrifugation (15 min, 1200× *g*, 4 °C). Plasma TNFα levels were quantified using commercial enzyme-linked immunosorbent assay (ELISA) kits as described in the manufacturer's protocol (R&D systems, Minneapolis, MN, USA).

4. Conclusions

The aim of this study was to design stealth pSiNPs using biodegradable pSiNPs and new surface-grafting with PEG and Man. When the PEGylated–pSiNPs were functionalized with Man, the pSiNPs–PEG–Man system exhibited a remarkable stealth property, with higher blood retention and a significant clearance in renal excretion. By contrast with studies reporting the influence of PEG on biodistribution [37,51], we observed that PEG at 368.5 g·mol^{-1} molecular weight had no significant effect on combined uptakes in major MPS organs such as the liver and spleen. Moreover, in vitro biodegradation kinetic studies were in accordance with in vivo studies indicating a fast biodegradation kinetic (~100% at 5 h in DMEM/F12-FBS medium). Based on the in vitro and in vivo biodegradation, biodistribution, clearance, and biocompatibility evaluations presented, the pSiNPs functionalized with Man and PEG-Man deserve to be tested in vivo to specifically target cancer sites in a non-invasive manner.

Supplementary Materials: The following are available online at http://www.mdpi.com/2079-4991/7/10/288/s1, Figure S1: Characterizations of the pristine pSiNPs. (A) Transmission electron microscopy (TEM) images, (B) N_2 adsorption/desorption isotherm, Figure S2: CP-MAS spectra (black line) and Bloch decay spectra (red line) of ^{29}Si NMR of pSiNPs suspended in absolute ethanol, Figure S3: Reaction pathway for the covalent binding of PEG on pSiNPs, Figure S4: Synthesis scheme for the functionalization of pSiNPs–PEG with Mannose, Figure S5: Reaction pathway for the covalent binding of mannose on pSiNPs, Figure S6: (A) DRIFT spectra of bare pSiNPs (brown), pSiNPs functionalized with PEG (blue) and pSiNP-PEG-Man (green), (B) DRIFT spectra of bare pSiNPs (brown), pSiNPs functionalized with Mannose phenyl squarate pSiNP-Man (green), Figure S7: UV-vis spectrum for quantification of mannose phenyl squarate in (A) pSiNPs–Man and (B) pSiNPs–PEG-Man, Figure S8: Size distribution curves in vol. % and num. % of four pSiNPs formulations in absolute ethanol.

Acknowledgments: We acknowledge with thanks Concours Chercheur d'Avenir Languedoc-Roussillon (2013-098085) and the ANR (Agence Nationale pour la Recherche, Programme Blanc inter I SIMI 10, edition 2012). This work is a contribution to the Labex Serenade (ANR-11-LABX-0064) funded by the «Investissements d'Avenir» French Government program of the French National Research Agency (ANR) through the A*MIDEX project (ANR-11-IDEX-0001-02).

Author Contributions: W.L. and M.A. designed the experiments and co-wrote the paper; W.L. performed in vitro experiments and analyzed the data; A.C. synthetized and characterized Si-based nanoparticles grafted or not with PEG or with mannose residues; M.G. and M.G-B. designed in vitro and in vivo experiments; B.A. performed the Si quantifications by ICP-MS; A.M. performed NMR analysis; ADS established the protocol for mice treatment; M.D. sacrificed and dissected the mice, and realized the TNF alpha level measurements; L.L. performed in vitro

cytotoxicity experiments; A.M. and K.E.C. designed and synthetized mannose residues and linkers adapted for silicon nanoparticle grafting; and J-O.D. and F.C. contributed in experimental design. All authors read and approved the final manuscript.

Conflicts of Interest: The authors declare no conflict of interest.

References

1. Lu, J.; Liong, M.; Li, Z.; Zink, J.I.; Tamanoi, F. Biocompatibility, biodistribution, and drug-delivery efficiency of mesoporous silica nanoparticles for cancer therapy in animals. *Small* **2010**, *6*, 1794–1805. [CrossRef] [PubMed]
2. Meng, H.; Xue, M.; Xia, T.; Ji, Z.; Tarn, D.Y.; Zink, J.I.; Nel, A.E. Use of size and a copolymer design feature to improve the biodistribution and the enhanced permeability and retention effect of doxorubicin-loaded mesoporous silica nanoparticles in a murine xenograft tumor model. *ACS Nano* **2011**, *5*, 4131–4144. [CrossRef] [PubMed]
3. Wilczewska, A.Z.; Niemirowicz, K.; Markiewicz, K.H.; Car, H. Nanoparticles as drug delivery systems. *Pharmacol Rep.* **2012**, *64*, 1020–1037. [CrossRef]
4. Mamaeva, V.; Sahlgren, C.; Lindén, M. Mesoporous silica nanoparticles in medicine—Recent advances. *Adv. Drug Deliv. Rev.* **2013**, *65*, 689–702. [CrossRef] [PubMed]
5. Santos, H.A.; Makila, E.; Airaksinen, A.J.; Bimbo, L.M.; Hirvonen, J. Porous silicon nanoparticles for nanomedicine: Preparation and biomedical applications. *Nanomedicine* **2014**, *9*, 535–554. [CrossRef] [PubMed]
6. Park, J.H.; Gu, L.; von Maltzahn, G.; Ruoslahti, E.; Bhatia, S.N.; Sailor, M.J. Biodegradable luminescent porous silicon nanoparticles for in vivo applications. *Nat. Mater.* **2009**, *8*, 331–336. [CrossRef] [PubMed]
7. Jarvis, K.L.; Barnes, T.J.; Prestidge, C.A. Surface chemistry of porous silicon and implications for drug encapsulation and delivery applications. *Adv. Colloid Interface Sci.* **2012**, *175*, 25–38. [CrossRef] [PubMed]
8. Gobin, A.M.; Lee, M.H.; Halas, N.J.; James, W.D.; Drezek, R.A.; West, J.L. Near-infrared resonant nanoshells for combined optical imaging and photothermal cancer therapy. *Nano Lett.* **2007**, *7*, 1929–1934. [CrossRef] [PubMed]
9. Sailor, M.J.; Wu, E.C. Photoluminescence-Based Sensing With Porous Silicon Films, Microparticles, and Nanoparticles. *Adv. Funct. Mater.* **2009**, *19*, 3195–3208. [CrossRef]
10. Gu, L.; Hall, D.J.; Qin, Z.; Anglin, E.; Joo, J.; Mooney, D.J.; Howell, S.B.; Sailor, M.J. In vivo time-gated fluorescence imaging with biodegradable luminescent porous silicon nanoparticles. *Nat. Commun.* **2013**, *4*, 2326–2332. [CrossRef] [PubMed]
11. Gary-Bobo, M.; Mir, Y.; Rouxel, C.; Brevet, D.; Basile, I.; Maynadier, M.; Vaillant, O.; Mongin, O.; Blanchard-Desce, M.; Morère, P.A. Mannose-functionalized mesoporous silica nanoparticles for efficient two-photon photodynamic therapy of solid tumors. *Angew. Chem.* **2011**, *123*, 11627–11631. [CrossRef]
12. Monopoli, M.P.; Walczyk, D.; Campbell, A.G.; Elia, G.; Lynch, I.; Bombelli, F.B.; Dawson, K.A. Physical-chemical aspects of protein corona: Relevance to in vitro and in vivo biological impacts of nanoparticles. *J. Am. Chem. Soc.* **2011**, *133*, 2525–2534. [CrossRef] [PubMed]
13. Gary-Bobo, M.; Hocine, O.; Brevet, D.; Maynadier, M.; Raehm, L.; Richeter, S.; Charasson, V.; Loock, B.; Morère, A.; Maillard, P. Cancer therapy improvement with mesoporous silica nanoparticles combining targeting, drug delivery and PDT. *Int. J. Pharm.* **2012**, *423*, 509–515. [CrossRef] [PubMed]
14. Graf, C.; Gao, Q.; Schütz, I.; Noufele, C.N.; Ruan, W.; Posselt, U.; Korotianskiy, E.; Nordmeyer, D.; Rancan, F.; Hadam, S. Surface functionalization of silica nanoparticles supports colloidal stability in physiological media and facilitates internalization in cells. *Langmuir* **2012**, *28*, 7598–7613. [CrossRef] [PubMed]
15. Perrier, M.; Gary-Bobo, M.; Lartigue, L.; Brevet, D.; Morère, A.; Garcia, M.; Maillard, P.; Raehm, L.; Guari, Y.; Larionova, J. Mannose-functionalized porous silica-coated magnetic nanoparticles for two-photon imaging or PDT of cancer cells. *J. Nanopart. Res.* **2013**, *15*, 1–17. [CrossRef]
16. Secret, E.; Maynadier, M.; Gallud, A.; Gary-Bobo, M.; Chaix, A.; Belamie, E.; Maillard, P.; Sailor, M.J.; Garcia, M.; Durand, J.-O. Anionic porphyrin-grafted porous silicon nanoparticles for photodynamic therapy. *Chem. Commun.* **2013**, *49*, 4202–4204. [CrossRef] [PubMed]

17. Secret, E.; Smith, K.; Dubljevic, V.; Moore, E.; Macardle, P.; Delalat, B.; Rogers, M.L.; Johns, T.G.; Durand, J.O.; Cunin, F. Antibody-Functionalized Porous Silicon Nanoparticles for Vectorization of Hydrophobic Drugs. *Adv. Healthc. Mater.* **2013**, *2*, 718–727. [CrossRef] [PubMed]
18. Vaillant, O.; Cheikh, K.E.; Warther, D.; Brevet, D.; Maynadier, M.; Bouffard, E.; Salgues, F.; Jeanjean, A.; Puche, P.; Mazerolles, C. Mannose-6-Phosphate Receptor: A Target for Theranostics of Prostate Cancer. *Angew. Chem.* **2015**, *127*, 6050–6054. [CrossRef]
19. Mogoşanu, G.D.; Grumezescu, A.M.; Bejenaru, C.; Bejenaru, L.E. Polymeric protective agents for nanoparticles in drug delivery and targeting. *Int. J. Pharm.* **2016**, *2*, 419–429. [CrossRef] [PubMed]
20. Debele, T.A.; Peng, S.; Tsai, H.C. Drug Carrier for Photodynamic Cancer Therapy. *Int. J. Mol. Sci.* **2015**, *16*, 22094–22136. [CrossRef] [PubMed]
21. Giret, S.; Wong Chi Man, M.; Carcel, C. Mesoporous-Silica-Functionalized Nanoparticles for Drug Delivery. *Chem. Eur. J.* **2015**, *21*, 13850–13865. [CrossRef] [PubMed]
22. Nigam, P.; Sarkar, D. Multifunctional silica nanoparticles for pancreatic cancer specific drug delivery and bioimaging. *J. Chem. Appl. Biochem.* **2015**, *2*, 110–116.
23. Xiao, L.; Gu, L.; Howell, S.B.; Sailor, M.J. Porous silicon nanoparticle photosensitizers for singlet oxygen and their phototoxicity against cancer cells. *ACS Nano* **2011**, *5*, 3651–3659. [CrossRef] [PubMed]
24. Secret, E.; Maynadier, M.; Gallud, A.; Chaix, A.; Bouffard, E.; Gary-Bobo, M.; Marcotte, N.; Mongin, O.; El Cheikh, K.; Hugues, V.; et al. Two-photon excitation of porphyrin-functionalized porous silicon nanoparticles for photodynamic therapy. *Adv Mater.* **2014**, *26*, 7643–7648. [CrossRef] [PubMed]
25. Nel, A.E.; Madler, L.; Velegol, D.; Xia, T.; Hoek, E.M.; Somasundaran, P.; Klaessig, F.; Castranova, V.; Thompson, M. Understanding biophysicochemical interactions at the nano-bio interface. *Nat. Mater.* **2009**, *8*, 543–557. [CrossRef] [PubMed]
26. Zhu, S.; Niu, M.; O'Mary, H.; Cui, Z. Targeting of tumor-associated macrophages made possible by PEG-sheddable, mannose-modified nanoparticles. *Mol. Pharm.* **2013**, *10*, 3525–3530. [CrossRef] [PubMed]
27. Immordino, M.L.; Dosio, F.; Cattel, L. Stealth liposomes: Review of the basic science, rationale, and clinical applications, existing and potential. *Int. J. Nanomed.* **2006**, *1*, 297–315.
28. Knop, K.; Hoogenboom, R.; Fischer, D.; Schubert, U.S. Poly(ethylene glycol) in drug delivery: Pros and cons as well as potential alternatives. *Angew. Chem. Int. Ed. Engl.* **2010**, *49*, 6288–6308. [CrossRef] [PubMed]
29. Morelli, C.; Maris, P.; Sisci, D.; Perrotta, E.; Brunelli, E.; Perrotta, I.; Panno, M.L.; Tagarelli, A.; Versace, C.; Casula, M.F. PEG-templated mesoporous silica nanoparticles exclusively target cancer cells. *Nanoscale* **2011**, *3*, 3198–3207. [CrossRef] [PubMed]
30. Hong, C.; Lee, J.; Zheng, H.; Hong, S.-S.; Lee, C. Porous silicon nanoparticles for cancer photothermotherapy. *Nanoscale Res. Lett.* **2011**, *6*, 1. [CrossRef] [PubMed]
31. Kuthati, Y.; Sung, P.-J.; Weng, C.-F.; Mou, C.-Y.; Lee, C.-H. Functionalization of mesoporous silica nanoparticles for targeting, biocompatibility, combined cancer therapies and theragnosis. *J. Nanosci. Nanotechnol.* **2013**, *13*, 2399–2430. [CrossRef] [PubMed]
32. Brevet, D.; Gary-Bobo, M.; Raehm, L.; Richeter, S.; Hocine, O.; Amro, K.; Loock, B.; Couleaud, P.; Frochot, C.; Morère, A. Mannose-targeted mesoporous silica nanoparticles for photodynamic therapy. *Chem. Commun.* **2009**, 1475–1477. [CrossRef] [PubMed]
33. Warther, D.; Jimenez, C.M.; Raehm, L.; Gérardin, C.; Durand, J.-O.; Morère, A.; El Cheikh, K.; Gallud, A.; Gary-Bobo, M.; Maynadier, M. Small sized mesoporous silica nanoparticles functionalized with mannose for retinoblastoma cell imaging. *RSC Adv.* **2014**, *4*, 37171–37179. [CrossRef]
34. Chaix, A.; El Cheikh, K.; Bouffard, E.; Maynadier, M.; Aggad, D.; Stojanovic, V.; Knezevic, N.; Garcia, M.; Maillard, P.; Morere, A.; et al. Mesoporous silicon nanoparticles for targeted two-photon theranostics of prostate cancer. *J. Mater. Chem. B* **2016**, *4*, 3639–3642. [CrossRef]
35. Tang, F.; Li, L.; Chen, D. Mesoporous silica nanoparticles: Synthesis, biocompatibility and drug delivery. *Adv. Mater.* **2012**, *24*, 1504–1534. [CrossRef] [PubMed]
36. He, Q.; Zhang, J.; Shi, J.; Zhu, Z.; Zhang, L.; Bu, W.; Guo, L.; Chen, Y. The effect of PEGylation of mesoporous silica nanoparticles on nonspecific binding of serum proteins and cellular responses. *Biomaterials* **2010**, *31*, 1085–1092. [CrossRef] [PubMed]
37. He, Q.; Zhang, Z.; Gao, F.; Li, Y.; Shi, J. In vivo biodistribution and urinary excretion of mesoporous silica nanoparticles: Effects of particle size and PEGylation. *Small* **2011**, *7*, 271–280. [CrossRef] [PubMed]

38. Anderson, S.; Elliott, H.; Wallis, D.; Canham, L.; Powell, J. Dissolution of different forms of partially porous silicon wafers under simulated physiological conditions. *Physica Status Solidi* **2003**, *197*, 331–335. [CrossRef]
39. Borkovec, M.; Papastavrou, G. Interactions between solid surfaces with adsorbed polyelectrolytes of opposite charge. *Curr. Opin. Colloid Interface Sci.* **2008**, *13*, 429–437. [CrossRef]
40. Lee, C.H.; Cheng, S.H.; Huang, I.; Souris, J.S.; Yang, C.S.; Mou, C.Y.; Lo, L.W. Intracellular pH-responsive mesoporous silica nanoparticles for the controlled release of anticancer chemotherapeutics. *Angew. Chem.* **2010**, *122*, 8390–8395. [CrossRef]
41. Pelaz, B.; del Pino, P.; Maffre, P.; Hartmann, R.; Gallego, M.; Rivera-Fernandez, S.; de la Fuente, J.M.; Nienhaus, G.U.; Parak, W.J. Surface functionalization of nanoparticles with polyethylene glycol: Effects on protein adsorption and cellular uptake. *ACS Nano* **2015**, *9*, 6996–7008. [CrossRef] [PubMed]
42. Milani, S.; Bombelli, F.B.; Pitek, A.S.; Dawson, K.A.; Radler, J. Reversible versus irreversible binding of transferrin to polystyrene nanoparticles: Soft and hard corona. *ACS Nano* **2012**, *6*, 2532–2541. [CrossRef] [PubMed]
43. Lesniak, A.; Fenaroli, F.; Monopoli, M.P.; Aberg, C.; Dawson, K.A.; Salvati, A. Effects of the presence or absence of a protein corona on silica nanoparticle uptake and impact on cells. *ACS Nano* **2012**, *6*, 5845–5857. [CrossRef] [PubMed]
44. Liu, W.; Rose, J.; Plantevin, S.; Auffan, M.; Bottero, J.-Y.; Vidaud, C. Protein corona formation for nanomaterials and proteins of a similar size: Hard or soft corona? *Nanoscale* **2013**, *5*, 1658–1668. [CrossRef] [PubMed]
45. Gref, R.; Lück, M.; Quellec, P.; Marchand, M.; Dellacherie, E.; Harnisch, S.; Blunk, T.; Müller, R. 'Stealth'corona-core nanoparticles surface modified by polyethylene glycol (PEG): Influences of the corona (PEG chain length and surface density) and of the core composition on phagocytic uptake and plasma protein adsorption. *Colloids Surf. B Biointerfaces* **2000**, *18*, 301–313. [CrossRef]
46. Aggarwal, P.; Hall, J.B.; McLeland, C.B.; Dobrovolskaia, M.A.; McNeil, S.E. Nanoparticle interaction with plasma proteins as it relates to particle biodistribution, biocompatibility and therapeutic efficacy. *Adv. Drug Deliv. Rev.* **2009**, *61*, 428–437. [CrossRef] [PubMed]
47. Godin, B.; Gu, J.; Serda, R.; Bhavane, R.; Tasciotti, E.; Chiappini, C.; Liu, X.; Tanaka, T.; Decuzzi, P.; Ferrari, M. Tailoring the degradation kinetics of mesoporous silicon structures through PEGylation. *J. Biomed. Mater. Res. A* **2010**, *94*, 1236–1243. [CrossRef] [PubMed]
48. Fu, C.; Liu, T.; Li, L.; Liu, H.; Chen, D.; Tang, F. The absorption, distribution, excretion and toxicity of mesoporous silica nanoparticles in mice following different exposure routes. *Biomaterials* **2013**, *34*, 2565–2575. [CrossRef] [PubMed]
49. Faure, A.C.; Dufort, S.; Josserand, V.; Perriat, P.; Coll, J.L.; Roux, S.; Tillement, O. Control of the in vivo biodistribution of hybrid nanoparticles with different poly (ethylene glycol) coatings. *Small* **2009**, *5*, 2565–2575. [CrossRef] [PubMed]
50. Kelly, C.; Jefferies, C.; Cryan, S.-A. Targeted liposomal drug delivery to monocytes and macrophages. *J. Drug. Deliv.* **2011**, *2011*. [CrossRef] [PubMed]
51. Perry, J.L.; Reuter, K.G.; Kai, M.P.; Herlihy, K.P.; Jones, S.W.; Luft, J.C.; Napier, M.; Bear, J.E.; De Simone, J.M. PEGylated PRINT nanoparticles: The impact of PEG density on protein binding, macrophage association, biodistribution, and pharmacokinetics. *Nano Lett.* **2012**, *12*, 5304–5310. [CrossRef] [PubMed]

ANNEXE 4

Journal of Controlled Release 269 (2018) 15–23

Contents lists available at ScienceDirect

Journal of Controlled Release

journal homepage: www.elsevier.com/locate/jconrel

Efficient therapy for refractory Pompe disease by mannose 6-phosphate analogue grafting on acid α-glucosidase

Ilaria Basile[a,1], Afitz Da Silva[a,b,1], Khaled El Cheikh[a], Anastasia Godefroy[a,b], Morgane Daurat[a,b], Alice Harmois[a], Marc Perez[c], Catherine Caillaud[d], Henry-Vincent Charbonné[a], Bernard Pau[e], Magali Gary-Bobo[b], Alain Morère[b,*], Marcel Garcia[b,*], Marie Maynadier[a,*]

[a] NanoMedSyn, 15 avenue Charles Flahault, 34093 Montpellier, France
[b] Institut des Biomolécules Max Mousseron IBMM, UMR 5247 CNRS-Université Montpellier-ENSCM, 34093 Montpellier, France
[c] INRA, UMR 1083, 34060 Montpellier, France
[d] Biochimie Métabolique et Protéique, AH-HP, Hopital Necker Enfants-Malades and Inserm U1151, Institut Necker Enfants Malades, Université Paris-Descartes, Paris, France
[e] BP Conseil, 34730 Saint-Gely-du Fesc, France

ARTICLE INFO

Keywords:
Lysosomal storage disease
Enzyme replacement therapy
Alpha acid glucosidase
Mannose 6-phosphate receptor targeting

ABSTRACT

Pompe disease is a rare disorder due to deficiency of the acid α-glucosidase (GAA) treated by enzyme replacement therapy. The present authorized treatment with rhGAA, the recombinant human enzyme, provides an important benefit in the infantile onset; however, the juvenile and adult forms of the disease corresponding to > 80% of the patients are less responsive to this treatment. This resistance has been mainly attributed to an insufficiency of mannose 6-phosphate residues in rhGAA to address lysosomes through the cation-independent mannose 6-phosphate receptor (CI-M6PR). As yet, several attempts to improve the enzyme delivery by increasing the number of mannose 6-phosphate on the enzyme were poorly effective on the late onset form of the disease. Here, we show that chemical conjugation of a synthetic analogue of the mannose 6-phosphate, named AMFA, onto rhGAA improves the affinity for CI-M6PR and the uptake of the enzyme in fibroblasts and myoblasts of adult Pompe patients. More importantly, only the conjugated rhGAA-AMFA was effective in aged Pompe mice when compared to rhGAA. Weekly treatment with 5–20 $mg{\cdot}kg^{-1}$ rhGAA-AMFA provided major improvements of the motor function and of the myofiber structure, whereas rhGAA was inactive. Finally, AMFA addition did not induce supplementary immune response to the enzyme. This modified enzyme, displaying a muscle recovery in aged Pompe mice that was never attained before, could be considered as a potential therapy for the late onset Pompe disease.

1. Introduction

Lysosomal storage disorders (LSD) are rare genetic diseases in which a lysosomal enzyme is deficient leading to a toxic accumulation of undigested substrate in lysosomes. Over the 53 identified disorders, only 8 have specific authorized treatments mostly based on enzyme replacement therapy (ERT) which consists in chronic human recombinant enzyme administration. Among LSD, Pompe disease is a myopathy due to the deficiency of acid α-glucosidase (GAA), a lysosomal enzyme responsible for glycogen degradation into glucose [1,2]. A total or partial GAA deficiency results in the accumulation of glycogen in cells and deleterious effects in cardiac, respiratory and skeletal muscles. The infantile form is the most severe one and presents < 1% GAA activity of normal subject, while the juvenile and adult onsets have a residual activity comprised between 1 and 30% [1]. Without any treatment, patients affected by the infantile Pompe disease die within the first year of age from a cardiac failure. In juvenile and adult forms, referred to as late-onset Pompe disease, clinical deterioration is progressive and is predominantly associated with proximal myopathy and respiratory failure. Currently, the proposed treatment consists in the ERT with a recombinant human acid α-glucosidase (rhGAA), the alglucosidase alfa (Myozyme®), produced in Chinese hamster ovary (CHO) cells. Clinical experience with Myozyme® indicates that this treatment is effective in treating the cardiomyopathy in infant patients and has a limited therapeutic efficacy in skeletal muscles of infants and of late-onset patients [3–6]. Still today, the late-onset Pompe disease

* Corresponding authors.
E-mail addresses: alain.morere@umontpellier.fr (A. Morère), marcel.garcia@inserm.fr (M. Garcia), m.maynadier@nanomedsyn.com (M. Maynadier).
[1] Authors contributed equally to this work.

https://doi.org/10.1016/j.jconrel.2017.10.043
Received 4 August 2017; Received in revised form 27 October 2017; Accepted 30 October 2017
Available online 03 November 2017

represents an unmet medical need since most of patients are poorly responsive to the treatment in terms of motor and respiratory functions and vital force. It has been proposed that this limited efficacy could be due to a low affinity for the cation-independent mannose 6-phosphate receptor (CI-M6PR), which recognizes the mannose 6-phosphate (M6P) moieties present on the recombinant enzymes and which is the key pathway to address the therapeutic enzyme to lysosomes [7–9]. The rhGAA contains a low number of M6P (between 0.9 and 1.2 mol M6P/mol enzyme) and an insufficient number of bis-M6P glycosylated chains allowing a high binding affinity to the two sites of CI-M6PR [10,11].

To overcome these limitations, several approaches have been developed to increase CI-M6PR affinity of the enzyme such as the grafting of multiple M6P on rhGAA [12–14], as Neo-GAA (Sanofi Genzyme), or the generation of hybrid recombinant protein (IGF2-GAA), BMN-701 (Biomarin) [15], that binds CI-M6PR through the high affinity IGF2 site present on this receptor. Both approaches improved efficacy in young mice but not in 9–10 month old mice representative of the late onset of the disease [14]. In connection to these proof-of concept results, Phase 2 clinical trials in adult patients showed only modest improvements as compared to the unmodified rhGAA (Myozyme®) [16,17].

Previously, we described the synthesis of isosteric analogues of M6P functionalized at the anomeric position (AMFAs) with ethyloxyamino linkers and their affinity and stability in human serum compared to M6P. The feasibility of conjugation of AMFA was described onto mannose-chains of recombinant GAA produced by baculovirus/Sf9 insect cell system. This conjugated enzyme showed a significant therapeutic efficacy on the motility of young 4–6 month old mice representative for a mild Pompe disease progression [18].

Here, we investigated the ability of the AMFA-enzyme to address the unmet medical need i.e. the muscular response of late-onset Pompe patients. AMFA were conjugated on the recombinant rhGAA produced in CHO cells and authorized in Pompe treatment. The chemical conjugation of AMFA on the enzyme was found to increase the affinity for CI-M6PR without altering the catalytic activity and to increase the uptake in fibroblasts and myoblasts of adult Pompe patients. Moreover, for the first time, Pompe mice aged of at least 10 months were significantly responsive to the treatment and provided muscular responses. The head to head comparison with rhGAA indicated that only rhGAA-AMFA had the capacity to increase the mobility of aged mice and to improve the muscular physiopathological parameters even at low doses. The relationship of these data with clinical studies and their potential therapeutic consequences will be discussed.

2. Materials and methods

2.1. Materials

Primary cultures of fibroblasts from infantile and adult Pompe patients were a kind gift of Dr. Catherine Caillaud. Cells were grown in DMEM containing 10% (v/v) fetal bovine serum and 100 IU/mL of penicillin-streptomycin in a humidified atmosphere containing 5% CO_2 at 37 °C. Primary cultures of myoblasts from Pompe adult patients, W172M01 BO and Y328 M01 BA, were obtained from CBC Biotec Biobank BB-0033-00046 (France) and cultured in HAM F10 medium supplemented with 20% fetal bovine serum on collagen-coated surface. The rhGAA used was alglucosidase alpha (Myozyme®) manufactured by Sanofi-Genzyme, and was recovered from excess material of the reconstituted commercial product used in patients. AMFA was synthesized from the commercial D-mannose as previously described [18]. D-Mannose was purchased from Senn Chemicals and other reagents were purchased from Acros Organics, Alfa Aesar, Expedeon and Sigma-Aldrich.

Pompe mice were a kind gift of Nina Raben [19] and were housed and cared according to protocols approved by the Languedoc-Roussillon ethical committee CEEA-LR-36 with agreement N4987-20l6l0lll6l32551.

2.2. Chemical conjugation of AMFA onto rhGAA

The rhGAA was oxidized with 1 mM sodium metaperiodate for 30 min at 4 °C. Excess sodium metaperiodate was consumed by the addition of 2% glycerol and by incubating on ice for 10 min. The oxidized enzyme was filtered on a G-25 sepharose column (GE Healthcare, UK) and conjugated to AMFA by mixing and incubating for 2 h at 25 °C. After conjugation, the rhGAA-AMFA was dialyzed against 25 mM sodium phosphate buffer (pH 6.2) containing 2% mannitol and 0.005% Tween 80 for 18 h at 4 °C. The samples were aliquoted and stored at − 20 °C until used.

2.3. rhGAA protein analysis

Western blot analyses were carried out on purified enzymes. The proteins were quantified by the Bradford method, and a constant amount were resolved by SDS-PAGE and transferred to nitrocellulose. Membranes were probed with anti-human GAA (anti-LYAG, Genetex) and actin (dilution 1:10,000, Sigma Aldrich), incubated with peroxidase-conjugated secondary antibodies (dilution 1:5000, Amersham) and analyzed by ECL detection system (Amersham). The apparent molecular weights were determined with prestained standard proteins (Ozyme).

2.4. Affinity for CI-M6PR

The affinity for CI-M6PR was tested at a concentration range from 10^{-8} to 10^{-6} M of enzymes. The assay was performed on a microtiter plate absorbed with pentamannose 6-phosphate (PM6P), which effectively binds CI-M6PR according to a method previously described [20]. After a 2 h pre-incubation of rhGAA enzymes with a biotinylated CI-M6PR (CI-M6PRb), the mixture was incubated in the microtiter plate coated with PM6P for 2 h, and CI-M6PRb linked to PM6P was then quantified by streptavidin peroxidase detection.

2.5. Uptake assays

For uptake experiments, primary human fibroblasts were grown to confluence and were incubated in low glucose DMEM supplemented with 5% (v/v) of fetal calf serum. Different concentrations of enzymes were added to culture medium and incubated for 24 h at 37 °C. For myoblast experiments, cells were grown to confluence and were incubated in HAM F12 supplemented with 10% fetal calf serum. Different concentrations of enzymes were added to culture medium and incubated for 24 h at 37 °C. After incubation, cells were washed three times with PBS and lysed by sonication in GAA assay buffer (0.2 M sodium acetate, 0.4 M potassium chloride, pH 4.3) containing 0.1% Triton X-100. The lysates were centrifuged at 14,000 × *g* for 10 min at 4 °C. Samples were tested for protein concentration and enzymatic activity was measured by using the fluorescent substrate 4-methylumbelliferyl-α-D-glucopyranoside (4-MUG). Cell lysates were incubated with 0.06 $mg{\cdot}mL^{-1}$ 4-MUG diluted in the GAA assay buffer for 3 h at 37 °C. The reaction was stopped by addition of 0.1 M Tris HCl pH 8 and the fluorescence was read with 355 nm excitation and 460 nm emission filters with a PerkinElmer 1420 VICTOR 2.

2.6. Confocal laser scanning microscopy

RhGAA and rhGAA-AMFA were coupled with Alexa-Fluor 488 Dye (Molecular Probes, USA) according to manufacturer instructions. By spectrophotometry, we checked that equal amounts of rhGAA-A488 and rhGAA-AMFA-A488 show equal fluorescence intensities. Few days prior to the experiment, myoblasts were grown onto collagen-coated glass dishes (World Precision Instrument, UK) at the density of 10^6 $cell.cm^{-2}$. On the day of the experiment, cells were washed once and incubated in 1 mL cultured medium containing fluorescent labeled

enzymes at a concentration of 100 nM for 16 h. For lysosome labeling, 2 h before visualization, 50 nM Lysotracker red DND-99 (Invitrogen, France) was added to medium. Fifteen minutes before the end of incubation, cells were loaded with Hoescht 33,342 (Invitrogen) for nuclear staining at a final concentration of 5 $\mu g \cdot mL^{-1}$. Before visualization cells were gently washed with phenol red-free medium. Cells were then scanned with a LSM 780 LIVE confocal laser scanning microscope (Carl Zeiss, France) with a slice depth (Z stack) of 0.62 µm. Merged images of fluorescent enzymes and lysosome marker allow the evaluation of enzyme level into lysosomes. Colocalizations of enzyme-A488 and Lysotracker were compared using Mander's overlap co-localization coefficient. This coefficient represents the sum of green colocalized pixels (yellow pixels, in merged image) as compared to the overall sum of green pixels above threshold. A value of 1 highlights a high co-localization and a value of 0 corresponds to an absence of co-localization.

2.7. In vivo studies

The GAA-/- Pompe mouse model [18] presents aspects of human disease, as mice exhibit systemic glycogen accumulation especially in heart, diaphragm and skeletal muscle and very low acid α-glucosidase activity (similar to the infantile onset). Two short term and one long term studies were performed. For all experiments, animals were injected intraperitoneally with 5 mg/kg diphenhydramine 15 min before enzyme administration. Enzyme treatment was injected into the tail vein. Throughout the treatment, sera were regularly collected in order to test the immunological response against the recombinant enzyme and animal motor function was tested on a Rotarod treadmill (Ugo Basile, Italy) using a constant acceleration program. At the end of the experiments, animals were sacrificed and several tissues were collected and stored at − 80 °C until assayed or fixed for histological analysis. A first in vivo study was performed on 11-month-old Pompe mice to evaluate the efficacy of the rhGAA-AMFA to improve the pathological parameters of the disease. Groups of Pompe mice (n = 6) were injected with vehicle, 5 mg/kg rhGAA or rhGAA-AMFA once a week. The animals were treated for 13 weeks and sacrificed 48 h after the last injection. For the second in vivo study, 11 month-old mice (n = 3) were administered vehicle, rhGAA-AMFA and rhGAA at 10 mg/kg/week. Animals received 4 injections and were sacrificed a week after the last treatment. A third experiment was performed on 12 month-old mice (n = 6), with 4 weekly doses of 20 mg/kg with rhGAA-AMFA, rhGAA or vehicle. Animals were euthanized 1 week after the 4th injection.

2.8. Activity of GAA in muscular biopsies

Pompe mice quadriceps were lysed in 0.2 M sodium acetate, 0.4 M potassium chloride, pH 4.3 containing 0.5% Triton X-100 and sonicated 3 × 6 s. The lysates were centrifuged at 14,000 × g for 10 min at 4 °C. Samples were assayed for protein concentration and the activity of GAA was tested using 4-MUG 1.3 $mg \cdot mL^{-1}$ as a substrate. Samples were incubated for 2 h at 37 °C. Reaction was stopped by adding 0.5 M sodium bicarbonate buffer pH10.65. Fluorescence was read with 355 nm excitation and 460 nm emission filters.

2.9. Glycogen quantification

The glycogen was extracted by digesting samples with 30% KOH for 2 h at 100 °C. Samples were cooled on ice and glycogen was precipitated with 95% ethanol. After centrifugation at 8000 × *g*, 10 min at room temperature, three series of acidification with 5 N HCl and precipitation with 95% ethanol were performed. Finally, glycogen extracts were reconstituted in deionized water. The glycogen content of the samples was tested by first digesting glycogen into glucose with *Aspergillus Niger* and consequently dosing the released glucose with Amplex Red reagent. Undigested samples were also tested for their glucose content. A standard curve was plotted with a glucose solution (Sigma). Values are expressed as µg glycogen/mg tissue.

2.10. Acid phosphatase quantification

Pompe mice tissue samples were lysed in 0.2 M sodium acetate, 0.4 M potassium chloride, pH 3.9 and sonicated 3 × 6 s. The lysates were centrifuged at 14,000 × g for 10 min at 4 °C. Samples were assayed for protein concentration and the activity of phosphatases was tested using 6,8-difluoro-4-methylumbelliferyl phosphate (DiFMUP) (Molecular Probes) as a substrate in 100 mM sodium acetate pH 5.5. Extract (10 µL) were incubated in sodium acetate buffer pH 5.5 and 0.2 mM DiFMUP for 45 min at room temperature. Fluorescence intensity was monitored with a 355 nm excitation and a 460 nm emission filters.

2.11. Histological analysis

For light microscopy, tissues were fixed in 10% formol buffered solution, embedded in paraffin, sectioned, and stained with hematoxylin-eosin by standard methods. For centralized nuclei counting, central and peripheral nuclei were counted in 400 fibers for each mouse and the mean values ± SD are indicated.

2.12. Statistical analysis

The statistical analysis was performed using either the Student's *t*-test or the Newman-Keuls test for repeated measures. A probability value of $p < 0.05$ was considered statistically significant.

3. Results

3.1. Characterization and cellular uptake of the new enzyme conjugate, rhGAA-AMFA

Chemical conjugation of the AMFA onto oligosaccharide chains of rhGAA was performed through the formation of oxime bonds between the carbonyl-reactive ethyloxyamino group of AMFA and the aldehyde residues generated at terminal sialic acid residues which are highly sensitive to periodate oxidation [21] (Scheme 1). The coupling reaction with a 300-fold molar excess of AMFA for 2 h at 25 °C led to the addition of a mean value of 4.8 ± 1 AMFA/rhGAA (mol/mol) from 3 independent experiments. The number of AMFA per enzyme was quantified by high-performance anion-exchange chromatography with pulse amperometric detection analysis as previously described [17].

The functionalities of the conjugated enzyme were characterized. AMFA coupling did not induce protein degradation, as shown by the unique band of the conjugated enzyme, corresponding to the 110 kDa GAA precursor, in SDS polyacrylamide gel (Fig. 1 a). Such result is coherent with the addition of 4.8 ± 1 AMFA per enzyme since the AMFA molecular weight is 0.317 kDa. In Western immunoblots

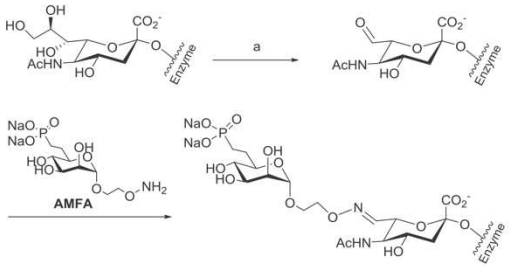

Scheme 1. AMFA grafting on oxidized sialic acid residues of rhGAA a) $NaIO_4$ (1 mM), 4 °C, 30 min, b) AMFA (300 eq) reaction with oxidized rhGAA, 25 °C, 2 h.

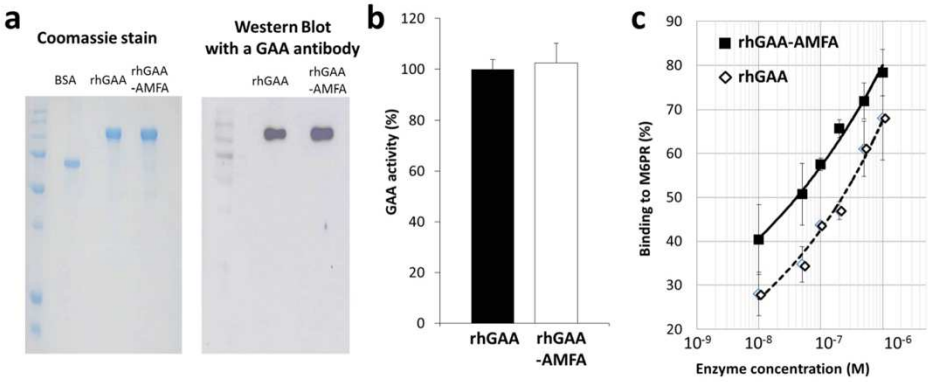

Fig. 1. Characterization of the immunoreactivity, CI-M6PR binding affinity and catalytic activity of the conjugate rhGAA-AMFA. a) SDS gel analysis of rhGAA and rhGAA-AMFA followed by Coomassie blue staining of total proteins (left) and Western immunoblot using anti-human GAA antibody (right). b) Catalytic activities of rhGAA-AMFA compared to rhGAA using the synthetic substrate 4-MUG, expressed in % of $nmol \cdot mg^{-1} \cdot h^{-1}$. n = 3 experiments in duplicate. c) Affinities of rhGAA and rhGAA-AMFA for CI-M6PR. To bind 50% of the CI-M6PR 2.4 10^{-7} M of rhGAA and 4 10^{-8} M of rhGAA-AMFA are necessary. n = 4.

performed with a specific anti-human GAA antibody, the recognition of rhGAA was unmodified after AMFA coupling (Fig. 1 a). The AMFA grafting also did not affect the catalytic activity of rhGAA assayed on a synthetic substrate (Fig. 1 b). In contrast, the affinity for the CI-M6PR, evaluated using an indirect ELISA method, was increased by 6-fold after AMFA addition (Fig. 1 c). These data indicated that AMFA coupling improved targeting and fully maintained the structural and the catalytic properties of the enzyme.

The uptakes of rhGAA-AMFA and rhGAA were then compared on adult Pompe fibroblast primary cultures (Fig. 2 a). While rhGAA showed a very limited internalization in these fibroblasts even at high concentrations, rhGAA-AMFA uptake was significantly increased. GAA activity in cells treated by 100 nM and 200 nM rhGAA-AMFA was by 233% and 411% versus control whereas for rhGAA treated cells it was only incremented by 132% and 164% respectively. The uptake of rhGAA-AMFA was also compared to that of rhGAA in Pompe myoblasts, a more relevant cell type for this myopathy. In primary cultures of myoblasts from two adult patients, a significant increase of rhGAA-AMFA internalization was also observed at 10 and 50 nM (Fig. 2 b). These data indicate that the AMFA conjugation has the capacity to increase the entry of rhGAA in different cell types of adult Pompe patients. The subcellular localization of rhGAA and rhGAA-AMFA was then analyzed after labeling each enzyme with a green fluorescent probe, Alexa-Fluor 488 (Fig. 2 c). The confocal analysis in living cells showed a higher fluorescent uptake of rhGAA-AMFA compared to rhGAA in accordance with the increased catalytic activity shown in Fig. 2a. More importantly, rhGAA-AMFA appeared more colocalized than rhGAA with the staining obtained by a Lysotracker (a fluorescent acidotropic probe). Manders' overlap coefficient which quantifies the colocalization between enzyme and Lysotracker fluorescences indicated a higher value for rhGAA-AMFA (0.38) than for rhGAA (0.22) (Fig. 2 d). All together, these data indicate that internalization of rhGAA in fibroblasts and myoblasts of adult patients is facilitated by AMFA that increases enzyme affinity to CI-M6PR. A higher localization of rhGAA-AMFA in acidic vesicles (lysosomes or phagolysosomes) as compared to rhGAA suggests that AMFA also favors the addressing to the acidic sites of action of the enzyme.

3.2. Mouse mobility is improved by AMFA grafting on rhGAA

To determine rhGAA-AMFA efficiency, the modified enzyme was assayed on Pompe mice aged of at least 10 months, since aged mice were previously found almost unresponsive to rhGAA [13]. The mobility of the mice was assessed using a Rotarod walking treadmill together with biochemical parameters in tissues. Three in vivo studies were performed: one 13-week study on 10 month-old mice at a low dose (5 mg/kg/week) and two distinct 4-week studies on older mice at 10 and 20 mg/kg/week. In all the experiments, the motor function was higher in mice treated with rhGAA-AMFA than in rhGAA treated ones. rhGAA-AMFA at the lowest dose stabilized the Pompe disease progression up to 13 weeks maintaining 90% of the initial mobility whereas in control and rhGAA-treated mice the mobility decreased to near 50% (Fig. 3 a). The intermediate dose (10 mg/kg/week) of rhGAA-AMFA showed an increase to 120% after 4 weeks whereas mobility decreased to near 75% in control and rhGAA-treated mice (Fig. 3 b). In the experiment with 4 injections at 20 mg/kg/week (Fig. 3 c) rhGAA-AMFA in 12 month-old mice, the mobility was more significantly increased raising 162% whereas rhGAA treated mice were stabilized at 98% and control mice mobility decreased to 58% of the initial values. It can be noticed that the effectiveness on mobility is rhGAA-AMFA dose dependent. Concerning rhGAA treatment, our data are consistent with previous studies of Zhu et al. [14] which tested higher doses of rhGAA and showed only marginal improvements of motor function in such aged mice.

3.3. Tissue GAA activity in aged Pompe mice

The biochemical and morphological effects of rhGAA-AMFA were then determined in the tissues of the Pompe mice treated in the three experiences described in Fig. 3, aged between 10 and 12 months. At this age, histological analysis of muscle sections exhibits a high degree of lysosomal rupture and elevated levels of extra-lysosomal glycogen [19]. These mice are considered as a representative model of an advanced stage of the disease observed in severe infantile form and advanced late onset in human [22]. This stage is associated with a degree of muscle wasting defined as a stage 4 according to Thurberg's classification [23] and is particularly resistant to ERT using rhGAA [24,25].

Tissues samples of mice were analyzed to assess enzyme activity. Higher levels of GAA activity were detected in heart, diaphragm and quadriceps muscles of Pompe mice treated with rhGAA-AMFA (Fig. 4). Importantly, even the treatment with very low doses of rhGAA-AMFA (5 mg/kg/week) resulted in a significantly higher level of enzyme activity in quadriceps and heart (Fig. 4 a-b). A dose-dependent activity in the heart was observed when comparing 5 mg/kg and 20 mg/kg experiments (Fig. 4 b-c). Importantly, only rhGAA-AMFA is able to ensure enzyme activity in the diaphragm (Fig. 4 d), an organ which is hardly

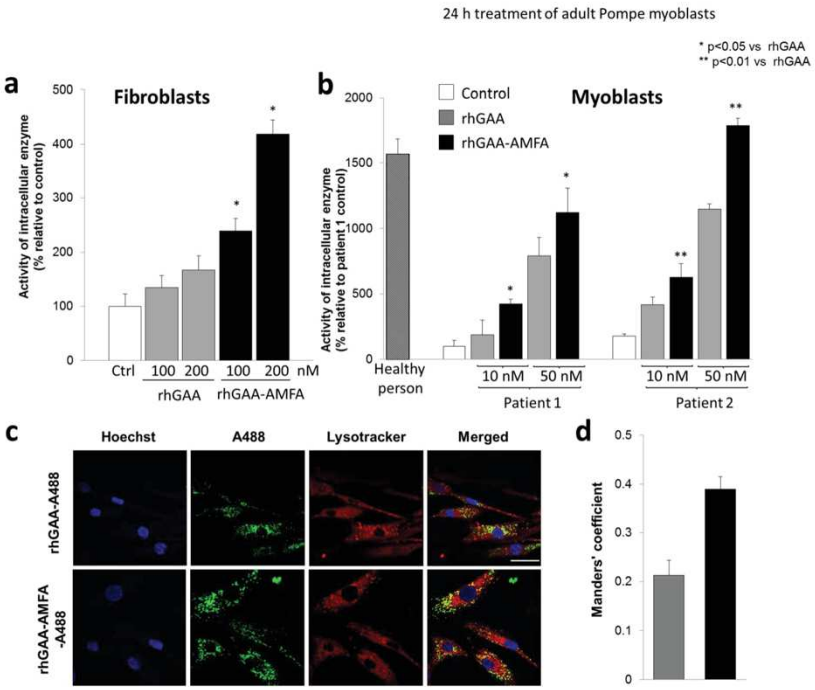

Fig. 2. Improvement of rhGAA uptake with AMFA and subcellular localization. a) GAA activities after enzymes internalization in primary cultures of adult patient fibroblasts. *p < 0.05 versus rhGAA, Student's *t*-test. b) Myoblasts issued from adult patients had a higher cellular uptake of rhGAA-AMFA. Myoblasts were incubated for 24 h with 10 and 50 nM rhGAA-AMFA or rhGAA and intracellular activity was quantified. c) Confocal microscopic analyses of rhGAA and rhGAA-AMFA in living adult Pompe myoblasts. Enzymes were labeled with Alexa 488 dye and incubated for 16 h. Before visualization, living cells were incubated with cell-permeable Hoescht solution and Lysotracker for the staining of nuclei and acidic vesicles (lysosomes, phagolysosomes) respectively. Data are from one representative of 3 experiments. d) Colocalization of rhGAA (grey bar) or rhGAA-AMFA (black bar) with Lysotracker staining. The Mander's overlap coefficient (varying between 0 and 1, with 0 = no overlap, and + 1 = perfect overlap) was calculated. Mean ± SD. n = 6.

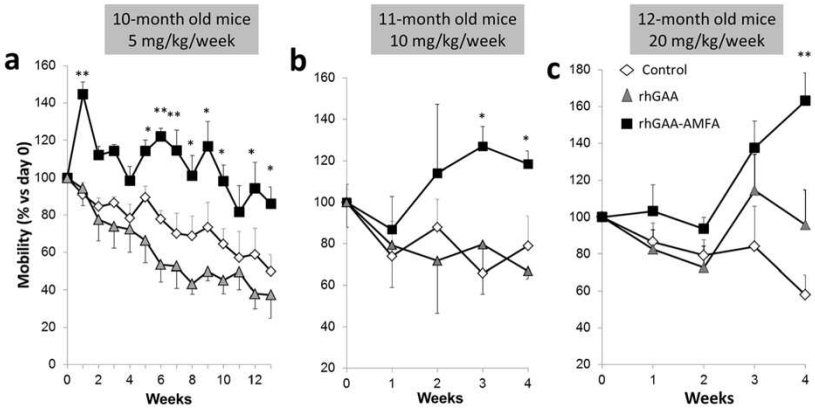

Fig. 3. Assessment of mobility after enzyme therapy of Pompe mice. Rotarod mobility test of a) 10-month old Pompe mice treated with 5 mg/kg/week with rhGAA, rhGAA-AMFA or dilution buffer (Control). n = 6 b) 11-month old Pompe mice treated with 10 mg/kg/week rhGAA, rhGAA-AMFA or dilution buffer (Control). n = 3 c) 12-month old Pompe mice treated with 20 mg/kg/week with rhGAA, rhGAA-AMFA or dilution buffer (Control). n = 6 *p < 0.05, **p < 0.01 vs rhGAA (Newman-Keuls test).

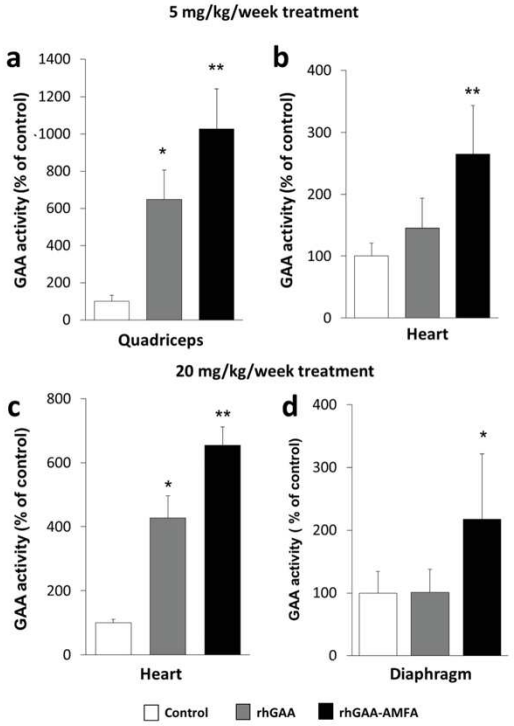

Fig. 4. GAA activity in aged Pompe mice muscles treated with rhGAA or rhGAA-AMFA. GAA activity in a) Quadriceps of 5 mg/kg/week treated mice. n = 4 b) Heart of 5 mg/kg/week-treated mice. n = 6 c) Heart of 20 mg/kg/week-treated mice. n = 6 d) Diaphragm of 20 mg/kg/week treated mice. *p < 0.05, **p < 0.01 versus Control (a,b) or rhGAA-AMFA versus rhGAA (c, d) (Student's *t*-test). n = 6.

treatable by present rhGAA treatment.

3.4. rhGAA-AMFA improves glycogen clearance in aged Pompe mice

A quantitative glycogen analysis was conducted on tissue extracts to determine if the increase in GAA activity was correlated with a reduction of glycogen accumulation (Fig. 5). In mice treated with rhGAA a modest reduction in glycogen levels was observed in heart (13.5%) and in triceps (40%). By contrast, treatment with rhGAA-AMFA led to a decrease of 35% in heart and 74.5% in triceps. This two-fold higher reduction of glycogen in GAA-AMFA group is in agreement with the higher GAA activity.

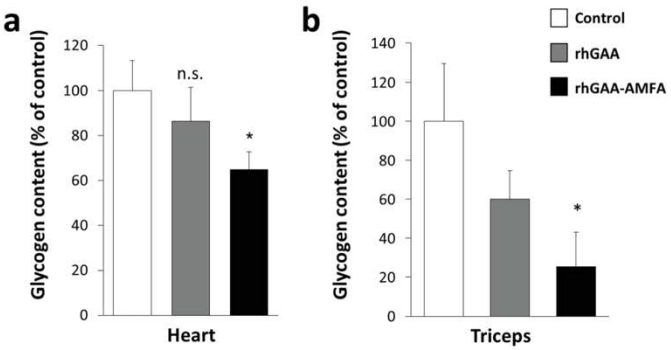

Fig. 5. Glycogen is decreased in aged Pompe mice muscles treated with rhGAA-AMFA. Glycogen content in a) Heart of 5 mg/kg/week-treated mice. n = 6 *p < 0.05 vs control. b) Triceps of 20 mg/kg/week-treated mice. n = 6 *p < 0.05 vs rhGAA.

3.5. rhGAA-AMFA reduces muscular cell damages and acid phosphatase activity

To corroborate the difference observed in the motor function, histopathological analyses of the muscles were performed. In normal muscle, only 2% of fibers have centralized nuclei. However, in response to stress, normal peripheral nuclei may migrate toward the center of the cells. Examination of quadriceps of Pompe old mice after 4 injections with vehicle or 20 mg/kg/week of each enzyme was realized (Fig. 6 a). rhGAA treated mice showed a pattern of centrally localized nuclei (31 ± 7%) similar to untreated mice (29 ± 9%) (Fig. 6 b). This is in agreement with the publication of Zhu et al. [14]. By contrast, the percentage of centralized nuclei is significantly reduced to 15 ± 2.5% by rhGAA-AMFA.

In complement, we assessed phosphatase acid activity since several clinical studies described that a decrease of this marker is associated with a good ERT response [26]. As shown in Fig. 6 c, the decrease of acid phosphatase activity by rhGAA-AMFA treatment is significantly stronger than that of rhGAA. The acid phosphatase values after rhGAA-AMFA treatment are close to those of healthy mice (39% ± 28% of control Pompe mice, data not shown).

Altogether, these data present the first evidence of ERT efficacy on the mobility of 10-month aged mice and of its ability to reduce muscle damages at an advanced stage of the disease.

3.6. Immunological response against rhGAA and rhGAA-AMFA

The presence of anti-GAA specific antibodies in mouse serum was assayed after each experiment. Fig. 7 presents the values of the longest experiment which corresponds to 13 weekly injections of 5 mg/kg/week rhGAA-AMFA and rhGAA. Serum analyses of treated mice revealed that the addition of AMFA did not increase the immunological response to rhGAA (Fig. 7 a). Interestingly, sera from rhGAA-AMFA treated mice reacted similarly to rhGAA-AMFA and rhGAA respectively (Fig. 7 b-c). The reactivity of the antibodies against rhGAA-AMFA is not statistically different from that against rhGAA, suggesting that AMFA grafting does not induce additional epitopes of hapten-type. However, immunological responses on Pompe mice model may not predict human responses.

4. Discussion

To our knowledge, the corrections of nuclear mispositioning and

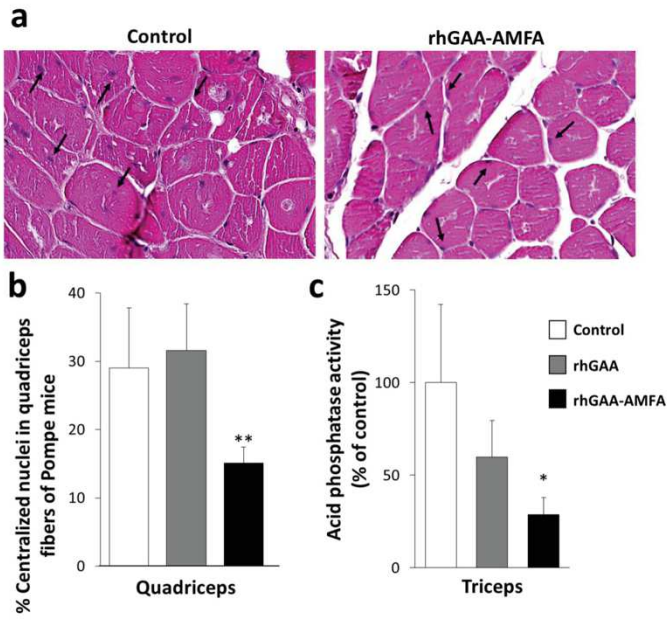

Fig. 6. Muscular cell corrections in aged Pompe mice treated with rhGAA-AMFA. a) Hematoxylin and eosin stained slides were prepared from mice treated either with dilution buffer (Control) or with 20 mg/kg/week rhGAA or rhGAA-AMFA for 4 weeks. Mice were 12 month-old at time 0. n = 6. b) Quantification of centralized nuclei on hematoxylin/eosin stained quadriceps sections. Twelve month-old Pompe mice were treated with 20 mg/kg/week rhGAA or rhGAA-AMFA or vehicle (Control) during 4 weeks. Central and peripheric nuclei were counted in 400 fibers for each mouse and the mean values ± SD are indicated. n = 6 mice. **p < 0.001 vs rhGAA. c) Phosphatase acid activity in triceps of 11 month-old Pompe mice treated with 10 mg/kg/week rhGAA, rhGAA-AMFA or vehicle (Control) during 4 weeks. Phosphatase activity is dosed using a fluorescent substrate 6,8-difluoro-4-methylumbelliferyl phosphate (DiFMUP). *p < 0.05 vs rhGAA. n = 3.

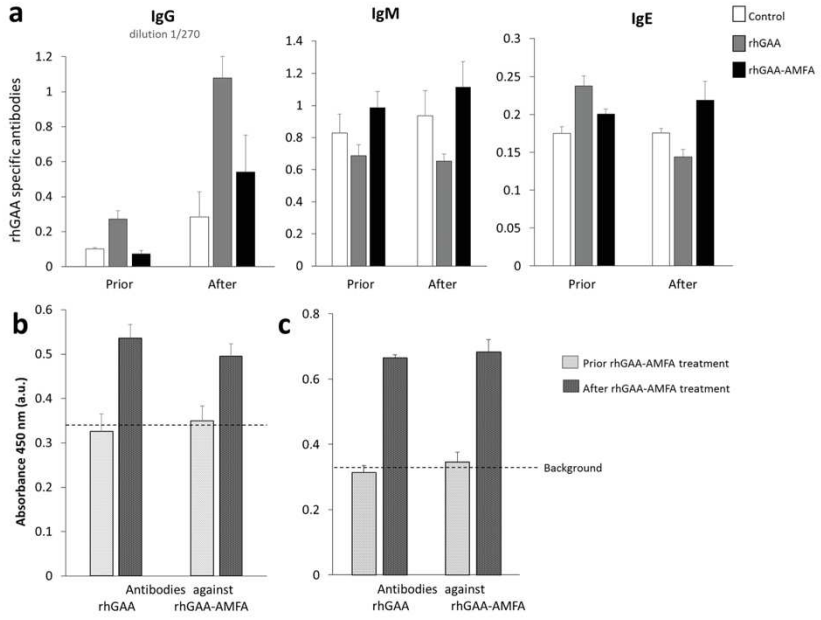

Fig. 7. Immunological responses against rhGAA and rhGAA-AMFA. a) Antibody titers against rhGAA were evaluated in sera of 10 month-old mice treated with 13 injections of vehicle (Control) or 5 mg/kg/week of rhGAA-AMFA and rhGAA. Sera were collected prior to treatment for comparison. ELISA plates were coated with rhGAA to determine the distribution of specific rhGAA antibodies in diluted sera. A dilution of 1:30 was used for IgM and IgE and a dilution of 1:270 for IgG (mean ± SD of two independent assays, *p < 0.05, **p < 0.01, Student's *t*-test) (n = 6 mice). b) Cross interaction of rhGAA-AMFA IgG with purified rhGAA or rhGAA-AMFA. Sera collected prior and after the treatment of 10 month-old mice with 13 injections of 5 mg/kg/week of rhGAA-AMFA were evaluated on microplates coated either with rhGAA or with rhGAA-AMFA. A 1:30 dilution of serum is used. c) Cross interaction of mice IgG from 12 month-old mice treated with 4 injections of 20 mg/kg/week of rhGAA-AMFA on microplates coated either with rhGAA or with rhGAA-AMFA. A 1:30 dilution of serum is used.

altered metabolic activity in muscle fibers and the increased motor function here described in 10–12 month-old mice had never been observed before, neither for higher doses of rhGAA [14] nor with other engineered rhGAA, such as Neo-GAA [10,14] or BMN701 [15]. In these previous studies, several hypotheses were proposed to explain the unresponsiveness of aged mice, such as (i) the reported decline in CI-M6PR expression with aging [27,28], (ii) an abnormal increase of the autophagic pathways [29] and (iii) a more established disease with irreversible damages [14].

The amount of CI-M6PR, although lowered with aging [9], appears not to be the only parameter to be taken into account. Indeed, some evidences support a sufficient internalization of glyco-engineered enzymes by aged muscle cells and prove that these enzymes are still metabolically active. For instance, the tissue glycogen levels in aged Pompe mice were significantly reduced with 40 mg/kg of hydrazone-neorhGAA [10] or with 20 mg/kg of oxime-neoGAA (Neo-GAA), which has a 20-fold increased affinity for CI-M6PR [14]. Nevertheless, in all previous studies, the reduction of glycogen levels in these more damaged muscle cells was not translated in improvements in the motor function. Therefore, the inability for rhGAA to restore muscle function in aged mice may involve other factors.

The abnormal autophagic pathways in Pompe mice were characterized in biopsies by clusters of densely packed late endosomes/lysosomes and autophagosomes [29,30]. These alterations were proposed to divert the recombinant enzyme from its destination, the lysosome, and induce its accumulation in autophagosomes [31]. In late-onset patients, autophagic abnormalities are also present in muscle biopsies [32,33]. This profound disorder in the intracellular recycling system is suggested as an important cause of unresponsiveness to therapy due to an altered routing and consequently a reduced lysosomal uptake of the rhGAA.

Irreversible damages due to lysosomal rupture, leading to release of glycogen and lytic enzymes into the cytoplasm, have been demonstrated in the most severe forms of the disease. Such muscle irreversible damages can explain the loss of sensitivity of aged tissue to ERT. However, in the milder non-classical infantile and juvenile/adult forms, this panel of muscle destruction is rarely observed at diagnosis. The unresponsiveness of these milder forms to rhGAA might be associated with the factors mentioned above that prevent the therapeutic enzyme to reach its final destination.

In this study, the enzyme rhGAA was chemically grafted with 4.8 ± 1 AMFA derivatives. The AMFA-enzyme displays a 6-fold higher affinity for CI-M6PR and a 2-fold higher uptake in adult patient fibroblasts and myoblasts compared to rhGAA. The subcellular analysis indicated that the conjugated enzyme rhGAA-AMFA is two-fold more localized in the acid vesicles than the native enzyme. These in vitro data, indicating a higher stability and a better delivery to lysosomes due to AMFA grafting, have been complemented by studies on the murine model of Pompe disease. The efficacy of rhGAA-AMFA on elderly mice, refractory to current treatment, was demonstrated as compared to rhGAA. An improved walking capacity is observed even at the low dose of 5 mg/kg/week rhGAA-AMFA and it increases in a dose-dependent manner. In line with this improved motor function, several biochemical and morphological analyses indicate the higher correction of muscle fibers impairment. The higher GAA activity and the lower level of glycogen recovered in different muscles indicate the higher uptake and efficacy of rhGAA-AMFA. These data are fully in agreement with those obtained from primary cell cultures.

The treatment efficacy was more evidenced by the reduction of the nuclei centralization in myofibers and by a decrease of acid phosphatase activity which are recognized as two key indicators of the ERT response. However, further examinations of specific muscle parameters are required to determine the extent of muscle regeneration. The enzyme activity detected in the diaphragm only with rhGAA-AMFA treatment could be particularly important because this tissue, which is considered as a difficult target for ERT, plays an important role in the frequent severe respiratory failures of the infantile and late onsets.

Another purpose of this study concerned the immunological responses against rhGAA-AMFA that AMFA grafting could induce. Interestingly, GAA antibodies analyses realized on the 13-week study at 5 mg/kg/week revealed the absence of an additional immunological response due to AMFA grafting and similar levels of specific antibodies against rhGAA-AMFA and rhGAA were observed.

In conclusion, for the first time, an ERT was demonstrated to be efficient both on motor function and muscle fibers in 10–12 month-old Pompe mice which were supposed to be almost unresponsive to therapy. The higher therapeutic potential of this new ERT may not be solely explained by the increased affinity for the CI-M6PR since another glyco-engineered enzyme, Neo-GAA, with higher affinity remains poorly active in elderly mice. We have shown that AMFA increase the affinity of rhGAA for CI-M6PR, are insensitive to phosphatases in opposite to M6P [17] and could modify the hydrophilicity of the enzyme. These properties of AMFA might interfere through different pathways in the stability, cell uptake, cell routing and intracellular processing of the enzyme. Therefore, we are now investigating to elucidate the mechanisms responsible of the greater efficacy of rhGAA-AMFA. Our findings in aged mice open the way to a new therapeutic option for late onset Pompe patients who are still in need of a successful therapy. AMFA technology could also be an answer for the treatment of other lysosomal diseases and likely improve the outcome for patients among the 53 lysosomal storage disorders.

Acknowlegments

This work was supported by Agence Nationale de la Recherche grant N13-RPIB-0012-03, Région ex-Languedoc-Roussillon, BPI France, French Ministère de l'Enseignement supérieur, de la Recherche et de l'Innovation for Crea-Dev (grant NA1211012J/AE AN 11 CC), Université de Montpellier, Vaincre les Maladies Lysosomales-Suisse, CNRS, NanoMedSyn and Transferts. We thank Pr Schaeffer from CBC Biotec Biobank, Montpellier RIO imaging platform for assistance in the microscopy experiments and METAMUS DMEM facility of Montpellier animal facilities (RAM) for animal housing and their support for the in vivo experiments.

References

[1] A.T. van der Ploeg, A.J. Reuser, Pompe's disease, Lancet 372 (9646) (2008) 1342–1353.
[2] A. Toscano, B. Schoser, Enzyme replacement therapy in late-onset Pompe disease: a systematic literature review, J. Neurol. 260 (4) (2013) 951–959.
[3] P.S. Kishnani, D. Corzo, M. Nicolino, B. Byrne, H. Mandel, W.L. Hwu, N. Leslie, J. Levine, C. Spencer, M. McDonald, J. Li, J. Dumontier, M. Halberthal, Y.H. Chien, R. Hopkin, S. Vijayaraghavan, D. Gruskin, D. Bartholomew, A. van der Ploeg, J.P. Clancy, R. Parini, G. Morin, M. Beck, G.S. De la Gastine, M. Jokic, B. Thurberg, S. Richards, D. Bali, M. Davison, M.A. Worden, Y.T. Chen, J.E. Wraith, Recombinant human acid [alpha]-glucosidase: major clinical benefits in infantile-onset Pompe disease, Neurology 68 (2) (2007) 99–109.
[4] A.T. van der Ploeg, P.R. Clemens, D. Corzo, D.M. Escolar, J. Florence, G.J. Groeneveld, S. Herson, P.S. Kishnani, P. Laforet, S.L. Lake, D.J. Lange, R.T. Leshner, J.E. Mayhew, C. Morgan, K. Nozaki, D.J. Park, A. Pestronk, B. Rosenbloom, A. Skrinar, C.I. van Capelle, N.A. van der Beek, M. Wasserstein, S.A. Zivkovic, A randomized study of alglucosidase alfa in late-onset Pompe's disease, N. Engl. J. Med. 362 (15) (2010) 1396–1406.
[5] B. Schoser, V. Hill, N. Raben, Therapeutic approaches in glycogen storage disease type II/Pompe disease, Neurotherapeutics 5 (4) (2008) 569–578.
[6] B. Schoser, A. Stewart, S. Kanters, A. Hamed, J. Jansen, K. Chan, M. Karamouzian, A. Toscano, Survival and long-term outcomes in late-onset Pompe disease following alglucosidase alfa treatment: a systematic review and meta-analysis, J. Neurol. 264 (4) (2016) 621–630.
[7] S. Kornfeld, Structure and function of the mannose 6-phosphate/insulinlike growth factor II receptors, Annu. Rev. Biochem. 61 (1992) 307–330.
[8] P. Ghosh, N.M. Dahms, S. Kornfeld, Mannose 6-phosphate receptors: new twists in the tale, Nat. Rev. Mol. Cell Biol. 4 (3) (2003) 202–212.
[9] M. Gary-Bobo, P. Nirde, A. Jeanjean, A. Morere, M. Garcia, Mannose 6-phosphate receptor targeting and its applications in human diseases, Curr. Med. Chem. 14 (28) (2007) 2945–2953.
[10] Y. Zhu, X. Li, A. McVie-Wylie, C. Jiang, B.L. Thurberg, N. Raben, R.J. Mattaliano, S.H. Cheng, Carbohydrate-remodelled acid alpha-glucosidase with higher affinity

for the cation-independent mannose 6-phosphate receptor demonstrates improved delivery to muscles of Pompe mice, Biochem. J. 389 (Pt 3) (2005) 619–628.
[11] A.J. McVie-Wylie, K.L. Lee, H. Qiu, X. Jin, H. Do, R. Gotschall, B.L. Thurberg, C. Rogers, N. Raben, M. O'Callaghan, W. Canfield, L. Andrews, J.M. McPherson, R.J. Mattaliano, Biochemical and pharmacological characterization of different recombinant acid alpha-glucosidase preparations evaluated for the treatment of Pompe disease, Mol. Genet. Metab. 94 (4) (2008) 448–455.
[12] J.E. Stefano, L. Hou, D. Honey, J. Kyazike, A. Park, Q. Zhou, C.Q. Pan, T. Edmunds, In vitro and in vivo evaluation of a non-carbohydrate targeting platform for lysosomal proteins, J. Control. Release 135 (2) (2009) 113–118.
[13] Q. Zhou, L.Z. Avila, P.A. Konowicz, J. Harrahy, P. Finn, J. Kim, M.R. Reardon, J. Kyazike, E. Brunyak, X. Zheng, S.M. Patten, R.J. Miller, C.Q. Pan, Glycan structure determinants for cation-independent mannose 6-phosphate receptor binding and cellular uptake of a recombinant protein, Bioconjug. Chem. 24 (12) (2013) 2025–2035.
[14] Y. Zhu, J.L. Jiang, N.K. Gumlaw, J. Zhang, S.D. Bercury, R.J. Ziegler, K. Lee, M. Kudo, W.M. Canfield, T. Edmunds, C. Jiang, R.J. Mattaliano, S.H. Cheng, Glycoengineered acid alpha-glucosidase with improved efficacy at correcting the metabolic aberrations and motor function deficits in a mouse model of Pompe disease, Mol. Ther. 17 (6) (2009) 954–963.
[15] J.A. Maga, J. Zhou, R. Kambampati, S. Peng, X. Wang, R.N. Bohnsack, A. Thomm, S. Golata, P. Tom, N.M. Dahms, B.J. Byrne, J.H. LeBowitz, Glycosylation-independent lysosomal targeting of acid alpha-glucosidase enhances muscle glycogen clearance in pompe mice, J. Biol. Chem. 288 (3) (2013) 1428–1438.
[16] L. Pena, R.J. Barohn, B. Byrne, C. Desnuelle, O. Goker-Alpan, S. Ladha, P. Laforet, E. Mengel, A. Pestronk, J. Pouget, B. Schoser, V. Straub, J. Trivedi, P. Van Damme, J. Vissing, P. Young, B. Thurberg, K. Culm-Merdek, G. Short, A. Van der Ploeg, Phase 1 exploratory efficacy of the novel enzyme replacement therapy NeoGAA in treatment- naïve and alglucosidase alfa-treated late-onset Pompe disease patients, Neurology 86 (16) (2015) S38006.
[17] T. Hiwot, R.J. Barohn, D. Bratkovic, B. Byrne, C. Desnuelle, D. Hughes, P. Laforêt, E. Mengel, M. Roberts, K. Yang, C. Heusner, W. Dummer, Reveglucosidase alfa (BMN701), a GILT-tagged recombinant human acid alpha glucosidase (rhGAA), evaluation in late-onset Pompe disease: preliminary clinical efficacy and safety results of an extension study (72-week results), Neuromuscul. Disord. (25) (2015) S184–S316.
[18] K. El Cheikh, I. Basile, A. Da Silva, C. Bernon, P. Cerutti, F. Salgues, M. Perez, M. Maynadier, M. Gary-Bobo, C. Caillaud, M. Cerutti, M. Garcia, A. Morere, Design of Potent Mannose 6-phosphate analogues for the functionalization of lysosomal enzymes to improve the treatment of Pompe disease, Angew. Chem. Int. Ed. Eng. 55 (47) (2016) 14774–14777.
[19] N. Raben, K. Nagaraju, E. Lee, P. Kessler, B. Byrne, L. Lee, M. LaMarca, C. King, J. Ward, B. Sauer, P. Plotz, Targeted disruption of the acid alpha-glucosidase gene in mice causes an illness with critical features of both infantile and adult human glycogen storage disease type II, J. Biol. Chem. 273 (30) (1998) 19086–19092.
[20] A. Jeanjean, M. Garcia, A. Leydet, J.L. Montero, A. Morere, Synthesis and receptor binding affinity of carboxylate analogues of the mannose 6-phosphate recognition marker, Bioorg. Med. Chem. 14 (10) (2006) 3575–3582.
[21] M. Thaysen-Andersen, M.R. Larsen, N.H. Packer, G. Palmisano, Structural analysis of glycoprotein sialylation- Part I: pre-LC-MS analytical strategies, RSC Adv. 3 (2013) 22683–22705.
[22] N. Raben, M. Danon, A.L. Gilbert, S. Dwivedi, B. Collins, B.L. Thurberg, R.J. Mattaliano, K. Nagaraju, P.H. Plotz, Enzyme replacement therapy in the mouse model of Pompe disease, Mol. Genet. Metab. 80 (1–2) (2003) 159–169.
[23] B.L. Thurberg, C. Lynch Maloney, C. Vaccaro, K. Afonso, A.C. Tsai, E. Bossen, P.S. Kishnani, M. O'Callaghan, Characterization of pre- and post-treatment pathology after enzyme replacement therapy for Pompe disease, Lab. Investig. 86 (12) (2006) 1208–1220.
[24] R.J. Ziegler, S.D. Bercury, J. Fidler, M.A. Zhao, J. Foley, T.V. Taksir, S. Ryan, B.L. Hodges, R.K. Scheule, L.S. Shihabuddin, S.H. Cheng, Ability of adeno-associated virus serotype 8-mediated hepatic expression of acid alpha-glucosidase to correct the biochemical and motor function deficits of presymptomatic and symptomatic Pompe mice, Hum. Gene Ther. 19 (6) (2008) 609–621.
[25] N. Raben, T. Fukuda, A.L. Gilbert, D. de Jong, B.L. Thurberg, R.J. Mattaliano, P. Meikle, J.J. Hopwood, K. Nagashima, K. Nagaraju, P.H. Plotz, Replacing acid alpha-glucosidase in Pompe disease: recombinant and transgenic enzymes are equipotent, but neither completely clears glycogen from type II muscle fibers, Mol. Ther. 11 (1) (2005) 48–56.
[26] R.S. Tsuburaya, K. Monma, Y. Oya, T. Nakayama, T. Fukuda, H. Sugie, Y.K. Hayashi, I. Nonaka, I. Nishino, Acid phosphatase-positive globular inclusions is a good diagnostic marker for two patients with adult-onset Pompe disease lacking disease specific pathology, Neuromuscul. Disord. 22 (5) (2012) 389–393.
[27] B. Funk, U. Kessler, W. Eisenmenger, A. Hansmann, H.J. Kolb, W. Kiess, Expression of the insulin-like growth factor-II/mannose-6-phosphate receptor in multiple human tissues during fetal life and early infancy, J. Clin. Endocrinol. Metab. 75 (2) (1992) 424–431.
[28] J. Wenk, A. Hille, K. von Figura, Quantitation of Mr 46000 and Mr 300000 mannose 6-phosphate receptors in human cells and tissues, Biochem. Int. 23 (4) (1991) 723–731.
[29] T. Fukuda, M. Ahearn, A. Roberts, R.J. Mattaliano, K. Zaal, E. Ralston, P.H. Plotz, N. Raben, Autophagy and mistargeting of therapeutic enzyme in skeletal muscle in Pompe disease, Mol. Ther. 14 (6) (2006) 831–839.
[30] C. Spampanato, E. Feeney, L. Li, M. Cardone, J.A. Lim, F. Annunziata, H. Zare, R. Polishchuk, R. Puertollano, G. Parenti, A. Ballabio, N. Raben, Transcription factor EB (TFEB) is a new therapeutic target for Pompe disease, EMBO Mol. Med. 5 (5) (2013) 691–706.
[31] J.A. Lim, L. Li, N. Raben, Pompe disease: from pathophysiology to therapy and back again, Front. Aging Neurosci. 6 (2014) 177.
[32] E. Lewandowska, T. Wierzba-Bobrowicz, R. Rola, J. Modzelewska, T. Stepien, A. Lugowska, E. Pasennik, D. Ryglewicz, Pathology of skeletal muscle cells in adult-onset glycogenosis type II (Pompe disease): ultrastructural study, Folia Neuropathol. 46 (2) (2008) 123–133.
[33] N. Raben, C. Schreiner, R. Baum, S. Takikita, S. Xu, T. Xie, R. Myerowitz, M. Komatsu, J.H. Van der Meulen, K. Nagaraju, E. Ralston, P.H. Plotz, Suppression of autophagy permits successful enzyme replacement therapy in a lysosomal storage disorder–murine Pompe disease, Autophagy 6 (8) (2010) 1078–1089.

ANNEXE 5

biomimetics

MDPI

Perspective

Biosafety of Mesoporous Silica Nanoparticles

Estelle Rascol [1,2,*], Cédric Pisani [3], Christophe Dorandeu [2], Jeff L. Nyalosaso [2], Clarence Charnay [2], Morgane Daurat [4], Afitz Da Silva [4], Jean-Marie Devoisselle [2], Jean-Charles Gaillard [5], Jean Armengaud [5], Odette Prat [3], Marie Maynadier [4], Magali Gary-Bobo [6], Marcel Garcia [4], Joël Chopineau [2] and Yannick Guari [2]

1 Institute of Chemistry and Biology of Membranes and Nano-objects (CBMN) UMR-5248, CNRS, University of Bordeaux, INP, Allée Geoffroy St Hilaire, 33600 Pessac, France
2 Institute Charles Gerhardt of Montpellier (ICGM), Place E. Bataillon, 34095 Montpellier, France; christophe.dorandeu@umontpellier.fr (C.D.); jeff.nyalosaso@gmail.com (J.L.N.); clarence.charnay@univ-montp2.fr (C.C.); jm.devoisselle@univ-montp1.fr (J.-M.D.); joel.chopineau@enscm.fr (J.C.); yannick.guari@univ-montp2.fr (Y.G.)
3 The French Alternative Energies and Atomic Energy Commission (CEA), Biosciences and Biotechnologies Institute (BIAM), 30200 Bagnols-sur-Cèze, France; pisani.cedric@gmail.com (C.P.); odette.prat@cea.fr (O.P.)
4 NanoMedSyn, 15 Avenue Charles Flahault, 34090 Montpellier, France; morgane.daurat2@gmail.com (M.D.); afitz@hotmail.fr (A.D.S.); m.maynadier@nanomedsyn.com (M.M.); m.garcia@nanomedsyn.com (M.G.)
5 Laboratoire Innovations technologiques pour la Détection et le Diagnostic (Li2D), Service de Pharmacologie et Immunoanalyse (SPI), CEA, INRA, 30207 Bagnols-sur-Cèze, France; jean-charles.gaillard@cea.fr (J.-C.G.); jean.armengaud@cea.fr (J.A.)
6 Max Mousseron Biomolecule Institute of Montpellier (IBMM), 15 Avenue Charles Flahault, 34090 Montpellier, France; magali.gary-bobo@inserm.fr
* Correspondance: estelle.rascol.c2i12@gmail.com

Received: 29 June 2018; Accepted: 2 August 2018; Published: 15 August 2018

Abstract: Careful analysis of any new nanomedicine device or disposal should be undertaken to comprehensively characterize the new product before application, so that any unintended side effect is minimized. Because of the increasing number of nanotechnology-based drugs, we can anticipate that regulatory authorities might adapt the approval process for nanomedicine products due to safety concerns, e.g., request a more rigorous testing of the potential toxicity of nanoparticles (NPs). Currently, the use of mesoporous silica nanoparticles (MSN) as drug delivery systems is challenged by a lack of data on the toxicological profile of coated or non-coated MSN. In this context, we have carried out an extensive study documenting the influence of different functionalized MSN on the cellular internalization and in vivo behaviour. In this article, a synthesis of these works is reviewed and the perspectives are drawn. The use of magnetic MSN (Fe_3O_4@MSN) allows an efficient separation of coated NPs from cell cultures with a simple magnet, leading to results regarding corona formation without experimental bias. Our interest is focused on the mechanism of interaction with model membranes, the adsorption of proteins in biological fluids, the quantification of uptake, and the effect of such NPs on the transcriptomic profile of hepatic cells that are known to be readily concerned by NPs' uptake in vivo, especially in the case of an intravenous injection.

Keywords: nanoparticles; safety; mesoporous silica; protein corona; internalization; adverse outcome pathways

1. Introduction

The growing interest of the scientific community for mesoporous silica nanoparticles (MSN) is particularly related to the degree of advanced sophistication that can be achieved in their design according to the objectives, in terms of properties or applications sought. Thanks to the silicon

chemistry, these nanoparticles (NPs) have a promising potential to constitute a new generation of smart drug nanocontainers, due to their high stability, large surface area, tunable pore size, and abundant surface functionalization sites [1,2].

For these reasons, MSN are one of the most studied nanotechnologies for use as drug delivery systems. Because there are an increasing number of nanotechnology-based drugs, we can anticipate that regulatory authorities might adapt the approval process for nanomedicine products due to safety concerns, e.g., request a more rigorous testing of the potential toxicity of NPs. Understanding the interactions of NPs with biological systems is clearly multifactorial and complex. Nanoparticles display different shapes and sizes, and can be decorated with a variety of functionality. They have increased surface area-to-volume ratios that dramatically increase their reactivity. The miniaturization of materials to the nanoscale has seen emergent properties due to their ultralarge surface area. Their surface reactivity can, depending on the type of coating, cause different behavior and toxicological profiles. Thus, careful analysis of any new nanomedicine device or disposal should be undertaken to completely characterize the new products before application, so that we can help avoid any unintended side effects.

This perspective aims to present a series of biological assays performed to obtain an integrated overview of the safety of coated or non-coated magnetic MSN (Fe_3O_4@MSN). In vitro studies at the molecular and cellular level allow for rapid knowledge generation, and their results could be used as predictors before a validation phase, in terms of toxicological outcome in vivo. This two-stage approach could limit the extent, volume, and cost of animal testing. In this context, we propose to review the safety profile of MSN [3] and the panel of methodologies associated. Our interest focuses on MSN's interaction with model membranes [4], the adsorption of proteins at their surface in biological fluids [5], the kinetics of internalization, and the effect of such NPs on the transcriptomic profile of hepatic cells [6] that are known to be readily concerned by NPs' uptake in vivo, especially in the case of an intravenous injection.

2. Preparation of Magnetic Mesoporous Silica Nanoparticles

Firstly, homogeneous NPs, reproducible synthesis, and extensive characterization are required to assess the toxicological profile of NPs. Before any biological assays, the NP synthesis has been designed to produce more potent NPs. Different aspects were even described as critical for NP safety, including biodegradability, surface properties (chemical composition, charge, hydrophilicity/hydrophobicity), and size. Mesoporous silica nanoparticles are biodegradable materials allowing drug release [7] while avoiding any accumulation and chronic toxicity, and which release silicic acid [8]. Dissolution of sol–gel-derived silica matrices occurs following two steps: an initial surface burst erosion followed by a slow bulk degradation [9]. The degradation rate and profile is dependent of the material composition [8], the production processes [10], the surface coating [11], and the body fluids [12]. It has been shown that surfactant-extracted MSN are more quickly degraded than calcined ones or amorphous silica NPs [10] in simulated body fluids. Plus, calcination influences the surface properties and reactivity. This step allow the dehydration of the MSN surface, reducing the proportion of silanol groups, leading to siloxane groups [13]. The surface then becomes more hydrophobic, reducing the availability of the silanol groups to functionalization by covalent ligands or electrostatic coupling [14]. Mesoporous silica nanoparticles were synthesized with a magnetic core to follow them by magnetic resonance imaging (MRI) [15], to induce a heat-triggered drug release [16], and to separate them from complex media by magnetization. Synthesis of magnetic MSN was challenging to obtain a homogenous population of spherical Fe_3O_4@MSN, presenting a primary diameter of 100 nm, all containing a unique magnetic core, and without any step of calcination. The optimization of all these aspects was deeply described previously [3] (Figure 1).

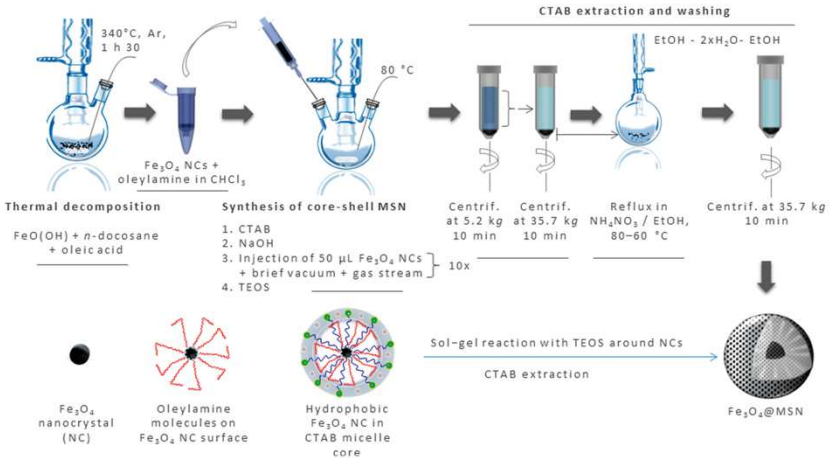

Figure 1. Schematic representation of the synthesis of bare magnetic mesoporous silica nanoparticles (Fe_3O_4@MSN). Firstly, Fe_3O_4 nanocrystals (NC) are obtained by thermal decomposition of FeO(OH). In another flask, cetyl trimethylammonium bromide (CTAB) micelles were obtained in alkaline water, at a temperature of 80 °C. Fe_3O_4 NC, after stabilization in oleylamine, were progressively added to the CTAB micelles, in 10 steps. After that, tetraethylorthosilicate (TEOS) has been added for sol–gel reaction and formation of Fe_3O_4MSN. Different washing steps were performed to extract CTAB surfactant from the pores.

3. Magnetic Separation for Corona Characterization

The use of magnetic nanoparticles allows for the efficient separation of the Fe_3O_4@MSN from biological media with a simple magnet [17]. Magnetic attraction of NPs is a useful method of separation to precisely characterize the protein corona, taking into account weak binding proteins, instead of very fast and drastic separation using centrifugation [17] (Figure 2a). This technique provides a true corona "interactome" of the MSN, with the characterization of the different protein–protein interactions around the NPs using next-generation shotgun proteomics [5] (Figure 2b). The timeline formation of the hard and the soft corona become accessible at low cost and relatively quickly, providing very interesting data for the development of future NPs.

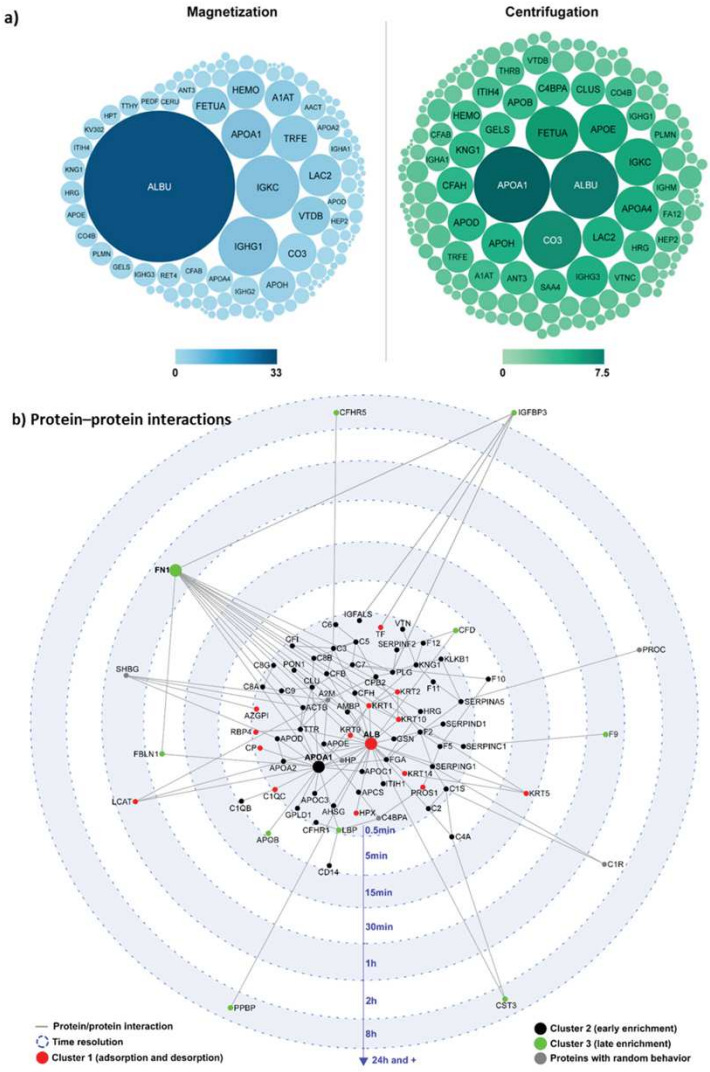

Figure 2. (**a**) Different proteomic profiles of the protein corona after Fe_3O_4@MSN separation by magnetization (blue) or centrifugation (green). Sizes and colors of human protein clues are proportional to their relative percentage within the corona. The 35 highest abundant proteins are labelled. The color scale unit is Normalized Spectral Abundance Factor (%). Reproduced from Pisani et al. 2017 [17] with permission from the Royal Society of Chemistry. (**b**) Protein–protein interactions are represented in a network developed using the NetworkAnalyst software [18,19], based on InnateDB [20]. The target represents the time scale (0.5 min to 7 days). Each protein (represented by its gene symbol) is placed according to its time of appearance within the corona. The colors indicate the cluster membership. The grey lines represent the protein–protein interactions. Proteins that have a lot of interactions with other proteins are represented by a larger visual cue. Reproduced from Pisani et al. 2017 [5] with permission from the Royal Society of Chemistry.

4. Influence of Magnetic Mesoporous Silica Nanoparticles' Coverage on Their Interaction with Proteins and Cell Membranes

To reduce the formation of the protein corona at the NPs' surfaces, NPs are generally covered by different layers. Numerous reported studies demonstrate that a polyethylene glycol (PEG) coating presents several advantages, like colloidal stability, inertia in biological media, and higher circulation time of NPs [11,21]. Another strategy consists of the deposition of a phospholipid bilayer on the inorganic NPs' surface, in order to create a biomimetic surface [22,23]. Fusion of liposomes to a spherical, high surface area, nanoporous silica core improves capacity, selectivity, and stability of NPs, and enables their targeted delivery and controlled release within the targeted cells [22,24,25]. Moreover, these two types of coverage can be easily applied to inorganic NPs [3,26,27] (Figure 3). Different strategies were employed for the functionalization of the NPs [28]. Concerning the lipid coating of MSN, this can be achieved by spontaneous adsorption of small unilamellar vesicles on the silica surface of NPs in suspension [27], or by thin-layer lipid rehydration in presence of the NPs [28,29]. Various parameters were investigated for their influence on effective NP coverage, such as buffer composition (pH, ionic strength) [30], lipid/NP ratio [31], temperature [32], or NP size [26]. Characterization of the lipid coating of the NPs is often done by cryogenic transmission electron microscopy (TEM), dynamic light scattering (DLS), zeta potential (ZP), or dynamic scanning calorimetry (DSC). These methods allow qualitative characterization of the NPs' coating, while quantitative methods can also be used, such as inorganic phosphorus dosage [30] or elemental analysis [29]. Preparation of PEG-grafted MSN is generally performed by direct addition of PEG-silane at the end of the NPs synthesis [33]. The silane groups are then able to condense with the silica surface of the NPs [34]. In this case, PEG is covalently bound to the NPs' surface [35]. Characterization is also frequently done by TEM imaging, DLS, or ZP [36]. Fourier-transformed infrared (FTIR) spectroscopy [35], DSC, or thermogravimetric analysis (TGA) allow deeper characterization [34]. It should be noted that combinations of surface decoration strategies are now described, leading to highly sophisticated nanocarriers that combines stealth properties, targeting, and controlled or triggered release [37]. For example, PEG–lipid assemblies are used for the functionalization of MSN [38].

The coating of Fe_3O_4@MSN by polymers or lipid bilayers was shown to influence the colloidal stability and interaction with proteins, model membranes, and cells in vitro [3]. Lipid bilayers allowed colloidal stability of MSN in a high ionic strength medium, in comparison to native or PEG-coated MSN (Figure 4a1). Native NPs were stabilized (meaning colloidal stability) in the presence of proteins by the formation of the corona, while PEG-coated MSN were very slowly stabilized by the presence of the proteins, due to the MSN's low adsorption of those proteins (Figure 4a2). The formation of a protein corona appeared to reduce the interaction between MSN and model membranes composed of an egg phosphatidylcholine (EPC)-supported lipid bilayer (SLB) as was observed using quartz crystal microbalance with dissipation (QCM-D) [4] (Figure 4b). Lipid-coated MSN were rapidly deposited on the top of the lipid bilayer, while PEG-coated MSN deposited slowly, and the native ones remained suspended in the medium.

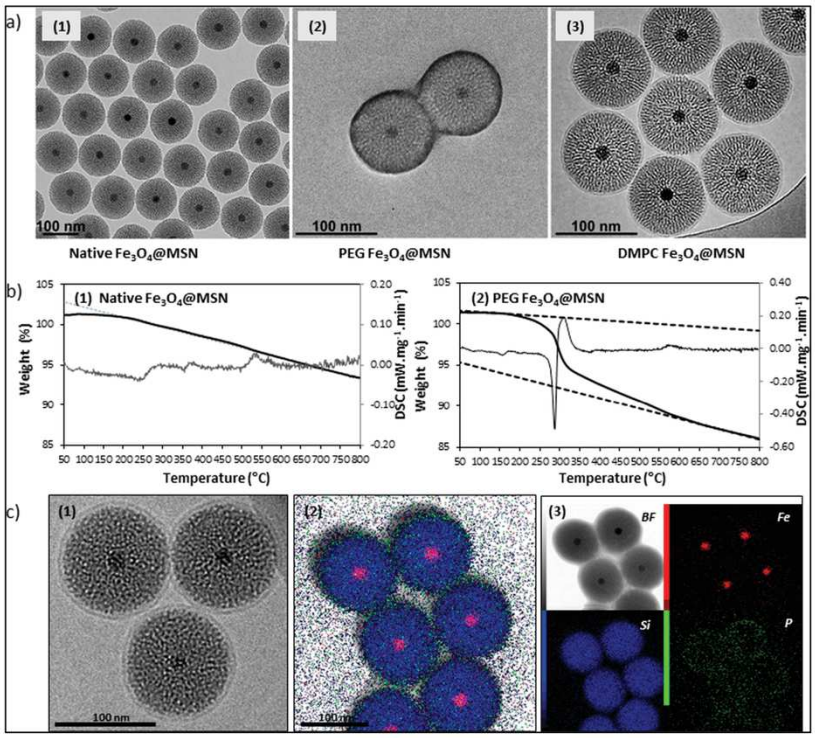

Figure 3. Characterization of native, polyethylene glycol (PEG)-grafted, and lipid-coated Fe_3O_4@MSN. (**a**) Transmission electron microscopy (TEM) imaging of (1) native Fe_3O_4@MSN, (2) PEG-grafted Fe_3O_4@MSN, and (3) lipid-coated Fe_3O_4@MSN with dimyristoyl phosphatidylcholine (DMPC) lipids, showing a primary diameter of 100 nm, with very homogeneous shape, porosity, and coverage. Reproduced from Pisani et al. 2017 [6], published under the Creative Commons attribution license CC BY-NC-ND 4.0 by Taylor & Francis publishers. (**b**) Characterization of Fe_3O_4@MSN PEG-grafting, with thermogravimetric analysis (TGA)/dynamic scanning calorimetry (DSC) spectra of (1) pristine Fe_3O_4@MSN and (2) PEG–Fe_3O_4@MSN. (**c**) Imaging of magnetic Fe_3O_4@MSN core–shell particles after incubation with DMPC small unilamellar vesicles (SUVs) (1). All the MSN are covered with a complete lipid bilayer, having a thickness of 5 nm. Three lipid-coated MSN are zoomed in on for a better observation of the lipid bilayer. (2) Scanning transmission electron microscopy (STEM) images of DMPC Fe_3O_4@MSN: DMPC Fe_3O_4@MSN overlay of TEM black field (BF), iron (Fe), silica (Si), and phosphorus (P) element cartography. (3) Each element is separately presented. The iron core localizes at the center of the silica nanoparticles and phosphorus is localized around the silica shell of the Fe_3O_4@MSN particles. (**b**) and (**c**) are reproduced and adapted from Nyalosaso et al. 2016 [3] with permission from the Royal Society of Chemistry.

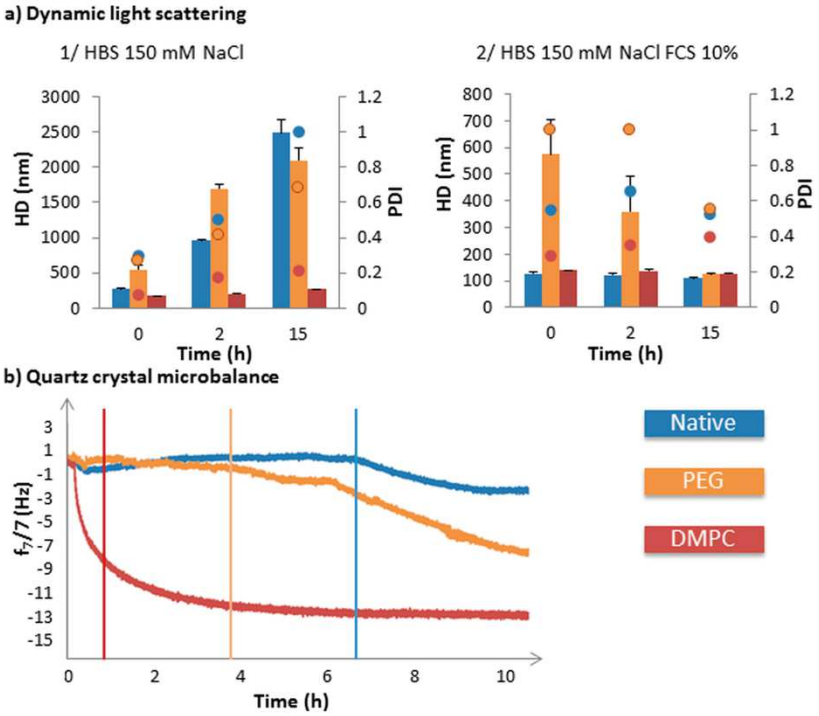

Figure 4. Characterization of native and coated Fe_3O_4@MSN behavior in suspension in complex media, with or without proteins. (**a**) (1) and (2): Hydrodynamic diameter (HD) and polydispersity index (PDI), represented respectively by bars and dots, for native (blue), polyethylene glycol (PEG) (orange) and dimyristoyl phosphatidylcholine (DMPC) (red) Fe_3O_4@MSN in (x) HEPES buffered saline (HBS) 150 mM NaCl (pH 7.4) and (y) HBS 150 mM NaCl (pH 7.4) containing 10% fetal calf serum (FCS). (**b**) Quartz crystal microbalance with dissipation (QCM-D) frequency sensorgram following the interaction between nanoparticles and the egg phosphatidyl choline (EPC)-supported lipid bilayer (SLB). Native (blue), PEG (orange), and DMPC (red) Fe_3O_4@MSN were flowed into HBS 150 mM NaCl 10% SCF medium on the top of EPC SLB, at a concentration of 0.25 mg mL^{-1} of nanoparticles. After adding Fe_3O_4@MSN into the medium on the top of the EPC SLB for 15 min, the flow was stopped for 10 h. The results on the variations of frequency are presented after the offset of the lipid bilayer formation. Reproduced and adapted from Rascol et al. 2017 [4], published under the Creative Commons Attribution (CC BY) license (http://creativecommons.org/licenses/by/4.0/).

5. Magnetic Mesoporous Silica Nanoparticles' In Vivo Toxicity and In Vitro Mechanisms

Functionalized Fe_3O_4@MSN with lipid bilayers or PEG polymers were administered to mice by intravenous injections, at a dose of 40 mg kg^{-1}, in order to compare their distribution and toxicity to bare Fe_3O_4@MSN [4]. Magnetic mesoporous silica nanoparticles were quantified by inductively coupled plasma–mass spectrometry (ICP–MS) analysis in the different organs obtained from sacrificed mice four days after injection (Figure 5a). All of the Fe_3O_4@MSN, functionalized or not, accumulated in the liver and spleen. However, lipid bilayer-coated Fe_3O_4@MSN accumulation was largely higher in the liver; these nanoparticles were found in a lower concentration in the lungs, and were cleared more quickly from the blood than the bare and PEG-grafted Fe_3O_4@MSN. PEG-grafted Fe_3O_4@MSN were always found in the blood 24 h after injection (Figure 5b). However, it was demonstrated that none

of the Fe_3O_4@MSN caused toxicity to liver, kidney, and spleen tissues at the administered doses [4]. Moreover, no immunotoxic effect was observed at the animal level.

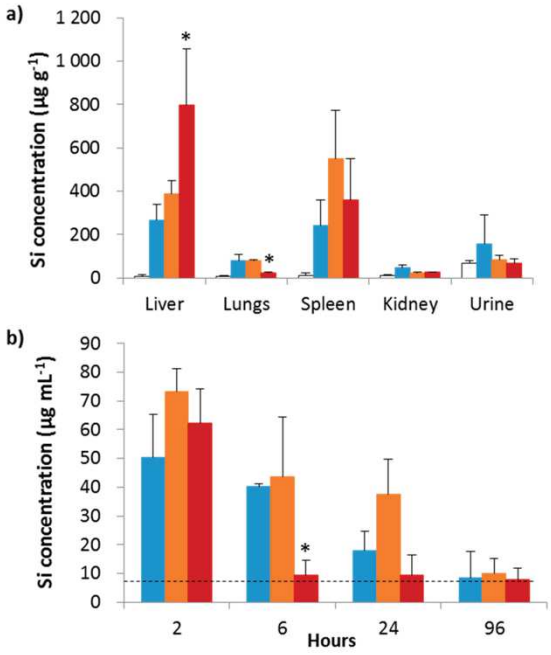

Figure 5. Biodistribution of Fe_3O_4@MSN in mice. (**a**) Quantification of silicon in different organs four days after injection. Inductively coupled plasma–mass spectrometry (ICP–MS) was used after acid digestion to quantify the silicon in the liver, lungs, spleen, kidneys, and urine four days after intravenous injection of native (blue), polyethylene glycol (PEG) (orange) and dimyristoyl phosphatidylcholine (DMPC) (red) Fe_3O_4@MSN at a concentration of 40 mg kg^{-1} in comparison to control mice (white). (**b**) Nanoparticle level in blood. The silicon levels in blood were measured 2, 6, 24 h, and 4 days after intravenous injection of native (blue), PEG (orange), and DMPC (red) Fe_3O_4@MSN at a concentration of 40 mg kg^{-1}. The dashed line indicates the silicon level found in blood of control mice. For this experiment, 20 mice were divided into four groups of five animals. The values of the histograms represent the mean ± standard deviation (SD) of values of each animal of a group. * $p < 0.05$ indicates that a group is statistically different from all other groups treated with nanoparticles. Reproduced and adapted from Rascol et al. 2017 [4], published under the Creative Commons Attribution (CC BY) license (http://creativecommons.org/licenses/by/4.0/).

Different techniques were combined to investigate the potential toxic effects of these Fe_3O_4@MSN, covered or not covered by PEG or lipid bilayers at the cellular level. First, in vitro analyses were performed by exposure of two liver cell lines to the different particles, the rational for choosing the cell lines being dictated by the preferential liver uptake of MSN. On one hand, HepG2 is a very frequently human hepatocarcinoma cell line studied for in vitro evaluation of anticancer therapy. On the other hand, HepaRG is a human hepatocarcinoma cell line which can be differentiated in vitro in hepatocyte-like colonies surrounded by clear primitive biliary cells [39,40]. The cell uptake of the Fe_3O_4@MSN was faster for those that were coated with DMPC than for the native ones, and slower for the PEG-grafted Fe_3O_4@MSN. This was observed by TEM cell imaging after exposure of HepG2 (Figure 6) and HepaRG cell lines to Fe_3O_4@MSN [6]. This observation was in accordance with the rapid

deposition of lipid-coated MSN on membrane models [4]. Moreover, the effect of Fe_3O_4@MSN on HepG2 and HepaRG cell lines was also investigated by cell impedance [3,6]. Impedance measurement of HepG2 cells showed a greater decrease in cell impedance by exposure to native Fe_3O_4@MSN than by exposure to the lipid-coated ones, and lastly, by exposure to the PEG-grafted Fe_3O_4@MSN [3,6] (Figure 7). Thus, impedance measurement represents an important metric to document.

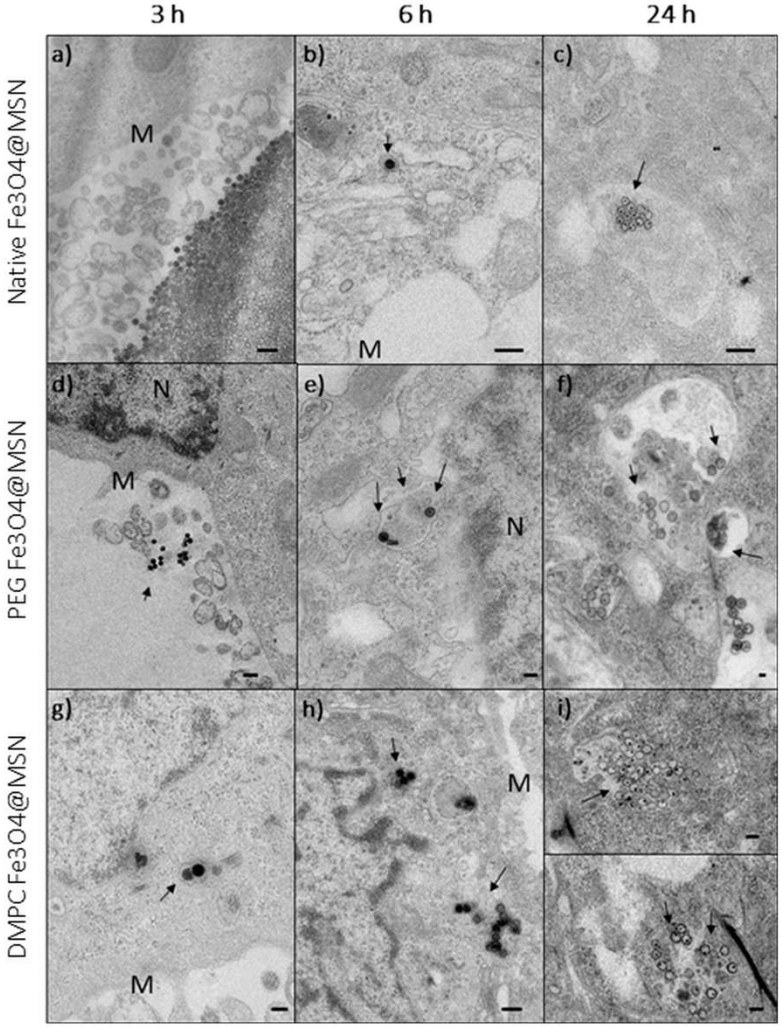

Figure 6. Transmission electron microscopy imaging of HepG2 cells exposed for 3, 6, and 24 h at 50 µg mL^{-1} for (**a**–**c**) native, (**d**–**f**) polyethylene glycol (PEG)-coated, or (**g**–**i**) dimyristoyl phosphatidylcholine (DMPC)-coated Fe_3O_4@MSN. The nanoparticles are indicated by arrows, near the cell membrane (M) or the nucleus (N). Reproduced from Rascol et al. 2017 [4], published under the Creative Commons Attribution (CC BY) license (http://creativecommons.org/licenses/by/4.0/).

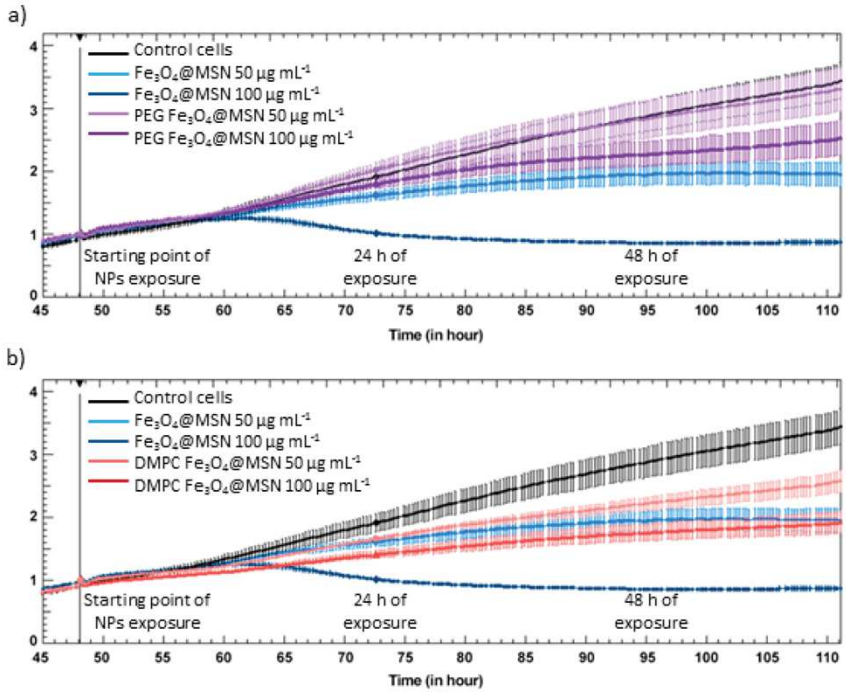

Figure 7. xCELLigence experiment. Real-time cell index (CI) monitoring of HepG2 cells (n = 3) exposed to 50 and 100 mg mL^{-1} of pristine, polyethylene glycol (PEG)-coated, and dimyristoyl phosphatidylcholine (DMPC)-coated Fe_3O_4@MSN. (**a**) Pristine Fe_3O_4@MSN versus PEG-coated Fe_3O_4@MSN. (**b**) Pristine Fe_3O_4@MSN versus DMPC-coated Fe_3O_4@MSN. Reproduced and adapted from Nyalosaso et al. 2016 [3] with permission from the Royal Society of Chemistry.

To get more insights into the molecular mechanisms explaining the biological effects of these Fe_3O_4@MSN in vitro, high-throughput transcriptomic assays were carried out [6]. Changes in the expression of thousands of genes were monitored for the HepaRG cell line after an exposure to different doses of the native, PEG-grafted, and lipid-coated Fe_3O_4@MSN. A transient change in the expressed gene profile has been observed for the lower doses between 24 and 48 h (Figure 8a,b, respectively), indicating that 16 µg cm^{-2} (or 60 µg mL^{-1}) could be the limit of biocompatibility for all of these Fe_3O_4@MSN. Slight differences could be observed depending on Fe_3O_4@MSN surface modifications. However, whatever the type of Fe_3O_4@MSN, 80 µg cm^{-2} (or 300 µg mL^{-1}) represents a concentration with strong and lasting adverse effects. At this concentration, initial molecular events and major pathways of toxicity elicited by these Fe_3O_4@MSN were easily identified by the methodology used. The hepatic cholestasis adverse pathway was triggered by a strong inhibition of the bile salt export pump transporter protein BSEP (gene ABCB11), responsible for intrahepatic accumulation of cytotoxic bile acids [6] (Figure 9).

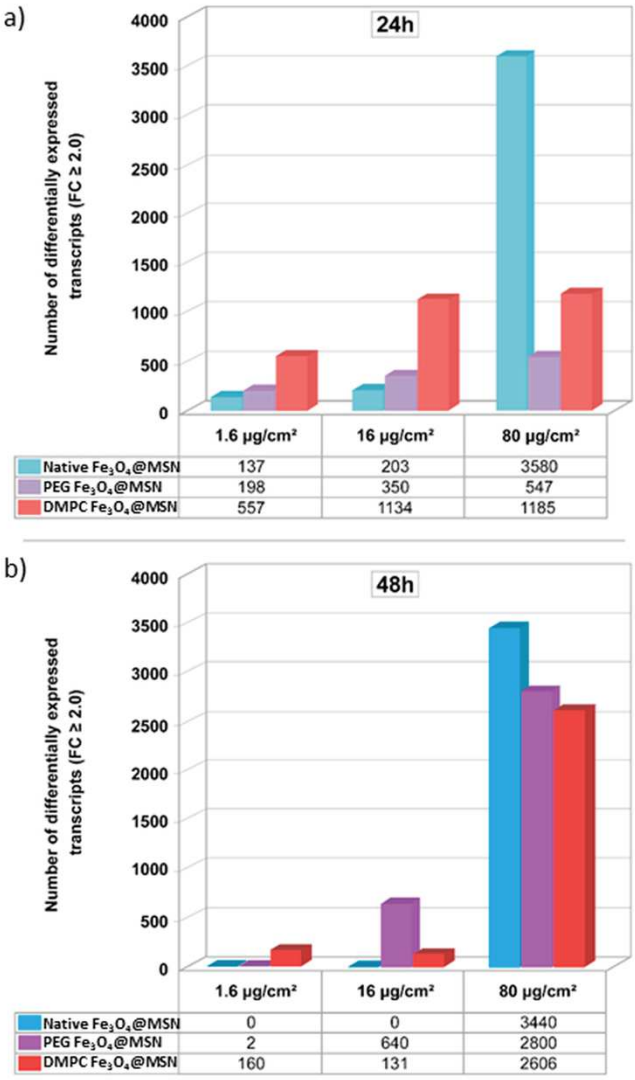

Figure 8. Time- and dose-dependent effects of exposure to Fe_3O_4@MSN on the number of significantly differentially expressed genes. HepaRG cells were exposed to 1.6, 16, and 80 µg cm^{-2} pristine, polyethylene glycol (PEG)-, and dimyristoyl phosphatidylcholine (DMPC)-coated Fe_3O_4@MSN for 24 (**a**) or 48 (**b**) h. After extraction and labeling, RNA was hybridized to a human oligonucleotide microarray (6 × 60 k Agilent V3 SurePrint). Bars represent the number of differentially expressed transcripts after statistical analysis, using Genespring GX13 software (Agilent), and with a p-value < 0.05 and a fold-change (FC) ≥ 2. Reproduced from Pisani et al. 2017 [6], published under the the Creative Commons Attribution (CC BY-NC-ND 4.0) license (https://creativecommons.org/licenses/by-nc-nd/4.0/).

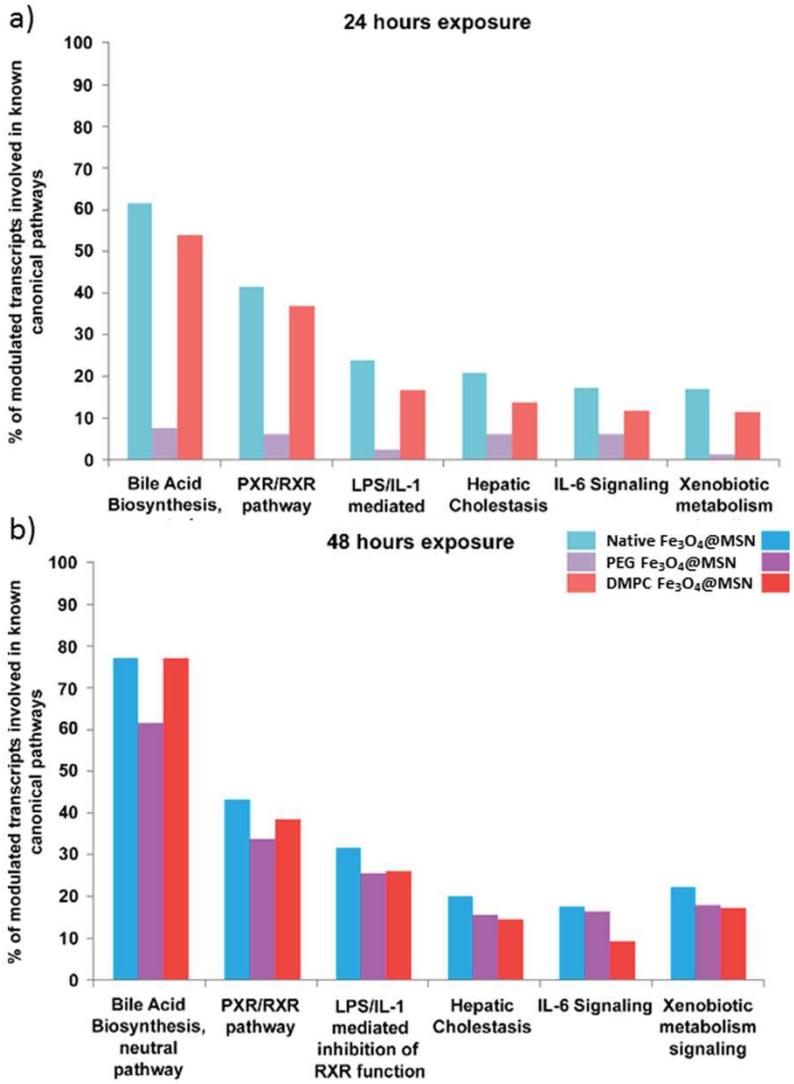

Figure 9. Canonical pathways elicited by each Fe_3O_4@MSN (80 mg cm^{-2}). The percentage of modulated transcripts of our datasets belonging to six major altered canonical pathways after (**a**) 24 and (**b**) 48 h exposure to Fe_3O_4@MSN. These pathways were all significant according to a Fisher's statistical test (p-value < 0.05), revealed with Ingenuity® Pathway Analysis (IPA®, QIAGEN). Reproduced from Pisani et al. 2017 [6], published under the Creative Commons Attribution (CC BY-NC-ND 4.0) license (https://creativecommons.org/licenses/by-nc-nd/4.0/).

6. Conclusions

This review highlighted the results of biological evaluation obtained on bare, PEG-grafted, and lipid-coated Fe_3O_4@MSN, presenting the same physical and chemical characterizations for all safety investigation performed. Some results presented here were previously discussed in other studies, such as NP aggregation at high ionic force, adsorption of proteins to the surface, or NP accumulation in the liver and spleen. However, this is the first time that all these aspects have been investigated, using different techniques to compare NPs with different surface properties, and the results have been reported as a whole here. This pioneering work allows for linking the different reported data and methodologies to a more in-depth analysis of the biological effects of Fe_3O_4@MSN at the animal, cellular, and molecular levels. This compendium is an example of integrated investigation of the safety of innovative technologies for biomedical applications. This multi-technology approach paves the way for the future trend of safety recommendations, including methodologies that are at the forefront of their disciplines while being rather cost- and time-effective.

Funding: This work was supported by the French National Research Agency (ANR-13-NANO-0007, BioSiPharm project).

Conflicts of Interest: The authors declare no conflict of interest. The founding sponsors had no role in the design of the study; in the collection, analyses, or interpretation of data; in the writing of the manuscript, and in the decision to publish the results.

References

1. Chang, B.; Guo, J.; Liu, C.; Qian, J.; Yang, W. Surface functionalization of magnetic mesoporous silica nanoparticles for controlled drug release. *J. Mater. Chem.* **2010**, *20*, 9941. [CrossRef]
2. Perrier, M.; Gary-Bobo, M.; Lartigue, L.; Brevet, D.; Morère, A.; Garcia, M.; Maillard, P.; Raehm, L.; Guari, Y.; Larionova, J.; et al. Mannose-functionalized porous silica-coated magnetic nanoparticles for two-photon imaging or PDT of cancer cells. *J. Nanoparticle Res.* **2013**, *15*, 1602. [CrossRef]
3. Nyalosaso, J.L.; Rascol, E.; Pisani, C.; Dorandeu, C.; Dumail, X.; Maynadier, M.; Gary-Bobo, M.; Kee Him, J.L.; Bron, P.; Garcia, M.; et al. Synthesis, decoration, and cellular effects of magnetic mesoporous silica nanoparticles. *RSC Adv.* **2016**, *6*, 57275–57283. [CrossRef]
4. Rascol, E.; Daurat, M.; Da Silva, A.; Maynadier, M.; Dorandeu, C.; Charnay, C.; Garcia, M.; Lai-Kee-Him, J.; Bron, P.; Auffan, M.; et al. Biological fate of Fe_3O_4 core-shell mesoporous silica nanoparticles depending on particle surface chemistry. *Nanomaterials* **2017**, *7*, 162. [CrossRef] [PubMed]
5. Pisani, C.; Gaillard, J.-C.; Odorico, M.; Nyalosaso, J.L.; Charnay, C.; Guari, Y.; Chopineau, J.; Devoisselle, J.-M.; Armengaud, J.; Prat, O. The timeline of corona formation around silica nanocarriers highlights the role of the protein interactome. *Nanoscale* **2017**, *9*, 1840–1851. [CrossRef] [PubMed]
6. Pisani, C.; Rascol, E.; Dorandeu, C.; Charnay, C.; Guari, Y.; Chopineau, J.; Devoisselle, J.-M.; Prat, O. Biocompatibility assessment of functionalized magnetic mesoporous silica nanoparticles in human HepaRG cells. *Nanotoxicology* **2017**, *11*, 871–890. [CrossRef] [PubMed]
7. Roggers, R.; Kanvinde, S.; Boonsith, S.; Oupický, D. The practicality of mesoporous silica nanoparticles as drug delivery devices and progress toward this goal. *AAPS PharmSciTech* **2014**, *15*, 1163–1171. [CrossRef] [PubMed]
8. Fontecave, T.; Sanchez, C.; Azaïs, T.; Boissiére, C. Chemical modification as a versatile tool for tuning stability of silica based mesoporous carriers in biologically relevant conditions. *Chem. Mater.* **2012**, *24*, 4326–4336. [CrossRef]
9. Bass, J.D.; Grosso, D.; Boissiere, C.; Belamie, E.; Coradin, T.; Sanchez, C. Stability of mesoporous oxide and mixed metal oxide materials under biologically relevant conditions. *Chem. Mater.* **2007**, *19*, 4349–4356. [CrossRef]
10. He, Q.; Shi, J.; Zhu, M.; Chen, Y.; Chen, F. The three-stage in vitro degradation behavior of mesoporous silica in simulated body fluid. *Microporous Mesoporous Mater.* **2010**, *131*, 314–320. [CrossRef]
11. Cauda, V.; Argyo, C.; Bein, T. Impact of different PEGylation patterns on the long-term bio-stability of colloidal mesoporous silica nanoparticles. *J. Mater. Chem.* **2010**, *20*, 8693–8699. [CrossRef]

12. Braun, K.; Pochert, A.; Beck, M.; Fiedler, R.; Gruber, J.; Lindén, M. Dissolution kinetics of mesoporous silica nanoparticles in different simulated body fluids. *J. Sol-Gel Sci. Technol.* **2016**, *79*, 319–327. [CrossRef]
13. Rimola, A.; Costa, D.; Sodupe, M.; Lambert, J.F.; Ugliengo, P. Silica surface features and their role in the adsorption of biomolecules: Computational modeling and experiments. *Chem. Rev.* **2013**, *113*, 4216–4313. [CrossRef] [PubMed]
14. Tarn, D.; Ashley, C.E.; Xue, M.; Carnes, E.C.; Zink, J.I.; Brinker, C.J. Masoporous Silica Nanocarriers: Biofunctionality and Biocompatibility. *Acc. Chem. Res.* **2013**, *46*, 792–801. [CrossRef] [PubMed]
15. Liu, J.; Qiao, S.Z.; Hu, Q.H.; Max Lu, G.Q. Magnetic Nanocomposites with Mesoporous Structures: Synthesis and Applications. *Small* **2011**, *7*, 425–443. [CrossRef] [PubMed]
16. Liu, J.; Detrembleur, C.; De Pauw-Gillet, M.C.; Mornet, S.; Elst, L.V.; Laurent, S.; Jérôme, C.; Duguet, E. Heat-triggered drug release systems based on mesoporous silica nanoparticles filled with a maghemite core and phase-change molecules as gatekeepers. *J. Mater. Chem. B* **2014**, *2*, 59–70. [CrossRef]
17. Pisani, C.; Gaillard, J.C.; Dorandeu, C.; Charnay, C.; Guari, Y.; Chopineau, J.; Devoisselle, J.M.; Armengaud, J.; Prat, O. Experimental separation steps influence the protein content of corona around mesoporous silica nanoparticles. *Nanoscale* **2017**, *9*, 5769–5772. [CrossRef] [PubMed]
18. Xia, J.; Gill, E.E.; Hancock, R.E.W. NetworkAnalyst for statistical, visual and network-based meta-analysis of gene expression data. *Nat. Protoc.* **2015**, *10*, 823–844. [CrossRef] [PubMed]
19. Xia, J.; Benner, M.J.; Hancock, R.E.W. NetworkAnalyst—integrative approaches for protein–protein interaction network analysis and visual exploration. *Nucleic Acids Res.* **2014**, *42*, W167–W174. [CrossRef] [PubMed]
20. Innate DB. Available online: www.innatedb.com (accessed on 1 May 2016).
21. He, Q.; Zhang, Z.; Gao, F.; Li, Y.; Shi, J. In vivo Biodistribution and Urinary Excretion of Mesoporous Silica Nanoparticles: Effects of Particle Size and PEGylation. *Small* **2011**, *7*, 271–280. [CrossRef] [PubMed]
22. Ashley, C.E.; Carnes, E.C.; Phillips, G.K.; Padilla, D.; Durfee, P.N.; Brown, P.A.; Hanna, T.N.; Liu, J.; Phillips, B.; Carter, M.B.; et al. The targeted delivery of multicomponent cargos to cancer cells by nanoporous particle-supported lipid bilayers. *Nat. Mater.* **2011**, *10*, 389–397. [CrossRef] [PubMed]
23. Butler, K.S.; Durfee, P.N.; Theron, C.; Ashley, C.E.; Carnes, E.C.; Brinker, J. Protocells: Modular Mesoporous Silica Nanoparticle- Supported Lipid Bilayers for Drug Delivery. *Small* **2016**, *12*, 1–13. [CrossRef] [PubMed]
24. Durfee, P.N.; Lin, Y.S.; Dunphy, D.R.; Muñiz, A.J.; Butler, K.S.; Humphrey, K.R.; Lokke, A.J.; Agola, J.O.; Chou, S.S.; Chen, I.M.; et al. Mesoporous Silica Nanoparticle-Supported Lipid Bilayers (Protocells) for Active Targeting and Delivery to Individual Leukemia Cells. *ACS Nano* **2016**, *10*, 8325–8345. [CrossRef] [PubMed]
25. Tada, D.B.; Suraniti, E.; Rossi, L.M.; Leite, C.A.P.; Oliveira, C.S.; Tumolo, T.C.; Calemczuk, R.; Livache, T.; Baptista, M.S. Effect of lipid coating on the interaction between silica nanoparticles and membranes. *J. Biomed. Nanotechnol.* **2014**, *10*, 519–528. [CrossRef] [PubMed]
26. Savarala, S.; Ahmed, S.; Ilies, M.A.; Wunder, S.L. Formation and colloidal stability of dmpc supported lipid bilayers on SiO 2 nanobeads. *Langmuir* **2010**, *26*, 12081–12088. [CrossRef] [PubMed]
27. Mornet, S.; Lambert, O.; Duguet, E.; Brisson, A. The formation of supported lipid bilayers on silica nanoparticles revealed by cryoelectron microscopy. *Nano Lett.* **2005**, *5*, 281–285. [CrossRef] [PubMed]
28. Weingart, J.; Vabbilisetty, P.; Sun, X.L. Membrane mimetic surface functionalization of nanoparticles: Methods and applications. *Adv. Colloid Interface Sci.* **2013**, *197–198*, 68–84. [CrossRef] [PubMed]
29. Ribeiro, R.T.; Braga, V.H.A.; Carmona-Ribeiro, A.M. Biomimetic Cationic Nanoparticles Based on Silica: Optimizing Bilayer Deposition from Lipid Films. *Biomimetics* **2017**, *2*, 20. [CrossRef]
30. Moura, S.P.; Carmona-Ribeiro, A.M. Biomimetic particles: Optimization of phospholipid bilayer coverage on silica and colloid stabilization. *Langmuir* **2005**, *21*, 10160–10164. [CrossRef] [PubMed]
31. Ahmed, S.; Savarala, S.; Chen, Y.; Bothun, G.; Wunder, S.L. Formation of lipid sheaths around nanoparticle-supported lipid bilayers. *Small* **2012**, *8*, 1740–1751. [CrossRef] [PubMed]
32. Wang, H.; Drazenovic, J.; Luo, Z.; Zhang, J.; Zhou, H.; Wunder, S.L. Mechanism of supported bilayer formation of zwitterionic lipids on SiO2nanoparticles and structure of the stable colloids. *RSC Adv.* **2012**, *2*, 11336–11348. [CrossRef]
33. Lin, Y.S.; Haynes, C.L. Synthesis and characterization of biocompatible and size-tunable multifunctional porous silica nanoparticles. *Chem. Mater.* **2009**, *21*, 3979–3986. [CrossRef]
34. Zhang, Q.; Ye, Z.; Wang, S.T.; Yin, J. Facile one-pot synthesis of PEGylated monodisperse mesoporous silica nanoparticles with controllable particle sizes. *Chinese Chem. Lett.* **2014**, *25*, 257–260. [CrossRef]

35. Maurice, V.; Georgelin, T.; Siaugue, J.M.; Cabuil, V. Synthesis and characterization of functionalized core-shell γFe_2O_3-SiO_2 nanoparticles. *J. Magn. Magn. Mater.* **2009**, *321*, 1408–1413. [CrossRef]
36. Graf, C.; Gao, Q.; Schütz, I.; Noufele, C.N.; Ruan, W.; Posselt, U.; Korotianskiy, E.; Nordmeyer, D.; Rancan, F.; Hadam, S.; et al. Surface functionalization of silica nanoparticles supports colloidal stability in physiological media and facilitates internalization in cells. *Langmuir* **2012**, *28*, 7598–7613. [CrossRef] [PubMed]
37. Van Schooneveld, M.M.; Vucic, E.; Koole, R.; Zhou, Y.; Stocks, J.; Cormode, D.P.; Tang, C.Y.; Gordon, R.E.; Nicolay, K.; Meijerink, A.; et al. Improved biocompatibility and pharmacokinetics of silica nanoparticles by means of a lipid coating: A multimodality investigation. *Nano Lett.* **2008**, *8*, 2517–2525. [CrossRef] [PubMed]
38. Ross, E.E.; Mok, S.W.; Bugni, S.R. Assembly of lipid bilayers on silica and modified silica colloids by reconstitution of dried lipid films. *Langmuir* **2011**, *27*, 8634–8644. [CrossRef] [PubMed]
39. Anthérieu, S.; Chesné, C.; Li, R.; Guguen-Guillouzo, C.; Guillouzo, A. Optimization of the HepaRG cell model for drug metabolism and toxicity studies. *Toxicol. Vitr.* **2012**, *26*, 1278–1285. [CrossRef] [PubMed]
40. Guillouzo, A. Liver cell models in in vitro toxicology. *Environ. Health Perspect.* **1998**, *106* (Suppl. 2), 511–532. [CrossRef]

ANNEXE 6

ChemComm

COMMUNICATION

View Article Online
View Journal | View Issue

Cite this: *Chem. Commun.*, 2018, 54, 13829

Received 15th September 2018,
Accepted 14th November 2018

DOI: 10.1039/c8cc07489e

rsc.li/chemcomm

Diazachlorin and diazabacteriochlorin for one- and two-photon photodynamic therapy†

Jean-François Longevial, ‡[ab] Ayaka Yamaji,‡[a] Dina Aggad, ‡[c] Gakhyun Kim,‡[d] Wen Xi Chia,[a] Tsubasa Nishimura,[a] Yoshihiro Miyake, [a] Sébastien Clément, [b] Juwon Oh,[d] Morgane Daurat, [c] Christophe Nguyen, [c] Dongho Kim, *[d] Magali Gary-Bobo, *[c] Sébastien Richeter *[b] and Hiroshi Shinokubo *[a]

Diazachlorin and diazabacteriochlorin have been prepared through reduction of diazaporphyrin and their *in vitro* and *in vivo* activity in photodynamic therapy has been investigated.

Photodynamic therapy (PDT) is a minimally invasive cancer treatment, which employs photosensitizers (PS) and light to generate singlet oxygen ($^1O_2$) and reactive oxygen species (ROS).[1] A number of porphyrin-based PS have been reported, some of which have been approved for clinical use.[1a,b] However, current PDT treatments are restricted to superficial cancers. This restriction mainly arises from the disability of the visible light to deeply penetrate into living tissues.[1i] To overcome this problem, new PDT approaches employ near infrared (NIR) light, ranging from 650 to 1000 nm. This NIR region corresponds to the window in which the endogenous chromophores have minimal absorbance.[1j] Consequently, the creation of NIR-PS has been extensively investigated.[2] These NIR-PS developments were followed by the emergence of the two-photon excited PDT (TPE-PDT). TPE-PDT relies on the simultaneous absorption of two NIR photons (750–1000 nm) by the PS at the focal point.[3] This feature allows high three-dimensional selectivity to enable targeted tumour treatments.

To access porphyrin-based NIR-PS, the introduction of saturated pyrrole units into the porphyrinic backbone is effective (Fig. 1).[4,5] However, the resulting chlorins or bacteriochlorins are generally unstable because they are readily oxidized back to the corresponding porphyrins when subjected to irradiation under aerobic conditions. To circumvent this issue, quaternary carbon centres have been introduced in the pyrroline ring.[6] This strategy has successfully created effective PS for PDT such as Visudyne®, Photrex® or *gem*-dialkylbacteriochlorins.[6c] However, the preparation of such elaborated molecules requires lengthy multistep synthesis.

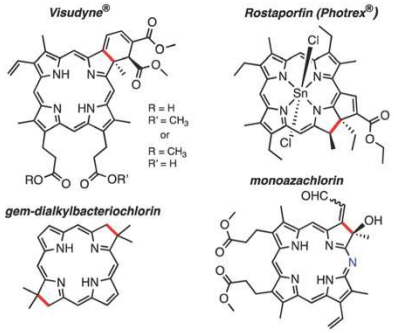

Fig. 1 Porphyrin-based photosensitizers for PDT. Saturated pyrrole C–C bonds are shown in red. Mes = 2,4,6-trimethylphenyl.

As previously shown by Dabrowski *et al.*, the presence of electron withdrawing groups at the porphyrin *meso* positions stabilizes bacteriochlorin type PS toward oxidation.[7] Consequently, we anticipated that the electron-deficient nature of the imine C=N double bonds of 5,15-diazaporphyrin **DAP**[8] would stabilize the corresponding chlorin **DAC** and bacteriochlorin **DAB** (Fig. 2). We disclose herein the study of **DAP**, **DAC** and **DAB** for either *in vitro* or *in vivo* PDT. Montforts *et al.* have synthesized monoazachlorins (Fig. 1) through a multistep reaction sequence, which exhibited absorption at longer wavelength and high $^1O_2$ generation efficiency (Φ_Δ = 0.65).[9] In contrast, both **DAC** and **DAB** were readily obtained.

DAC and **DAB** were synthesised through the reaction of **DAP** with *p*-tosylhydrazide in the presence of bases in pyridine at

[a] *Department of Molecular and Macromolecular Chemistry, Graduate School of Engineering, Nagoya University, Nagoya 464-8603, Japan. E-mail: hshino@chembio.nagoya-u.ac.jp*
[b] *Institut Charles Gerhardt de Montpellier, UMR 5253 CNRS-ENSCM-UM, 34095 Montpellier Cedex 05, France. E-mail: sebastien.richeter@umontpellier.fr*
[c] *Institut des Biomolécules Max Mousseron, UMR 5247 CNRS-UM, 34093 Montpellier Cedex 05, France. E-mail: magali.gary-bobo@inserm.fr*
[d] *Spectroscopy Laboratory for Functional π-Electronic Systems and Department of Chemistry, Yonsei University, Seoul 03722, Korea. E-mail: dongho@yonsei.ac.kr*

† Electronic supplementary information (ESI) available. CCDC 1865986. For ESI and crystallographic data in CIF or other electronic format see DOI: 10.1039/c8cc07489e

‡ These authors contributed equally to this work.

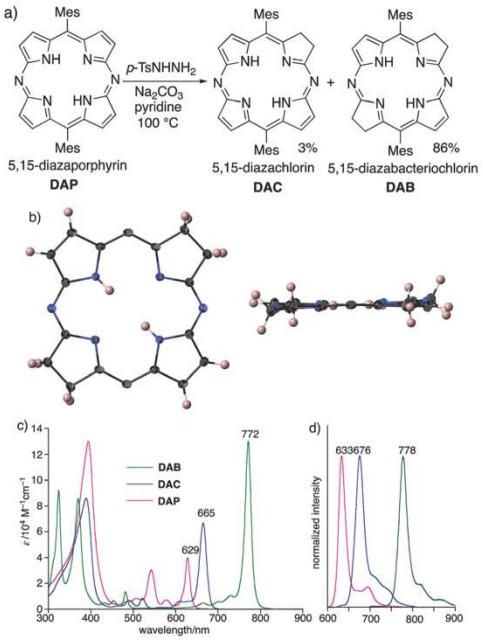

Fig. 2 (a) Preparation of **DAC** and **DAB** from **DAP**. (b) X-ray crystal structure of **DAB**. Atomic displacement parameters are set at 50% probability and mesityl groups are omitted. (c) UV/Vis/NIR absorption and (d) emission spectra of **DAP**, **DAC** and **DAB** in CH_2Cl_2 (excitation wavelength = 400, 420 and 480 nm, respectively).

100 °C (Fig. 2a).[10] The use of KOH as the base predominantly afforded **DAC** in 36% yield. On the other hand, **DAB** was obtained in 86% yield with Na_2CO_3 as the base. Importantly, **DAC** and **DAB** were stable in air and under ambient light (Fig. S5, ESI†). The structure of **DAB** was clearly confirmed by the X-ray diffraction analysis (Fig. 2b and ESI†). It is noteworthy that diagonal two saturated C–C bonds (1.508(2) Å) are substantially longer than other pyrrole C=C double bonds (1.368(2) Å).

As shown in Fig. 2c, **DAP** exhibits a relatively large Q band as compared to that of regular porphyrins. With the change in symmetry by a sequential saturation of the macrocycle, the Q bands of **DAC** and **DAB** were significantly red-shifted and intensified compared to **DAP**.[11] The largest molar extinction coefficient of the Q band of **DAB** is 1.3×10^5 M^{-1} cm^{-1} at 772 nm. The introduction of the saturated pyrrole unit also intensified and red-shifted emission bands (Fig. 2c). The fluorescence quantum yields (Φ_f) of **DAP**, **DAC** and **DAB** are 0.031, 0.043 and 0.08 in CH_2Cl_2, respectively.

Considering PDT applications, we evaluated the ability of **DAP**, **DAC** and **DAB** to generate singlet oxygen ($^1O_2$) by monitoring its photoluminescence (PL) at 1270 nm in aerated toluene using H_2TPP as a reference (Φ_Δ = 0.70) (Fig. S6, ESI†).[12] The $^1O_2$ yields of **DAP** (Φ_Δ = 0.74) and **DAC** (Φ_Δ = 0.68) are comparable to that of H_2TPP,[13] whereas **DAB** showed a relatively low $^1O_2$ yield (Φ_Δ = 0.04). Since the generation of $^1O_2$ requires the triplet–triplet energy transfer process, we performed sub-nanosecond and nanosecond transient absorption (TA) measurements to observe the triplet state of diazaporphyrin derivatives in deaerated toluene. Based on the femtosecond TA spectra, we monitored the kinetic profiles of **DAP**, **DAC** and **DAB** upon excitation at the Q bands (Fig. S7 and S8, ESI†). Two exponential components, composed of a fast nanosecond decay and a constant residual, were observed. The fast decay components were attributed to the singlet excited state lifetimes (Fig. S10, ESI†). The triplet state lifetimes of **DAP**, **DAC** and **DAB**, which correspond to the constant residual, were determined to be 14, 54 and 210 μs, respectively (Fig. S9, ESI†). Considering the fraction of the triplet state, we can conclude that these observations are in good agreement with the results of $^1O_2$ PL measurements. The high Φ_Δ values of **DAP** and **DAC** result from an efficient intersystem crossing process.

These diazaporphyrin derivatives were then used for *in vitro* PDT experiments. The internalization of **DAP**, **DAC** and **DAB** in MCF-7 breast cancer cells was clearly observed by fluorescence microscopy, although these compounds have none of the hydrophilic groups (Fig. 3a and Fig. S11, ESI†). Then, MCF-7 cells were incubated for 24 h with diazaporphyrin derivatives and subjected or not to laser irradiation at 650 nm for 15 min (6 mW cm^{-2}). A 3-(4,5-dimethylthiazol-2-yl)-2,5-diphenyltetrazolium bromide assay was performed two days after irradiation to determine the cell viability.[14] Excellent phototoxicity was

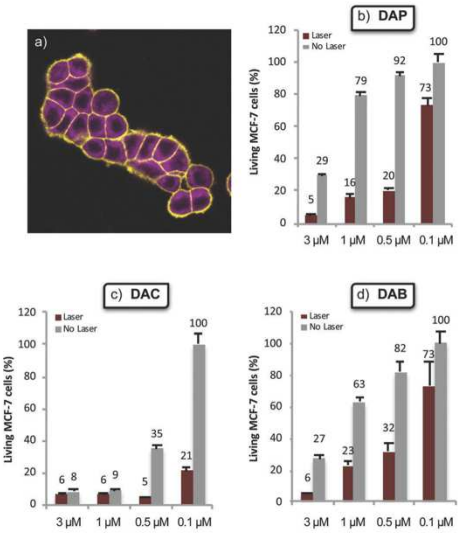

Fig. 3 (a) Fluorescence imaging of MCF-7 cells incubated for 24 h with 15 μM of **DAB**. The cell membranes appear in yellow and **DAB** in purple. PDT evaluations of (b) **DAP**, (c) **DAC** and (d) **DAB** on MCF-7 cells under irradiation at 650 nm.

observed in the micromolar range for **DAP**, **DAC** and **DAB** (Fig. 3b–d). Surprisingly, despite its lower $^1O_2$ generation yield, **DAB** is as efficient as **DAP**. In particular, **DAC** presents an efficient phototoxicity at the nanomolar range (79% cell death at 100 nM) without significant toxicity in the dark and is still effective at 50 nM (Fig. S12, ESI†). The generation of ROS in MCF-7 cells after irradiation was confirmed by a 2′,7′-dichlorodihydrofluorescein diacetate test (Fig. S13, ESI†). The fact that **DAB** exhibited a high PDT effect despite the low $^1O_2$ generation indicates that the PDT effect by **DAB** could occur through different mechanisms such as a type I mechanism.[1a]

The use of diazaporphyrin derivatives for TPE-PDT was investigated. Their TPA cross-section values were determined by the open-aperture Z-scan method (Fig. S14, ESI†). The maximum TPA cross-section values of **DAP**, **DAC** and **DAB** were determined to be 60, 90 and 240 GM, respectively (Fig. S15, ESI†). The relatively large TPA value of **DAB** revealed its prospective feature as PS for TPE-PDT. For this purpose, we used 760, 800 and 980 nm focused lasers and employed another human breast cancer cell line, namely MDA-MB-231. These highly invasive cells are widely used for *in vivo* studies and enable tumor establishments into zebrafish larvae.[15] Preliminary *in vitro* confocal imaging studies confirmed **DAB** internalization by MDA-MB-231 cells (Fig. 4a).

Moreover, *in vitro* TPE-PDT on these cells demonstrated the phototoxicity of **DAB** under 760, 800 and 980 nm biphotonic excitation (Fig. 4b and Fig. S16, S17, ESI†). **DAB** induced significant phototoxicity at 760 and 800 nm and the effect was observed even at 980 nm. Because **DAB** has no one-photon absorption at 980 nm, TPE-PDT should contribute the high activity of **DAB**. As in the case of monophotonic excitation, ROS production was associated with the observed phototoxicity induced after PDT (Fig. S18, ESI†). These *in vitro* experiments demonstrate the ability of **DAB** as stable PS for TPE-PDT.

With excellent *in vitro* PDT activity of **DAB**, we performed *in vivo* experiments using a zebrafish larva model, which is a promising animal model for cancer research (Fig. 5 and Fig. S19, ESI†).[16] MDA-MB-231 cells were implanted in the zebrafish larvae

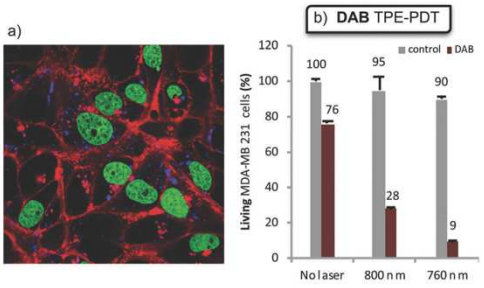

Fig. 4 (a) Intracellular distribution of **DAB** in the MDA-MB-231 cells. The cell membranes appear in red, the nuclei in green and **DAB** in blue (biphotonic excitation at 760 nm). (b) PDT evaluations of **DAB** under 760 or 800 nm biphotonic irradiation at 5 μM.

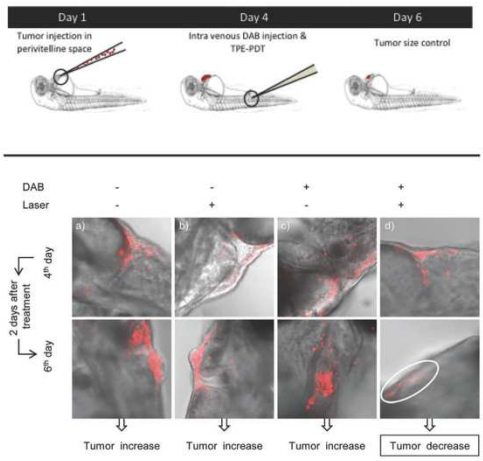

Fig. 5 Top: Xenografted tumor implantation protocol. Bottom: Tumor evolution after treatment (a) without **DAB** or irradiation, (b) with irradiation but no **DAB**, (c) with **DAB** but no irradiation and (d) with **DAB** and irradiation.

and kept until the 4th day to develop and establish the tumor (Fig. 5, top). Then, the larvae were intravenously injected or not with **DAB** (40 μM, 5 nL) and subjected or not to PDT at 760 nm. Finally, the tumor size was monitored on the 6th day.

Clear growth of the xenografted tumor was observed in zebrafish larvae injected with MDA-MB-231 cells (Fig. 5a). A comparable evolution was confirmed with laser irradiation alone or in the presence of **DAB** without irradiation (Fig. 5b and c). In sharp contrast, the intravenous injection of **DAB** and subsequent two-photon irradiation significantly reduced the tumor size (Fig. 5d). To investigate how **DAB** leads to tumor regression, zebrafish larvae aged 6 days were fixed. These fixed larvae were treated with a primary antibody specific to caspase 3, a protease which is induced during the apoptosis death activation. Clearly, the tumor size reduction is associated with the activation of caspase 3, demonstrating that the tumor reduction occurs through the apoptotic pathway (Fig. S20, ESI†).

In conclusion, we have synthesized and investigated the photophysical properties of diazaporphyrin derivatives and used them for one- and two-photon excitation PDT. We demonstrated that **DAC** exhibited potent *in vitro* PDT activity at a nanomolar level under monophotonic excitation at 650 nm. Moreover, **DAB** is also an efficient PS for PDT applications despite its low $^1O_2$ production yield. The enhanced nonlinear optical properties of **DAB** allowed its use in TPE-PDT. Indeed, biological studies clearly showed excellent *in vitro* and *in vivo* PDT performance of **DAB** enabling tumor size reduction in xenografted zebrafish larvae.

The authors thank Profs Aiko Fukazawa and Shigehiro Yamaguchi (Nagoya Univ.) for the help with the measurement of NIR emission spectra. This work was supported by JSPS KAKENHI Grant Numbers JP26102003, JP15K21721 and

JP17H01190. AY appreciates the JSPS Research Fellowship for Young Scientists. JFL is grateful to the JSPS for a short-term postdoctoral fellowship. MGB and SR are grateful to the Région Languedoc-Roussillon (Research Grant "Chercheur(se)s d'Avenir – Editions 2013 and 2015", 2013-098085 and 2015-005984) and the program FEDER for financial support. SR and MGB also thank the French Ministère de l'Enseignement Supérieur et de la Recherche. Laure Lichon is acknowledged for her technical assistance. The work at Yonsei was supported by the Global Research Laboratory (GRL) Program funded by the Ministry of Science, ICT & Future, Korea (2013K1A1A2A02050183).

Conflicts of interest

There are no conflicts to declare.

Notes and references

1 (*a*) M. Ethirajan, Y. Chen, P. Joshi and R. K. Pandey, *Chem. Soc. Rev.*, 2011, **40**, 340; (*b*) M. Ethirajan, N. J. Patel and R. K. Pandey, in *Handbook of Porphyrin Science*, ed. K. M. Kadish, K. M. Smith and R. Guilard, World Scientific, Singapore, 2010, vol. 4, p. 249; (*c*) C. A. Robertson, D. H. Evans and H. Abrahamse, *J. Photochem. Photobiol., B*, 2009, **96**, 1; (*d*) A. E. O'Connor, W. M. Gallagher and A. T. Byrne, *Photochem. Photobiol.*, 2009, **85**, 1053; (*e*) M. C. DeRosa and R. Crutchley, *Coord. Chem. Rev.*, 2002, **233-234**, 351; (*f*) R. Bonnett, *Chem. Soc. Rev.*, 1995, **24**, 19; (*g*) D. E. J. G. J. Dolmans, D. Fukumura and R. K. Jain, *Nat. Rev. Cancer*, 2003, **3**, 380; (*h*) S. B. Brown, E. A. Brown and I. Walker, *Lancet Oncol.*, 2004, **5**, 497; (*i*) P. Agostinis, K. Berg, K. A. Cengel, T. H. Foster, A. W. Girotti, S. O. Gollnick, S. M. Hahn, M. R. Hamblin, A. Juzeniene, D. Kessel, M. Korbelik, J. Moan, P. Mroz, D. Nowis, J. Piette, B. C. Wilson and J. Golab, *Ca-Cancer J. Clin.*, 2011, **61**, 250; (*j*) F. Bolze, S. Jenni, A. Sour and V. Heitz, *Chem. Commun.*, 2017, **53**, 12857.

2 (*a*) E. A. Lukyanets, *J. Porphyrins phthalocyanines*, 1999, **3**, 424; (*b*) M. Soncin, A. Busetti, R. Biolo, G. Jori, G. Kwag, Y.-S. Li, M. E. Kenney and M. A. J. Rodgers, *J. Photochem. Photobiol., B*, 1998, **42**, 202; (*c*) R. Biolo, G. Jori, M. Soncin, R. Pratesi, U. Vanni, B. Rihter, M. E. Kenney and M. A. J. Rodgers, *Photochem. Photobiol.*, 1994, **59**, 362; (*d*) D. M. Guldi, T. D. Mody, N. N. Gerasimchuk, D. Magda and J. L. Sessler, *J. Am. Chem. Soc.*, 2000, **122**, 8289; (*e*) A. Harriman, B. G. Maiya, T. Murai, G. Hemmi, J. L. Sessler and T. E. Mallouk, *J. Chem. Soc., Chem. Commun.*, 1989, 314; (*f*) J. L. Sessler, M. R. Johnson and V. Lynch, *J. Org. Chem.*, 1987, **52**, 4394; (*g*) S. W. Young, K. W. Woodburn, M. Wright, T. D. Mody, Q. Fan, J. L. Sessler, C. Dow and W. R. A. Miller, *Photochem. Photobiol.*, 1996, **63**, 892.

3 (*a*) H. A. Collins, M. Khurana, E. H. Moriyama, A. Mariampillai, E. Dahlstedt, M. Balaz, M. K. Kuimova, M. Drobizhev, V. X. D. Yang, D. Phillips, A. Rebane, B. C. Wilson and H. L. Anderson, *Nat. Photonics*, 2008, **2**, 420; (*b*) M. Gary-Bobo, Y. Mir, C. Rouxel, D. Brevet, I. Basile, M. Maynadier, O. Vaillant, O. Mongin, M. Blanchard-Desce, A. Morère, M. Garcia, J.-O. Durand and L. Raehm, *Angew. Chem., Int. Ed.*, 2011, **50**, 11425; (*c*) Y. Shen, A. J. Shuhendler, D. Ye, J.-J. Xu and H.-Y. Chen, *Chem. Soc. Rev.*, 2016, **45**, 6725.

4 (*a*) C. Brückner, L. Samankumara and J. Ogikubo, in *Handbook of Porphyrin Science*, ed. K. M. Kadish, K. M. Smith and R. Guilard, World Scientific, Singapore, 2012, vol. 17, p. 1; (*b*) F.-P. Montforts, B. Gerlach and F. Hoeper, *Chem. Rev.*, 1994, **94**, 327; (*c*) M. Taniguchi and J. S. Lindsey, *Chem. Rev.*, 2017, **117**, 344.

5 (*a*) B. W. Henderson, D. A. Bellnier, W. R. Greco, A. Sharma, R. K. Pandey, L. A. Vaughan, K. R. Weishaupt and T. J. Dougherty, *Cancer Res.*, 1997, **57**, 4000; (*b*) Ch. Grewer, G. Schermann, R. Schmidt, A. Völcker, H.-D. Brauer, A. Meier and F.-P. Montforts, *J. Photochem. Photobiol., B*, 1991, **11**, 285; (*c*) T. Y. Ohulchanskyy, I. Roy, L. N. Goswami, Y. Chen, E. J. Bergey, R. K. Pandey, A. R. Oseroff and P. N. Prasad, *Nano Lett.*, 2007, **7**, 2835; (*d*) Y. Chen, G. Li and R. K. Pandey, *Curr. Org. Chem.*, 2004, **8**, 1105; (*e*) R. Bonnett, R. D. White, U.-J. Winfield and M. C. Berenbaum, *Biochem. J.*, 1989, **261**, 277.

6 (*a*) Y.-Y. Huang, P. Mroz, T. Zhiyentayev, S. K. Sharma, T. Balasubramanian, C. Ruzié, M. Krayer, D. Fan, K. E. Borbas, E. Yang, H. L. Kee, C. Kirmaier, J. R. Diers, D. F. Bocian, D. Holten, J. S. Lindsey and M. R. Hamblin, *J. Med. Chem.*, 2010, **53**, 4018; (*b*) P. Mroz, Y.-Y. Huang, A. Szokalska, T. Zhiyentayev, S. Janjua, A.-P. Nifli, M. E. Sherwood, C. Ruzié, K. E. Borbas, D. Fan, M. Krayer, T. Balasubramanian, E. Yang, H. L. Kee, C. Kirmaier, J. R. Diers, D. F. Bocian, D. Holten, J. S. Lindsey and M. R. Hamblin, *FASEB J.*, 2010, **24**, 3160; (*c*) H.-J. Kim and J. S. Lindsey, *J. Org. Chem.*, 2005, **70**, 5475.

7 (*a*) J. M. Dabrowski, L. G. Arnaut, M. M. Pereira, K. Urbanska and G. Stochel, *Med. Chem. Commun.*, 2012, **3**, 502; (*b*) C. J. P. Monteiro, J. Pina, M. M. Pereira and L. G. Arnaut, *Photochem. Photobiol. Sci.*, 2012, **11**, 1233.

8 Y. Matano, *Chem. Rev.*, 2017, **117**, 3138.

9 (*a*) F.-P. Montforts and B. Gerlach, *Tetrahedron Lett.*, 1992, **33**, 1985; (*b*) K. Schiwon, H.-D. Brauer, B. Gerlach, C. M. Müller and F.-P. Montforts, *J. Photochem. Photobiol., B*, 1994, **23**, 239; (*c*) B. Gerlach and F.-P. Montforts, *Liebigs Ann.*, 1995, 1509.

10 H. W. Whitlock Jr, R. Hanauer, M. Y. Oester and B. K. Bower, *J. Am. Chem. Soc.*, 1969, **91**, 7485.

11 (*a*) C. Muthiah, M. Taniguchi, H.-J. Kim, I. Schmidt, H. L. Kee, D. Holten, D. F. Bocian and J. S. Lindsey, *Photochem. Photobiol.*, 2007, **83**, 1513; (*b*) M. A. Grin and A. F. Mironov, in *Chemical Processes with Participation of Biological and Related Compounds*, ed. T. N. Lomova and G. E. Zaikov, Taylor & Francis Group, Boston, 2008, p. 5.

12 F. Wilkinson, W. P. Helman and A. B. Ross, *J. Phys. Chem. Ref. Data*, 1993, **22**, 113.

13 $^1O_2$ generation efficiency of 5,15-diazaporphyrins has been reported. (*a*) H. Shinmori, F. Kodaira, S. Matsugo, S. Kawabata and A. Osuka, *Chem. Lett.*, 2005, **34**, 322; (*b*) S. Omomo, T. Sugai, M. Minoura, H. Nakano and Y. Matano, *Angew. Chem., Int. Ed.*, 2018, **57**, 3797.

14 T. Mosmann, *J. Immunol. Methods*, 1983, **65**, 55.

15 M. Konantz, T. B. Balci, U. F. Hartwig, G. Dellaire, M. C. André, J. N. Berman and C. Lengerke, *Ann. N. Y. Acad. Sci.*, 2012, **1266**, 124.

16 (*a*) S. Nicoli, D. Ribatti, F. Cotelli and M. Presta, *Cancer Res.*, 2007, **67**, 2927; (*b*) K. Stoletov and R. Klemke, *Oncogene*, 2008, **27**, 4509; (*c*) R. White, K. Rose and L. Zon, *Nat. Rev. Cancer*, 2013, **13**, 624.

ANNEXE 7

ChemPubSoc Europe

DOI: 10.1002/slct.201802107

Chemistry SELECT Communications

Materials Science inc. Nanomaterials & Polymers

Hollow Organosilica Nanoparticles for Drug Delivery

Saher Rahmani,[a] Alia Akrout,[a] Jelena Budimir,[a] Dina Aggad,[b] Morgane Daurat,[b, c] Anastasia Godefroy,[b, c] Christophe Nguyen,[b] Hanene Largot,[a] Magali Dr. Gary-Bobo,*[b] Laurence Raehm,[a] Jean-Olivier Durand,[a] and Clarence Charnay*[a]

The sol-gel synthesis of hollow organosilica nanoparticles incorporating amino groups with uniform size are described. These nanoparticles were successfully prepared *via* a micro-emulsion method. Then, the hollow nanoparticles were loaded with gemcitabine hydrochloride or methotrexate and studied in MCF-7 breast cancer cells.

Owing to their unique structural features, organosilica nanoparticles have attracted much attention the last few years particularly for bio-applications and the field has been recently reviewed.[1,2] Indeed, recent results demonstrate their high biocompatibility which makes them promising candidates for cancer treatment applications. These nanoparticles are obtained from triethoxysilyl-functionalized organic precursors without the presence of SiO_2, leading to ca 80–90% of organic moieties, thereby maximizing the impact of the organic fragment on the resulting material properties. Furthermore, porous systems have also been described and recently reviewed[3–5] which opens new possibilities of development for these nanoparticles when applied to drug adsorption and delivery. Indeed the properties of these nanoparticles are very different from that of mesoporous silica nanoparticles in terms of stability,[6,7] drug loading capacity and delivery. The synthesis consists of using a small bis-triethoxysilyl functionalized organic precursor in the presence of a surfactant which acts as the template during the sol-gel process thus leading to porous structures. Among several shapes, the synthesis of hollow organosilica nanoparticles is still a great challenge. The first synthesis was reported in 2006 by Lu and co-workers. They described a successful synthesis of periodic mesoporous organosilica hollow nanospheres with a size of 300–800 nm with the use of a fluorocarbon surfactant (FC-4) and the cationic surfactant cetyltrimethylammonium bromide (CTAB) as co-structure directing agent with 1,2-bis(trimethoxysilyl)ethane (BTME) as the precursor.[8] Liu and co-workers synthesized hybrid hollow nanospheres with controllable size (12-20 nm) and shell thickness (4-7 nm) through the condensation of BTME around an inorganic-electrolyte-stabilized F127 micelle.[9] Another strategy consists in the condensation of an organosilica shell around silica nanoparticles as hard template, then to dissolve the template to prepare hollow periodic mesoporous organosilica nanospheres.[10–15] The typical precursors used for the syntheses of these hollow nanoparticles are bistriethoxysilyl or trimethoxysilyl ethane (BTSE or BTME), bistriethoxysilyl ethylene or bistriethoxysilyl benzene. The use of more functional precursors such as bis(triethoxysilylproyl)amine has been scarcely described and only as a mixture of precursors with BTSE[16] or BTME.[17] Herein, we report the synthesis of amino-based hollow organosilica nanoparticles *via* an O/W microemulsion method, with the organic precursor bis(triethoxysilylpropyl)amine solely as the oil phase and cetyltrimethylammonium bromide (CTAB) as the template. The encapsulation of two anti-cancer drugs, methotrexate (MTX, hydrophobic) or gemcitabine (hydrophilic) was studied and their delivery *in vitro* in MCF-7 cancer cells was investigated. Note that the encapsulation of methotrexate and gemcitabine was previously studied with mesoporous silica nanoparticles (MSN). The hydrophobic drug MTX could be encapsulated in MSN[18–21] whereas gemcitabine is challenging and necessitated to cap the pores in order to avoid its premature release due to its hydrophilic character.[22–26]

The monodisperse hollow organosilica nanoparticles (HONPs) were prepared through the condensation of bis (triethoxysilylpropyl) amine solubilized in a water/ethanol solution (100:1, v:v) with the cetyltrimethylammonium bromide (CTAB) surfactant used as template. The sol-gel process was carried out for 2 h at 75 °C in highly diluted conditions with ammonium hydroxide as catalyst. Afterwards, the surfactant was extracted thrice using an ethanolic mixture of ammonium nitrate. The as-prepared material was dried under air flow for few hours.

The HONPs were then characterized *via* transmission electron microscopy (TEM) (Figure 1), which clearly depicted about 200 nm hollow spherical particles with the presence of a cavity inside the nanoparticles.

The narrow size distribution of the nanoparticles was confirmed by dynamic light scattering measurement (DLS, Figure S.1).

[a] *S. Rahmani, A. Akrout, J. Budimir, H. Largot, L. Raehm, Jean-Olivier Durand, Dr. C. Charnay*
Institut Charles Gerhardt Montpellier, UMR-5253 CNRS-UM-ENSCM cc 1701, Place Eugène Bataillon, 34095, Montpellier cedex 05 (France).
E-mail: clarence.charnay@umontpellier.fr
[b] *D. Aggad, M. Daurat, A. Godefroy, C. Nguyen, M. Dr. Gary-Bobo*
Institut des Biomolécules Max Mousseron, UMR 5247 CNRS, UM-Faculté de Pharmacie, 15 Avenue Charles Flahault, 34093, Montpellier cedex 05 (France).
E-mail: magali.gary-bobo@inserm.fr
[c] *M. Daurat, A. Godefroy*
NanoMedSyn, 15 avenue Charles Flahault, 34093 Montpellier

Supporting information for this article is available on the WWW under https://doi.org/10.1002/slct.201802107

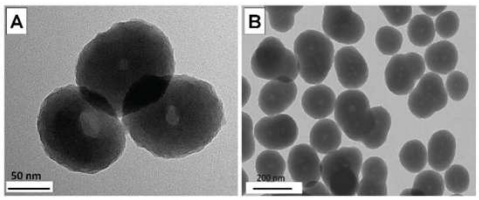

Figure 1. A) Transmission electron microscopy (TEM) image of Hollow Organosilica Nanoparticles (Scale bar: 50 nm) where the porosity can be observed. B) TEM image at lower magnification (scale bar 200 nm).

The zeta potentials of the nanocarriers dispersed in a solution of NaCl (1 mM) were checked at pH 5 and at pH 7 and positive values of 49 and 45 mV were respectively obtained.

Nitrogen-adsorption desorption analysis (BET model) showed a low specific surface area of 15 $m^2.g^{-1}$ with 10 nm pore diameters (Figure 2) determined from BJH (Barrett-Joyner-Halenda) analysis. The composition of the material was then studied by elemental analysis and showed that the nanoparticles contain about 8 wt% of nitrogen and 24 wt% of carbon (Table S1). The incorporation of organic bridges into the silica framework of porous organosilica nanoparticles was proven by FTIR spectroscopy (Figure S2) with $\delta_{N\text{-}H}$ at 1635 cm^{-1} and $\nu_{C\text{-}H}$ at 2964 cm^{-1}. The high degree of condensation of siloxanes was confirmed by the shift of the ν_{Si-O} value from 1090 to 1136 cm^{-1}. The HONPs were further characterized by solid state nuclear magnetic resonance (NMR) ^{29}Si and ^{13}C CPMAS spectra (Figure S3). The ^{29}Si CPMAS NMR spectrum of nanocarriers (Figure S3-A) showed the presence of the siloxane network with a high condensation of the precursor (bis (triethoxysilylpropyl) amine) with a ^{3}T resonance at −68 ppm and a small amount of less-condensed material with a ^{2}T peak (-58 ppm). Moreover, NMR ^{13}C cross-polarization magic angle spinning (CPMAS) spectrum in Figure S3-B displayed the three types of carbon found in the precursor, at 10, 18 and 48 ppm. The organization of the porous framework was then controlled by XRD. Figure S4-A confirms the presence of the porosity with a small angle diffraction at $2\theta = 1.8°$. Moreover, no wide angle X-ray diffraction is observed (Figure S4-B).

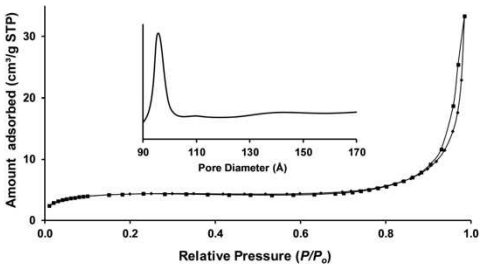

Figure 2. N_2 adsorption (diamonds)-desorption (squares) isotherms and pore size distribution of HONPs.

The loading of these nanoparticles with two different drugs (gemcitabine hydrochloride (GEM) and methotrexate (MTX)) was then examined in water at room temperature. The loading capacity with GEM or MTX was obtained by UV-Vis absorption spectra of the supernatants and the absolute loading was 0.3 $mg.mg^{-1}$ of particles or 0.35 $mg.mg^{-1}$ of particles respectively. Drug release experiments were first carried out at pH 7 in ultrapure water, with GEM and MTX loaded nanoparticles. No release of drugs was observed in these conditions showing the intense interactions between both of the drugs and the organosilica matrix. The pH was then adjusted to 5.5 (lysosomal pH) to trigger the drug release.[27] The release amount of GEM and MTX were 45 $\mu g.mL^{-1}$ and 160 $\mu g.mL^{-1}$ respectively (Figure S5), and were sufficient for further studies in cancer cells.

The endocytosis of the nanoparticles in MCF-7 breast cancer cells was then investigated. The nanoparticles were loaded with fluorescein isothiocyanate (HONPs-FITC) and incubated with MCF-7 cancer cells for 24 h. Observation of the cells whose membranes were stained with cell mask clearly showed nanoparticles taken up by the cells (Figure 3).

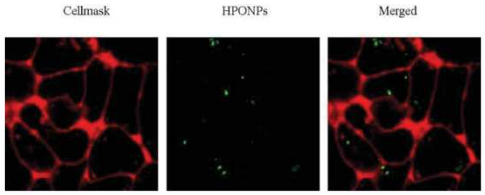

Figure 3. Endocytosis of fluorescein-loaded nanoparticles (50 $\mu g.mL^{-1}$, 24 h incubation) in MCF-7 cancer cells analyzed by confocal microscopy ($\lambda = 488$ nm). Membranes were stained with cell mask (red), and the nanoparticles (green) were clearly taken up by cell.

To determine the kinetics of HONPs-FITC internalization, flow cytometry experiments were performed, demonstrating progressive endocytosis by MCF-7 cells. After 18 h of incubation, a maximal internalization level (54% stained cells) was reached (Figure 4).

Since the endocytosis of the nanoparticles was established by flow cytometry experiments, HONPs were then examined as vectors for GEM and MTX deliveries. The deliveries of GEM and MTX were tested in MCF-7 breast cancer cells as depicted in Figure 5. Moreover, it was observed no significant cytotoxicity of empty hollow organosilica nanoparticles up to a concentration of 100 $\mu g.mL^{-1}$, showing their biocompatibility.

Furthermore, the GEM and MTX delivery-mediated cancer killing was highly efficient, with down to 40% and 60% of cell survival respectively at only 1 $\mu g.mL^{-1}$ of nanomaterials. As comparative points, free gemcitabine or methotrexate were also tested and added in the graph in dotted lines. It was

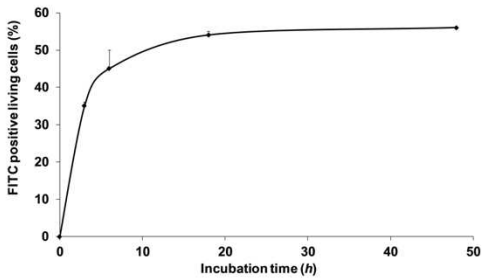

Figure 4. Internalization of HONPs-FITC by living MCF-7 cells. Cells were treated with 50 μg mL^{-1} of HONPs-FITC for 3, 6, 18, 48 h. Non-fixed cells were incubated with propidium iodide (1 μg mL^{-1}) to remove dead cells and FITC fluorescence was analysed by flow cytometry on living cells only. Data represent means ± SEM of two experiments.

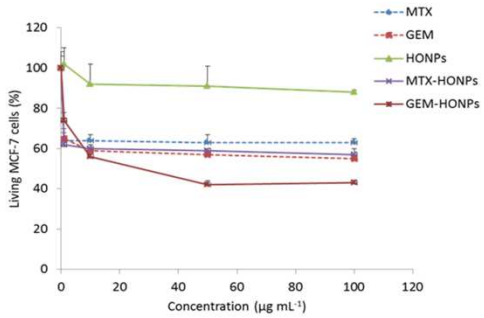

Figure 5. GEM or MTX delivery in MCF-7 cancer cells with hollow organosilica nanoparticles. Cytotoxic assay of a range (from 1 to 100 μg mL^{-1}) of GEM, MTX, HONPs loaded or not with these 2 drugs. Cells were incubated 72 h with the different samples and then submitted to MTT assay to quantify the living cells. Values are means ± standard deviations of 3 experiments. * $p < 0.05$ statistically different from control.

observed that the drug encapsulated into the HONPs was more efficient to kill the cells than the free drug for the same amount of material (HONPs + drug versus drug alone).

In summary, we have designed new hollow organosilica nanoparticles from bis (triethoxysilylpropyl) amine as a bis-silylated precursor via a microemulsion system. The morphology and compositions were fully characterized by various techniques. The nanoscaled particles displayed a large cavity, enabling drug loading and release. In particular, the hydrophilic gemcitabine was loaded without early release and no chemical coupling was required. Besides, the gemcitabine hydrochloride and the methotrexate-loaded HONPs were very efficient to be internalized by cancer cells and to induce cancer cell killing showing promising potential for biomedical applications.

Supporting Information Summary

The different procedures and experimental details are described in supporting information, notably the synthesis of HONPs that was not yet reported. Moreover, the HONPs characterizations (DLS, elemental analysis, X-ray diffraction, FTIR and solid NMR) are also reported.

Acknowledgements

The grant "Chercheur d'Avenir Languedoc-Roussillon" attributed to MGB and the Erasmus Mundus program for S. Rahmani are gratefully acknowledged. We thank L. Lichon for technical assistance. We thank MRI (Montpellier RIO Imaging platform) for confocal imaging facilities.

Conflict of Interest

The authors declare no conflict of interest.

Keywords: Gemcitabine · MCF-7 breast cancer cells · Methotrexate · Organosilica Nanoparticles

[1] J. G. Croissant, X. Cattoen, J.-O. Durand, M. Wong Chi Man and N. M. Khashab, *Nanoscale*, **2016**, *8*, 19945–19972.
[2] M. Nakamura, *Nanotechnol. Rev.*, **2012**, *1*, 469–491.
[3] X. Du, X. Li, L. Xiong, X. Zhang, F. Kleitz and S. Z. Qiao, *Biomaterials*, **2016**, *91*, 90–127.
[4] Y. Chen and J. Shi, *Adv. Mater.*, **2016**, *28*, 3235–3272.
[5] J. G. Croissant, X. Cattoen, M. W. C. Man, J.-O. Durand and N. M. Khashab, *Nanoscale*, **2015**, *7*, 20318–20334.
[6] C. Urata, H. Yamada, R. Wakabayashi, Y. Aoyama, S. Hirosawa, S. Arai, S. Takeoka, Y. Yamauchi and K. Kuroda, *J. Am. Chem. Soc.*, **2011**, *133*, 8102–8105.
[7] S. Datz, H. Engelke, C. v. Schirnding, L. Nguyen and T. Bein, *Microporous Mesoporous Mater.*, **2016**, *225*, 371–377.
[8] H. Djojoputro, X. F. Zhou, S. Z. Qiao, L. Z. Wang, C. Z. Yu and G. Q. Lu, *J. Am. Chem. Soc.*, **2006**, *128*, 6320–6321.
[9] J. Liu, Q. Yang, L. Zhang, H. Yang, J. Gao and C. Li, *Chem. Mater.*, **2008**, *20*, 4268–4275.
[10] Y. Chen, Q. Meng, M. Wu, S. Wang, P. Xu, H. Chen, Y. Li, L. Zhang, L. Wang and J. Shi, *J. Am. Chem. Soc.*, **2014**, *136*, 16326–16334.
[11] N. Koike, W. Chaikittisilp, A. Shimojima and T. Okubo, *RSC Adv.*, **2016**, *6*, 90435–90445.
[12] N. Koike, T. Ikuno, T. Okubo and A. Shimojima, *Chem. Commun.*, **2013**, *49*, 4998–5000.
[13] X. Qian, W. Wang, W. Kong and Y. Chen, *RSC Adv.*, **2014**, *4*, 17950–17958.
[14] Y. Yang, W. Zhang, Y. Zhang, A. Zheng, H. Sun, X. Li, S. Liu, P. Zhang and X. Zhang, *Nano Research*, **2015**, *8*, 3404–3411.
[15] Y. Chen, P. Xu, H. Chen, Y. Li, W. Bu, Z. Shu, Y. Li, J. Zhang, L. Zhang, L. Pan, X. Cui, Z. Hua, J. Wang, L. Zhang and J. Shi, *Adv. Mater.*, **2013**, *25*, 3100–3105.
[16] F. Chen, E. Zhao, T. Kim, J. Wang, G. Hableel, P. J. T. Reardon, S. J. Ananthakrishna, T. Wang, S. Arconada-Alvarez, J. C. Knowles and J. V. Jokerst, *ACS Appl. Mater. Interfaces.*, **2017**, *9*, 15566–15576.
[17] S. Bai, J. Liu, J. Gao, Q. Yang and C. Li, *Microporous Mesoporous Mater.*, **2012**, *151*, 474–480.
[18] L. B. d. O. Freitas, L. d. M. Corgosinho, J. A. Q. A. Faria, V. M. dos Santos, J. M. Resende, A. S. Leal, D. A. Gomes and E. M. B. d. Sousa, *Microporous Mesoporous Mater.*, **2017**, *242*, 271–283.
[19] H. Zheng, C.-W. Tai, J. Su, X. Zou and F. Gao, *Dalton Trans.*, **2015**, *44*, 20186–20192.
[20] N. Vadia and S. Rajput, *Eur. J. Pharm. Sci.*, **2012**, *45*, 8–18.
[21] J. M. Rosenholm, E. Peuhu, L. T. Bate-Eya, J. E. Eriksson, C. Sahlgren and M. Linden, *Small*, **2010**, *6*, 1234–1241.

[22] M. R. Zeiderman, D. E. Morgan, J. D. Christein, W. E. Grizzle, K. M. McMasters and L. R. McNally, *ACS Biomater. Sci. Eng.*, **2016**, *2*, 1108–1120.
[23] A. Pourjavadi and Z. M. Tehrani, *Mater. Sci. Eng. C*, **2016**, *61*, 782–790.
[24] H. Meng, M. Wang, H. Liu, X. Liu, A. Situ, B. Wu, Z. Ji, C. H. Chang and A. E. Nel, *Acs Nano*, **2015**, *9*, 3540–3557.
[25] J. G. Croissant, D. Zhang, S. Alsaiari, J. Lu, L. Deng, F. Tamanoi, A. M. Al Malik, J. I. Zink and N. M. Khashab, *J. Control. Release*, **2016**, *229*, 183–191.
[26] Z. Bahrami, A. Badiei and G. M. Ziarani, *J. Nanopart. Res.*, **2015**, *17*, 1–12.
[27] D. Aggad, C. M. Jimenez, S. Dib, J. G. Croissant, L. Lichon, D. Laurencin, S. Richeter, M. Maynadier, S. K. Alsaiari, M. Boufatit, L. Raehm, M. Garcia, N. M. Khashab, M. Gary-Bobo, J.-O. Durand, *ChemNanoMat* **2018**, *4*, 46.

Submitted: July 7, 2018
Accepted: September 20, 2018

COMMUNICATIONS

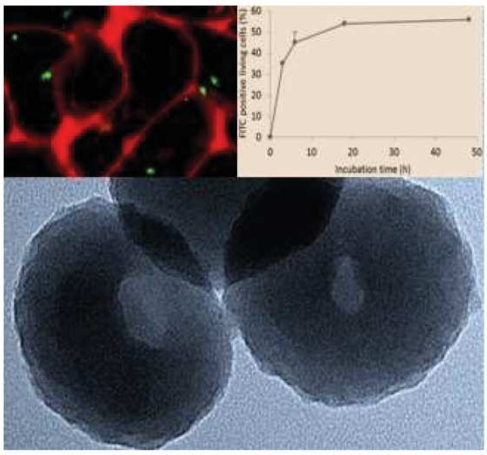

Hollow Organosilica Nanoparticles (HONPs) with uniform size and incorporating amino groups were achieved via a microemulsion method. These hollow nanoparticles displayed a large cavity, enabling drug loading and release. In particular, the hydrophilic gemcitabine was loaded without early release and no chemical coupling was required. HONPs loaded with gemcitabine were very efficient to be internalized by cancer cells and to induce MCF-7 cell killing.

Author Contributions

S.R. Investigation:Lead; Writing – original draft:Equal
A.A. Investigation:Equal
J.B. Investigation:Equal
D.A. Investigation:Equal
M.D. Investigation:Equal
A.G. Investigation:Equal
C.N. Investigation:Equal
H.L. Investigation:Equal
M.M.-B. Methodology:Lead; Supervision:Equal; Writing – original draft:Equal
L.R. Methodology:Equal; Writing – original draft:Equal
J.-O.D. Supervision:Lead; Writing – original draft:Equal

ANNEXE 8

molecules

MDPI

Article

Large Pore Mesoporous Silica and Organosilica Nanoparticles for Pepstatin A Delivery in Breast Cancer Cells

Saher Rahmani [1], Jelena Budimir [1], Mylene Sejalon [1], Morgane Daurat [2,3], Dina Aggad [2], Eric Vives [4], Laurence Raehm [1], Marcel Garcia [4], Laure Lichon [2], Magali Gary-Bobo [2,*], Jean-Olivier Durand [1] and Clarence Charnay [1,*]

1 Institut Charles Gerhardt Montpellier, UMR-5253 Univ Montpellier, CNRS, ENSCM, cc 1701, Place Eugène Bataillon, CEDEX 5, 34095 Montpellier, France; rahmeni.sahar@yahoo.fr (S.R.); jelena.budimir@uni-goettingen.de (J.B.); mylene.sejalon@enscm.fr (M.S.); laurence.raehm@univ-montp2.fr (L.R.); durand@univ-montp2.fr (J.-O.D.)

2 Institut des Biomolécules Max Mousseron, UMR 5247 CNRS, UM-Faculté de Pharmacie, 15 Avenue Charles Flahault, CEDEX 5, 34093 Montpellier, France; morgane.daurat2@gmail.com (M.D.); dina.aggad@umontpellier.fr (D.A.); laure.lichon@umontpellier.fr (L.L.)

3 NanoMedSyn, Faculté de Pharmacie, 15 Avenue Charles Flahault, CEDEX 5, 34093, Montpellier, France

4 Centre de Recherche en Biologie cellulaire de Montpellier (CRBM), UMR 5237 CNRS, Université Montpellier, 1919 Route de Mende, CEDEX 5, 34293 Montpellier, France; eric.vives@umontpellier.fr (E.V.); marcel.garcia@inserm.fr (M.G.)

* Correspondence: magali.gary-bobo@inserm.fr (M.G.-B.); clarence.charnay@umontpellier.fr (C.C.); Tel.: +33-467-14-38-64 (C.C.)

Received: 11 December 2018; Accepted: 11 January 2019; Published: 17 January 2019

check for updates

Abstract: (1) Background: Nanomedicine has recently emerged as a new area of research, particularly to fight cancer. In this field, we were interested in the vectorization of pepstatin A, a peptide which does not cross cell membranes, but which is a potent inhibitor of cathepsin D, an aspartic protease particularly overexpressed in breast cancer. (2) Methods: We studied two kinds of nanoparticles. For pepstatin A delivery, mesoporous silica nanoparticles with large pores (LPMSNs) and hollow organosilica nanoparticles (HOSNPs) obtained through the sol–gel procedure were used. The nanoparticles were loaded with pepstatin A, and then the nanoparticles were incubated with cancer cells. (3) Results: LPMSNs were monodisperse with 100 nm diameter. HOSNPs were more polydisperse with diameters below 100 nm. Good loading capacities were obtained for both types of nanoparticles. The nanoparticles were endocytosed in cancer cells, and HOSNPs led to the best results for cancer cell killing. (4) Conclusions: Mesoporous silica-based nanoparticles with large pores or cavities are promising for nanomedicine applications with peptides.

Keywords: pepstatin A; mesoporous silica nanoparticles; mesoporous organosilica nanoparticles; cancer

1. Introduction

Mesoporous silica nanoparticles (MSNs) hold great promise for biological applications, particularly in the field of theranostics and drug delivery, and the field has been extensively reviewed [1–15]. Indeed, these nanoparticles (NPs) exhibit adjustable diameters (10 to 200 nm) and pore size (2–15 nm), leading to wide ranges of encapsulated drugs and biomolecules. The synthesis of these NPs, especially those presenting a large pore and which are targeted, has recently been performed [16] and both methods for their preparation and colloidal stability studies have been

reviewed [17]. Large-pore mesoporous silica nanoparticles (LPMSNs) are of interest for the delivery of large molecules, such as nucleic acids or peptides [18]. The release and delivery of peptides for antibacterial [19,20] and anticancer applications has been recently reported [21–23]. Although less described than MSNs, organosilica NPs [24,25] and their porous systems [26–28] are very promising for bioapplications. The properties of organosilica NPs are very different from those of MSNs in terms of stability, drug loading, and release capacities, due to the high content of organic groups, which constitute the structure [29,30]. Recently, large-pore mesoporous organosilica NPs have been synthesized for the delivery of therapeutic proteins in cells [31]. LPMSNs and organosilica NPs seem good candidates for the delivery of pepstatin A ($C_{34}H_{63}N_5O_9$), a small hydrophobic pentapeptide which is the most potent inhibitor of cathepsin D, a lysosomal aspartic endopeptidase overexpressed in solid tumors and breast cancer [32]. Overexpression of cathepsin D is associated with tumor growth. Therefore, an efficient system which would inhibit cathepsin D could be of high interest for cancer therapy. As pepstatin A does not cross cell membranes, it has to be vectorized in cancer cells; nevertheless, very few studies report the vectorization of pepstatin A with NPs. One study used pepstatin A covalently linked to superparamagnetic iron oxide NPs to target P-glycoproteins in the brain of epilepsy rats [33]. In this work, we present the syntheses of LPMSNs functionalized with fluorescein isothiocyanate (FITC) and of new tertiary amine-based hollow organosilica nanoparticles (HOSNPs) obtained with a pore expanding agent. Then, their noncovalent loading was investigated with two short peptides, pepstatin A, and a model cyclic protected Arg-Gly-Asp (RGD) peptide whose adsorption and release can be monitored by UV-visible spectroscopy, unlike pepstatin A. The endocytosis of these NPs was monitored in MCF-7 breast cancer cells, and delivery of pepstatin A was successfully demonstrated in MCF-7 breast cancer cells.

2. Results and Discussion

The synthesis of LPMSNs was performed as already described [16]. Monodispersed NPs with 100 nm diameter were observed by transmission electron microscopy (TEM) images and had 7 nm in pore diameter radial mesopores (Figure 1). Although some spontaneous nuclei were observed, incorporation of fluorescein isothiocyanate (FITC) linked to aminopropyltriethoxysilane (APTES) in the walls did not modify the mesostructure. N_2 adsorption–desorption measurements showed type IV isotherms and the specific surface area was 817 $m^2 \cdot g^{-1}$. The pore size distribution shows that LPMSNs had 3-nm- and 7-nm-sized pores (Supplementary Figure S1). Zeta potential was negative at pH 7.4 (−19.5 mV), which is consistent with the deprotonation of the surface silanol groups.

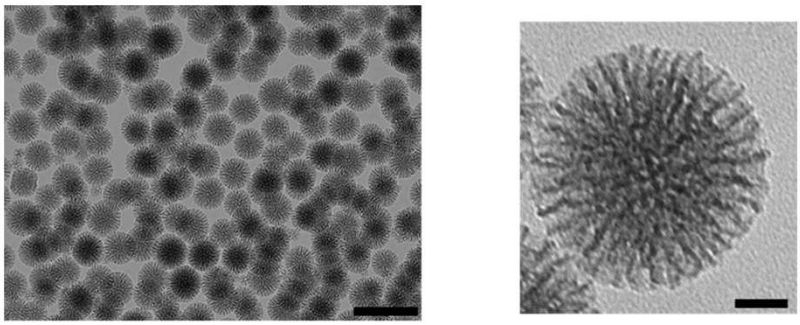

Figure 1. TEM image of large-pore mesoporous silica nanoparticles (LPMSNs). Scale Bar 200 nm (**left**) and 50 nm (**right**), respectively.

HOSNPs were synthesized by hydrolysis and polycondensation of bis (3-tri-methoxysilyl)-*N*-methylamine (BMSPMA) at 75 °C in basic media (pH = 10) using cetyltrimethylammonium bromide (CTAB) as the template and 1,3,5-triethylbenzene (TEB) as

the pore-expanding agent. The surfactant was extracted with a solution of ammonium nitrate in ethanol. TEM images showed a hollow structure with small NPs of 20–30 nm diameter and larger NPs with a mean diameter of 100 nm and with 10–15 nm thick walls (Figure 2A). Dynamic light scattering in EtOH confirmed two populations of HOSNPs with mean hydrodynamic diameters of 228 nm and 460 nm, respectively (Figure 2B), in agreement with the TEM observations; however, some aggregates were observed with hydrodynamic diameters around 900 nm. HOSNPs were further characterized by solid-state ^{29}Si and ^{13}C cross-polarization magic angle spinning nuclear magnetic resonance (CP/MAS NMR) spectroscopy (Figure S2). ^{29}Si CP/MAS NMR spectrum (Figure S2A) showed signals at −64, −72, and −82 ppm, corresponding to T^1, T^2, and T^3 units (T^m: $CSi(OSi)_m(OH)_{3-m}$), respectively, in agreement with a well-condensed structure. ^{13}C CP/MAS NMR spectrum (Figure S2B) clearly displayed three signals at 10, 21, and 43 ppm, corresponding to the propyl chains of condensed BMSPMA and the signal of the methyl group linked to nitrogen was found at 64 ppm. In addition, XRD patterns at small angles (Figure S3A) displayed the presence of a diffraction peak at around 1.9°, which suggests porosity in the walls. In addition, the wide angle XRD of HOSNPs (Figure S3B) showed a broad peak at 23° characteristic of nonregular repetitions within the siloxane framework. N_2 adsorption–desorption isotherm showed a specific surface area of 58 $m^2 \cdot g^{-1}$ with a pore size of 26 nm. The type II isotherm (IUPAC) is consistent with nonporous materials at 77 K with adsorption–desorption of nitrogen in interparticle voids, which suggests that the large cavity is not accessible to nitrogen at cryogenic temperature of 77 K (Figure S4). Zeta potential was positive at pH 7.4 (+32 mV), in agreement with the protonation of tertiary amine group.

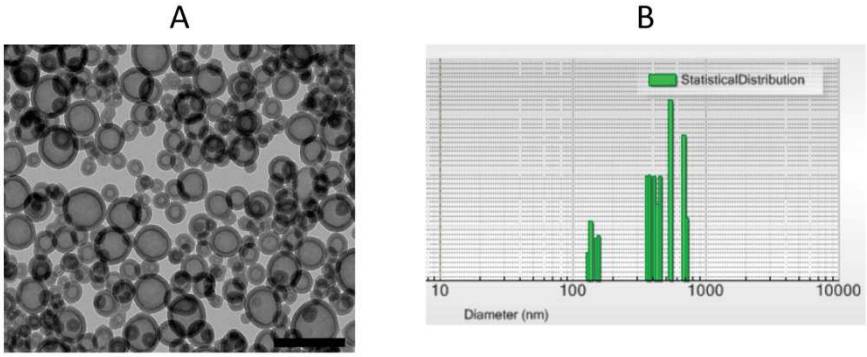

Figure 2. (**A**) TEM image of hollow organosilica nanoparticles (HOSNPs). Scale Bar 100 nm. (**B**) Dynamic light scattering in intensity mode of HOSNPs (dispersed in EtOH).

We then examined the prepared NPs for the vectorization of peptides. First, a model cyclic protected RGD peptide was loaded in HOSNPs in water under stirring for 24 h. After centrifugation for 20 min and washes with water, the NPs were dried under vacuum. The loading capacity of the HOSNPs with the RGD peptide was 28 wt% (Figure S6). The release of the RGD peptide was analyzed in water at pH 7 (Figure S7). No release was observed in these conditions. We observed 16 wt% peptide release after adjusting the pH to 5. This experiment shows the versatility of HOSNPs for the adsorption/release of different short peptides. The prepared LPMSNs and HOSNPs were then loaded with hydrophobic pepstatin A (Figure 3) in EtOH, under stirring for 48 h. After centrifugation, the NPs were washed with EtOH, dried under vacuum, and stored at 0 °C. The dosage of the supernatants with HPLC/MS allowed to determine the loading capacities of the NPs: 18 wt% for HOSNPs and 32 wt% for LPMSNs, respectively. After loading of pepstatin A, the zeta potential of LPMSNs decreased from −19.5 mV to −22.6 mV, whereas the zeta potential of HOSNPs decreased from +32 mV to −13.2 mV. This latest high variation of zeta potential suggests that pepstatin A was mainly adsorbed onto the

external surface of HOSNPs, whereas hydrophobic pepstatin A was mainly adsorbed into the pores of LPMSNs.

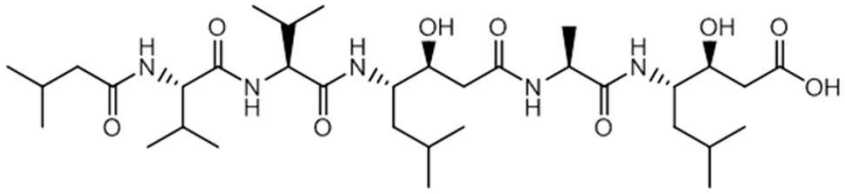

Figure 3. Chemical structure of the pepstatin A ($C_{34}H_{63}N_5O_9$, Mw = 686 g·mol^{-1}).

Pepstatin A release was then investigated. The loaded NPs were placed at the bottom of a cuvette that was carefully filled with water to avoid the nanoparticle swirling. Pepstatin A release from the NPs was monitored with the analysis of the solution by HPLC/MS. No significant release of pepstatin A from the HOSNPs was observed and a low release from LPMSNs was noticed over time (Figure S5A,B). The strong electrostatic interactions between negatively charged pepstatin A and the ammonium moieties of HOSNPs prevented the release of the peptide.

The endocytosis of the NPs was then investigated with MCF-7 breast cancer cells. HOSNPs were loaded with FITC in order to monitor the uptake of the NPs in the cells by confocal microscopy. LPMSNs (already functionalized with FITC) and loaded HOSNPs were incubated for 24 h with MCF-7 cells at a concentration of 50 µg·mL^{-1}. The membranes of the cells were stained with a cell mask 15 min before observation (Figure 4). After 24 h of incubation, the presence of the NPs in the cytoplasm of the cells was clearly observed, showing the endocytosis of LPMSNs and HOSNPs.

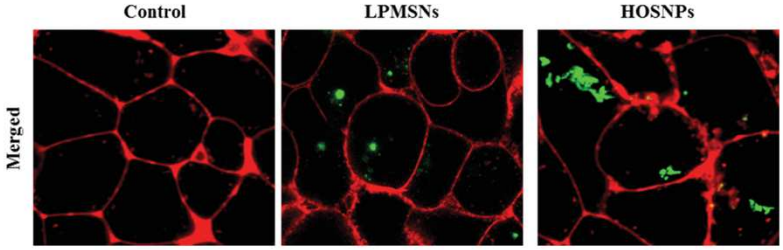

Figure 4. Fluorescence confocal imaging of live MCF-7 cells incubated for 24 h with LPMSNs or HOSNPs. The presence of the NPs is marked by green dots and membranes of cells appear in red.

The delivery of pepstatin A was investigated in MCF-7 cancer cells, as pepstatin A does not cross cell membranes and the peptide has to be encapsulated to be efficiently vectorized. The pepstatin A-loaded NPs or unloaded NPs were incubated with MCF-7 cancer cells for 72 h at several concentrations and MTT assay allowed to determine cancer cell death. The unloaded NPs were not toxic, even with HOSNPs, which have a positive zeta potential. These ammonium-based NPs were thus biocompatible. When loaded with pepstatin A, LPMSNs led to 20% of cancer cell death, whereas up to 60% cancer cell death was observed with HOSNPs (Figure 5). As shown by pepstatin A release monitoring, LPMSNs slightly released pepstatin A, whereas no release was noticed for HOSNPs. Although the loading capacity was higher with LPMSNs, we assume that premature release occurred with LPMSNs before endocytosis when incubated with cancer cells. More sustained delivery of pepstatin A in cells with HOSNPs could explain the results, due to stronger interactions between HOSNPs and pepstatin A than with LPMSNs.

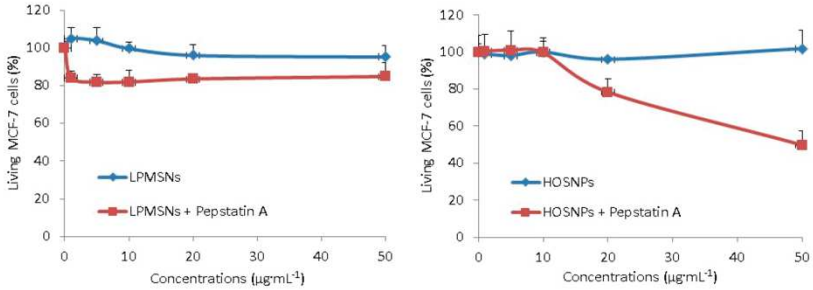

Figure 5. Cytotoxic study of LPMSNs and HOSNPs loaded or not with pepstatin A. Human breast cancer cells (MCF-7) were incubated during 72 h with increasing concentrations (from 1 to 50 $\mu g \cdot mL^{-1}$) of NPs loaded or not with pepstatin A. Values are means ± standard deviations of 3 experiments.

3. Materials and Methods

Cetyltrimethylammonium bromide (CTAB), ammonium hydroxide, ammonium nitrate (NH_4NO_3), potassium bromide, 1,3,5-triethylbenzene (TEB), and pepstatin A were purchased from Sigma-Aldrich (Saint-Quentin-Fallavier, France). Absolute ethanol was purchased from Fisher Chemicals. Bis (3-trimethoxysilyl propyl)-*N*-methylamine (BMSPMA) was purchased from Abcr GmbH&Co (Karlsruhe, Germany) and hydrochloric acid from VWR PROLABO. Triethanolamine (TEA) as a base catalyst, and acetic acid were purchased from Wako Pure Chem. Ind., Ltd (Osaka, Japan). Tetraethoxysilane (TEOS: $Si(OC_2H_5)_4$), tetrapropoxysilane (TPOS: $Si(OC_3H_7)_4$), 3-aminopropyltriethoxysilane (APTES), and fluorescein 5-isothiocyanate (FITC) were purchased from Tokyo Chemical Industry Co., Ltd (Osaka, Japan).

The complete characterization of the synthesized NPs requires a complementary panel of techniques. In this study, techniques focusing on the properties of NPs, such as transmission electron microscopy (TEM), dynamic light scattering (DLS), X-ray diffraction (XRD), and nitrogen adsorption–desorption were implemented. TEM images were recorded with a JEOL 1200 EXII microscope to visualize the shape and size of the NPs. For the purpose of TEM analysis, the sample particles were dispersed in ethanol and then dropped onto copper grids with porous carbon films. Dynamic light scattering analyses were performed using a Cordouan Technologies DL 135 particle size analyzer instrument. For zeta potential, the suspensions were prepared by dilution in NaCl (1 mM) in order to impose the ionic strength and analysis was performed using a Malvern Zetasizer nano ZS (ZEN 3600) instrument. The zeta potential was calculated from the measured electrophoretic mobility based on the theoretical analysis related to the Helmholtz–Smoluchowski equation. [34] For ^{13}C CP/MAS NMR spectra, solid-state NMR experiments were performed on a Varian VNMRS 600 MHz (14.1 T) NMR spectrometer. The specific area and pore structure parameters of the studied NPs were determined from the measurements of nitrogen adsorption–desorption at 77 K with a TRISTAR 3000 Micromeritics using the Brunauer–Emmet–Teller (BET) method. For the sorption experiments, the samples (about 70 mg) were evacuated under vacuum at 80 °C for 12 h. The organization of the porous framework was controlled by XRD and performed with a PANalytical X'Pert MPD (Philips 1710) diffractometer. The small angles measurements (2θ from 1.5 to 10) were recorded with an adapted slit of 1/16.

3.1. Synthesis of HOSNPs

A total of 20 mg of CTAB (5.5×10^{-5} mol) and 1.5 mL of TEB (8×10^{-3} mol) were mixed in 60 mL of water and 300 µL of ethanol and stirred for one night at 75 °C/1000 rpm. A total of 40 µL of NaOH solution at 1 M (4×10^{-5} mol) was then added and the mixture vigorously stirred for 50 min at 75 °C/1000 rpm. Then, 156 µL (0.44×10^{-3} mol) of BMSPMA was added. The reaction was stirred

for 2 h at 80 °C/1400 rpm. The reaction mixture was cooled to room temperature and centrifuged for 15 min, 20,000 rpm. Surfactants were removed by three extractions, with 30 mL of a solution of ammonium nitrate (NH_4NO_3) in ethanol (0.075 M), followed by three ethanol washes (20 mL each). NPs were dried under vacuum at room temperature.

3.2. Synthesis of LPMSNs

Triethanolamine (4.7×10^{-3} mol) and 3.33 g of CTAB (9.1×10^{-3} mol) were dissolved in 400 mL of deionized water in a round-bottomed flask (500 mL), and the mixture was stirred at 900 rpm for 1 h at 80 °C using a magnetic stirrer with a football-type stirring bar. Then, 0.8 mL of tetraethoxysilane (3.6×10^{-3} mol) was added to the solution with stirring at 900 rpm. After stirring the mixture at 80 °C for 1 h, the obtained colloidal solution was cooled to room temperature with stirring. Then, ethanol containing FITC-APTES and 1,3,5-triisopropylbenzene (1.8×10^{-3} mol) was added to the obtained colloidal solution (200 mL). FITC–APTES was synthesized by adding FITC (2.2×10^{-5} mol) and APTES (8×10^{-8} mol) into the ethanol (2.5 mL) and stirring the mixture in a dark and cool place overnight. Then, tetrapropoxysilane (TPOS) (4×10^{-3} mol) was added into the colloidal solution, and the colloidal solution was stirred for 2 days at room temperature. The process of the addition of TPOS was repeated up to four times. The prepared colloidal solution (50 mL) was transferred into a dialysis membrane tube composed of cellulose (molecular weight cutoff 12,000–14,000 Da) and was dialyzed for 24 h against a mixture (250 mL) of 2 M aqueous acetic acid and 2-propanol (1:1, v/v) to remove organic species. This process was repeated five times. After that, the colloidal solution was dialyzed for 24 h against water (250 mL), and this process was repeated four times.

3.3. Loading of Nanoparticles with Pepstatin A

A total of 10 mg of NPs and 5 mg of pepstatin A in 4 mL of ethanol were sonicated (45 kHz) for 5 min and stirred for 48 h at room temperature at 320 rpm. Then, the NPs were centrifuged at 12,000 rpm for 25 min, washed 2 times with ethanol (1 mL each), and dried for five hours under vacuum.

The loading capacity was calculated through the following formula: Loading Capacity (wt%) = [(initial mass of loaded pepstatin − mass of unloaded pepstatin A)/mass of NPs obtained + mass of loaded pepstatin A] × 100. The mass of unloaded pepstatin was calculated from the titration of the supernatant of pepstatin A in a solution with HPLC/MS. The loading capacity was 18 wt% for HOSNPs and 32 wt% for LPMSNs.

3.4. Loading of HOSNPs with Protected RGD Peptide

A total of 5 mg of HOSNPs was sonicated (45 kHz) for 10 min in 5 mL of deionized water. A total of 3.9 mg of peptide was then added to the mixture. The solution was stirred at 320 rpm at room temperature for 24 h. Finally, the NPs were collected by centrifugation for 12 min at 12,000 rpm, washed three times with water (2 mL each), and dried for five hours under vacuum. A total of 3.6 mg of loaded NPs was obtained. UV-visible allowed to determine the loading capacity of the HOSNPs: 28 wt%.

3.5. Loading of HOSNPs with Fluorescein Isothiocyanate (FITC)

First, 10 mg of NPs was added in an ethanol solution (4 mL) of fluorescein isothiocyanate (FITC, 7 μmol) and stirred for 48 h at room temperature. The NPs were collected by centrifugation for 12 min at 12,000 rpm, washed twice with ethanol (2 mL each), and dried overnight under air.

3.6. Cell Culture

Human breast cancer cells MCF-7 were purchased from ATCC (American Type Culture Collection, Manassas, VA, USA). Cells were cultured in Dulbecco's Modified Eagle's Medium (DMEM-F12)

supplemented with 10% fetal bovine serum and 50 $\mu g \cdot mL^{-1}$ gentamycin. These cells were allowed to grow in a humidified atmosphere at 37 °C under 5% CO_2.

3.7. Fluorescence Imaging of Cell Uptake of NPs

Human breast cancer cells MCF-7 were seeded into a tissue culture chamber with a cover glass bottom in 300 µL of culture medium. The culture medium is based on a Dulbecco's Modified Eagle Medium: Nutrient Mixture F-12 (DMEM/F12) that is a commercial medium intensively used for the culture of mammalian cells and available in all consumable providers for cell biology. Moreover, 10% fetal bovine serum was added for proteins, fatty acids, and growth factor addition. To finish, this medium was supplemented with antibiotics to assure cell safety. Then, the cells were incubated for 24 h with fluorescein functionalized NPs at a concentration of 50 $\mu g \cdot mL^{-1}$. After incubation, the cells were washed twice with 1 mL of culture medium. Fluorescence imaging (488 nm excitation wavelength) was performed on living cells with a Carl Zeiss confocal microscope.

3.8. Cytotoxic Study

MCF-7 cells were seeded into 96-well plates at 500 cells per well in 200 µL of the previously described culture medium and allowed to grow for 24 h. Increasing concentrations of NPs with or without pepstatin A were added in a culture medium of MCF-7 cells. Three days after treatment, an MTT assay was performed to determine the drug delivery potential of the NPs. Briefly, cells were incubated for 4 h with 0.5 $mg \cdot mL^{-1}$ of MTT (3-(4,5-dimethylthiazol-2-yl)-2,5-diphenyltetrazolium bromide; Promega) in media. The MTT/media solution was then removed, and the precipitated crystals were dissolved in 150 µL of EtOH/DMSO (v/v). The solution absorbance was read at 540 nm in a microplate reader.

4. Conclusions

The syntheses of LPMSNs or HOSNPs were successfully achieved through the sol–gel procedure in mild conditions, and the NPs were loaded with pepstatin A, a hydrophobic peptide inhibitor of cathepsin D. The loading capacities of the NPs were high with at 32 wt% and 18 wt%, respectively. After incubation with MCF-7 breast cancer cells, the NPs (50 $\mu g \cdot mL^{-1}$) were endocytosed as monitored by fluorescence confocal microscopy. LPMSNs and HOSNPs loaded with pepstatin A and incubated with cancer cells led to significant 20% and 60% cancer cell death, respectively. We assume that electrostatic interactions between pepstatin A and HOSNPs were stronger than the interactions between LPMSNs and pepstatin A, which could explain the better activity of HOSNPs through a more sustained delivery of pepstatin A in cells. Organosilica-based nanoparticles thus represent an interesting tool for the vectorization of peptides for nanomedicine applications.

Supplementary Materials: The following are available online at http://www.mdpi.com/1420-3049/24/2/332/s1, Figure S1: N_2 adsorption desorption isotherm, BET and BJH of LPMSN, Figure S2: ^{29}Si (A) and ^{13}C CP/MAS (B) Solid-state NMR of HOSNPs Figure S3: XRD patterns at small angles (A) and wide angles (B). Figure S4: N_2 adsorption desorption, BET and BJH of HOSNPs. Figure S5: Release of pepstatin A from HOSNPs and LPMSNs monitored with HPLC/MS, Figure S6: Structure of the RGD peptide and UV-Vis analysis in water, Figure S7: Release of the RGD peptide from HOSNPs at pH 7 and pH 5.

Author Contributions: J.-O.D., C.C., M.G., and M.G.-B. conceived and designed the experiments; S.R., J.B., M.S., M.D., E.V., L.L. and D.A., performed the experiments; L.R. analyzed the data; C.C., S.R. and J.-O.D. wrote the paper.

Funding: This research received no external funding.

Acknowledgments: The Erasmus Mundus grant for S.R. is gratefully acknowledged. G. Cazals is gratefully acknowledged for the technical assistance. We thank K. Kuroda and E. Yamamoto for proving LPMSNs.

Conflicts of Interest: The authors declare no conflict of interest.

References

1. Ruehle, B.; Saint-Cricq, P.; Zink, J.I. Externally controlled nanomachines on mesoporous silica nanoparticles for biomedical applications. *ChemPhysChem* **2016**, *17*, 1769–1779. [CrossRef] [PubMed]
2. Castillo, R.R.; Colilla, M.; Vallet-Regi, M. Advances in mesoporous silica-based nanocarriers for co-delivery and combination therapy against cancer. *Expert Opin. Drug Deliv.* **2017**, *14*, 229–243. [CrossRef] [PubMed]
3. Yang, Y.; Yu, C. Advances in silica based nanoparticles for targeted cancer therapy. *Nanomedicine* **2016**, *12*, 317–332. [CrossRef]
4. Pasqua, L.; Leggio, A.; Sisci, D.; Ando, S.; Morelli, C. Mesoporous silica nanoparticles in cancer therapy: Relevance of the targeting function. *Mini-Rev. Med. Chem.* **2016**, *16*, 743–753. [CrossRef] [PubMed]
5. Moreira, A.F.; Dias, D.R.; Correia, I.J. Stimuli-responsive mesoporous silica nanoparticles for cancer therapy: A review. *Microporous Mesoporous Mater.* **2016**, *236*, 141–157. [CrossRef]
6. Feng, Y.; Panwar, N.; Tng, D.J.H.; Tjin, S.C.; Wang, K.; Yong, K.-T. The application of mesoporous silica nanoparticle family in cancer theranostics. *Coord. Chem. Rev.* **2016**, *319*, 86–109. [CrossRef]
7. Wang, Y.; Zhao, Q.; Han, N.; Bai, L.; Li, J.; Liu, J.; Che, E.; Hu, L.; Zhang, Q.; Jiang, T.; et al. Mesoporous silica nanoparticles in drug delivery and biomedical applications. *Nanomedicine* **2015**, *11*, 313–327. [CrossRef]
8. Giret, S.; Man, M.W.C.; Carcel, C. Mesoporous-silica-functionalized nanoparticles for drug delivery. *Chem. Eur. J.* **2015**, *21*, 13850–13865. [CrossRef] [PubMed]
9. Bharti, C.; Nagaich, U.; Pal, A.K.; Gulati, N. Mesoporous silica nanoparticles in target drug delivery system: A review. *Int. J. Pharm. Investig.* **2015**, *5*, 124–133. [CrossRef]
10. Nadrah, P.; Planinsek, O.; Gaberscek, M. Stimulus-responsive mesoporous silica particles. *J. Mater. Sci.* **2014**, *49*, 481–495. [CrossRef]
11. Dave, P.N.; Chopda, L.V. A review on application of multifunctional mesoporous nanoparticles in controlled release of drug delivery. *Mater. Sci. Forum* **2014**, *781*, 17–24. [CrossRef]
12. Argyo, C.; Weiss, V.; Bräuchle, C.; Bein, T. Multifunctional mesoporous silica nanoparticles as a universal platform for drug delivery. *Chem. Mater.* **2014**, *26*, 435–451. [CrossRef]
13. Mamaeva, V.; Sahlgren, C.; Linden, M. Mesoporous silica nanoparticles in medicine-recent advances. *Adv. Drug. Deliv. Rev.* **2013**, *65*, 689–702. [CrossRef] [PubMed]
14. Chen, Y.; Chen, H.; Shi, J. In vivo bio-safety evaluations and diagnostic/therapeutic applications of chemically designed mesoporous silica nanoparticles. *Adv. Mater.* **2013**, *25*, 3144–3176. [CrossRef]
15. Chen, N.-T.; Cheng, S.-H.; Souris, J.S.; Chen, C.-T.; Mou, C.-Y.; Lo, L.-W. Theranostic applications of mesoporous silica nanoparticles and their organic/inorganic hybrids. *J. Mater. Chem. B* **2013**, *1*, 3128–3135. [CrossRef]
16. Yamamoto, E.; Mori, S.; Shimojima, A.; Wada, H.; Kuroda, K. Fabrication of colloidal crystals composed of pore-expanded mesoporous silica nanoparticles prepared by a controlled growth method. *Nanoscale* **2017**, *9*, 2464–2470. [CrossRef] [PubMed]
17. Yamamoto, E.; Kuroda, K. Colloidal mesoporous silica nanoparticles. *Bull. Chem. Soc. Jpn.* **2016**, *89*, 501–539. [CrossRef]
18. Knezevic, N.Z.; Durand, J.-O. Large pore mesoporous silica nanomaterials for application in delivery of biomolecules. *Nanoscale* **2015**, *7*, 2199–2209. [CrossRef]
19. Braun, K.; Pochert, A.; Gerber, M.; Raber, H.F.; Linden, M. Influence of mesopore size and peptide aggregation on the adsorption and release of a model antimicrobial peptide onto/from mesoporous silica nanoparticles in vitro. *Mol. Syst. Des. Eng.* **2017**, *2*, 393–400. [CrossRef]
20. Braun, K.; Pochert, A.; Lindén, M.; Davoudi, M.; Schmidtchen, A.; Nordström, R.; Malmsten, M. Membrane interactions of mesoporous silica nanoparticles as carriers of antimicrobial peptides. *J. Colloid Int. Sci.* **2016**, *475*, 161–170. [CrossRef]
21. Xie, J.; Yang, C.; Liu, Q.; Li, J.; Liang, R.; Shen, C.; Zhang, Y.; Wang, K.; Liu, L.; Shezad, K.; et al. Encapsulation of hydrophilic and hydrophobic peptides into hollow mesoporous silica nanoparticles for enhancement of antitumor immune response. *Small* **2017**, *13*, 1701741. [CrossRef] [PubMed]
22. Cao, J.; Zhang, Y.; Shan, Y.; Wang, J.; Liu, F.; Liu, H.; Xing, G.; Lei, J.; Zhou, J. A pH-dependent antibacterial peptide release nano-system blocks tumor growth in vivo without toxicity. *Sci. Rep.* **2017**, *7*, 11242. [CrossRef] [PubMed]

23. De la Torre, C.; Domínguez-Berrocal, L.; Murguía, J.R.; Marcos, M.D.; Martínez-Máñez, R.; Bravo, J.; Sancenón, F. ϵ-polylysine-capped mesoporous silica nanoparticles as carrier of the c9h peptide to induce apoptosis in cancer cells. *Chem. Eur. J.* **2018**, *24*, 1890–1897. [CrossRef] [PubMed]
24. Croissant, J.G.; Cattoen, X.; Durand, J.-O.; Wong Chi Man, M.; Khashab, N.M. Organosilica hybrid nanomaterials with a high organic content: Syntheses and applications of silsesquioxanes. *Nanoscale* **2016**, *8*, 19945–19972. [CrossRef] [PubMed]
25. Nakamura, M. Biomedical applications of organosilica nanoparticles toward theranostics. *Nanotechnol. Rev.* **2012**, *1*, 469–491. [CrossRef]
26. Du, X.; Li, X.; Xiong, L.; Zhang, X.; Kleitz, F.; Qiao, S.Z. Mesoporous silica nanoparticles with organo-bridged silsesquioxane framework as innovative platforms for bioimaging and therapeutic agent delivery. *Biomaterials* **2016**, *91*, 90–127. [CrossRef] [PubMed]
27. Chen, Y.; Shi, J. Chemistry of mesoporous organosilica in nanotechnology: Molecularly organic-inorganic hybridization into frameworks. *Adv. Mater.* **2016**, *28*, 3235–3272. [CrossRef]
28. Croissant, J.G.; Cattoen, X.; Man, M.W.C.; Durand, J.-O.; Khashab, N.M. Syntheses and applications of periodic mesoporous organosilica nanoparticles. *Nanoscale* **2015**, *7*, 20318–20334. [CrossRef]
29. Urata, C.; Yamada, H.; Wakabayashi, R.; Aoyama, Y.; Hirosawa, S.; Arai, S.; Takeoka, S.; Yamauchi, Y.; Kuroda, K. Aqueous colloidal mesoporous nanoparticles with ethenylene-bridged silsesquioxane frameworks. *J. Am. Chem. Soc.* **2011**, *133*, 8102–8105. [CrossRef]
30. Datz, S.; Engelke, H.; Schirnding, C.V.; Nguyen, L.; Bein, T. Lipid bilayer-coated curcumin-based mesoporous organosilica nanoparticles for cellular delivery. *Microporous Mesoporous Mater.* **2016**, *225*, 371–377. [CrossRef]
31. Yang, Y.; Niu, Y.; Zhang, J.; Meka, A.K.; Zhang, H.; Xu, C.; Lin, C.X.C.; Yu, M.; Yu, C. Biphasic synthesis of large-pore and well-dispersed benzene bridged mesoporous organosilica nanoparticles for intracellular protein delivery. *Small* **2015**, *11*, 2743–2749. [CrossRef] [PubMed]
32. Maynadier, M.; Vezenkov, L.L.; Amblard, M.; Martin, V.; Gandreuil, C.; Vaillant, O.; Gary-Bobo, M.; Basile, I.; Hernandez, J.-F.; Garcia, M.; et al. Dipeptide mimic oligomer transporter mediates intracellular delivery of cathepsin D inhibitors: A potential target for cancer therapy. *J. Control. Release* **2013**, *171*, 251–257. [CrossRef] [PubMed]
33. Yu, X.; Wang, J.; Liu, J.; Shen, S.; Cao, Z.; Pan, J.; Zhou, S.; Pang, Z.; Geng, D.; Zhang, J. A multimodal pepstatin A peptide-based nanoagent for the molecular imaging of p-glycoprotein in the brains of epilepsy rats. *Biomaterials* **2016**, *76*, 173–186. [CrossRef] [PubMed]
34. Hunter, R.J. *Zeta Potential in Colloid Science: Principles and Applications*; Academic Press: London, UK, 1981; pp. 59–124.

Sample Availability: Not available.